

THE CATHOLIC UNIVERSITY OF AMERICA

Oxygen-Enriched Fuel Reforming of Heavy Liquid Hydrocarbon Fuels for Fuel Cells

A DISSERTATION

Submitted to the Faculty of the
Department of Mechanical Engineering
School of Engineering
Of The Catholic University of America
In Partial Fulfillment of the Requirements

For the Degree
Doctor of Philosophy

©

Copyright
All Rights Reserved

by
Terry Grice DuBois

Washington, D.C.

2011

Oxygen-enriched Fuel Reforming of Heavy Liquid Hydrocarbon Fuels for Fuel Cells

Terry Grice DuBois, Ph.D.

Director: Sen Nieh, Ph.D.

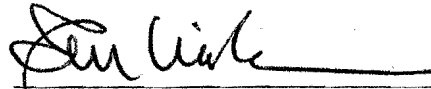
The effect of oxygen-enriched catalytic reforming of heavy liquid hydrocarbon fuels has been theoretically and experimentally investigated. The objective of this research is to analyze the reactions, reaction products, and reformer and system level effects from oxygen enriched reforming of heavy hydrocarbon fuels (JP-8). To achieve the objective of this dissertation analytical modeling was employed to develop a theoretical basis for experimental work; a research grade experimental apparatus was designed, constructed, and tested; via experimentation, a JP-8 surrogate fuel was developed; and autothermal reformer performance was characterized with air and enriched oxygen under various operating scenarios.

Notable contributions of this work were: good carbon conversion (~100%) and hydrogen yield can be achieved in autothermal reforming of heavy liquid hydrocarbon fuels; the development of a JP-8 surrogate fuel through experimental evaluation of the major hydrocarbon chemical classes present in JP-8: n-paraffin, cyclo-paraffin and mono-aromatics; a detailed study of the influence of each chemical class was evaluated under broad operating conditions and the contribution of each along with synergistic effects in mixtures was studied and contrasted with a target JP-8 fuel; oxygen enriched reforming of the surrogate fuel under varying oxygen concentration, fuel flows, and oxygen-to-

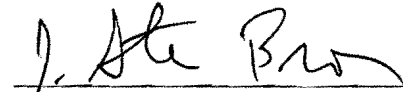
carbon ratios was experimentally evaluated; and the influence of oxygen enriched reforming on the fuel cell system was analyzed.

Oxygen enrichment is shown to allow for independent control of both reactor space time and the oxygen-to-carbon ratio during autothermal reforming. This allows for much better control over the reformer and allows for significant gains in reformer through-put without negative impacts to reformer performance. Additionally, the use of oxygen enriched reforming is shown to result in enhanced reformer performance and also enhanced fuel cell stack performance due to greatly increased hydrogen concentration in the reformat.

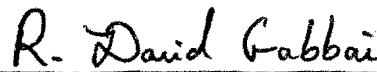
This dissertation by Terry Grice DuBois fulfills the dissertation requirement for the doctoral degree in mechanical engineering approved by Sen Nieh, Ph.D., as Director, and by Steven Brown, Ph.D., Rene Gabbai, Ph.D., and Neal E. Blackwell, Ph.D., as Readers.



Sen Nieh, Ph.D., Director



Steven Brown, Ph.D., Reader



Rene Gabbai, Ph.D., Reader



Neal E. Blackwell, Ph.D., Reader

To my wife Tracy for her love, patience and support.

CONTENTS

List of Illustrations	viii
List of Tables	xvi
Foreword	xvii
Preface	xix
Acknowledgements	xx
Chapter 1 – Introduction	1
1.0 Motivation	1
1.1 Background	2
1.1.1 Population growth	2
1.1.2 Natural resources	5
1.1.3 Global warming	7
1.1.3.1 Transportation fuels in the United States	10
1.2 History of fuel cell technology	13
1.2.1 Fuel cells	15
1.2.2 Fuel cell types for mobile applications	15
1.2.2.1 Proton exchange membrane fuel cell and solid oxide fuel cell	17
1.3 Reforming chemistries	21
1.4 Oxygen enrichment of air	28
1.5 Research objectives and approach	30
Chapter 2 – Scientific Background and Technical Discussion	32
2.0 Introduction	32
2.1 Overview of hydrogen production for fuel cells	32
2.2 Hydrogen storage for mobile applications	33
2.2.1 Gaseous hydrogen storage	36
2.2.2 Liquid hydrogen storage	38
2.2.3 Solid hydrogen storage	39
2.2.4 Metal hydrides	39
2.2.5 Chemical hydrides	42
2.2.5.1 Hydrolysis reactions	42
2.2.5.2 Thermolysis of ammonia borane (NH_3BH_3)	44
2.3 Catalytic fuel reforming	47
2.3.1 Early history of catalysts development	47

2.3.1.1	Ammonia synthesis	49
2.3.1.2	Liquid and gaseous hydrocarbon catalysts development	52
2.3.1.3	Vehicle emissions control	54
2.3.2	Liquid hydrocarbon fuel reforming	56
2.3.2.1	Basic overall reactions in liquid hydrocarbon fuel reforming	57
2.3.2.2	Reforming of heavy hydrocarbon fuels (diesel, kerosene, jet fuels)	62
2.3.2.3	ATR operating conditions	69
2.3.2.3.1	ATR operating temperature	69
2.3.2.3.1.1	Fuel atomization/vaporization	70
2.3.2.3.1.2	Steam-to-carbon (S/C) ratio and oxygen-to-carbon (O/C) ratio	75
2.3.2.4	Reforming catalysts and support materials	77
2.3.2.5	Carbon formation	82
2.4	Oxygen enrichment	84
2.4.1	Oxygen enriched air reforming	85
2.5	Chapter summary	86
Chapter 3 – Experimental Apparatus, Instrumentation and Operation		90
3.0	Introduction	90
3.1	Experimental apparatus	90
3.1.1	Air delivery subsystem	94
3.1.2	Nitrogen delivery/blanketing gas subsystem	95
3.1.3	Water/steam delivery subsystem	96
3.1.4	Diesel delivery subsystem	98
3.1.5	ATR reactor subsystem	98
3.1.5.1	ATR reactor build	100
3.1.6	Reformate cooler/condenser/liquid separation subsystem	106
3.1.7	Control and data acquisition	110
3.1.8	Insulation of tubing	111
3.2	Safety	113
3.2.1	Personnel safety	115
3.2.2	Equipment safety	119
3.3	Analysis of reaction products	121
3.3.1	Fuel analysis	123
3.4	ATR operational characteristics	125
3.4.1	ATR reactor design/thermal characteristics	125

3.4.2	Instabilities with vaporization of liquids	128
3.4.3	ATR reactor start-up and shutdown	131
3.4.4	Light-off temperature	134
3.5	Data analysis	135
3.5.1	Propagation of experimental errors	139
3.6	Chapter summary	144
	Chapter 4 – Analysis of Oxygen Enriched Liquid Heavy Hydrocarbon Fuel Reforming	148
4.0	Introduction	148
4.1	Operating regimes for catalytic processes	148
4.2	Principles of membrane oxygen enrichment	152
4.3	Equilibrium analysis of autothermal reforming with oxygen enrichment	154
4.3.1	Enrichment number and heat transfer	158
4.3.2	Enrichment number and reactor design	159
4.4	Enrichment number and space time	162
4.5	Elementary reaction rates	164
4.6	Fuel cell performance as a function of hydrogen concentration	169
4.6.1	Effect of hydrogen partial pressure on fuel cell performance	170
4.6.2	Effect of hydrogen partial pressure on fuel cell, fuel utilization	173
4.7	Chapter summary	176
	Chapter 5 – Surrogate Fuel Development	178
5.0	Introduction	178
5.1	Jet fuel hydrocarbon composition	181
5.1.1	Autothermal reforming (ATR)	181
5.2	Method	184
5.2.1	Experimental apparatus	184
5.2.2	Analysis	184
5.2.3	Reactor operation	187
5.3	Surrogate fuel results and discussion	187
5.3.1	Jet fuel (JP-8) and surrogate JP-8 fuel	188
5.3.2	Reforming of JP-8 surrogate fuels	195
5.4	Chapter summary	208
	Chapter 6 – Experimental Results and Discussion	211
6.0	Introduction	211
6.1	Operating procedures and notes	211
6.2	Low sulfur JP-8 reforming with air ($\Psi = 1$)	213

6.2.1 Reactor temperature profile and space velocity (space time)	213
6.2.2 JP-8 reformat composition	219
6.2.3 Nitrogen dilution in reformat product	220
6.2.4 Reformer efficiency and product yields for reformed JP-8	222
6.3 JP-8 fuel reforming with varying S/C ratios, $\Psi = 1$	224
6.3.1 Fuel conversion, operating temperatures, and GHSV under varying S/C ratios	225
6.3.2 Hydrogen and carbon monoxide yields under varying S/C ratios	229
6.3.3 Hydrocarbon and olefin conversion under varying S/C ratios	231
6.3.4 Reformer efficiency under varying S/C ratios	234
6.4 JP-8 surrogate reforming at varying fuel flows	236
6.5 JP-8 reforming with air ($\Psi = 1$) summary	253
6.6 JP-8 surrogate fuel reforming with enriched air	255
6.6.1 JP-8 surrogate fuel reforming with enriched oxygen at 5.0 kW _{th}	256
6.6.2 JP-8 surrogate fuel reforming with enriched oxygen and varying fuel flows	265
6.7 Fuel cell power system implications from oxygen enriched reforming	282
Chapter 7 – Conclusions and Recommendations	287
7.0 Introduction	287
7.1 Conclusions	287
7.2 Recommendations for further study	292
Appendix A - Propagation of Experimental Error Analysis	294
Appendix B - Determining Experimental Operating Conditions	311
Appendix C - Operational Calculations Based on Carbon and Hydrogen Content of Fuel	314
Appendix D - Gas Chromatograph Calibration Properties	317
Bibliography	324

LIST OF ILLUSTRATIONS

Figure 1.1. World population growth and demographics.	3
Figure 1.2. CO ₂ emissions Showing Developed and Developing Nations Trends.	4
Figure 1.3. Energy and Prosperity Trends.	4
Figure 1.4. Global energy demand Growth by sector (1971-2030)	6
Figure 1.5 Carbon dioxide (CO ₂) concentrations (parts per million) for the past 1100 years, measured from air trapped in ice (Vostok, Antarctica Ice-Core record) and as measured directly at Mauna Loa, Hawaii.	8
Figure 1.6 Greenhouse gas equivalent emissions on a per capita basis, also showing population.	9
Figure 1.7 Carbon emissions from fossil fuels and cement showing top five emitters.	9
Figure 1.8 Global fossil fuel emissions by fuel type.	10
Figure 1.9 Gravimetric energy density and volumetric energy density for a number of future postulated mobile energy sources. Based on 150 kW-hr net energy storage (equivalent to 16 gallons of JP-8 with a 26% efficient conversion).	12
Figure 1.10 Comparison of future fuels on net CO ₂ emissions.	13
Figure 1.11 Comparisons of Electric Power Technologies.	16
Figure 1.12 Simplified Schematic of Fuel Cell.	17
Figure 1.13 Ionic transport through the electrolyte of a PEMFC and SOFC.	20
Figure 1.14 Process schemes for SOFC and PEMFC system operating on heavy hydrocarbon liquid fuels.	21
Figure 1.15 Leading reforming techniques and their characteristics.	23
Figure 1.16 Ternary diagram showing carbon formation boundaries for selected temperatures.	26
Figure 2.1 Simplified process flow diagram for a typical refinery.	55
Figure 2.2 Ceramic monolith used in automotive catalytic converters.	57
Figure 2.3 Temperature profile within an ATR reactor.	65
Figure 2.4 The effect of oxygen-to-fuel molar ratio on the concentration of hydrogen in the reformat stream and the reactor adiabatic temperature using Eqn. 2.27.	67
Figure 2.5 Equilibrium product composition n-dodecane at a molar oxygen-to-carbon (O/C) ratio of 1.0 and a molar steam-to-carbon (S/C) ratio of 1.0.	68
Figure 2.6 Lattice structure of a single perovskite cell.	81
Figure 3.1 Photo of autothermal reformer test apparatus.	92
Figure 3.2 Experimental instrumentation and process flow schematic.	93
Figure 3.3 Subsystem function layout.	93
Figure 3.4 Design of ATR reactor assembly.	100
Figure 3.5 In-line static mixer.	101
Figure 3.6 Photographs of the ATR reactor installed in the Nicrofer cylinder. Panel (a) entrance of reactor showing metal foam insert, panel (b) show the reactor exit of the reactor, panel (c) shows exit with thermocouples installed.	101
Figure 3.7 BASF catalysts ATR-7B prior to coring. Washcoated cordierite dimensions of 127 mm diameter and 101.6 mm depth.	102
Figure 3.8 Corded Reactor Section with depth of 101.6 mm and diameter 19.05 mm.	103
Figure 3.9 Reactor construction, (a) three ceramic cordierite sections with alignment wire and metal foam being wrapped by 3M Interam mat, (b) Provoir metal foam.	104
Figure 3.10 Reactor assembly into Nicrofer metal shell and initial heating to fit the reactor in place.	105
Figure 3.11 Complete reactor vessel assembly: (a) design drawing showing ceramic reactor in red and Zircar ceramic insulation in black cross hatch, (b) end view of reactor showing Zircar ceramic insulation, (c) initial build of reactor full assembly with mating stainless steel reformat distribution manifold.	107

Figure 3.12 Installation of reactor thermocouples: (a) thermocouples (6) inserted into reactor channels and threaded through reformat distribution piping, (b) inserting thermocouples through Conex multi-element sealing gland, (c) applying sealer to Conex fitting and (d) Conex end-cap attached.	108
Figure 3.13 Reactor installation onto Reformer Test Bed experimental setup: (a) applying heat tape to reactor outer shell, (b) applying ½" of Fiberfrax Durablanket S insulation and (c) reactor installed in Reformer Test Bed.	109
Figure 3.14 iFIX Control and Monitoring screens (a) and heating element PID screen for the air heater (PD 1124), fuel vaporizer (PD 1321), water vaporizer/superheater (PD 1421), reactant tubing heat trace (PD 1515), and reactor outer shell heat trace (PD 1517).	111
Figure 3.15 Steps taken to minimize heat loss in lines upstream of the reactor: (a) heat trace, (b) high temperature woven tape is layered over the heat trace, (c) kaowool insulation and (d) fiberfrax insulating blanket is applied.	114
Figure 3.16 Effects of carbon monoxide exposure from (a) direct exposure to the reformat and (b) unventilated exposure assuming a well mixed environment.	116
Figure 3.17 Laboratory reformer test apparatus, control and work space. Desk with multiple computer LCD monitors is the operator control desk. Large gray panel on the left is the electrical power and signal distribution panel. Walk-in hood is shown in the background of the photo.	118
Figure 3.18 Reactor leak rate over time.	121
Figure 3.19 System integrity test consisting of operating the reactor test apparatus at indicated flowrates and noting the pressure drop through the system.	122
Figure 3.20 Chromatograms from on-line Agilent 5000A micro Gas Chromatograph identifying selected column for each channel and carrier gas.	124
Figure 3.21 Infrared based Jet fuel analyzer, PetroSpec Turbine Fuel Analyzer (TD-PPA).	126
Figure 3.22 Elemental Analyzer for total carbon, nitrogen and sulfur content; Analytik-Jena, ea3100.	126
Figure 3.23 Cross Section View of Reactor and Insulating Housing.	128
Figure 3.24 Reactor skin temperatures compared to modeled results under two scenarios: 1) reactor heat tape off, and 2) reactor heat tape set at 325 °C.	129
Figure 3.25 Calculated reactor thermal losses (solid line) against measured under four different operating conditions.	130
Figure 3.26 n-Dodecane at 6 ml/min. fuel flow with S/C = 2.0 and O/C = 0.8. The reformer test apparatus water vaporization system consists of a single stage vaporizer/superheater and this design resulted in high temperature and pressure fluctuations.	132
Figure 3.27 Comparison of water vaporizer/superheater with design improvements to minimize flow instabilities.	132
Figure 3.28 Start-up and light-off of an ATR reactor on low-sulfur JP-8 at 6 ml/min., S/C = 2.0 and O/C = 1.0.	134
Figure 3.29 Light-off of JP-8 in dry partial oxidation mode with reactor pre-heated to 324 °C.	136
Figure 4.1 Equilibrium calculations with n-dodecane at 6.0 ml/min. (3.33 kW _{th}), S/C ratio of 1.0, adiabatic reactor and reactor inlet temperature of 25 °C. For H ₂ , CO, CO ₂ , and N ₂ the composition is on a dry basis.	150
Figure 4.2 Oxygen enrichment membrane depiction.	153
Figure 4.3 Performance of a polymer membrane air separation module with membrane selectivity of 3.0, membrane thickness of 0.035 µm, membrane permeability of 3.0 Barrier and area of 6 m ² .	155
Figure 4.4 Total power required to produce required enriched air flow for a 5.9 ml/min. (3.33 kW _{th}) ATR at an O/C ratio of 1.0 and S/C ratio of 2.0. Based on the membrane of Fig. 4.3 with membrane selectivity of 3.0, membrane thickness of 0.035 µm, membrane permeability of 3.0 Barrier, and area of 6 m ² .	156
Figure 4.5 ATR composition, temperature, and efficiency (a); and molar flow rates of hydrogen and carbon monoxide (b) for a fuel flow of 5.9 ml/min. (3.33 kW _{th}), S/C of 2.0, O/C of 1.0, reactor thermal losses of 5%, and reactant initial temperatures of 25 °C.	157

- Figure 4.6 Specific heat of reactants and reformat products as a function of enrichment number (Ψ). For an ATR with operating conditions of fuel flow equal to 5.9 ml/min. (3.33 kW_{th}), S/C of 2.0, O/C of 1.0, reactor thermal losses of 5%, and reactant initial temperatures of 25 °C. 159
- Figure 4.7 Reactor space time and pressure drop as a function of enrichment number. For an ATR with operating conditions of fuel flow equal to 5.9 ml/min. (3.33 kW_{th}), S/C of 2.0, O/C of 1.0, reactor thermal losses of 5%, and reactant initial temperatures of 25 °C. 160
- Figure 4.8 Reynolds number as a function of enrichment number. For an ATR with operating conditions of fuel flow equal to 5.9 ml/min. (3.33 kW_{th}), S/C of 2.0, O/C of 1.0, reactor thermal losses of 5%, and reactant initial temperatures of 25 °C. 162
- Figure 4.9 Potential for reactor volume reduction maintaining constant reactor space time and pressure drop. Reactor volume change is relative to reactor size for an enrichment number of 1.0. With ATR operating conditions of fuel flow of 5.9 ml/min. (3.33 kW_{th}), S/C of 2.0, O/C of 1.0, reactor thermal losses of 5%, and reactant initial temperatures of 25 °C. 163
- Figure 4.10 Relationship between the O/C ratio for reforming with air (a) and with enriched oxygen reforming with enrichment number (Ψ) between 0.477 (10% O₂/N₂) and 4.77 (100% O₂/N₂). Fuel flow of 6.94 g/min. (5.0 kW_{th}, LHV_{fuel} = 43.2 MJ/kg), S/C of 2.0 and for a reactor volume of 86.9 cm³. 165
- Figure 4.11 Fuel reaction time (τ_{fuel}) as a function of molar oxygen-to-carbon (O/C) ratio for three JP-8 fuel flow rates: 5.9 ml/min. (3.33 kW_{th}), 8.9 ml/min. (5.0 kW_{th}) and 11.8 ml/min. (6.67 kW_{th}), S/C at 2.0, and enrichment number of 1. Opened symbols (\diamond , \circ , \square) represent space time and closed symbols (\blacklozenge , \bullet , \blacksquare) represent time needed to achieve full fuel conversion (τ). 169
- Figure 4.12 Fuel reaction time (τ_{fuel}) as a function of enrichment number (Ψ) for t JP-8 fuel flow rate of 5.9 ml/min. (3.33 kW_{th}), S/C at 2.0, and O/C of 1.06. 170
- Figure 4.13 Effect of hydrogen concentration entering the fuel cell stack on the overall stack efficiency based on the lower heating value of hydrogen. Initial stack voltage assumed at 0.7 volts/cell, with an anode hydrogen entrance concentration of 33.9 % (dry basis), cell temperature of 800 °C, pressure of 1 atm, and steam and oxygen concentrations are assumed constant. 173
- Figure 4.14 Effect of hydrogen concentration entering the fuel cell stack on the overall stack efficiency based on the lower heating value of hydrogen. Initial stack voltage assumed at 0.7 volts/cell, with an anode hydrogen entrance concentration of 33.9% (dry basis), cell temperature of 800 °C, pressure of 1 atm, and steam and oxygen concentrations are assumed constant. Fuel utilization is based on maintaining 15% hydrogen in the exit of the fuel cell anode. 176
- Figure 5.1 Major hydrocarbon classes represented in JP-8 and a chromatogram showing hydrocarbon distribution within JP-8 with normal-paraffins identified against boiling point temperatures. 182
- Figure 5.2 Typical hydrocarbon class composition for JP-8. 182
- Figure 5.3 Hydrocarbon Class approximate composition as a function of boiling range. 183
- Figure 5.4. U.S. Department of Defense JP-8 fuel composition data: (a) mean values of naphthalene, density, hydrogen content and heating values for 2001-2007; (b) aromatic content distribution for 2007; (c) hydrogen content distribution for 2007. 189
- Figure 5.5. Results comparison of gas hourly space velocity with H₂O/C = 2.0, fuel feed at 3.33 kW thermal and entrance temperature 425 °C. 196
- Figure 5.6. Results of fuel conversion for surrogate fuels and target JP-8 (a) and fuel conversion for surrogate fuel components (b) with H₂O/C = 2.0, fuel feed at 3.33 kW thermal, entrance temperature 425 °C and the GHSV between 21,000 hr⁻¹ and 28,000 hr⁻¹. 197
- Figure 5.7. Results of reactor peak measured temperature (a) and exit temperature for surrogate fuels, surrogate fuel components and JP-8 with H₂O/C = 2.0, fuel feed at 3.33 kW thermal, entrance temperature 425 °C and the GHSV between 21,000 hr⁻¹ and 28,000 hr⁻¹. 199
- Figure 5.8. Hydrogen yield for surrogate fuels (a) and surrogate fuel components (b) with H₂O/C = 2.0, fuel feed at 3.33 kW thermal, entrance temperature of 425 °C and the GHSV between 21,000 hr⁻¹ and 28,000 hr⁻¹. 201

- Figure 5.9. Carbon monoxide yield for surrogate fuels (a) and surrogate fuel components (b) with $H_2O/C = 2.0$, fuel feed at 3.33 kW thermal, entrance temperature of 425 °C and the GHSV between 21,000 hr^{-1} and 28,000 hr^{-1} . 203
- Figure 5.10. Hydrogen produced in the reformat for surrogate fuels, surrogate fuel components and the target JP-8 fuel, under conditions of $H_2O/C = 2.0$, fuel feed at 3.33 kW thermal, entrance temperature of 425 °C and the GHSV between 21,000 hr^{-1} and 28,000 hr^{-1} . 204
- Figure 5.11. Molar concentrations of methane for surrogate fuels (a) and surrogate fuel components (b) and on a dry basis with $H_2O/C = 2.0$, fuel feed at 3.33 kW thermal, entrance temperature of 425 °C and the GHSV between 21,000 hr^{-1} and 28,000 hr^{-1} . 205
- Figure 5.12. Molar concentrations of olefins for surrogate fuels (a) and surrogate fuel components (b) on a dry basis with $H_2O/C = 2.0$, fuel feed at 3.33 kW thermal, entrance temperature of 425 °C and the GHSV between 21,000 hr^{-1} and 28,000 hr^{-1} . 206
- Figure 5.13. Results comparison of reforming efficiency for JP-8 surrogate fuels and low-sulfur JP-8 with $H_2O/C = 2.0$, fuel feed at 3.33 kW thermal, entrance temperature of 425 °C and the GHSV between 21,000 hr^{-1} and 28,000 hr^{-1} . 207
- Figure 5.14. Results comparison of reforming efficiency for JP-8 surrogate fuels and low-sulfur JP-8 with $H_2O/C = 2.0$, fuel feed at 3.33 kW thermal, entrance temperature of 425 °C and the GHSV between 21,000 hr^{-1} and 28,000 hr^{-1} . 208
- Figure 6.1. Reactor temperature profile at selected thermocouple locations under conditions of JP-8 fuel at fuel flow = 5.9 ml/min. (3.33 kW_{th}), S/C = 2.0, enrichment number (Ψ) of 1.0 (air), and O/C ratio's as shown. 214
- Figure 6.2. Gas Hourly Space Velocity (GHSV) (a) and Space Time (b) for JP-8 at fuel feeds of 5.9 ml/min (3.33 kW_{th}), 8.85 ml/min. (5.0 kW_{th}), and 11.8 ml/min. (6.67 kW_{th}) at S/C = 2.0, variable O/C ratios, GHSV between 20,500 hr^{-1} and 26,000 hr^{-1} , and enrichment number (Ψ) of 1.0 (air). 215
- Figure 6.3. Reactor temperature profiles at JP-8 fuel feeds of 5.9 ml/min (3.33 kW_{th}), 8.85 ml/min. (5.0 kW_{th}), and 11.8 ml/min. (6.67 kW_{th}) at S/C = 2.0, O/C = 1.05, GHSV between 20,500 hr^{-1} and 26,000 hr^{-1} , and enrichment number (Ψ) of 1.0 (air). 216
- Figure 6.4. Molar concentrations of reformat products N_2 , H_2 , CO_2 , CO and CH_4 with JP-8 fuel feed of 5.9 ml/min. (3.33 kW_{th}), S/C = 2.0, reactor entrance temperature 425 °C \pm 25 °C, GHSV between 20,500 hr^{-1} and 26,000 hr^{-1} , and enrichment number (Ψ) of 1.0 (air). 220
- Figure 6.5. Molar concentrations of reformat products of CH_4 and Olefins, and reactor pressures with JP-8 fuel feed of 5.9 ml/min. (3.33 kW_{th}), S/C = 2.0, reactor entrance temperature 425 °C \pm 25 °C, GHSV between 20,500 hr^{-1} and 26,000 hr^{-1} , and enrichment number (Ψ) of 1.0 (air). 221
- Figure 6.6. Maximum and minimum reactor temperatures, and gas hourly space velocity with JP-8 fuel feed of 5.9 ml/min. (3.33 kW_{th}), S/C = 2.0, reactor entrance temperature 425 °C \pm 25 °C and enrichment number (Ψ) of 1.0 (air). 222
- Figure 6.7. Relationship between reformer efficiency, fuel conversion, hydrogen yield and carbon monoxide yield with JP-8 fuel feed of 5.9 ml/min. (3.33 kW_{th}), S/C = 2.0, reactor entrance temperature 425 °C \pm 25 °C, GHSV between 20,500 hr^{-1} and 26,000 hr^{-1} and enrichment number (Ψ) of 1.0 (air). 223
- Figure 6.8. Normalized fuel conversion for JP-8 fuel flows of 5.9 ml/min. and S/C ratios of 1.5, 2.0, 2.5, and 3.0; reactor entrance temperature 425 °C \pm 25 °C, and enrichment number (Ψ) of 1.0 (air). The GHSV for S/C = 1.5 was from 19,200 hr^{-1} to 23,200 hr^{-1} , for S/C = 2.0 was from 21,900 hr^{-1} to 27,300 hr^{-1} , for S/C = 2.5 was from 24,000 hr^{-1} to 30,000 hr^{-1} , and for S/C = 3.0 was from 26,700 hr^{-1} to 32,000 hr^{-1} . 225
- Figure 6.9. Reactor maximum and exit temperatures (a) and reactor temperature profiles at O/C = 1.05 (b) with JP-8 fuel flows of 5.9 ml/min. and S/C ratios of 1.5, 2.0, 2.5, and 3.0; reactor entrance temperature 425 °C \pm 25 °C, and enrichment number (Ψ) of 1.0 (air). The GHSV for S/C = 1.5 was from 19,200 hr^{-1} to 23,200 hr^{-1} , for S/C = 2.0 was from 21,900 hr^{-1} to 27,300 hr^{-1} , for S/C = 2.5 was from 24,000 hr^{-1} to 30,000 hr^{-1} , and for S/C = 3.0 was from 26,700 hr^{-1} to 32,000 hr^{-1} . Temperature profiles measurements are with the reactor entrance being 0.0 mm. 227

- Figure 6.10 Input water consumed in the reactor with JP-8 fuel flows of 5.9 ml/min. and S/C ratios of 1.5, 2.0, 2.5, and 3.0; reactor entrance temperature $425\text{ }^{\circ}\text{C} \pm 25\text{ }^{\circ}\text{C}$, and enrichment number (Ψ) of 1.0 (air). The GHSV for S/C = 1.5 was from $19,200\text{ hr}^{-1}$ to $23,200\text{ hr}^{-1}$, for S/C = 2.0 was from $21,900\text{ hr}^{-1}$ to $27,300\text{ hr}^{-1}$, for S/C = 2.5 was from $24,000\text{ hr}^{-1}$ to $30,000\text{ hr}^{-1}$, and for S/C = 3.0 was from $26,700\text{ hr}^{-1}$ to $32,000\text{ hr}^{-1}$. 228
- Figure 6.11 Gas hourly space velocity (GHSV) for JP-8 with flows of 5.9 ml/min. and S/C ratios of 1.5, 2.0, 2.5, and 3.0; reactor entrance temperature $425\text{ }^{\circ}\text{C} \pm 25\text{ }^{\circ}\text{C}$, and enrichment number (Ψ) of 1.0 (air). 229
- Figure 6.12 Hydrogen yield (a) and carbon monoxide yield (b) with JP-8 fuel flows of 5.9 ml/min. and S/C ratios of 1.5, 2.0, 2.5, and 3.0; reactor entrance temperature $425\text{ }^{\circ}\text{C} \pm 25\text{ }^{\circ}\text{C}$, and enrichment number (Ψ) of 1.0 (air). The GHSV for S/C = 1.5 was from $19,200\text{ hr}^{-1}$ to $23,200\text{ hr}^{-1}$, for S/C = 2.0 was from $21,900\text{ hr}^{-1}$ to $27,300\text{ hr}^{-1}$, for S/C = 2.5 was from $24,000\text{ hr}^{-1}$ to $30,000\text{ hr}^{-1}$, and for S/C = 3.0 was from $26,700\text{ hr}^{-1}$ to $32,000\text{ hr}^{-1}$. 230
- Figure 6.13 Hydrocarbon concentration as a function of S/C ratio with JP-8 fuel flows of 5.9 ml/min. and S/C ratios of 1.5, 2.0, 2.5, and 3.0; reactor entrance temperature $425\text{ }^{\circ}\text{C} \pm 25\text{ }^{\circ}\text{C}$, and enrichment number (Ψ) of 1.0 (air). The GHSV for S/C = 1.5 was from $19,200\text{ hr}^{-1}$ to $23,200\text{ hr}^{-1}$, for S/C = 2.0 was from $21,900\text{ hr}^{-1}$ to $27,300\text{ hr}^{-1}$, for S/C = 2.5 was from $24,000\text{ hr}^{-1}$ to $30,000\text{ hr}^{-1}$, and for S/C = 3.0 was from $26,700\text{ hr}^{-1}$ to $32,000\text{ hr}^{-1}$. 232
- Figure 6.14 Olefin concentration as a function of S/C ratio with JP-8 fuel flows of 5.9 ml/min. and S/C ratios of 1.5, 2.0, 2.5, and 3.0; reactor entrance temperature $425\text{ }^{\circ}\text{C} \pm 25\text{ }^{\circ}\text{C}$, and enrichment number (Ψ) of 1.0 (air). The GHSV for S/C = 1.5 was from $19,200\text{ hr}^{-1}$ to $23,200\text{ hr}^{-1}$, for S/C = 2.0 was from $21,900\text{ hr}^{-1}$ to $27,300\text{ hr}^{-1}$, for S/C = 2.5 was from $24,000\text{ hr}^{-1}$ to $30,000\text{ hr}^{-1}$, and for S/C = 3.0 was from $26,700\text{ hr}^{-1}$ to $32,000\text{ hr}^{-1}$. 233
- Figure 6.15 Reformer efficiency and combined hydrogen and carbon monoxide flow rates (a), and reformer efficiency when energy for water vaporization is considered (b) with JP-8 fuel flows of 5.9 ml/min. and S/C ratios of 1.5, 2.0, 2.5, and 3.0; reactor entrance temperature $425\text{ }^{\circ}\text{C} \pm 25\text{ }^{\circ}\text{C}$, and enrichment number (Ψ) of 1.0 (air). The GHSV for S/C = 1.5 was from $19,200\text{ hr}^{-1}$ to $23,200\text{ hr}^{-1}$, for S/C = 2.0 was from $21,900\text{ hr}^{-1}$ to $27,300\text{ hr}^{-1}$, for S/C = 2.5 was from $24,000\text{ hr}^{-1}$ to $30,000\text{ hr}^{-1}$, and for S/C = 3.0 was from $26,700\text{ hr}^{-1}$ to $32,000\text{ hr}^{-1}$. 235
- Figure 6.16 Normalized fuel conversion for JP-8 fuel flows of 4.42 ml/min. (2.5 kWth), 5.9 ml/min. (3.33 kWth), 8.84 ml/min. (5.0 kWth) and 11.8 ml/min. (6.67 kWth) with S/C = 2.0, reactor entrance temperature $425\text{ }^{\circ}\text{C} \pm 25\text{ }^{\circ}\text{C}$, and enrichment number (Ψ) of 1.0 (air). The GHSV for 2.50 ml/min. was from $16,000\text{ hr}^{-1}$ to $20,000\text{ hr}^{-1}$, for 3.33 kWth was from $20,500\text{ hr}^{-1}$ to $26,000\text{ hr}^{-1}$, for 5.0 kWth was from $32,500\text{ hr}^{-1}$ to $40,000\text{ hr}^{-1}$, and for 6.67 kWth was from $42,500\text{ hr}^{-1}$ to $53,500\text{ hr}^{-1}$. 237
- Figure 6.17 Reactor differential pressure as a function of fuel flow with JP-8 fuel flows of 4.42 ml/min. (2.5 kWth), 5.9 ml/min. (3.33 kWth), 8.84 ml/min. (5.0 kWth), and 11.8 ml/min. (6.67 kWth) with S/C = 2.0, reactor entrance temperature $425\text{ }^{\circ}\text{C} \pm 25\text{ }^{\circ}\text{C}$, and enrichment number (Ψ) of 1.0 (air). The GHSV for 2.50 ml/min. was from $16,000\text{ hr}^{-1}$ to $20,000\text{ hr}^{-1}$, for 3.33 kWth was from $20,500\text{ hr}^{-1}$ to $26,000\text{ hr}^{-1}$, for 5.0 kWth was from $32,500\text{ hr}^{-1}$ to $40,000\text{ hr}^{-1}$, and for 6.67 kWth was from $42,500\text{ hr}^{-1}$ to $53,500\text{ hr}^{-1}$. 238
- Figure 6.18 Reactor maximum and exit temperatures with JP-8 fuel flows of 4.42 ml/min. (2.5 kWth), 5.9 ml/min. (3.33 kWth), 8.84 ml/min. (5.0 kWth) and 11.8 ml/min. (6.67 kWth) with S/C = 2.0, reactor entrance temperature $425\text{ }^{\circ}\text{C} \pm 25\text{ }^{\circ}\text{C}$, and enrichment number (Ψ) of 1.0 (air). The GHSV for 2.50 ml/min. was from $16,000\text{ hr}^{-1}$ to $20,000\text{ hr}^{-1}$, for 3.33 kWth was from $20,500\text{ hr}^{-1}$ to $26,000\text{ hr}^{-1}$, for 5.0 kWth was from $32,500\text{ hr}^{-1}$ to $40,000\text{ hr}^{-1}$, and for 6.67 kWth was from $42,500\text{ hr}^{-1}$ to $53,500\text{ hr}^{-1}$. 239
- Figure 6.19 Space time for JP-8 fuel flows of 4.42 ml/min. (2.5 kWth), 5.9 ml/min. (3.33 kWth), 8.84 ml/min. (5.0 kWth) and 11.8 ml/min. (6.67 kWth) with S/C = 2.0, reactor entrance temperature $425\text{ }^{\circ}\text{C} \pm 25\text{ }^{\circ}\text{C}$, and enrichment number (Ψ) of 1.0 (air). Ideal gas behavior is assumed under standard conditions. 240

- Figure 6.20 Graphical determination of optimum reactor thermal rating to achieve minimum O/C ratio for full fuel conversion with JP-8 fuel flows of 4.42 ml/min.(2.5 kW_{th}), 5.9 ml/min. (3.33 kW_{th}), 8.84 ml/min. (5.0 kW_{th}) and 11.8 ml/min. (6.67 kW_{th}) with S/C = 2.0, reactor entrance temperature 425 °C ± 25 °C, and enrichment number (Ψ) of 1.0 (air). The GHSV for 2.50 ml/min. was from 16,000 hr⁻¹ to 20,000 hr⁻¹, for 3.33 kW_{th} was from 20,500 hr⁻¹ to 26,000 hr⁻¹, for 5.0 kW_{th} was from 32,500 hr⁻¹ to 40,000 hr⁻¹, and for 6.67 kW_{th} was from 42,500 hr⁻¹ to 53,500 hr⁻¹. 242
- Figure 6.21 Hydrogen yield (a) and carbon monoxide yield (b) with JP-8 fuel flows of 4.42 ml/min.(2.5 kW_{th}), 5.9 ml/min. (3.33 kW_{th}), 8.84 ml/min. (5.0 kW_{th}) and 11.8 ml/min. (6.67 kW_{th}) with S/C = 2.0, reactor entrance temperature 425 °C ± 25 °C, and enrichment number (Ψ) of 1.0 (air). The GHSV for 2.50 ml/min. was from 16,000 hr⁻¹ to 20,000 hr⁻¹, for 3.33 kW_{th} was from 20,500 hr⁻¹ to 26,000 hr⁻¹, for 5.0 kW_{th} was from 32,500 hr⁻¹ to 40,000 hr⁻¹, and for 6.67 kW_{th} was from 42,500 hr⁻¹ to 53,500 hr⁻¹. 243
- Figure 6.22 Reformers efficiency with JP-8 fuel flows of 4.42 ml/min.(2.5 kW_{th}), 5.9 ml/min. (3.33 kW_{th}), 8.84 ml/min. (5.0 kW_{th}) and 11.8 ml/min. (6.67 kW_{th}) with S/C = 2.0, reactor entrance temperature 425 °C ± 25 °C, and enrichment number (Ψ) of 1.0 (air). The GHSV for 2.50 ml/min. was from 16,000 hr⁻¹ to 20,000 hr⁻¹, for 3.33 kW_{th} was from 20,500 hr⁻¹ to 26,000 hr⁻¹, for 5.0 kW_{th} was from 32,500 hr⁻¹ to 40,000 hr⁻¹, and for 6.67 kW_{th} was from 42,500 hr⁻¹ to 53,500 hr⁻¹. 244
- Figure 6.23 Molar concentration of hydrocarbons with JP-8 fuel flows of 4.42 ml/min.(2.5 kW_{th}), 5.9 ml/min. (3.33 kW_{th}), 8.84 ml/min. (5.0 kW_{th}), and 11.8 ml/min. (6.67 kW_{th}) with S/C = 2.0, reactor entrance temperature 425 °C ± 25 °C, and enrichment number (Ψ) of 1.0 (air). The GHSV for 2.50 ml/min. was from 16,000 hr⁻¹ to 20,000 hr⁻¹, for 3.33 kW_{th} was from 20,500 hr⁻¹ to 26,000 hr⁻¹, for 5.0 kW_{th} was from 32,500 hr⁻¹ to 40,000 hr⁻¹, and for 6.67 kW_{th} was from 42,500 hr⁻¹ to 53,500 hr⁻¹. 246
- Figure 6.24 Molar concentration of olefins with JP-8 fuel flows of 4.42 ml/min.(2.5 kW_{th}), 5.9 ml/min. (3.33 kW_{th}), 8.84 ml/min. (5.0 kW_{th}), and 11.8 ml/min. (6.67 kW_{th}) with S/C = 2.0, reactor entrance temperature 425 °C ± 25 °C, and enrichment number (Ψ) of 1.0 (air). The GHSV for 2.50 ml/min. was from 16,000 hr⁻¹ to 20,000 hr⁻¹, for 3.33 kW_{th} was from 20,500 hr⁻¹ to 26,000 hr⁻¹, for 5.0 kW_{th} was from 32,500 hr⁻¹ to 40,000 hr⁻¹, and for 6.67 kW_{th} was from 42,500 hr⁻¹ to 53,500 hr⁻¹. 247
- Figure 6.25 Hydrogen concentration (a) and maximum allowable hydrogen concentration points identified (b) with JP-8 fuel flows of 4.42 ml/min.(2.5 kW_{th}), 5.9 ml/min. (3.33 kW_{th}), 8.84 ml/min. (5.0 kW_{th}), and 11.8 ml/min. (6.67 kW_{th}) with S/C = 2.0, reactor entrance temperature 425 °C ± 25 °C, and enrichment number (Ψ) of 1.0 (air). The GHSV for 2.50 ml/min. was from 16,000 hr⁻¹ to 20,000 hr⁻¹, for 3.33 kW_{th} was from 20,500 hr⁻¹ to 26,000 hr⁻¹, for 5.0 kW_{th} was from 32,500 hr⁻¹ to 40,000 hr⁻¹, and for 6.67 kW_{th} was from 42,500 hr⁻¹ to 53,500 hr⁻¹. 249
- Figure 6.26 Reactor performance degradation as a result of exposure to periodic high levels (≥ 1 mole%) of olefins. All at fuel flows 5.9 ml/min. (3.33 kW_{th}) JP-8 with S/C = 2.0, O/C of 1.0 (for Fig. 6.18a and as shown for Fig. 6.18b), reactor entrance temperature 425 °C ± 25 °C, and enrichment number (Ψ) of 1.0 (air). The GHSV was from 20,500 hr⁻¹ to 26,000 hr⁻¹. [* all percentages are liquid volume percent]. 252
- Figure 6.27 Normalized fuel conversion (a) and reactor maximum and exit temperatures (b) with JP-8 fuel flows of 8.84 ml/min.(5.0 kW_{th}) with oxygen enrichment (Ψ) of 0.477, 1.0, 1.432 and 1.91. The GHSV for Ψ = 0.477 was from 48,600 hr⁻¹ to 69,500 hr⁻¹, for Ψ = 1.0 was from 32,400 hr⁻¹ to 40,400 hr⁻¹, for Ψ = 1.432 was from 26,600 hr⁻¹ to 31,400 hr⁻¹, and for Ψ = 1.91 was from 23,600 hr⁻¹ to 27,800 hr⁻¹. 257
- Figure 6.28 Space time for JP-8 fuel flows of 8.84 ml/min.(5.0 kW_{th}) with oxygen enrichment (Ψ) of 0.477, 1.0, 1.432 and 1.91 and reactor entrance temperature 425 °C ± 25 °C. Ideal gas behavior is assumed under standard conditions. 258
- Figure 6.29 Hydrogen yield with surrogate JP-8 fuel flows of 8.84 ml/min.(5.0 kW_{th}) with oxygen enrichment (Ψ) of 0.477, 1.0, 1.432 and 1.91. The GHSV for Ψ = 0.477 was from 48,600 hr⁻¹ to 69,500 hr⁻¹, for Ψ = 1.0 was from 32,400 hr⁻¹ to 40,400 hr⁻¹, for Ψ = 1.432 was from 26,600 hr⁻¹ to 31,400 hr⁻¹, and for Ψ = 1.91 was from 23,600 hr⁻¹ to 27,800 hr⁻¹. 259

- Figure 6.30 Carbon monoxide yield with surrogate JP-8 fuel flows of 8.84 ml/min.(5.0 kW_{th}) with oxygen enrichment (Ψ) of 0.477, 1.0, 1.432 and 1.91. The GHSV for $\Psi = 0.477$ was from 48,600 hr⁻¹ to 69,500 hr⁻¹, for $\Psi = 1.0$ was from 32,400 hr⁻¹ to 40,400 hr⁻¹, for $\Psi = 1.432$ was from 26,600 hr⁻¹ to 31,400 hr⁻¹, and for $\Psi = 1.91$ was from 23,600 hr⁻¹ to 27,800 hr⁻¹. 259
- Figure 6.31 Molar hydrocarbon and olefin composition in reformat with surrogate JP-8 fuel flows of 8.84 ml/min.(5.0 kW_{th}) with oxygen enrichment (Ψ) of 0.477, 1.0, 1.432 and 1.91. The GHSV for $\Psi = 0.477$ was from 48,600 hr⁻¹ to 69,500 hr⁻¹, for $\Psi = 1.0$ was from 32,400 hr⁻¹ and 40,400 hr⁻¹, for $\Psi = 1.432$ was from 26,600 hr⁻¹ to 31,400 hr⁻¹, and for $\Psi = 1.91$ was from 23,600 hr⁻¹ to 27,800 hr⁻¹. 261
- Figure 6.32 Reformer efficiency with surrogate JP-8 fuel flows of 8.84 ml/min.(5.0 kW_{th}) with oxygen enrichment (Ψ) of 0.477, 1.0, 1.432 and 1.91. The GHSV for $\Psi = 0.477$ was from 48,600 hr⁻¹ to 69,500 hr⁻¹, for $\Psi = 1.0$ was from 32,400 hr⁻¹ to 40,400 hr⁻¹, for $\Psi = 1.432$ was from 26,600 hr⁻¹ to 31,400 hr⁻¹, and for $\Psi = 1.91$ was from 23,600 hr⁻¹ to 27,800 hr⁻¹. 262
- Figure 6.33 Molar hydrogen composition in reformat with surrogate JP-8 fuel flows of 8.84 ml/min.(5.0 kW_{th}) with oxygen enrichment (Ψ) of 0.477, 1.0, 1.432 and 1.91. The GHSV for $\Psi = 0.477$ was from 48,600 hr⁻¹ to 69,500 hr⁻¹, for $\Psi = 1.0$ was from 32,400 hr⁻¹ to 40,400 hr⁻¹, for $\Psi = 1.432$ was from 26,600 hr⁻¹ to 31,400 hr⁻¹, and for $\Psi = 1.91$ was from 23,600 hr⁻¹ to 27,800 hr⁻¹. 262
- Figure 6.34 Reactor differential pressure with surrogate JP-8 fuel flows of 8.84 ml/min.(5.0 kW_{th}) with oxygen enrichment (Ψ) of 0.477, 1.0, 1.432 and 1.91. The GHSV for $\Psi = 0.477$ was from 48,600 hr⁻¹ to 69,500 hr⁻¹, for $\Psi = 1.0$ was from 32,400 hr⁻¹ to 40,400 hr⁻¹, for $\Psi = 1.432$ was from 26,600 hr⁻¹ to 31,400 hr⁻¹, and for $\Psi = 1.91$ was from 23,600 hr⁻¹ to 27,800 hr⁻¹. 264
- Figure 6.35 Normalized fuel conversion for enrichment number (Ψ) of 0.477 (a) and 1.0 (b) with surrogate JP-8 fuel flows of 5.9 ml/min. (3.33 kW_{th}), 8.84 ml/min.(5.0 kW_{th}), 11.8 ml/min. (6.67 kW_{th}), and 14.7 ml/min (8.33 kW_{th}). The GHSV for $\Psi = 0.477$ (a) was from 33,900 hr⁻¹ to 40,900 hr⁻¹ (3.33 kW_{th}), 48,600 hr⁻¹ to 69,500 hr⁻¹ (5.0 kW_{th}), and 54,700 hr⁻¹ to 67,200 hr⁻¹ (6.67 kW_{th}). The GHSV for $\Psi = 1.0$ (b) was from 22,200 hr⁻¹ to 26,900 hr⁻¹ (3.33 kW_{th}), 32,400 hr⁻¹ to 40,400 hr⁻¹ (5.0 kW_{th}), and 43,200 hr⁻¹ to 53,800 hr⁻¹ (6.67 kW_{th}). 266
- Figure 6.35 (con't) Normalized fuel conversion for enrichment number (Ψ) of 1.432 (c) and 1.91 (d) with surrogate JP-8 fuel flows of 5.9 ml/min. (3.33 kW_{th}), 8.84 ml/min.(5.0 kW_{th}), 11.8 ml/min. (6.67 kW_{th}), and 14.7 ml/min (8.33 kW_{th}). The GHSV for $\Psi = 1.432$ (c) was from 18,800 hr⁻¹ to 21,500 hr⁻¹ (3.33 kW_{th}), 26,600 hr⁻¹ to 31,300 hr⁻¹ (5.0 kW_{th}), 35,600 hr⁻¹ to 42,900 hr⁻¹ (6.67 kW_{th}), and 45,500 hr⁻¹ to 53,400 hr⁻¹ (8.33 kW_{th}). The GHSV for $\Psi = 1.91$ (d) was from 16,500 hr⁻¹ to 19,200 hr⁻¹ (3.33 kW_{th}), 23,600 hr⁻¹ to 27,800 hr⁻¹ (5.0 kW_{th}), and 31,900 hr⁻¹ to 37,400 hr⁻¹ (6.67 kW_{th}), and 41,100 hr⁻¹ to 46,800 hr⁻¹ (8.33 kW_{th}). 267
- Figure 6.36 Reactor maximum and exit temperatures for enrichment number (Ψ) of 0.477 (a) and 1.0 (b) with surrogate JP-8 fuel flows of 5.9 ml/min. (3.33 kW_{th}), 8.84 ml/min.(5.0 kW_{th}), 11.8 ml/min. (6.67 kW_{th}), and 14.7 ml/min (8.33 kW_{th}). The GHSV for $\Psi = 0.477$ (a) was from 33,900 hr⁻¹ to 40,900 hr⁻¹ (3.33 kW_{th}), 48,600 hr⁻¹ to 69,500 hr⁻¹ (5.0 kW_{th}), and 54,700 hr⁻¹ to 67,200 hr⁻¹ (6.67 kW_{th}). The GHSV for $\Psi = 1.0$ (b) was from 22,200 hr⁻¹ to 26,900 hr⁻¹ (3.33 kW_{th}), 32,400 hr⁻¹ to 40,400 hr⁻¹ (5.0 kW_{th}), and 43,200 hr⁻¹ to 53,800 hr⁻¹ (6.67 kW_{th}). 269
- Figure 6.36 (con't) Reactor maximum and exit temperatures for enrichment number (Ψ) of 1.432 (c) and 1.91 (d) with surrogate JP-8 fuel flows of 5.9 ml/min. (3.33 kW_{th}), 8.84 ml/min.(5.0 kW_{th}), 11.8 ml/min. (6.67 kW_{th}), and 14.7 ml/min (8.33 kW_{th}). The GHSV for $\Psi = 1.432$ (c) was from 18,800 hr⁻¹ to 21,500 hr⁻¹ (3.33 kW_{th}), 26,600 hr⁻¹ to 31,300 hr⁻¹ (5.0 kW_{th}), 35,600 hr⁻¹ to 42,900 hr⁻¹ (6.67 kW_{th}), and 45,500 hr⁻¹ to 53,400 hr⁻¹ (8.33 kW_{th}). The GHSV for $\Psi = 1.91$ (d) was from 16,500 hr⁻¹ to 19,200 hr⁻¹ (3.33 kW_{th}), 23,600 hr⁻¹ to 27,800 hr⁻¹ (5.0 kW_{th}), and 31,900 hr⁻¹ to 37,400 hr⁻¹ (6.67 kW_{th}), and 41,100 hr⁻¹ to 46,800 hr⁻¹ (8.33 kW_{th}). 270

- Figure 6.37 Carbon monoxide yields for enrichment number (Ψ) of 0.477 (a) and 1.0 (b) with surrogate JP-8 fuel flows of 5.9 ml/min. (3.33 kW_{th}), 8.84 ml/min.(5.0 kW_{th}), 11.8 ml/min. (6.67 kW_{th}), and 14.7 ml/min (8.33 kW_{th}). The GHSV for $\Psi = 0.477$ (a) was from 33,900 hr⁻¹ to 40,900 hr⁻¹ (3.33 kW_{th}), 48,600 hr⁻¹ to 69,500 hr⁻¹ (5.0 kW_{th}), and 54,700 hr⁻¹ to 67,200 hr⁻¹ (6.67 kW_{th}). The GHSV for $\Psi = 1.0$ (b) was from 22,200 hr⁻¹ to 26,900 hr⁻¹ (3.33 kW_{th}), 32,400 hr⁻¹ to 40,400 hr⁻¹ (5.0 kW_{th}), and 43,200 hr⁻¹ to 53,800 hr⁻¹ (6.67 kW_{th}). 271
- Figure 6.37 (con't) Carbon monoxide yield for enrichment number (Ψ) of 1.432 (c) and 1.91 (d) with surrogate JP-8 fuel flows of 5.9 ml/min. (3.33 kW_{th}), 8.84 ml/min.(5.0 kW_{th}), 11.8 ml/min. (6.67 kW_{th}), and 14.7 ml/min (8.33 kW_{th}). The GHSV for $\Psi = 1.432$ (c) was from 18,800 hr⁻¹ to 21,500 hr⁻¹ (3.33 kW_{th}), 26,600 hr⁻¹ to 31,300 hr⁻¹ (5.0 kW_{th}), 35,600 hr⁻¹ to 42,900 hr⁻¹ (6.67 kW_{th}), and 45,500 hr⁻¹ to 53,400 hr⁻¹ (8.33 kW_{th}). The GHSV for $\Psi = 1.91$ (d) was from 16,500 hr⁻¹ to 19,200 hr⁻¹ (3.33 kW_{th}), 23,600 hr⁻¹ to 27,800 hr⁻¹ (5.0 kW_{th}), and 31,900 hr⁻¹ to 37,400 hr⁻¹ (6.67 kW_{th}), and 41,100 hr⁻¹ to 46,800 hr⁻¹ (8.33 kW_{th}). 272
- Figure 6.38 Hydrogen yield for enrichment number (Ψ) of 0.477 (a) and 1.0 (b) with surrogate JP-8 fuel flows of 5.9 ml/min. (3.33 kW_{th}), 8.84 ml/min.(5.0 kW_{th}), 11.8 ml/min. (6.67 kW_{th}), and 14.7 ml/min (8.33 kW_{th}). The GHSV for $\Psi = 0.477$ (a) was from 33,900 hr⁻¹ to 40,900 hr⁻¹ (3.33 kW_{th}), 48,600 hr⁻¹ to 69,500 hr⁻¹ (5.0 kW_{th}), and 54,700 hr⁻¹ to 67,200 hr⁻¹ (6.67 kW_{th}). The GHSV for $\Psi = 1.0$ (b) was from 22,200 hr⁻¹ to 26,900 hr⁻¹ (3.33 kW_{th}), 32,400 hr⁻¹ to 40,400 hr⁻¹ (5.0 kW_{th}), and 43,200 hr⁻¹ to 53,800 hr⁻¹ (6.67 kW_{th}). 274
- Figure 6.38 (con't) Hydrogen yields for enrichment number (Ψ) of 1.432 (c) and 1.91 (d) with surrogate JP-8 fuel flows of 5.9 ml/min. (3.33 kW_{th}), 8.84 ml/min.(5.0 kW_{th}), 11.8 ml/min. (6.67 kW_{th}), and 14.7 ml/min (8.33 kW_{th}). The GHSV for $\Psi = 1.432$ (c) was from 18,800 hr⁻¹ to 21,500 hr⁻¹ (3.33 kW_{th}), 26,600 hr⁻¹ to 31,300 hr⁻¹ (5.0 kW_{th}), 35,600 hr⁻¹ to 42,900 hr⁻¹ (6.67 kW_{th}), and 45,500 hr⁻¹ to 53,400 hr⁻¹ (8.33 kW_{th}). The GHSV for $\Psi = 1.91$ (d) was from 16,500 hr⁻¹ to 19,200 hr⁻¹ (3.33 kW_{th}), 23,600 hr⁻¹ to 27,800 hr⁻¹ (5.0 kW_{th}), and 31,900 hr⁻¹ to 37,400 hr⁻¹ (6.67 kW_{th}), and 41,100 hr⁻¹ to 46,800 hr⁻¹ (8.33 kW_{th}). 275
- Figure 6.39 Space time for enrichment number (Ψ) of 0.477 (a) and 1.0 (b) with surrogate JP-8 fuel flows of 5.9 ml/min. (3.33 kW_{th}), 8.84 ml/min.(5.0 kW_{th}), 11.8 ml/min. (6.67 kW_{th}), and 14.7 ml/min (8.33 kW_{th}). 276
- Figure 6.39 (con't) Carbon monoxide yield for enrichment number (Ψ) of 1.432 (c) and 1.91 (d) with surrogate JP-8 fuel flows of 5.9 ml/min. (3.33 kW_{th}), 8.84 ml/min.(5.0 kW_{th}), 11.8 ml/min. (6.67 kW_{th}), and 14.7 ml/min (8.33 kW_{th}). 277
- Figure 6.40 Reformer efficiency for enrichment number (Ψ) of 0.477 (a) and 1.0 (b) with surrogate JP-8 fuel flows of 5.9 ml/min. (3.33 kW_{th}), 8.84 ml/min.(5.0 kW_{th}), 11.8 ml/min. (6.67 kW_{th}), and 14.7 ml/min (8.33 kW_{th}). The GHSV for $\Psi = 0.477$ (a) was from 33,900 hr⁻¹ to 40,900 hr⁻¹ (3.33 kW_{th}), 48,600 hr⁻¹ to 69,500 hr⁻¹ (5.0 kW_{th}), and 54,700 hr⁻¹ to 67,200 hr⁻¹ (6.67 kW_{th}). The GHSV for $\Psi = 1.0$ (b) was from 22,200 hr⁻¹ to 26,900 hr⁻¹ (3.33 kW_{th}), 32,400 hr⁻¹ to 40,400 hr⁻¹ (5.0 kW_{th}), and 43,200 hr⁻¹ to 53,800 hr⁻¹ (6.67 kW_{th}). 279
- Figure 6.40 (con't) Reformer efficiency for enrichment number (Ψ) of 1.432 (c) and 1.91 (d) with surrogate JP-8 fuel flows of 5.9 ml/min. (3.33 kW_{th}), 8.84 ml/min.(5.0 kW_{th}), 11.8 ml/min. (6.67 kW_{th}), and 14.7 ml/min (8.33 kW_{th}). The GHSV for $\Psi = 1.432$ (c) was from 18,800 hr⁻¹ to 21,500 hr⁻¹ (3.33 kW_{th}), 26,600 hr⁻¹ to 31,300 hr⁻¹ (5.0 kW_{th}), 35,600 hr⁻¹ to 42,900 hr⁻¹ (6.67 kW_{th}), and 45,500 hr⁻¹ to 53,400 hr⁻¹ (8.33 kW_{th}). The GHSV for $\Psi = 1.91$ (d) was from 16,500 hr⁻¹ to 19,200 hr⁻¹ (3.33 kW_{th}), 23,600 hr⁻¹ to 27,800 hr⁻¹ (5.0 kW_{th}), and 31,900 hr⁻¹ to 37,400 hr⁻¹ (6.67 kW_{th}), and 41,100 hr⁻¹ to 46,800 hr⁻¹ (8.33 kW_{th}). 280
- Figure 6.41 Reformer thermal capacity as a function of enrichment number. The reformer was operating at a S/C ratio of 2 and the O/C ratio was adjusted to achieve a constant reformer efficiency. 281
- Figure 6.42 Overall power system performance based assumptions shown in Table 6.4. 284
- Figure 6.43 Impact to fuel cell power source performance on system efficiency, power density, and specific power as a function of oxygen enrichment of air. For comparison, the performance of a fuel cell power source without oxygen enrichment is shown. Overall power system performance based on assumptions of Table 6.4. 285

LIST OF TABLES

Table 1.1 Comparison of fuel cells	18
Table 1.2 Typical reformat streams by reforming technique.	23
Table 2.1 Properties of hydrogen compared to other common fuels.	34
Table 2.2 Comparison of hydrogen fuel system for mobile applications (based on 150kW-hr energy storage).	35
Table 2.3 Comparison of some metal hydrides.	41
Table 3.1 Output data collected during all experimental work.	112
Table 3.2 Logic/Status data collected during all experimentation.	113
Table 3.3 Instrument measurement accuracy	143
Table 3.4 Variable definitions	144
Table 3.5 Example experimental data from n-dodecane, fuel flow = 4.436 gm/min. (3.3 kWth): S/C = 2.0; O/C = 1.07	145
Table 3.6 Calculation results for n-dodecane with fuel flow = 4.436 gm/min., S/C = 2.0, O/C = 1.07 and oxygen enrichment number = 1.0.	146
Table 5.1 Properties of JP-8 sample	191
Table 5.2 JP-8 sample chemical composition analysis	192
Table 5.3 Surrogate mixtures for JP-8 fuel	193
Table 5.4 Comparison of surrogate JP-8 fuel properties	194
Table 6.1 Full fuel conversion	240
Table 6.2 Comparison of peak full fuel conversion, hydrogen yield and reformer efficiency	244
Table 6.3 Reformer operating constraints	250
Table 6.4 System level modeling assumptions	283
Table 6.5 Emissions comparisons	286

FOREWORD

This research topic has, since its inception in October 2006 and through discussion with my thesis advisor, Dr. Sen Nieh, resulted in productivity outside the scope of the original research effort. Shortly after proposing the topic to my advisory committee in February 2007, I developed a proposal and received financial support from the Army for laboratory analytical instrumentation in the amount of \$45k in 2007. I also prepared a two-year proposal for in-house research funding with the Army under an In-House Laboratory Independent Research (ILIR) program and received \$177k funding in total for 2008 through 2010. In addition, to the external funding my Branch, Advanced Power Technology Branch, under the US Army Research and Development Command, provided financial support for my labor of approximately \$160k in support this research topic.

I, along with Dr. Nieh, have participated in presenting our in-progress research through conferences and technical reports. I prepared as 1st author with my advisor Dr. Nieh as second author, and presented a technical paper, published in the conference proceedings, at the 43rd 2008 Power Sources Conference, Philadelphia, PA, July 2008 entitled, “Design and Performance of an Experimental 3 kWth Autothermal Reformer Test Bed for Heavy Hydrocarbon Fuels”. In April 2009, I prepared and submitted a technical report to the US Army on the results from the first year of my ILIR project. I prepared as 1st author with my advisor Dr. Nieh as second author, and presented a

technical paper, published in the conference proceedings, at the 44th 2010 Power Sources Conference, Las Vegas, NV, July 2010 entitled, “Effects of Hydrocarbon Chemical Class Composition on Autothermal Reforming of JP-8 Fuel”. In March 2010, I prepared a second technical report to the US Army on the results from the final year of my ILIR project. In addition, in March 2011, I submitted an abstract as first author, Richard Scenna (MS ME, CUA, 2010) as second author, and Dr. Nieh as third author, entitled, “Autothermal reforming of JP-8 and model fuels: experimental study and application in multi-kW power sources” to the Interagency Advanced Power Group (IAPG), Mechanical Working Group for presentation at their meeting on May 3-5, 2011 at The Catholic University of America.

Additionally, I have prepared and submitted manuscripts to journals for archival publication. I prepared and submitted a manuscript entitled, “Simulation of a fuel reforming system based on catalytic partial oxidation”, which was published in Elsevier’s Journal of Power Sources, in August 2008 (*J. Power Sources* 2008;183:295-302). In April 2010, I prepared as first author and Dr. Nieh as second author a paper entitled, “Selection and performance comparison of jet fuel surrogates for autothermal reforming”, which was published in Elsevier’s Journal Fuel, in April 2011 (*Fuel* 2011;90(4):1439-1448). A technical manuscript entitled “Experimental design and investigation of a JP-8 autothermal reformer” has been submitted to Elsevier’s International Journal of Hydrogen Sources for peer review.

PREFACE

The term “oxygen enrichment” refers to any process that results in increasing the concentration of oxygen to a level greater than the level found in air under standard conditions; approximately 21%. Oxygen enrichment of air appears to imply that additional oxygen is added to air in order to raise the molar concentration of oxygen; however, this is not the case. Oxygen enrichment as used in this research work, is achieved through selective removal of nitrogen from air.

Others terms used in describing the quantity of oxygen and steam that are reacted in the reformer along with heavy hydrocarbon fuel are the oxygen-to-carbon (O/C) ratio and the steam-to-carbon (S/C) ratio. The O/C ratio is the molar ratio of oxygen (monatomic oxygen) to carbon; where carbon is from the hydrocarbon fuel. In a similar fashion, the S/C ratio is the molar ratio of steam to carbon.

ACKNOWLEDGEMENTS

I first, would like to thank Tracy, my wife, for her love, support and encouragement throughout this long course of study. I would also like to acknowledge the contribution from my son, Matthew, who has brought joy and excitement to my life, and reminds me that the simple things in life are most important. I am also indebted to my parents, Marvin and Joyce DuBois, for their many years of investment of love, encouragement, and confidence in me under all circumstances.

I would also like to thank my adviser, Dr. Sen Nieh, for his advice in technical, professional and personal matters. Dr. Nieh's broad knowledge and experience has greatly influenced the direction of the research presented in this dissertation and he served as a constant source of inspiration and enthusiasm for this work. I am indebted to him for his wise council and thoughtful guidance. I also want to acknowledge my committee for their generous contribution of time on my behalf: Dr. Neal Blackwell, Dr. Steve Brown, and Dr. Gene Gabbai. Special thanks go to Mrs. Ruth Hicks who has assisted me greatly throughout my program of study.

I have been the recipient of generous technical advice, guidance and assistance throughout my career from many individuals. I would like to acknowledge Mr. Richard Belt for taking me on in my first engineering position in the Fuel Cell Group at Fort Belvoir, Virginia and for giving me the opportunity to work with an outstanding group of engineers and technicians: Mr. Walter Taschek, Mr. Stan Kurpit, Mr. Richard Jacobs,

Mr. Ed Starkovich, and Mr. Milt Jakola. I want to recognize my current colleagues at the US Army Research, Development and Engineering Center, Power Division at Fort Belvoir, Virginia who have provided technical assistance, advice and comradery. To my branch chiefs for their support during the completion of my studies and experimental work I would like to thank Dr. Ashok Patil, Mr. Darwin Reckart, Dr. Scott Coombe and Mrs. Selma Matthews. To my co-workers for their encouragement, council, engineering and technical support, and humor, I want to acknowledge: Dr. Neal Blackwell, Mr. Michael Connaghan, Mr. John Manizone, Mr. Chris Bolton, Mr. William Campbell, Mr. Byrd Pritchett, Mr. Andrew Thompson, Mr. Narinder Gulati, Mr. Jason Shoop, Mr. Robert Bruce, Mr. Michael Seibert, and Mr. Richard Scenna. Finally, I want to acknowledge Mr. James Stephens, retired Team Leader of the Fuel Cell Technology Team at Fort Belvoir, for expending an opportunity to me to return to Fort Belvoir and supporting me in my pursuit of a doctoral degree.

During the course of conducting the experimental work, I received valuable advice from a large number of researchers who generously shared from their research experienced; the number of individuals is too long to list here in its entirety, but I do wish to recognize a few individuals whose contributions were very significant: Dr. Shabbir Ahmed, Argonne National Laboratory; Mr. Ajaib Randhava, Unitel Technologies, Inc.; Dr. Subir Roychoudhury and Dr. Christian Junaedi, Precision Combustion, Incorporated.

I would not have been able to accomplish the design, fabrication, and build (and re-build) of my experimental test stand without the aid, assistance and technical advice from

a group of extremely experienced and capable technicians at Fort Belvoir: Mr. Byrd Pritchett (Army Power Division) , Mr. Andrew Thompson (Army Power Division), Mr. Ricky Bowers (Night Vision Shop), and Mr. Andy Cerutti (Night Vision Shop).

Special recognition goes to Mr. Walter Taschek, who provided a technical review of this manuscript and offered technical advice, guidance, and encouragement throughout this research effort.

This work was sponsored in part by the U.S. Army's Research, Development, and Engineering Command (RDECOM), Communications-Electronics Research, Development and Engineering Center (CERDEC). Additionally, funding was received for instrumentation through a Director's Research Initiative, provided by Dr. Gerardo Melendez, and multi-year research funding was received through the Army's In-House Laboratory Independent Research (ILIR) program sponsored by Dr. Arthur Ballato, Chief Scientist, CERDEC. I gratefully acknowledge the above support received, without which, this doctoral program could not have been pursued.

Chapter 1

Introduction

1.0 Motivation

This thesis is concerned with improving the efficiency and reduction of environmental pollutants for mobile power systems. Specifically, the thesis is targeting mobile multi-kW fuel cell power sources employing oxygen enriched air reforming of heavy hydrocarbon fuels.

Mobile power systems represent a segment of energy consuming equipment that operate almost exclusively on oil based fuels. Petroleum oil based fuels provide an energy storage source that has high specific energy, high energy density, and is affordable. Internal combustion engines, operating on oil based fuels, results in an energy conversion device that is very attractive in terms of cost, specific power and power density. Unfortunately, combustion based power sources are inefficient and are a primary source of greenhouse gases and other pollutants (NO_x , ozone, VOCs, particulate matter, etc.). The combination of catalytic fuel reforming and fuel cells may provide a solution for many mobile power applications.

1.1 Background

At the writing of this chapter the world is facing the convergence of three major interrelated global challenges that are beginning to impact the planet and shape future geopolitical discussion and decisions. These are: soaring population growth, depletion of natural resources and global warming. With the exception of global warming, these factors have been recognized for a long time; however, the consequences of these factors have only recently been recognized at the global level. Developing future energy sources, and efficient non-polluting energy conversion devices, can play a significant role in addressing the three cited global challenges.

1.1.1 Population growth

World population is currently estimated at 6.4 billion people with this number projected to rise to 8.9 billion by 2050 [1]. As seen in Fig. 1.1, the largest contributors to population are developing countries (China, India, and Africa). Many of these countries are also entering into a period of rapid industrialization, which is accompanied by significant increases in both per capita income and gross domestic product resulting in the development and growth of a middle class. These positive economic trends in some developing countries have resulted in a significant reduction in global poverty [2], but also a significant increase in energy use and associated equivalent carbon dioxide emissions [3] that are increasing at alarming rates. The strong relationship between rapid economic growth and rapid carbon dioxide emissions is shown in Fig. 1.2. Figure 1.3 shows a very strong correlation between prosperity and per capita electricity consumption

as measured by the United Nations Human Development Index, the index is composed from data on life expectancy, education and per-capita GDP [4,1]. The path to better economic conditions in developing countries is through industrialization, which is still very resource intensive (both energy and natural resources).

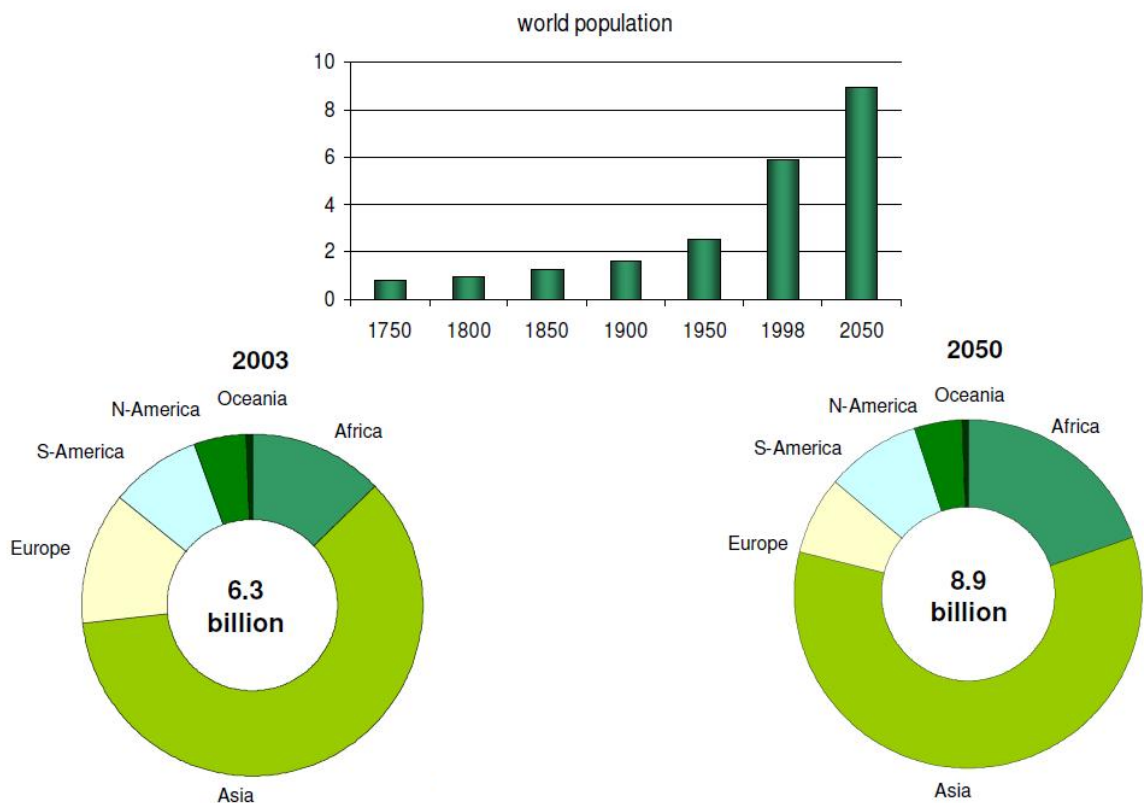


Figure 1.1. World population growth and demographics [1].

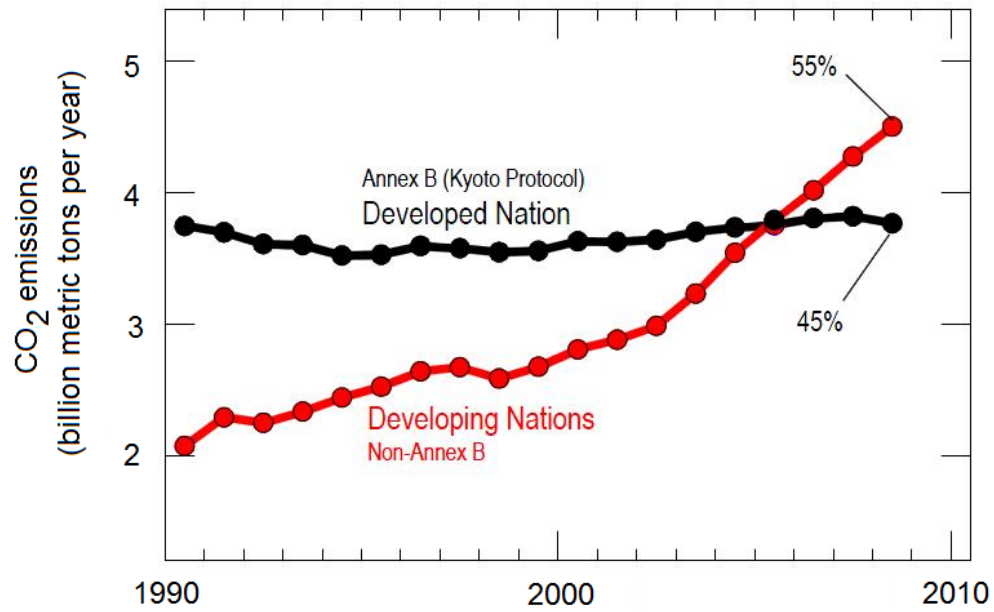


Figure 1.2. CO₂ emissions Showing Developed and Developing Nations Trends [3].

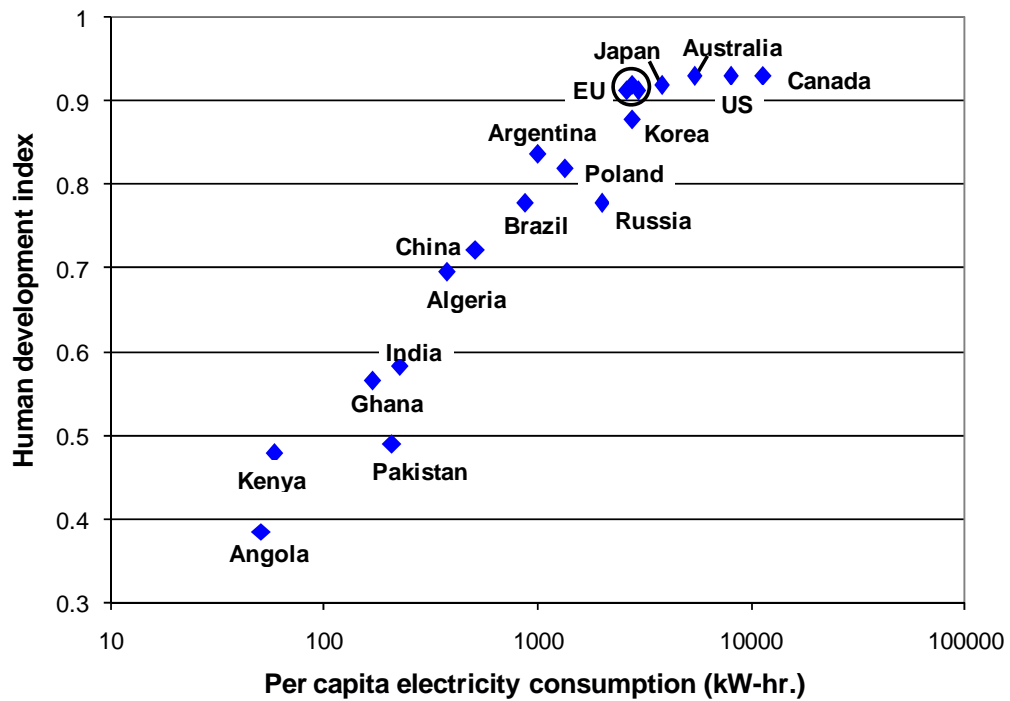


Figure 1.3. Energy and Prosperity Trends [4,1].

1.1.2 Natural resources

The United States has enjoyed a sustained period of industrial and economic dominance, where scientific and engineering ingenuity were unhampered by commodity scarcity. During this period, we consumed the majority of most resources and we rarely faced stiff competition from any other country. Today, we face a very different situation. With China and India having the largest populations and fastest growing economies, competition for natural resources will be heightened. Additionally, sustainable methods in both energy and manufacturing will have to be pursued to continue global economic growth. As anecdotal evidence of the changes taking place, the World Monetary Fund reported that China is the world's largest coal consumer country. In 2005, China consumed 25 percent of the world's aluminum, 22 percent of its copper, 18 percent of its nickel, and 44 percent of its iron. China's economic growth and appetite for natural resources is believed to continue until its per capita GDP reaches approximately \$15,000 (2010 US\$); currently at \$6500 [5].

Today approximately 1.5 billion people do not have access to electricity. Eight-five percent of these people live in rural areas primarily in sub-Saharan Africa and South Asia [5]. In his Technology, Entertainment and Design (TED) 2010 conference presentation [6], Bill Gates identified affordable energy as the most significant need of impoverished people; more pressing than vaccines, food, and education – energy being critical to each. Lack of access to dependable, available, sustainable and affordable energy will significantly differentiate the developed and developing/underdeveloped populations of

the world. Energy is now seen as the lynch-pin to addressing social, economic and educational needs for all people and universal access to energy is being promoted as a crucial human right [7,8].

Strong population and economic growth in some large developing nations has resulted in a very large projection in future global energy demand [9]. Past, current, and future energy needs out to 2030 are shown in Fig. 1.4. All sectors project growth in energy consumption with transportation energy growth having the largest percentage increase of approximately 75%.

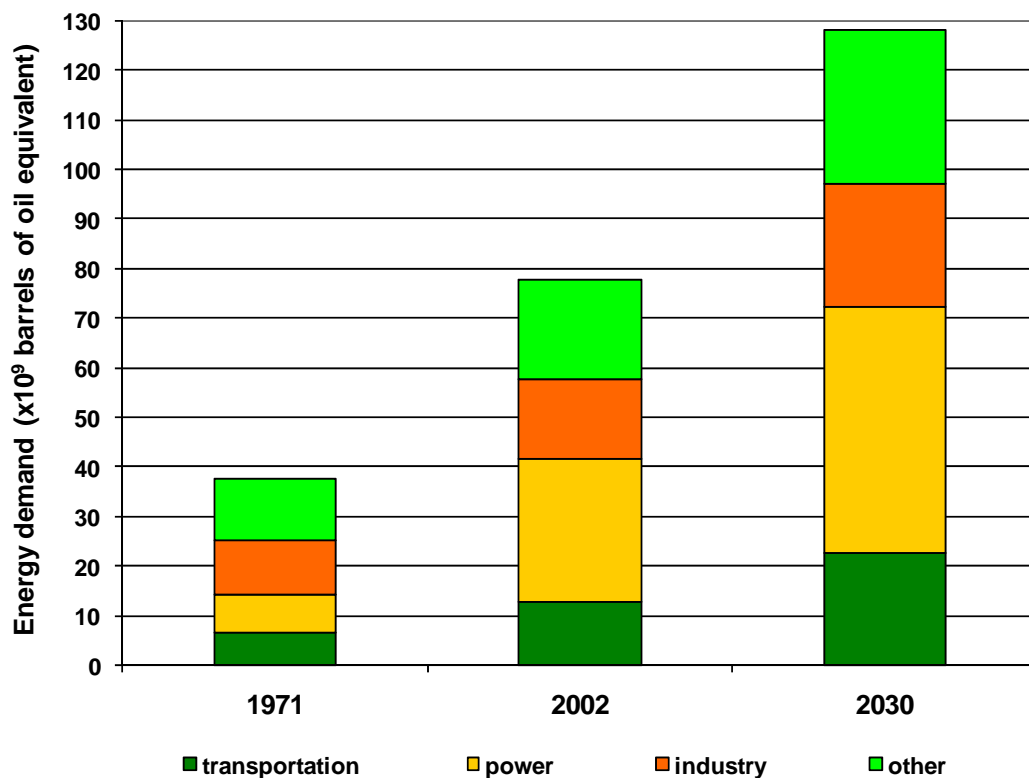


Figure 1.4. Global energy demand Growth by sector (1971-2030) [9].

1.1.3 Global warming

The world's energy needs are principally met by energy stored in the chemical bonds of hydrocarbon compounds that are converted into mechanical or electrical power. The release of reaction products into the atmosphere is unavoidable and products such as carbon dioxide are associated with trapping heat within earth's atmosphere and raising the average temperature on earth; termed global warming. Although widely debated in the latter decades of the 20th century, consensus has emerged on the negative and potentially severe present and future impacts of elevated average global temperatures. Figure 1.5 shows the CO₂ concentration overtime from data collected from air trapped in ice cores at Vostok, Antarctica and reading taken at Manna Loa, Hawaii after 1976. As can be seen, there is a significant increase beginning around 1800 and continuing to today. The timeframe in which the dramatic increase in atmospheric CO₂ occurred matches closely with the timeframe for Western industrialization. Figure 1.6 shows the per capita greenhouse gas pollution by country with the more industrialized countries producing more greenhouse gas pollution per capita [10]. However, when total greenhouse gas pollution is considered (area under the curve in Fig. 1.6), China leads and India is fourth as shown in Fig. 1.7 [3]. In fact, future projections of all additional energy related CO₂ emissions above current levels are attribute to non-Organization for Economic Co-operation and Development (OECD)¹ countries [9]. These are largely underdeveloped countries with rapidly growing populations and escalating energy

¹ OECD consists of thirty industrialized countries that work together to address economic, social and environmental challenges of globalization. Member countries are: Australia, Austria, Belgium, Canada, Czech Republic, Denmark, Finland, France, Germany, Greece, Hungary, Ireland, Italy, Japan, Korea (Republic of), Luxembourg, Netherlands, New Zealand, Norway, Poland, Portugal, Slovak Republic, Spain, Sweden, Switzerland, turkey, United Kingdom, and the United States.

demands. A primary contributor to atmospheric CO_2 is the burning of oil principally for transportation purposes. Figure 1.8 shows CO_2 emission trends over the past twenty years by fossil fuel source. Until 2005, oil was the primary source of CO_2 emissions. Oil has recently been displaced by coal, with China and India accounting for 90% of this increased use of coal [3]. In the United States, oil (petroleum) is the single largest energy source for CO_2 emissions [11] and transportation represents the single largest carbon emitter among end-user sectors and the largest consumer of oil [12,13].

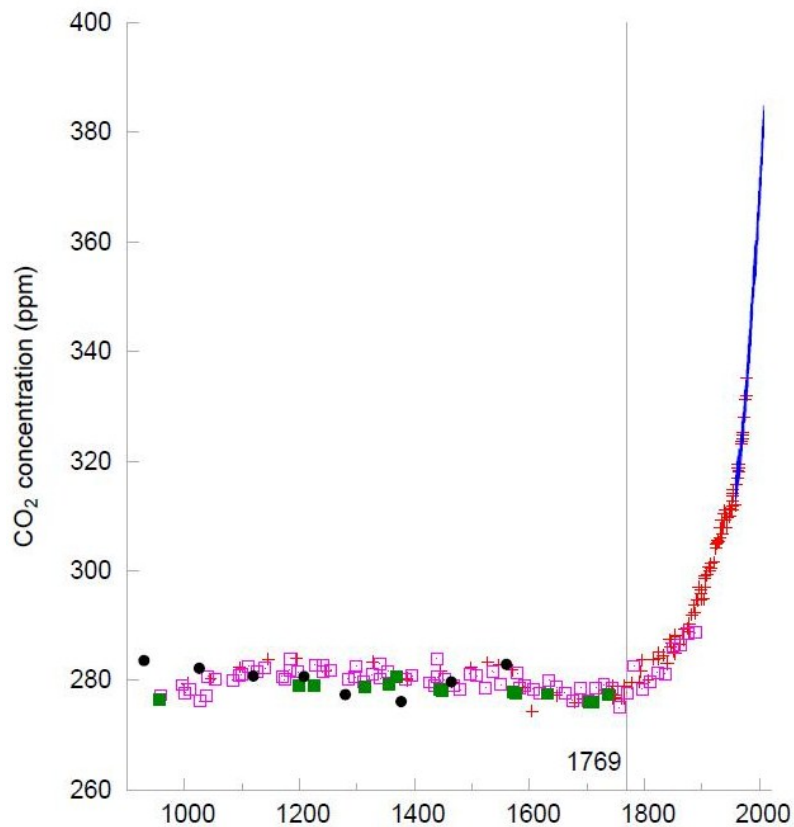


Figure 1.5 Carbon dioxide (CO_2) concentrations (parts per million) for the past 1100 years, measured from air trapped in ice (Vostok, Antarctica Ice-Core record) and as measured directly at Mauna Loa, Hawaii [10].

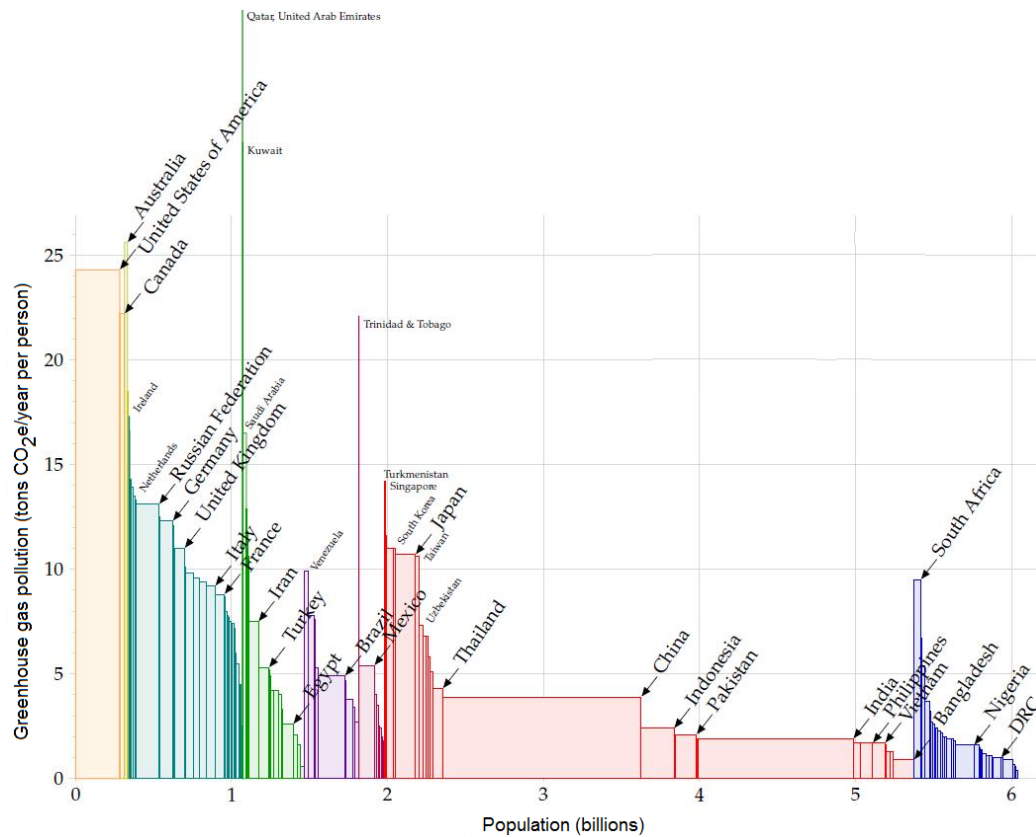


Figure 1.6 Greenhouse gas equivalent emissions on a per capita basis, also showing population [3,10].

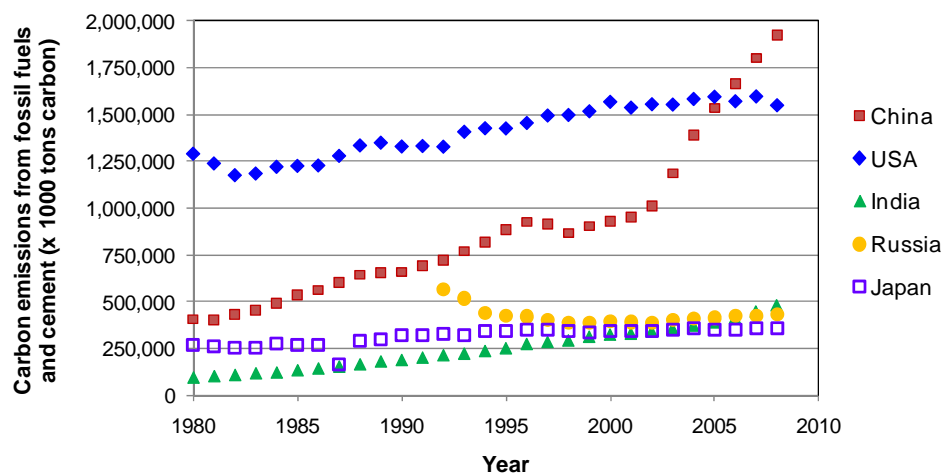


Figure 1.7 Carbon emissions from fossil fuels and cement showing top five emitters [3].

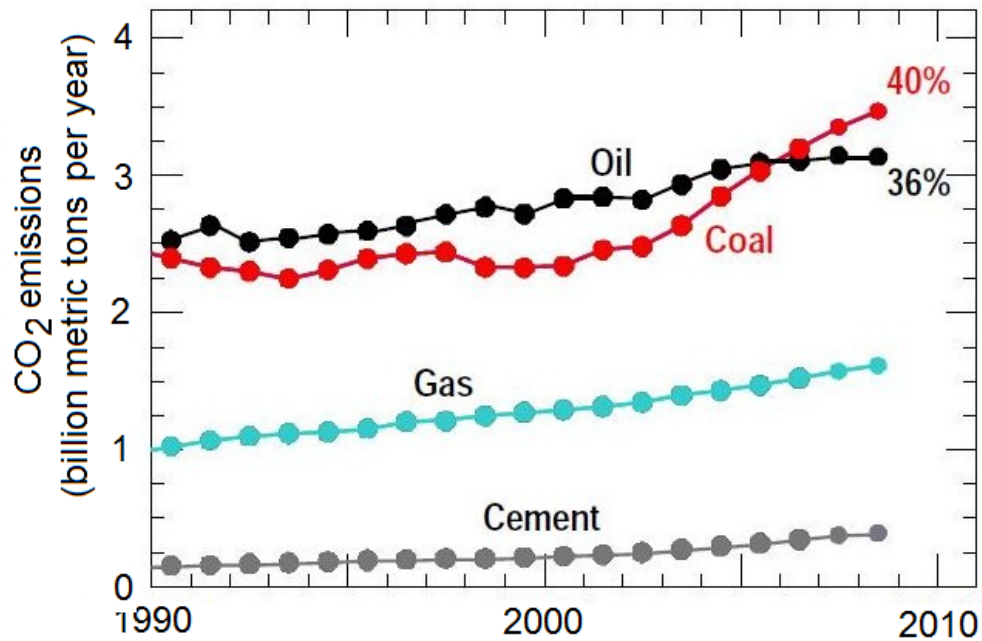


Figure 1.8 Global fossil fuel emissions by fuel type [3].

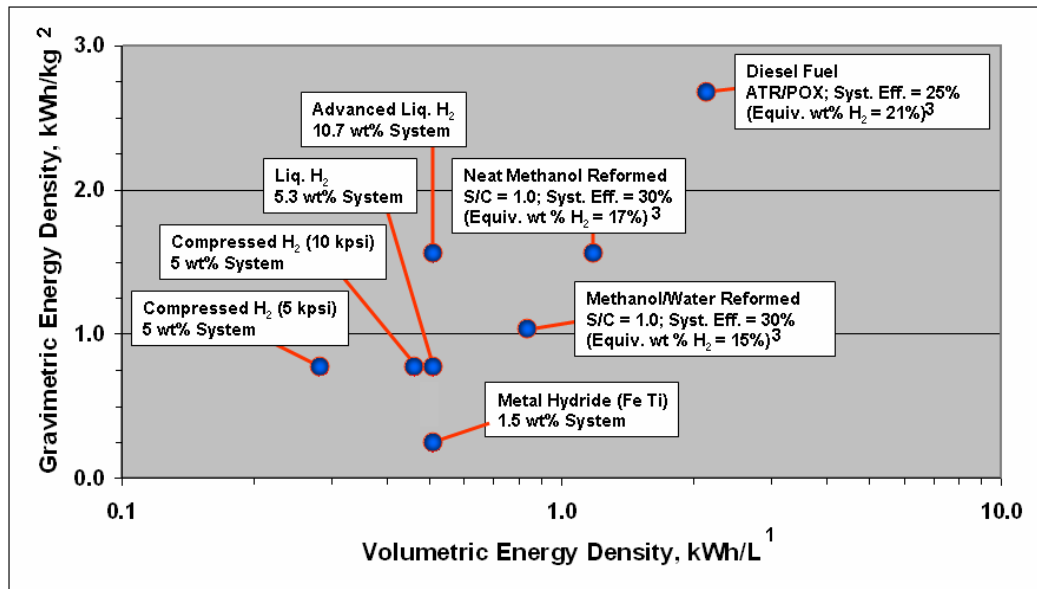
1.1.3.1 Transportation fuels in the United States

Heavy liquid hydrocarbon fuels, such as gasoline, aviation and diesel fuels exhibit both high specific energy and high energy density which has made them the fuels of choice for mobile power applications. The United States consumes about 3.85 million barrels per day of diesel fuel, 1.59 million barrels per day of kerosene based jet fuels and 8.9 million barrels per day of gasoline. Approximately, 67% of the diesel fuel consumed in the United States is used by the heavy trucking industry with the remained primarily used by the rail transportation industry [14]. Transportation represents 29% [15] of the total energy consumed in the United States and is substantially supplied through imports; for 2010 net imports for crude to support transportation needs were 58% of total

consumption [12]. In addition to being a large energy consumer, transportation represented 32% of green house gases emitted in the United States; the largest identified sector [13]. For heavy transportation (long haul trucking) a significant contribution to fuel consumption and pollution is engine idling, which is estimated to represent an average 1830 hrs/year per truck and consumes 838 million gallons of diesel fuel annually [16].

Fuel cells, supported by on-board fuel reformers, have emerged as a technology that could, as a direct replacement for spark ignition engines, as an auxiliary electric power source for compression ignition engines, or as a stand alone power source for mobile power applications, provide an opportunity for efficiency improvements and environmental benefits. The use of fuel cell auxiliary electric power units for removing truck auxiliary loads from the engine is being studied widely and is projected to improve vehicle fuel economy by 10% while driving and 600% when idling [17,18,19,20,21,22]. Fuel reforming of heavy hydrocarbon fuels is also being developed for pollution abatement in transportation applications where the primary propulsive engine is compression ignition diesel. Reformed fuel consisting of simple hydrocarbons, hydrogen, carbon dioxide and carbon monoxide, when introduced into the combustion chamber along with diesel fuel creates a fuel mixture that burns cleanly, reducing exhaust emissions [23,24,13]. Additionally, for diesel compression ignition engines the abatement of NO_x is difficult due to the lean burn nature of the engines. Nitrogen-oxides are usually removed via absorbent materials that require periodic regeneration. Here

hydrogen from reformed diesel fuel has been proposed as a means of regenerating NO_x absorbers [25,26]. Fig. 1.9 shows the gravimetric energy density and volumetric energy density for a number of future mobile energy sources. Both high gravimetric energy density and high volumetric energy density are desired. Middle distillate fuels, such as diesel and jet fuels, are very attractive and are unlikely to be displaced for many mobile applications in the near future. Additionally, there are sustainable approaches to producing middle distillate fuels via bio-mass fuel synthesis that can significantly reduced equivalent CO_2 emissions (see Fig. 1.10 [27]) and are attractive as future low carbon footprint fuels.



- 1 Net electric power divided by fuel storage mass and volume.
- 2 System Efficiency assumed at 45%
- 3 H₂ equivalent weight % is calculated on a gross energy storage basis

Figure 1.9 Gravimetric energy density and volumetric energy density for a number of future postulated mobile energy sources. Based on 150 kW-hr net energy storage (equivalent to 16 gallons of JP-8 with a 26% efficient conversion).

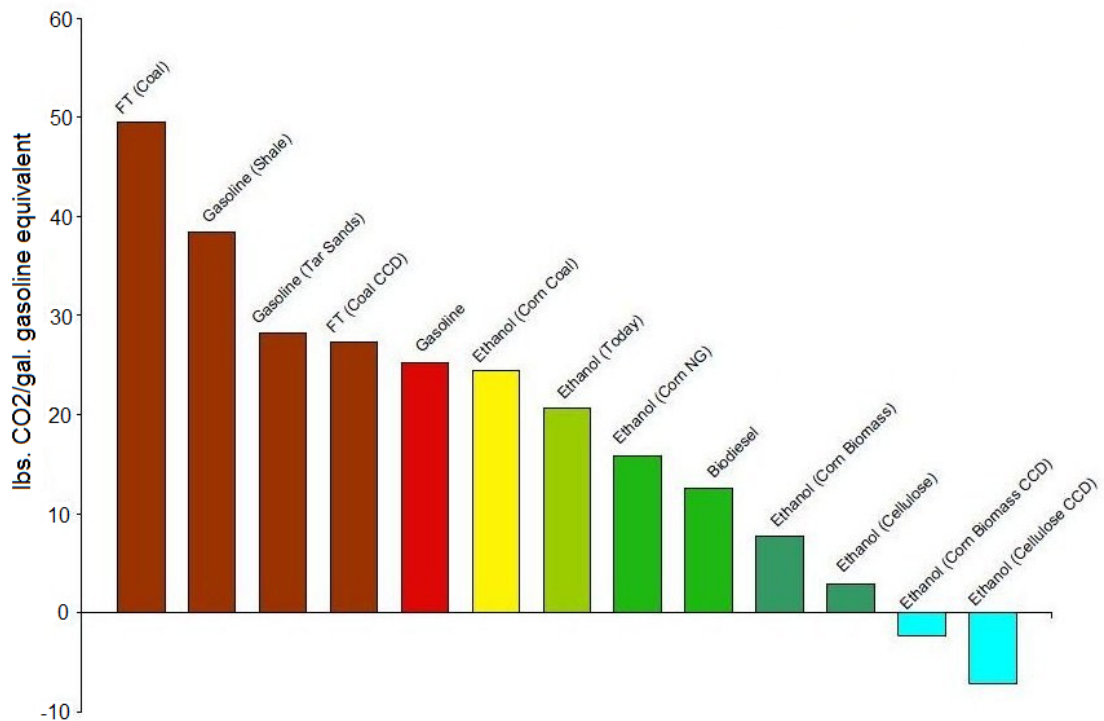


Figure 1.10 Comparison of future fuels on net CO₂ emissions [27].

1.2 History of fuel cell technology [28,29]

In 1839, the British physicist William R. Grove demonstrated the first electrochemical combination of oxygen and hydrogen via a sulfuric acid electrolyte producing electricity. Fuel cells largely remained a laboratory curiosity with some notable contribution from a number of chemists. In 1889, Ludwig Mond and Charles Langer attempted to build a practical electrochemical apparatus using perforated platinum electrodes with platinum black catalysts working with air and coal gas (CO and H₂). Mond and Langer were also the first to use the term “fuel cell”. In 1932, Francis T. Bacon, modified the design of Mond and Langer creating the first ‘practical’ fuel cell. Bacon pursued a fuel cell with

an alkaline electrolyte allowing the use of non-noble metal electrodes in order to avoid the expensive platinum materials used in the Mond and Langer design. Bacon encountered and overcame many problems and by the mid 1950's produced a successful 6kW fuel cell stack. Commercial success did not follow Bacon's invention, but patents were licensed to Pratt & Whitney and these patents formed the basis of the fuel cell technology that powered the NASA manned Apollo missions.

The first notable development of fuel cells occurred in the late 1950's lead by NASA and the Department of Defense. NASA was interested in a lightweight power source for spacecraft and DoD was interested in mobile electric power sources that ranged from 10's of watts to multi-kW sizes. Work at NASA largely took place at Johnson Space Center, Houston Texas [30]. The Department of Defense in the late 1950's, pursued early research and development of fuel cells through the Navy for marine applications and the Army Labs at Fort Belvoir² and Fort Monmouth³ for multi-kW mobile power generation and man portable power units [31]. The federal government has continued to be a primary supporter of fuel cell development work through government labs, national labs, the Department of Energy, and NASA, as well as, supporting commercial pilot plant development and field evaluation.

² Then the US Army Engineer Research and Development Laboratories, Fort Belvoir, VA. Now known as the US Army RDECOM, Army Power Division, Fort Belvoir.

³ The US Army Signal Research and Development Laboratories, Fort Monmouth, NJ. Now known as the US Army RDECOM, Army Power Division, Fort Monmouth.

1.2.1 Fuel cells

Fuel cell development has seen significant progress in the last several decades because of increased recognition of the need to improve energy efficiency and to address environmental concerns, particularly those associated with mobile power applications [32]. Because fuel cells transform chemical energy directly into electrical energy, its theoretical efficiency is not limited by Carnot efficiencies associated with traditional heat engines [33]. Therefore, a fuel cell system can exhibit high fuel to electric efficiencies in comparison to most conventional heat engine cycles. Figure 1.11 provides a diagram comparing various mobile electric power technologies in the net electrical power range of 1 to 500 kWe [34] and shows that fuel cell power system in this power range have efficiency advantages over other power technologies. Additionally, the emission from fuel cell power systems will be reduced due to reduced fuel consumption and also because combustion does not take place with its associated pollution such as: thermal NO_x generation, carbon monoxide, unconverted hydrocarbons and particulate emissions.

1.2.2 Fuel cell types for mobile applications

Fuel cells are electrochemical devices for converting chemical energy into electrical direct current energy. Typically, fuel cells react hydrogen and oxygen in the presence of catalysts creating an electrical current with byproducts of heat and water. The physical structure of a fuel cell consists of an electrolyte in contact with an anode and a cathode.

Figure 1.12 gives a simplified schematic of a generic fuel cell using hydrogen as the anode fuel source. Fuel is fed continuously to the anode and an oxidant (usually air) is

feed continuously to the cathode. The anode electrode consists of a porous gas diffusion layer and an anodic catalysts layer. The anode conducts electrons to an external circuit and returns the electrons to the cathode where they recombine with oxygen forming water. The cathode is similar in construction to the anode and consists of a porous gas diffusion layer and a cathodic catalysts layer. The electrolyte separating the two electrodes consists of a solid matrix having ion-conducting properties. There are many different types of fuel cells being developed for many power applications. Fuel cell types are usually designated by the type of electrolyte used. Table 1.1 provides a listing of the major types of fuel cells and some characteristics of each.

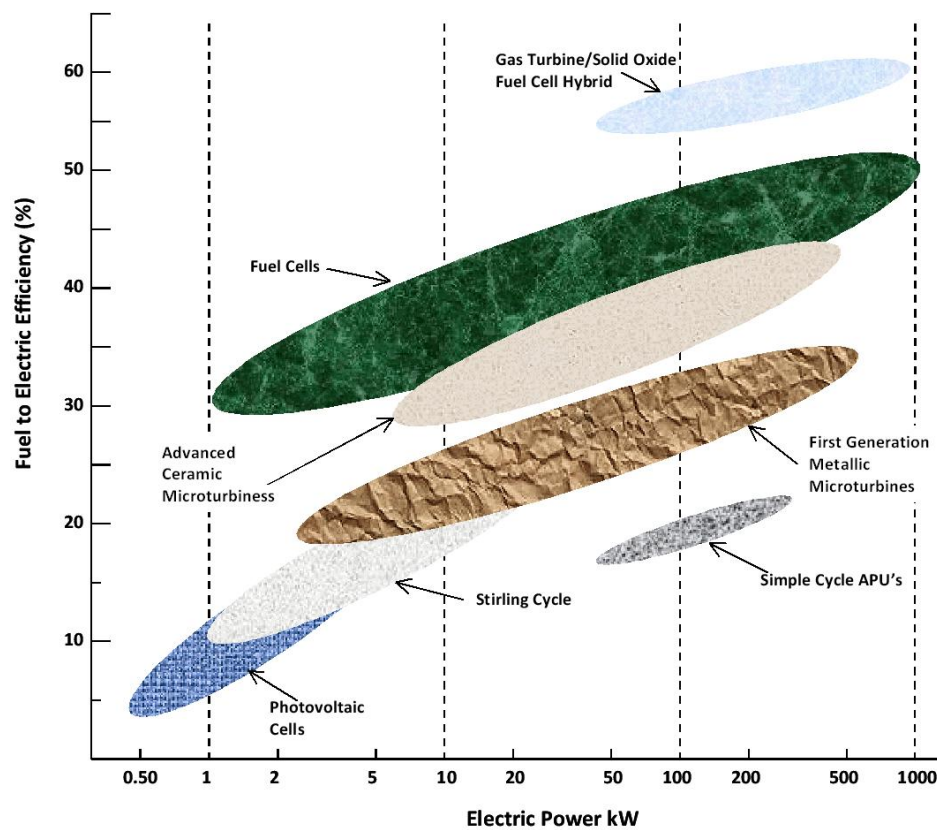


Figure 1.11 Comparisons of Electric Power Technologies [34].

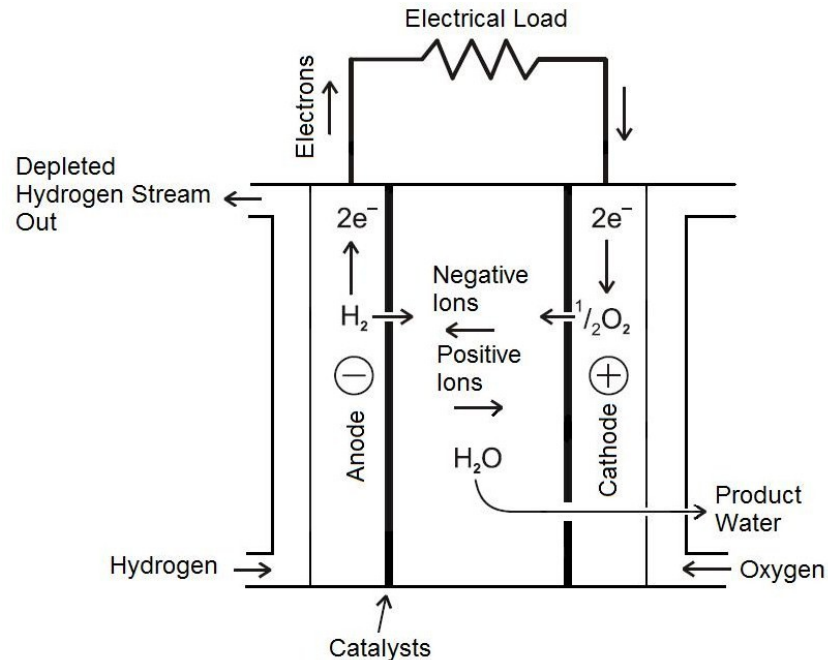


Figure 1.12 Simplified Schematic of Fuel Cell

1.2.2.1 Proton exchange membrane fuel cell and solid oxide fuel cell

Of the six types of fuel cells presented in Table 1.1 the two candidates most applicable to multi-kW mobile applications are the proton exchange membrane (PEMFC) and the solid oxide fuel cell (SOFC). The primary difference between these two types of fuel cells is their electrolyte which dictates their operating temperature. Figure 1.13 provides a simplified schematic of their operation and ion transport. A PEMFC transports hydrogen ions (H^+) and typically operates in the temperature range of 60°C to 80 °C with nafion membranes (low temperature PEM) and can operate as high as 180 °C (high temperature PEM) when the electrolyte is phosphoric acid doped polybenzimidazole membranes (PBI-membranes). In a SOFC, the transport of oxygen ions (O^{2-}) through a ceramic membrane requires temperatures in the range of 800°C to

Table 1.1 Comparison of Fuel Cells

	Proton Exchange	Direct Methanol Fuel Cell	Alkaline Fuel Cell	Phosphoric Acid Fuel Cell	Solid Oxide Fuel Cell	Molten Carbonate Fuel
Applications	Automotive power, portable power, small scale stationary (mW to multi - kW)	Portable/mobile power for < 500W	Portable power source	Portable power, small scale stationary, cogeneration	Auxiliary power units, stationary power (Watt to multi-kW), cogeneration	Auxiliary power units, stationary power (sub-MW), cogeneration
Electrolyte	Polymer membrane, proton mobile, electrolyte immobile.	Polymer membrane, proton mobile, electrolyte immobile.	Solution of concentrated (30-50%) KOH in water	Liquid concentrated 100% phosphoric acid retained in a matrix of silicon carbide particles held by PTFE.	Solid oxide ceramic yttrium-stabilized zirconium dioxide (ZrO_2/Y_2O_3)	Liquid molten carbonate (Li_2CO_3/K_2CO_3 or Li_2CO_3/Na_2CO_3) retained in a ceramic matrix of $LiAlO_2$
Operating temperature range	50 -100°C	25-90°C	50-200°C	150-220°C	600-1000°C	600-700°C
Charge carrier through electrolyte	H^+	H^+	OH^-	H^+	O^-	CO_3^-
Catalysts	Platinum (Pt, Pt/Ru)	Pt/Ru on anode, Pt on cathode	Platinum	Platinum	Nickel, Perovskites	Nickel
Primary fuel	H_2	Methanol (CH_3OH)	H_2	H_2	H_2 , CO , CH_4	H_2 , CO , CH_4
Fuel cell efficiency	50-60%	20-30%	50-60%	55%	60-65%	55-65%
Reformer	External	N/A	External	External	Internal and/or external	Internal and/or external
Status of development	Prototype and early commercial products in the 10's W to multi-kW.	Early commercial products in <20W size and prototype up to 100W	Commercialized for unique applications.	Numerous 250 kW systems have been demonstrated and some up to MW size.	Demonstration system in the low multi-kW to 300 kW.	Commercial/pre-commercial units available in the 250 kW, 1 M We and 3 MWe sizes.

1000°C. The advantages of PEMFC for mobile applications are short start-up and shutdown times, and because of the low operating temperatures, low cost materials can be used. Because of these advantages, this type of fuel cell is being explored for future automotive propulsive power and stand alone power applications [35,36,37,38,39]. However, for PEMFCs, carbon monoxide is a reversible poison which deactivates the anode electrode catalysts severely reducing performance. Carbon monoxide tolerance level is low (10 ppm CO for low temperature PEM and 1-2% CO for PBI high temperature PEM) and expensive CO management process step(s) have to be used when reformed hydrocarbon fuels. The SOFC, because it is an oxygen ion transport fuel cell, CO is not a poison but a fuel. This makes the SOFC more compatible with reformed hydrocarbon fuels. The drawback of SOFC's for mobile applications are their slow start-up times and performance degradation under thermal cycling; both problems are associated with thermal stresses in the cells and progress is being made to ameliorate this problem.

Figure 1.14 provides a depiction of the process steps required to implement a heavy hydrocarbon fueled fuel cell with PEMFCs and SOFCs. Two process paths are indicated: path 1 is PEMFC, where additional carbon monoxide removal steps are required, and path 2, is for SOFC where the reformed fuel can usually be used without further modification. In Fig. 1.14, if the PEMFC is substituted with a high temperature PEM (PBI), some reduction in carbon monoxide process steps can be taken. All petroleum derived liquid heavy hydrocarbon fuels contain organic sulfur compounds.

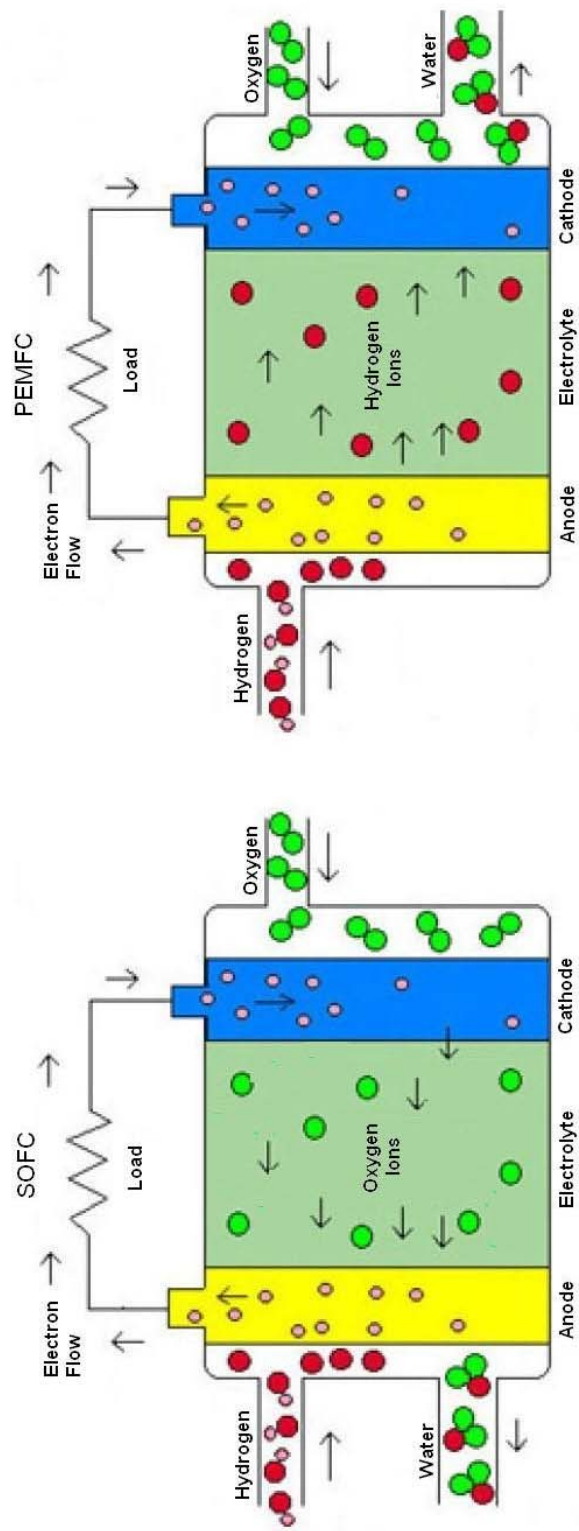


Figure 1.13 Ionic transport through the electrolyte of a PEMFC and SOFC.

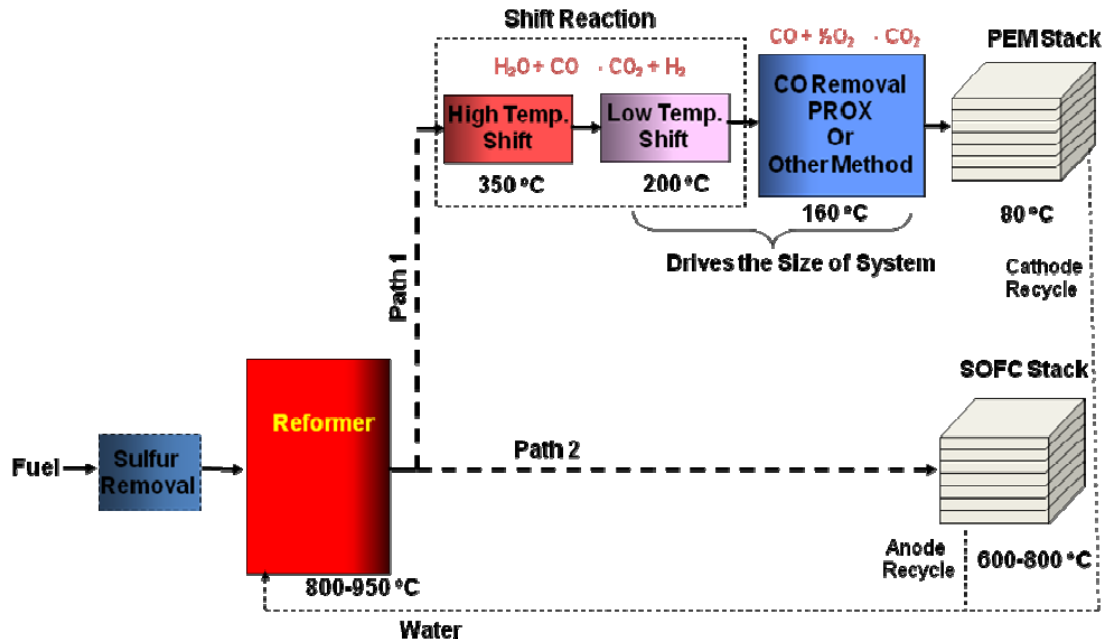


Figure 1.14 Process schemes for SOFC and PEMFC system operating on heavy hydrocarbon liquid fuels.

Sulfur has an affinity for metals. Most commercially available catalysts (reforming catalysts and fuel cell electrocatalysts) are metal based and can be deactivated when exposed to sulfur compounds. On-going research and development work is underway to improve the sulfur tolerance of reforming catalysts and electrocatalysts [40,41] (for SOFC), but at the present time sulfur absorption technologies are needed for both reforming catalysts and fuel cell electrocatalysts.

1.3 Reforming chemistries

Fuel cells combine hydrogen and oxygen electrochemically to produce electricity cleanly, efficiently, and quietly. While oxygen is typically obtained from air, hydrogen may be

extracted from a variety of primary fuels, such as natural gas, petroleum distillate fuels, or alcohols, by a process termed fuel reforming. Catalytic reforming of fuels into hydrogen and synthesis gases (H_2 and CO) has been employed in the chemical industry since the 1950's [42]. Reforming of liquid hydrocarbon fuels into a gaseous stream compatible with fuel cells requires a multi-step process that typically employs fuel desulfurization, fuel reforming (sometimes using a pre-reformer reactor step) and post-reformer step(s) to remove or convert product gases not suitable for fuel cells. For most compact mobile applications, fuel reforming is accomplished with metal catalysts that demonstrate good activity for the fuel selected [43,44,45,46]. The application of fuel cells for mobile power imposes new constraints such as size, weight, rapid transient response and variable process flows that must be addressed. The focus of the research proposed herein deals solely with the fuel reforming step.

The conversion of hydrocarbon fuels to hydrogen rich gaseous streams can be carried out by a number of different reaction processes, including: steam reforming (SR), catalytic partial oxidation (CPOx) and autothermal reforming (ATR). Figure 1.15 gives a depiction of the three primary fuel reforming techniques. Only the primary reforming step is depicted, as any additional processing steps will be dictated by the type of fuel cell selected. A typical reformate stream produced from these three reforming techniques is shown in Table 1.2.

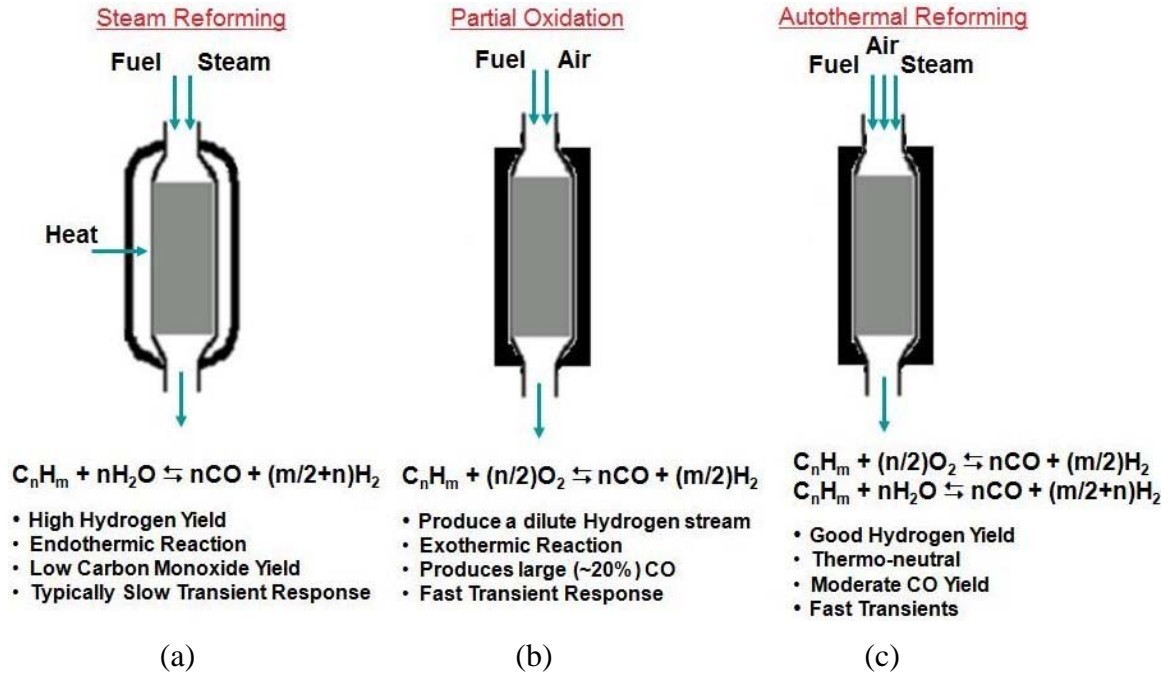


Figure 1.15 Leading reforming techniques and their characteristics.

Table 1.2 Typical reformat streams by reforming technique

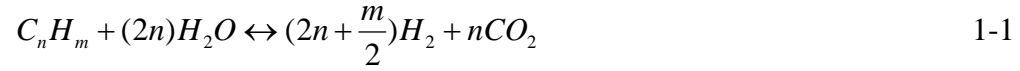
Product per mole of fuel fed to the reformer	Steam Reformer (SR) ^a		Autothermal Reformer (ATR) ^b		Catalytic Partial Oxidation (CPO _x) ^c	
	mol/hr	mol %	mol/hr	mol %	mol/hr	mol %
H ₂	2.52	71.7	1.61	41	1.05	26.7
CO	0.43	12.3	0.6	15.2	0.95	24.3
CH ₄	0.01	0.3	0.02	0.4	0.03	0.7
CO ₂	0.56	15.9	0.39	9.9	0.01	0.4
N ₂	0	0	1.33	33.8	1.88	47.8

a Operating at 700 °C and S/C = 2.0

b Operating at 700 °C, with thermoneutral air feed and stoichiometric H₂O

c Operating at 800 °C and an O/C = 1.

Steam reforming, shown in Fig. 1.15 (a) involves the catalyzed reaction of steam with fuel. The steam reforming reaction for n-dodecane is shown below:



$$\Delta H_{R(C_{12}H_{26})} = +1371.4 \text{ kJ/kmol}$$

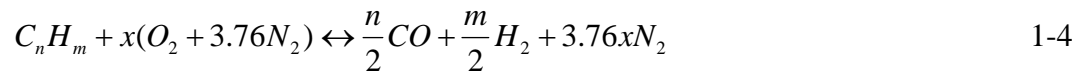
As shown above in Eqn. 1-1, the SR reaction is strongly endothermic and the reaction must be carried out in a furnace, micro-channel heat exchanger reactor or other apparatus at elevated temperatures. Almost all industrial production of hydrogen is through SR of natural gas which occurs at around 775 °C and 30 atm [47]. Typically, excess steam, beyond the stoichiometric ratio, is used to minimize solid carbon formation which can occur via thermal cracking (Eqn. 1-2) or through the Boudouard reaction (Eqn. 1-3).



Carbon formation is an insidious problem in fuel reforming and can lead to catalysts deactivation. Figure 1.16 shows a ternary carbon-hydrogen-oxygen diagram depicting carbon deposition limits for several reactor operating temperatures. The carbon rich side corresponds to the carbon deposition region at each temperature. Steam reforming is

typically characterized by high hydrogen concentrations, long residence times and slow transient responses to step changes in product demand. Negative characteristics include the need to provide external heat input through conductive materials (reactor walls, water vaporizer walls). However, recent advances in reactor design have demonstrated that with improved heat transfer, transient responds and residence times can be greatly improved [48]. Also, steam reformers typically require quantities of water, greater than are produced from a fuel cell, resulting in the need for importing water from an external source. For heavy hydrocarbon steam reforming the quantity of water on a mass basis is four to six times the fuel mass consumed [49]. Therefore, for mobile applications steam reforming is usually not attractive.

Partial oxidation, shown in Fig. 1.15 (b), involves the reaction of oxygen in air with fuel to produce hydrogen and carbon monoxide. In partial oxidation the oxygen to fuel ratio is typically around one-third the stoichiometric quantity needed to achieve full oxidation. The reaction for n-dodecane is shown below:



$$\Delta H_{R(C_{12}H_{26})_{at \frac{x}{n}=1}} = -1035.4 \quad \text{kJ/kmol}$$

As shown by the heat of reaction above, this is an exothermic reaction. The reaction usually takes place in the presences of a catalysts, but can be accomplished without a

catalysts but at much higher temperatures. Reaction rates are much faster than with SR, but the hydrogen product concentration is much lower typically around 25%⁴ versus 72%⁴ for SR. The bulk of the reformat products is nitrogen (typically ~50%⁴) from air which does not participate in the reactions in catalytic partial oxidation (CPOx). Because of its fast reaction rates, CPOx reactors are usually small compared to SR and have very good transient response (for power systems this translates into fast start-up and good load following characteristics).

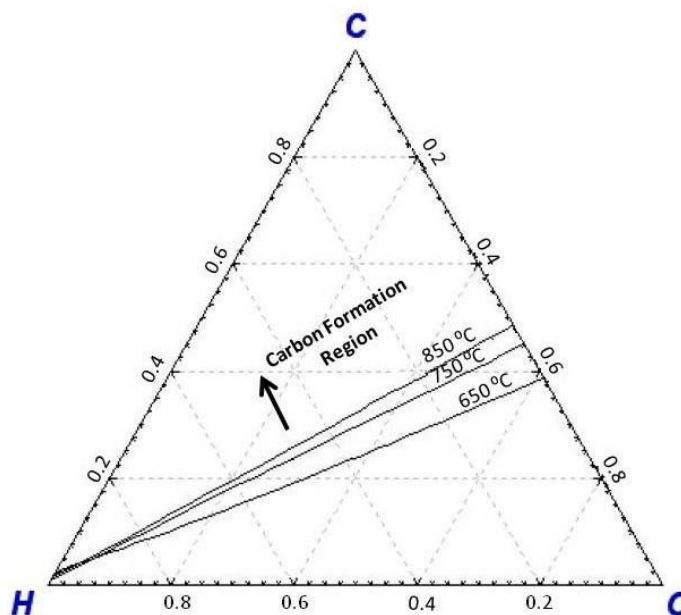
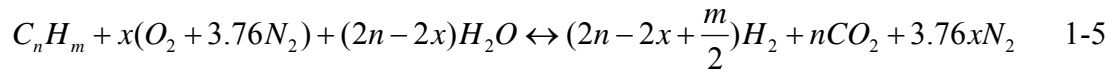


Figure 1.16 Ternary diagram showing carbon formation boundaries for selected temperatures.

⁴ Percentages are given as molar percentages on a dry basis (i.e. with water removed).

Autothermal (ATR) reforming, shown in Fig. 1.15 (c), involves the reactions of oxygen, steam and fuel. This reforming process can be thought of as a combination of SR and CPOx. The ideal chemistry equation is as shown below:



where, x is the oxygen-to-fuel molar ratio. When x is equal to zero, Eqn. 1-5 reduces to the SR equation (Eqn. 1-1). The reactions associated with ATR consist of an oxidative exothermic reaction and an endothermic steam reforming reaction. The overall reaction can be either exothermic or endothermic depending on the molar ratio of oxygen-to-carbon (x/n). Assuming an adiabatic reactor, the thermal neutral point for catalytic partial oxidation results in an oxygen-to-carbon ratio of approximately 0.46. To account for the sensible heat in the reformat gas stream and reactor thermal losses the carbon-to-oxygen (O/C) ratio is typically around 1.0.

The design of fuel reforming reactors for heavy hydrocarbon fuels is constrained by the need to avoid excessive operating temperatures, localized oxygen deficiencies and the need for good axial heat transport from exothermic reactions to endothermic reactions. The kinetics of the partial oxidation reaction [3] is much faster than that of steam reforming [1], therefore, the energy liberated via the partial oxidation reaction tends to occur in the front end of the reactor followed by steam reforming in the middle and back end of the reactor [50,51]. In order to maintain acceptable operating temperatures in the

front end of the reactor and provide necessary heat to the tail end of the reactor, good thermal transport is needed. Additionally, within the reactor poor mixing of fuel and oxygen can create localized areas with high oxygen-to-carbon ratios which can lead to high localized temperatures ($>1200\text{ }^{\circ}\text{C}$). High temperature operation of fuel reformers can affect catalysts durability due to catalysts sintering⁵, catalysts vaporizing and failure of supporting support structure (typically ceramic cordierite monoliths). Conversely, localized oxygen deficiencies can result in hydrocarbon pyrolysis resulting in solid carbon formation that can quickly deactivate reforming catalysts and plug the reactor [52,53,54,55]. In order to assure acceptable operation of catalytic reactors, both good heat transfer and mass transfer must be achieved. Recent research has shown that for heavy hydrocarbon liquid fuels being reformed by a catalytic processes the reactions are heat and mass transfer limited [56,57,58,59,60,61]. Therefore, improvements to heat and/or mass transfer are likely to result in improved performance.

1.4 Oxygen enrichment of air

As can be seen from Eqn. 1-4, for most terrestrial applications oxygen for the partial oxidation reaction comes from air. Air consists of approximately 78.08% nitrogen, 20.95% oxygen, 0.93% argon, 0.035% carbon dioxide and 0.005% other gases (for simplicity air is shown at 79% N_2 and 21% O_2 in Eqn. 1-4). Over 79% of air consists of gases carried through the fuel reforming process that do not participate in the reforming

⁵ Catalyst sintering refers to the mobility of catalysts materials at elevated temperatures where the catalysts tend to agglomerate. This greatly reduces the active surface area and results in a loss of overall catalysts activity.

reactions. These additional gases place a burden on processing equipment (parasitic power requirements), result in over sized components which negatively impact system size, weight, cost and thermal losses. Recent developments in membrane technology have made oxygen enrichment of air practical for mobile applications. There are two primary approaches to oxygen-enrichment of air for mobile applications: polymeric membranes and ceramic membranes. Membranes can separate a feed gas (in this case, air) into a permeate (O_2 rich) and a retentate (N_2 rich) through a number of mechanisms, such as: a pressure difference, a concentration difference, a chemical potential difference, or an electrical potential difference [62,63]. Polymer membrane-based air intake systems operate at ambient temperatures and have been used successfully as oxygen enrichment systems for internal combustion engine applications and for nitrogen enrichment purposes providing an inert gas blanket in aircraft fuel compartments [64]. Ceramic membranes often referred to as oxygen transport membranes, are fabricated from a ceramic oxide material with the perovskite crystal structure and operate at elevated temperatures (700 – 800 °C) [65]. The membrane material is designed to conduct both oxygen anions (O^{2-}) and electrons (e^-). Under the influence of an oxygen partial pressure gradient, oxygen ions move through the dense, nonporous membrane lattice at high rates with very high selectivity [63]. Recent developments with both ceramic and polymeric membranes make the application of oxygen enrichment of air for combustion and reforming purposes feasible and of practical interest.

1.5 Research objective and approach

The objective of the research herein is to investigate the characteristics of oxygen-enriched fuel reforming. Nitrogen represents 30% to 50% (molar basis) of the reformat flow from a heavy hydrocarbon fuel reformer. Reducing the amount of nitrogen in the process flow stream will have a significant positive effect on both the fuel cell system (reducing parasitic pumping power, reducing the physical size of all process components and their associated heat losses, and will ultimately result in a reformat stream with high concentrations of hydrogen resulting in improved fuel cell stack performance) and on the heat and mass transfer characteristics within fuel reformers. The proposed research program will focus on conducting experimentation to gain insight into the effects of oxygen enrichment on fuel reformers while also evaluating system level effects through analytical modeling.

The proposed research will focus on oxygen enriched reforming of hydrocarbon fuels with a goal of gaining insight into jet fuel, oxygen enriched fuel reforming. A detailed survey of relevant literature and technical discussion is presented in Chapter 2. The experimental design and equipment are described in Chapter 3. A thermodynamic analysis of enriched oxygen reforming is presented in Chapter 4. Jet fuels are middle-distillate fuels consisting of many hydrocarbons that are broadly defined in terms of boiling point range, aromatic content, heating value, sulfur content and other physical characteristics. The broad definition of these fuels makes definitive conclusions difficult; therefore, the use of well defined surrogate was used to evaluate reformer performance.

The use of simplified surrogate fuels for research purposes is a well recognized and accepted approach for combustion and fuel reforming research. The approach used to determine the selected surrogate fuel along with experimental results is presented in Chapter 5. Result and discussion of both air and oxygen enriched reforming of jet fuel is presented in Chapter 6. Chapter 7 summarizes our findings and conclusions and also makes recommendations for future work.

Chapter 2

Scientific Background and Technical Discussion

2.0 Introduction

This chapter will provide a historical backdrop on prior work occurring in fuel reforming; focusing on catalytic partial oxidation and autothermal reforming of middle distillate liquid hydrocarbon fuels (i.e. diesel, jet fuels and model fuel hydrocarbon components). Recent advances in fuel cell technology have heightened the interest in the reforming of supported infrastructure fuels as a means of producing hydrogen. Some discussion on alternative hydrogen generation and storage techniques is also presented to highlight the status of these competing technologies. Additionally, some discussion on catalysts historical development and use, catalysts material selection, catalysts deactivation resulting from solid phase carbon formation is presented. Published results relevant to oxygen enrich reforming will also be discussed. Not covered in this chapter are pre and post reforming processes such as: water-gas-shift reactors, preferential oxidation reactors used in post reforming reformat clean-up, pre-reformers, and desulfurization technologies.

2.1 Overview of hydrogen production for fuel cells

Fuel cells are electrochemical devices that are analogous to batteries except that the electrodes are not consumed in reactions and the fuel and oxidant are continuously

supplied to the anode and cathode, respectively. For fuel cell applications the preferred anode feed stream is hydrogen, a hydrogen rich reformat stream, or a hydrogen rich synthesis gas (H_2 and CO) stream for high temperature fuel cells. These preferred anode feed streams are not widely available and do not have infrastructure support, therefore, they must either be created from available fuels and stored at the point of use or converted *in-situ* at the point of use via fuel reforming using existing infrastructure fuels.

2.2 Hydrogen storage for mobile applications

As a result of its low molecular weight and high molar heat of combustion, hydrogen is a very attractive fuel on a unit mass basis. However, the low density of hydrogen in gaseous and liquid states results in hydrogen having a very low energy density compared to other alternative fuels, as shown in Table 2.1 [66]. Hydrogen is often cited as one of the most abundant elements in the universe. However, it readily reacts with other elements and does not naturally exist in quantity as diatomic hydrogen on earth. Therefore, energy must be expended to separate hydrogen from other chemically bound atoms (e.g. water, hydrocarbons). At standard conditions (101,325 Pa and 293.15 °C), 1 kg of hydrogen occupies a volume of 11 m³ resulting in a very low energy density of 0.003 kW-hr/L (on a lower heating value basis). Therefore, to increase the storage energy density, hydrogen must be stored as a compressed gas, liquefied, stored in other materials (such as metal hydrides, chemical hydrides, carbon nanotubes, etc.), or extracted from other hydrogen containing materials or liquids such as alcohols or hydrocarbons. Table 2.2 shows a number of potential sources of hydrogen based on 150

Table 2.1 Properties of hydrogen compared to other common fuels

	Hydrogen	Gasoline	JP-8	Methane	Methanol
Boiling point, (°C)	-253	77-127	163-371	-161.5	64
Liquid density, (kg/m ³)	70.8	~700	~753	425	797
Gas density, (kg/m ³)	0.08	~4.7	1.15	0.66	—
Heat of vaporization, (kJ/kg)	444	~300	~441	577	1168
Heat of combustion, (MJ/kg)	120	44.5	42.8	50	20.1
Heat of combustion, (MJ/m ³)	8960	31,170	37,792	21,250	16,020
Autoignition temperature, (°C)	585	222	257	534	385

Table 2.2: Comparison of Hydrogen Fuel Systems for Mobile Applications (based on 150 kW-hr energy storage)

	Compressed H2 (5 kpsi)	Compressed H2 (10 kpsi)	Liquid H2	Metal Hydrides (Fe Ti)	Methanol Reformer (SR)	JP-8 Reformer (ATR)
H2 Vol. Density	19.1 g H ₂ /L	31.0 g H ₂ /L	36.4 g H ₂ /L	36 g H ₂ /L	29-37 g H ₂ /L	37-45 g H ₂ /L
Fuel Volume for 10 kg H ₂	523.6 L	322.6 L	274.7 L	277.8 L	270-345 L	270-345 L
Fuel System H2 Mass Fraction	Current: 3.5-4.5 wt% Near term: 7-9 wt%	Current: 3.3-4.3 wt% Near term: 6-8 wt%	3.8-7.9 wt%	1.1-1.6 wt%	~7.9 wt%	~14.2 wt%
H2 Purity	99.9 %	99.9 %	99.9 %	99.9 %	75 %	30%
Recharge Time	< 2 min. (to 99% useable capacity)	< 2 min. (to 99% useable capacity)	< 2 min. (to 80% useable capacity)	> 30 min. to 80% capacity	< 2 minutes	< 2 minutes
Specific Energy, Net Energy Basis (kWh/kg)	0.74	0.74	0.54	0.21	0.79	1.39
Energy Density, Net Energy Basis (kWh/kg)	0.28	0.46	0.37	0.51	0.69	1.37

kW-hr (540 MJ) of energy storage. Also, shown is the volume required to store 10 kg of hydrogen which is approximately the amount of hydrogen needed for automotive applications. Automotive use of fuel cells as prime power sources continues to receive substantial attention and research support, where the current preferred approach is to carry hydrogen in a compressed or liquid state. Hydrogen can be produced from hydrogen rich infrastructure fuels or via electrolysis at the point of use or at localized plants and then distributed to the local fueling stations. Under this scenario, development of an onboard hydrogen storage system is critical and is an active area of research and development [67,68]. For mobile applications energy density and specific energy are important design factors. Specific energy relates to the weight of the energy conversion device and fuel on a unit kW-hr basis. Energy density compares the size of the energy conversion device and fuel on a unit kW-hr basis. On the basis of specific energy and energy density the reformed fuel approach presents advantages over other methods of carrying and/or chemically generating of hydrogen. In operating environments where ready supplies of hydrogen or chemical hydrides are not available, reformed infrastructure fuels are the only alternative.

2.2.1 Gaseous hydrogen storage

Hydrogen has excellent specific energy density at standard pressure and temperature; higher than any other fuel. However, it has very poor energy density due to its low density. In order for hydrogen to compete with hydrocarbon fuels in terms of energy

density it must be stored under pressure, in a liquefied form, or a hybrid approach of cyro-compressed hydrogen storage. This requires material and design improvements in order to ensure tank integrity and to minimize hydrogen losses. Specially, carbon composite tanks are being pursued for both 35 MPa and 70 MPa tank pressure options [69]. These tanks require specialty liners to avoid reactions between hydrogen and the composite materials and will require pressure controls to accommodate a variable pressure delivery [70]. Achieving higher pressures is energy intensive and will have a negative impact on overall efficiency of the approach. Modern large scale compressor typically have an iso-thermal compression efficiency of approximately 70% [71] and multistage “adiabatic” compressor can achieve up to 93% efficiency [72]. In addition, to compressed hydrogen tanks, two other approaches are being explored: 1) cryo-compressed tanks and 2) conformal tanks. Cryo-compressed tanks are a combination of compressed liquid hydrogen with compressed gaseous hydrogen in the tank headspace [73]. This approach allows you to achieve liquid hydrogen densities at higher hydrogen storage temperatures ($-196\text{ }^{\circ}\text{C}$) which reduces heat transfer into the tank and minimizes hydrogen loss through venting. Conformal tanks used with compressed hydrogen consist of tanks with internal material structures which provide both strength and better thermal properties. Conformal tanks also can be fabricated to fit non cylindrical spaces opening up the possibility to take advantage of available space [74]. Volumetric capacity, high pressure and cost are key challenges for compressed and cryo-compressed hydrogen storage.

2.2.2 Liquid hydrogen storage

The energy density of hydrogen can be improved by storing hydrogen in the liquid state. However, the liquefaction of hydrogen is complex requiring the use of multiple compression and expansion cycles (e.g. Joule-Thompson cycle) to condense the gas to below its condensation temperature of -252.9°C (at 1 atm) [75]. Liquid hydrogen tanks are well insulated and vented to prevent excessive pressure buildup [76]. Liquid hydrogen is widely used today for storing and transporting hydrogen and can store more hydrogen in a given volume than compressed gas tanks. The volumetric capacity of liquid hydrogen is 0.070 kg/L, compared to 0.030 kg/L for 10,000 psi gas tanks. However, the issues with liquid hydrogen tanks are hydrogen boil-off, the energy required for hydrogen liquefaction, and tank cost [74]. Storage tanks must be well insulated to minimize boil off and insulation adds significantly to size and the cost of this approach. Typically, hydrogen boil-off constitutes approximately 1-3% of hydrogen stored per day and is strongly influenced by ambient conditions, tank insulation, tank size, and dormancy (non-use) of the hydrogen during the day. Even assuming that hydrogen boil-off is minimized, the energy needed to liquefy hydrogen is typically around 30% of the lower heating value of the storage hydrogen. For most mobile application the higher energy consumption associated with liquefying hydrogen is the primary issue resulting in high fuel cost and fuel cycle energy efficiency. In addition, safety concerns related to hydrogen boil off limit applications to well ventilated applications.

2.2.3 Solid hydrogen storage

Hydrogen can be adsorbed onto certain high surface area materials, like carbon nanotubes, that have the advantages of fast hydrogen kinetics and low hydrogen binding energies resulting in easier thermal management during charging and recharging [77,78]. Single-walled carbon nanotubes (SWNT) were reported as hydrogen storage materials with hydrogen gravimetric capacities in the range of 3-10 wt% at room temperature. However, there has been continued difficulty in the measurement of hydrogen storage capacity in SWNT and in reproducing results. Recent results at the National Renewable Energy Laboratory (NREL) show that while no hydrogen storage was observed in pure single-walled carbon nanotubes, roughly 3 wt% was measured in metal-doped nanotubes at room temperature [79]. For many mobile applications, the room temperature gravimetric hydrogen storage capacity performance target is typically around 6 wt% hydrogen [74]; therefore, further research and development will be required before nanotubes are competitive options. In addition, low cost, high volume manufacturing processes must be developed for this technology to be economically attractive for mobile applications.

2.2.4 Metal hydrides

Under appropriate conditions, most metals will react with hydrogen to form metal hydrides. Some metal hydrides have the potential for reversible or hydrogen decomposition reactions, which is needed for practical mobile applications. Group A I, II, and III elements, (e.g. Li, Mg, B and Al) form a large variety of metal-hydrogen

complexes. Table 2.3 provides examples of metal hydride compounds along with their theoretical maximum hydrogen absorption potential (wt% hydrogen; where, wt% hydrogen is the amount of hydrogen absorbed to material weight)[66,80, 81,82,83,84]. As seen in Table 2.3, the lighter element metal hydrides give the highest hydrogen absorption and are, therefore, viewed as the best technology candidates for mobile applications. Key issues with metal hydrides for hydrogen storage are reversibility, favorable thermodynamics and fast kinetics.

Formation and decomposition of a metal hydride is represented in the following equation:



Where, M is a metal and ΔH_f^0 is the enthalpy of formation of the metal hydride ($MH_{2(s)}$).

Equation 2-1, as written, is for hydrogen formation. A condition for thermodynamic stability of metal hydrides is that $\Delta H_f^0 > 0$; the larger ΔH_f^0 , the more stable the compound. Stability of absorbed hydrogen materials gives an indication of their tendency to release hydrogen spontaneously or “leak” hydrogen (less stable materials result in more hydrogen released). This also shows that hydrogen absorption is exothermic and that for good operation good heat transfer is needed. For hydrogen decomposition (Eqn. 2-2 read from right to left) the enthalpic term will be the same magnitude but opposite in sign:

$$\Delta H_d^0 = -\Delta H_f^0 \quad 2-2$$

Table 2.3 Comparison of some metal hydrides

Materials	Maximum wt% H ₂	T _d (°C)	Ref.
LiBH ₄ /½MgH ₂	11.4	400	[80]
NaAlH ₄ (Ti)	5.5	35-130	[81]
NaAlH ₄ (TiCl ₃)	4	100-125	[82]
NaAlH ₄ (TiO ₂)	5.5	125	[83]
MgH ₂ /2LiH ₂	5.6	180-200	[84,82]
Mg ₂ NiH ₄	3.6	ambient	[83]

Where, ΔH_d^0 is the metal hydride decomposition enthalpy. A simple thermodynamic relationship (pure metal hydride at equilibrium pressure) for the minimum temperature needed to achieve decomposition of hydrogen is given in Eqn. 2-3 below:

$$T_d = \frac{\Delta H^0}{\Delta S^0} \quad 2-3$$

Here, ΔS^0 is the entropy change associated with the formation of the metal hydride. For many mobile applications, being able to absorb and desorb hydrogen under prevailing environmental conditions is usually desirable and considering Eqn. 2-3 you will want to minimize ΔH^0 or look at less stable metal hydrides.

Another means of reducing hydrogenation-dehydrogenation, is to add additional chemical species that destabilizes the metal hydride. An example of this is the additional of MgH₂

to LiBH_4 . The addition of MgH_2 to LiBH_4 reduces the hydrogen absorption capacity of LiBH_4 from 13.6 wt% to 11.4 wt%, but drops the hydrogenation-dehydrogenation enthalpy from 67 kJ/(mol H_2) to 42 kJ/(mol H_2) [80]. Active research is underway via experimentation and atomic modeling to evaluate combination of materials that may be able to balance high hydrogen absorption at ambient temperatures with fast kinetics [85,86,87].

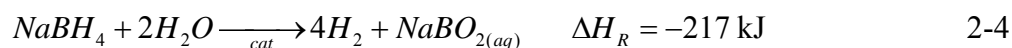
2.2.5 Chemical hydrides

Chemical hydrides are materials that produce hydrogen through reactions with other substances. Many chemical hydrides can produce hydrogen rapidly with the help of catalysts and chemical stabilizers. This type of hydrogen storage also exhibits very high gravimetric energy density and is stable. However, most materials currently being developed are not reversible *in-situ* and many cannot be recycled. Additionally, there can be substantial size and weight requirements associated the chemical hydride reactor which can significantly reduce the gravimetric and volumetric energy densities. Two of the most promising chemical hydrides are sodium borohydride (NaBH_4) which produces hydrogen via hydrolysis and ammonia borane (NH_3BH_3) where a dehydrogenation (thermolysis) reaction produces hydrogen.

2.2.5.1 Hydrolysis reactions

Hydrolysis reactions involve the oxidation reaction of chemical hydrides with water to produce hydrogen. A stabilized aqueous solution of sodium borohydride is a safe, simple

and compact source of high-purity hydrogen. Schlesinger et al. [88] have reported that alkaline borohydride solutions undergo hydrolysis in the presence of various transition metal catalysts to produce hydrogen. Based on this, various catalysts such as Pt, Ru, Ni, Co, etc. have been developed for hydrogen production from borohydride solutions [89, 90, 91, 92]. The reaction of sodium borohydride has been widely studied, can theoretically produce hydrogen at 10.8 wt% and is a leading chemical hydride candidate. This reaction is shown below in Eqn. 2-4:

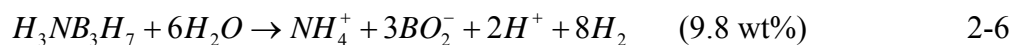
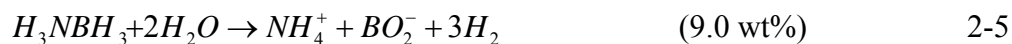


The exothermic reaction of sodium borohydride with water produces hydrogen gas and sodium metaborate. The uncatalyzed reaction is very slow, but with the use of catalysts, the reaction rate can be easily controlled to produce hydrogen at varying rates or “on demand”. The hydride is sensitive to moisture and needs to be stored and transported in an inert stabilizing liquid. The exothermic reaction in Eqn. 2-4 does require good thermal management of the reactor system. The reaction can be carried out on a catalyst in an aqueous medium of typically, 30 wt% NaBH₄ in water [93]. The byproduct of the reaction produces NaBO₂ which is carried on-board and must be removed for regeneration. Millennium Cell, Inc. has reported that their NaBH₄ based hydrogen on demand system possessed a system gravimetric capacity of about 4 wt% [94].

Sodium borohydride hydrolysis is a promising hydrogen generation approach, however additional development work is needed to improve reactor designs, catalysts efficiency, and reaction controllability. Recycling sodium borohydride and the use of fuel cell generated water are ways to help meet certain weight limitations for fuel cell applications. Cost effective production of sodium borohydride and the catalysts used is also essential to the future of this method. Additionally, other chemical hydrides such as lithium borohydride, calcium hydride and sodium aluminum hydride are also being investigated and may contribute to a chemical hydride hydrogen storage solution [95, 96, 97].

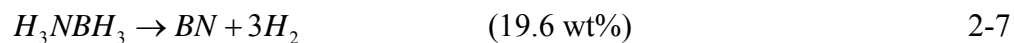
2.2.5.2 Thermolysis of ammonia borane (NH₃BH₃)

Ammonia borane (AB) is a very promising hydrogen storage materials due to its high hydrogen storage of 19.6 wt% [98]. Ammonia borane is a colorless solid that melts at 110 °C – 114 °C, but is stable at room temperature. There are two main methods to release hydrogen from a chemical hydride; hydrolytically and thermolytically. The requirements for hydrogen release for many mobile applications are fast kinetics, variable and controlled generation, and complete release. The area that received the most attention early was AB hydrolysis. General reactions for amine borane hydrolysis are given below in Eqns. 2-5 and 2-6:



Ammonia borane will undergo hydrolysis only very slowly at room temperature in basic water, but the rate is accelerated by lowering the pH or increasing the temperature. Most of the research in this area has focused on the search for transition-metal catalysts to increase the rate of AB-hydrolysis and to reduce the temperature needed to achieve good conversion [99, 100, 101]. Metal catalyzed hydrolysis can give fast hydrogen release with very controllable rates. This method also drives the dehydrogenation of AB to near completion. However, the use of hydrolysis as a method for hydrogen delivery for mobile applications is impractical for several reasons. AB is only moderately soluble in water resulting in a practical hydrogen storage capacity of 5 wt% (materials weight percent basis). Difficulty in regeneration of the spent fuel due to the strong B-O bonds is another reason hydrolytic hydrogen release is not well suited for mobile applications.

The simplest hydrogen release method for AB is thermal decomposition or thermolysis. Thermolysis offers several benefits over hydrolysis, with the main advantage being the system can achieve much higher material weight percent, as shown in the general reaction for AB thermolysis given below in Eqn. 2-7:



Wolf, *et al.* [102, 103] first showed that there are two exotherms occurring at different temperatures associated with hydrogen release events. The first exothermic event starts

in the temperature range of 70 °C - 100 °C. This is followed by an endothermic reaction at approximately 110 °C associated with the melting of AB. The second exothermic event is much broader and starts at around 130 °C and continues until well above 400 °C. According to Autrey, raising the temperature of reaction to above 500 °C can result in the complete release of stored hydrogen [104].

Most research in AB thermolysis has focused on increasing the extent of hydrogen release as well as the rate. Another important research area is in understanding product pathways of AB dehydrogenation; products can include cyclotriborane (one hydrogen molecule released), borazine (two hydrogen molecules released) and polymeric analogues [74]. Some of these products can have negative effect such as borazine, which can poison proton exchange membrane fuel cells.

While ammonia borane looks promising as a hydrogen storage medium, given the high volumetric and gravimetric density of hydrogen in the material, there are still technical challenges and work continues in evaluating AB in both solid state and solutions, developing an understanding of the underlying kinetics of AB dehydrogenation, and evaluation of transition metal catalysts to enhance the amount and rate of hydrogen release. Another critical area of research is developing acceptable and feasible means to regenerate AB.

2.3 Catalytic fuel reforming

Although the historic use of catalysts goes back hundreds of years it has only been in fairly recent history that scientific recognition and study of catalysts has occurred. There are two broad definitions of catalyst: homogeneous catalysts and heterogeneous catalysts. Homogeneous catalysts describe a catalytic reaction where the reactant and the catalysts are in the same physical phase (i.e. gas, solid, liquid); and conversely, heterogeneous catalysts describe reactions where the reactants and catalysts are not in the same phase. This dissertation concerns fuel reforming with heterogeneous catalysts where the catalyst is a solid (typically, metals) and the reactants are gases (hydrocarbons, steam and oxygen). Therefore, all subsequent discussions on catalysts development and use are from a heterogeneous catalysts perspective. The following three subsections will address the early scientific history of catalysis discovery, industrial use in ammonia production and in petroleum refining, and more recent use in pollution abatement in automobiles. Each of these historical topics serve as critical technology breakthroughs and provide a scientific foundation for the experimental research presented in this dissertation.

2.3.1 Early history of catalysts development

The recognition that some materials could aid in enhancing reactions was first recognized in 1836 by the Swedish chemist J. J. Berzelius in a review for the Stockholm Academy of Science [105]. Berzelius was the first to use the term “catalysis” and referred to it as a force that was present in the decomposition of chemical compounds. Metallic catalysts

had been in use earlier by Joseph Priestly and Martinus van Marum in 1800 while studying the decomposition of alcohols [106]. However, these earlier studies suggest that the purpose of the metals was only to transfer heat to the reaction. Louis Jacques Thenard and Pierre Dulong, in 1813, studied the decomposition of ammonia with a number of metals and correlated ammonia's reactivity to these metals; this was the first documented study of reactivity. Later in 1818, while working on hydrogen peroxide, Thenard concluded that some chemical substances sped up reactions without being chemically changed. Humphry Davy is credited with providing insight into the use of heterogeneous metal catalysts (platinum) and correctly concluding that gaseous oxidation reactions of "coal gas" and oxygen took place on the catalysts surface without any chemical change to the metal [107]. In 1843, Faraday published a review paper in which he stated that the reactants must simultaneously adsorb on the surface of a catalysts for reactions to proceed, however, he did not attempt to describe the reactions that take place [108].

These catalytic experimental discoveries ushered in both the industrial use of catalysts and the foundation of physical chemistry. Although catalysts had been used for some time (beer and wine production), the first, often cited, industrial use of catalysts is the oxidation of ammonia over platinum in the manufacture of nitric acid (CF Huhlmann, 1838) [109]. At around the same time, the manufacturing of sulphuric acid was achieved, where sulfur dioxide (SO_2) is oxidized with nitrous oxide as catalyst to SO_3 and then reacted with steam to sulfuric acid (Peregrine Phillips, 1831) [110]. In parallel with the

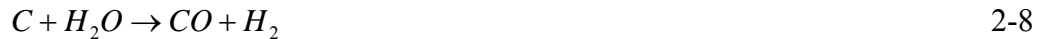
industrial development, many chemists were developing an understanding of chemical reaction phenomena, most notably among these was Wilhelm Ostwald, Professor of Physical Chemistry at Leipzig University. Ostwald provided a more complete definition of catalysts, stating that a catalysts does not change the thermodynamic equilibrium of reactant, it only affects the rate of reactions [111]. Ostwald received the noble prize in chemistry in 1909 based on his work in catalysis, chemical equilibria and reaction kinetics. He is regarded as one of the founders of classical physical chemistry and many of his students went on to have very distinguished academic careers: Svante Arrhenius (Noble Prize 1903, activation energy of reactions), Van't Hoff (Nobel Prize 1901, reaction kinetics), Walther Nernst (Nobel Prize 1920, chemical affinity)[112].

2.3.1.1 Ammonia synthesis

A significant development in the early twentieth century was the ammonia synthesis process. Sources of ammonia up until this point in time had been derived from saltpeter mined principally in Chile. Ammonia was used extensively in agriculture fertilizer and as a critical ingredient in military explosives. At the turn of the twentieth century, population growth in Europe was rising at a pace that the present available arable land and current agricultural methods would be unsustainable; leading scientific and political figures at the time were appealing to the scientific community to develop a solution to the imminent crisis. As a result, many chemists were working on a way to synthesis ammonia from atmospheric nitrogen [113]. In 1905, Fritz Haber (of the Karlsruhe Institute of Technology and later the Kaiser Wilhelm Institute for Physical Chemistry and

Electrochemistry) was able to catalytically combine atmospheric nitrogen with hydrogen forming ammonia. Initially, the process yielded only trace amounts of ammonia, but with significant catalysts research and development along with innovative engineering high pressure reactor designs, chiefly lead by Carl Bosch (mechanical and metallurgy engineer, Technische Hochschule, Charlottenburg, Germany) of BASF, an improved process was achieved that could economically produce ammonia. The development of ammonia synthesis (the Haber-Bosch ammonia synthesis process) was one of the most important inventions for mankind and also became the prototype of how science and engineering could work together to solve a global problem. Fritz Haber's scientific contribution to ammonia synthesis earned him the Nobel Prize award in chemistry in 1918. In an unprecedented decision, Carl Bosch received the Nobel Prize award in chemistry in 1931 for his innovative scientific and engineering design for the industrial production of ammonia; this award is notable in that the Nobel Prize typically goes to significant scientific discoveries and not the translation of laboratory research into practical engineering designs.

The development of ammonia synthesis also created a need for an affordable hydrogen production process. Hydrogen had been produced in small quantities through electrochemical means. This approach was not economically feasible for large scale production. As an alternative approach, coal gasification (Eqn. 2-8) in combination with the water-gas shift reaction (Eqn. 2.9) was initially used to produce hydrogen.



Later in the 1950's, steam methane reforming (SMR) was used to produce hydrogen using nickel based catalysts (Eqn. 2-10):



SMR is still the dominant method for hydrogen production representing over 95% of the total amount of hydrogen produced in the United States in 2007 [114]. A parallel development to SMR for hydrogen production was catalytic autothermal reforming (ATR). Catalytic ATR was pioneered by SBA (*Societe Belge de l'Azote*) and BASF (Badische Anilin- und Soda-Fabrik, translated to Baden Aniline and Soda Factory) in the 1930's and improved by Topsoe and SBA in the 1950's [115].

The synthesis of ammonia addressed many problem related to chemical reaction kinetic, high pressure reactor design, and catalysts analysis all of which contributed greatly to a growing need for energy as industrialization swept through Western Europe and the United States.

2.3.1.2 Liquid and gaseous hydrocarbon catalysts development

Prior to the wide industrial use of liquid and gaseous hydrocarbons, coal was the fuel resource of choice. Coal gas generated from coke production ovens, a mild pyrolysis process, was used to manufacture ethylene a significant building block hydrocarbon for plastics and synthetic lubricants. Coal was also gasified producing a syngas stream of hydrogen, carbon monoxide and carbon dioxide. Coal derived syngas was used in a number of important processes:

- the manufacture of ammonia; where the ammonia synthesis process employed iron based catalyst at elevated pressures.
- the synthesis of methanol using a chromium and manganese oxide catalysts at 450 °C and 200 atms)
- liquid fuel synthesis where the syngas is put into a Fischer-Tropsch process using cobalt, iron, and ruthenium catalysts.

Coal could also be hydrogenated to produce a liquid fuel directly using Mo, W and Co catalysts. Much of the research related to catalytic processes with coal occurred in the late 1800's and early 1900's. By the 1920's, automotive use was driving the need for gasoline and new catalytic process were developed for the conversion of liquid petroleum.

The first refinery operating on crude oil was built in 1860 in Titusville, Pennsylvania.

The refiner process was based on batch distillation to separate kerosene and heating oil out from the remaining crude oil fractions [116]. Crude oil consists principally of

paraffins which are very unreactive and when distilled do not produce high volumes of gasoline. Initially, thermal cracking was used to breakup large molecule hydrocarbons and produce more liquid transportation fuels that were in great demand. In the 1930's, Eugene Houdry, a French mechanical engineer, invented catalytic cracking which greatly improved gasoline yield and also increase the octane rating of the produced fuel (catalysts was activated clay) in comparison with gasoline obtained from petroleum distillation alone (referred to as straight run gasoline). The Houdry process was a semi-batch process and was subsequently improved in the 1940's by the Standard Oil Company of New Jersey using the Fluid Catalytic Cracking (FCC) process. The FCC process is a continuous process employing fluidized beds of silica-alumina catalysts (replace by zeolite-based catalysts in the 1960's). An outcome of catalytic processes being put into practice at refineries was that large amounts of by-products gases were being produced. This lead to the invention of a number of additional catalytic processes (i.e. polymerization, alkylation, isomerization) all aimed at converting low value gases and light hydrocarbons into higher valued hydrocarbon products. Today's refineries consist of many catalytic processes all designed to convert the crude oil feedstock into high values fuels and lubricants. Figure 2.1 provides a simplified process flow diagram of a typical refinery and the end products that are created [117]. An additional challenge that refineries are facing today are the environmental fuel composition mandates (e.g. reduced sulfur and aromatic content for transportation fuels) occurring simultaneously with the declining quality of crude oil feedstock as oil wells are reaching the end of their productive life. This has resulted in a growing demand for hydrogen at the refineries for

fuel “upgrading” (catalytic process for increasing the hydrogen content in fuels) and has resulted in refineries being the largest hydrogen consumers in the United States at 33% of total hydrogen production [118, 119].

Refinery catalytic process development over the past hundred years has been a significant driving force in heterogeneous catalysts development. Much of what is known today regarding hydrocarbon reforming can be traced back to petroleum processing and the petroleum industry which continues to grow and innovate. Global refinery catalysts sales in 2007 constitutes approximately \$3.7 billion or approximately 90% of total energy related catalysts sales [120, 121]. Annual sales growth is projected to be 3.22% from 2007 to 2012 [120]. Within the energy and environmental catalysts market, refinery catalysts sales are second to environmental catalysts which represent \$9.5 billion in global sales for 2007 and are expected to grow at an annual rate of 7.28% between 2007 and 2012 [120]. Within the environmental catalysts market, vehicular catalytic converters account for 50% of global sales.

2.3.1.3 Vehicle emissions control

The clean air act of 1970, mandated carbon monoxide and hydrocarbon emission levels in spark ignition automobiles that could not be met solely by improvements in engines designs [122]. This emission standard necessitated the use of catalytic converters placed in the engine exhaust stream. The catalytic converters were initially termed two-way converters using platinum and rhodium catalysts for the oxidation of unburned

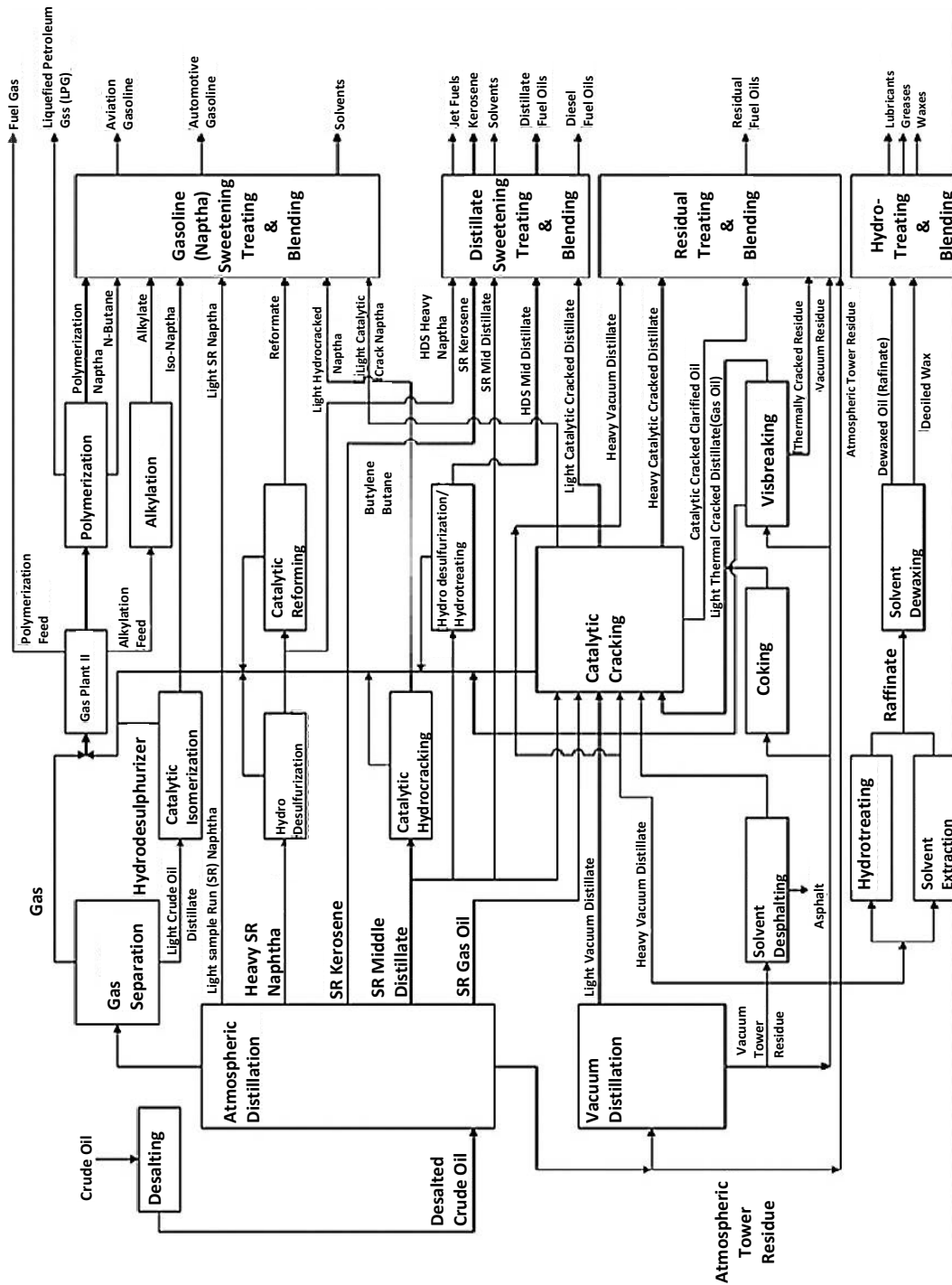


Figure 2.1 Simplified process flow diagram for a typical refinery.

hydrocarbons and the reduction of carbon monoxide via the water-gas-shift reaction (see Eqn. 2-9) [123]. The use of catalysts in the engine exhaust stream also resulted in the removal of tetraethyl lead, an anti-knock additive, from gasoline [124]; lead being a poison to many metallic catalysts. Initially (1975 – 1980), catalytic converters consisted of packed bed designs with pelletized catalysts. These early designs were not very durable in automobiles due to catalyst attrition resulting from the high shock and vibration operating environment. By 1980, most automobile catalytic converters were of the solid ceramic or metallic monolithic designs; shown in Fig. 2.2. The monolithic designs are characterized by large open frontal areas which greatly reduces pressure drop and large geometric surface area available to support catalysts. The flow down the reactor is laminar with Reynold numbers typically below 100. Catalytic reactions take place on the channel surface with reactant transport taking place via diffusion. The basic design of these reactors hasn't changed much since the 1980's, however, higher cell densities (measured as cells per square inch) are being used today [125]. ATR reactor designs based on catalytic monoliths are now being used widely in research and development for many mobile fuel reforming applications [126,127,128] and was used for all experimental work in this dissertation.

2.3.2 Liquid hydrocarbon fuel reforming

Reforming of liquid hydrocarbon fuels is receiving considerable attention due to fuel availability, infrastructure support and because sustainable low carbon emitting approaches for synthesizing middle distillates fuels (such as the Fischer-Tropsch) from

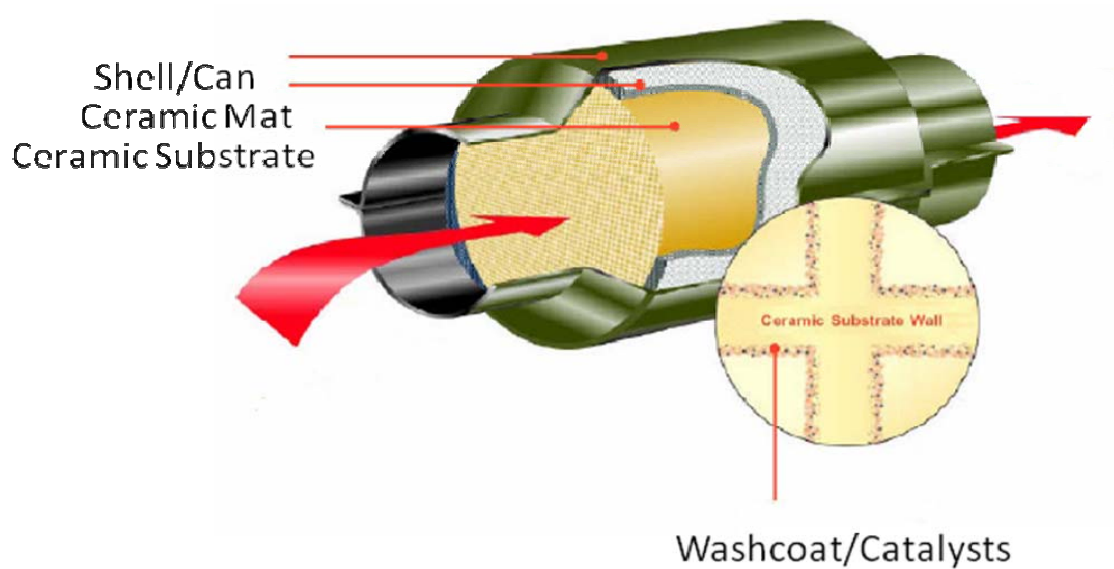


Figure 2.2 Ceramic monolith used in automotive catalytic converters.

bio-mass are being demonstrated [129, 130]. Additionally, mobile applications using diesel and kerosene based fuels (i.e jet fuels) do not lend themselves to an electric energy storage solution; so, these fuels will likely be around in some form for the foreseeable future. The next sections will address overall reactions that take place within a catalytic reactor, some discussion on middle distillate fuel reforming, ATR operating conditions, catalysts materials and challenges associated with carbon formation.

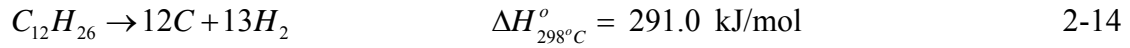
2.3.2.1 Basic overall reactions in liquid hydrocarbon fuel reforming

Although, detailed analysis of all reaction taking place during the reforming of complex liquid hydrocarbon fuels are not known, it is instructive to review a number of dominant reactions believed to strongly influence the operation of catalytic partial oxidation or

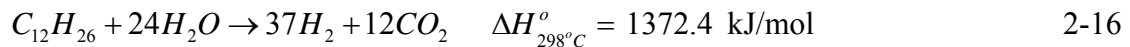
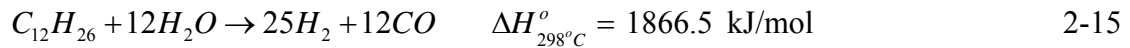
autothermal reformers. Fortunately, the field of hydrocarbon reforming has received much attention over the past fifty years and there are many good references that can be used in selecting basic reactions for analysis [131, 132, 133, 134, 135]. Additionally, for a well designed reactor, the product stream compares very closely to predicted equilibrium results at the exit temperature and pressure. For this analysis, n-dodecane ($C_{12}H_{26}$) is being used as a surrogate for the liquid hydrocarbon fuel in the equations below. Reactions shown in Eqns. 2-11, 2-12, and 2-13 consist of oxidative reactions which are believed to occur rapidly and concurrently, near the entrance of the reactor [136, 137, 138].



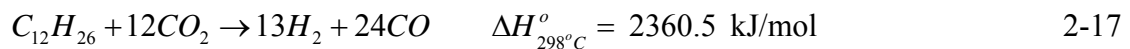
All the equations above are exothermic and are ordered from highest to lowest in terms of heat given off. Equation 2-13 is often cited as the partial oxidation equation; however, oxidation can occur completely or incompletely depending on localized conditions and concentration of reactants. In addition to oxidation, some researchers have suggested that pyrolysis reactions can also take place early in the reactor, as shown in Eqn. 2-14 below:



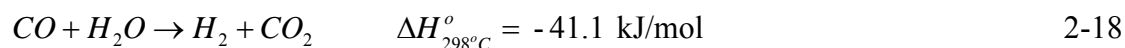
The pyrolysis reaction is endothermic and can, along with early initiation of steam reforming reactions, help to reduce the temperature at the entrance of a catalytic reactor. The pyrolysis reaction, under atmospheric conditions is favored at low temperatures. If sufficient oxygen is not present in the vicinity of a pyrolysis reaction solid carbon formation can occur which is deleterious to reforming catalysts and can lead to deactivation. Steam reforming reactions, shown below in Eqn. 2-15 and 2-16 are generally considered much slower than oxidation and tend to become more dominant from the mid-point to the end of the reactor [139].



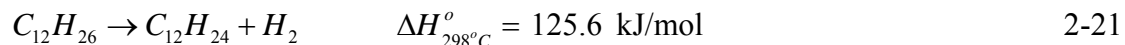
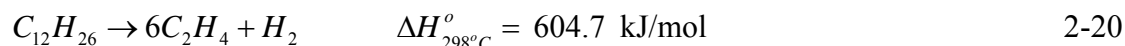
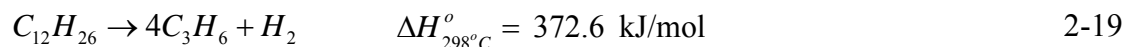
In addition to steam reforming carbon dioxide reforming, shown in Eqn. 2-17 (sometimes referred to as dry reforming) can also take place and is more endothermic than steam reforming.



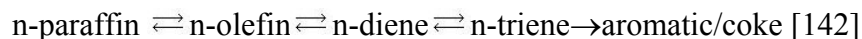
The water-gas-shift reaction is active over a wide temperature range and can occur throughout the catalytic reactor. This equation is very important in determining the final composition from a reactor. The forward reaction, shown in Eqn. 2-18, is favored at decreasing temperatures and is slightly exothermic.



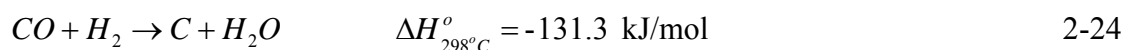
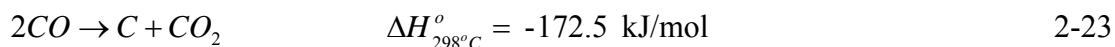
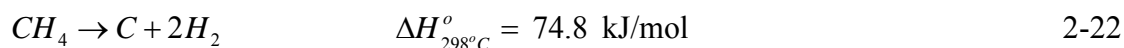
Other important side reactions can occur in catalytic reformer including dehydrogenation, thermal cracking and catalytic cracking. The preference and degree to which these reactions occur is strongly influenced by the catalysts and support structure being used. Shown below are often cited reactions representing thermal cracking (Eqn. 2-19)[140], catalytic cracking (Eqn. 2-20) [140] and dehydrogenation (Eqn. 2-21) [141]:



An area of concern related to reforming of heavy hydrocarbon fuels is the formation of solid carbon deposits. Formation of carbon within a catalytic reactor can proceed through a number of reactions as described below:



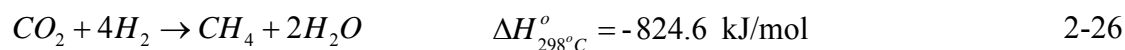
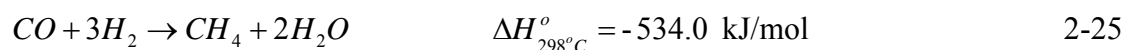
Here paraffins are hydrocarbon with single carbon-carbon bonds. Olefins are hydrocarbon with one double carbon-carbon bond; dienes contain two double carbon-carbon bonds and trienes contain three double carbon-carbon bonds. Of note is that the final formation of aromatics or coke is a non-reversible event and is the principal reason that carbon formation can quickly accumulate within a reactor and deactivate catalysts. There are also studies that suggest that carbon itself is a catalyst for carbon formation further accelerating carbon deactivation once it begins [143]. In addition to pyrolysis of jet fuel (Eqn. 2-14), other common carbon formation reactions are methane pyrolysis (Eqn. 2-22), the Boudouard reaction (Eqn. 2-23) and the CO reduction to carbon and water (Eqn. 2-24).



Carbon formation at atmospheric pressures, is favored by the Boudouard reaction (Eqn. 2-23) and carbon monoxide reduction reaction (Eqn. 2-24) at low temperatures and at high temperatures the methane pyrolysis reaction (Eqn. 2-22) is favored. Carbon

deposition can be avoided by proper selection of operating oxygen-to-carbon ration, operating temperature and reactor designs that ensures good mixing of reactants.

Some additional reactions are needed to allow for the formation of hydrocarbons from non-hydrocarbon components. In their simplest form these are the methanation reactions show below in Equations 2-25 and 2-26.



Although Eqn.s 2-11 to 2-26 are not all inclusive, they can be used in equilibrium calculations to closely predict reformat products at reactor exit conditions. This approach will be taken in Chapter 4, Analysis of Oxygen Enriched Liquid Heavy Hydrocarbon Fuel Reforming, to predict catalytic reforming results under a number of operating conditions. Prior to performing experimental work, extensive modeling was undertaken in order to better understand and predict operating conditions that could be damaging to the reactor (carbon formation, excessive temperature, etc.) and invalidate experimental results.

2.3.2.2 Reforming of heavy hydrocarbon fuels (diesel, kerosene, jet fuels)

Catalytic fuel reforming generally refers to steam reforming (SR), catalytic partial oxidation (CPOx), or autothermal reforming (ATR). Steam reforming has been used in

industrial production of hydrogen and syngas since the 1950's and accounts for 95% [144] of current hydrogen production in the United States and 48% of the global production of hydrogen [145]. Steam reforming takes place at lower operating temperatures than ATR and CPO_x and produces high hydrogen concentrations. Low temperature operation is beneficial to catalysts long-term durability. However, because SR is endothermic heat must be transferred across a material boundary which results in slow response to transient conditions (i.e. start-up, load following, etc.). In addition, good system heat recovery is needed to achieve high efficiency and this has generally resulted in physically large designs better suited for stationary applications [146]. Recent advances in miniaturization of components and close coupling of endothermic/exothermic processes have allowed SR to be considered in compact mobile applications [147, 148]. Hydrogen and syngas production via steam reforming of hydrocarbons has been studied by many researchers over the years [149, 150, 151, 152, 153]. For heavy liquid hydrocarbon fuels, SR has been reported to be limited to naphtha or lighter hydrocarbons due to the strong tendency for carbon deposition [148, 154](see Section 2.3.2.5 Carbon formation). Catalytic partial oxidation (CPO_x) has been investigated for automotive and industrial applications [155, 156, 157, 158]. CPO_x reactors are noted for their fast response to transients and fast reactions resulting in physically small reactors. However, CPO_x reactor operate at high temperatures and their overall reactions are strongly exothermic requiring good thermal management. High operating temperatures also can result in reduced catalysts durability due to catalysts sintering and volatilization [159].

For compact mobile fuel reforming applications autothermal reforming (ATR), a combination of steam reforming and partial oxidation, is often a good compromise.

ATRs operate with two easily distinguishable thermal zones as shown in Fig. 2.3: 1) near the entrance of the reactor a higher temperature zone where oxidative reactions dominate and 2) a lower temperature zone where endothermic steam reforming reactions dominate towards the exit of the reactor. These two zones also provide insight into the rates of reactions with oxidative reactions proceeding more rapidly than steam reforming reactions [160, 161]. The heat generated in the oxidative zone provides heat to drive the downstream endothermic reactions. These zones create a distinctive temperature profile for ATRs of a rapid rise in temperature near the entrance to the reactor followed by a gradual decrease in temperature as you move to the reactor exit [162]. ATRs retain the fast response of CPOx, but operate at more moderate temperatures (typically, between 850 °C and 950 °C, when reforming JP-8) and produce a reformat stream higher in hydrogen concentration than CPOx. Recently, Argonne National Labs conducted extensive research and development on automotive on-board reforming for fuel cell [163, 164, 165]. Through their research and development, ATRs were seen as the best approach due to their cost, compact size, long life under thermal transients, quick start-up and good load following ability [139].

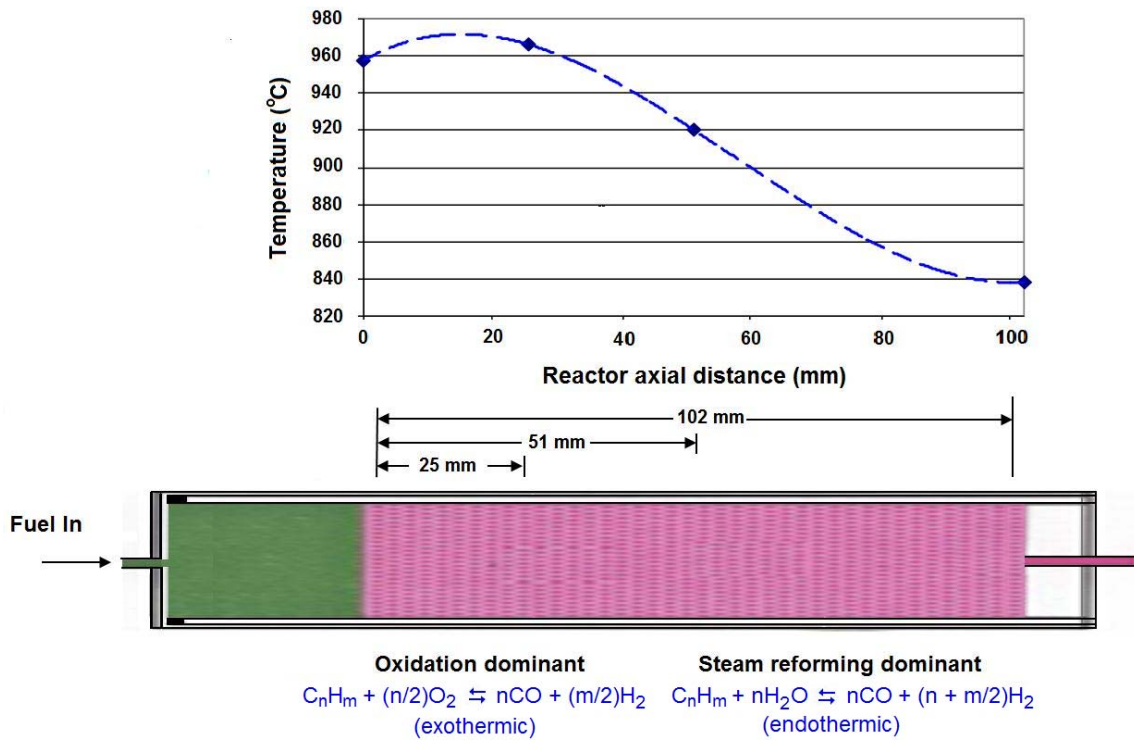
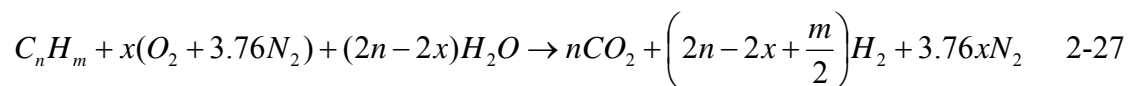


Figure 2.3 Temperature profile within an ATR reactor.

ATRs have found wide use because the reformat products and operating temperature can be altered by adjusting the amount of fuel, oxygen and water admitted into the reactor.

The overall ATR reaction is shown below in Eqn. 2-27:



where the net enthalpy change for the ATR reaction is:

$$\Delta H_R = nh_{CO_2}^f + \left(2n - 2x + \frac{m}{2}\right)h_{H_2O}^f - \left[h_{C_nH_m}^f + xh_{O_2}^f + (2n - 2x)h_{H_2O}^f\right]$$

which simplifies to,

$$\Delta H_R = nh_{CO_2}^f - \left[h_{C_nH_m}^f + (2n - 2x)h_{H_2O}^f\right] \quad 2-28$$

The overall ATR reaction can be either exothermic or endothermic depending on the selection of the molar oxygen to carbon ratio (O_2/C)⁶, here designated as (x/n) and the molar steam-to-carbon ratio (S/C) [166]. The effect on hydrogen product concentration and adiabatic operating temperature as a result of molar oxygen-to-fuel ratio, where oxygen is obtained from air, is shown in Fig. 2.4. The thermoneutral operating point (exothermic reactions balance endothermic reactions) is determined by adjusting the values for n and x in Eqn. 2-28 until ΔH_R equals zero at 298°C. For n-dodecane ($C_{12}H_{26}$), a single component normal alkane that approximates diesel and jet fuel (JP-8), the conditions of thermal neutrality is $O/C = 0.726$ ($x/n = 0.363$, $x = 4.356$) and the molar steam-to-carbon ration (S/C) of 1.274 ($2n - 2x + \frac{m}{2} = 15.290$). The thermoneutral point is also the optimum condition for achieving maximum theoretical efficiencies in ATRs

⁶ The molar oxygen-to-carbon number can either be represented as (O_2/C) or (O/C), where $O/C = 2 \times O_2/C$. Throughout this manuscript I represent my data as O/C , but in this section I have chosen to use O_2/C as is more simply correlates with (x/n) .

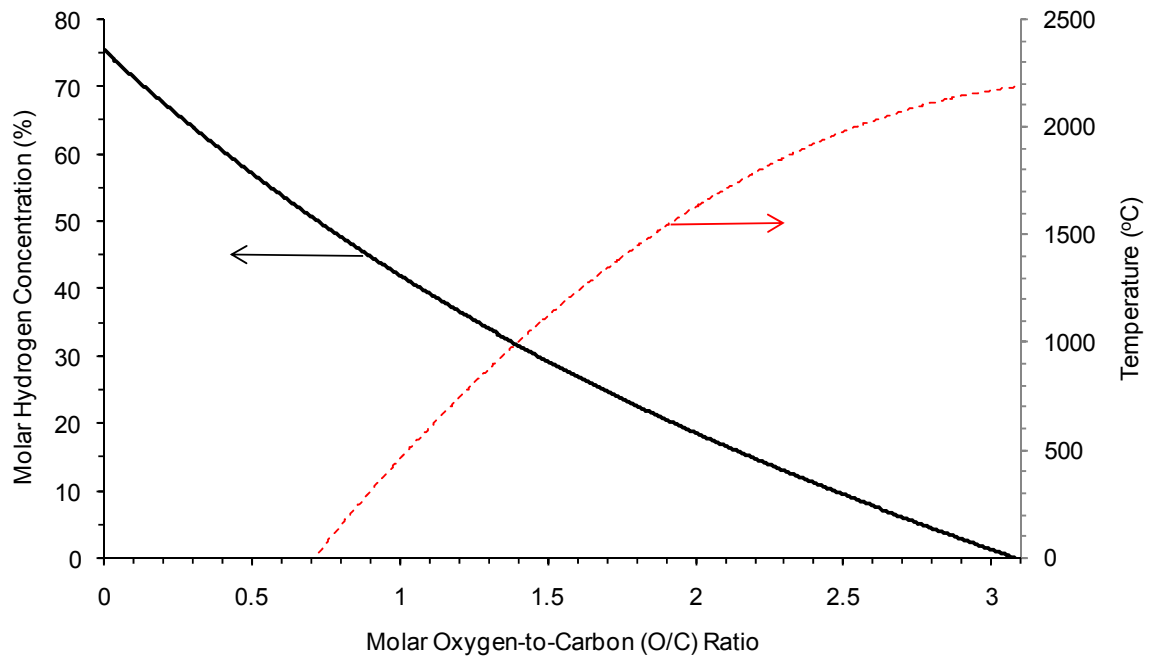


Figure 2.4 The effect of oxygen-to-fuel molar ratio on the concentration of hydrogen in the reformat stream and the reactor adiabatic temperature using Eqn. 2.27.

[163, 139]. As the O/C ratio is reduced to zero you move towards steam reforming which will produce the maximum hydrogen concentration (75.5%) from the reformer. As the O/C ratio is raised above the thermoneutral point you are moving toward complete combustion (for n-dodecane complete combustion is reached at, $O/C = 3.08$; $x = 18.5$). This results in the complete conversion of hydrogen and carbon in the reactant fuel to water and carbon dioxide and is accompanied by very high operating temperatures. Also, as you move from steam reforming ($O/C = 0$) in the direction of complete oxidation the hydrogen concentration drops as a result of dilution due to nitrogen in the product stream. Although, an oxygen-to-carbon ratio of 0.726 is the theoretical optimum operating point, ATR reactors are generally operated at higher O/C ratios (e.g. $0.95 \leq O/C \leq 1.10$) to compensate for thermal losses, and to ensure complete conversion of fuel.

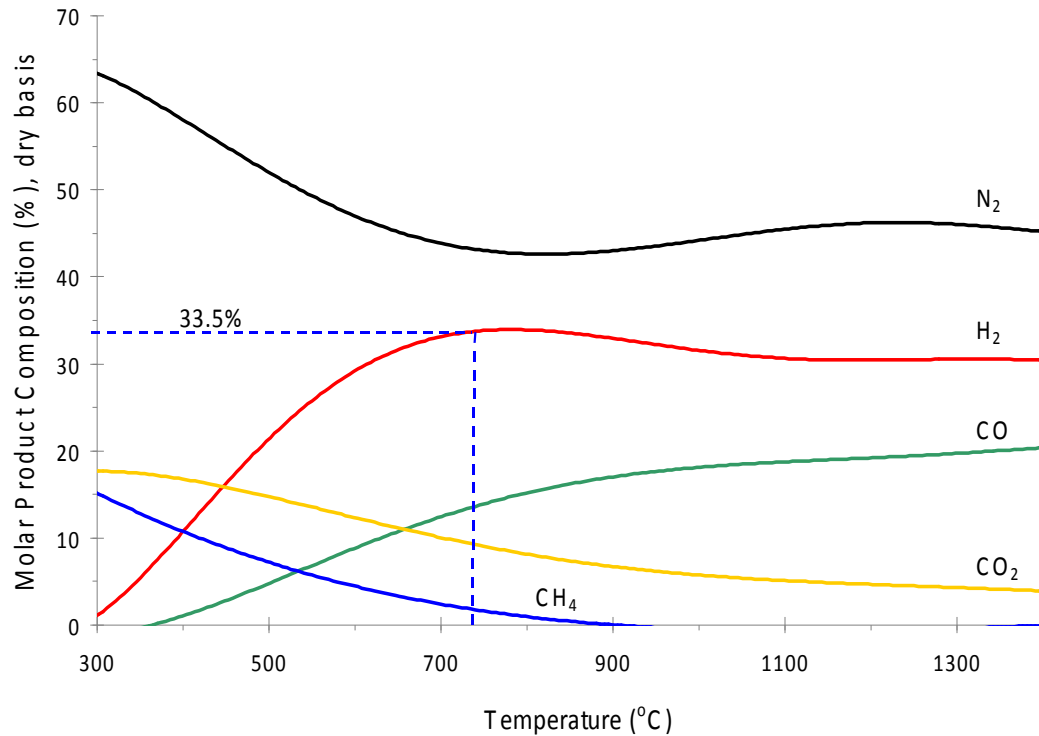


Figure 2.5 Equilibrium product composition n-dodecane at a molar oxygen-to-carbon (O/C) ratio of 1.0 and a molar steam-to-carbon (S/C) ratio of 1.0.

Figure 2.5 shows the equilibrium product composition for reforming of n-dodecane with an oxygen-to-carbon ratio of 1.0 ($O/C = 1.0$) and a molar steam-to-carbon ratio of 1.0 ($S/C = 1.0$). Here the maximum hydrogen produced is 33.5% at an equilibrium temperature of approximately 730 °C. Operating at temperatures above 730 °C results in a reverse bias of the water-gas-shift equilibrium equation (Eqn. 2-18) towards greater production of carbon monoxide and water which reduces the hydrogen in the product stream. At temperatures below 730 °C production of methane increases (Eqn.'s 2-25 and 2-26) which consumes hydrogen reducing the amount in the reformer product stream.

2.3.2.3 ATR operating conditions

Many researchers [167, 163, 168] have demonstrated that for ATRs controlling input parameters (i.e. reactor inlet temperature, steam-to-carbon ratio, and oxygen-to-carbon ratio) has a direct influence on the reactor operating temperature, composition of products produced, the reformer efficiency, and the performance of downstream processes and fuel cell efficiency. Other factors such as residence time, catalysts reactivity, peak temperatures, and catalysts deactivation also can have a significant effect on reactor performance, but will not be included in this section (for discussion on these areas see Chapter 6 Experimental Results and Discussion). The following sections will provide technical backgrounds and prior experimental work on the effects of operating conditions on ATR performance; additional, discussion and analysis is presented in Chapter 4 Analysis of Oxygen Enriched Liquid Heavy Hydrocarbon Fuel Reforming.

2.3.2.3.1 ATR operating temperature

The control of reactor temperature has a strong and direct effect on the reformer product composition and efficiency. Assuming a fixed oxygen-to-carbon ratio, the primary means to effect the reactor operating temperature is through the reactant temperature at the entrance to the reactor, the thermal design of the reactor, and, in this thesis, the oxygen enrichment number (Ψ), defined as shown below in Equation 2-29.

$$\Psi = \frac{\text{percent oxygen in enriched air}}{\text{percent oxygen in air}} \quad 2-29$$

In general, maintaining higher reactor operating temperatures (everything else being equal) results in faster reactions, improved efficiency and small reactors for a given product output. Higher temperatures result in better fuel conversion to hydrogen and carbon monoxide and decreased concentration of methane and higher hydrocarbons. A major technical challenge with achieving good reactor entrance temperature control is achieving fuel vaporization without initiating thermal decomposition of the fuel resulting in carbon formation.

2.3.2.3.1.1 Fuel atomization/vaporization

The reactor entrance temperature is usually controlled to a level that is sufficiently above the boiling temperature of the fuel to avoid the possibility of liquid fuel condensing before, or in the reactor, which can leach out catalysts; but below the temperature at which either pre-ignition could occur or where the hydrocarbons in the fuel could begin to crack and form carbon deposits [169, 163]. For JP-8 fuel, the final boiling temperature at 1 atm is 300 °C [170]. The upper temperature bounds where carbon could form from JP-8 fuel exposed to elevated temperatures is not well defined. The Air Force Research Laboratory has funded The Pennsylvania State University Laboratory for Hydrocarbon Process Chemistry to perform a number of studies to investigate the thermal stability of JP-8 flowing through tubes at elevated temperatures [171, 172, 173, 174]. These studies evaluated stainless steels, inconel, and superalloys (e.g FeCrAlloy, Hastelloys) and determined the propensity for carbon formation at elevated temperatures. In general, the

findings indicated that at temperatures above 470 °C pyrolysis of JP-8 is likely and preferentially occurs in the following order:

Ni > SS 316 > SS 304 > Inconel 600 > silcosteel > glass-lined SS

Where, SS is an acronym for stainless steel and silcosteel is a stainless steel passivation process developed by Restek Company (Bellefonte, PA). Penn State conducted their tests with pure fuels and not mixtures of fuel, steam, and air as is the case in ATR reforming. Therefore, the Penn State test conditions are not identical to reforming, but should produce more conservative results as the steam present in reforming should significantly help to avoid carbon formation [175].

Diesel and jet fuel vaporization has been identified as a critical challenge and has received some attention from researchers. In general, vaporization of diesel and jet fuels need to either take place very rapidly in order to avoid thermal cracking reactions leading to carbon formation or vaporization needs to take place in an environment containing oxygen (e.g. steam, carbon dioxide) which suppresses carbon formation (see Eqn. 2-24). Research into diesel and jet fuel vaporization and atomization is synopsized below:

Liu *et al.* [162] working at Argonne National Labs suggested a number of experimental design considerations for preconditioning of fuel, water, and air prior to their introduction into a multi-kilowatt ATR: i) as a minimum, the fuel stream should be vaporized to a

temperature of 30 °C to 50 °C above the final boiling point of the fuel, ii) that the water be vaporized and superheated using a multiple heating zone approach with a superheat temperature of the vaporized fuel, iii) that the vaporized fuel and superheated steam be mixed prior to introducing air, iv) that all lines be wrapped with heat tape and well insulated to prevent condensation prior to the ATR reactor, and vi) that the reactor be well insulated to minimize heat loss.

Ming *et al.* [176] recommends that for higher hydrocarbon fuels, such as JP-8 and diesel, that the fuel should be atomized into a superheated steam stream where the heat from the steam vaporizes the fuel. This is recommended as a means to avoid solid phase carbon formation from thermal cracking of fuel during vaporization. In a similar approach, Szydlowski *et al.* of International Fuel Cells, Inc. [177] designed a combined fuel and steam injection system as a means to atomize and vaporize liquid heavy hydrocarbon fuels for ATRs. In this design the fuel is atomized to a mean particle diameter of 10 microns and heat from steam fully vaporizes the fuel without carbon formation.

Sarioglan *et al.* [178] investigate the vaporization of F-76 (military grade marine diesel fuel) under two operating conditions: i) direct vaporization of F-76 flowing through a tube in a tube furnace and ii) indirect vaporization where a shell and tube heat exchanger is used with nitrogen flowing in the shell and F-76 is vaporized in the tube⁷. The results strongly indicated that the indirect method produced less thermal decomposition of the

⁷ This use of indirect vaporization with heated nitrogen was chosen to simulate the effects of vaporizing fuel through the use of reforming off-gases.

fuel as compared to direct vaporization. Additionally, short residence time (i.e. fast vaporization) resulted in reduced thermal decomposition.

Lindstrom *et al.* [179] presents engineering vaporization and mixing designs for five different ATRs operating on commercial grade diesel fuel. Results showed that poor mixing of air, fuel and water creating fuel rich zones are associated with soot formation. The use of cool flame oxidation⁸ as a vaporization technique as described by Hartmann *et al.* [169] resulted in unstable operation, incomplete conversion of aromatics and autoignition prior to the reactor. Chen *et al.* [175] noted similar challenges with cool flame oxidation/vaporization approaches. Lindstrom *et al.* achieved a successful design by reducing the residence time in the vaporization chamber to 0.7 s. In addition to short residence times, Lindstrom *et al.* cited the addition of steam as a means to inhibit autoignition.

Kang *et al.* [180] investigated the effect of using an ultrasonic injector atomizing fuel to 40 μm and then vaporizing versus an electric vaporizer with an ATR reactor. The ultrasonic vaporizer was believed to provide superior mixing of reactants prior to introduction into the ATR reactor. Results show that reactor efficiency increased by 20% when a well mixed ultrasonic injector was used. Additionally, deactivation of the

⁸ Cool flame oxidation is a low temperature (<400 °C) combustion process where combustion is accompanied by a decrease in heat released and an increase in temperature (referred to as a negative temperature coefficient).

catalysts when using the electrical vaporizer occurred after 26 hours of operation accompanied by increased ethylene in the product stream and reduced hydrogen yield.

Most researchers have concluded that very rapid transition from liquid to vapor must take place with diesel and jet fuel in order to avoid carbon formation when operating in an oxygen deficient environment. Rapid vaporization of liquid fuels through convective heat transfer generally requires that the liquid particle be no larger than 10 μm [181]. Alternatively, Boutin *et al.* [182] using focused radiant heat from a xenon lamp determined that with heat fluxes on the order of 10^6 W/m^2 that solid bio-mass pellets could be volatilized without the formation of carbon or char. Salge *et al.* [183] at the University of Minnesota recognized that heat fluxes of similar magnitude used by Boutin *et al.* existed at the face of a catalytic partial oxidation/ATR reactor. Salge *et al.* performed experimentation using fuels such as soy oil, glucose-water solutions, and biodiesel⁹. These fuels were atomized to 400 μm and then were impinged on the surface of a ceramic foam reactor with Rh-Ce catalysts and flash volatilized to hydrogen, carbon monoxide, carbon dioxide and C2 olefins. Experimental results for test of up to 20 hours produced no detectable carbon formation (operating in the oxygen-to-carbon ratio range of 0.83 to 1.25).

Based on the cited references and additional information from others conducting experimental ATR research [179, 184, 185, 186], a reactor entrance operating

⁹ The research group at the University of Minnesota has successfully conducted further work with JP-8 using reactive flash volatilization under a US Army R&D program.

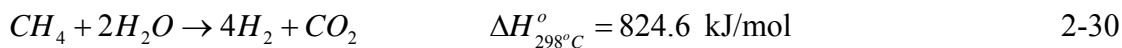
temperature for experimental testing in this thesis was set at $425\text{ }^{\circ}\text{C} \pm 10\text{ }^{\circ}\text{C}$.

Additionally, the vaporization of fuel was accomplished by flowing liquid JP-8 into a superheated steam stream where the heat from the steam vaporized the JP-8. The reactants were further mixed by a static mixer and then by a metal foam prior to introduction into the ATR reactors (See Chapter 3 Experimental Apparatus and Instrumentation).

2.3.2.3.1.2 Steam-to-carbon (S/C) ratio and oxygen-to-carbon (O/C) ratio

Reformer operating temperature and product gas composition are functions of the molar S/C ratio and the O/C ratio's. The reactor operating temperature is not a strong function of the S/C ratio resulting in a slight decrease in temperature as more steam is added. Liu *et al.* [162] showed that increasing the S/C ratio from 1.1 to 2.8 while holding the O/C at 0.68 with n-dodecane resulted in a $\sim 40\text{ }^{\circ}\text{C}$ drop in temperature at the front of the reactor and a $\sim 10\text{ }^{\circ}\text{C}$ drop at the exit of the reactor. The temperature drop is attributed to a higher concentration of water at the front of the reactor which results in more endothermic steam reforming reactions occurring. As the S/C ratio is increased the hydrogen production increases and methane production is reduced. This can be explained by looking at the water-gas-shift reaction, Eqn. 2-18, and the methane steam reforming reaction (or reverse methanation reaction) shown in Eqn. 2-26. With the addition of water, the water-gas-shift reaction is driven towards the conversion of carbon monoxide to carbon dioxide and hydrogen. The reverse methanation reaction, rewritten below as

the steam reforming of methane reaction (Eqn. 2-30), is driven towards the production of hydrogen and carbon dioxide as steam is increased.



These results from the increase of steam in an ATR reactor have been shown experimentally by many researchers [161, 162, 167, 187, 188]. Although, the results from steam addition appear to only be positive, there is a significant energy requirement for vaporization of water which can have a negative impact on system level performance. The overall performance impact from increased steam can only be evaluated at the system level which is outside of the scope of this thesis, but is a function of available waste heat and waste energy of the fuel cell system.

The O/C ratio has a very strong effect on the reactor operating temperature. The production of hydrogen and reactor performance increases until an optimal O/C ratio is achieved. In section 2.3.2.2, the theoretical optimal O/C ratio was determined to occur at the thermoneutral point which for n-dodecane (a good single component surrogate for JP-8 and diesel) was found to be 0.726. Experimental data by Royshoudhury *et al.* [189] on JP-8 fuel indicates that an optimum O/C ratio is approximately 1.0; Dreyer *et al.* [190] found that an O/C ratio of 1.0 resulted in maximum hydrogen production and minimization of olefins. The higher O/C level above the theoretical operating point is needed to compensate for reactor thermal losses and to elevate the reactor operating

temperature to obtain more favorable kinetics for difficult to reform hydrocarbon components. Operating below the optimum O/C ratio results in incomplete conversion of fuel, production of olefins, a lower reactor temperature and an increased likelihood of solid carbon formation (Eqn.'s 2-23 and 2-24). Operating above the optimum O/C ratio results in conversion of hydrogen to water, higher reactor operating temperatures, and the dilution of product gases by nitrogen.

2.3.2.4. Reforming catalysts and support materials

A number of different catalyst materials and supports have been used in reforming of hydrocarbon fuels. The hydrocarbon fuel type and presence and type of heteroatoms often dictate catalysts and support selection. Shekhawat *et al.* [159] and Navarro *et al.* [191] provide very good review articles on catalyst selection for a number of hydrocarbon fuels and reforming approaches. The market potential for fuel cell use in mobile applications such as automobiles, heavy trucking auxiliary power units (APUs), and for portable power has received the attention of commercial catalysts developers who have recently come out with products for liquid hydrocarbon reforming: BASF Corporation, through the acquisition of Englehard Corporation, has a family of noble metal based SR and ATR catalysts for heavy hydrocarbon reforming [192], Sud-Chemie has developed both CPOx and ATR catalysts for liquid hydrocarbon reforming [193], and Johnson-Matthey [194] has a family of non-precious metal catalysts for reforming processes and is developing catalysts for higher hydrocarbons fuels. Although, active research and development on catalysts for heavy liquid hydrocarbon fuel reforming is

occurring, most commercial products are targeted towards natural gas, alcohol fuels (methanol and ethanol), and lighter liquid hydrocarbon fuels; reforming of middle distillate fuels is still considered an developmental area.

Commercial ATR catalysts had initially relied on Ni based catalysts developed for steam methane reforming. Nickel based catalysts have generally been avoided when reforming diesel and jet fuels due to their tendency to form carbon, particularly, with fuels having a high carbon-to-hydrogen ratio and also because nickel is easily deactivated by sulfur present in these fuels. Flytzani-Stephanaopoulos and Voecks [154] conducted testing in a multi-zone ATR reactor with Ni based catalysts to better understand the coking tendency of aliphatic and aromatic hydrocarbons. They concluded that aliphatic compounds (80% of jet fuels) underwent thermal cracking resulting in a significant amount of olefins production; a precursor to carbon deposition. Hansen and Rostrup-Nielsen [195] describe the mechanisms for chemisorptions of hydrogen sulfide on metal surfaces and the sensitivity of nickel to this process. The vast majority of sulfur entering an ATR (or any reformer designed for hydrogen production) under normal reforming conditions is converted to hydrogen sulfide (H_2S)¹⁰. The sulfur chemisorptions reactions on metals (Me) is shown below in Equation 2-31.



¹⁰ Under some conditions sulfur can be converted to carbonyl sulfide (COS), however, the quantities of COS are generally very small in comparison to H_2S .

The forward reaction is favored at low temperatures and is reversible under low concentration (typically ≤ 10 ppm sulfur wt% in liquid fuel), but at moderate sulfur concentration and low temperatures, deactivation of catalysts by sulfur poisoning can be rapid and irreversible. Because of its low cost, research work continues with nickel based catalysts often combining it with noble metal catalysts and other elements, such as potassium, which have shown the ability to reduce the carbon formation tendencies of nickel [196, 197, 159].

For the ATR of middle distillate fuels, the use of the platinum metals group (PMG) catalysts (Pt, Ru, Rh, Pd, Os, Ir) have successfully been demonstrated and a number of commercial catalysts developers offer products targeting higher hydrocarbon ATR reforming. PMG catalysts such as Rh, Pt and Pd have better stability, higher activity, and are less prone to carbon formation than nickel based catalysts [198, 199, 200]. These PMG catalysts are often combined with an oxide ion conducting substrate such as ceria, gadolinium, zirconia, or others that serve to transport oxygen. Sud-Chemie working with Argonne National Laboratory developed one of the first ATR catalysts specifically targeting gasoline [201]. The Sud-Chemie ATR catalysts (HyProGen™ [193]) consist of Rh and Pt dispersed on a gadolinium-doped ceria substrate. Lenz *et al.* [184] conducted tests with Sud-Chemie ATR catalysts with jet fuel under varying fuel sulfur content levels. With fully desulfurized jet fuel good reformer performance was achieved with hydrogen production of 33% (dry basis, S/C = 3, O/C = 1), but with jet fuel containing 290 ppmw sulfur the hydrogen production immediately drops to 26% (dry basis);

switching back to initial desulfurized jet fuel regenerates the catalysts, but does not fully recover initial performance levels.

Other catalysts under investigation include perovskite based materials of the form ABO_3 where A is a lanthanide element (La, Ce, and Yb) and B is a first row transition metal (e.g. Ni, Co); see Figure 2.6 for representation of the structure of a perovskite [202].

Pure perovskite materials such as $LaNiO_3$ and $LaCoO_3$ have been reported to exhibit excellent catalytic activity, however, these materials have demonstrated poor structural stability under ATR operating conditions [203]. Perovskite catalysts can be doped with an additional transition metal (e.g. Mn, Cr, Fe, Co, Ni, Cu) which provides better durability. The B sites in perovskite catalysts can also be doped with noble metals (e.g. Ru, Rh, etc.) that can be selected by application. The benefits of perovskite catalysts are good catalytic activity, low cost, and with doping, the function of the catalysts can be altered for steam reforming, partial oxidation, or a combination of both as needed with ATR. Another benefit of perovskite catalysts is that unlike traditional catalysts which typically deposit catalysts on the surface of a substrate material, perovskite's distribute active metal catalysts within the lattice structure of the material. Dispersion of catalysts within a structure avoids catalysts clusters which are associated with carbon and sulfur adsorption. Liu and Mawdsley [204,205] improved perovskite based catalysts ATR sulfur tolerance by partially incorporating Ru into a B site ($LaCr_{0.95}Ru_{0.05}O_3$). The catalysts compared favorably to a non-perovskite Rh based ATR catalysts and exhibited superior sulfur tolerance while reforming n-dodecane doped with 50 ppmw sulfur.

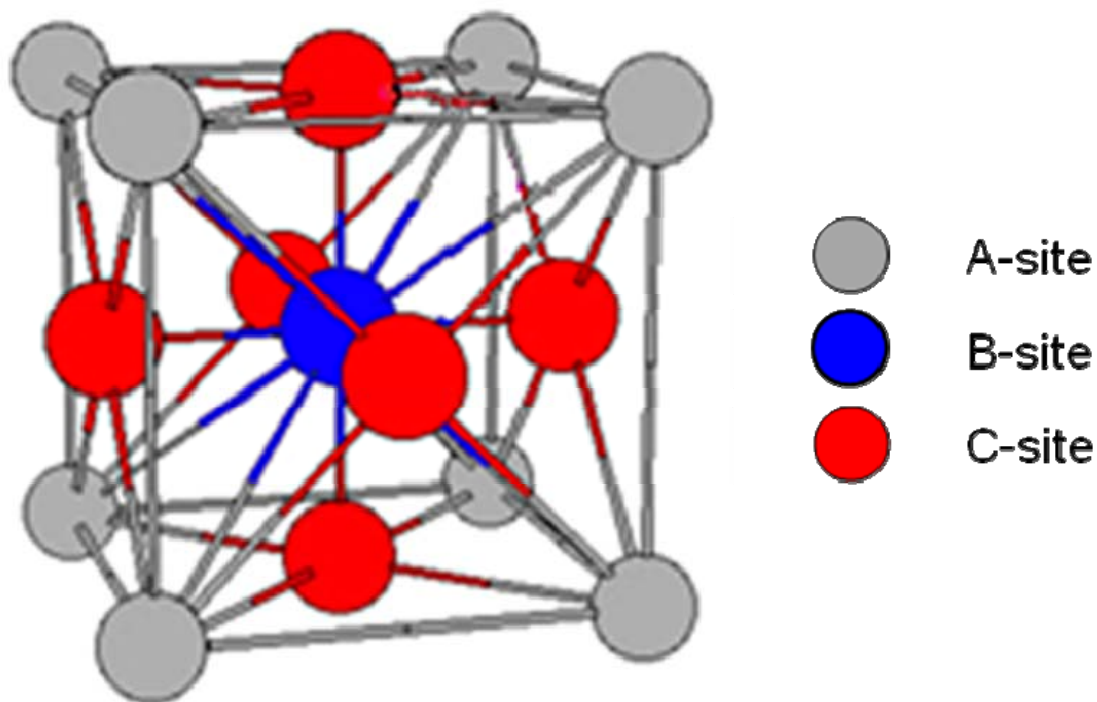


Figure 2.6 Lattice structure of a single perovskite cell [187].

Perovskites materials when partially substituted with rare earth elements at the B site can create an oxygen defect which can increase oxygen mobility within the catalysts resulting in reduced carbon formation. Erri et al. [206] developed a cerium and nickel substituted lanthanum iron perovskite ($\text{La}_{0.6}\text{Ce}_{0.4}\text{Fe}_{(1-x)}\text{Ni}_x\text{O}_3$) and tested under conditions of $S/C = 3.0$, $O/C = 0.728$ and reforming temperature of 775°C . Results indicated that the amount of nickel incorporated into the perovskite had little effect on reactant conversion, but the propensity for coking is reduced greatly as the amount of nickel is reduced. The addition of cerium caused the oxygen ions to be more weakly bound in the perovskite, allowing oxygen to be released from the catalysts material where it can oxidize carbon.

2.3.2.5 Carbon formation

Carbon formation is a significant concern with fuels containing a large portion of long chain ($>C_{12}$) n-alkanes and/or polynucleate aromatics; diesel and jet fuels contain both of these problematic hydrocarbons. Carbon formation can deactivate catalysts [207], plugs the flow within a reactor [208] and can self catalyze to produce more carbon [209, 210]. Shekhawat *et al.* [159] describes carbon formation within reactors as occurring through two distinct types of carbon containing materials formed on the catalysts surface: elemental carbon formation and “coke” formation. Both carbon formation types can lead to catalysts deactivation.

Elemental carbon formation is created through decomposition of the hydrocarbon fuel or through reactions with carbon monoxide. This type of carbon formation is often referred to as “whisker” carbon or filamentous carbon which describes its morphology. Whisker carbon, often associated with nickel catalysts, is formed when carbon dissolves on the metal catalysts, diffuses through the metal and forms a filament that can delaminate the catalysts from the support. Whisker carbon forms under the reactor conditions of high temperatures, low steam to hydrocarbon ratios, and higher aromatic content.

The second type of carbon is termed “coke” which can occur through polyaromatic hydrocarbons that go through a series of dehydrogenation/condensation steps or through pyrolysis of olefins in the gas phase (homogeneous reactions). The result of carbon formation is the deactivation of catalysts either by physical blockage of active sites or

through mechanical breakage of catalysts and support materials that can result in loss of catalysts surface area and blockage within the reaction leading to increased pressure drops. Mundschau *et al.* [143] states that coke can be formed through the breaking of carbon-carbon bonds in long chain n-alkanes forming alkyl free radicals which at temperatures above their autoignition temperatures, and in the absence of oxygen, can react with other fuel molecules initiating radical polymerization and the forming of tar. Alternatively, coke can be formed in aromatics by the breaking of carbon-hydrogen bonds (because of the unique structure of aromatics carbon-carbon bonds are very strong and stable) leaving aromatic rings intact to nucleate graphitic soot.

Carbon formation is a formidable problem when reforming higher hydrocarbons. Localized fuel rich conditions within a reformer can exacerbate the problem. Steps to control carbon formation in ATRs is to incorporate good mixing of reactants prior to entering the reactor, operate at high steam to carbon ratios, and the use of non-nickel based catalysts. Krause *et al.* [211] evaluated the ATR of diesel and JP-8 and concluded that operating with a S/C ratio at 2.0 would eliminate carbon formation under typical ATR operating temperatures. Minimizing production of olefins in the reformate, particularly, ethylene a carbon formation precursor should also help to avoid favorable conditions for carbon formation [149]. Additionally, some researchers [212, 213] have incorporated pre-reformers that operate at moderate temperatures (500 °C – 550 °C) where long chain n-alkanes can be broken-up under conditions that are kinetically

unfavorable to carbon formation. The use of noble metal catalysts, such as Ru and Rh, have also shown strong resistance to carbon formation [200].

2.4 Oxygen enrichment [214, 215]

Four methods are generally considered for oxygen enrichment; cryogenic distillation (or fractional distillation), electrolysis, pressure swing adsorption (PSA), and membrane separation. The latter two have evolved to full commercial status. Cryogenic distillation and PSA are practical for large-scale applications, and only membrane separation is deemed economical at small (50W-5kW) scale [216, 217]. For small-scale power applications, membrane separation material options generally fall into one of two categories, polymeric or ceramic. These two membrane types provide very different performance and operating characteristics.

Polymer membrane technology is generally more mature and commercial products enjoy widespread availability relative to the ceramic membrane products. Ceramic membranes are characterized by high O₂/N₂ selectivity, but they exhibit low airflow permeability, and require high pressure ratios and operating temperatures. More specifically, polymer membrane separators typically contain small hollow fibers of 100 to 500 μm in diameter and 0.25 to 0.3 m in length. These are assembled into bundles of 0.03 to 0.25 m diameter. A dense polymer layer as thin as 35 nm is supported on thick porous walls. Examples of polymers are polysulfone, polycarbonate, and polyimides. The separation mechanism is known as the dissolution / diffusion model whereby a three-step process

takes place: 1) dissolution of the gas into the high-pressure (or high chemical potential) upstream face of the polymer, 2) diffusion of the gas through the polymer, and 3) desorption from the low-pressure (low chemical potential) downstream face of the polymer. The driving force for transport is the partial pressure difference between the upstream and downstream sides of the membrane.

The membrane materials that appear to be best suited for small reforming applications are from the perfluorodioxide family [218]. Perfluorodioxole membrane materials have been employed in portable medical oxygen-assisted breathing apparatus [219] as a safer, less expensive, and more portable alternative to pressurized oxygen canisters.

2.4.1 Oxygen enriched air reforming

Oxygen enriched air or pure oxygen reforming is not an entirely new concepts and was first proposed by Haldor Topsoe in 1958 [220] for the ATR of methane to syngas for ammonia plant operation. Syngas plant incorporating oxygen ATR of methane have been demonstrated and has economic advantages over steam methane reforming. For large industrial applications PSA is the selected oxygen production approach [221], however, experimental work suggests that membrane enrichment of oxygen in air for ATR syngas production from natural gas is feasible [222].

The ATR of diesel and jet fuels under enriched oxygen conditions for small mobile applications, as undertaken in this thesis has not received much attention in the published

literature. Some work on diesel fuel distillates CPOx reforming using higher temperature ceramic membrane reactors has been published by Eltron Research and Development, Inc. a ceramic membrane developer [223]. Mundschau *et al.* [143] (Eltron R&D) reformed diesel fuel distillates using a ceramic membrane to produce essentially pure oxygen for CPOx reforming of ultra low sulfur diesel distillates. Interest in the use of oxygen reforming was also discussed by Czernichowski *et al.* [224] as an avenue that could improve plasma¹¹ reforming of fuels if applied; however, no published work was found by the author demonstrating oxygen-enriched plasma reforming. In combustion process, Lamber *et al.* cites a number of benefits attributed to oxygen enrichment which are likely to be similar in an ATR reactor: (i) reduces the fraction of parasitic nitrogen in the combustion gases, thus decreasing the amount of sensible heat needed to heat nitrogen, and (ii) it improves heat transfer by elevating reaction temperatures and also by increased flame emissivity as a result of high concentration of CO₂ and H₂O [²²⁵].

2.5 Chapter summary

A number of different approaches are available for delivering hydrogen to fuel cells for mobile applications to include compressed and liquid hydrogen storage, chemical and metal hydrides and fuel reforming approaches. Active research and development is continuing in all these areas primarily driven by automotive applications. For mobile applications, where power system size and weight are key performance parameters,

¹¹ Plasma reforming uses an electric arc in an oxidative environment to partially oxidize fuel without the use of catalysts.

hydrogen produced from reformed heavy hydrocarbon fuels provides very clear advantages in terms of specific energy and energy density as shown in Table 2.2.

Significant research into fuel reforming, experimental design, catalysts selection, and reactor operating conditions has been published on various fuels most notably methane and octane and more recently, but with less quantity, with diesel and jet fuels. From the cited literature the following experimental design and operating guidelines have been followed in conducting the research in this thesis:

- Penn State University recommended maximum fuel vaporization temperatures to avoid fuel cracking and carbon formation of 470 °C for jet fuels [169, 170, 171, 172] based on the materials of construction in the fuel vaporizer and reactor feed lines.
- Liu *et al.* [162] of Argonne National Labs recommended that a multi-stage steam vaporizer/superheaters be used.
- A number of researchers (Liu *et al.* [162], Ming *et al.* [176], and Szydlowski *et al.* [177]) noted that vaporizing fuel in superheated steam (i.e. injecting liquid fuel into a superheat steam line, where the heat from the superheated steam vaporizes the fuel) was a proven method for carbon formation avoidance.
- To assure good reactor operation and avoid the possibility of fuel condensation, all reactor feed lines and the reactor should be well insulated (Liu *et al.* [162]).
- Good mixing of all reactants prior to entering the reactor is needed to avoid: hot spots leading to catalysts failure, oxygen lean zones within the reactor leading to

carbon formation, and good utilization of catalysts (Liu *et al.* [162], Lindstrom *et al.* [179], and Kang *et al.* [180]).

- For heavy hydrocarbon fuels (diesel and Jet fuels), operation at molar steam-to-carbon ratios at 2.0 or higher will prevent the likelihood of carbon formation within ATR reactors (Krause *et al.* [211]).
- Operation at a molar oxygen-to-carbon ratio of around 1.0 to 1.10 has been demonstrated to result in optimum ATR reactor operation when operating on heavy hydrocarbon fuels by a number of researchers (Royshoudhury *et al.* [189], Dreyer *et al.* [190], and Krause *et al.* [211]).
- Operation at low O/C ratios can create conditions favorable for carbon formation and the concentration of ethylene in the reformat should be kept very low (less than 0.05% [226]) to minimize carbon formation. Olefins are a good precursor for carbon formation (Rostrup-Nielson *et al.* [149]); O/C ratios can be adjusted to avoid olefin production.
- Catalysts selection from noble metals or perovskites with substituted noble metals, particularly, Rh and Ru, have shown a resistance to carbon adsorption lead to carbon formation (Heck *et al.* of BASF [192], Rostrup-Neilsen *et al.* [200]).
- Use of monolithic supports for catalysts is recommended for mobile application to avoid problems with shock and vibration, and also to reduce pressure drop (and associated power requirements) through the reactor (Heck *et al.* [125], Boger *et al.* [126], and Cybulski *et al.* [127]).

- Oxygen enrichment of air could play an important role in improving ATR reforming as nitrogen dilution accounts for 40% - 50% of an ATR's product stream. In combustion process, oxygen enrichment reduces parasitic nitrogen in reactant gases thus decreasing the amount of sensible heat associated with heat of nitrogen, improves heat transfer within the reactor due to higher operating temperature, higher heat transfer due higher emissivity of CO₂ and H₂O in reactant gases (Lambert *et al.* [225]).
- Many researchers have determined that the use of thermodynamic equilibrium modeling of reactions produces results that are very accurate in predicting reformat product concentrations based upon reactor exit conditions (United Catalysts, Inc. [131], Pacheco *et al.* [132], Villegas *et al.* [133], Eroz *et al.* [134], Oosthuizen *et al.* [135]). Equilibrium modeling can be used to predict reactor operating characteristics that can help in avoiding operating regimes that could damage the reactor.

Chapter 3

Experimental Apparatus, Instrumentation and Operation

3.0 Introduction

Heavy hydrocarbon fuels pose many challenges including those related to volatilizing distillates, varying and complex compositions, and high aromatic hydrocarbon content. To address these challenges a multi-kilowatt laboratory test bed was developed that would allow independent control and operation of the fuel reformer. The experimental test apparatus consists of a fully controllable reformer test bed; ceramic monolithic catalytic partial oxidation/autothermal reforming reactor instrumented with imbedded thermocouples; analytical equipment for measuring the composition of reformat gas stream; analytical equipment for analyzing the fuel input stream; test apparatus needed to accurately meter the fuel, water, and air streams; and a data acquisition system for recording reforming operating parameters during testing. This chapter will address test bed design and operation considerations, operational characteristics of the experimental apparatus, and instrumentation and experimental errors.

3.1 Experimental apparatus

The design of fuel reforming reactors for heavy hydrocarbon fuels is constrained by the need to avoid excessive operating temperatures, localized oxygen deficiencies, and the need for good axial heat transport from exothermic oxidative reactions to endothermic steam reforming reactions [227, 228]. Poor mixing of fuel and oxygen within the reactor

can create localized areas with high oxygen-to-carbon ratios that can lead to high localized temperatures ($>1100\text{ }^{\circ}\text{C}$). High temperature operation of fuel reformers can affect catalysts durability due to catalysts sintering, catalysts vaporization, and failure of support structures (typically ceramic cordierite monoliths) [229]. Conversely, localized oxygen deficiencies can result in hydrocarbon pyrolysis producing solid carbon formation that can quickly deactivate reforming catalysts and/or plug the reactor [230, 231, 54]. In order to assure acceptable operation of catalytic partial oxidation reactors, both good heat transfer and mass transfer must be achieved.

The use of heavy hydrocarbon middle distillate fuels (e.g. kerosene based fuels, diesel fuel) as a feed stock also poses a number of challenges. Primary among these challenges is the selection of appropriate catalysts and operating conditions to maximize the production of hydrogen while avoiding carbon formation. Additionally, heavy hydrocarbon fuels consist of hundreds of organic compounds, some of which are easily reformed and other refractory compounds that are very difficult to reform under normal operating conditions.

Key to the introduction of fuel cells for mobile applications will be a greater understanding of the performance of reforming catalysts and how these catalysts perform with various organic compounds present in the fuel. The reformer test apparatus, shown in Fig. 3.1, was developed to support fuel cell power system development at the multi-



Figure 3.1 Photo of autothermal reformer test apparatus.

kW electric size (typically $0.3W_e$ to 10 kW_e net). The experimental apparatus was designed to be capable of operating over a range of 300 W_{th} to 7 kW_{th} while varying the steam-to-carbon ratio (S/C) from 0 to 4 and oxygen-to-carbon ratio up to 0.5 to 1.5 (or up to the thermal limits of the reactor).

Figure 3.2 presents a simplified diagram of the experimental setup. The apparatus is designed to support carbon balance calculations and because of the sensors and balances upstream and downstream of the reactor, a complete elemental mass balance can also be determined. The experimental setup (Fig. 3.1) has dimensions of 2.44 m height, 0.76 m depth and 2.44 m length. The experimental design consists of seven major functional subsystems as shown in Fig. 3.3 and described in the following sections.

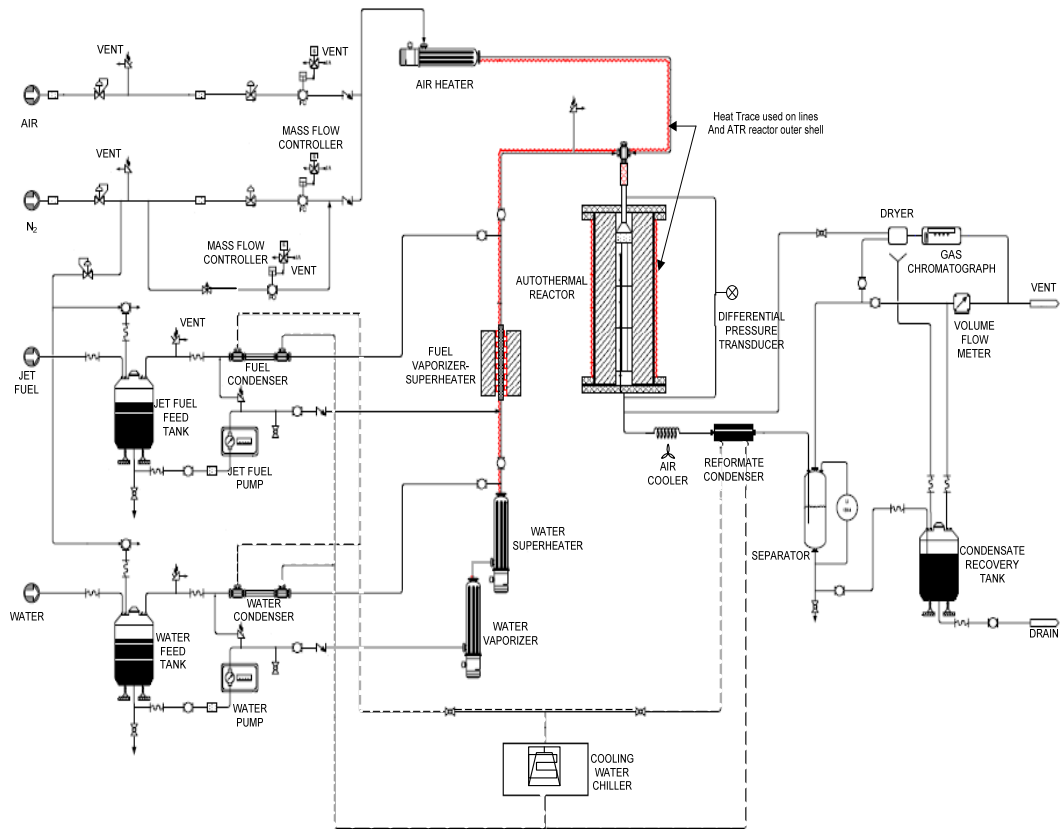


Figure 3.2 Experimental instrumentation and process flow schematic.

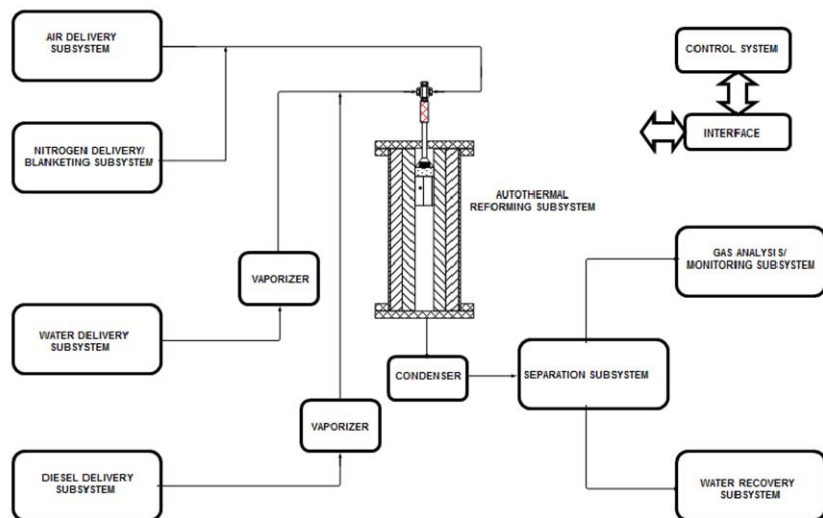


Figure 3.3 Subsystem function layout.

3.1.1 Air delivery subsystem

This subsystem is designed to accept a pressurized source of air and to regulate, monitor, condition and control its delivery into the reactor. The module is designed for a maximum gas inlet pressure of 15.3 MPa psig and a maximum gas supply pressure into the thermal mass flow meter of 515 kPa. The incoming gas is filtered through a 40 micron filter to ensure appropriate particulate removal. The inlet pressure is monitored with a pressure gauge (Ashcroft 0-16,000 kPa Gauge, $\pm 1\%$ full scale accuracy) and regulated through a forward pressure regulator (Swagelok, SS Pressure-Reducing Regulator, 0-791 kPa). The regulated gas pressure is monitored locally using a pressure gauge (Ashcroft 1009 series, 0-600 kPa, $\pm 1\%$ full scale) and remotely using an electronic pressure transducer (Serta 209 series, $\pm 0.25\%$ of full scale). The compressed air is further filtered using a 5 micron filter and the flow rate is monitored and controlled using a thermal mass flow sensor and control valve combination (Brooks, 5851E, $\pm 1\%$ full scale). Air flow rates up to 54 slpm can be controlled and conditioned. This mass flow controller enables accurate maintenance of the selected air flow rate through a feed back proportional-integral-derivative (PID) control algorithm. A fail-close air actuated shutoff valve (Swagelok, SS-44S6-33C) is incorporated downstream of the mass flow control element to shut off the gas into the system in the event of an alarm shutdown. This entire module is isolated from the rest of the system via a check valve (Swagelok, poppet check valve, SS-6C-1/3). Heating of air is accomplished by a 1600 W electric resistance heater (Sylvania, Threaded Inline Process Heater) with PID controller.

3.1.2 Nitrogen delivery/blanketing gas subsystem

The function of this subsystem is to provide low pressure nitrogen gas for flushing (start-up, shutdown, and alarm actions) and/or blanketing applications. This subsystem is also designed to accept a maximum nitrogen gas inlet pressure of 10.4 MPa and a maximum gas supply pressure into the system of 515 kPa. In this module, the incoming nitrogen is split into two paths with one stream used for flushing applications and the other stream used for blanketing applications. The primary system purge stream is identical to the air delivery system and can provide up to 54 slpm of flow and the flushing stream can provide a variable flow up to 50 slpm, but is typically set at 20 slpm.

Purge/emergency shutdown nitrogen is filtered through a 40 micron filter to ensure appropriate particulate removal. The inlet pressure is monitored with a pressure gauge and regulated through a forward pressure regulator (Swagelok, SS Pressure-Reducing Regulator, 0-791 kPa). The regulated gas pressure is monitored locally using a pressure gauge (Ashcroft 1009 series, 0-600 kPa, $\pm 1\%$ full scale) and remotely using an electronic pressure transducer (Serta 2091 series, $\pm 0.25\%$ of full scale). The nitrogen gas is further filtered using a 5 micron filter and the flow rate is monitored and controlled using a thermal mass flow sensor and control valve combination (Brooks, 5851E, $\pm 1\%$ full scale). A fail-open actuated shutoff valve (Swagelok, SS-44S6-33C) is incorporated downstream of the mass flow control element to allow nitrogen to flow into the system in the event of an alarm shutdown or loss of power. This entire module is isolated from the rest of the system via a check valve (Swagelok, poppet check valve, SS-6C-1/3).

In the blanketing application, nitrogen is regulated with a forward pressure regulator (Swagelok, SS Pressure-Reducing Regulator, 0-690 kPa) and the regulated pressure is monitored using a pressure gauge. This regulated low pressure nitrogen line is then directed into the fuel and water liquid tanks for blanketing applications.

3.1.3 Water / steam delivery subsystem

This subsystem is designed to store water, meter it, convert it into steam, and deliver it to the reactor under highly controlled conditions. Water as used in this thesis refers to de-ionized water with an electrical resistivity of approximately 18 M Ω (conductivity of 0.056 μ Siemens). The subsystem consists of a stainless steel feed tank (Alloy Product Corp., 18.9 L, 316 stainless steel, 72-05) that allows an inert blanketing gas (nitrogen) to be used with a low head pressure (the inert gas pressure is typically ≤ 205 kPa). The tank is mounted on an electronic weight platform (Sartorius laboratory balance, CP34001S, ± 0.1 g) that enables the liquid quantity to be monitored by the computer on a real time basis. The data acquisition software being used (iFIX, see paragraph 3.1.7 Control and Data Acquisition) can enable summation of the water and/or calculation of flow rates. A chromatographic type metering pump (Gilson pump, GA-360261; 0-40 ml/min. head, GA-360520) is used to provide a constant liquid feed flow. The feed rate is varied by entering the appropriate number through the computer keyboard. A 40 micron filter is provided to ensure particulate free water stream into the chromatographic metering pump. The feed tank is isolated from the rest of the tubing network by using flex lines.

Appropriate drain and shutoff valves are provided to ensure filling and draining flexibility. A pressure (Ashcroft, 0-40000 kPa Gauge, $\pm 1\%$ full scale) gauge is incorporated in the line downstream of the pump discharge to assist with setting backpressure on the pump. A relief valve (Swagelok, stainless steel relief valve, R3A series) is also put in the line in the high pressure discharge to protect the pump from a downstream pressure excursion. A ball valve / drain valve combination is incorporated for flushing and calibration of the feed pump. Additionally, check valves are placed on the feed and return lines to isolate the pumping section from the rest of the system (Swagelok, poppet check valve, SS-6C-1/3).

The water stream then flows into a vaporizer where heat is added to produce steam at a selected temperature. Water vaporization and superheating are accomplished by two electric heaters (Watlow, Rapid Response Electric Heat Exchanger). The first heater is dedicated to vaporizing water to just above its boiling point ($101\text{ }^{\circ}\text{C}$ - $105\text{ }^{\circ}\text{C}$). The second Watlow heater provides superheated steam at the desired temperature. To assist in setting the electric power level to the two water heaters, thermocouples (Watlow, 1.5875 mm diameter, stainless steel sheathed, type-K, 3.5 s time constant, $1.1\text{ }^{\circ}\text{C}$ or 0.40%, whichever is greater) are placed at the midpoint and exit of the water vaporizer and superheater. Watlow heaters are capable of delivering a combined maximum heat input of 4 kW. Superheated steam may either be recycled back, through a double tube condenser, to the feed tank or can be directed into the reactor. High temperature ball valves (Swagelok Severe Service Union-Bonnet Needle Valve with Grafoil Packaging,

SS-12NBS8-G) are incorporated to enable this function. This configuration enables the production of an appropriate vapor stream at the right temperatures and steady state conditions. Control of the water vaporizers is accomplished via power controls through two variable a/c transformers (Staco Energy Products, 3PN Series, $\pm 5\%$ full scale).

3.1.4 Diesel delivery subsystem

This subsystem is configured identical to the water /steam delivery subsystem with the exception that fuel vaporization is accomplished via a tube reactor (Applied Test Systems 3210, split tube furnace, 19 mm inner diameter and 533 mm length, 1140 W). To minimize the potential for pyrolysis of the fuel and carbon formation during normal ATR mode operation, the liquid fuel is delivered into the superheated steam prior to entering the tube heater/vaporizer. A chromatographic type metering pump (Gilson pump, GA-360261; 0.125-30 ml/min. head, GA-360520) is used to provide a constant liquid feed flow.

3.1.5 ATR reactor subsystem

The reforming reactor was designed for a nominal 3.33 kW thermal capacity when operating on jet fuel or equivalent surrogate fuel. This size was selected to scale easily with the application power range of interest of between 500 W_e to 10 kW_e (net). The resultant design was an 87 cm³ catalyst volume reactor. For this thesis, a BASF proprietary noble metal based catalysts (ATR-7B) was used. The catalyst was supported on a 600 cells per square inch cordierite monolith with an overall dimension of 19.81 mm

in diameter and 305 mm length. The monolith was wrapped in 3M InteramTM Intumescent Mat according to 3M's design instructions [232] and inserted into a 31 mm outside diameter Nicrofer 6020 hMo (Alloy 625) tube. Figure 3.4 shows a dimensioned drawing of the reactor. To ensure good reactant mixing an inline stainless steel, six element, static mixer (Koflo Corp., series 275) is incorporated after the fuel/water and air streams are mixed (upstream of the reactor); shown in Fig. 3.5. Additionally, to aid in providing a homogeneous composition and mass velocity entering the reactor a porous metal foam material 19 mm in diameter and 25.4 mm long (Provair FeCrAlY, 20 PPI) is incorporated just upstream and adjacent to the reactor (Fig. 3.6, panel (a)). The porous metal foam also serves as a radiation shield minimizing the possibility of preoxidation of the incoming gas stream. Figure 3.6, panel (b) shows the reactor exit prior to insertion of thermocouples. To monitor the bed temperature, six type-K thermocouples (Omega, 0.25 mm diameter, inconel 600 sheathed, 0.23 s time constant, 1.1 °C or 0.40% of reading whichever is greater) are inserted into the channels of the reactor (Fig. 3.6, panel (c)). Two additional 1.59 mm diameter, type-K thermocouple (Watlow, stainless steel sheathed, 3.5 s time constant, 1.1 °C or 0.40% of reading, whichever is greater) is used to measure the temperature at the exit of the reactor and also at the entrance to the reactor. Thermocouples located within the reactor channels are spaced at 51 mm intervals axially down the reactor with the first thermocouple placed 25 mm from the leading edge of the reactor. The thermocouples are placed approximately midway between the centerline and outer edge of the reactor.

3.1.5.1 ATR reactor build

There are a number of steps required to build and assemble a reactor into the reactor subsystem which is mounted into the reformer test apparatus (Fig. 3.1). The catalysts samples were cored out of a larger cordierite structure (wash coated with catalysts) with a maximum depth of 101.6 mm and diameter of 19.05 mm; see Fig. 3.7. For the length of the reactor (304.8 mm), 3 cored catalysts sections were required as shown in Fig. 3.8. The reactor assembly consisted of a 25.4 mm length of metal foam (Provair FeCrAlY, 20 PPI) followed by the three cordierite reactor sections. Figure 3.9 (a) shows a reactor assembly during construction. Figure 3.9 (b) shows a photo of the Provair metal foam segment. Alignment of the channels in the reactor is important and several strains of piano wire (0.737 mm diameter, carbon steel) were threaded through the reactor channels

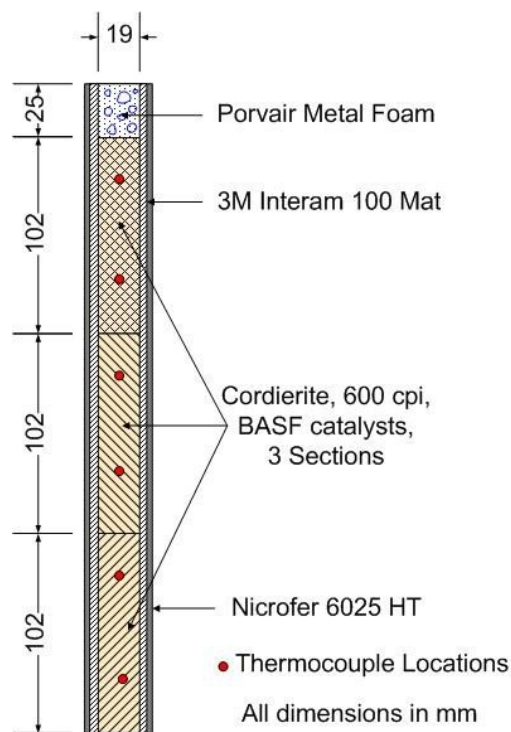


Figure 3.4 Design of ATR reactor assembly.

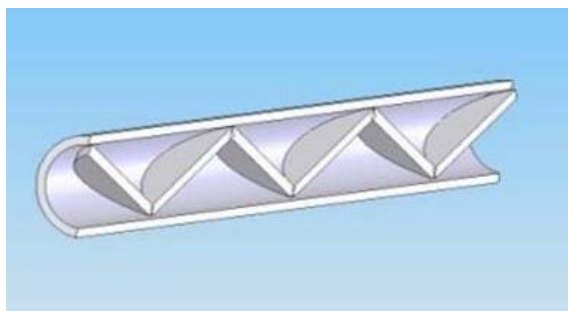
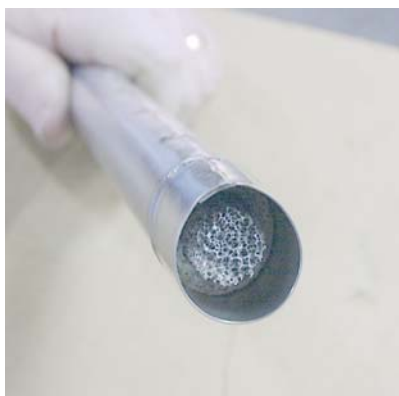


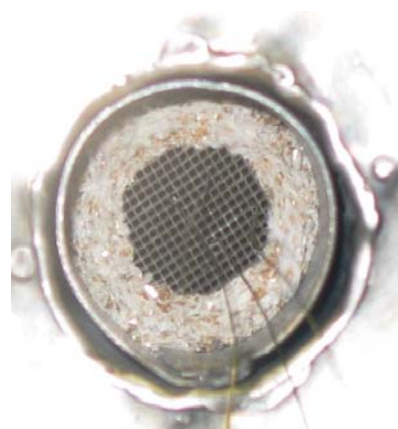
Figure 3.5 In-line static mixer.



(a)



(b)



(c)

Figure 3.6 Photographs of the ATR reactor installed in the Nicrofer cylinder. Panel (a) entrance of reactor showing metal foam insert, panel (b) show the reactor exit of the reactor, panel (c) shows exit with thermocouples installed.

(reactor channels have approximately open channel dimensions of 0.8 mm x 0.8 mm) to assure proper alignment during reactor construction; wire can be seen in Fig. 3.9 (a) coming out of the rear of the reactor assembly. The reactor and metal foam are surrounded by a mat (3M InteramTM Intumescent Mat) which when installed in the reactor provides three primary functions: i) a friction fit between the reactor metal containment tube (see Fig. 3.4), ii) a seal between the tube and the ceramic reactor, and iii) thermal insulation between the reactor and the Nicrofer tube. The 3M Interam mat was developed for the automotive catalytic converter market to hold ceramic converters



Figure 3.7 BASF catalysts ATR-7B prior to coring. Washcoated cordierite dimensions of 127 mm diameter and 101.6 mm depth.

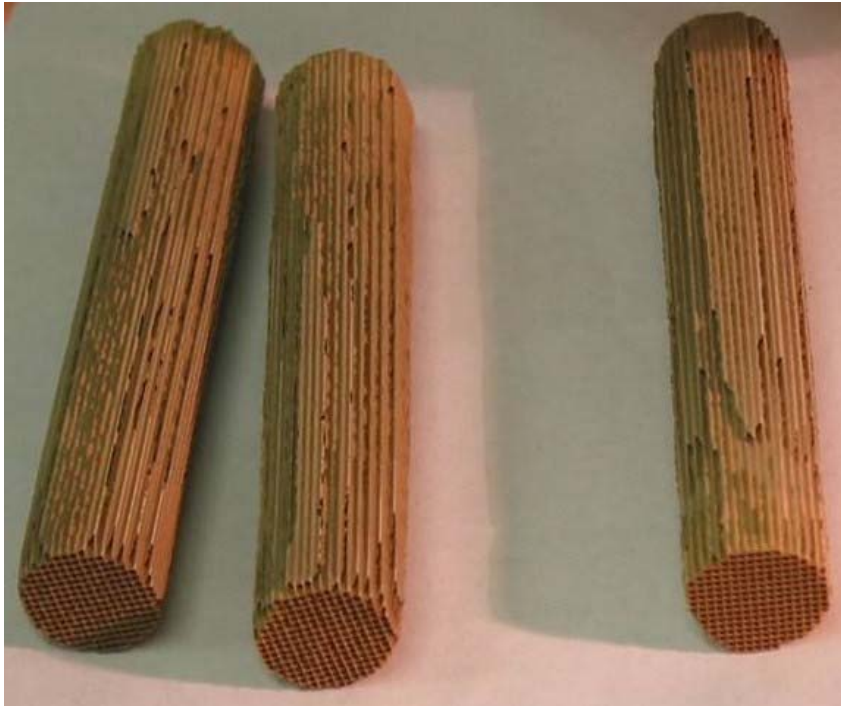


Figure 3.8 Corded Reactor Section with depth of 101.6 mm and diameter 19.05 mm.

into their metal shells. Interam has the unique property that when initially heated it expands providing a tight friction fit. Figure 3.10 (a) shows the reactor assembly being inserted into the Nicrofer metal shell and Fig. 3.10 (b) shows initial heating of the mat to set the reactor in place (alignment wires are still in place). Once the reactor is set via heating, the alignment wires can be removed. Figure 3.11 provides details on the reactor vessel which houses the reactor and Nicrofer tube, provides 50 mm thickness of high temperature ceramic insulation (Zircar Ceramics, Alumina Insulation Type ALC-AA, fiber density of 15 lbm/ft³), incorporates thermal breaks to minimize heat conduction and loss, and allows for manifolding of the reformat stream. Prior to connecting the



(a)



(b)

Figure 3.9 Reactor construction, (a) three ceramic cordierite sections with alignment wire and metal foam being wrapped by 3M Interam mat, (b) Provair metal foam.



(a)



(b)

Figure 3.10 Reactor assembly into Nicorfer metal sheel and initial heating to fit the reactor in place.

reformat manifold, thermocouples (Omega, grounded 0.254 mm diameter, type-K, KMTXL-010G-36, inconel sheathed) were threaded into channels in the reactor as shown in Fig. 3.12. The thermocouples are introduced into the reformat distribution manifold leading to the exit of the reactor through a unique fitting developed by Conax Technologies. The Conax seal is designed to withstand high temperatures and high pressures without leaking: Multi-Element Sealing (Multi-Hole Metal Gland; MHM5) $\frac{3}{4}$ " NPT (National Pipe Thread) with six (6), 0.254 mm diameter holes and grafoil soft sealant capable of withstanding 690 bar pressure (69 MPa) and 1650 °C. Final steps in construction of the reactor are shown in Figure 3.13 and include wrapping the reactor outer shell with heat tape (maintained at 325 °C for all tests), insulating the outer shell and the reformat distribution manifold with an insulation blanket (Unifrax LLC, Fiberfrax Durablanket S, 4 lbm/ft³. $\frac{1}{2}$ " thickness), and mounting the reactor assembly onto the reformer test apparatus.

3.1.6 Reformat cooler/condenser/liquid separation subsystem

The reaction products are directed first into an air cooler and then into a water cooled condenser. Water at an appropriate rate is metered into the outer jacket to ensure appropriate condensing of water from the reactor effluent. Reaction gases and condensing liquids are directed into a separator where the water separates from the

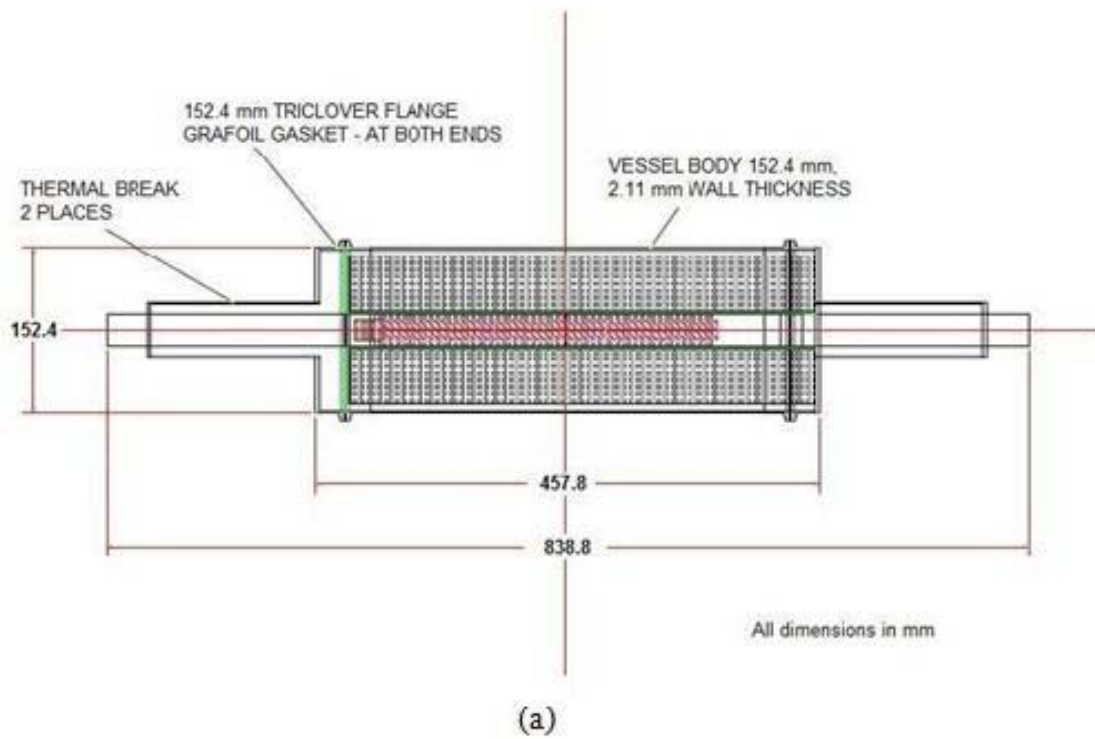


Figure 3.11 Complete reactor vessel assembly: (a) design drawing showing ceramic reactor in red and Zircar ceramic insulation in black cross hatch, (b) end view of reactor showing Zircar ceramic insulation, (c) initial build of reactor full assembly with mating stainless steel reformat distribution manifold.

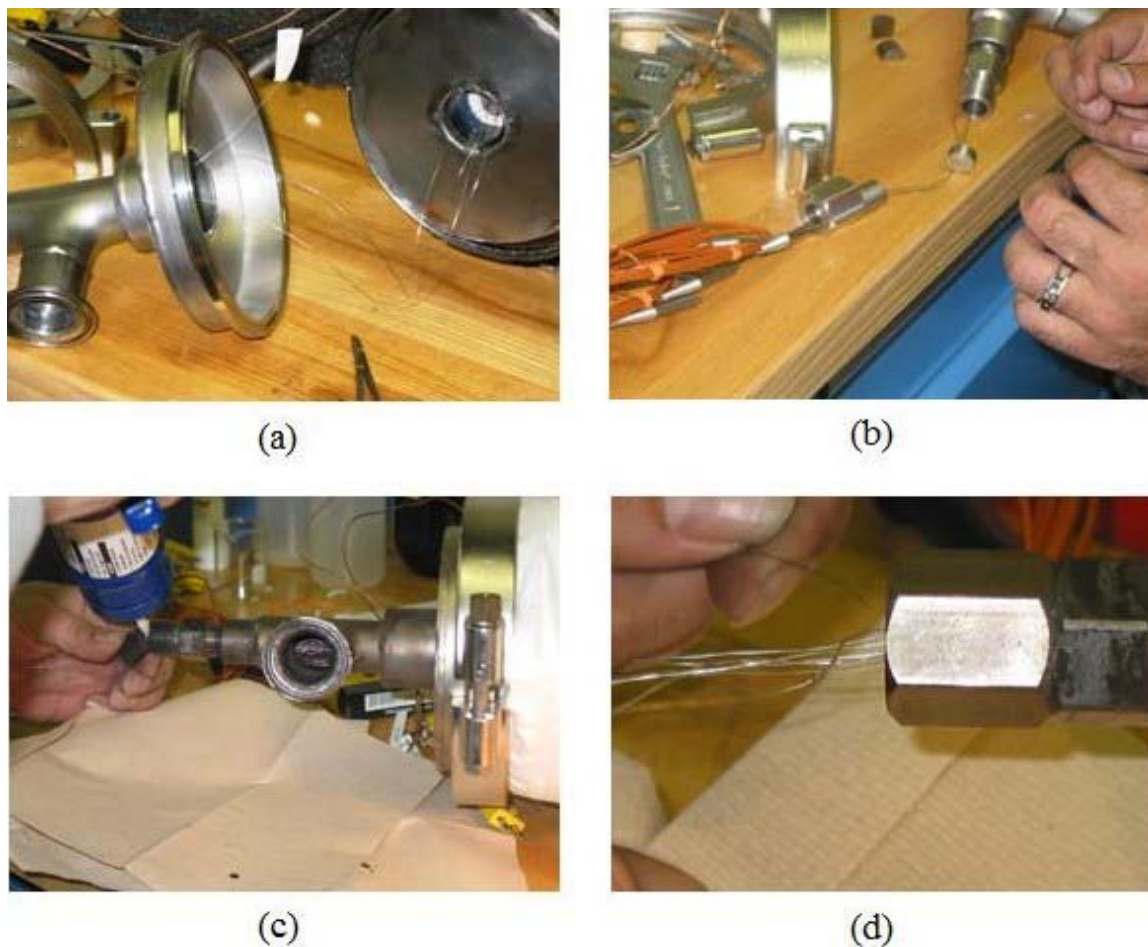


Figure 3.12 Installation of reactor thermocouples: (a) thermocouples (6) inserted into reactor channels and threaded through reformat distribution piping, (b) inserting thermocouples through Conex multi-element sealing gland, (c) applying sealer to Conex fitting and (d) Conex end-cap attached.

reaction gases. A site gauge is incorporated for visual monitoring of the liquid levels. The discharge line is configured in an overflow mode to maintain a constant level in the separator. Gases leaving the separator flow through a volume flow meter (American Meter, diaphragm meter, AC-250, $\pm 1\%$) that has a rotary encoder incorporated into its face (BEI, Incremental Optical Encoder, model L25). The rotary encoder digitizes the sweep down to 1,000th of a full rotation and sends this information into the computer



(a)



(b)



(c)

Figure 3.13 Reactor installation onto Reformer Test Bed experimental setup: (a) applying heat tape to reactor outer shell, (b) applying $\frac{1}{2}$ " of Fiberfrax Durablanket S insulation and (c) reactor installed in Reformer Test Bed.

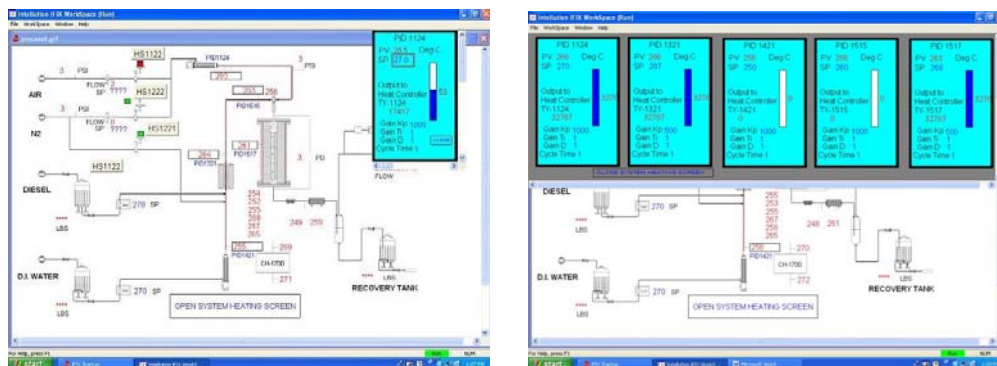
control and data acquisition system. The algorithms in the control system takes this digital information and converts it either into a real time flow rate or integrates this information over a period of time to yield net gas flow.

Condensate in the reactor effluent flows from the gas liquid separator to a receiver vessel which is mounted on a weigh scale (Sartorius laboratory balance). The information from

the weigh scale is directed into the computer control system that has the appropriate algorithms for generating liquid product flow rate information and also the total condensate collected over a predetermined period of time. Appropriate drain and sample valves are provided to be able to discharge the liquid.

3.1.7 Control and data acquisition

All components are controlled and data is electronically collected at 1 s intervals via a data acquisition system/computer interface that uses iFIXTM (General Electric) process control software. The iFIX software allows easy monitoring and rapid changes in input flow rates and operating parameters. Figure 3.14 shows iFIX control screens with the following input and control parameters: air flow (slpm), water flow (ml/min.), fuel flow (ml/min.), water vaporizer/superheater set point (temperature °C), air heater set point (temperature °C), fuel vaporizer set point (temperature °C), input line heat trace set point (temperature °C), and the reactor outer shell heat trace set point (temperature °C). All heating elements are PID controlled as shown in Fig. 3.14 (b). Within the iFIX platform all critical operational parameters can be designated with graduated alarms and procedures if values become “out of range” (see section, 3.2 Safety). Alarm values are designated as variables and can be modified for every experimental run or can be altered during operation. All data recorded during an experimental run can be exported to an excel spreadsheet for archiving and data reduction. Data is collected and archived as shown in Table 3.1 and additional logic information (valve position, power activation of components) is also recorded as shown in Table 3.2.



(a)

(b)

Figure 3.14 iFIX Control and Monitoring screens (a) and heating element PID screen for the air heater (PD 1124), fuel vaporizer (PD 1321), water vaporizer/superheater (PD 1421), reactant tubing heat trace (PD 1515), and reactor outer shell heat trace (PD 1517).

3.1.8 Insulation of tubing

All lines and tubing that carry vaporized gases or liquids are well insulated to minimize heat loss and the possibility of liquids condensing prior to reaching the reactor. All lines are wrapped with heat trace (Amptek Standard Laboratory Heating Tape, ½" x 10', 240 Vac, 520 W) that is controlled through PID controllers with interface to iFIX; see Fig. 3.15 panel (a). A High temperature woven tape (Hot Spot Tape 1500-M, 3 lbm/100 ft roll, Industrial Energy Products, Inc.) is layered over the heat tape to insure good thermal contact between the heat tape and stainless steel tubing; Fig. 3.15, panel (b). Two insulating layer are then applied: 25.4 mm of kaowool (Thermal Ceramics, kaowool, $k = 0.3 \text{ W/m-}^\circ\text{C @ } 1000 \text{ C}$) and 12.7 mm to 25.4 mm of fiberfrax (Unifrax, fiberfrax durablanket 2600, $k = 0.1 \text{ W/m-}^\circ\text{C @ } 1000 \text{ C}$); shown in Fig. 3.15 panels (b) and (c).

Table 3.1 Output data collected during all experimental work

Parameter	iFIX Nomenclature	Note	Alarm Shutdown
Temperatures			
Air Heater (mid-point)	FIX.TE1125_HEATER	Used to control air heater via PID algorithm	$\geq 700\text{ }^{\circ}\text{C}$
Fuel Vaporizer Heater Outlet	FIX.TE1322	Used to control fuel heater via PID algorithm	$\geq 1000\text{ }^{\circ}\text{C}$
Water Vaporizer/Superheater	FIX.TE1422	Used to control water heat power input	$\geq 1000\text{ }^{\circ}\text{C}$
Reactor Entrance	FIX.TE1514	Used to control reactor inlet temperature via air heater	$\geq 1000\text{ }^{\circ}\text{C}$
Tubing prior to reactor	FIX.TE1515	Used to control tubing heat trace input power via PID.	$\geq 1000\text{ }^{\circ}\text{C}$
Reactor Outer Shell	FIX.TE1518		$\geq 500\text{ }^{\circ}\text{C}$
Reactor Internal, Position #1	FIX.TE1519		$\geq 1150\text{ }^{\circ}\text{C}$
Reactor Internal, Position #2	FIX.TE1520		$\geq 1150\text{ }^{\circ}\text{C}$
Reactor Internal, Position #3	FIX.TE1521		$\geq 1150\text{ }^{\circ}\text{C}$
Reactor Internal, Position #4	FIX.TE1522		$\geq 1150\text{ }^{\circ}\text{C}$
Reactor Internal, Position #5	FIX.TE1523		$\geq 1150\text{ }^{\circ}\text{C}$
Reactor Internal, Position #6	FIX.TE1524		$\geq 1150\text{ }^{\circ}\text{C}$
Entrance to reformat liquid HX	FIX.TE1611		$\geq 1150\text{ }^{\circ}\text{C}$
Exit of reformat liquid HX	FIX.TE1612		$\geq 1150\text{ }^{\circ}\text{C}$
Chiller Outlet	FIX.TE1713		$\geq 1150\text{ }^{\circ}\text{C}$
Chiller Return	FIX.TE1714		$\geq 1150\text{ }^{\circ}\text{C}$
Reactor Exit	see note		
Reformer Flow Meter Entrance	see note	Recorded via Aglient Data Acquisition System 34970A Recorded via Aglient Data Acquisition System 34970A	
Pressures			
ATR Differential Pressure	FIX.PDI530_PRESS-DIFF	Differential pressure of ≥ 5 psig triggers reactor by-pass.	≤ 10 psig
Air Pressure	FIX.P1117_PRESS_ENTRY		≤ 10 psig
Nitrogen Pressure	FIX.P1217_PRESS_ENTRY		
System Total Pressure	FIX.P1511_PRESS_REACTOR	Pressure of ≥ 10 psig triggers valve.	
Reformer Flow Meter Entrance	see note	Recorded via Aglient Data Acquisition System 34970A	
Flow Meters			
Air Flow Rate (slpm)*	FIX.1120.FLOW		
Nitrogen Flow Rate (slpm)*	FIX.1220.FLOW		
Reformate Flow Meter	FIX.EN_FQT1850	Encrypted reading is converted to volume flow.	
High Performance Liquid Chromatographic Pumps			
Fuel Flow Rate (ml/min)	FIX.P-1350_RATE		
Water Flow Rate (ml/min)	FIX.P-1450_RATE		

* Standard condition of 1 bar and 21 °C.

Table 3.2 Logic/Status data collected during all experimentation

Parameter	iFIX Nomenclature	Note
Solenoid Valve		
Air Vent	FIX.HS1122_VENT_SOL	
Nitrogen Vent	FIX.HS1221_VENT_SOL	Primary nitrogen line
Nitrogen Vent	FIX.HS1222_VENT_SOL	By-pass nitrogen line
Electric Power		
Air Heater	FIX.1124.CV	Binary indicator (on/off)
Fuel Vaporizer	FIX.1321.CV	Binary indicator (on/off)
Water Vaporizer/Superheater	FIX.1421.CV	Binary indicator (on/off)
Tube Heat Trace	FIX.1521.CV	Binary indicator (on/off)
Reactor Shell Heat Trace	FIX.1517.CV	Binary indicator (on/off)
Reformer Flow Meter	FIX.FQT1850.SAVE.CV	
Flow Rates		
Air Flow Rate	FIX.SP1120_FLOW_SETPOINT	Flow rate input values.
Nitrogen Flow Rate	FIX.SP1220_FLOW_SETPOINT	Flow rate input values.

3.2 Safety

Autothermal reforming and catalytic partial oxidation reforming of liquid heavy hydrocarbon fuels involves operation at elevated temperatures, produces carbon monoxide at levels that are lethal, requires that vaporized fuel and oxidants be mixed at temperatures greater than the autoignition temperature of the fuel, and, if full oxidation should occur, the flame temperature would greatly exceed the melting point of the reactor, reactor containment vessel, and tubing in the experimental setup. These operating conditions require that safety be considered and that safety precautions be incorporated into the experimental design. Prior to construction of the fuel reforming apparatus, a safety risks assessment was conducted by a board consisting of engineers, technicians, and safety personnel working at the US Army Communication-Electronics Research, Development and Engineering Center, Night Vision Laboratory, Fort Belvoir,

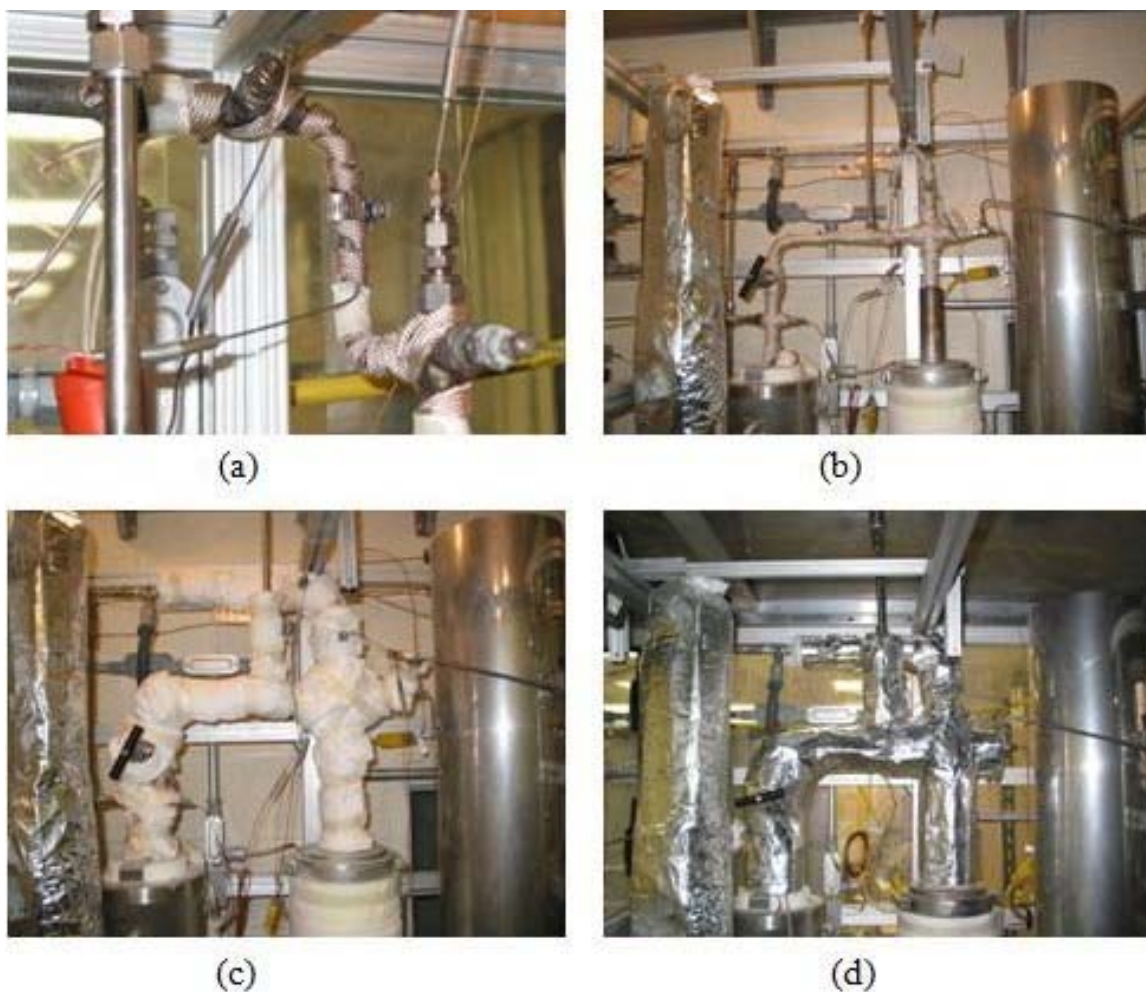


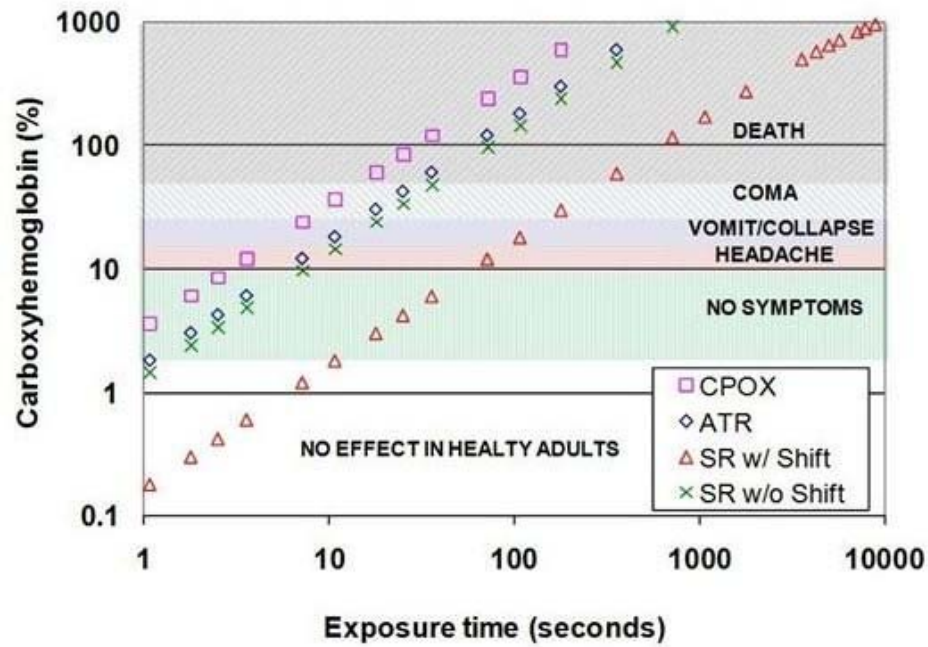
Figure 3.15 Steps taken to minimize heat loss in lines upstream of the reactor: (a) heat trace, (b) high temperature woven tape is layered over the heat trace, (c) kaowool insulation and (d) fiberfrax insulating blanket is applied.

Virginia. Risk assessment included visits to other laboratories conducting similar experimentation (Argonne National Laboratory, Argonne, IL; Army Research Laboratory, Delphi, MD) to incorporate their approaches to safety. Safety can be divided into personnel safety (anything affecting the safety of people in the vicinity of the laboratory)

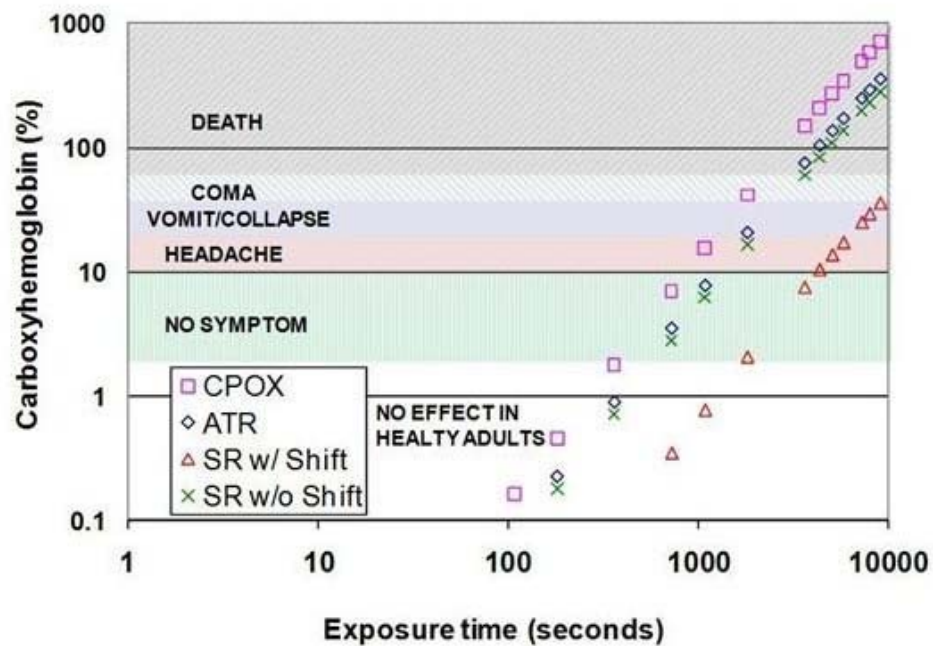
and equipment safety (precautions taken to minimize risk of damage to the reformer test apparatus).

3.2.1 Personnel safety

The greatest threat to human safety associated with the fuel reformer apparatus is carbon monoxide poisoning. Depending on operating conditions, carbon monoxide concentrations in the reformat stream can reach 25% (molar percent on a dry basis) although 10% is more typical. Figure 3.16 panel (a) shows that direct exposure to reformat gases can cause very severe health risks, even brief exposure. To mitigate personnel risks associated with fuel reforming, a dedicated walk-in hood with chemical sensors and alarms (audible and visual), and the ability to remotely control experiments was incorporated into the reformer test apparatus. The reformer test apparatus is housed entirely within a walk-in hood which was designed and built at the Night Vision Lab facilities. The design ventilation flow rate was based on a number of parameters, including: maintaining a minimum duct flow velocity of 45.8 m/min., maintaining an exit exhaust velocity of 305 m/min., maintaining sufficient flow for hydrogen and carbon monoxide concentrations to be below their lower explosive limits of 4% and 12.5%, respectively, having adequate ventilation to assure that carbon monoxide concentration did not exceed 50 ppm (OSHA eight hour exposure limit), being sized to handle future reforming requirements up to 66.6 kW_{th} (approximately, a reformer sized for a 20 kW_e fuel cell) regardless of reforming technology, and being able to remove any heat



(a)



(b)

Figure 3.16 Effects of carbon monoxide exposure from (a) direct exposure to the reformat and (b) unventilated exposure assuming a well mixed environment.

generated during reforming (including heat generated by combustion of the entire reformat stream). Based on these criteria, the walk-in hood ventilation was designed with a maximum flow rate of 113.3 m³/min. (4000 std. ft³/min.) controlled through a motor controller (Safronics, GP10, General Purpose Open Loop AC Drive) which allows the user to reduce flow to meet application needs. Figure 3.16 panel (b) provides a more likely scenario of the failure of the ventilation fan while under operation in a well mixed environment; under these conditions adequate time is available to safely terminate operation and leave the experimental laboratory. The walk-in hood was designed with a foot print of 3.04 m x 2.18 m and can be seen in the background of Fig. 3.17. Gaseous chemical sensor for carbon monoxide, hydrogen and hydrocarbons are continuously monitored (Scott Instrument, QuadScan II) and alarms and visual signals are actuated in case of unacceptable levels (typically set at ½ the lower explosive limit or at the maximum allowable 8 hour exposure limit set by ACGIH¹²). Inspection of the hood and its performance is performed annually.

Personnel safety equipment and devices such as safety glasses, gloves (compatible with fuels being used), high temperature mittens, fuel spill mitigation supplies, fire extinguishers, unblocked and marked exit doors, eyewash, and showers are also readily available and accessible. The laboratory area is periodically inspected by the U.S. Army Night Vision Safety Office for compliance with U.S. Army safety regulations [233]. In addition, all personnel working with hazardous materials and waste (fuels used in this

¹² American Conference of Industrial Hygienists (ACGIH)

experimental work, gases generated during reforming and liquids and gases used in the calibration of instrumentation are considered hazardous materials) are trained and licensed in accordance with Environmental Protection Agency (EPA) 40 Code of Federal Regulation (CFR), Resource Conservation and Recovery Act (RCRA), Part 261 [234] and 262 [235].



Figure 3.17 Laboratory reformer test apparatus, control and work space. Desk with multiple computer LCD monitors is the operator control desk. Large gray panel on the left is the electrical power and signal distribution panel. Walk-in hood is shown in the background of the photo.

3.2.2 Equipment safety

Incorporated into the hardware and control of the reformer test apparatus are a number of automated, manual, and fail safe components designed to protect the test setup and personnel from harm. Automated shutdowns occur when predefined operating limits are exceeded; see Table 3.1 for values. Most automated shutdowns are temperature driven, however, the reformer test apparatus will not start if nitrogen pressure is not present; nitrogen is critical to unit operation, shutdown, and emergency conditions. Automated shutdowns occur without input from an operator and consist of shutting off fuel, air and water flows, opening the nitrogen valve with a predetermined flow of 20 slpm, and removing power from all heating elements. A shutdown condition, once initiated, will continue until reset by the operator. The unit shut down can also be initiated manually by hitting the emergency shutdown button on the electrical power and signal distribution panel (see Fig. 3.17, manual shutdown button is red button in the center of the panel). In case of loss of power, the air flow valve is designed as a normally closed valve and the nitrogen valve is a normally open valve; thus, loss of power will result in a nitrogen purge situation returning the unit to a safe condition.

Other equipment safety measures incorporated into the design are:

- i. The air heater cannot be powered until air pressure is detected at the inlet of the unit. This is to minimize the possibility of burning out the electrical air heater.

- ii. Both the water and fuel pumps have pressure relief check valves downstream of the pumps which return to the respective tanks. This is to avoid damage to the pumps due to a blockage in the line.
- iii. Up stream of the reactor a pressure relief valve to atmosphere set at 10 psig is incorporated to avoid over pressurizing components in the reformer test apparatus.
- iv. A differential pressure relief valve operates across the reactor and allows flow to bypass the reactor when 5 psig is exceeded. This is to protect the reactor vessel that is designed for a maximum differential pressure of 10 psig.

As a test of the reactor seals and integrity of the reformat system, the reformer test apparatus is leak tested before and after every experimental run. Leak testing consisted of valving off all gas paths and pressurizing the reactor to approximately 1 psig and measuring the time until 0.6 psig was reached. A leak rate of 1272.6 Pa/min. (0.185 psig/min.) has been used as a minimum acceptable leak rate for the system. This leak rate is empirically determined and for this experimental setup is based upon the conditions of no measureable external leakage of components (checked with Snoop Leak Detection Solution, Swagelok) and seals. Figure 3.18 shows system leak rates which have occurred over many thermal cycles and hours of elevated temperature operation. In addition to leak testing, a system integrity tests which consists of measuring the pressure drop through the unit at flow rates of 5, 10, 15, 20, 30, 40 and 50 slpm is also conducted before and after every experimental run. The system integrity test is used to identify any

potential damage to the reactor or blockage within the system. Figure 3.19 shows the results from the integrity testing showing minor pressure drop increase over the time period in which experimental work supporting this thesis was undertaken.

3.3 Analysis of reaction products

The gaseous reformat stream was analyzed by an on-line gas chromatograph (Agilent Technologies, Inc., Micro GC 3000) with four columns using thermal conductivity detectors (TCD). Hydrogen (H_2), Nitrogen (N_2), Methane (CH_4), and carbon monoxide (CO) concentrations were determined by GC on a Molecular Sieve column (10 m x 0.32 mm) at 100 °C with argon carrier gas. Carbon Dioxide (CO_2), Ethylene (C_2H_2), Ethane (

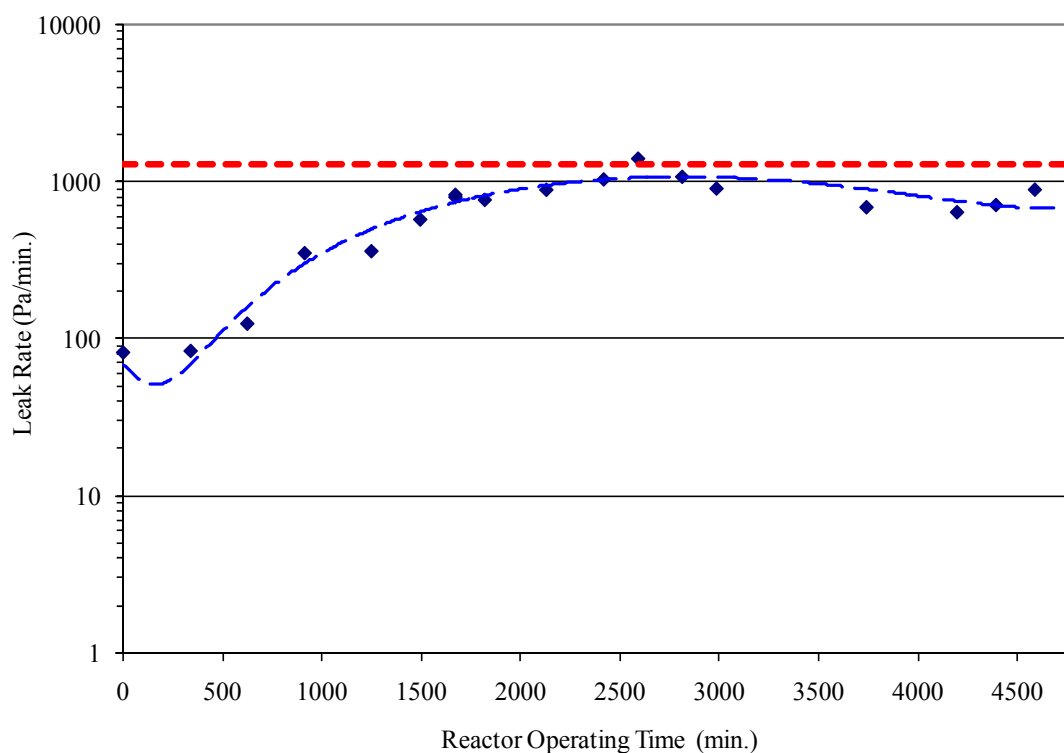


Figure 3.18 Reactor leak rate over time.

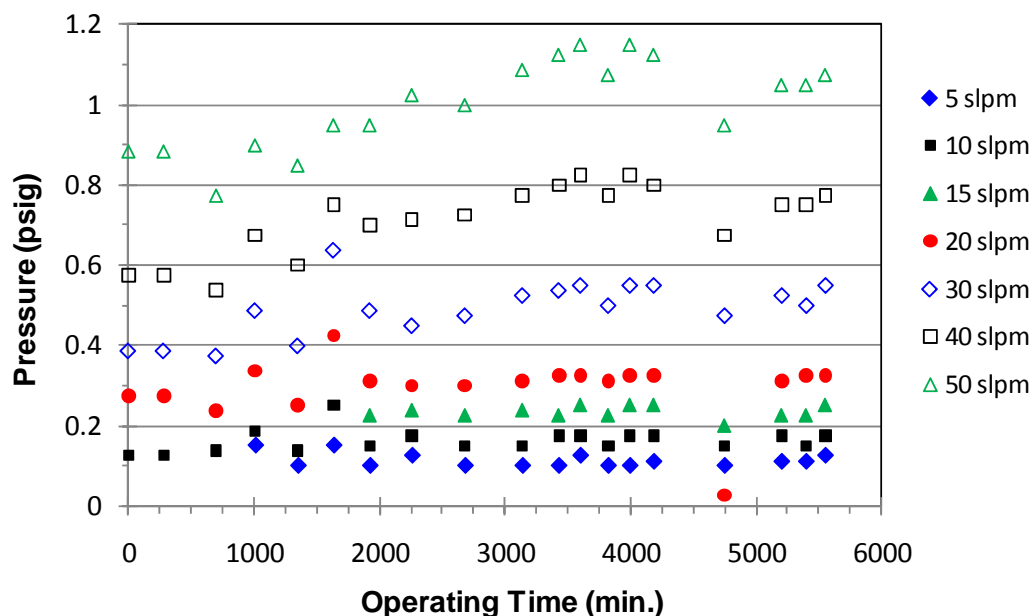


Figure 3.19 System integrity test consisting of operating the reactor test apparatus at indicated flowrates and noting the pressure drop through the system.

C_2H_4), and Acetylene (C_2H_2) were determined by GC on a Plot U column (8 m x 0.32 mm) at 75 °C with helium carrier gas. Propylene (C_3H_6), propane (C_3H_8), n-butane (C_4H_{10}), trans-2-butene (C_4H_8), iso-butene (C_4H_8), 1-butene (C_4H_8), cis-2-butene (C_4H_8), iso-pentane (C_5H_{12}), n-pentane (C_5H_{12}), 1,3 Butadiene (C_4H_6), trans-2-butene (C_4H_6), 2-methyl-2-butene (C_5H_{10}), 1-pentene (C_5H_{10}), and cis-2-pentene (C_5H_{10}) were determined by GC on an Alumina column (10 m x 0.32 mm) at 145 °C with helium carrier gas. Iso-butane (C_4H_{10}) was determined by GC on an OV1 column (10m x 0.15 mm x 2.0 μ m) at 90 °C with helium carrier gas. While the Micro-GC was capable of detecting hydrocarbon compounds up to C_6 , the reformat condensers would remove compounds greater than C_4 . Figure 3.20 shows a typical chromatogram identifying peaks versus

elution time for compounds of interest. Multiple level calibration curves were used for all compounds with the calibration gases at ± 0.02 % analytical accuracy. Additional details regarding calibration standards used with the gas chromatograph can be found in Appendix D Gas Chromatograph Calibration. The instrument was recalibrated on a weekly basis preceded by a column bake-out¹³ procedure recommended by Agilent [236].

3.3.1 Fuel analysis

Jet fuel (JP-8) was obtained from Haltermann Products, Channelview, Texas in accordance with MIL-T-83133 (Turbine Fuels, Aviation, Kerosene Types, NATO F-34 (JP-8), NATO F-35, and JP-8+100). The following selected fuel properties were obtained through analysis by Southwest Research Institute, San Antonio, Texas: Heat of Combustion (ASTM D240) of 12.0 kW-hr/kg; carbon and hydrogen mass percent (ASTM D5291), 85.72%¹⁴ and 13.91%¹⁴, respectively; aromatic content (ASTM D5186), mono-aromatics of 19.2%¹⁴, poly-aromatics of $< 0.1\%$ ¹⁴, and total aromatics of 19.3%¹⁴; and, sulfur content (ASTM D2622) of $< 0.001\%$ ¹⁴. The heating value was confirmed by the author using a PetroSpec, Turbine Fuel Analyzer (TD-PPA); see Fig. 3.21 for photo of the turbine fuel analyzer. Sulfur and carbon content of the JP-8 fuel was further characterized by the author using an Analytik-Jena Elemental Analyzer 3100ea (Fig. 3.22), calibrated against a six point calibration curve for sulfur over a range of 0.1 to 50

¹³ The bake-out procedure consists of raising the temperature of the columns for a specified period of time. This procedure removes hydrocarbon compounds and fixed gas from the columns which may build up over time. Recommended bake-out procedures by column type are: molecular 5A sieve (8-12 hrs. @ 180 °C, weekly), plot U (8-12 hrs. @ 160 °C, weekly), alumina plot (8-12 hrs. @ 180 °C, weekly) and OV-1 (2 hrs. @ 180 °C, weekly).

¹⁴ Percentage is in mass percent.

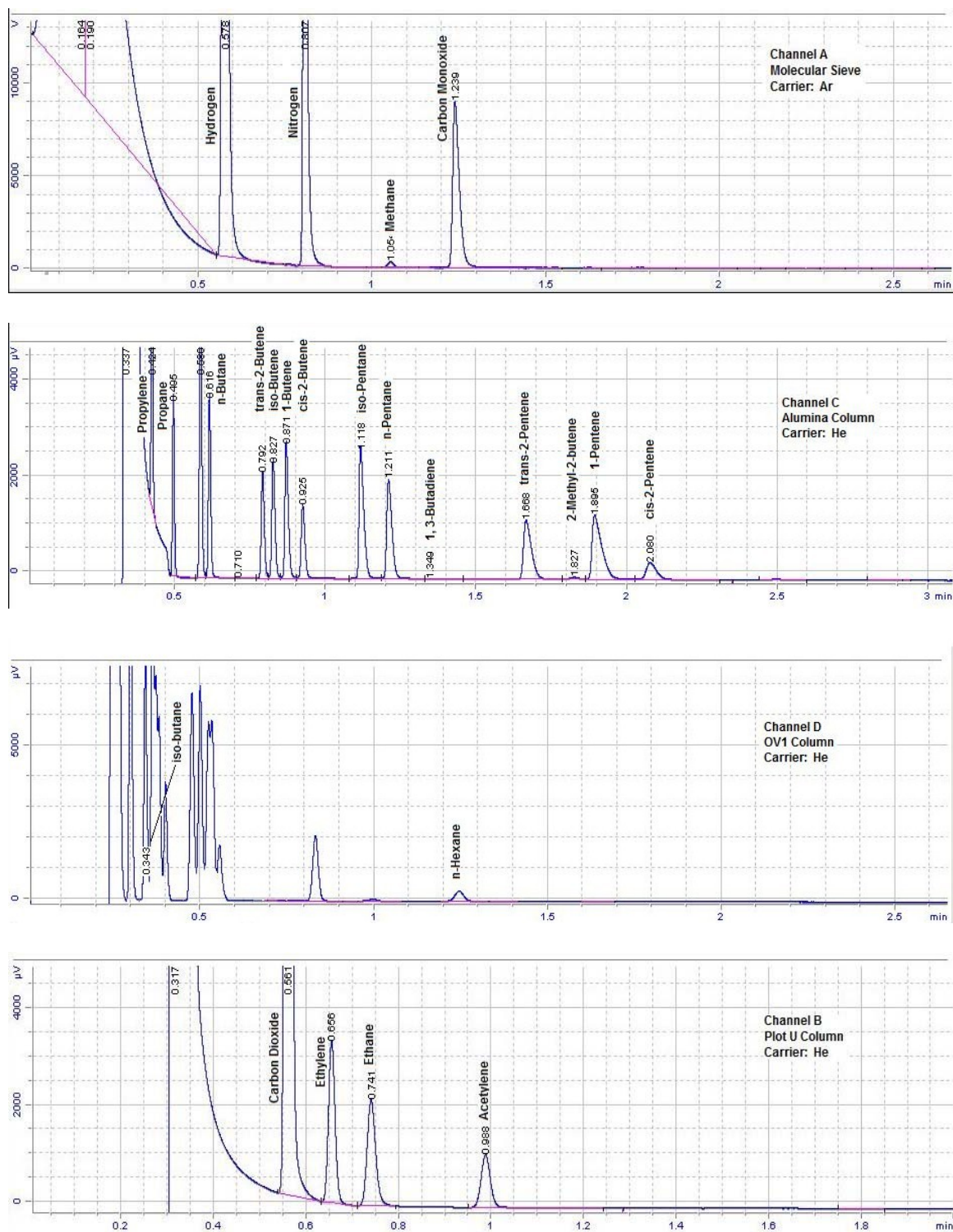


Figure 3.20 Chromatograms from on-line Agilent 5000A micro Gas Chromatograph identifying selected column for each channel and carrier gas.

ppm and a five point carbon calibration curve of over a range of 85%¹⁴ to 86%¹⁴ with calibration standards obtained from O2SI, Charleston, South Carolina. The sulfur analysis resulted in a total sulfur content of 3.8 ppm mass basis (average of five samples run with a variance of 0.5%).

3.4 ATR operational characteristics

The experimental reformer test apparatus was designed to have an adiabatic reactor, the ability to control input parameters over a wide operating range, and to acquire data directly or through mathematical reduction with acceptable error. The following four sections will address the operating characteristics of the test apparatus, unique operating conditions observed during initial experiments and corrective actions taken, and instrument error.

3.4.1 ATR reactor design/thermal characteristics

The design goal for the reactor was to achieve adiabatic operation and to successfully reform liquid heavy hydrocarbon fuels (for this study JP-8) under ATR and CPOx operating conditions. Figure 3.23 gives a cross-sectional view of the reactor design. The reactor is surrounded by 4mm of InteramTM 100 Mat ($k = 0.2 \text{ W/m-K @ } 900 \text{ }^{\circ}\text{C}$) all enclosed by a 35 mm outside diameter tube with 1.6 mm thickness made of Nicrofer 6020 hMo ($k = 24.6 \text{ W/m-K @ } 900 \text{ }^{\circ}\text{C}$). Surrounding the reactor tube is a 50.8 mm thick rigid zirconia insulation (Zircar, Microsil Microporous Insulation, $k = 0.038 \text{ W/m-K @ }$



Figure 3.21 Infrared based Jet fuel analyzer, PetroSpec Turbine Fuel Analyzer (TD-PPA).

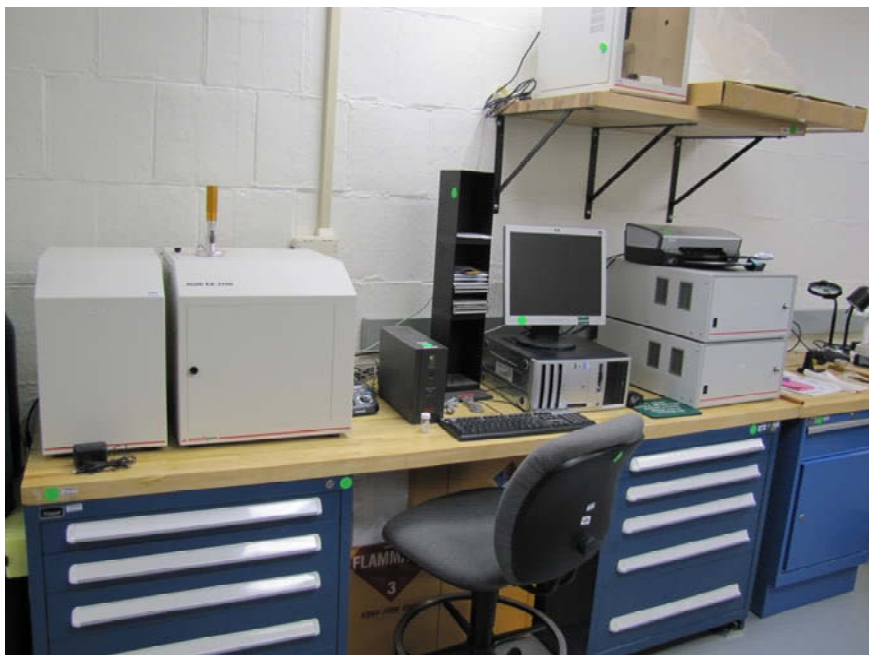


Figure 3.22 Elemental Analyzer for total carbon, nitrogen and sulfur content; Analytik-Jena, ea3100.

800 °C). The above materials are housed in a 151 mm outside diameter stainless steel enclosure. The enclosure is wrapped with heat tape and insulated with 25.4 mm of kaowool insulation (Thermal Ceramics, kaowool, $k = 0.3 \text{ W/m-}^\circ\text{C @ } 1000 \text{ C}$). The thermal losses from the reactor were simulated by a modified one-dimensional model (modified to account for end losses) and verified against laboratory test data. Figure 3.24 provides a comparison of reactor skin temperatures measured experimentally, while the reactor is heated to 550 °C with air, against modeled results. The air heater is only capable of producing a maximum reactor temperature of approximately 550 °C to 600 °C; this is the reason for not testing under conditions more typical for JP-8 fuel reforming (850 °C to 950 °C). In this test, the reactor skin temperature was experimentally measured using a Fluke Infrared Thermometer (model 566, accuracy of $\pm 1\%$ of reading or 1°C whichever is larger). Results indicate that the simple one-dimensional model provides reasonable results and can probably be extended to JP-8 fuel reforming conditions without introducing unacceptable errors. Figure 3.25 shows the predicted model thermal losses against reactor operating temperature and experimental data taken from reformer operating runs. Here the modeled thermal loss result are in close agreement with the experimental data with the model over predicting thermal losses at temperatures below 775 °C and under predicting thermal losses above 775 °C. For the experimental data, the reactor operating temperature is averaged by temperature and area for comparison purposes. For ATR operation on JP-8, we are generally interested in operating in the temperature range of 850 °C to 950 °C. In this temperature range, the

thermal losses are between 80W and 110W which corresponds to a 2.4% to 3.2% loss respectively, based on incoming fuel at 6 ml/min ($3.33 \text{ kW}_{\text{th}}$).

3.4.2 Instabilities with vaporization of liquids

Flow instabilities, observed as fluctuations in temperature and pressure within the reactor during reforming were noted during initial experimental runs. Figure 3.26 shows early results while reforming n-dodecane. Temperature fluctuations of over 100°C and pressure variations of $\pm 12 \text{ kPa}$ (1.74 psi) were observed. Initially the liquid pumps were believed to be the source of the pressure and temperature variations. To diagnosis the problem, both the fuel vaporizer and water vaporizer were observed while operating in

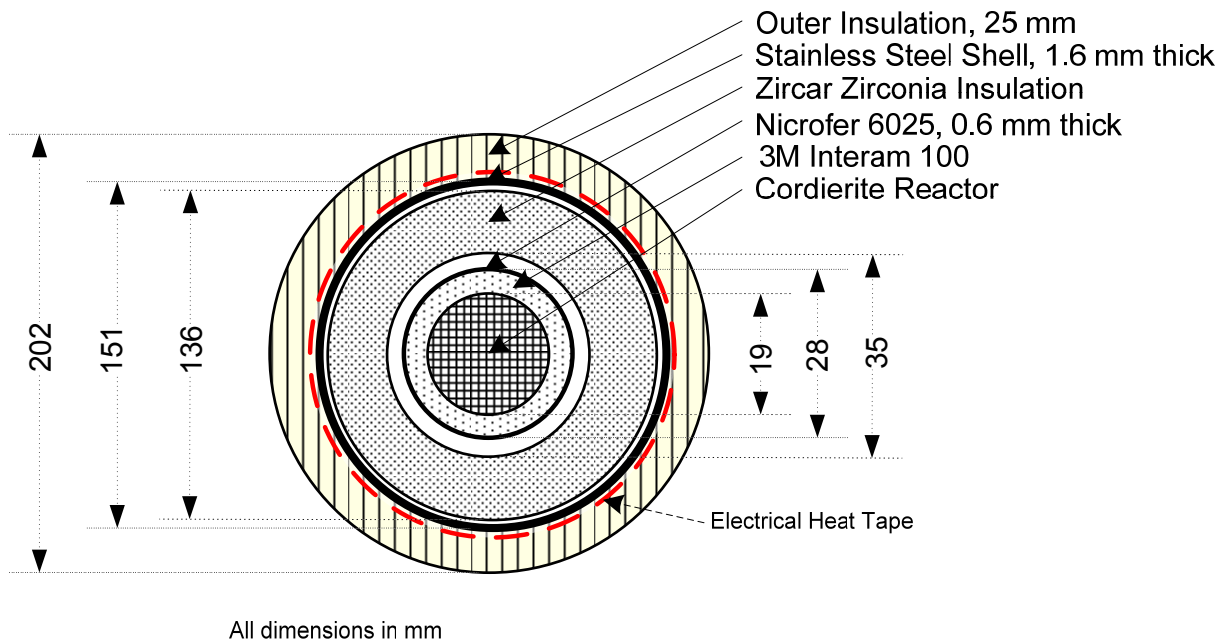
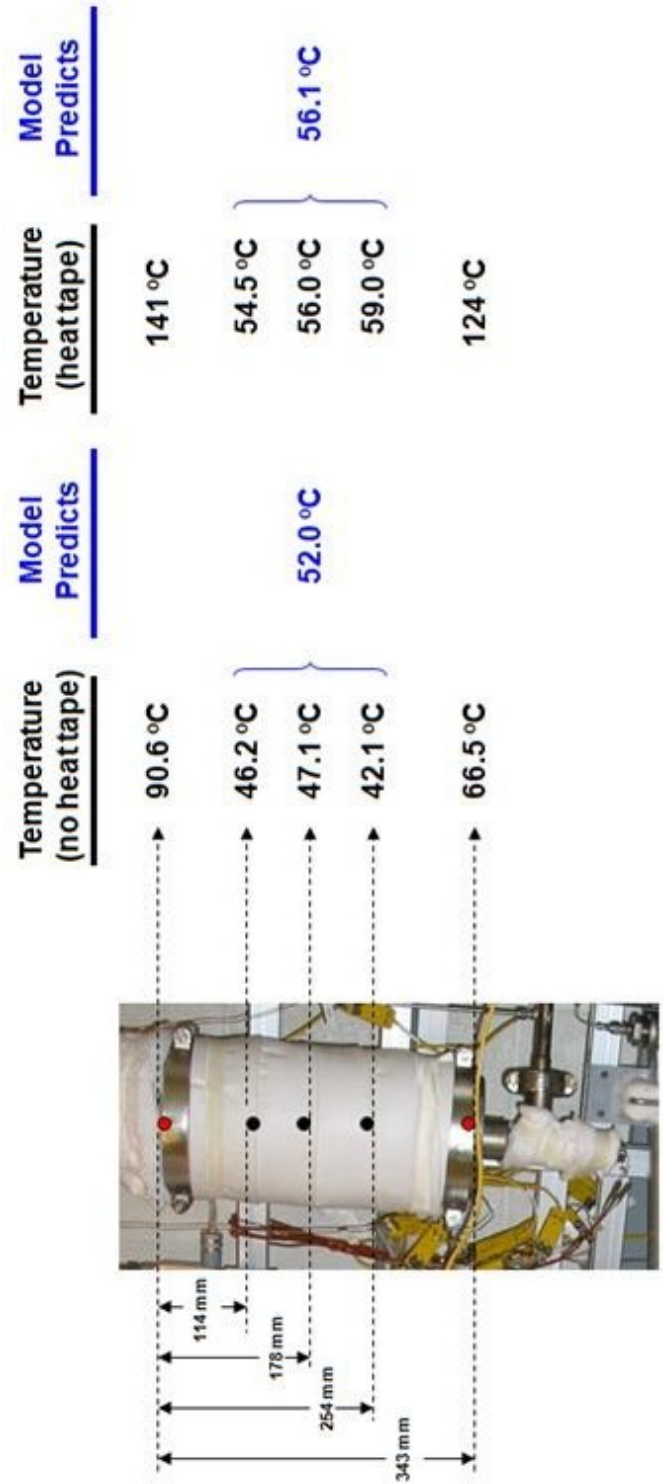
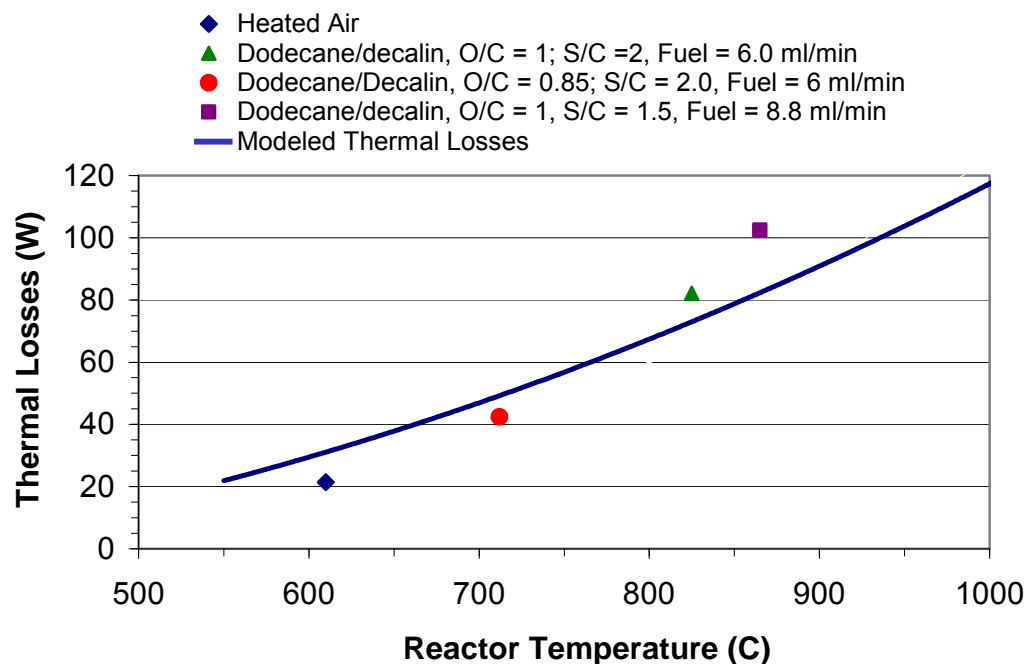


Figure 3.23 Cross Section View of Reactor and Insulating Housing.



* Heat air at 50 slpm producing an average reactor temperature of 550 °C .

Figure 3.24 Reactor skin temperatures compared to modeled results under two scenarios: 1) reactor heat tape off and 2) reactor heat tape set at 325 °C.



3.25 Calculated reactor thermal losses (solid line) against measured under four different operating conditions.

recirculation mode (i.e. isolated from other components in the system). From variation in the outlet temperature as measured by a 1.6 mm diameter K-type thermocouple (0.4 s response time, $\pm 0.75\%$) positioned in the flow stream at the exit of the vaporizer, the water vaporizer was seen to be the primary contributor to flow instabilities. The fluctuation within the water vaporizer appeared random and could not be directly correlated with pressure pulsations from the water pump. The primary cause of the water vaporizer flow instabilities was attributed to unstable film boiling. Unstable film boiling is a well documented [237, 238, 239, 240, 241], yet complex phenomena that is

still the subject of active research [242]. Unstable film boiling can usually be avoided by increasing the heat transfer surface area and minimizing the temperature difference between the bulk fluid and the wall (heater element in the present case). To minimize temperature fluctuations several modifications on the water vaporizer design were undertaken while operating in a “recirculation” mode (vaporizer/superheater is isolated from the system). Figures 3.27 depicts improved water vaporizer designs and the resulting decrease in temperature fluctuation. Figure 3.27, Curve A is for a single electric vaporizer module with 25.4 mm insulation ($k = 0.09 \text{ W/m-K @ } 400^\circ\text{C}$), a 319.2 cm^2 heat transfer surface area, and an average heat flux of 4.7 W/cm^2 . Figure 3.27, Curve B shows the addition of a second vaporizer/superheater (with the same amount of insulation as for Curve A), a total heat transfer surface area of 752.4 cm^2 , and with a heat flux of 3.8 W/cm^2 . Figure 3.27, Curve C, has the same heat transfer surface area as Curve B, but with improved insulation ($k_{\text{equiv.}} = 0.07 \text{ W/m-K @ } 400^\circ\text{C}$) applied with a thickness of 38 mm resulting in a heat flux of 3.3 W/cm^2 . With each design modification the maximum heat flux was reduced as well as the temperature difference between the bulk fluid and heat element surface temperature.

3.4.3 ATR reactor start-up and shutdown

Upon start-up the liquid streams (fuel and water) are valved into a recirculation mode that returns the vaporized liquids to their reservoirs through a tube in tube condensing heat exchanger (see Fig. 3.2). This allows the fuel and water to independently achieve a desired temperature prior to mixing with air and introduction into the reactor. For the

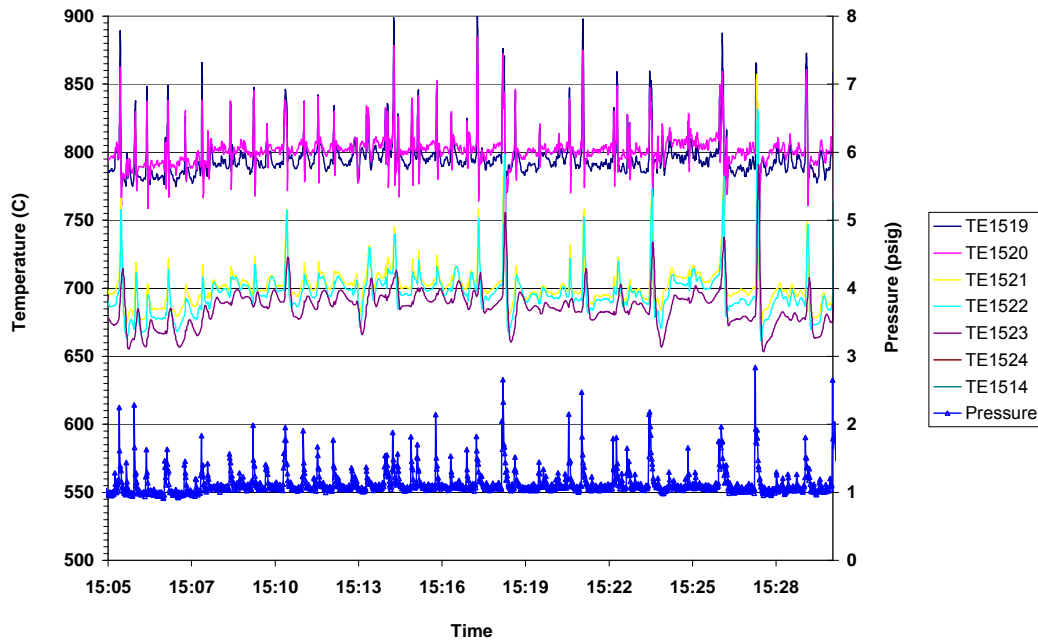


Figure 3.26 n-Dodecane at 6 ml/min. fuel flow with $S/C = 2.0$ and $O/C = 0.8$. The reformer test apparatus water vaporization system consists of a single stage vaporizer/superheater and this design resulted in high temperature and pressure fluctuations.

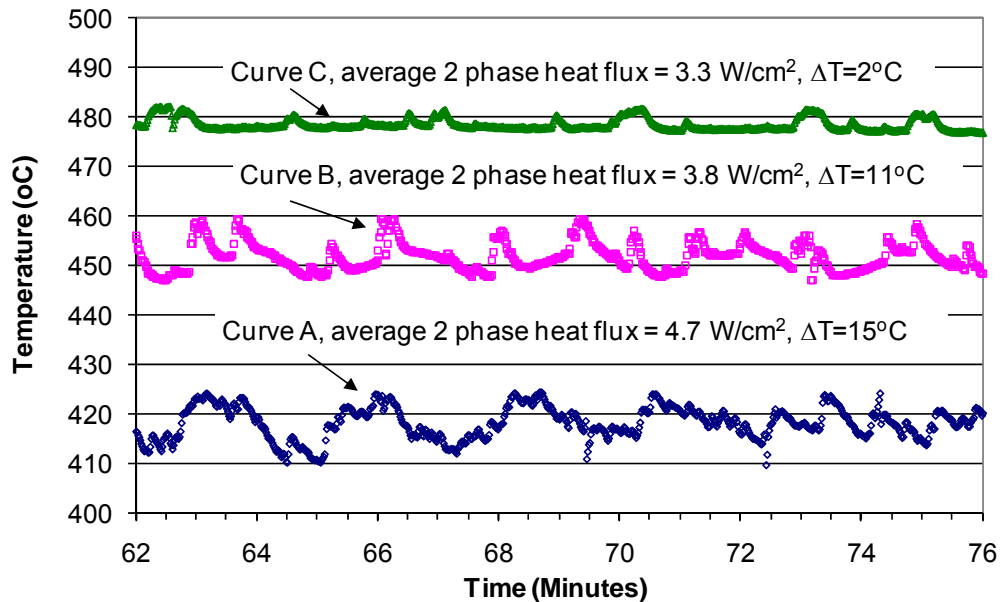


Figure 3.27 Comparison of water vaporizer/superheater with design improvements to minimize flow instabilities.

testing performed, a reactor entrance temperature of 425 °C (± 10 °C) was selected.

Under this condition, the water vaporization temperature is typically set in the range of 425 °C to 475 °C and the superheated fuel temperature is set at approximately 50 °C to 100 °C above its boiling point, which for JP-8 is 261 °C to 311 °C. The reactor is preheated by air to 270 °C to 300 °C prior to light-off. Once start-up conditions are achieved, the air flow path is purged of air by flowing nitrogen at 20 slpm for approximately 1 minute prior to allowing the vaporized fuel to flow into the reactor.

Once the vaporized fuel is allowed into the reactor, air is then incrementally increased to the predetermined oxygen-to-carbon level (O/C) with corresponding incremental decreases for nitrogen. Light-off occurs under dry catalytic partial oxidation conditions.

Within approximately 30 s the reactor comes up to temperature and steam is added.

Figure 3.28 shows typical conditions of the input stream as the reactor starts-up. As can be seen from the figure, start-up takes from 60 to 90 minutes and the reactor achieves stable operating temperature within 1-2 minutes after light-off. Full thermal stability of the reactor after light-off is determined by reformat product analysis and typically takes from 20 to 30 minutes. The limiting conditions for start-up are water vaporization/superheat and reactor preheat.

Reactor shutdown is accomplished by switching from air to nitrogen (at the same flow rate), temporarily shutting off the fuel and placing the fuel and water delivery system in recirculation mode. At this time all electrical heating components are turned off and the fuel is restarted to assist with fuel vaporizer cool down. While the reactor is still at an

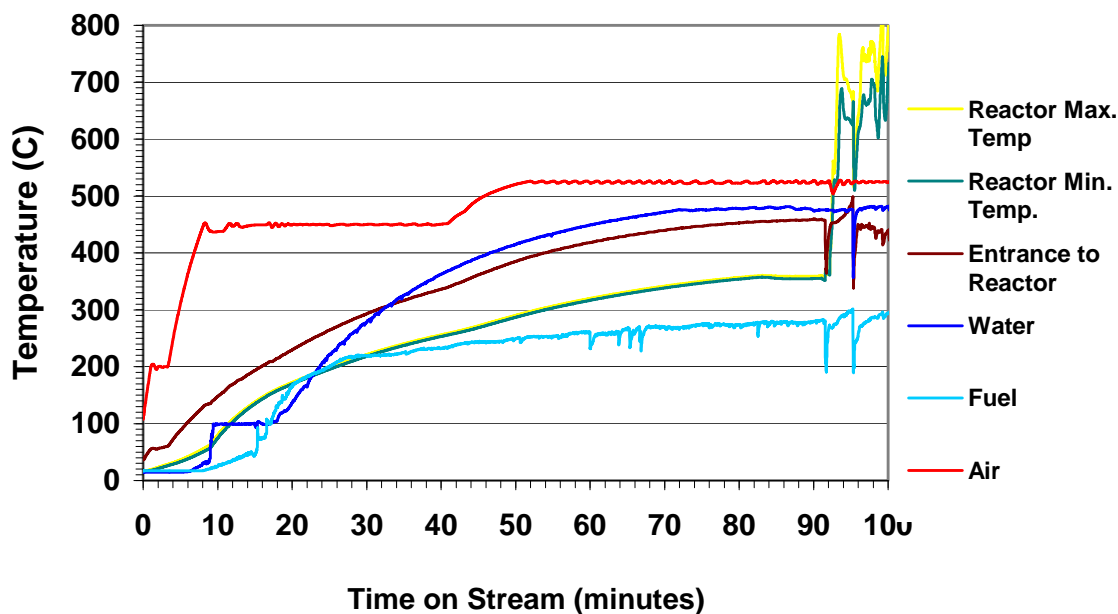


Figure 3.28 Start-up and light-off of an ATR reactor on low-sulfur JP-8 at 6 ml/min., S/C = 2.0 and O/C = 1.0.

elevated temperature (≥ 500 °C), air is slowly reintroduced into the nitrogen flow in order to oxidize any residual carbon or unconverted hydrocarbon present in the reactor. The reactor is then slowly cooled with air flow at 10-14 slpm. Reactor cool down under these conditions takes approximately 90 minutes.

3.4.4 Light-off temperature

The light-off temperature, as used here, is defined as the minimum temperature that partial oxidation reactions will begin and proceed to full reactor operation. For many mobile applications, rapid system start-up is desired and an understanding of light-off is a key parameter for improving system start and in avoiding pre-ignition/oxidation upstream of the reactor. The procedure used in determining light-off was to operate under flow

conditions that had resulted in good reactor operation in previous experiments. For light-off of JP-8, a fuel flow rate of 5.86 ml/min (3.33 kW_{th}) and an oxygen-to-carbon ratio of 1.0 was used. The reactor was preheated and started as described above. For the determination of the light-off temperature, a maximum of 60 s was allowed for the reactor to achieve full temperature operation. If light-off was unsuccessful, the reactor was purged with nitrogen for approximately 60 s, after which the next reactor operating temperature was set with air flow. Figure 3.29 shows a successful light-off of JP-8. The reactor temperature conditions just prior to light-off were T_{max} of 228.5 °C (reactor inlet) and T_{min} of 224.2 °C (exit of reactor). At time equal to 0.0 s, air is introduced into the fuel/nitrogen stream. After 60 s, an O/C ratio of 1.0 is achieved. During the transition from nitrogen to air (at O/C = 1.0) a slight rise in temperature is observed ($\Delta T_{0-60s} = 14$ °C, $\Delta T/dt = 0.23$ °C/s). In general, the reactor heats up from the front to the rear. From 60 s to 90 s, the temperature rises more rapidly ($\Delta T_{60-90s} = 34$ °C, $\Delta T/dt = 1.13$ °C/s). After 90s the reactor temperature rises rapidly exceeding 700 °C at t = 93 s ($\Delta T/t = 140$ °C/s). Of note is that once air is flowing at an O/C ratio of 1.0 there is an approximate 30 s delay prior to light-off. At t = 100 s, steam at 475 °C (10.47 ml/min) is introduced into the reactor resulting in a slight decrease in temperature that is recovered and stabilized within 60 s.

3.5 Data analysis

For small, mobile reactors designed for fuel cell power systems, reactor product yield, fuel conversion to CO_x (CO and CO₂), reformer efficiency, gas hourly space velocity (or

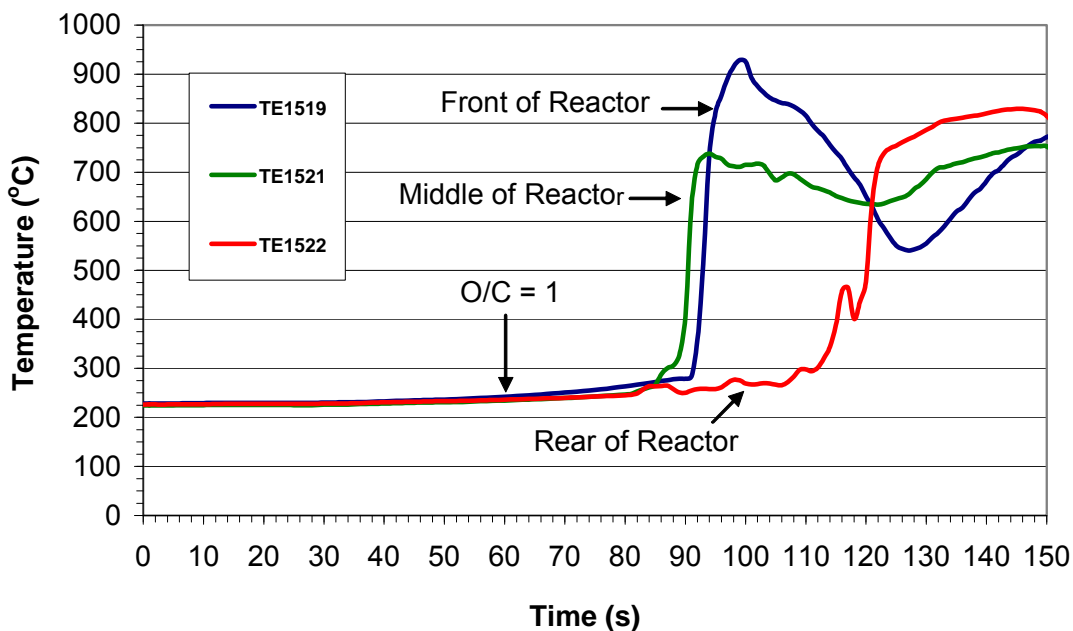


Figure 3.29 Light-off of JP-8 in dry partial oxidation mode with reactor pre-heated to 324 °C.

space-time), and carbon balance provide good insight into the overall performance of the reactor. High fuel conversion, as defined here, assures that hydrocarbon slip which could have deleterious effects for downstream process is not occurring. High yield indicates that proper sizing and operating conditions are achieved for the reactor. Efficiency provides an indication of the reactors contribution to an overall power system performance and also is an indirect measure of the selectivity of the reactor for products of interest. The gas hourly space velocity (GHSV) or space time is defined as the volume flow rate of products into the reactor at standard conditions divided by the volume of the reactor with units of hr^{-1} . The term space-time is analogous to residence time, assuming plug flow reactor conditions, and is the reciprocal of GHSV (space time = $(\text{GHSV})^{-1}$).

Carbon balance provides a means to assure that all fuel compounds are being accounted for in product analysis.

For the data presented, yield for a product is defined as:

$$\text{Yield of R} = \frac{\text{moles of R formed}}{m \cdot \text{moles of hydrocarbon fuel consumed}} \quad 3-1$$

For hydrogen yields, m is the number of moles of H_2 per mole of hydrocarbon; for CO , CO_2 , CO_x and CH_4 , m is the number of carbon atoms in the hydrocarbon fuel. Under favorable conditions, the hydrogen yield can be greater than 1 due to the contribution of hydrogen from water. Fuel conversion is defined in Eqn. 3-2 below:

$$\text{Fuel conversion to } CO_x (\%) = \frac{CO + CO_2}{(X_C)_{fuel} \cdot (\text{hydrocarbon fuel})_{in}} \cdot 100\% \quad 3-2$$

where, $(X_C)_{fuel}$ is the number of carbon atoms in the hydrocarbon fuel fed to the reactor.

Reforming efficiency (η) is defined assuming that the reformat will be used with a solid oxide fuel cell and includes both the lower heating value for hydrogen and carbon monoxide as shown in Eqn. 3-3:

$$\eta_{\text{reformer}} (\%) = \frac{\dot{n}_{H_2} (LHV)_{H_2} + \dot{n}_{CO} (LHV)_{CO}}{\dot{n}_{fuel} (LHV)_{fuel}} \cdot 100\% \quad 3-3$$

where, $(LHV)_x$ is the lower heating value of x . The gas hourly space velocity or space-time gives an indication of the length of time that reactants spend within a reactor and can be calculated by Eqn. 3-4 below:

$$GHSV = \frac{(\dot{V}_{\text{Reactant}})_{\text{Inlet}}}{V_{\text{Reactor}} - V_{\text{Catalysts}}} = (\text{space - time})^{-1} \quad 3-4$$

where, $(\dot{V}_{\text{Reactant}})_{\text{Inlet}}$ is the volume flow rate of the reactants under standard conditions, V_{Reactor} is the total volume of the reactor, and $V_{\text{Catalysts}}$ is the volume occupied by the catalysts or catalysts support materials. In Eqn. 3-4 the term $V_{\text{Catalysts}}$ is optional, and if included, the calculated value is termed corrected GHSV.

In fuel reforming or for most processes that involve reactions, it is important to make sure that the principle reactant is accounted for in reaction products. For hydrocarbon fuels this would mean that an atom balance for both carbon and hydrogen would need to be performed. Since hydrogen is introduced into the reactor via fuel and water and often condenses out of the reformat stream; accounting for hydrogen is difficult. Therefore, carbon balance is used as a means to account for all fuel atoms and is shown in Eqn. 3-5 below:

$$\text{Carbon Balance} = \frac{\text{Carbon atoms in reformat}}{N \cdot \text{moles of hydrocarbon fuel fed to the reactor}} \quad 3-5$$

where, N is the average number of carbon atoms per mole of fuel. Mathematically the Carbon Balance can be represented as:

$$\text{Carbon Balance} = \frac{\dot{V}_{\text{Ref}} \cdot (CO + CO_2 + \sum_{i=1}^6 iC_iH_n) \cdot t}{(X_C)_{\text{fuel}} \frac{(Fuel)_{\text{In}}}{MW_{\text{fuel}}} \cdot 24.144} \quad 3-6$$

here, $(CO + CO_2 + \sum_{i=1}^6 iC_iH_n)$ represents the sum of carbon atoms in the reformat stream,

\dot{V}_{Ref} is the reformat volume flow rate, $(Fuel)_{\text{In}}$ is the mass of fuel which enters the reactor in time t , MW_{fuel} is the average molecular weight of fuel, $(X_C)_{\text{fuel}}$ is the average number of carbon atoms per average molecule of fuel and the value 24.144 is the number of liters per mole for an ideal gas.

3.5.1 Propagation of experimental errors

Although determining absolute error in any measurement or calculation is impossible, a Taylor series expansion of a function can provide “order of magnitude” approximation of error given some knowledge of underlying instrument error. The error approximation equation determined by Taylor series expansion is given below in Eqn. 3-7¹⁵:

¹⁵ Additional details on instrument error and error propagation is presented in Appendix A. Propagation of Experimental Error Analysis.

$$\Delta f(x_1, x_2, \dots, x_n) \cong \left| \frac{\partial f(\tilde{x})}{\partial x_1} \right| \cdot \Delta \tilde{x}_1 + \left| \frac{\partial f(\tilde{x})}{\partial x_2} \right| \cdot \Delta \tilde{x}_2 + \dots + \left| \frac{\partial f(\tilde{x})}{\partial x_n} \right| \cdot \Delta \tilde{x}_n \quad 3-7$$

where,

$\Delta f(x) \equiv$ approximate error of a function

$f(\tilde{x}) \equiv$ function dependent on x

$\tilde{x} \equiv$ approximate value of x (i.e. measured value)

$\Delta \tilde{x} \equiv$ measurement error of x

Applying Eqn. 3-5 to Eqn.'s 3-1, 3-2, 3-3, and 3-4 and incorporating instrument error as shown in Table 3.3 results in the following error propagations equations (variables are defined in Table 3.4):

$$\begin{aligned} \Delta Yield_{H_2} = & \frac{t}{\frac{(Fuel)_{in}}{MW_{fuel}} (\tilde{X}_{H_2})_{fuel} \cdot 24.144} \cdot \Delta \dot{V}_{H_2} + \frac{\dot{V}_{H_2}}{\frac{(Fuel)_{in}}{MW_{fuel}} (\tilde{X}_{H_2})_{fuel} \cdot 24.144} \cdot \Delta t + \\ & \frac{\dot{V}_{H_2} \cdot t}{\frac{(Fuel)_{in}^2}{MW_{fuel}} (\tilde{X}_{H_2})_{fuel} \cdot 24.144} \cdot \Delta (Fuel)_{in} + \frac{\dot{V}_{H_2} \cdot t}{\frac{(Fuel)_{in}}{MW_{fuel}} (\tilde{X}_{H_2})_{fuel}^2 \cdot 24.144} \cdot \Delta (\tilde{X}_{H_2})_{fuel} \end{aligned} \quad 3-8$$

$$\Delta (Fuel\ Conversion)_{CO_x} = \frac{(X_{CO} + X_{CO_2})}{(X_C)_{fuel} \cdot \frac{\dot{m}_{fuel}}{MW_{fuel}} \cdot 24.144 \text{ l/mol}} \cdot \Delta \dot{V}_{Reformate}$$

$$\begin{aligned}
& + \frac{\dot{V}_{\text{Reformat}} \cdot (X_{CO_2})}{(X_C)_{fuel} \cdot \frac{\dot{m}_{fuel}}{MW_{fuel}} \cdot 24.144 \text{ l/mol}} \cdot \Delta \tilde{X}_{CO} + \frac{\dot{V}_{\text{Reformat}} \cdot (X_{CO})}{(X_C)_{fuel} \cdot \frac{\dot{m}_{fuel}}{MW_{fuel}} \cdot 24.144 \text{ l/mol}} \cdot \Delta \tilde{X}_{CO_2} \\
& + \frac{\dot{V}_{\text{Reformat}} \cdot (X_{CO} + X_{CO_2})}{(X_C)_{fuel} \cdot \frac{(\dot{m}_{fuel})^2}{MW_{fuel}} \cdot 24.144 \text{ l/mol}} \cdot \Delta \dot{m}_{fuel}
\end{aligned} \tag{3-9}$$

$$\begin{aligned}
\Delta \eta \cong & \left[\frac{\tilde{X}_{H_2} \cdot \tilde{LHV}_{H_2} \cdot \tilde{t} \cdot \tilde{MW}_{H_2}}{\tilde{LHV}_f \cdot (\tilde{Fuel})_m \cdot 24.144} \right] \cdot \Delta \dot{V}_{\text{Reformat}} + \left[\frac{\dot{V}_{\text{Reformat}} \cdot \tilde{LHV}_{H_2} \cdot \tilde{t} \cdot \tilde{MW}_{H_2}}{\tilde{LHV}_f \cdot (\tilde{Fuel}) \cdot 24.144_{in}} \right] \cdot \Delta \tilde{X}_{H_2} \\
& + \left[\frac{\dot{V}_{\text{Reformat}} \cdot \tilde{X}_{H_2} \cdot \tilde{t} \cdot \tilde{MW}_{H_2}}{\tilde{LHV}_f \cdot (\tilde{Fuel})_m \cdot 24.144} \right] \cdot \Delta \tilde{LHV}_{H_2} + \left[\frac{\dot{V}_{\text{Reformat}} \cdot \tilde{X}_{H_2} \cdot \tilde{LHV}_{H_2} \cdot \tilde{MW}_{H_2}}{\tilde{LHV}_f \cdot (\tilde{Fuel})_m \cdot 24.144} \right] \cdot \Delta(\tilde{t}) \\
& + \left[\frac{\dot{V}_{\text{Reformat}} \cdot \tilde{X}_{H_2} \cdot \tilde{LHV}_{H_2} \cdot \tilde{t} \cdot \tilde{MW}_{H_2}}{(\tilde{Fuel})_m \cdot (\tilde{LHV}_f)^2 \cdot 24.144} \right] \cdot \Delta \tilde{LHV}_f \\
& + \left[\frac{\dot{V}_{\text{Reformat}} \cdot \tilde{X}_{H_2} \cdot \tilde{LHV}_{H_2} \cdot \tilde{MW}_{H_2}}{\tilde{LHV}_f \cdot (\tilde{Fuel})_m^2 \cdot 24.144} \right] \cdot \Delta(\tilde{Fuel})_m
\end{aligned} \tag{3-10}$$

$$\Delta GHSV = \frac{1}{V_{\text{Reactor}}} \cdot \Delta(\dot{V}_{\text{Reactant}})_{\text{Inlet}} + \frac{(\dot{V}_{\text{Reactant}})_{\text{Inlet}}}{(V_{\text{Reactor}})^2} \cdot \Delta V_{\text{Reactor}} \tag{3-11}$$

$$\begin{aligned}
\Delta(\text{Carbon Balance}) = & \frac{(CO + CO_2 + \sum_{i=1}^6 iC_iH_n) \cdot t}{(X_C)_{fuel} \frac{(Fuel)_{In}}{MW_{fuel}} \cdot 24.144} \cdot \Delta \dot{V}_{Ref} + \frac{\dot{V}_{Ref} \cdot (CO + CO_2 + \sum_{i=1}^6 iC_iH_n)}{(X_C)_{fuel} \frac{(Fuel)_{In}}{MW_{fuel}} \cdot 24.144} \cdot \Delta t \\
& + \frac{\dot{V}_{Ref} \cdot (CO + CO_2 + \sum_{i=1}^6 iC_iH_n) \cdot t}{(X_C)_{fuel}^2 \frac{(Fuel)_{In}}{MW_{fuel}} \cdot 24.144} \cdot \Delta(X_C)_{fuel} + \frac{\dot{V}_{Ref} \cdot (CO + CO_2 + \sum_{i=1}^6 iC_iH_n)}{(X_C)_{fuel} \frac{(Fuel)_{In}^2}{MW_{fuel}} \cdot 24.144} \cdot \Delta(Fuel)_{In}
\end{aligned}$$

3-12

To gain some insight into the impact of error propagation into typical calculations used throughout this thesis, a series of calculation at a real operating point is provided. The operating point selected was with n-dodecane at a fuel flow of 4.436 g/min. which equates to a 3.33 kW thermal fuel flow, a steam-to-carbon ratio (S/C) of 2.0, an oxygen-to-carbon ratio (O/C) of 1.07, and an enrichment number of 1.0 (reforming with standard air). Example data is shown in Table 3.5. Calculated results, error value and percentage error of calculated values are shown in Table 3.6. For many parameters shown in Table 3.5 two answers are possible; this results from two methods of calculating the total reformat flow from the reactor: 1) direct measurement by a volume flow meter and 2) indirect calculation using a nitrogen balance method. The error values and error percentages are not fixed and vary with reforming operating parameters, but values presented provide some insight into the magnitude of error associated with calculated parameters. Appendix A Propagation of Experimental Error Analysis provides additional details on the results shown in Table 3.6.

Table 3.3 Instrument measurement accuracy

Instrument	Error	Notes:
Agilent micro GC 3000A (4 channel)	1.02%	GC has a 1% error, but is calibrated to a primary standard with a 0.02% analytical error
Brooks 5851E mass flow controller	1%	Error is 1% of full scale (50 slpm for air and N ₂)
Ashcroft Analogue Guages	1%	Error is 1% of full scale reading
Reformate pressure, Dwyer Magnehelic Differential Pressure Gages	2%	full scale is 10 inches water gage
Reformate Flow Metrer (American Meter Company), AR250	1%	of reading
Thermocouples		
- Watlow, 1/16" stainless steel 316 sheathed	1.1 °C or 0.4%	response time is 0.22 s
- Watlow, 1/8" stainless steel 316 sheathed	1.1 °C or 0.4%	response time is 0.50 s
- Omega, K-type, 0.02" diameter	1.1 °C or 0.4%	which ever is greater; response time is 0.8s with 0.02"
Gilson Piston Pump	1%	of reading
Sartorius Laboratory Balance	0.1 gm	fuel, water, and reformate condensate

Table 3.4 Variable definitions

Variable	Variable Definition
\dot{V}_x	Volume flow rate of X
\tilde{X}_x	Molar fraction of X
\tilde{Fuel}_{in}	Mass of fuel into the reactor in grams.
\tilde{LHV}_x	Lower Heating Value of X .
\tilde{t}	Time in minutes.
$(\tilde{X}_x)_{fuel}$	Mass fraction of X in fuel.
MW_X	Molecular weight of X .
CO	Moles of carbon monoxide.
CO_2	Moles of carbon dioxide.

3.6 Chapter summary

The overall goal for the experimental reformer test apparatus and supporting laboratory equipment was to develop a test fixture and capability that had the following attributes: adiabatic ATR reactor operation; ability to control and vary input parameters (fuel flow, air flow, steam flow) values and reactor inlet conditions; good fuel analysis and reactor product analysis; safe operation; automated control, acquisition and archiving of operating data; quality analytical instrumentation and measurement equipment which would support analysis with acceptable calculation errors. The resultant laboratory capability addressed in this chapter resulted in a near adiabatic reactor (approximately 2-

Table 3.5 Example experimental data from n-dodecane, fuel flow = 4.436 gm/min. (3.3 kWth); S/C = 2.0; O/C = 1.07

Experimental value	Error
$\tilde{T} = T_{std}$	$\Delta\tilde{T} = \pm 1.1 \text{ } ^\circ C = \pm 1.1 \text{ } K$
$\tilde{P} = P_{std}$	$\Delta\tilde{P} = 24.89 \text{ } Pa = 0.1'' \text{ } wg$
$\dot{V}_{meter} = 33.728 \text{ } slpm$	$\Delta\dot{V}_{meter} = 0.3 \text{ } slpm$
$\dot{V}_{Air} = 19.4 \text{ } slpm$	$\Delta\dot{V}_{Air} = 0.5 \text{ } slpm$
$\tilde{X}_{N_2} = 0.4493$	$\Delta\tilde{X}_{N_2} = 0.004583$
$(\tilde{X}_{N_2})_{Air} = 0.7809$	$\Delta(\tilde{X}_{N_2})_{Air} = 0$
$\tilde{Fuel}_{in} = 88.72 \text{ } g$	$\Delta\tilde{Fuel}_{in} = 0.1 \text{ } g$
$\tilde{Water}_m = 217.5 \text{ } g$	$\Delta\tilde{Water}_m = 0.1 \text{ } g$
$\dot{V}_{Reformate} = 33.728 \text{ } slpm$	$\Delta\dot{V}_{Reformate} = 1.2225 \text{ } slpm$
$\tilde{X}_{H_2} = 0.3281$	$\Delta\tilde{X}_{H_2} = 0.003347$
$\tilde{LHV}_{H_2} = 33.603 \text{ } kW - hr/kg$	$\Delta\tilde{LHV}_{H_2} = 0.33603 \text{ } kW - hr/kg$
$\tilde{t} = 1200 \text{ } s$	$\Delta\tilde{t} = 0.5 \text{ } s$
$\tilde{LHV}_f = 12.26 \text{ } kW - hr/g$	$\Delta\tilde{LHV}_f = 0.01226 \text{ } kW - hr/g$
$(\tilde{X}_{H_2})_{fuel} = 11.4175 \frac{H_2 \text{ } atoms}{molecule \text{ } fuel}$	$\Delta(\tilde{X}_{H_2})_{fuel} = 0$
$(\tilde{X}_C)_{Fuel} = 12.277 \frac{H_2 \text{ } atoms}{molecule \text{ } fuel}$	$\Delta(\tilde{X}_C)_{Fuel} = 0$
$MW_{fuel} = 170.32 \frac{g}{mol}$	$\Delta MW_{fuel} = 0$
$MW_{Water} = 18.0153 \frac{g}{mole}$	$\Delta MW_{Water} = 0$
$MW_{H_2} = 2.01588 \frac{g}{mole}$	$\Delta MW_{H_2} = 0$
$(CO + CO_2 + \sum_{i=1}^6 iC_iH_n) = 0.21925$	$\Delta(CO + CO_2 + \sum_{i=1}^6 iC_iH_n) = 0.0022364$

Table 3.6 Calculation results for n-dodecane with fuel flow = 4.436 g/min., S/C = 2.0, O/C = 1.07 and oxygen enrichment number = 1.0.

Parameter*	Value	Error Value	Error %
\dot{m}_{fuel}	$4.436 \frac{g}{min.}$	$\pm 0.05185 \frac{g}{min.}$	$\pm 1.2\%$
$\dot{V}_{Reformate}$	$32.728 \frac{l}{min.}$	$\pm 0.4233 \frac{l}{min.}$	$\pm 1.2\%$
$\dot{V}_{Ref. N_2 Bal.}$	$32.728 \frac{l}{min.}$	$\pm 1.21295 \frac{l}{min.}$	$\pm 3.6\%$
η_{H_2}	57.07%	$\pm 1.4708 \%$	$\pm 2.6\%$
		$\pm 2.774 \%$	$\pm 4.9\%$
\dot{V}_{H_2}	$11.066 \frac{l}{min.}$	$\pm 0.2536 \frac{l}{min.}$	$\pm 2.6\%$
		$\pm 0.5108 \frac{l}{min.}$	$\pm 4.6\%$
$Yield_{H_2}$	$1.542 \frac{moles H_2}{moles H_2 \text{ in fuel}}$	$\pm 0.0377 \frac{moles H_2}{moles H_2 \text{ in fuel}}$	$\pm 2.4\%$
		$\pm 0.07396 \frac{moles H_2}{moles H_2 \text{ in fuel}}$	$\pm 4.8\%$
Fuel Conversion CO_x	95.75%	$\pm 1.021\%$	$\pm 1.1\%$
		$\pm 3.678\%$	$\pm 3.8\%$
Carbon Balance	96.00%	$\pm 1.492\%$	$\pm 1.6\%$
		$\pm 3.601\%$	$\pm 3.8\%$
GHSV	$22,622 hr^{-1}$	$351 hr^{-1}$	$\pm 1.5\%$

*Where given, second values are based on using the nitrogen balance method to determine reformate flowrate.

3% thermal losses under fuel flow conditions of $3.33 \text{ kW}_{\text{th}}$, and lower at higher flowrates); incorporated laboratory equipment which could vary fuel flow from 0 – 10 ml/min, water flow from 0 – 30 ml/min., and air flow up to 54 slpm – capable of supporting a thermal capacity of $300 \text{ W}_{\text{th}}$ to $7.5 \text{ kW}_{\text{th}}$ ¹⁶ (assuming $(\text{O/C})_{\text{max}} = 1.25$ and $(\text{S/C})_{\text{max}} = 3.0$). Minimizing error propagation through key calculated parameters was an early design criterion in the selection of measurement equipment and analytical instrumentation. Finally, since hydrocarbon fuel reforming results in high concentration of carbon monoxide, personnel safety was paramount. To address personnel and facility safety numerous redundant safety controls as well as fail safe designs were considered and incorporated into the overall laboratory environment and experiments.

¹⁶ The maximum thermal capacity of the reformer test apparatus is limited by the maximum air flow when operating with standard air. Higher maximum capacities can be achieved when operating under oxygen enriched conditions.

Chapter 4

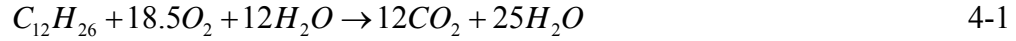
Analysis of Oxygen Enriched Liquid Heavy Hydrocarbon Fuel Reforming

4.0 Introduction

An important conclusion drawn from a review of reforming literature is that the use of thermodynamic equilibrium modeling, based upon the exit conditions of the reactor, provides very good predictions of reforming products. This coupled with the fact that little published data on oxygen enriched reforming is available in the literature, suggests that an analytical approach could be beneficial in understanding oxygen enriched reforming. Where analytical values are presented they are based on process simulator calculation using *Design II* (WinSim, Inc.) with the thermodynamic equilibrium assumption of Gibb's free energy minimization. In addition, the impact of oxygen enrichment on reforming performance, heat transfer, pressure drop, and kinetics as well as the impact on the fuel cell stack are discussed.

4.1 Operating regimes for catalytic processes

Autothermal reforming can be thought of as catalytic combustion under moist, fuel rich conditions. Figure 4.1 shows equilibrium calculations for n-dodecane at a flow rate of 6.0 ml/min. (3.33 kW_{th}), a S/C ratio of 1.0, and adiabatic reactor operation. For n-dodecane the balanced equation for complete oxidation with an S/C of 1.0 is shown below in Eqn. 4-1.



There are a number of conventions used in engineering and science to describe the relationship between fuel and oxygen in combustion processes. Fig. 4.1 provides four commonly used designations to describe the amount of oxygen and fuel being used. The terms are: oxygen to carbon ratio, equivalency ratio, air to fuel ratio, and lambda. These terms are briefly described below.

The oxygen to carbon ratio is the molar mono-atomic oxygen (O) divided by the carbon atoms in fuel.

$$O/C \text{ ratio} = \frac{n_{O,air}}{n_{C,C_nH_m}} \quad 4-2$$

where n_x represents the number of moles of x . The O/C ratio is commonly used in fuel reforming and is used throughout this thesis. The O/C ratio corresponding to stoichiometric full combustion for n-dodecane is 3.0833.

The equivalency ratio (ϕ) is the ratio of the fuel-to-oxidizer to the stoichiometric fuel-to-oxidizer ratio shown in Eqn. 4-3 below:

$$\phi = \frac{\frac{m_{fuel}}{m_{ox}}}{\left(\frac{m_{fuel}}{m_{ox}}\right)_{stoich}} = \frac{\frac{n_{fuel}}{n_{ox}}}{\left(\frac{n_{fuel}}{n_{ox}}\right)_{stoich}} \quad 4-3$$

here, m_x is the mass of x , the subscript OX stands for oxidizer and $stoich$ is the stoichiometric ratio. As shown above the equivalency ratio can be expressed as either mass or molar ratios. Equivalency ratio values greater than 1.0 represent a fuel rich condition and values less than one represent an excess of oxygen.

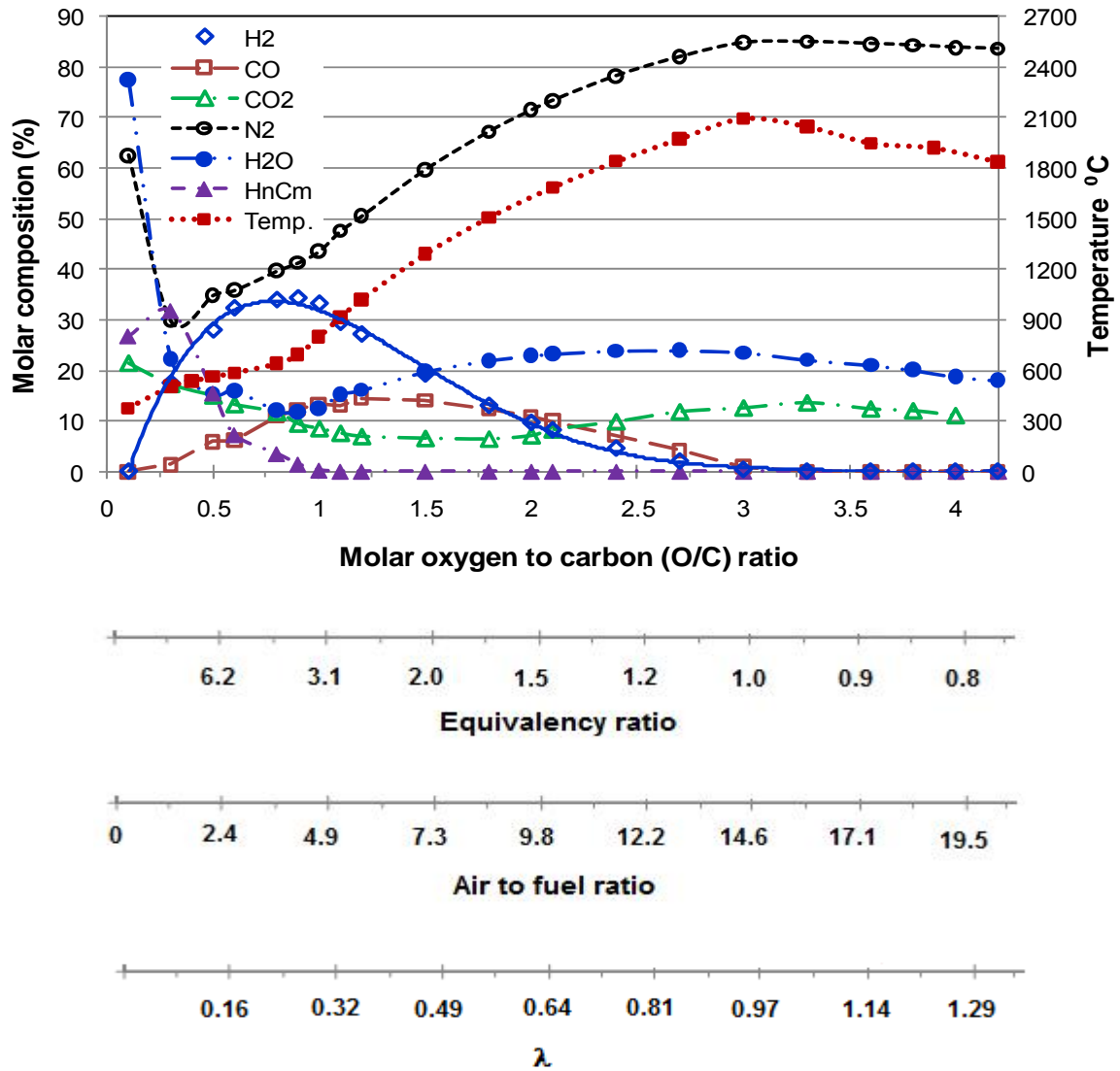


Figure 4.1 Equilibrium calculations with n-dodecane at 6.0 ml/min. (3.33 kW_{th}), S/C ratio of 1.0, adiabatic reactor and reactor inlet temperature of 25 °C. For H₂, CO, CO₂, and N₂ the composition is on a dry basis.

The air-to-fuel ratio (AFR) is very commonly used with internal combustion engines.

The AFR is the mass of air divided by the mass of fuel shown in Eqn. 4-4 below:

$$AFR = \frac{m_{air}}{m_{fuel}} \quad 4-4$$

For n-dodecane the stoichiometric mixture (Eqn. 4-1) results in an AFR of 15.02.

Lambda (λ) is the ratio of the operating AFR to the stoichiometric AFR shown in Eqn. 4-5 below:

$$\lambda = \frac{AFR}{(AFR)_{stoich}} \quad 4-5$$

Lambdas greater than 1.0 are fuel lean mixtures and lambdas less than 1.0 are fuel rich mixtures.

Figure 4.1 shows the general composition of products with n-dodecane oxidation at increasing oxygen levels. Here oxygen is obtained from air (i.e. unenriched). As would be expected, increasing the amount of oxygen that reacts with n-dodecane when below the stoichiometric amount of oxygen ($O/C_{stoich} = 3.08333$) results in increased product temperature and a shift in products towards carbon dioxide and water. In fuel reforming for fuel cell applications, the production of syngas (H_2 and CO) is desired and this takes place in the O/C range of 0.95 to 1.10. In this syngas region, hydrogen and carbon monoxide reach their maximum composition and hydrocarbon species are fully converted.

4.2 Principles of membrane oxygen enrichment

The use of polymer membrane for air separation purposes can be traced to Generon (Innovative Gas Systems, Inc.) where the first air separation membranes were introduced in the 1980's. Today polymer membranes for air separation are manufactured by many companies [243,244,245] and can economically produce oxygen concentrations of approximately 35% for single pass membranes and up to approximately 50% for a cascaded design. The predominant application for air separation is for nitrogen enrichment which has many safety applications where nitrogen is used as a blanketing or inerting agent to displace oxygen in environments containing hydrocarbons or reactive environments. Polymer air separation membrane are characterized as a low power alternative to other separation processes and have no moving parts which makes them robust, reliable and well suited for mobile applications.

Figure 4.2 [246] shows a graphic representation of an oxygen enrichment tube bundle. Each membrane tube is designed to have preferential diffusion for the desired gas; in this case oxygen. Gases permeating through the fibers are collected in the shell and leave the tube as the permeate stream. Because oxygen, water vapor, and carbon dioxide are more permeable than nitrogen, the gases which exit as permeate are oxygen enriched and the gases exiting the fiber bore are nitrogen enriched. As shown in Fig. 4.2, gas separation membranes are usually tubular in design and packaged together into bundles. For industrial applications, it is not unusual for tube bundles to consist of 500,000 tubes, each tube 250 to 300 μm in outside diameter, each tube bundle 150 mm to 300 mm in

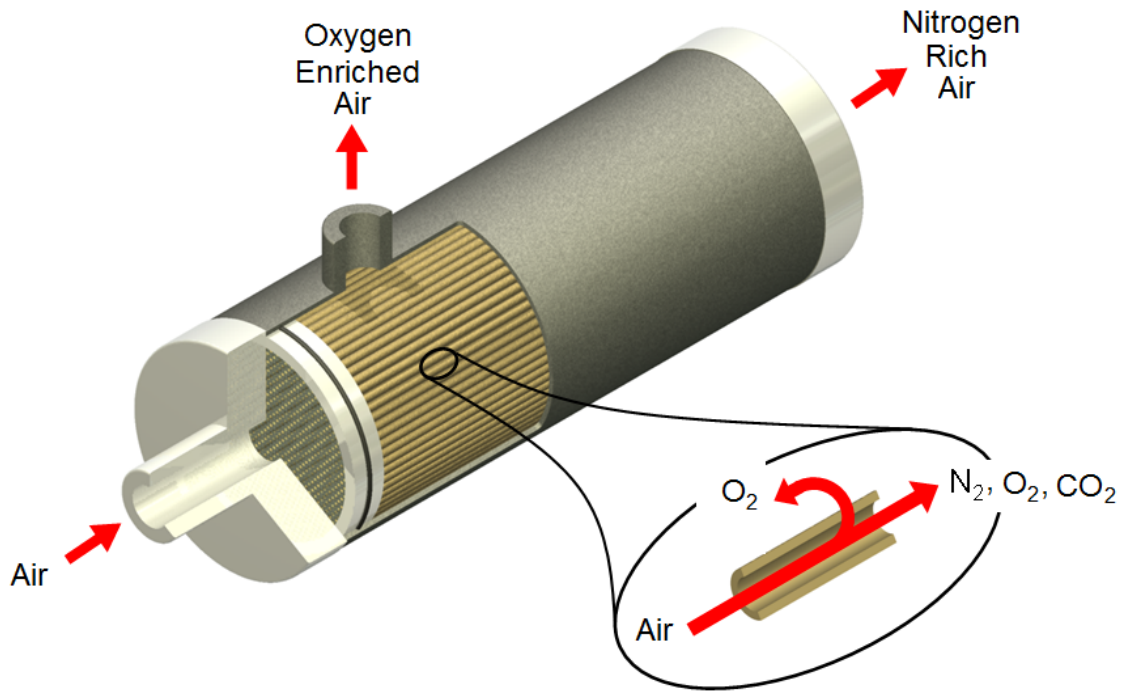


Figure 4.2 Oxygen enrichment membrane depiction [246].

diameter, with lengths varying up to 1000 mm. A typical polymer wall thickness is on the order of 75 μm and on this wall a dense gas separation layer of 500 to 1000 \AA is applied. Key design parameters and quantities for membrane materials are:

$$\text{Permeability} = \frac{(\text{solubility}) \cdot (\text{diffusion coefficient})}{\text{membrane thickness}} \quad 4-6$$

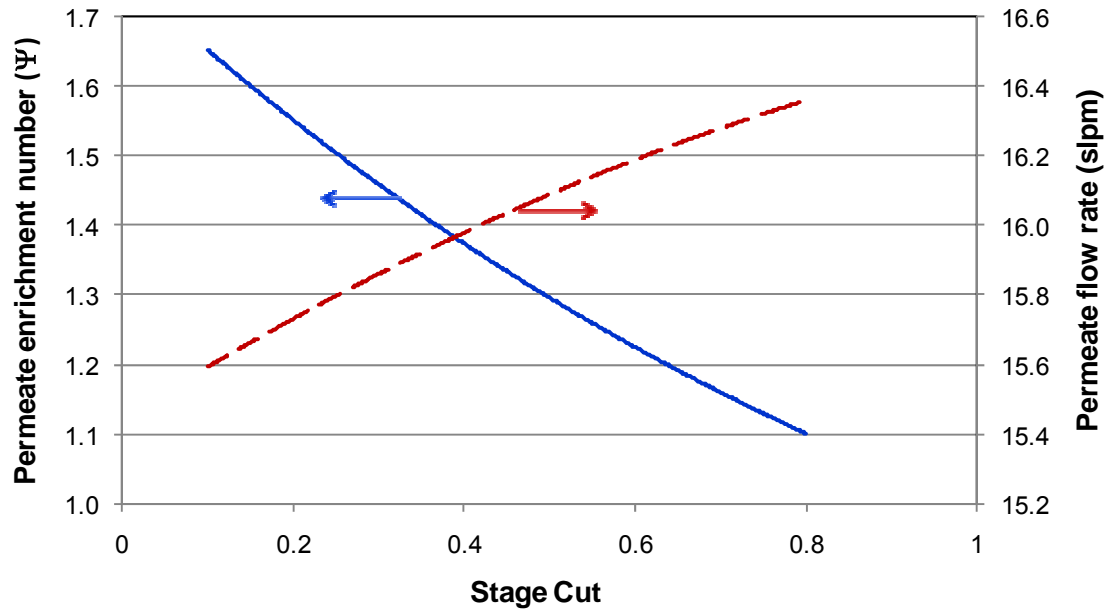
$$\text{Stage cut} = \frac{\text{permeate flow}}{\text{inlet flow}} \quad 4-7$$

$$\text{Membrane selectivity}_{\text{oxygen}} = \frac{\text{flow of oxygen across membrane}}{\text{flow of nitrogen across membrane}} \quad 4-8$$

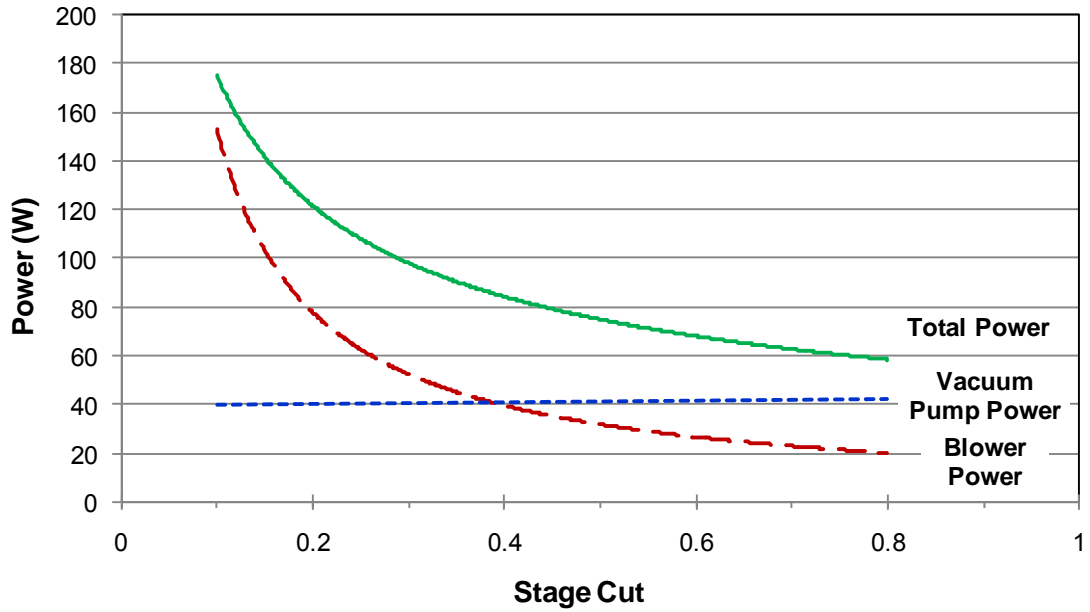
Figure 4.3 gives performance curves for a polymer membrane based on the permeability of polyaramid materials. This membrane material has not been optimized for this particular application, but is based on earlier experimental work conducted by Coombe and Nieh [247,248] for oxygen enriched combustion. From Fig. 4.3a, to achieve high oxygen enrichment, the stage cut is reduced resulting in reduced permeate flow. Fig. 4.3b provides the total power consumption as a function of stage cut. Figure 4.4 provides an estimate of the power required to support ATR of JP-8 at a flow rate of 6.0 ml/min. (3.33 kW_{th}, n-dodecane) at an O/C ratio of 1.0 and a S/C ratio of 2.0. In Fig. 4.4, power is the delivered power and to determine the input power blower and vacuum pump efficiencies would need to be applied. As can be seen, the power increases with enrichment number and rises very rapidly for an enrichment number of 1.7 (35.6% O₂) or higher.

4.3 Equilibrium analysis of autothermal reforming with oxygen enrichment

The equilibrium equations used in modeling the reactor are the sixteen equations identified in section 2.3.2.1 Basic overall reactions in liquid hydrocarbon fuel reforming. All modeling was performed assuming a fuel flow rate of 6.0 ml/min. (3.33 kW_{th}, n-dodecane), S/C ratio of 2.0, O/C ratio of 1.0 and a 5% thermal loss in the reactor.



(a)



(b)

Figure 4.3 Performance of a polymer membrane air separation module with membrane selectivity of 3.0, membrane thickness of 0.035 μm , membrane permeability of 3.0

Barrier [$1 \text{ Barrier} = \frac{10^{-10} \text{ cm}^2 (\text{STP}) \text{ cm}}{\text{cm}^2 \cdot \text{cm} \cdot \text{Hg}}$], and area of 6 m^2 .

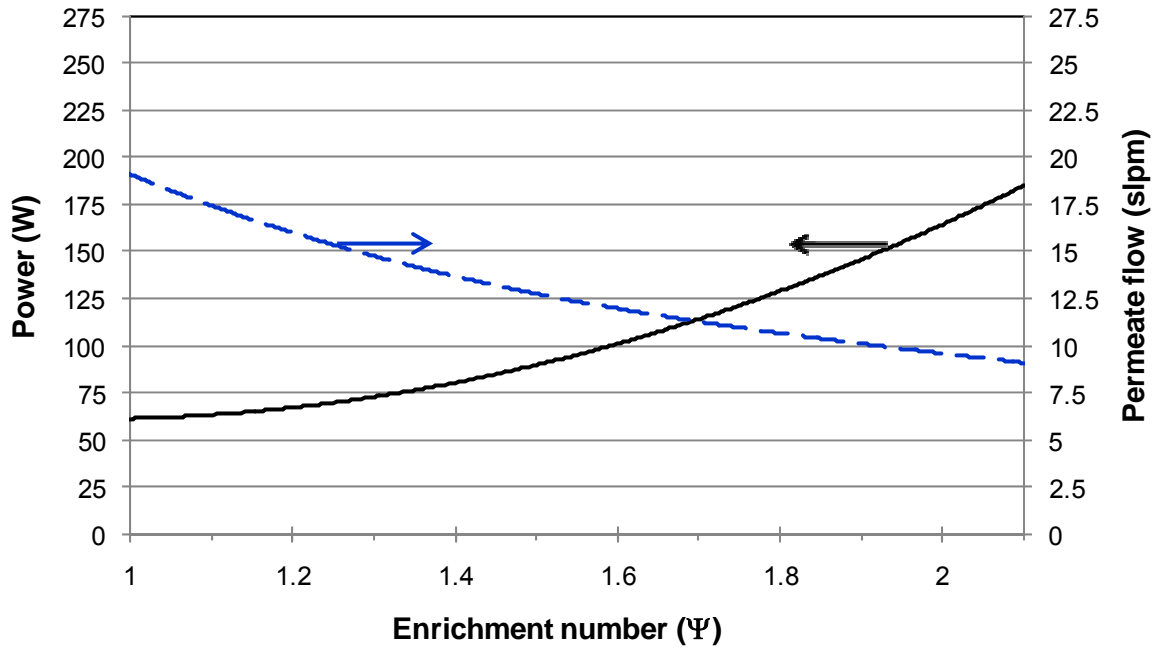
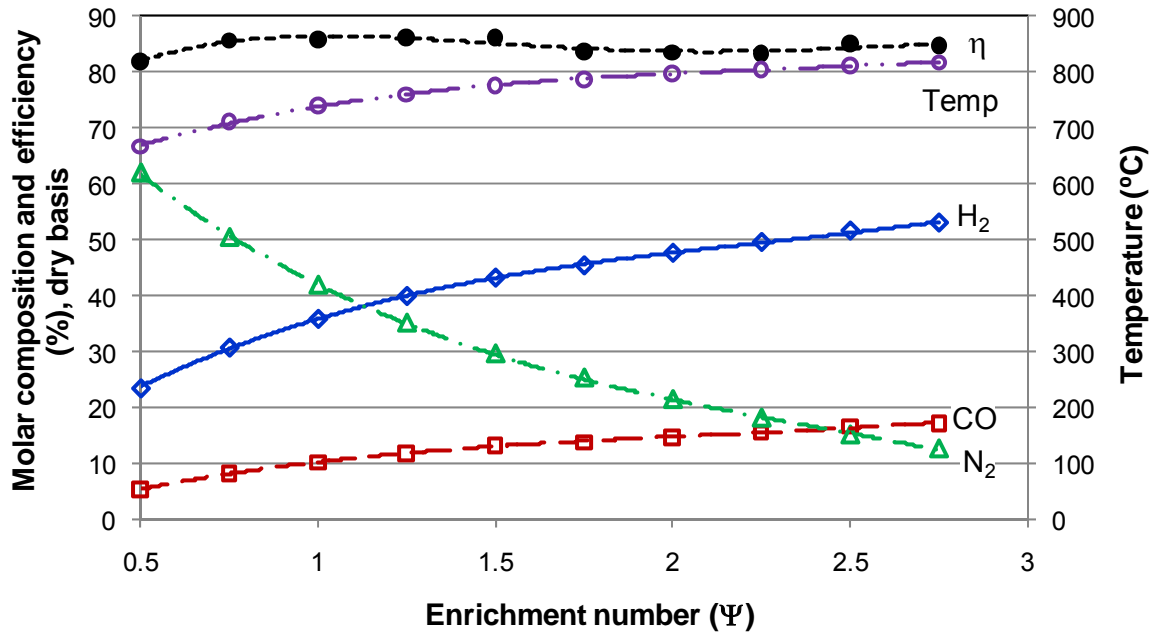
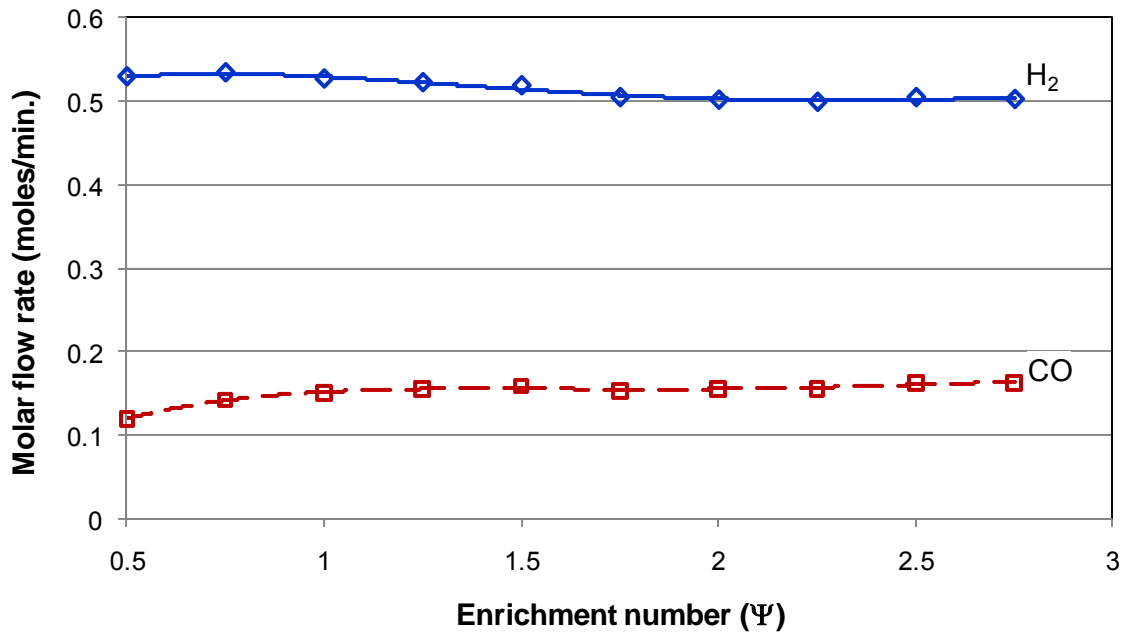


Figure 4.4 Total power required to produce required enriched air flow for a 5.9 ml/min. ($3.33 \text{ kW}_{\text{th}}$) ATR at an O/C ratio of 1.0 and S/C ratio of 2.0. Based on the membrane of Fig. 4.3 with membrane selectivity of 3.0, membrane thickness of $0.035 \mu\text{m}$, membrane permeability of 3.0 Barrier [$1 \text{ Barrier} = \frac{10^{-10} \text{ cm}^2 (\text{STP}) \text{ cm}}{\text{cm}^2 \cdot \text{cm} \cdot \text{Hg}}$], and area of 6 m^2 .

Figure 4.5a displays reactor composition, exit temperature and reforming efficiency as a function of enrichment number. With the O/C ratio held constant, a fixed quantity of heat is generated under all enrichment number scenarios. As nitrogen is removed (increasing enrichment number) more energy is available to heat other reforming constituents and the overall reactor temperature rises. Also displayed in Fig. 4.5a, is that with increasing enrichment number, the concentration of hydrogen rises rapidly. Increasing hydrogen concentration also has a direct positive impact on fuel cell performance as will be discussed later in this chapter.



(a)



(b)

Figure 4.5 ATR composition, temperature, and efficiency (a); and molar flow rates of hydrogen and carbon monoxide (b) for a fuel flow of 5.9 ml/min. (3.33 kW_{th}), S/C of 2.0, O/C of 1.0, reactor thermal losses of 5%, and reactant initial temperatures of 25°C .

Figure 4.5b shows that there is a slight reduction in hydrogen production as the enrichment number is increased and a slight increase in carbon monoxide production. The increase in carbon monoxide is likely a result of increased reactor operating temperature which through the water-gas-shift reaction (Eqn. 2-18) favors carbon monoxide production over hydrogen production. Although, Fig. 4.5b shows a reduction in hydrogen with increasing enrichment number, this may not necessarily be true, as the data is for a fixed O/C ratio and has not been optimized for each enrichment number.

4.3.1 Enrichment number and heat transfer

An important characteristic of ATRs are that they have two distinct reaction zones: one zone is oxidation/exothermic reaction dominant and the other zone is steam reforming/endothermic reaction dominant. Good reactor operation requires that heat generated in the exothermic zone be efficiently moved to the endothermic zone to drive the steam reforming reactions. Since the reactor is constructed of ceramic material which is a poor heat conductor ($k_{\text{cordierite}} = 2.0 \text{ W/m-K}$), the principle means for moving heat within the reactor is via heat convection. Figure 4.6 shows the average constant pressure specific at the inlet and exit of the reactor as a function of enrichment number. Constant pressure specific heat is used as a convenient means to measure the capacity of the flow to absorb heat. As is shown in Fig. 4.6, increasing oxygen enrichment results in increased constant pressure specific heat when measured by either the reactor inlet composition or exit composition. Therefore, oxygen enrichment appears to have no negative impact on heat transfer and may enhance heat transfer within the reactor.

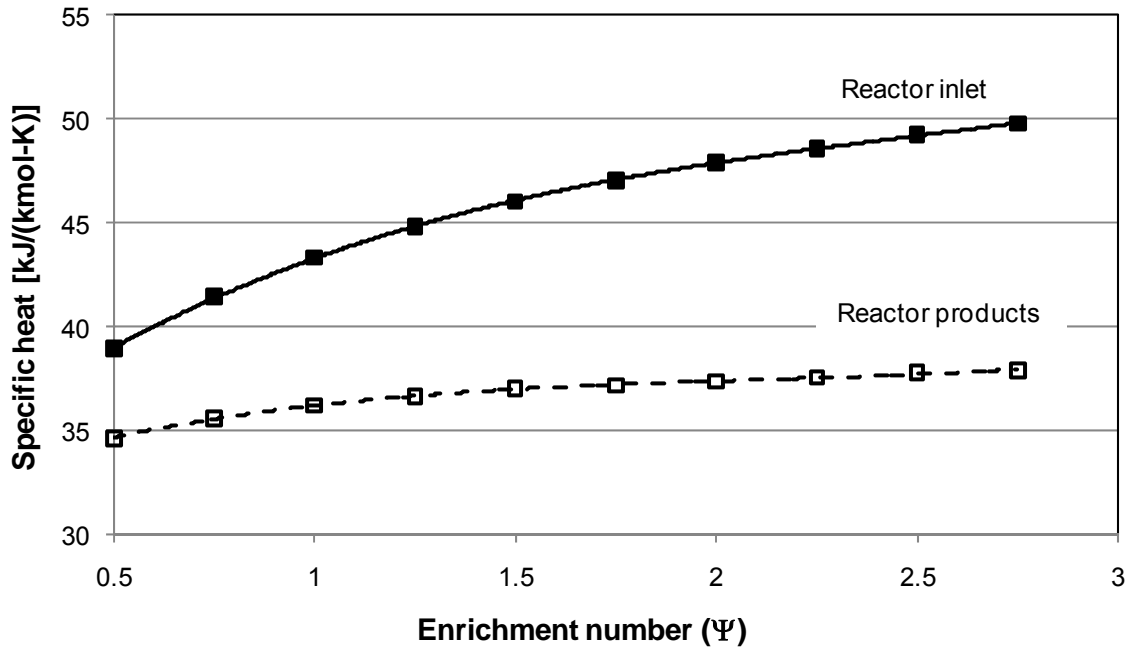


Figure 4.6 Specific heat of reactants and reformat products as a function of enrichment number (Ψ). For an ATR with operating conditions of fuel flow equal to 5.9 ml/min. (3.33 kW_{th}), S/C of 2.0, O/C of 1.0, reactor thermal losses of 5%, and reactant initial temperatures of 25 °C.

4.3.2 Enrichment number and reactor design

With increasing oxygen enrichment, the volume flow rate within the reactor is reduced and reactants, on average, have a longer time within the reformer to fully convert.

Figure 4.7 shows the increased reactor space time as a function of enrichment number.

For these calculations a reactor volume of 87 cm³ was used, which is the volume of the reactor for all experimental work described in this thesis. Oxygen enrichment results in increases in reactor space time and reactor operating temperatures (Fig. 4.5a); this indicates that with oxygen enrichment, reactor throughput can be increased.

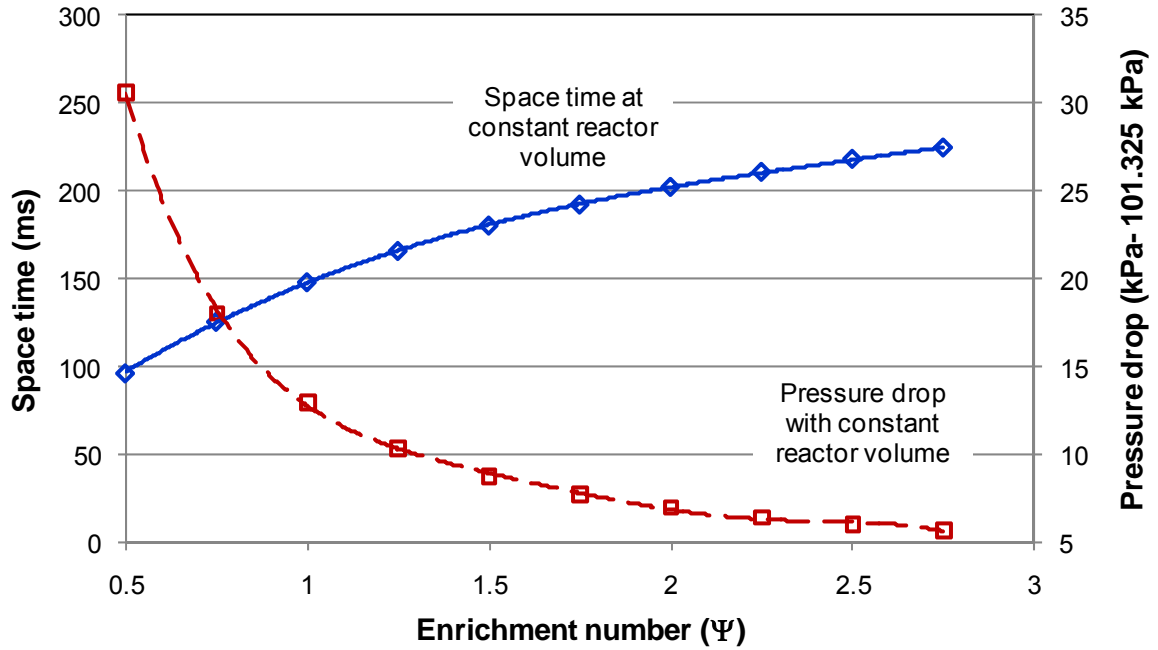


Figure 4.7 Reactor space time and pressure drop as a function of enrichment number. For an ATR with operating conditions of fuel flow equal to 5.9 ml/min. (3.33 kW_{th}), S/C of 2.0, O/C of 1.0, reactor thermal losses of 5%, and reactant initial temperatures of 25 °C.

As the velocity of the gases within the reactor drops, the pressure loss is reduced.

Equation 4-9 below shows the relationship between the average gas velocity (u) within the reactor and reactor pressure drop:

$$\Delta P = \left(\frac{L}{d_H} \right) \left(\frac{u^2}{2} \right) \cdot f \cdot \rho \quad 4-9$$

where, L is the reactor channel length, d_H is the hydraulic diameter of the channel, ρ is the average density and f is the channel friction factor. For laminar flow, f can be approximated by Eqn. 4-10 below:

$$f = \frac{64}{\text{Re}} \quad 4-10$$

where, Re is the Reynolds number of the flow. Figure 4.8 gives the Reynolds numbers as a function of enrichment number; for all conditions the flow is within the laminar region ($\text{Re} < 2300$). Therefore, movement of reactants within the reactor to reactions sites on the channel walls is governed by mass diffusion. As can be seen in Eqn. 4-9, pressure drop is proportional to fluid velocity squared; therefore, modest reductions in flow velocity can result in large reductions in pressure drop. Based on Eqn. 4-9 above, the reactor pressure drop as a function of enrichment number was determined and is presented in Fig. 4.8. Here enrichment number has a strong effect on pressure with a 50% reduction in pressure drop when going from an enrichment number of 1.0 to 2.0. Because monolithic reactors were designed for low pressure drop, the absolute reduction in pumping power associated with the reformer is low. However, the system level impacts could be significant.

As an alternative to increasing space time and reducing pressure drop within a reactor, the use of oxygen enrichment could be used for system size and weight reduction. Here the space time and pressure drop were held constant by adjusting the volume of the reactor. Fig. 4.9 shows the percentage change in reactor volume that can be achieved by adjusting the enrichment number. For this figure an enrichment number of 1.0 was used as the baseline comparison point. As an example, going from an enrichment number of 1.0 to 2.0 can result in a 27% reduction in size.

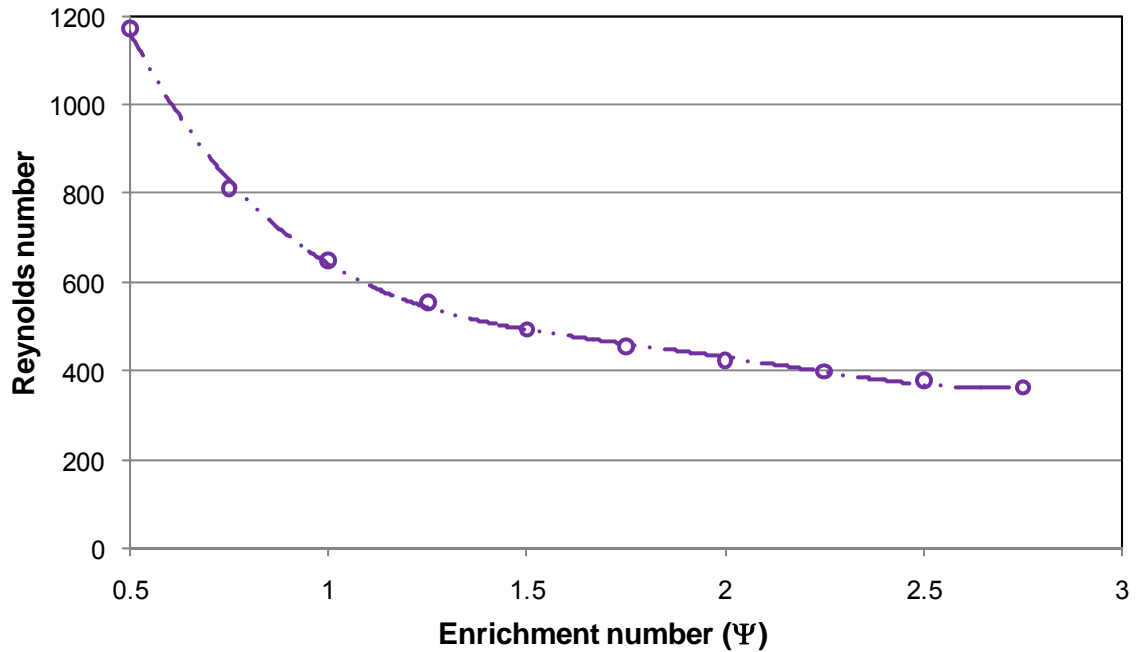


Figure 4.8 Reynolds number as a function of enrichment number. For an ATR with operating conditions of fuel flow equal to 5.9 ml/min. (3.33 kW_{th}), S/C of 2.0, O/C of 1.0, reactor thermal losses of 5%, and reactant initial temperatures of 25 °C.

4.4 Enrichment number and space time

An interesting and potentially valuable consequence of oxygen enrichment is that reactor space time and the O/C ratio are no longer directly dependent. With enrichment you can vary reactor space time while maintaining O/C ratios fixed. The definition of space time is given by Eqn. 3.4 and repeated below:

$$\text{space time} = (GHSV)^{-1} = \frac{V_{\text{Reactor}}}{(\dot{V}_{\text{Reactor}})_{\text{Inlet}}} \quad 4-11$$

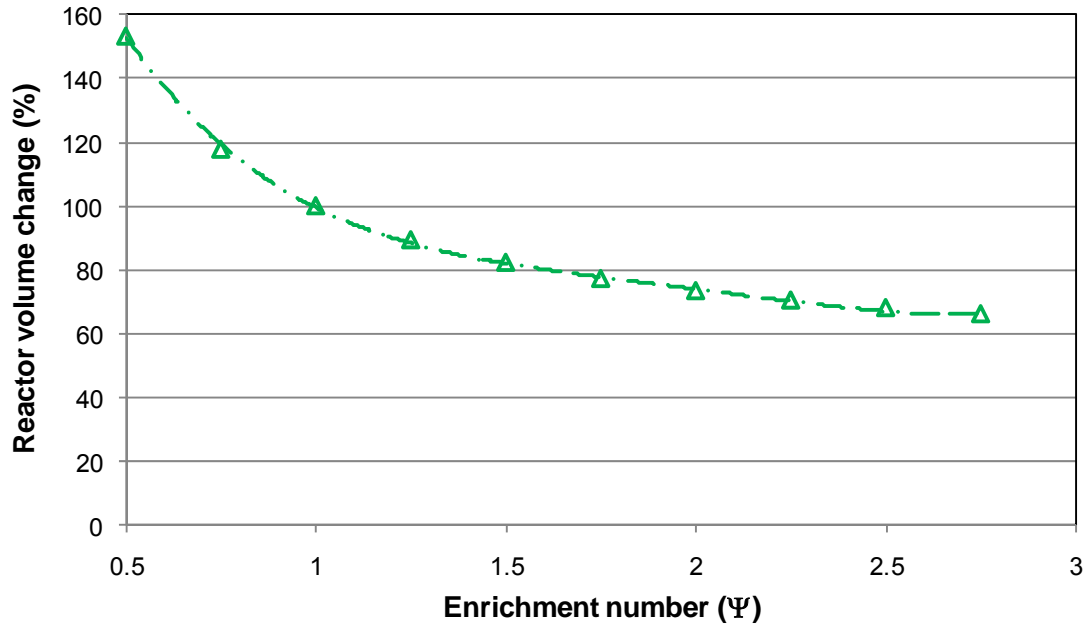
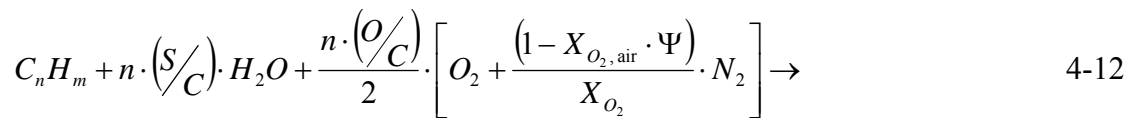


Figure 4.9 Potential for reactor volume reduction maintaining constant reactor space time and pressure drop. Reactor volume change is relative to reactor size for an enrichment number of 1.0. With ATR operating conditions of fuel flow of 5.9 ml/min. (3.33 kW_{th}), S/C of 2.0, O/C of 1.0, reactor thermal losses of 5%, and reactant initial temperatures of 25 °C.

From the definition of space time above, only the reactor inlet conditions need to be specified to analyze the relationship between space time and O/C ratio. Equation 4-12 below is the reactant equation for ATR where the oxygen enrichment number (Ψ) has been incorporated.

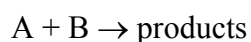


where, $X_{O_2, \text{air}}$ is the fractional oxygen concentration in air and X_{O_2} is the fractional oxygen of the enriched air. With a specified fuel flow and knowing the composition for the selected fuel, the molar flow rate of fuel can be determined. Defining the S/C ratio

and knowing the volume of the reactor, a relationship between O/C ratio and reactor space time can also be determined. Figure 4.10a displays the results for a 6.95 g/min. (8.85 ml/min., 5.0 kW_{th}) fuel flow with S/C of 2.0 and variable O/C ratio. For air reforming ($\Psi = 1.0$), there is a single value for reactor space time for each O/C ratio selected. With enriched oxygen reforming the space time for each O/C ratio can vary significantly. In Fig. 4.10b, the oxygen enrichment is varied between pure oxygen and 10% oxygen ($\Psi = 0.477$) and the reactor space time varies from approximately 60 ms to 170 ms. The lower limit of oxygen enrichment would likely be constrained by the acceptable pressure drop of the reactor or other system constraint. The ability to vary reactor space time and the O/C ratio can potentially have benefits in reforming of hydrocarbon species with broad reactivities¹⁷. This may have implication in creating a fuel flexible reformer that could operate on a number of available fuels by adjusting the reactor space time. In addition, the ability to vary O/C ratio and reactor space time could have implication in kinetics research and performance mapping of reactors.

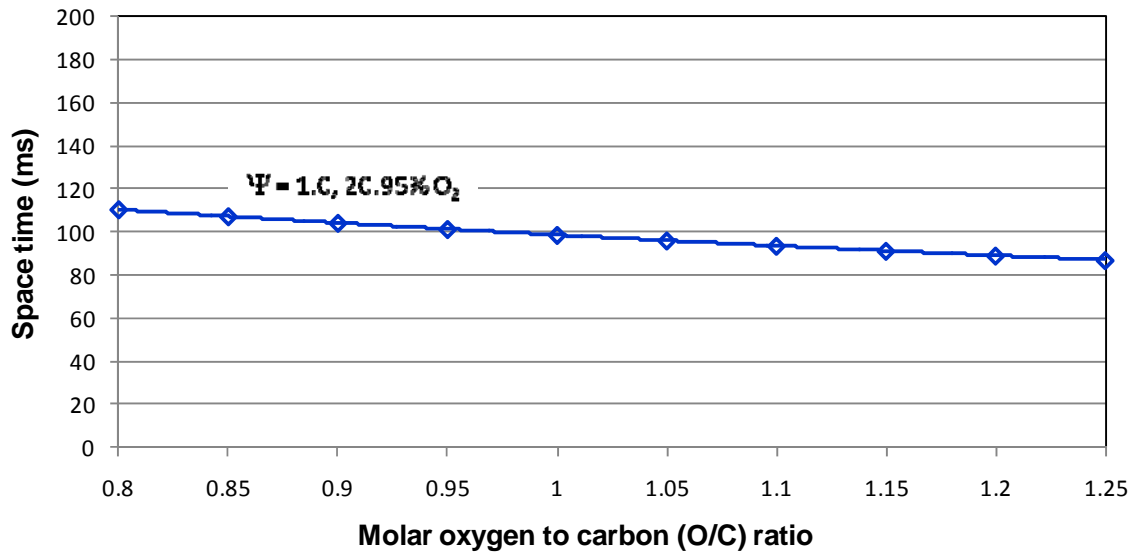
4.5 Elementary reaction rates

A basic understanding of chemical kinetics can provide insight into factors that influence chemical reaction rates. Assuming a simple reaction involving two molecules which collide and produce a product:



4-13

¹⁷ Chemical reactivity is the tendency of a substance to undergo chemical reactions.



(a)

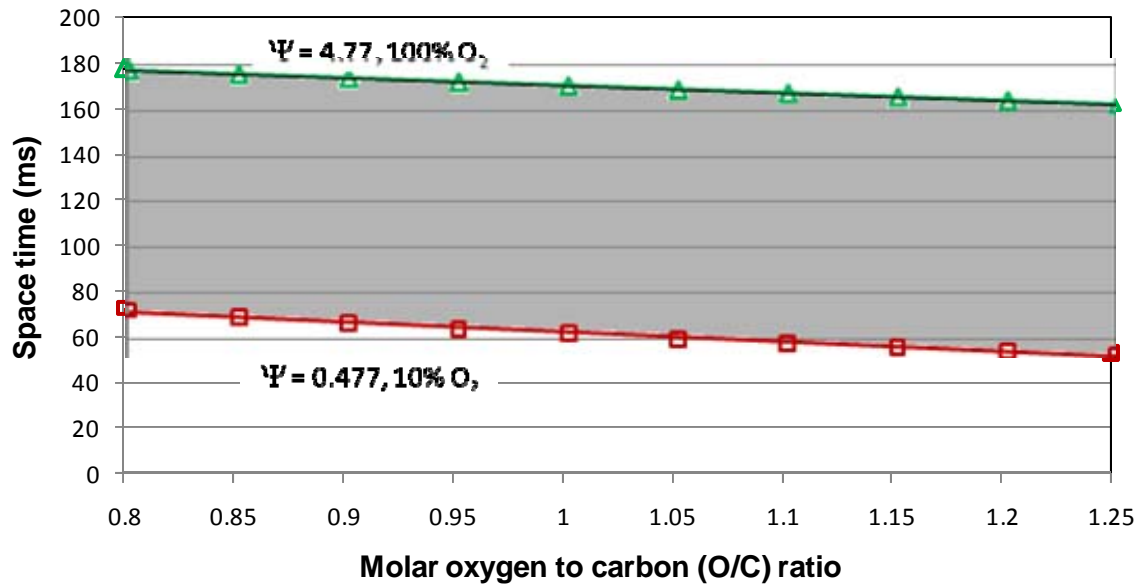


Figure 4.10 Relationship between the O/C ratio for reforming with air (a) and with enriched oxygen reforming with enrichment number (Ψ) between 0.477 (10% O_2/N_2) and 4.77 (100% O_2/N_2). Fuel flow of 6.94 g/min. (5.0 kW_{th} , $LHV_{fuel} = 43.2 \text{ MJ/kg}$), S/C of 2.0 and for a reactor volume of 86.9 cm^3 . (b)

Collision theory states that the rate that reaction Eqn. 4-13 proceeds is proportional to the concentration of A and B and the probability that a collision of A and B produces a reaction. Mathematically, this can be expressed as:

$$\frac{d[A]}{dt} = -k_{AB}[A] \cdot [B] \quad 4-14$$

where, $[X]$ is the concentration of X in units of mol/cm^3 and k_{AB} is the rate constant for the reaction with units of $\text{cm}^3/\text{mol}\cdot\text{s}$. The rate coefficient k_{AB} , as a function of temperature is given by the modified Arrhenius equation below:

$$k(T) = A \cdot \left(\frac{T}{T_o} \right)^n \cdot e^{\frac{-E_a}{RT}} \quad 4-15$$

where, A is the pre-exponential factor, R is the gas constant, and E_a is the activation energy of the reaction. The pre-exponential factor is usually determined experimentally and can be thought of as the number of collisions of A and B. The activation energy is the energy barrier that must be overcome for a reaction to proceed. The beneficial use of catalysts to promote reactions is usually described in terms of reducing the activation energy of reactions and therefore making them more likely to occur. The exponential term in Eqn. 4-15 is the probability that a collision will result in a reaction.

Combining Eqns. 4-14 and 4-15 gives:

$$\frac{d[A]}{dt} = -A \cdot \left(\frac{T}{T_o} \right)^n \cdot e^{\frac{-E_a}{RT}} \cdot [A] \cdot [B] \quad 4-16$$

Equation 4-16 above shows that reactions rates are linear functions of reactant concentration and are strong functions of temperature. Berry *et al.*[249] of the National Energy Technology Laboratory developed a simplified reaction model for autothermal reforming of diesel shown in eqn. 4-17, below:

$$r_{C_nH_m} = -A \cdot e^{\left(\frac{8315}{T} \right)} [C_nH_m]^{0.87} [H_2O]^{-1.02} [O_2]^{0.13} \quad 4-17$$

Berry does not provide the pre-exponential factor, but values can be obtained from other sources [250, 251, 252] that range from 2.23×10^5 to $6.4 \times 10^4 \text{ cm}^3/(\text{mol}\cdot\text{s})$.

Concentrations of components in Eqn. 4-17 are determined by Eqn. 4-18 below:

$$[Y] = \frac{X_Y \cdot P}{R \cdot T} \quad 4-18$$

Where, X is the molar concentration of species Y , P is the pressure, T is the absolute temperature and R is the universal gas constant. Substituting Eqn. 4-18 for all components into Eqn. 4-17 will result in the reaction rate for JP-8 under ATR operating conditions. The time required for the fuel to fully react, τ_{fuel} , is calculated by Eqn. 4-19 below:

$$\tau_{\text{fuel}} = -\frac{n_{\text{fuel}}}{r_{C_nH_m}} \quad 4-19$$

where, n_{fuel} is the total number of moles of fuel entering the reactor.

The fuel reaction time is strongly influenced by the O/C ratio and the enrichment number (Ψ). Figure 4.11 shows that as the O/C ratio increases, the time for the fuel to fully react decreases. This result is strongly influenced by temperature which increases with increasing O/C ratio. The slope of the fuel reaction time line (i.e. reaction rate) is greatest between O/C of 0.8 to 1.05; at O/C ratio's greater than 1.05 the reaction rate is low. Also to be considered is that as the O/C ratio is increased, the total space time available (available residence time of the reactor for all reactions) decreases linearly. Therefore, at O/C ratios above 1.05, reaction rates are approaching a constant value as the total reactor space time continues to decrease; this ultimately can result in incomplete fuel conversion which will jeopardize reactor performance. At low O/C ratios and high fuel flow rates (such as 6.67 kW_{th}) the time required to reach full fuel conversion increases rapidly as the O/C ratio is reduced. For 6.67 kW_{th}, at an O/C ratio of approximately 0.90 the available space time and fuel conversion time lines cross indicating that there is just sufficient time to fully convert the fuel at this O/C ratio. At lower O/C ratios incomplete fuel conversion should be expected. Figure 4.12 shows the impact of enrichment number on fuel reaction time and on reactor space time under fixed

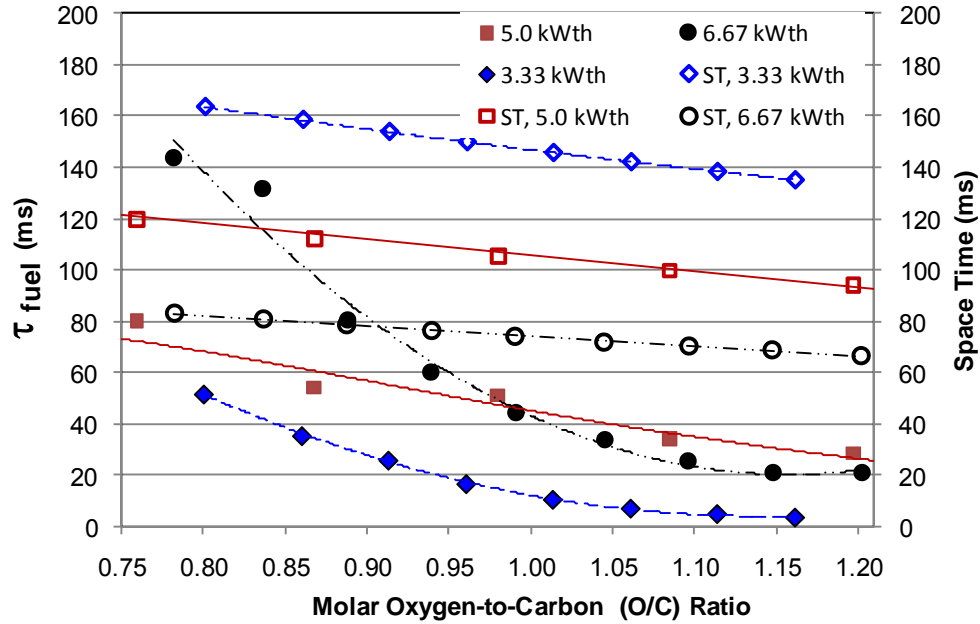


Figure 4.11 Fuel reaction time (τ_{fuel}) as a function of molar oxygen-to-carbon (O/C) ratio for three JP-8 fuel flow rates: 5.9 ml/min. (3.33 kW_{th}), 8.9 ml/min. (5.0 kW_{th}) and 11.8 ml/min. (6.67 kW_{th}), S/C at 2.0, and enrichment number of 1. Opened symbols (\diamond , \circ , \square) represent space time and closed symbols (\blacklozenge , \bullet , \blacksquare) represent time needed to achieve full fuel conversion (τ).

ATR operating conditions of fuel feed equal to 5.9 ml/min. (3.33 kW_{th}), O/C ratio of 1.06 and S/C ratio of 2. Here increasing the enrichment number results in both a reduced time to achieve fuel conversion and an increase in reactor space time; both very positive results. This result indicates that oxygen enrichment could allow for either larger fuel throughput or a substantial reduction in reactor volume.

4.6 Fuel cell performance as a function of hydrogen concentration

Increasing the concentration of hydrogen in the anode feed stream to a fuel cell can have positive impacts on fuel cell performance. The following two sections address these fuel cell performance improvements resulting from increased hydrogen concentration.

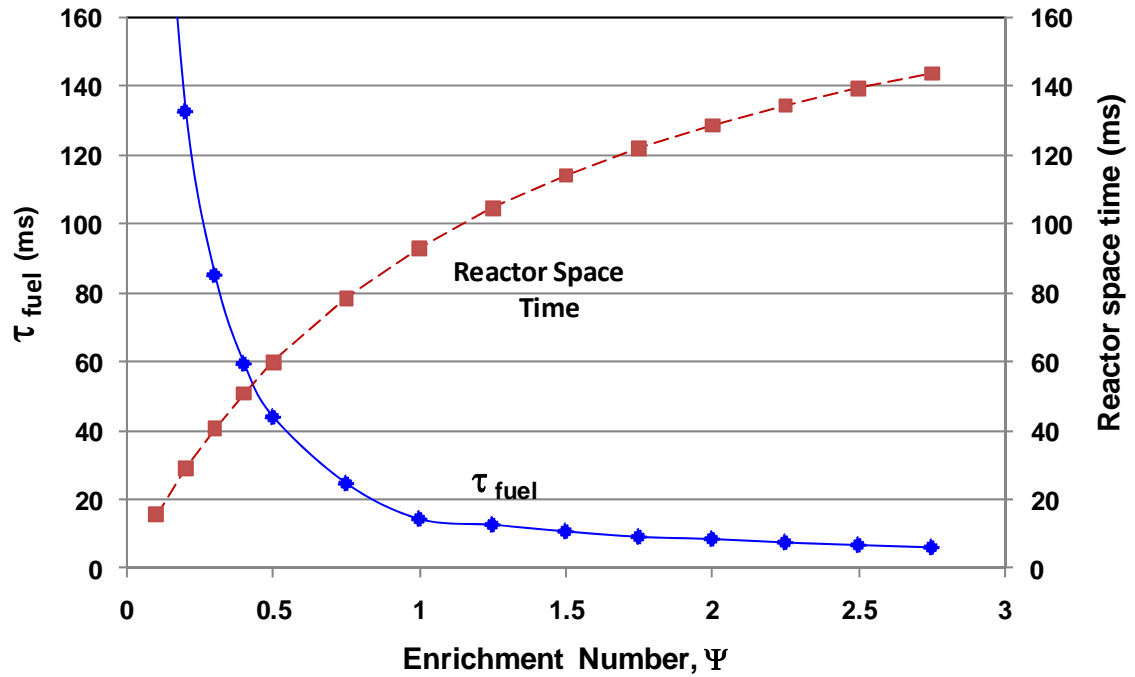


Figure 4.12 Fuel reaction time (τ_{fuel}) as a function of enrichment number (Ψ) for t JP-8 fuel flow rate of 5.9 ml/min. (3.33 kWth), S/C at 2.0, and O/C of 1.06.

Section 4.6.1 discusses the thermodynamic efficiency of a fuel cell and the role hydrogen partial pressure plays. Section 4.6.2 addresses fuel cell mass transport design considerations and the influence that hydrogen concentration has on the ability of a fuel cell to utilize available fuel.

4.6.1 Effect of hydrogen partial pressure on fuel cell performance

A consequence of oxygen-enrichment is that reformat hydrogen concentration will increase considerably as a result of reducing the nitrogen content going into the reactor.

The overall reaction taking place within a fuel cell is given below:



The Nernst equation below gives the ideal cell voltage as a function of operating temperature and partial pressures of reactants and products:

$$E = E^o + \frac{RT}{2\mathfrak{F}} \cdot \ln \frac{X_{H_2}}{X_{H_2O}} + \frac{RT}{2\mathfrak{F}} \cdot \ln \frac{X_{O_2}^{0.5}}{X_{H_2O}} \quad 4-21$$

where, E^o is the ideal cell voltage, R is the ideal gas constant (8.314 J/mol-K), \mathfrak{F} is Faraday's constant (96,485 Coulombs/mol), and X_i is the partial pressure of i .

Considering changes in the hydrogen concentration between two conditions where all other values remain the same, Eqn. 4-21 can be rewritten as follows:

$$E_2 = E_1 - \Delta E_{2-1} = E_1 - \frac{RT}{2\mathfrak{F}} \cdot \ln \frac{(X_{H_2})_2}{(X_{H_2})_1} \quad 4-22$$

The cell voltage corrected for hydrogen concentration can be related to the cell efficiency by:

$$\eta_{LHV} = \frac{E}{E^o} \cdot 100\%$$

The ideal voltage for a fuel cell can be determined by:

$$E^o = \frac{-\Delta \bar{h}_f}{2F} \quad 4-23$$

Here $\Delta \bar{h}_f$ is the heat released through oxidation of the fuel (i.e. heating value where the $(\Delta \bar{h}_f)_{\text{Lower}}$ is -241.83 kJ/mole $(\Delta \bar{h}_f)_{\text{Higher}}$ is -285.84 kJ/mole). Using the lower heating value you obtain an ideal cell voltage of 1.25 V. Where the fuel cell efficiency based on the lower heating value of hydrogen is:

$$\eta_{LHV} = \frac{E}{1.25} \cdot 100\% \quad 4-24$$

Combining Eqns. 4-24 and 4-23 a relationship between fuel cell efficiency and entering hydrogen concentration is developed.

$$\eta_{LHV} = \frac{E_1 - \frac{RT}{2\mathfrak{F}} \cdot \ln \left(\frac{X_{H_2}_2}{X_{H_2}_1} \right)}{1.25} \cdot 100\% \quad 4-25$$

Assuming a baseline operating voltage of 0.7 V/cell, an initial hydrogen concentration of 33.9%¹⁸, and a cell operating temperature of 800 °C, the impact of hydrogen concentration on fuel cell efficiency is displayed in Fig. 4.13. Comparing the hydrogen concentration (Fig. 4.5a) with the fuel cell stack efficiency (Fig. 4.13) for enrichment numbers of 1.0 (33.9%¹⁸ H₂) and 2.0 (46.5%¹⁸ H₂) will result in a 4% increase in fuel cell stack efficiency (56.7% to 59.0%).

¹⁸ Molar percentage on a dry basis.

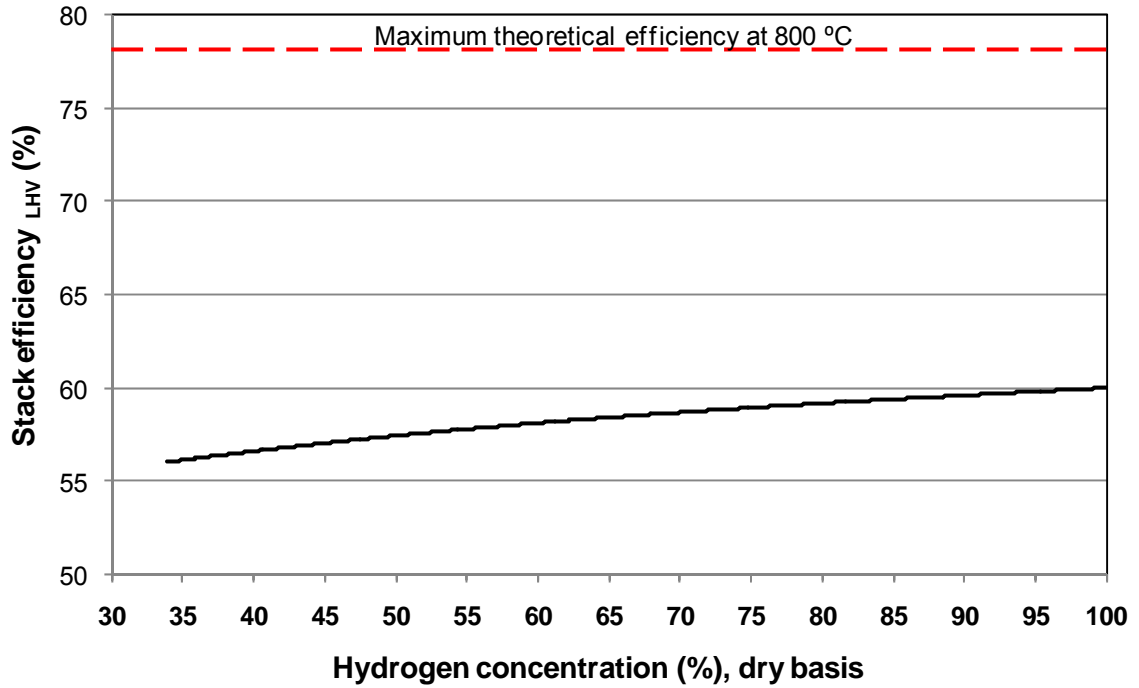


Figure 4.13 Effect of hydrogen concentration entering the fuel cell stack on the overall stack efficiency based on the lower heating value of hydrogen. Initial stack voltage assumed at 0.7 volts/cell, with an anode hydrogen entrance concentration of 33.9 %(dry basis), cell temperature of 800 °C, pressure of 1 atm, and steam and oxygen concentrations are assumed constant.

4.6.2 Effect of hydrogen partial pressure on fuel cell, fuel utilization

The fuel utilization within a fuel cell stack describes the ability of the stack to effectively use the incoming fuel without incurring performance losses due to mass transfer limitations. The efficiency of a fuel cell as presented in Eqn. 4-24 assumes that all fuel entering the fuel cell is consumed. This assumption is not valid for practical applications and Eqn. 4-26 [253] below modifies Eqn. 4-24 by incorporating the fuel utilization of the stack.

$$\eta_{LHV} = \frac{E}{1.25} \cdot u_{fuel} \cdot 100\% \quad 4-26$$

where,

$$\text{Fuel utilization} \equiv u_{fuel} = \frac{\text{mass of fuel reacted in the cell}}{\text{mass of fuel input to the cell}} \quad 4-27$$

Fuel utilization is determined empirically and is a function of the design of the fuel cell flow fields, operating voltage, cell operating temperature and composition of anode feed. A typical fuel utilization for reformed fuel is approximately 70% when operating at 0.7V cell voltage, with hydrogen concentrations of approximately 29-34%, and 800 °C (solid oxide fuel cell). Under these acceptable operating conditions, hydrogen exiting the stack is at a concentration of approximately 15% and this condition is sufficient to avoid stack performance losses resulting from mass transport limitations of fuel at the anode (termed concentration polarization losses). An equation for fuel utilization within the fuel cell anode as a function of anode entrance conditions and the constraint of anode exit molar fuel concentration can be derived from the following relationships.

$$\dot{n}_{anode, exit} = \dot{n}_{anode, entrance} - u_{fuel} \cdot \dot{n}_{fuel, entrance} \quad 4-28$$

$$\dot{n}_{fuel, exit} = \dot{n}_{fuel, entrance} - u_{fuel} \cdot \dot{n}_{fuel, entrance} \quad 4-29$$

$$X_{fuel, exit} = \frac{\dot{n}_{fuel, exit}}{\dot{n}_{anode, exit}} \quad 4-30$$

Eqn. 4-28 describes the molar flow rate at the anode exit in terms of the anode entrance molar flow and the fuel consumed by the fuel cell. Eqn. 4-29 provides a similar evaluation for the fuel as it passes through the fuel cell anode. Eqn. 4-30 gives a definition of the molar concentration of fuel at the anode exit. Combining Eqns. 4-28,

4-29 and 4-30 results in a relationship for fuel utilization as a function of entrance conditions and the exit fuel concentration.

$$u_{fuel} = \frac{\dot{n}_{fuel, exit} - X_{fuel, exit} \cdot \dot{n}_{fuel, entrance}}{\dot{n}_{fuel, entrance} (1 - X_{fuel, exit})} \quad 4-31$$

The power that a fuel cell can produce can be determined from Eqn. 4-32 below:

$$P_{fuel\ cell} = \dot{n}_{fuel, ent.} \cdot u_{fuel} \cdot \mathfrak{F} \cdot V_{cell} \quad 4-32$$

where, \mathfrak{F} is Faraday's constant (96485 C/mol), and $\dot{n}_{fuel, ent.}$ is the molar flow rate of fuel entering the fuel cell. Rearranging Eqn. 4-32 in terms of fuel flow rate, results in Eqn. 4-33 below.

$$\dot{n}_{fuel, ent.} = \frac{u_{fuel} \cdot \mathfrak{F} \cdot V_{cell}}{P_{fuel\ cell}} \quad 4-33$$

Increasing anode fuel concentration results in increased allowable fuel utilization within the fuel cell stack (Eqn. 4-31), reduced fuel delivery requirements (Eqn. 4-33), and improved fuel cell efficiency (Eqn. 4-26). Figure 4.14 displays graphically these results for a SOFC operating at 800 °C, at a cell voltage of 0.7 V, and at 1 atm. Comparing the hydrogen concentration (Fig. 4.5a) with fuel cell stack efficiency (Fig. 4.14) for enrichment numbers of 1.0 (33.9% H₂) and 2.0 (46.5% H₂) results in a 15.6 % increase in fuel cell stack efficiency (39.2% to 45.3%).

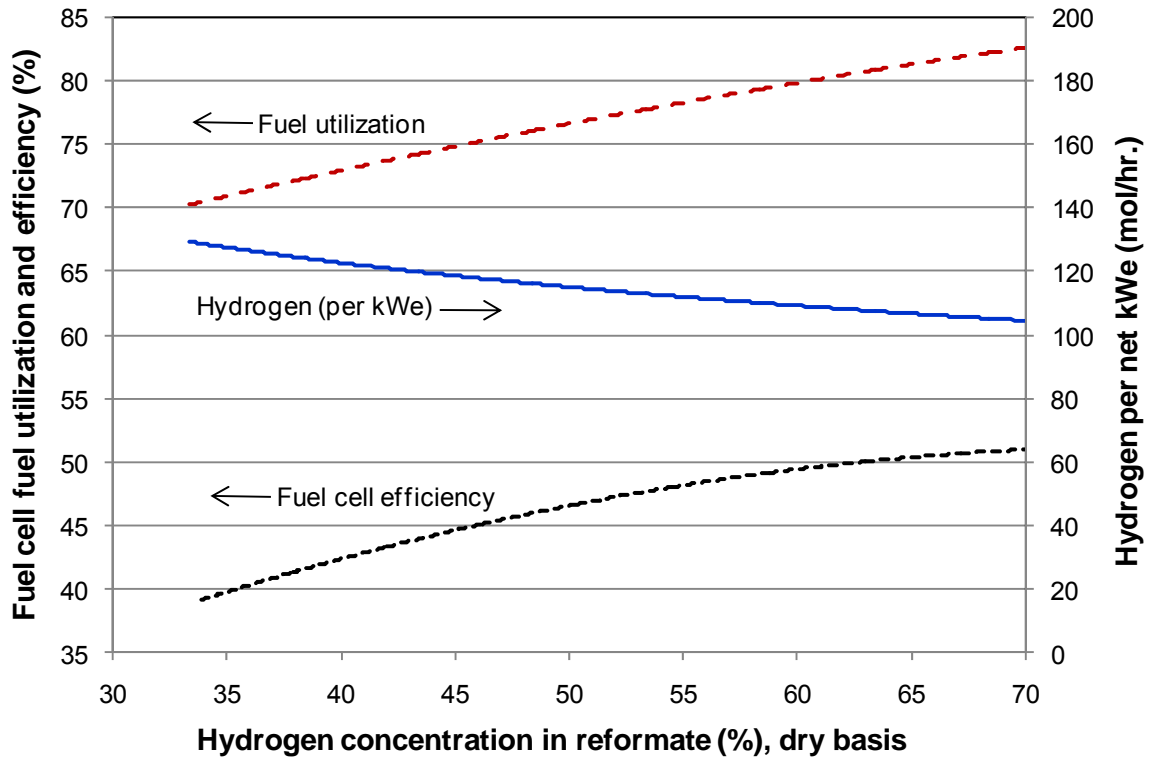


Figure 4.14 Effect of hydrogen concentration entering the fuel cell stack on the overall stack efficiency based on the lower heating value of hydrogen. Initial stack voltage assumed at 0.7 volts/cell, with an anode hydrogen entrance concentration of 33.9% (dry basis), cell temperature of 800 °C, pressure of 1 atm, and steam and oxygen concentrations are assumed constant. Fuel utilization is based on maintaining 15% hydrogen in the exit of the fuel cell anode.

4.7 Chapter summary

Through the use of analytical modeling a number of observations regarding the influence of oxygen enrichment on reforming can be drawn:

- Based on equilibrium reactions, oxygen enrichment may result in a slight reformer efficiency reduction of approximately 3.5% when going from an enrichment of 1.0 to 2.0. The reformer efficiency reduction results from increased reactor temperature which reduces hydrogen production.

- Oxygen enrichment results in a significant increase in hydrogen concentration. This increased concentration of hydrogen will have a positive performance benefit to the fuel cell stack.
 - Increased fuel partial pressure at the anode results in a 4% performance increase when going from enrichment number of 1 to 2.
 - Increased fuel concentration allows for operation at higher stack fuel utilizations resulting in a 15.6% increase when going from enrichment number of 1 to 2.
- Increased reactor convective heat transfer as measured by constant pressure specific heat results from oxygen enrichment.
- Oxygen enrichment reduces reformer volume flow resulting in a reduction in reactor pressure drop and an associated pumping power. Reduced reformer volume flow also increases reactor space time.
 - Or alternatively, the size of the reactor can be reduced while maintaining a constant reactor space time and pressure drop.
- Oxygen enrichment allows for independent variation of reactor space time and O/C ratio. This could have significant benefits for experimental research and control applications.
- With increasing oxygen enrichment, the time to reach full fuel conversion is reduced.

Chapter 5

Surrogate Fuel Development

5.0 Introduction

Jet fuel is an important transportation fuel in the United States, with an annual consumption of 591 million barrels in 2008. Jet fuel is the fourth most consumed transportation fuel in the United states after gasoline, distillate fuel oil and liquefied petroleum gases; representing 11.1% of the total energy consumed for transportation purposes [254]. The U.S. military is the single largest petroleum consumer in the world and jet fuel represents 62% (volume basis) of all petroleum products consumed (82 million barrels per year) [255]. The large consumption of jet fuel in the military has resulted from a 1988 decision to pursue a single battlefield fuel as a means to simplify the supply chain and gain logistics efficiencies [256]. Specifically, the U.S. military identified JP-8 as the preferred battlefield fuel for all ground and land-based forces [257]. The selection of JP-8 was based on the following factors: flight and ground force safety (high fuel flash point of 38 °C minimum), good low temperature operations (-47 °C freezing point), worldwide availability and interoperability with NATO forces [258]. Military grade jet fuel (JP-8) is a kerosene based fuel that is very similar to commercial grade Jet-A1 fuel, but contains trace additives, such as: static dissipating additive, corrosion inhibitor/lubricity improver, fuel system icing inhibitor, and may contain antioxidant and metal deactivator [259,260]. JP-8 is obtained from the fractional distillation of petroleum between 150 °C and 300 °C, resulting in a mixture with an

approximate carbon number distribution between 8 and 16. Jet fuels are middle distillate fuels consisting of hundreds of hydrocarbons that are broadly defined in terms of boiling point range, aromatic content, heating value, sulfur content and other physical characteristics. The chemical composition of jet fuel is highly variable and is influenced by geographic origin of feedstock crude oil and refinery processes, but can also vary locally from batch to batch [261]. The broad definition and composition variation of JP-8 fuel makes fair comparison and definitive conclusion from experimental studies difficult; therefore, surrogate fuel blends are desirable and can be used to evaluate combustion and reactive flows.

Surrogate fuels are well defined, reproducible, mixtures of high purity hydrocarbon fuels that reflect the desired properties of the real fuel with as few components as necessary. Surrogates are typically based on either physical or chemical models. Physical surrogates are single component or mixtures whose physical properties (e.g. density, viscosity, thermal conductivity, etc.) are comparable to the real fuel. Chemical surrogates are single component or mixtures that have generally the same chemical-class (e.g. aromatics, naphthenes, olefins, alkanes, etc.) composition and average molecular weight as the real fuel. There has been a practical need and significant interest in developing surrogates for jet fuels in order to establish baseline performance characteristics for real fuels. Recently, on-going collaborative work to establish a surrogate JP-8 fuel databases and kinetic models have been undertaken with a goal of developing a consensus between industry, academia, and government laboratories so that future efforts could focus on

experimental and kinetic modeling [262,263]. A large body of published work on the development of surrogate jet fuels exists. A number of often cited review papers [264,265] and recent studies [266, 267, 268, 269] on multi-component jet fuel surrogates for combustion applications are available. Surrogate fuels have also been applied to fuel reforming studies of diesel and kerosene based jet fuels: steam reforming [270, 271, 196, 272], catalytic partial oxidation [272, 190] and autothermal reforming [272, 273, 230, 162, 274, 275, 276].

This chapter presents experimental investigation of three low-sulfur JP-8 surrogate fuels for application in a catalytic reactor under near atmospheric pressures (1.05 bar to 1.15 bar) with a molar steam-to-carbon ratio of 2.0, gas hourly space velocity of between $21,000 \text{ hr}^{-1}$ and $28,000 \text{ hr}^{-1}$, and varying molar oxygen-to-carbon ratios between 0.8 and 1.2. The three selected surrogate fuels were down-selected from a field of eighteen separate hydrocarbon candidate surrogates as being the most representative of JP-8. The developed surrogate fuel is intended for study of the product composition and heat and mass transfer characteristics of catalytic autothermal reforming (ATR) reactions for small (1-10 kWe), mobile, fuel cell applications. The target fuel, low-sulfur JP-8, was selected as many approaches to jet fuel reforming for fuel cell applications incorporate sulfur removal prior to reforming [277, 278, 279].

5.1 Jet fuel hydrocarbon composition

Jet fuels consist of blends of hundreds of hydrocarbons with carbon numbers between 8 and 18 and principally fall into five hydrocarbon classes; normal-paraffins, iso-paraffins, cyclo-paraffins, mono-aromatics, and di-aromatics. Trace amounts of olefins and tri-aromatics can also be found, but are generally not considered in surrogate fuel development where the objective is to mimic fuel reactions. Figure 5.1 provides a depiction of the five hydrocarbon classes showing their carbon bond structure and arrangement and also a chromatogram of JP-8 against boiling range. Figure 5.2 shows the hydrocarbon class distribution found in JP-8. The largest hydrocarbon class found in JP-8 are paraffins with normal-paraffins and iso-paraffins each representing approximately one-third of the fuel components and naphthenes ranging from ten to twenty percent. Naphthenes with one, two, and three rings have been identified in JP-8 with relative abundances of approximately, 35:6:1, respectively. Aromatics are another major component of JP-8 consisting of mono-aromatics (15% to 20%) and polyaromatics (1% to 3%), with polyaromatics primarily composed of two ring aromatics with trace amounts (typically $\leq 0.2\%$) of tri-benzene ring compounds. Figure 5.3 provides a depiction of jet fuel hydrocarbon classes based upon boiling range.

5.1.1 Autothermal reforming (ATR)

Although diesel and JP-8 fuels are composed on hundreds of hydrocarbon species that undergo thousands of reaction steps during reforming, the reforming process can be

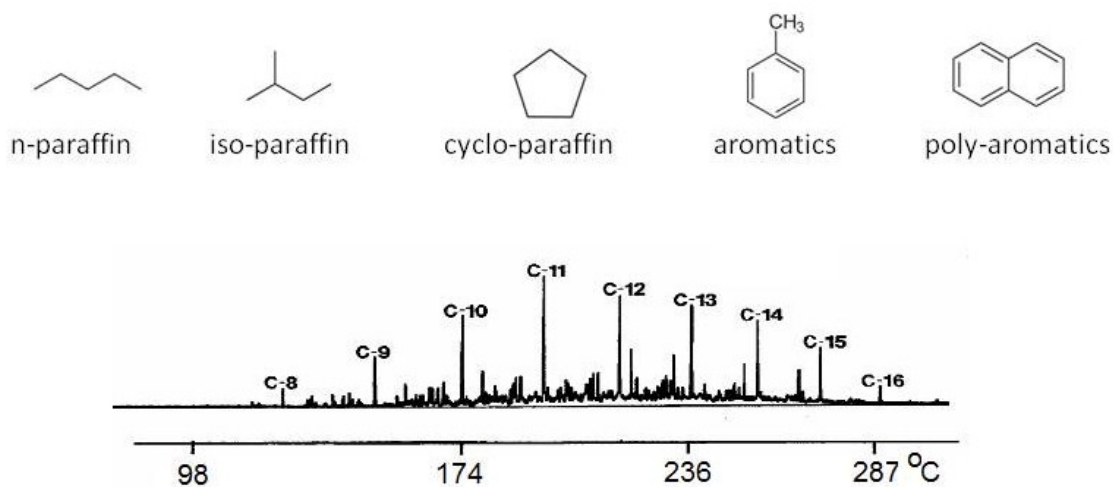


Figure 5.1 Major hydrocarbon classes represented in JP-8 and a chromatogram showing hydrocarbon distribution within JP-8 with normal-paraffins identified against boiling point temperatures.

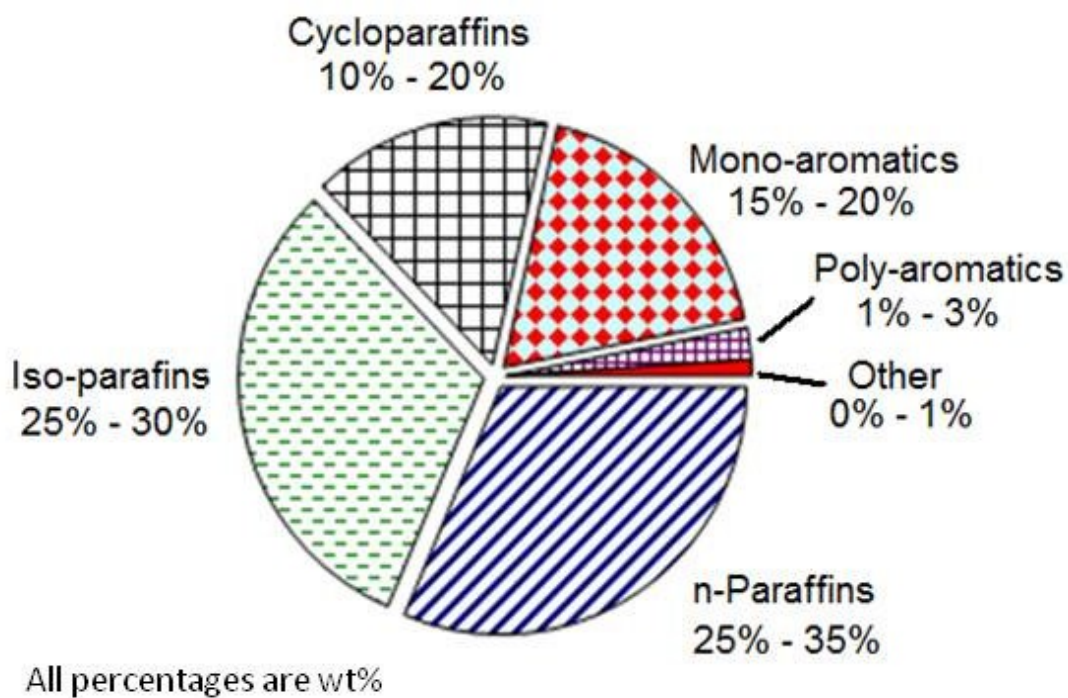


Figure 5.2 Typical hydrocarbon class composition for JP-8.

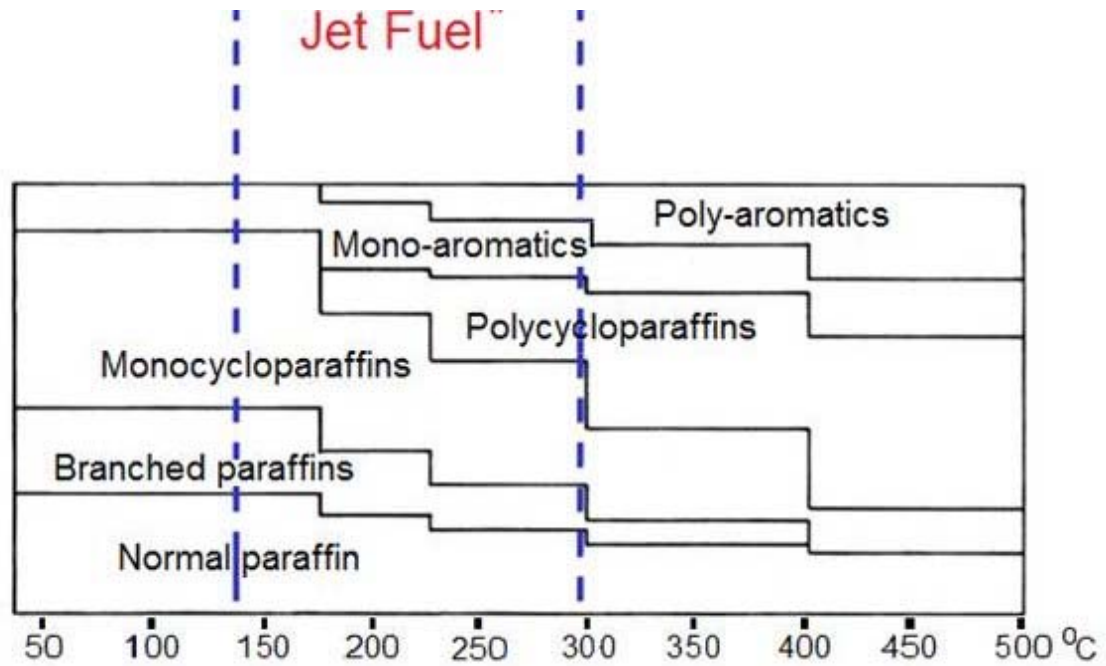
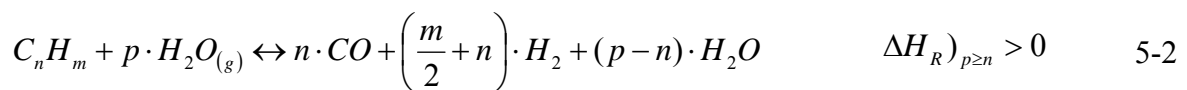


Figure 5.3 Hydrocarbon Class approximate composition as a function of boiling range.

explained through a few simplified reactions. The simplified reactions associated with autothermal fuel reforming consist of an exothermic oxidation reaction Eqn. 5-1, followed by endothermic steam reforming Eqn. 5-2 and a slightly exothermic water-gas-shift reaction Eqn. 5-3. The overall partial oxidation reactions can be exothermic or endothermic depending on the molar ratio of oxygen-to-carbon (x/n).



Autothermal reforming has been in use since the 1950's with initial applications in ammonia and methanol synthesis [280]. Primary ATR characteristics are low energy requirements, high gas space velocities, quick transient response and start-up; these operating characteristics have made ATRs an attractive choice for mobile power equipment.

5.2 Method

The following three sections briefly review the experimental apparatus, data analysis and experimental operation which is described in more detail in Chapter 3, Experimental Apparatus, Instrumentation and Operation.

5.2.1 Experimental apparatus

Experiments were performed on a reformer test bed as described in Chapter 3 [281]. The experimental apparatus was designed to closely control the reactor influx conditions: fuel, steam and air flow rates and temperatures. The goal for the reformer test bed is to deliver a vaporized and temperature selectable stream of steam (for the present experiments $425^{\circ}\text{C} \pm 10^{\circ}\text{C}$), fuel, and air to the entrance of the continuous flow autothermal reformer reactor and to be able to quantify the amount and composition of the gaseous effluents.

5.2.2 Analysis

The target jet fuel (JP-8, MIL-T-83133) was obtained from Haltermann Products, Channelview, Texas. Fuel analysis conducted by Southwest Research Institute gave the

following: 43.2 MJ/kg heat of combustion; carbon and hydrogen mass percent of 85.72% and 13.91%, respectively; mono-aromatics of 19.2 mass %, poly-aromatics of <0.1 mass %, and total aromatics of 19.3 mass %; and, sulfur content of <0.001 mass %. Sulfur content was further characterized by the authors using an Elemental Analyzer, and determined to be 3.8 ppm mass basis. Fuel blends were prepared from commercial supplier with n-dodecane (99+%), decalin (decahydronaphthalene, cis, trans, 98%) and toluene (methylcyclohexane, 99%).

The gaseous reformat stream was analyzed by an on-line chromatograph (Agilent Technologies, Micro GC 3000) with four columns using thermal conductivity detectors. Column type, carrier gas and hydrocarbon gases analyzed are as described in section 3.3 Analysis of reaction products. For hydrocarbon species the gas chromatograph had a lower calibration point of 10 to 20 ppm, so any non-detectable quantity was below this value. Gas chromatograph samples were taken approximately every four minutes, for each experimental run.

For small, mobile reactors, designed for fuel cell power systems, reactor product yield, fuel conversion to CO_x (CO and CO_2), and reformer efficiency provide good insight into the overall performance of the reactor. High fuel conversion, as defined here, assures that hydrocarbon slip which could have deleterious effects for downstream process is not occurring. High yield indicates that proper sizing and operating conditions are achieved for the reactor. Efficiency provides an indication of the reactors contribution to an

overall power system performance and also is an indirect measure of the selectivity of the reactor for products of interest. These parameters are described in section 3.5 Data Analysis and repeated below.

For the data presented, yield for a product is defined as:

$$\text{Yield of R} = \frac{\text{moles of R formed}}{m \cdot \text{moles of hydrocarbon fuel consumed}} \quad 5-4$$

For hydrogen yields, m is the number of moles of H_2 per mole of hydrocarbon; for CO , CO_2 , CO_x and CH_4 , m is the number of carbon atoms in the hydrocarbon fuel. Under favorable conditions, the hydrogen yield can be greater than 1 due to the contribution of hydrogen from water. Fuel conversion is defined as:

$$\text{Fuel conversion to } CO_x (\%) = \frac{CO + CO_2}{m \cdot (\text{hydrocarbon fuel})_{in}} \cdot 100\% \quad 5-5$$

where, m is the number of carbons in the hydrocarbon fuel fed to the reactor. Reforming efficiency (η), is defined assuming that the reformat will be used with a solid oxide fuel cell:

$$\eta_{\text{reformer}} (\%) = \frac{(LHV)_{H_2} + (LHV)_{CO}}{(LHV)_{\text{fuel}}} \cdot 100\% \quad 5-6$$

where, $(LHV)_x$ is the lower heating value of x .

Under all test conditions oxygen conversion was 100% and has been reported in the literature for methane reforming to be consumed rapidly within the first few millimeters of the reactor [282]. Rapid oxygen conversion is also believed to hold for heavier hydrocarbons. Values presented are based on the averages of gas chromatograph results taken after steady state conditions were observed at each experimental point. Reformate condensate was collected and visually inspected but not analyzed. Reformate condensate under conditions of $O/C \geq 1.0$ appeared to consist of water with no visible sign of fuel, but for $O/C \leq 1.0$ a fuel film could be observed indicating incomplete conversion. Under conditions where complete fuel conversion are anticipated, $O/C \geq 1.0$, the carbon balance were in the range of 96% - 100%.

5.2.3 Reactor operation

The experimental apparatus operation for surrogate fuel development is identical to normal operation as described in sections 3.4.3 ATR reactor start-up and shutdown and 3.4.4 Light-off temperatures.

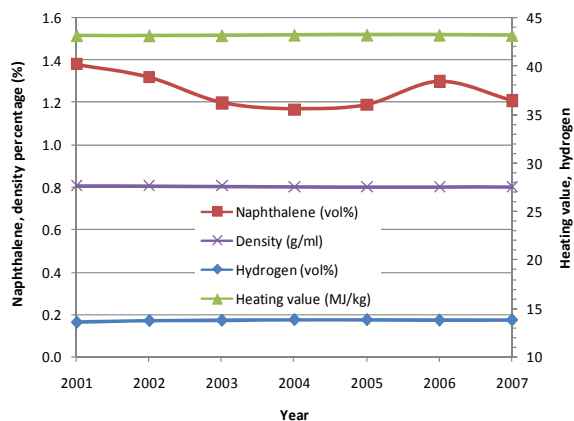
5.3. Surrogate fuel results and discussion

The following two sections discuss the composition of JP-8 fuel, describe criteria used in developing a surrogate JP-8 fuel for ATR, provide a review of surrogate JP-8 fuel compositions developed previously principally in support of combustion research, and give a detailed discussion of fuel components selected under this thesis, and results obtained in reforming.

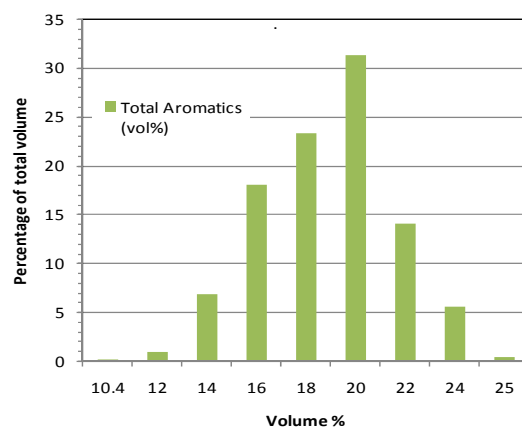
5.3.1 Jet fuel (JP-8) and surrogate JP-8 fuel

The military grade JP-8 specification is based on broad parameters that typically specify a wide acceptable range or that set minimum or maximum acceptable physical fuel properties. The broad fuel definition helps in minimizing refinery costs and subsequently fuel prices. From Fig. 5.4, selected mean values are shown for a number of fuel parameters obtained from the Petroleum Quality Information System, maintained by the Defense Energy Support Center [283]; statistical data reflects all Department of Defense (DoD) fuel purchases worldwide. In 2007, 1982 million gallon of JP-8 fuel was purchased by DoD. Figure 5.4a indicates that for many fuel properties such as heating value, density, and hydrogen content the mean values are consistent from year to year. However, looking more closely, Figures 5.4b and 5.4c, reveal that significant variance can occur from the mean values; as shown for aromatic and hydrogen content. These variances can be even more pronounced when comparing fuel properties on a regional basis.

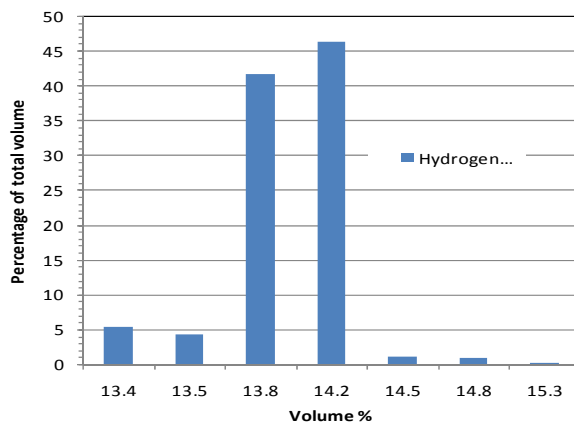
An analysis of the target low-sulfur JP-8 fuel is shown in Table 5.1 along with JP-8 specification values and the mean values for all JP-8 fuel purchased by DoD in 2007 [261]. The low sulfur JP-8 values are in general, in close agreement to mean value data for JP-8 except for sulfur content, di-aromatic content, and the evaporation point on the distillation range. The low sulfur fuel has an evaporation point of 211 °C and the mean JP-8 value is 268.8 °C and the low sulfur JP-8 also contains very low di-aromatic content compared to typical values shown in Table 5.2. Both the reduced evaporation point and



(a)



(b)



(c)

Figure 5.4. U.S. Department of Defense JP-8 fuel composition data: (a) mean values of naphthalene, density, hydrogen content and heating values for 2001-2007; (b) aromatic content distribution for 2007; (c) hydrogen content distribution for 2007.

reduced di-aromatic content could be a function of the desulfurization processes used at the refinery. For the target low-sulfur JP-8, the hydrogen to carbon ratio (H/C) is 1.93 and the average empirical formula was assumed to be $C_{12.2}H_{23.5}$.

Surrogate fuel selection criteria was based on constraining the hydrocarbon components to three, having an average carbon number close to the target fuel, maintaining a hydrogen to carbon ratio close to the target fuel, minimizing fuel costs and having a fuel that reflected the real fuel behavior in terms of fuel ignition, heat transfer, oxidative behavior, and reaction behavior. Based on these criteria, a chemical surrogate fuel that represented the major chemical hydrocarbon classes in the target fuel was followed. In developing the surrogate fuel formulation for fuel reforming, six chemical compound classes representing JP-8 were considered: normal paraffins, cyclo-paraffins, iso-paraffins, olefins, mono-aromatics, and poly-aromatics [262]. In order to simplify the surrogate fuel, chemical compound classes not abundant in the target sample were eliminated from consideration. Also strongly considered in developing the chosen surrogate fuels were chemical surrogate JP-8 fuels proposed by other researchers, shown in Table 5.3. With the exception of Gould, et al [274], all the remaining surrogates in Table 5.3 were proposed for combustion and kinetics research. Gould et al developed their surrogate jet fuel to study autothermal reforming of a nickel-ceria-zirconia based catalyst for solid oxide fuel cell auxiliary power units. The University of Utah (Violi 2) [284] developed their surrogate fuel to simulate pool fires where fuel volatility and compositional characteristics (eg. flash point, smoke point, heat of combustion, flash

Table 5.1 Properties of JP-8 sample

Property	JP-8 specification ^a	JP-8 weighted mean ^b	JP-8 target sample ^c
Aromatics (vol%)	25 max.	17.90	19.3 ^d
Olefin (vol%)	5 max.		0.5
Napthalenes (vol%)	3 max.	1.21	<0.10 ^d
Alkanes (% vol)	N/A		83.2
American petroleum institute (API)	37 - 51		48.6
Density @ 15 °C (kg/L)	0.775-0.840	0.8031	0.785
Heat of combustion (MJ/kg)	42.8 min.	43.225	43.1 ^d
Hydrogen content (wt%)	13.5 min.	13.81	13.91 ^d
Carbon content (wt%)	N/A		85.72 ^{d,e}
Hydrogen-to-carbon ratio			1.93
Total sulfur (ppm wt basis)	3000 max.	790	3.8 ^e
Distillation (°C)			
Initial boiling point		149.3	152
10%	205	171.0	162
20%		179.5	168
50%		201.1	186
90%		242.6	202
Evaporation point	300	268.80	211

a. MIL-DTL-83133E Turbine Fuel, Aviation, Kerosene Types, NATO F34 (JP-8).

b. Defense Energy Support, Center, Defense Logistics Agency,
Petroleum Quality Information System (PQIS) 2007; Figure 4-1,
JP8 - 2007 Data Summary.

c. Haltermann Products, product Information, JP-8 HF0162, product:
MIL-DTL-83133E, JP-8, F-34; product cCode: TR 819.

d. Southwest Research Institute, testing per ASTM D240, ASTM D2622,
ASTM D5291, ASTM D5186.

e. Conducted or confirmed by authors

Table 5.2 JP-8 sample chemical composition analysis

Sample ^a	JP8001 ^b	JP8002 ^b	JP8003 ^b
Heat of combustion (MJ/kg)	42.96	43.22	42.48
Sulfur (wt%)	0.0799 ^c	0.0273 ^c	0.0644 ^c
Aromatic content			
mono-aromatic (wt%)	21.2	22.6	17.0
di-aromatic (wt%)	2	2.2	2.0
total (wt%)	23.2	24.8	19.0
Carbon (wt%)	86.06 ^c	86.00 ^c	85.47 ^c
Hydrogen (wt%)	14.02	13.65	13.70

- a. Periodic samples taken from Communications-Electronics Research, Development and Engineering Center, Army Power Division, Ft. Belvoir, VA over an eighteen month time frame.
- b. Southwest Research Institute, testing per ASTM D240, ASTM D2622, ASTM D5291, ASTM D5186.
- c. Confirmed by authors.

point) were emphasized. The surrogates proposed by Drexel University (designated “Drexel S1” [285] and “Drexel S5” [266]) were developed to mimic the low and intermediate temperature reactivity of JP-8 for preignition oxidation studies. The last two surrogate fuels shown in Table 5.3, designated UCSD (University of California at San Diego) and Aachen (RWTH Aachen University) [286] were developed to investigate laminar nonpremixed combustion for compression ignition engine studies. In addition to these multi-component surrogates, many researchers have chosen to use single component hydrocarbon fuels such as n-dodecane as a surrogate for JP-8. Within the area of catalytic autothermal fuel reforming there is little, if any, published surrogate fuel research beyond single and binary blends.

Table 5.3. Surrogate mixtures for JP-8 fuel

surrogate component	Content (mol%)					
	Gould	Violi 2	Drexel S1	Drexel S5	UCSD	Aachen
<u>normal alkanes</u>						
n-decane		25			48.5	68.4
n-dodecane	50	25	43	26		
n-tetradecane		20				
<u>branched alkanes</u>						
iso-octane		5				
iso-cetane			27	36		
<u>cyclo-alkanes</u>						
methyl cyclohexane		5	15	14	29.9	
decalin				6		
<u>mono-aromatics</u>						
toluene		20				
tetralin	50					
o-xylene					21.6	
trimethylbenzene						31.6
<u>poly-aromatics</u>						
1-methyl naphthalene			15	18		

The surrogate fuels selected for this investigation, shown in Table 5.4, consisted of single, binary and tertiary-component mixtures of n-dodecane, decalin and toluene in liquid volume ratios of 10:0:0, 9:1:0 and 7:1:2. The surrogate fuel components represented the hydrocarbon classes of normal paraffin, cyclo-paraffin (naphthene) and mono-aromatic. In moving from the single, to binary, to tertiary surrogate mixtures the overall fuel densities moved towards the target value of 0.785 kg/L (Table 5.1), the hydrogen content moved down towards the target of 13.91 wt%, the hydrogen to carbon ratio moved

Table 5.4 Comparison of surrogate JP-8 fuel properties

	Surrogate JP-8 fuels		
	1-Component (1-Comp.)	2-Component (2-Comp.)	3-Component (3-Comp.)
<u>Physical properties</u>			
Average formula	C ₁₂ H ₂₆	C _{11.7} H _{24.9}	C _{10.1} H _{19.0}
Density (kg/L) @ 20 °C	0.7493	0.764	0.788
Hydrogen/carbon (moles/moles)	2.167	2.123	1.886
Lower heating value (Mj/kg)	44.14	43.85	43.06
Average molecular weight	170.3	165.8	140.4
<u>Chemical properties</u>			
<u>Composition (vol %):</u>			
alkane (n-dodecane)	100%	90%	70%
cyclo-alkane (decalin)	0%	10%	10%
mono-aromatic (toluene)	0%	0%	20%
poly-aromatic	0%	0%	0%
olefins	0%	0%	0%
<u>Economics</u>			
Cost per liter (2010\$)	\$117	\$108	\$92

toward the target value of 1.93, the lower heating value moved down toward the target value of 43.1 MJ/kg, the average molecular weight resceded from the assumed target value of 170 g/g-mole and the surrogate fuel cost was reduced. The costs of the fuels when obtained in small quantities (~ 1 - 2.5 L) for n-dodecane, decalin, and toluene were \$117/L, \$27/L, and \$37/L, respectively; resulting in a surrogate fuel cost for the 1-component, 2-component and 3-component fuels of \$117/L, \$108/L, and \$92/L, respectively.

The three surrogate fuels were reacted in a ceramic monolith reactor over a noble metal based catalysts. In order to minimize potential deleterious effects from carbon formation, the steam-to-carbon ratio was held at 2.0 and the minimum molar oxygen-to-carbon ratio (O/C) was set at 0.8. These conditions generally resulted in low ethane and ethylene production ($< 0.2\%$) which have been identified as carbon formation precursors [154, 287, 288]. To avoid the potential of catalyst sintering or damage to the reactor support structure the maximum operating temperature was limited to $1,100\text{ }^{\circ}\text{C}$ which limited the maximum O/C ratio to approximately 1.2. The reactor space velocities, defined as the standard volume flow into the reactor divided by the reactor volume, at each test condition and fuel are shown in Fig. 5.5, varying from $21,000\text{ hr}^{-1}$ to $28,000\text{ hr}^{-1}$. Variation in space velocity at each test point among the fuels is a maximum of 3% resulting from differences in fuel densities and lower heating values.

5.3.2 Reforming of JP-8 and surrogate fuels

A comparison of the effect on fuel conversion to COx and reactor maximum and exit temperatures as a function of molar oxygen to carbon ratio is shown in Fig. 5.6. The stoichiometric combustion oxygen to carbon ratio (O/C) for n-dodecane, n-dodecane/decalin mixture and the n-dodecane/decalin/toluene mixture are 3.08, 3.06 and 2.94, respectively. With the assumption of an average chemical formula for JP-8 of $\text{C}_{12.2}\text{H}_{23.5}$ the stoichiometric combustion oxygen to carbon ratio is 2.95. For all fuels operating below the stoichiometric combustion oxygen to carbon ratio, as the oxygen to carbon ratio is increased the conversion to COx increases and the reactor exit and maximum

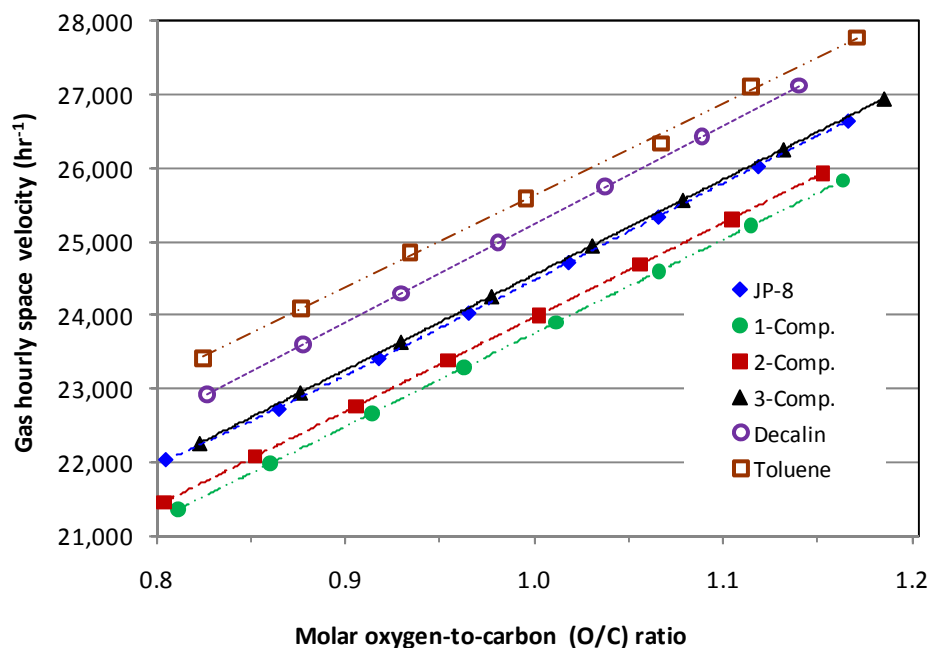
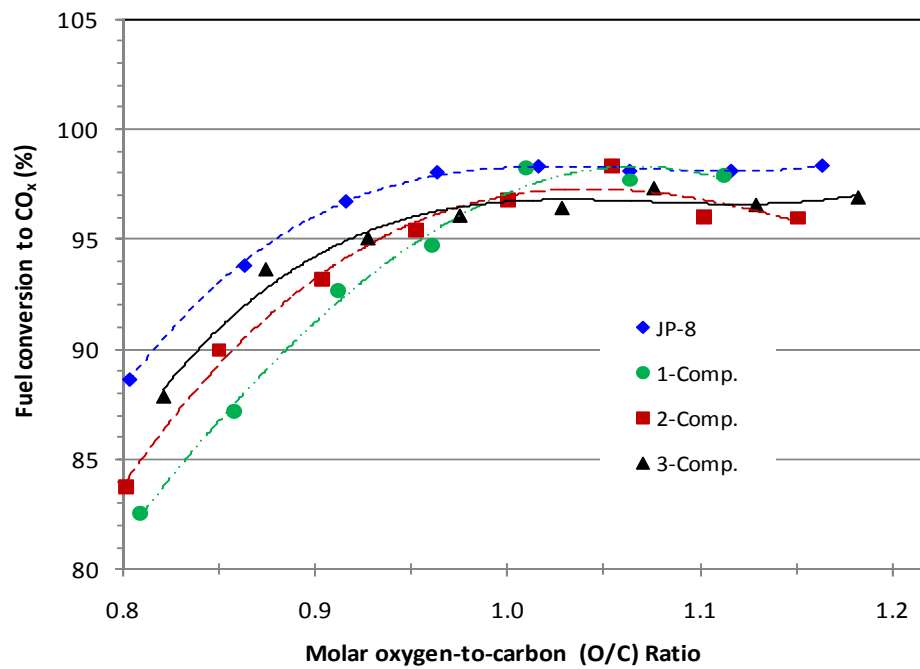
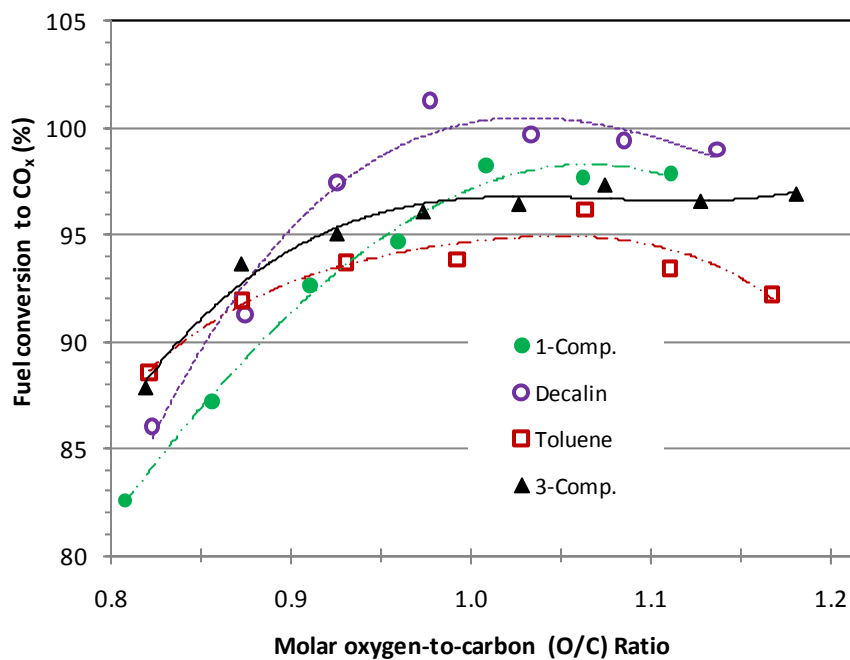


Figure 5.5. Results comparison of gas hourly space velocity with $\text{H}_2\text{O}/\text{C} = 2.0$, fuel feed at 3.33 kW thermal and entrance temperature 425 °C.

measured temperature increases. At oxygen to carbon ratios between 0.95 and 1.05 all fuels achieved maximum conversion of 96 – 98% which is consistent with the carbon balances achieved over the same range. Observing the oxygen to carbon range between 0.8 to 1.0, it can be seen in Fig. 5.6 a that fuel conversion increases with number of fuel components present in the fuel. Of note is that the fuel showing the highest apparent reactivity is JP-8 followed by the three component surrogate (n-dodecane/decalin/toluene). Both of these two fuels contain aromatic components which are noted for their stability and are typically associated with increased difficulty in reforming as compared to paraffins [273, 154]. Similar results were found by Gould et al. [274] when reforming n-dodecane, tetralin, and equal molar mixtures of the two. Wang and Gorte [289] in their experiments with steam reforming on palladium/ceria catalysts showed that aromatics



(a)

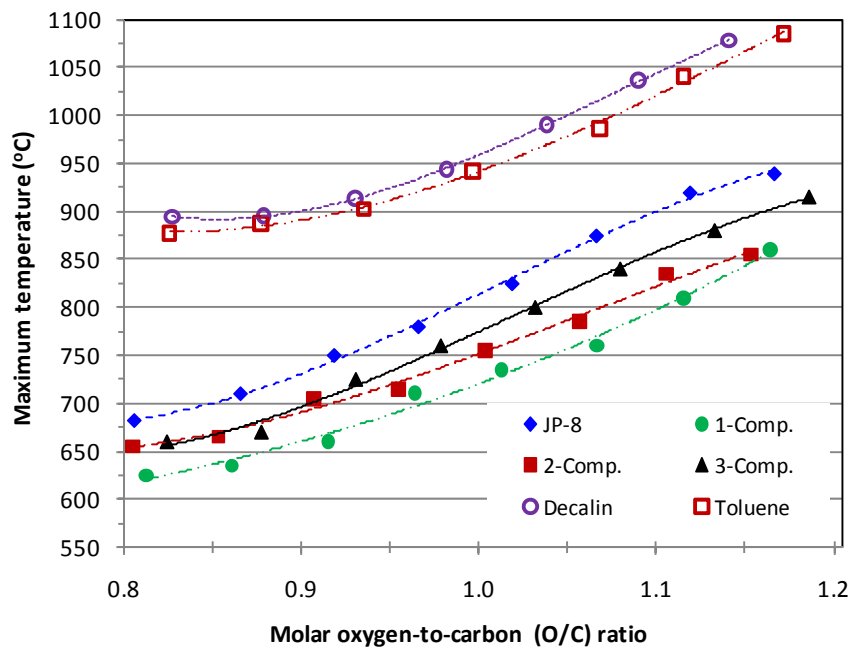


(b)

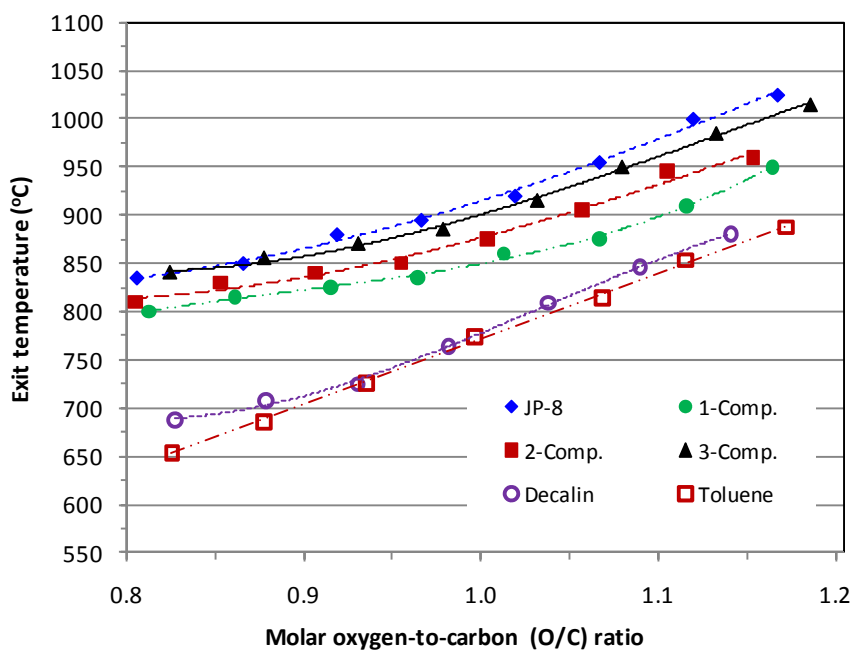
Figure 5.6. Results of fuel conversion for surrogate fuels and target JP-8 (a) and fuel conversion for surrogate fuel components (b) with $\text{H}_2\text{O}/\text{C} = 2.0$, fuel feed at 3.33 kW thermal, entrance temperature 425 °C and the GHSV between 21,000 hr^{-1} and 28,000 hr^{-1} .

possess higher activation energies than normal alkanes and are therefore usually more difficult to reform. Figure 5.6 b provides some additional insight into the contribution of individual surrogate fuel components on fuel conversion. Here decalin achieves rapid fuel conversion and the inclusion of this hydrocarbon class appears to contribute to the order of fuel conversion seen in Fig. 5.6 a. However, the target JP-8 fuel achieves the best surrogate fuel conversion (reaching maximum fuel conversion at the lowest O/C ratio) and other hydrocarbon classes present in JP-8 but not part of this experimental study could be contributing to the observed results. Wang and Gorte also showed that hydrocarbon size also influences reforming and that for normal alkanes larger than C₆ there is a tendency to form cyclohexane, which can react to benzene. The reaction path of large straight chain hydrocarbons such as n-dodecane to benzene may explain why n-dodecane is the least reactive JP-8 surrogate fuel in this study. Additionally, Figs. 5.7 a and 5.7 b show that the order of surrogate and surrogate component apparent reactivities corresponds with both the reactor maximum and exit temperatures. Therefore, increased reactor temperatures for JP-8 and the three component surrogate could have contributed to improved kinetics and better fuel conversion at oxygen to carbon ratios below 0.95. Figures 5.7 a and 5.7 b also show that the surrogate fuel components, decalin, and toluene, are strong contributors to the temperature profiles of the two and three component surrogate fuels.

Also observed from Fig. 5.6 is that reactivities of mixtures can be strongly influenced by small changes in fuel composition. Subramania, et al. [288] and Gould et al. [274] noted



(a)

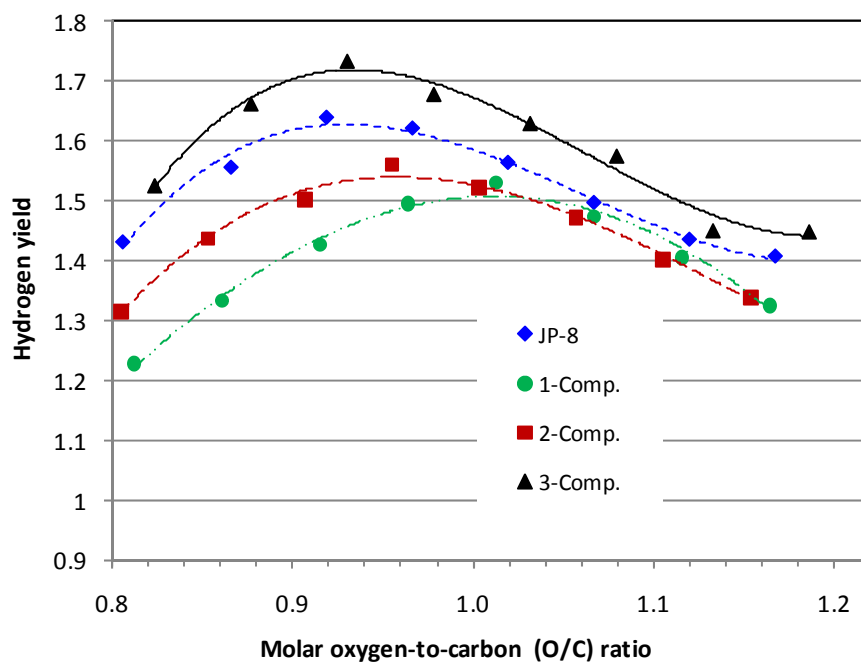


(b)

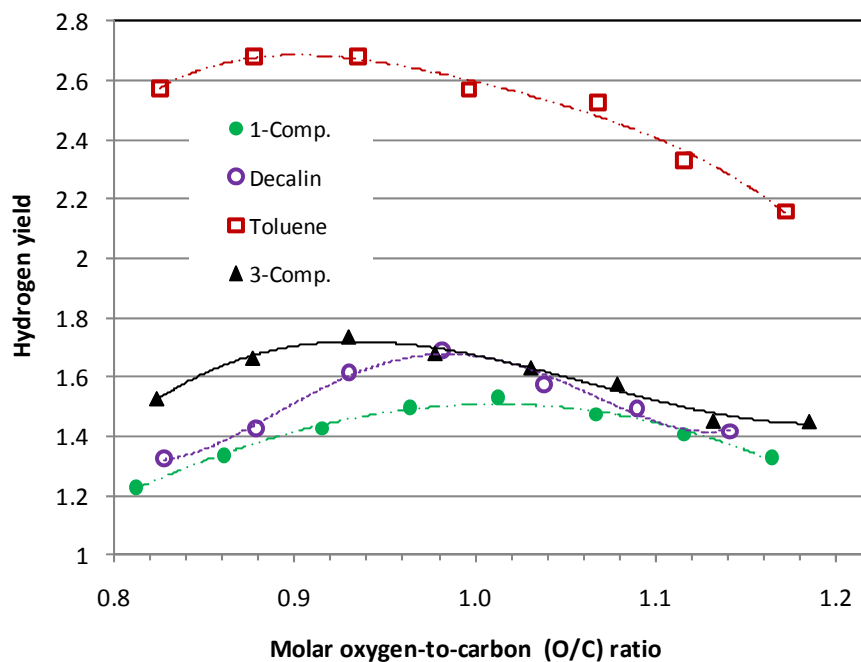
Figure 5.7. Results of reactor peak measured temperature (a) and exit temperature for surrogate fuels, surrogate fuel components and JP-8 with $H_2O/C = 2.0$, fuel feed at 3.33 kW thermal, entrance temperature 425 °C and the GHSV between 21,000 hr^{-1} and 28,000 hr^{-1} .

similar result and concluded that results from surrogate mixtures are not simple averages of their components. Evidence of this relationship can be seen in comparing n-dodecane/decalin and n-dodecane in Fig. 5.6 a at oxygen to carbon ratio below 0.95. Even though the mixture of n-dodecane/decalin is very similar to n-dodecane the reactivity correlates better with n-dodecane/decalin/toluene (variance = 2.11) than with n-dodecane (variance = 4.92) over the oxygen-to-carbon range observed. This result indicates that hydrocarbon classes that are not strongly represented in JP-8 cannot necessarily be ignored as hydrocarbon components can have a disproportionate influence on reforming.

Hydrogen yields are shown in Fig. 5.8. The three component surrogate fuel of n-dodecane/decalin/toluene produces the highest hydrogen yield of 1.72 moles H/mole H in fuel, at an oxygen-to-carbon ratio between 0.92 to 0.94. The peak hydrogen yield for JP-8 also occurs in the same O/C range as the 3-component surrogate, but at lower yield of 1.64 moles H/mole H in fuel. The peak yields for the two-component and one-component surrogate are lower at 1.55 and 1.53, respectively, and occur at higher O/C ratios of 0.96 and 1.0. In general, the results follow a similar pattern as with fuel conversion; for surrogate fuels containing large quantities of n-dodecane (straight chain normal paraffin) which are difficult to convert, higher oxygen to carbon ratios and corresponding higher reactor operating temperatures are needed to achieve full conversion. With the reformate composition being close to predicted equilibrium composition at the reactor exit temperatures; higher exit temperatures will favor carbon



(a)



(b)

Figure 5.8. Hydrogen yield for surrogate fuels (a) and surrogate fuel components (b) with $\text{H}_2\text{O}/\text{C} = 2.0$, fuel feed at 3.33 kW thermal, entrance temperature of 425 °C and the GHSV between 21,000 hr^{-1} and 28,000 hr^{-1} .

monoxide production over hydrogen production via the water-gas-shift reaction Eqn. 5-3. Yields of carbon monoxide, Fig. 5.9 a and 5.9 b, show the water-gas-shift influence with peak hydrogen yields corresponding to minimum carbon monoxide yields and vice-versa. Of note in Fig. 5.8 a is the very high hydrogen yield associated with toluene. Toluene has the lowest hydrogen to carbon ratio of 1.143 (decalin has the next lowest ratio at 1.80, for other fuels see Table 5.4), yet produces hydrogen in the reformat stream that is approximately equivalent to all other fuels tested, as seen in Figure 5.10. The additional hydrogen for toluene comes from water via the endothermic steam reforming reaction, Eqn. 5-2. The suppressed exit temperatures and large temperature difference between the maximum and exit temperatures for decalin and toluene shown in Figures 5.7a and 5.7b supports the conclusion that for these components, steam reforming is very active.

Reformat molar composition for methane and olefin compounds shown in Fig. 5.11 and Fig. 5.12, provide additional insight into fuel conversion. Once again the 3-component surrogate fuel and JP-8 are very nearly identical with methane production reduced from a few hundredths at an O/C of 0.8 to zero above an $O/C > 1.0$. The 2-component and 1-component surrogate fuels are also able to fully convert methane but at a higher oxygen to carbon ratio of 1.10. Figure 5.11b shows more conclusively that n-dodecane is responsible for delayed conversion of methane as toluene and decalin achieve full methane conversion at an O/C ratio of approximately 1.0. Olefin composition shown in Fig. 5.12 a and 5.12b, predominantly ethylene, is reduced to zero for both the 3-

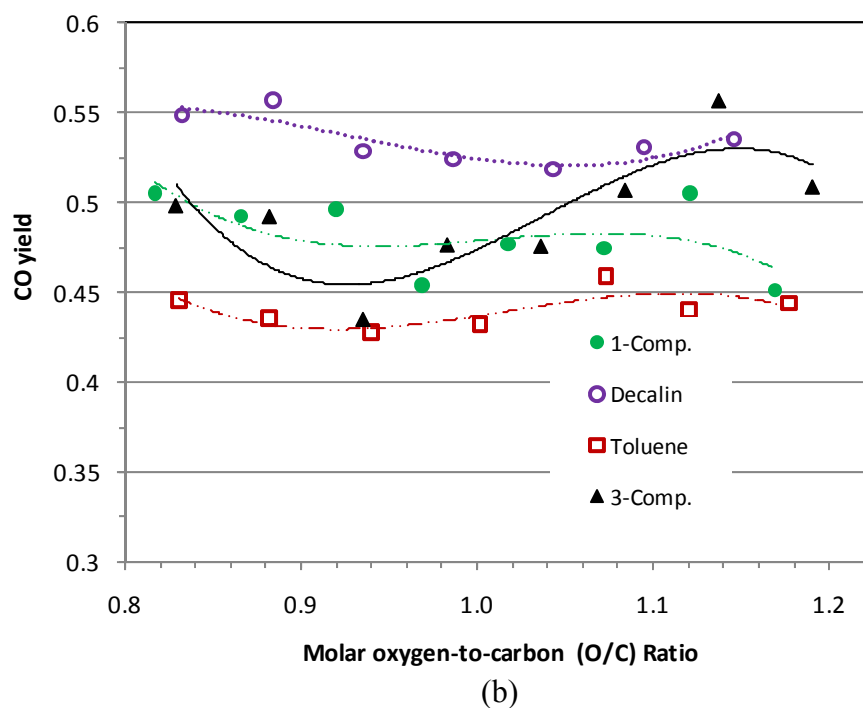
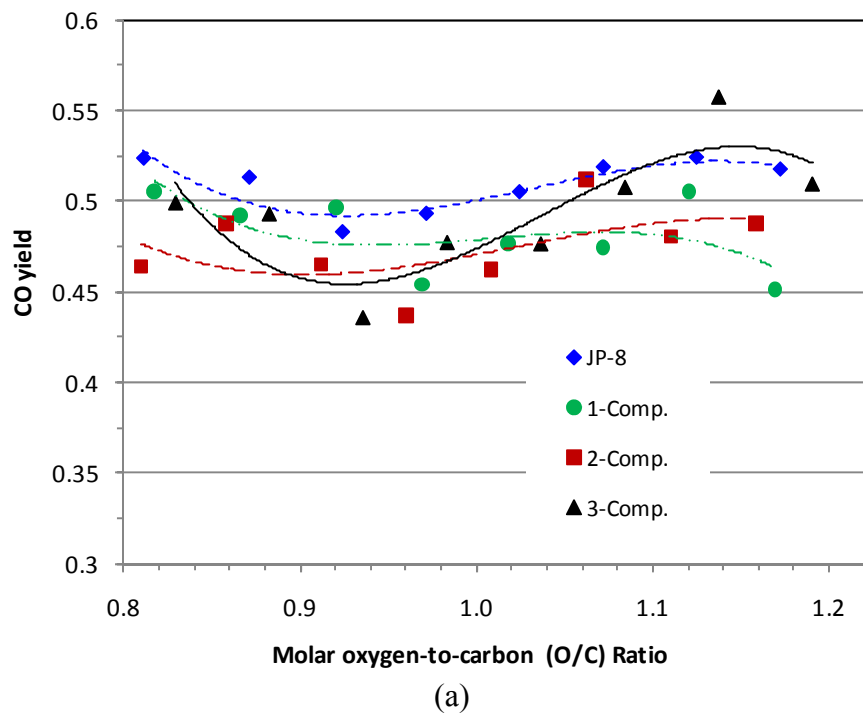


Figure 5.9. Carbon monoxide yield for surrogate fuels (a) and surrogate fuel components (b) with $H_2O/C = 2.0$, fuel feed at 3.33 kW thermal, entrance temperature of 425 °C and the GHSV between 21,000 hr^{-1} and 28,000 hr^{-1} .

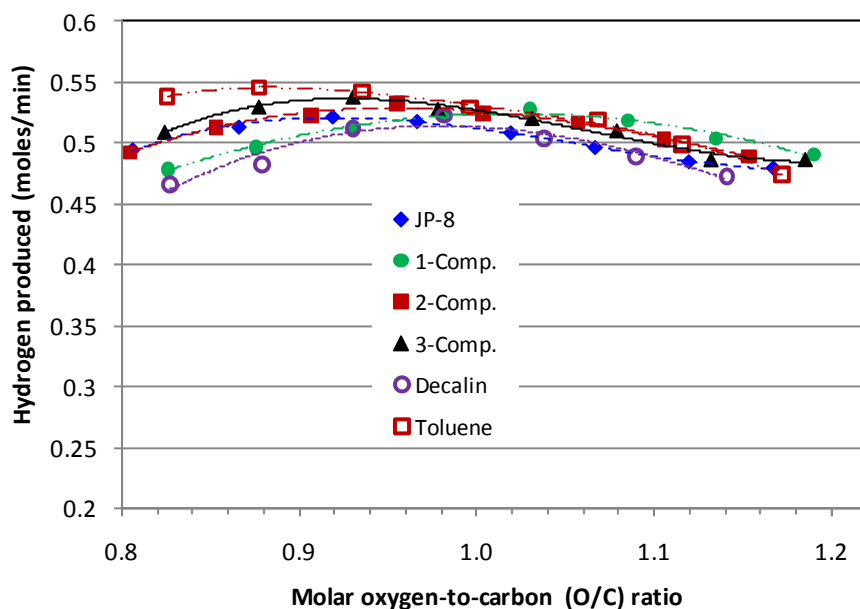
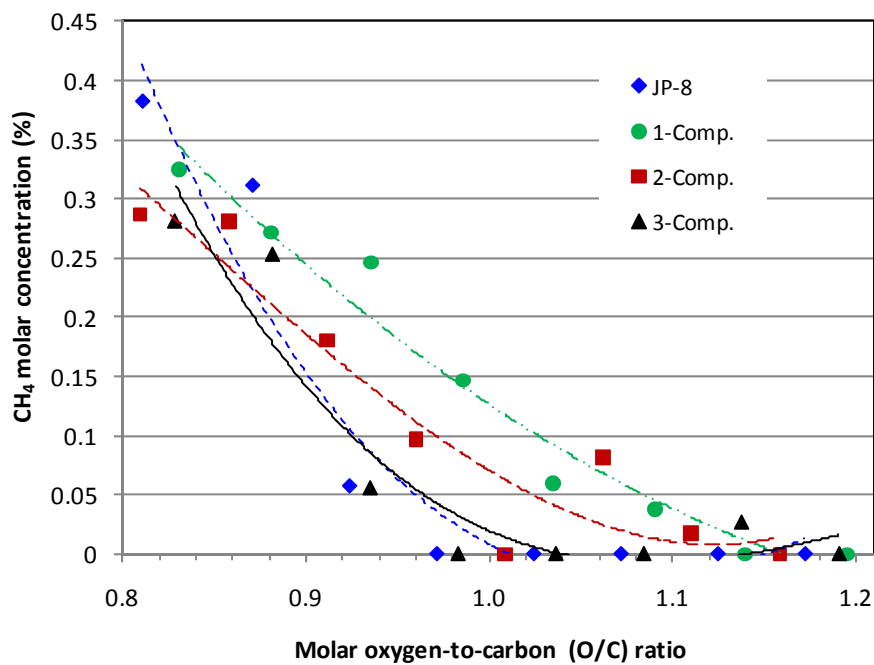
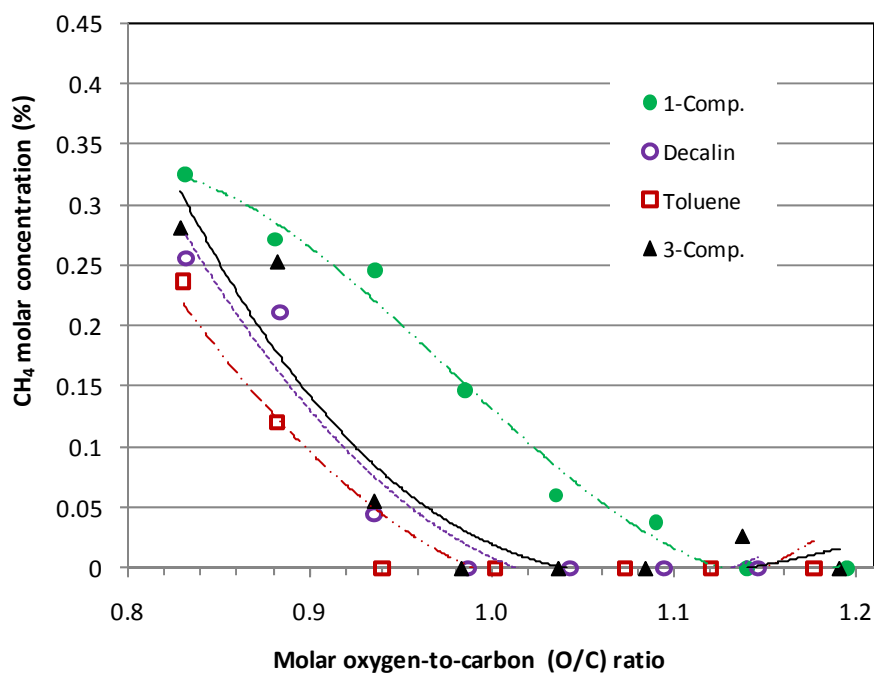


Figure 5.10. Hydrogen produced in the reformat for surrogate fuels, surrogate fuel components and the target JP-8 fuel, under conditions of $H_2O/C = 2.0$, fuel feed at 3.33 kW thermal, entrance temperature of 425 °C and the GHSV between 21,000 hr^{-1} and 28,000 hr^{-1} .

component fuel and JP-8 at O/C ratio above 0.96. However, for the one-component and two-component surrogate fuels the olefin composition is reduced to a minimum composition of 0.04%, but is never fully converted. Figure 5.12 b shows that the inability to fully convert olefins in the one and two component surrogate fuels is related to the presence of n-dodecane. Kaila and Krause [273] observed that olefin products of reforming are associated with thermal cracking of aliphatic compounds at elevated temperatures. This appears to be supported by the results of Fig. 5.12b as the aliphatic mixtures of the single-component and two-component surrogates produce noticeably more olefins throughout the oxygen to carbon range and that JP-8 and the 3-component mixture, having aromatic content, have significantly reduced olefin products.

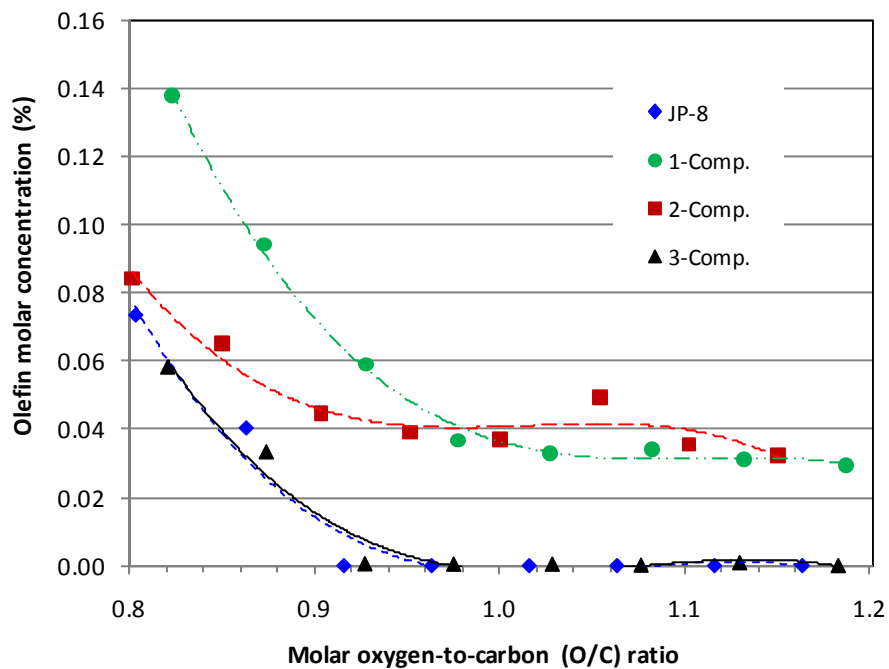


(a)

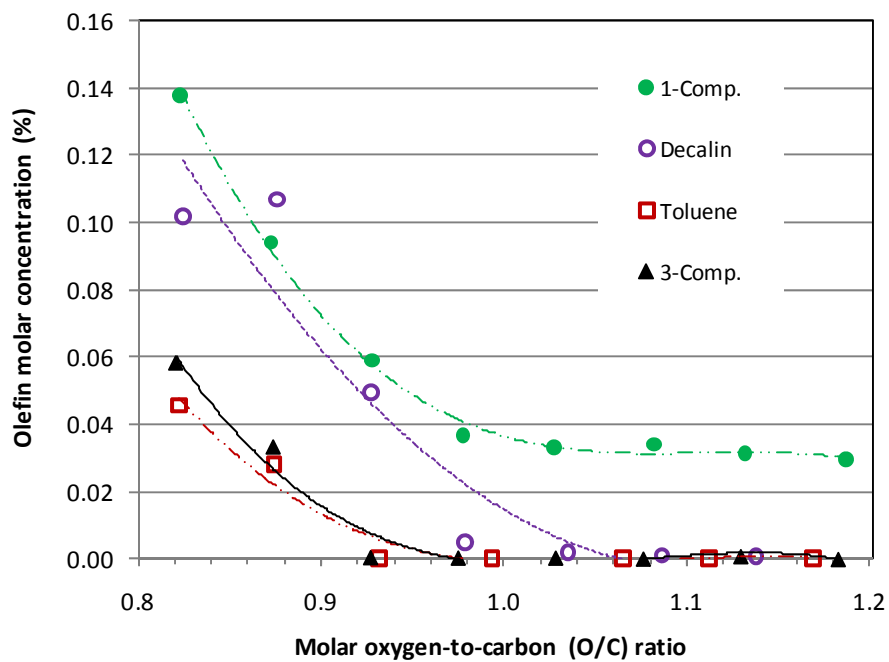


(b)

Figure 5.11 Molar concentrations of methane for surrogate fuels (a) and surrogate fuel components (b) and on a dry basis with $\text{H}_2\text{O}/\text{C} = 2.0$, fuel feed at 3.33 kW thermal, entrance temperature of 425 °C and the GHSV between 21,000 hr^{-1} and 28,000 hr^{-1} .



(a)



(b)

Figure 5.12 Molar concentrations of olefins for surrogate fuels (a) and surrogate fuel components (b) on a dry basis with $\text{H}_2\text{O}/\text{C} = 2.0$, fuel feed at 3.33 kW thermal, entrance temperature of 425 °C and the GHSV between 21,000 hr^{-1} and 28,000 hr^{-1} .

Reformer efficiency is shown in Fig. 5.13 with the 3-component fuel having the highest peak efficiency of 87% for all surrogates followed by the two-component fuel, JP-8 and the one-component surrogate all at 82% to 83%. Peak efficiencies occur at O/C ratios for peak hydrogen yields for all fuels tested. The 3-component fuel and JP-8 efficiency curves have a very similar shape with peak efficiencies occurring at an O/C of 0.95; and equivalent efficiencies of 70% at an O/C of 0.8 and also equivalent values of 75% at an O/C of 1.15. The operating region resulting in high fuel conversion, minimal olefin production and good efficiency appears to be between an O/C ratio of 0.95 to 1.10 for JP-8. In this operating region the 3-component fuel efficiency curve most closely matches the JP-8 curve with a variance of 4.4 followed by the 2-component fuel at 9.1 and the single component fuel at 13.0.

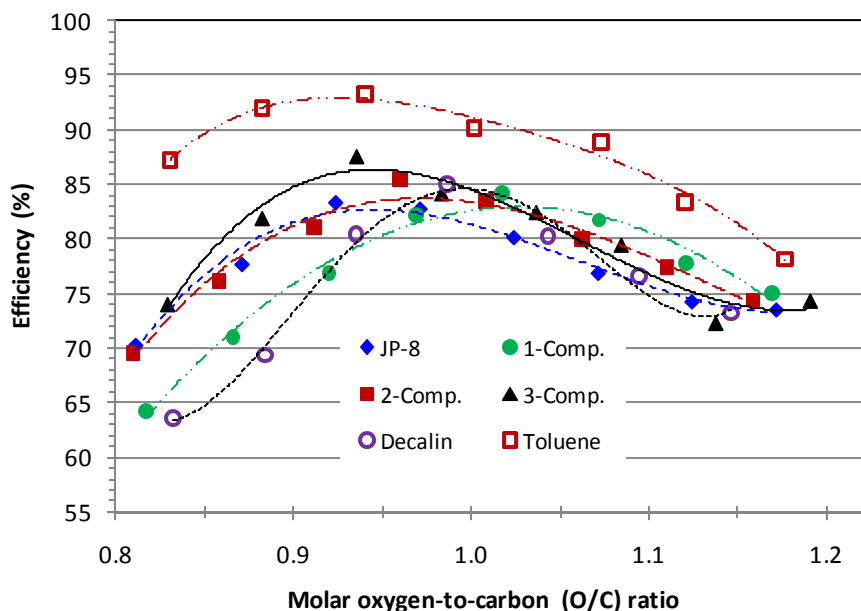


Figure 5.13 Results comparison of reforming efficiency for JP-8 surrogate fuels and low-sulfur JP-8 with $\text{H}_2\text{O}/\text{C} = 2.0$, fuel feed at 3.33 kW thermal, entrance temperature of 425 °C and the GHSV between 21,000 hr^{-1} and 28,000 hr^{-1} .

Overall, reformat composition profiles for the 3-component surrogate fuel and the target JP-8 is shown on a dry basis in Fig. 5.14 under conditions of fuel flow of $3.33 \text{ kW}_{\text{th}}$ and $S/C = 1.75$. Here the 3-component fuel matches very closely to the target fuel over O/C ratios from 0.85 to 1.20.

5.4 Chapter summary

Three fuels were investigated as possible JP-8 surrogate fuels under autothermal reforming conditions using a noble-metal based catalyst. Liquid hydrocarbons n-dodecane, decalin, and toluene were selected as components representing paraffins, cyclo-paraffins and aromatics. The surrogate fuels selected consisted of single, binary and tertiary-component mixtures of n-dodecane, decalin, and toluene in liquid volume

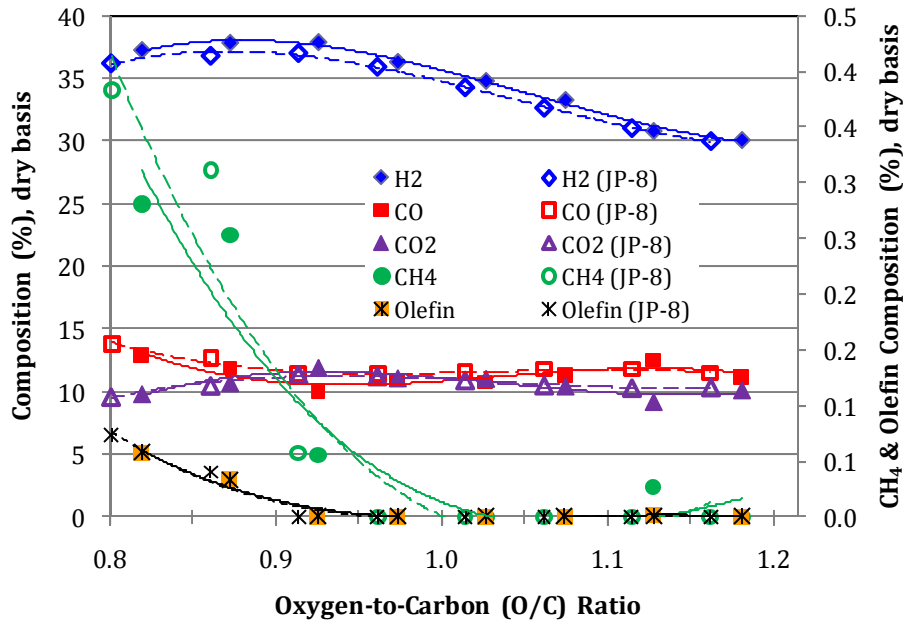


Figure 5.14 Results comparison of reforming efficiency for JP-8 surrogate fuels and low-sulfur JP-8 with $\text{H}_2\text{O}/\text{C} = 2.0$, fuel feed at $3.33 \text{ kW}_{\text{th}}$, entrance temperature of 425°C and the GHSV between $21,000 \text{ hr}^{-1}$ and $28,000 \text{ hr}^{-1}$.

ratios of 10:0:0, 9:1:0 and 7:1:2. As the number of components in the surrogate fuels increased, the surrogate fuel more closely matched the target real fuel in terms of density, hydrogen content, hydrogen to carbon ratio, and lower heating value, but diverged in terms of average molecular weight. An additional benefit with the addition of components to the surrogate fuel was that the fuel cost per liquid volume decreased.

The surrogate fuels were reacted in an autothermal reactor operated under equivalent fuel heating value input of 3.33 kW thermal, steam to carbon ratio of 2.0, and variable oxygen to carbon ratios between 0.8 to 1.20, resulting in gas hourly space velocities between 21,000 hr^{-1} to 27,000 hr^{-1} . Of the surrogates tested the three-component surrogate fuel was found to more closely match the performance of JP-8 in terms of major performance parameters, such as, fuel conversion, hydrogen yield, reactor temperature profile and reforming efficiency. Variation in results among the surrogate fuels were most pronounced at oxygen to carbon ratios below 1.0; with, in general, better correlations to JP-8 observed in the order of three-component, two-component and single-component surrogate.

The conversion of the single component fuel, n-dodecane, proved to be the most difficult requiring higher oxygen to carbon ratios and corresponding higher temperatures to achieve full conversion. Dodecane also resulted in higher production of hydrocarbons and olefins in the reformat stream over all conditions tested. Additions of a small amount of a cycloparafin (decalin at 10% liquid volume) to n-dodecane, resulted in

significant changes in fuel conversion, hydrogen yield, and reformer efficiency. Further, addition of a third component, toluene, resulted in better fuel conversion and higher hydrogen yields.

Results show that that a three-component mixture of n-dodecane, decalin and toluene in the liquid volume ratios of 7:1:2 results in a good approximation to the behavior of JP-8, particularly, in the oxygen to carbon ratio range of 0.95 to 1.10. Results also indicate that a single component surrogate fuel is not representative of JP-8 for reforming applications. Additionally, as is seen with the addition of decalin to n-dodecane, addition of some hydrocarbon components can have a pronounced effect on reforming and, therefore, surrogate fuel selection cannot be based solely on the most prevalent hydrocarbon classes represented in the targeted fuel. Further improvement and understanding of hydrocarbon class effects would likely result from additional work with additional hydrocarbon classes not represented in this study such as iso-parafins, olefins and polyaromatics.

Chapter 6

Experimental Results and Discussion

6.0 Introduction

This chapter addresses three primary areas of experimental work all associated with an adiabatic autothermal reformer operating on low sulfur JP-8 and a surrogate JP-8 fuel¹⁹ under atmospheric reforming conditions. Autothermal reforming of JP-8 with air is first addressed to establish a baseline of performance for comparison. The effects of operating parameters variation such as oxygen-to-carbon (O/C) ratio, steam-to-carbon ratio, and fuel feed rate on reformer operating characteristics and performance are quantified and discussed. The results of enriched oxygen in autothermal reforming is addressed next and contrasted to air autothermal reforming. Unique aspects of enriched oxygen enrichment such as the ability to independently vary space-time, O/C ratio, and S/C ratio are addressed. The final area addressed is an analysis of system level effects from oxygen enrichment.

6.1 Operating procedures and notes

In order to minimize potential deleterious effects from carbon formation, the minimum steam-to-carbon ratio was set at 1.5 and the minimum molar oxygen-to-carbon ratio (O/C) was generally kept at 0.75. These conditions resulted in relatively low ethane and ethylene production (typically < 0.3%), compounds that have been identified as carbon

¹⁹ The surrogate JP-8 fuel consists of three components as follows: 70 vol% n-dodecane, 10 vol% decalin, and 20 vol% toluene.

formation precursors. To avoid the potential of catalyst sintering or damage to the reactor support structure, the maximum operating temperature was limited to 1,100 °C which limited the maximum O/C ratio to approximately 1.2. Over all testing conditions, no change in reactor pressure drop was observed indicating that no significant carbon disposition occurred. In addition, the three component surrogate fuel was periodically tested throughout all experimental runs under consistent conditions²⁰ and no degradation in catalysts performance was noted, indicating that catalysts deactivation due to carbon formation was not a factor in the experimental results. Under all test conditions oxygen conversion was 100%. All experimental values presented are based on the averages of gas chromatograph results taken after steady state conditions were observed at each experimental point. Reformate condensate was collected and visually inspected but not analyzed. In general for fuel flow of 8.85 ml/min.²¹ (5.0 kW_{th} on a lower heating value basis) or below, reformate condensate under conditions of $O/C \geq 1.0$ appeared to consist of water with no visible sign of fuel, but for $O/C \leq 1.0$ a fuel film could be observed indicating incomplete conversion. At fuel flows greater than 8.85 ml/min. (5.0 kW_{th}), higher O/C ratios were needed before oil residue in the condensate was abated. Under conditions where complete fuel conversion is anticipated, $O/C \geq 1.0$ (for fuel flows ≤ 5.0 kW_{th}), the carbon balance was in the range of 96% - 103% which is in agreement with experimental error associated with carbon balance which has an error on the order of $\pm 4\%$.

²⁰ Test conditions were fuel flow of 5.9 ml/min. (3.33 kW_{th}), S/C of 2.0 and variable O/C ratio.

²¹ Fuel flows are often given in terms of thermal capacities based on the lower heating value of the fuel. The thermal capacities tested and their corresponding fuel flows are: 2.5 kW_{th} (4.42 ml/min.), 3.33 kW_{th} (5.9 ml/min.), 5.0 kW_{th} (8.85 ml/min), and 8.33 kW_{th} (14.8 ml/min.).

Fuel flow into the reactor was maintained at equivalent energy flows based on the lower heating value of the fuel. Additionally, the entrance temperature into the reactor for reactants was fixed at $425\text{ }^{\circ}\text{C} \pm 10\text{ }^{\circ}\text{C}$. These experimental controls are typical for this type of experimental work, however, these experimental constraints allow for some variation in enthalpy at the entrance of the reactor which can affect operating temperatures and kinetics.

6.2 Low sulfur JP-8 reforming with air ($\Psi = 1$)

The following sections address JP-8 fuel ATR reforming with air. In general, the section addresses reactor performance responses to changes in operating parameters such as O/C ratio, S/C ratio, and fuel flow rates.

6.2.1 Reactor temperature profile and space velocity (space time)

Thermocouples were inserted into the open channels of the reactor monolith at locations measured from the entrance of 13 mm, 38 mm, 102 mm, 178 mm, 203 mm and 229 mm with additional thermocouple measurements at 305 mm, -152mm and -26 mm. Figure 6.1 shows the reactor's temperature profiles while operating on JP-8 fuel with fuel flow rate of 5.7 ml/min. ($3.33\text{ kW}_{\text{th}}$), S/C = 2.0, inlet temperature controlled to $425\text{ }^{\circ}\text{C} \pm 10\text{ }^{\circ}\text{C}$, and O/C ratio as shown. The temperature profile exhibits a characteristic shape for ATR operation with fast oxidative reactions occurring near the entrance of the reactor followed by a steady drop in temperature as endothermic steam reforming reactions begin to

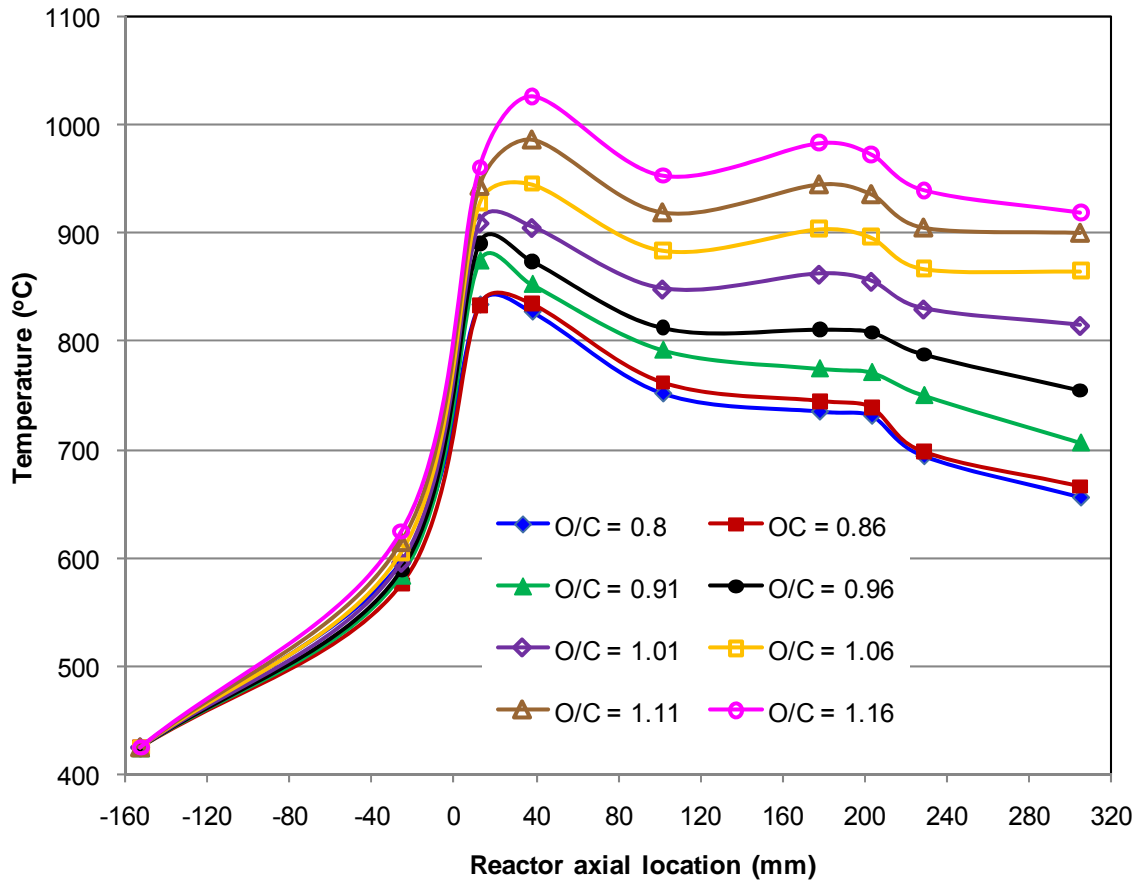
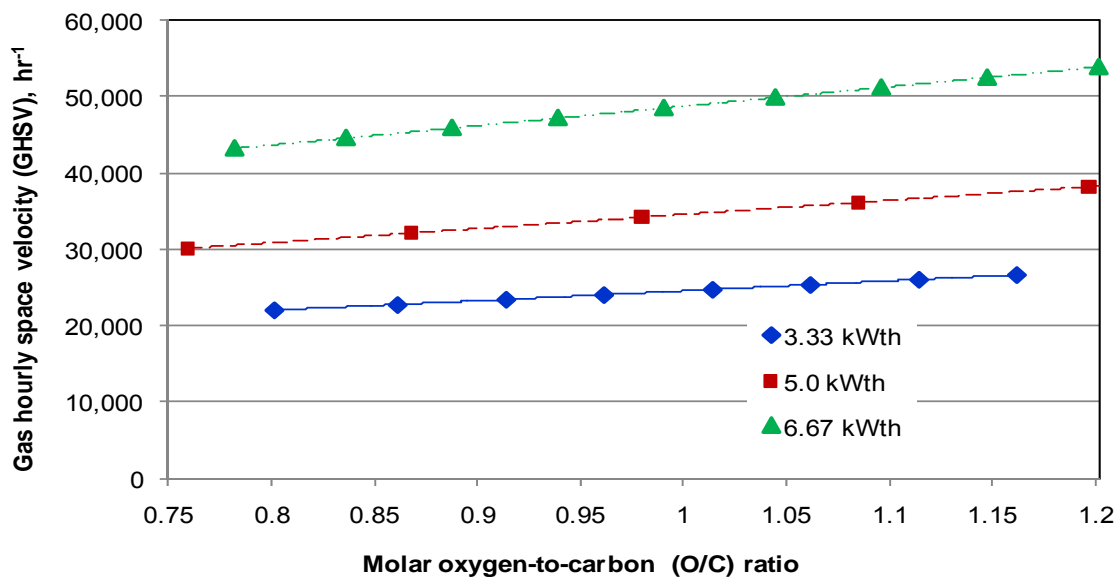


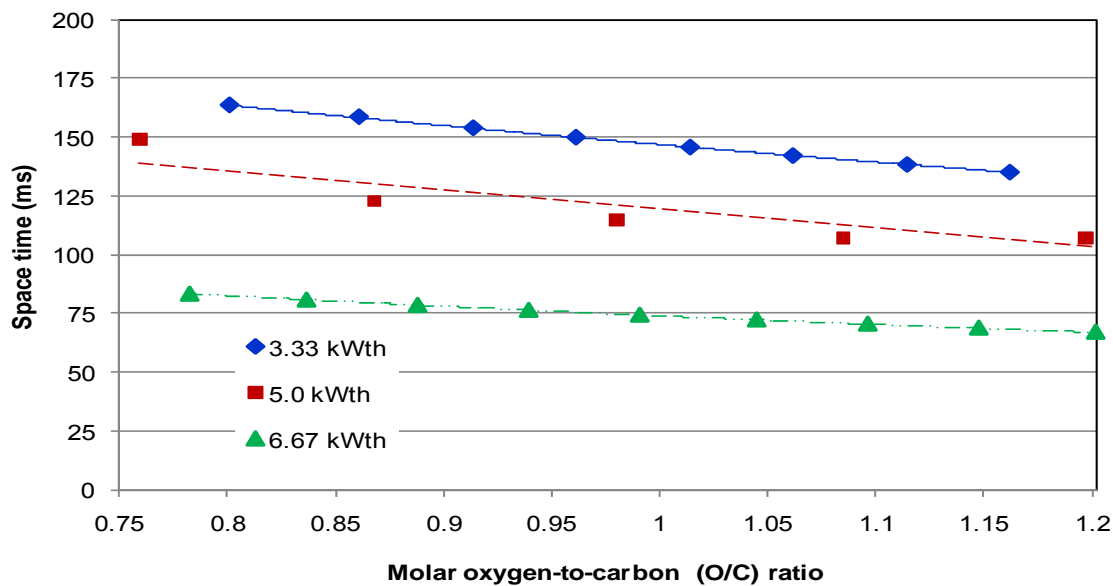
Figure 6.1 Reactor temperature profile at selected thermocouple locations under conditions of JP-8 fuel at fuel flow = 5.9 ml/min. ($3.33 \text{ kW}_{\text{th}}$), S/C = 2.0, enrichment number (Ψ) of 1.0 (air), and O/C ratio's as shown.

dominate towards the back end of the reactor. Also, evident from Fig. 6.1 is that the overall reactor temperature increases with increasing O/C ratio (theoretical O/C for complete oxidation is 2.963, assuming an average fuel composition of $\text{C}_{12.2}\text{H}_{23.5}$).

Increased O/C ratio also results in increased reactant flow and gas-hourly-space-velocity (or conversely, a decrease in space time) as shown in Fig. 6.2. A consequence of higher average volume flow into the reactor is that reforming reactions will reach completion



(a)



(b)

Figure 6.2 Gas Hourly Space Velocity (GHSV) (a) and Space Time (b) for JP-8 at fuel feeds of 5.9 ml/min (3.33 kWth), 8.85 ml/min. (5.0 kWth), and 11.8 ml/min. (6.67 kWth) at $S/C = 2.0$, variable O/C ratios, GHSV between $20,500 \text{ hr}^{-1}$ and $26,000 \text{ hr}^{-1}$, and enrichment number (Ψ) of 1.0 (air).

further down the reactor. This can be seen in Fig. 6.1 where the peak temperature resulting from oxidative reactions shifts from thermocouple position at 13 mm to the 38 mm position with increasing O/C ratio. This shift in reaction zone within the reactor can also be seen in Fig. 6.3, where a single operating condition ($O/C = 1.05$ and $S/C = 2.0$) is maintained while the fuel feed is changed. Here the effects of increased reactor flow shifts the peak reactor temperature further towards the exit of the reactor as the fuel flow is increased.

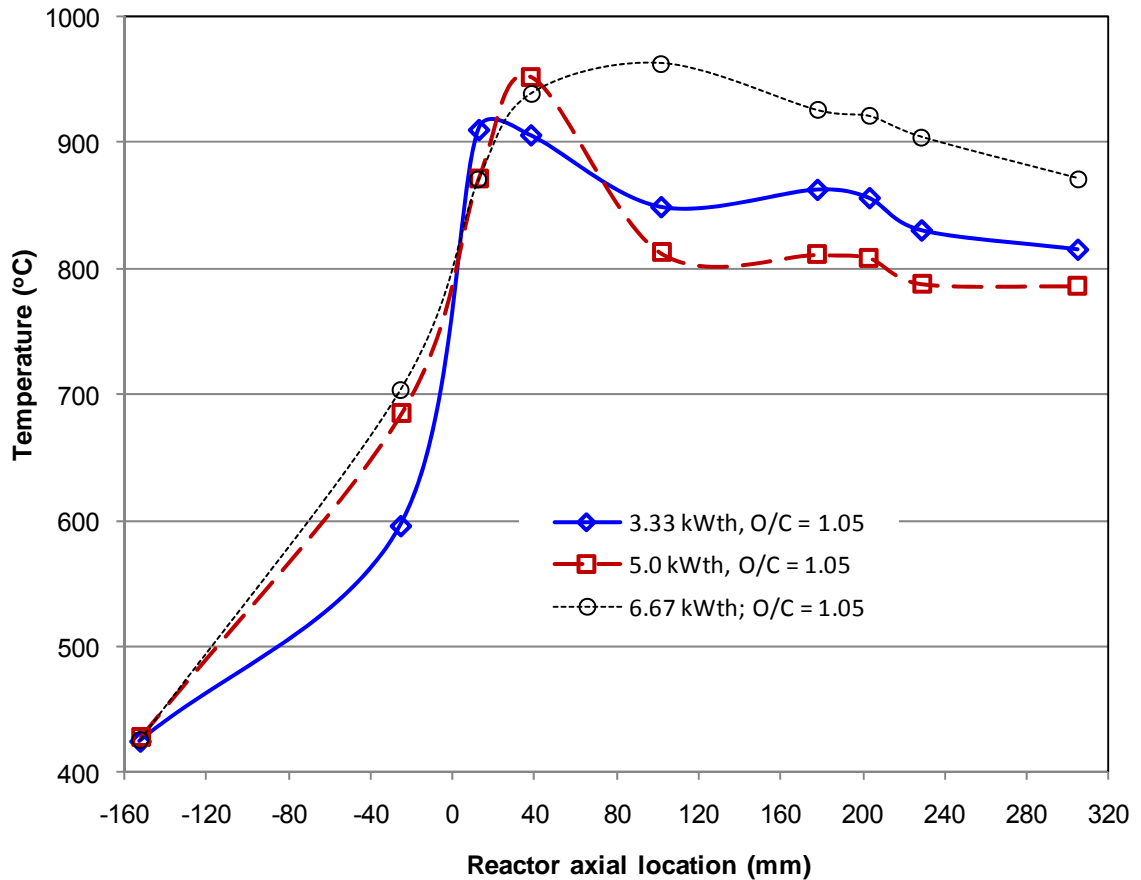


Figure 6.3 Reactor temperature profiles at JP-8 fuel feeds of 5.9 ml/min (3.33 kWth), 8.85 ml/min. (5.0 kWth), and 11.8 ml/min. (6.67 kWth) at $S/C = 2.0$, $O/C = 1.05$, GHSV between $20,500 \text{ hr}^{-1}$ and $26,000 \text{ hr}^{-1}$, and enrichment number (Ψ) of 1.0 (air).

Also of interest in Fig. 6.1, is that at the 102 mm thermocouple position the reactor temperature appears to be a strong function of O/C ratio. For O/C ratios greater than 1.0, the temperature at position 102 mm is lower than the temperature at position 178. At an O/C of 0.96 the temperatures at thermocouple position 102 mm and 178 mm are nearly identical, and below an O/C ratio of 0.96, the temperature at thermocouple position 102 mm is greater than at thermocouple position 178 mm. Because of the error associated with thermocouples (0.4%, ~ 3.4 °C) the absolute values between thermocouples could be misleading, however the relative value of a given thermocouple (or between thermocouples) under varying operating conditions is meaningful to discuss. The large drop in temperature following the oxidative exotherm at thermocouple position at 38 mm indicates that endothermic reactions are very active. Likely endothermic reactions at this location are steam reforming and pyrolysis reactions. Higher reactor temperatures would multiply these endothermic reactions and could explain the more pronounced temperature dip seen at higher O/C ratios. Similar work performed by Voecks and Flytzani-Stephanopoulos [154] with ATR of n-tetradecane, n-hexane, benzene and naphthalene showed that the shape of the temperature profile is strongly determined by the hydrocarbon constituents in the fuel. Voecks *et al.* noted that aromatics resulted in high peak temperatures during oxidation followed by rapid cooling from steam reforming, aliphatics exhibited cooler oxidation temperatures as a result of endothermic fuel pyrolysis to olefins and then a gradual temperature drop down the reactor as olefins were steam reformed.

Figure 6.3 provides some insight into the effects of increasing fuel flow. As space velocities are increased through higher fuel flow rates the reactor temperature profiles give an indication of the optimum operating condition. In short, for a reactor under conditions of full fuel conversion (an O/C ratio of 1.05 achieves full fuel conversion for the fuel flows given) the operating condition resulting in the largest temperature difference between maximum temperature and exit temperature will usually produce optimum performance. This condition indicates that sufficient heat and temperature is being generated via oxidation to support endothermic steam reforming, that heat is being effectively transported from exothermic reaction zones to endothermic reaction zones, and that sufficient residence time for reactants is available to support preferred reactions. Looking at the fuel flow of 3.33 kW_{th} in Fig. 6.3, there is a noticeable peak temperature at 18 mm followed by a temperature drop at 102 mm indicating that there is a close coupling of needed exothermic and endothermic reactions. Fuel flows at 5.0 kW_{th} show a similar temperature profile as the 3.33 kW_{th} curve, but both higher peak temperatures (shift downstream to thermocouple position at 38 mm) and lower exit temperatures are achieved indicating a better operating condition has been achieved. Also, the slope of the temperature profile between thermocouple position at 38 mm and 102 mm is steeper for 5.0 kW_{th} in comparison to 3.33 kW_{th}, indicating that relative to flow, more endothermic reactions are occurring. The curve for 6.67 kW_{th} shows a high peak temperature but a gradual temperature decline and small temperature difference between peak and exit temperatures. This temperature profile (6.67 kW_{th}) indicating that endothermic reactions are not occurring at a rate high enough to offset exothermic reactions and heat transfer.

This may be indicative of insufficient residence time for endothermic reactions to go to completion. More detailed discussion on determining optimum fuel flow rating will be discussed in later sections.

6.2.2 JP-8 reformat composition

A representative plots of the ATR reformat stream products under conditions of 5.9 ml/min. JP-8 surrogate fuel (3.33 kW_{th}), S/C of 2.0, reactor inlet temperature of 425 °C ±10 °C, and gas hourly space velocities between 20,500 hr⁻¹ and 26,000 hr⁻¹ is shown in Fig. 6.4 and Fig. 6.5. Full fuel conversion was achieved at an O/C ratio of approximately 1.05 and good hydrogen concentrations were obtained with a peak concentration of 34.5 % at and O/C ratio of 0.97. These results are also in close agreement with other [190, 290, 291] published results. In order to ensure durability of reactor catalysts by avoiding carbon formation, the olefin concentration (olefins are precursors for carbon formation) must be very low ($\sim \leq 0.03\%$) and all hydrocarbons should be kept low ($\sim \leq 0.1\%$). Figure 6.5 shows that olefin concentration is reduced to zero at an O/C ratio of 1.03 and hydrocarbons (represented by methane) are at 0.1% concentration or less at O/C ratios of approximately 1.04 and above. Based on the results from Fig.'s 6.4 and 6.5 the preferred operating O/C ratio is 1.05 which ensures complete fuel conversion, good hydrogen concentration of approximately 33%, no olefin components, and low hydrocarbon species. Looking at Fig. 6.6 the maximum temperature under these conditions is approximately 930 °C; in general, lower reactor

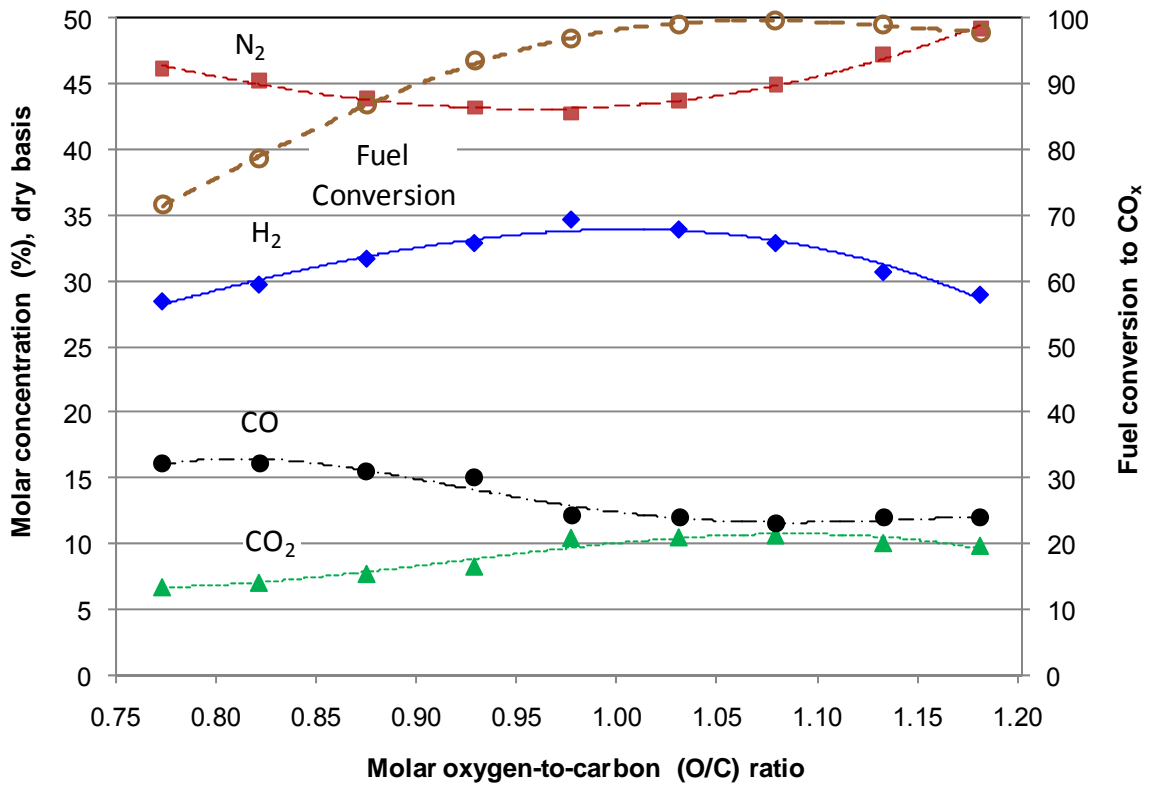


Figure 6.4 Molar concentrations of reformate products N₂, H₂, CO₂, CO and CH₄ with JP-8 fuel feed of 5.9 ml/min. (3.33 kW_{th}), S/C = 2.0, reactor entrance temperature 425 °C ± 25 °C, GHSV between 20,500 hr⁻¹ and 26,000 hr⁻¹, and enrichment number (Ψ) of 1.0 (air).

operating temperatures result in better catalysts durability and prolonged operation at temperatures above 1000 °C are associated with more rapid catalysts degradation.

6.2.3 Nitrogen dilution in reformate product

From Fig. 6.4 it can be seen that nitrogen is the largest constituent of the reformate product stream, representing 40 to 50 percent of the reformate product stream. With catalyzed reforming, where reactor temperatures are low and well controlled (in comparison to combustion), nitrogen does not oxidize or participate in reforming

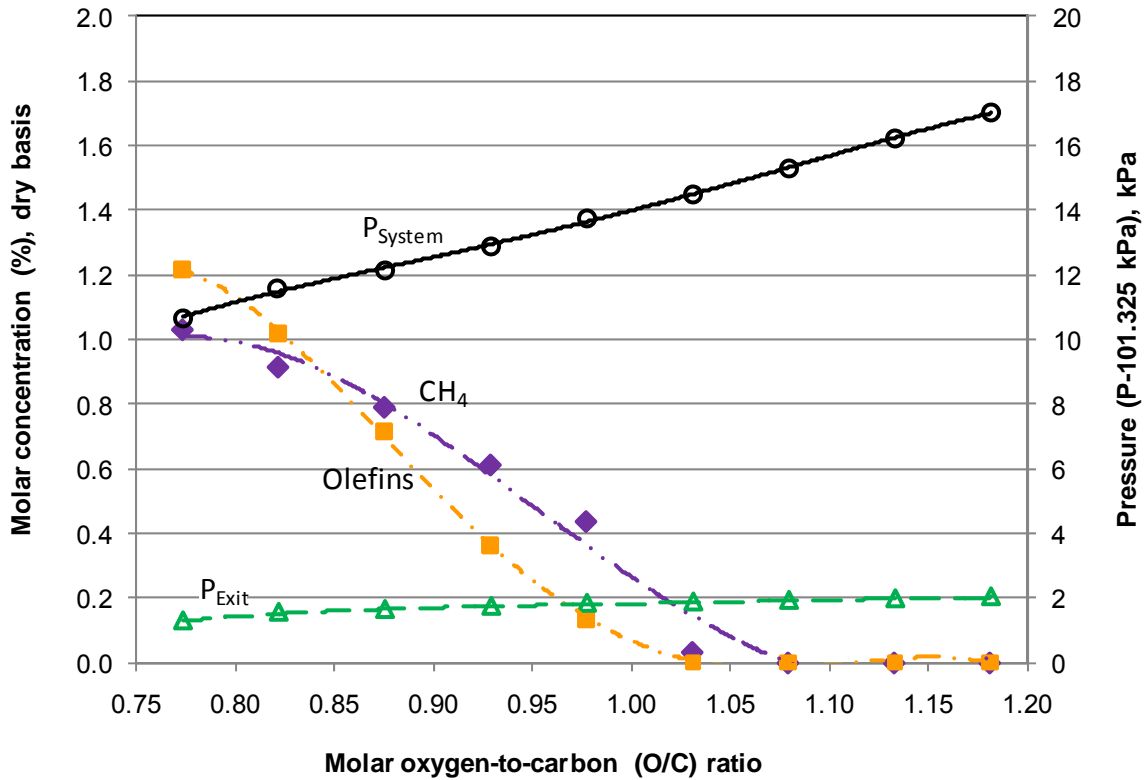


Figure 6.5 Molar concentrations of reformate products of CH_4 and Olefins, and reactor pressures with JP-8 fuel feed of 5.9 ml/min. (3.33 kW_{th}), $S/C = 2.0$, reactor entrance temperature $425 \text{ }^\circ\text{C} \pm 25 \text{ }^\circ\text{C}$, GHSV between $20,500 \text{ hr}^{-1}$ and $26,000 \text{ hr}^{-1}$, and enrichment number (Ψ) of 1.0 (air).

reactions. Therefore, nitrogen is present only as a constituent of air and beyond acting as a heat transfer medium provides little benefit to the reforming process, but does negatively impact reformer size, parasitic pumping power, may interfere with reforming reactions, and dilutes the reformate product stream resulting in negative performance impacts on the fuel cell stack.

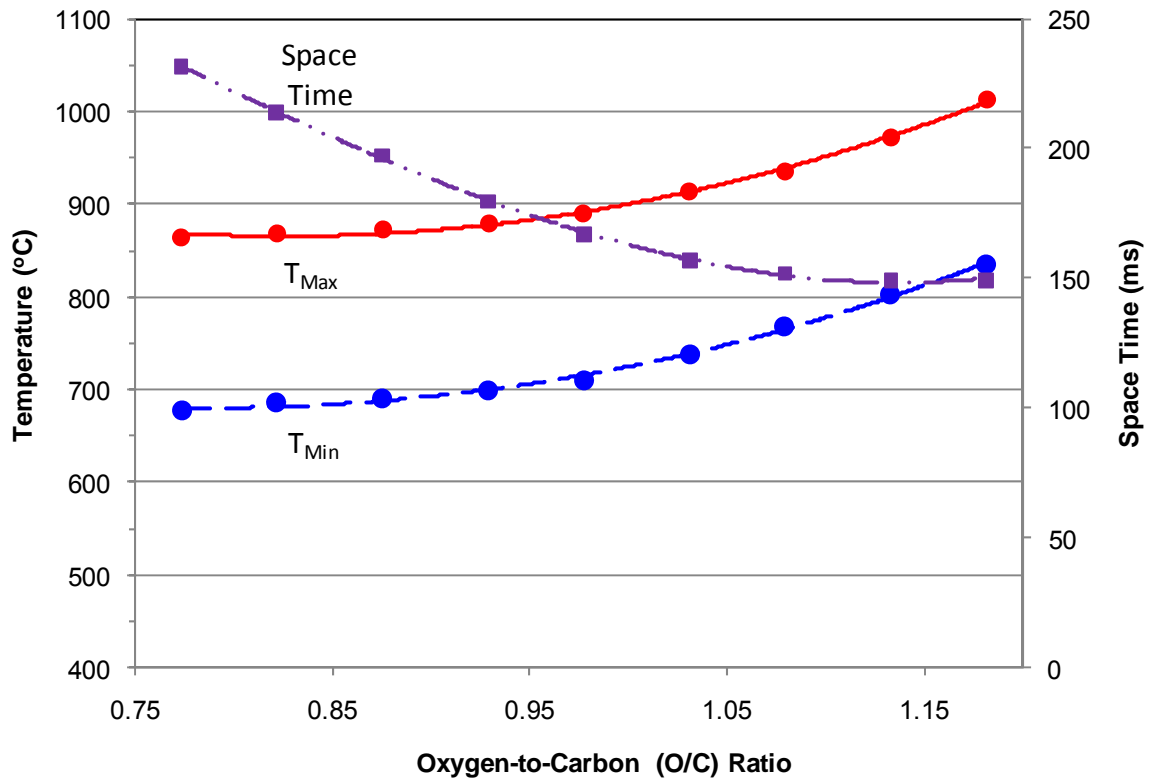


Figure 6.6 Maximum and minimum reactor temperatures, and gas hourly space velocity with JP-8 fuel feed of 5.9 ml/min. (3.33 kW_{th}), $S/C = 2.0$, reactor entrance temperature $425^\circ\text{C} \pm 25^\circ\text{C}$ and enrichment number (Ψ) of 1.0 (air)

6.2.4 Reformer efficiency and product yields for reformed JP-8

Although, reformat composition provides a convenient means of assessing the reactor operating characteristics and determining best reactor operating conditions, it does not give a clear indication of the efficiency of the reformer or provide a measure of the reactor's ability to produce hydrogen and carbon monoxide. Figure 6.7 shows the relationship between product yields of hydrogen and carbon monoxide, efficiency and fuel conversion. Peak reformer efficiency is nearly coincident with peak hydrogen yield and, therefore, hydrogen yield is a very good measure of the performance of a reformer.

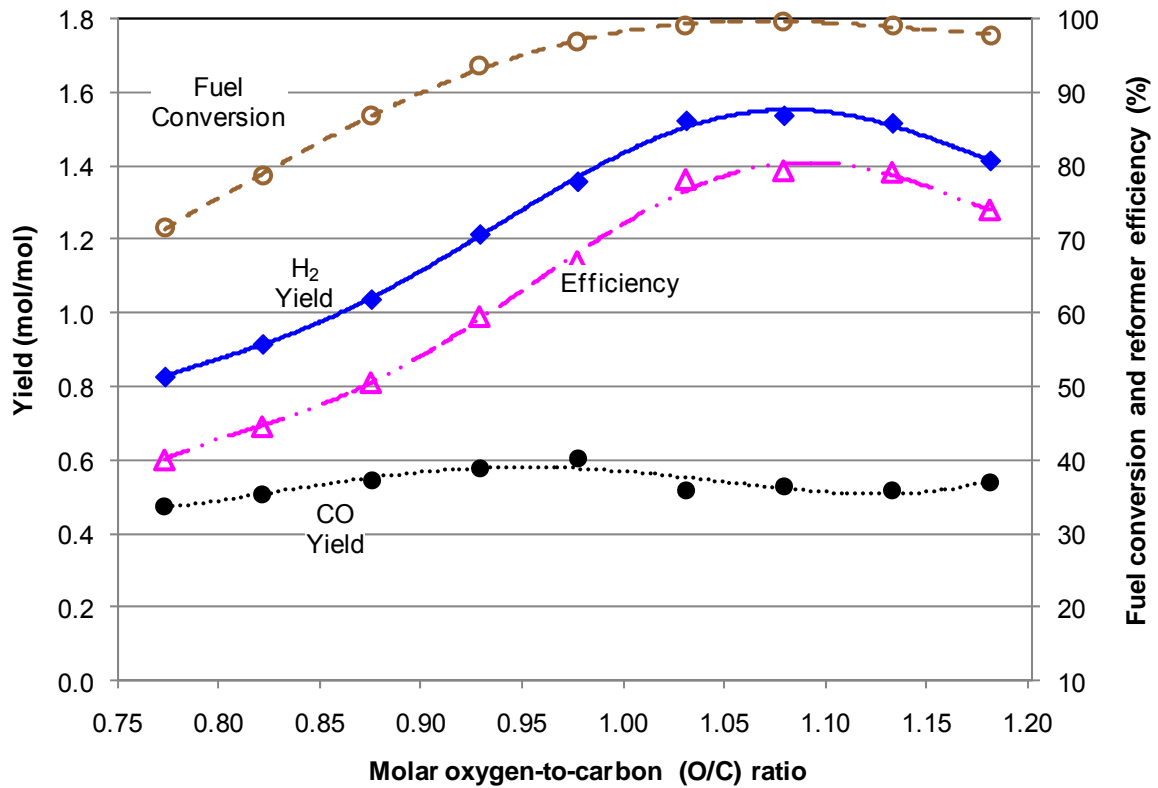


Figure 6.7 Relationship between reformer efficiency, fuel conversion, hydrogen yield and carbon monoxide yield with JP-8 fuel feed of 5.9 ml/min. ($3.33 \text{ kW}_{\text{th}}$), $S/C = 2.0$, reactor entrance temperature $425 \text{ }^{\circ}\text{C} \pm 25 \text{ }^{\circ}\text{C}$, GHSV between $20,500 \text{ hr}^{-1}$ and $26,000 \text{ hr}^{-1}$ and enrichment number (Ψ) of 1.0 (air).

Carbon monoxide yield generally peaks prior to hydrogen yield, but usually stays within a narrow range; here the carbon monoxide yield peaks at 0.6 mol/mol at an O/C ratio of 0.98. The peak values for hydrogen yield and efficiency occur just after full fuel conversion is achieved.

The shape of the carbon monoxide yield curve in Fig. 6.7 may provide some insight the impact that the water-gas-shift (WGS) reaction has on reforming. The water-gas-shift equation was given in Eqn. 2.18 and is provided below:



The forward reaction is favored at lower temperatures. At low O/C ratios from 0.75 to 0.98 the carbon monoxide yield increases along with fuel conversion, however, the rate of increase is less than fuel conversion due to excess water favoring the forward direction towards conversion to carbon dioxide. At O/C ratios between 0.98 and 1.12, carbon monoxide yield goes down which is likely due to more rapid kinetics resulting in increased production of hydrogen (forward reaction direction) and increased temperature (forward WGS reaction is moderately exothermic). At O/C ratios greater than 1.12 the carbon monoxide yield rises as oxidative reactions increase. In this region (O/C > 1.12) the reformer's temperature is rising quickly which favors the reverse WGS reaction (Eqn. 6-1) producing increasing amounts of carbon monoxide.

6.3 JP-8 fuel reforming with varying S/C ratios $\Psi = 1$

The ATR was operated at 5.9 ml/min. JP-8 (3.33 kW_{th}) and at varying steam to carbon ratio's corresponding to water flows of 9.03 ml/min. (S/C = 1.5), 12.04 ml/min. (S/C = 2.0), 15.05 ml/min. (S/C = 2.5), and 18.06 ml/min. (S/C = 3.0). The purposes of these experiments were to assess the impact of S/C ratio on reactor performance and the likelihood of long term catalysts durability. Additionally, minimizing water consumption and the need to import water into a fuel cell power unit has been recognized as a

desirable attribute for commercial and military applications [292,293]. Therefore, operation at the lowest S/C ratio that is practical will be a selection criterion.

6.3.1 Fuel conversion, operating temperatures, and GHSV under varying S/C ratios

Figure 6.8 displays the fuel conversion as a function of S/C ratio and shows that at all four S/C ratios full fuel conversion was achieved. The S/C ratio does appear to have some effect on fuel conversion with higher S/C ratio's resulting in better conversion (i.e. reaching full conversion at lower O/C ratio's), but the variation among the four

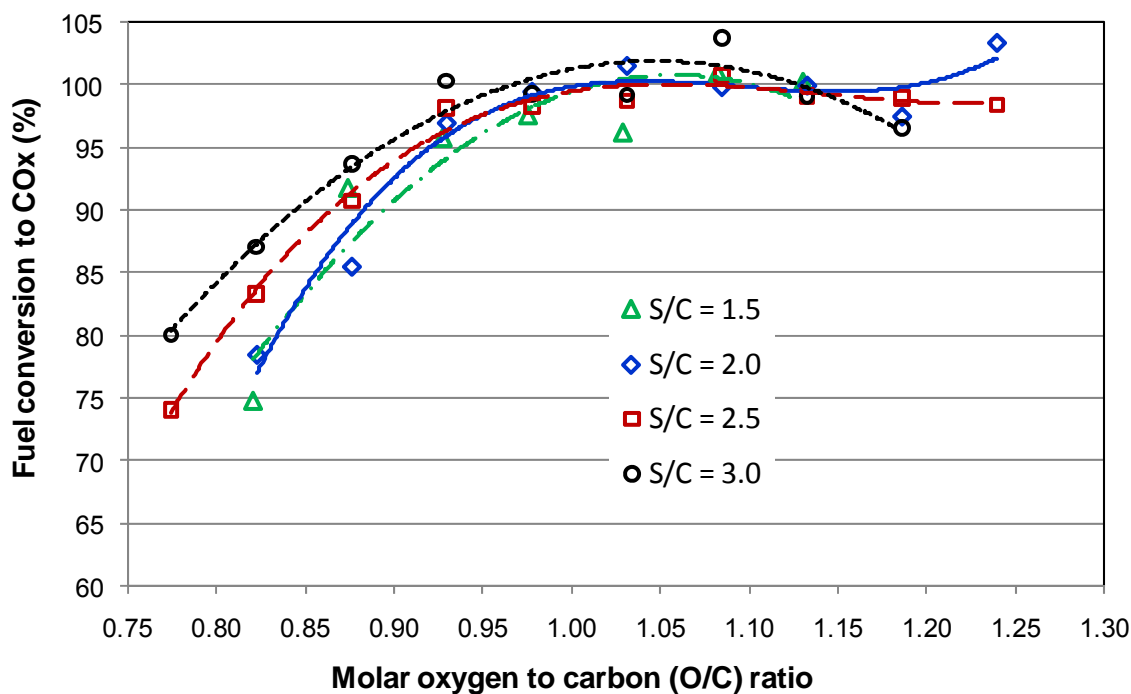


Figure 6.8 Normalized fuel conversion for JP-8 fuel flows of 5.9 ml/min. and S/C ratios of 1.5, 2.0, 2.5, and 3.0; reactor entrance temperature $425\text{ }^{\circ}\text{C} \pm 25\text{ }^{\circ}\text{C}$, and enrichment number (Ψ) of 1.0 (air). The GHSV for S/C = 1.5 was from $19,200\text{ hr}^{-1}$ to $23,200\text{ hr}^{-1}$, for S/C = 2.0 was from $21,900\text{ hr}^{-1}$ to $27,300\text{ hr}^{-1}$, for S/C = 2.5 was from $24,000\text{ hr}^{-1}$ to $30,000\text{ hr}^{-1}$, and for S/C = 3.0 was from $26,700\text{ hr}^{-1}$ to $32,000\text{ hr}^{-1}$.

experiments is not very significant considering that experimental error can account for approximately $\pm 3.7\%$ error in the readings. Variation in reactor operating temperature is shown in Fig. 6.9a where both the maximum temperatures and exit temperature are inversely related to S/C ratio. Figure 6.9b shows reactor temperature profiles taken with an O/C ratio of 1.05; where the higher reactor temperature bias shown in Fig. 6.9a for lower S/C ratios can be seen throughout the reactor. For all S/C ratio's tested, the maximum and exit reactor operating temperatures are closely grouped within approximately $\pm 25^\circ\text{C}$. Therefore increasing the concentration of water in the reactor does appear to favor endothermic steam reforming reactions. Figure 6.10 displays the amount of water consumed in the reactor which is determined analytically from Eqn. 6-2 below:

$$(H_2O)_{\text{consumed}} = H_{2,\text{reformat}} + \left(\sum C_n H_m \cdot \frac{m}{2} \right)_{\text{reformat}} - H_{2,\text{fuel}} \cdot \text{Fuel Conversion} \quad 6-2$$

where $(H_2O)_{\text{consumed}}$, $H_{2,\text{reformat}}$, $H_{2,\text{fuel}}$ are the molar flow rates of steam consumed, hydrogen in the reformat stream, and hydrogen present in the fuel respectively. The term "Fuel Conversion" is the fraction amount of fuel that is converted for a given operating condition. Equation 6-2 is a hydrogen balance on the reformer where unaccounted hydrogen is assumed to be water. From Fig. 6.10 water consumption within the reactor is directly related to the concentration of water input into the reactor. Additionally, it is clear that under all tested conditions excess water is available in the

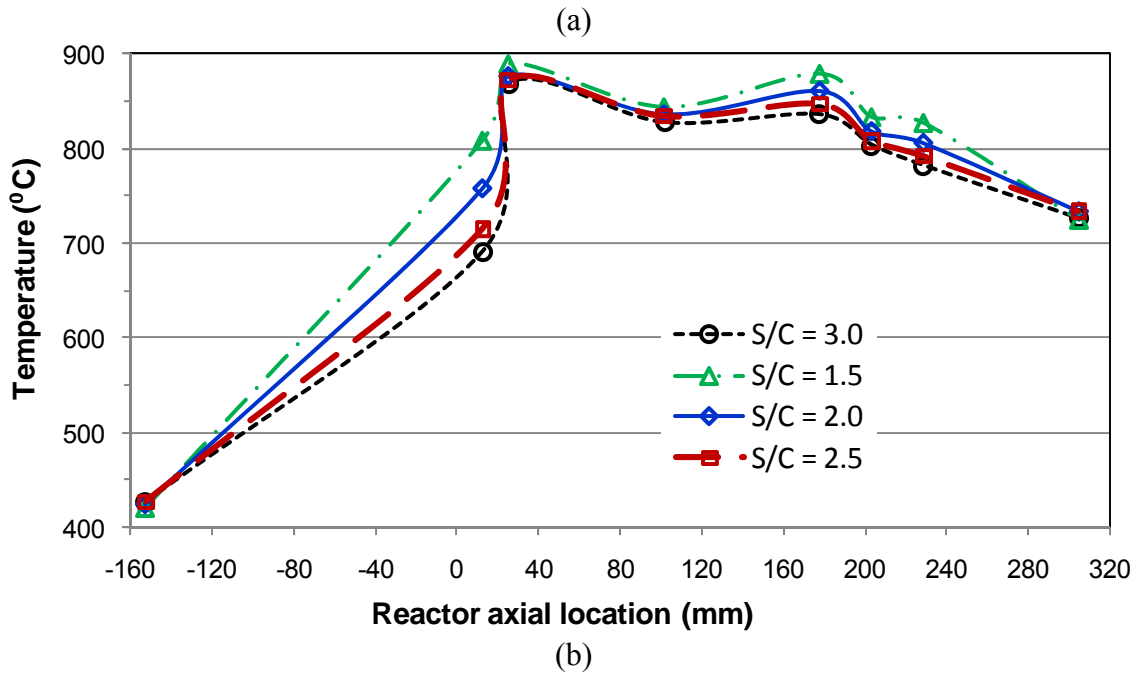
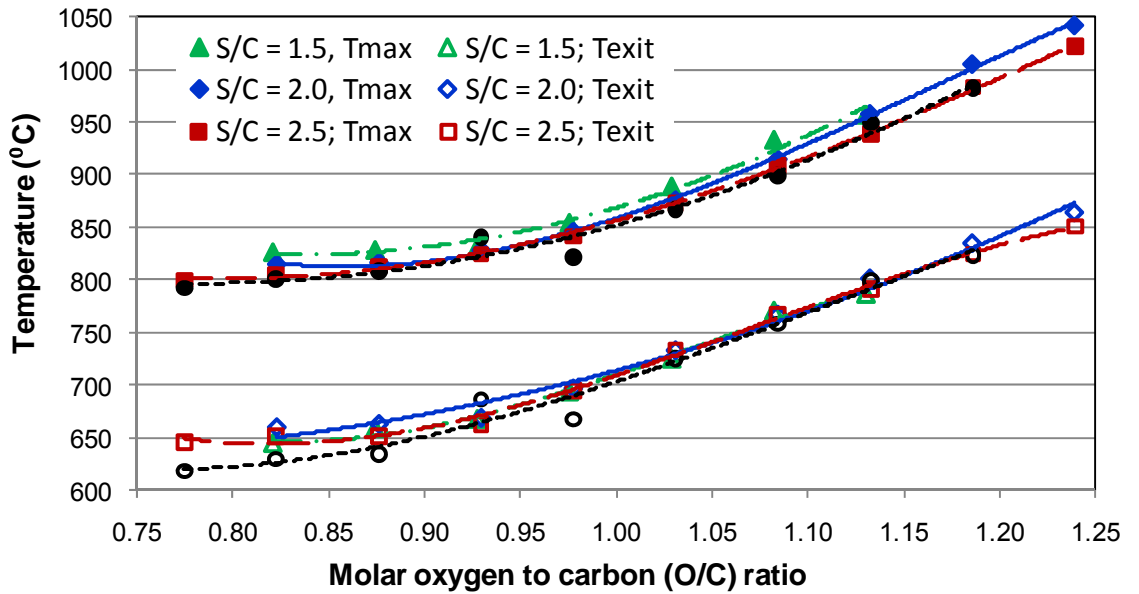


Figure 6.9 Reactor maximum and exit temperatures (a) and reactor temperature profiles at O/C = 1.05 (b) with JP-8 fuel flows of 5.9 ml/min. and S/C ratios of 1.5, 2.0, 2.5, and 3.0; reactor entrance temperature $425^{\circ}\text{C} \pm 25^{\circ}\text{C}$, and enrichment number (Ψ) of 1.0 (air). The GHSV for $S/C = 1.5$ was from $19,200\text{ hr}^{-1}$ to $23,200\text{ hr}^{-1}$, for $S/C = 2.0$ was from $21,900\text{ hr}^{-1}$ to $27,300\text{ hr}^{-1}$, for $S/C = 2.5$ was from $24,000\text{ hr}^{-1}$ to $30,000\text{ hr}^{-1}$, and for $S/C = 3.0$ was from $26,700\text{ hr}^{-1}$ to $32,000\text{ hr}^{-1}$. Temperature profiles measurements are with the reactor entrance being 0.0 mm.

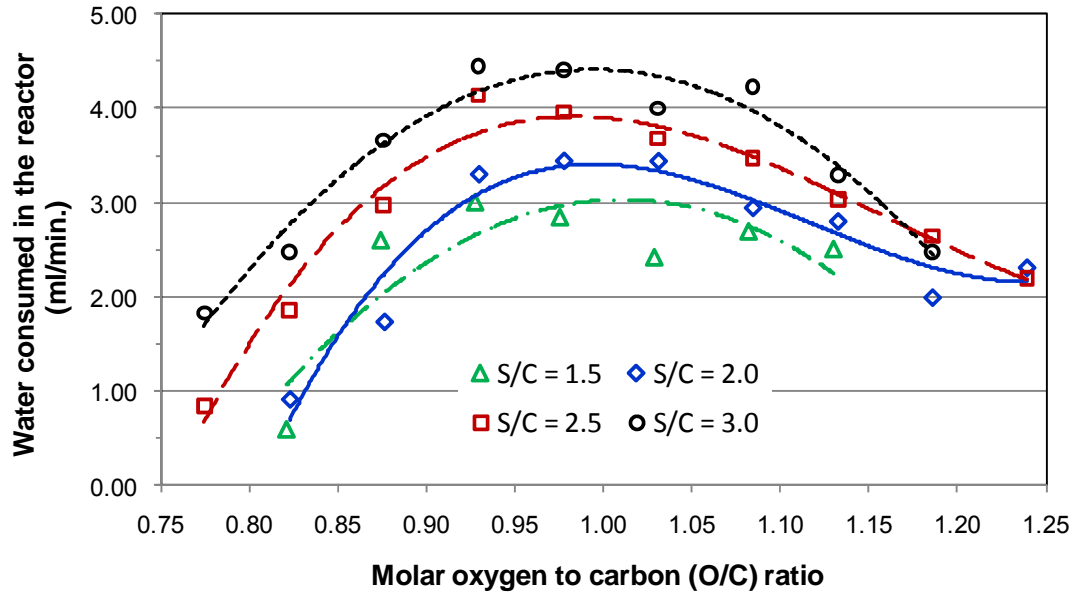


Figure 6.10 Input water consumed in the reactor with JP-8 fuel flows of 5.9 ml/min. and S/C ratios of 1.5, 2.0, 2.5, and 3.0; reactor entrance temperature $425^{\circ}\text{C} \pm 25^{\circ}\text{C}$, and enrichment number (Ψ) of 1.0 (air). The GHSV for S/C = 1.5 was from $19,200\text{ hr}^{-1}$ to $23,200\text{ hr}^{-1}$, for S/C = 2.0 was from $21,900\text{ hr}^{-1}$ to $27,300\text{ hr}^{-1}$, for S/C = 2.5 was from $24,000\text{ hr}^{-1}$ to $30,000\text{ hr}^{-1}$, and for S/C = 3.0 was from $26,700\text{ hr}^{-1}$ to $32,000\text{ hr}^{-1}$.

reactor. Since water consumption is associated with endothermic steam reforming reactions, the results of Fig. 6.10 and the conclusions drawn from the reactor temperatures in Fig. 6.9 are consistent. Also, as a consequent of introducing more water into the reformer the space velocity shown in Fig. 6.11 increases. The increase in space velocity does not appear to have a negative impact on the reformer operation, but as will be seen in later sections, the reformer is capable of operating at higher space velocities (i.e. the S/C variation experiments at $3.33\text{ kW}_{\text{th}}$ is well within the capability of this reactor).

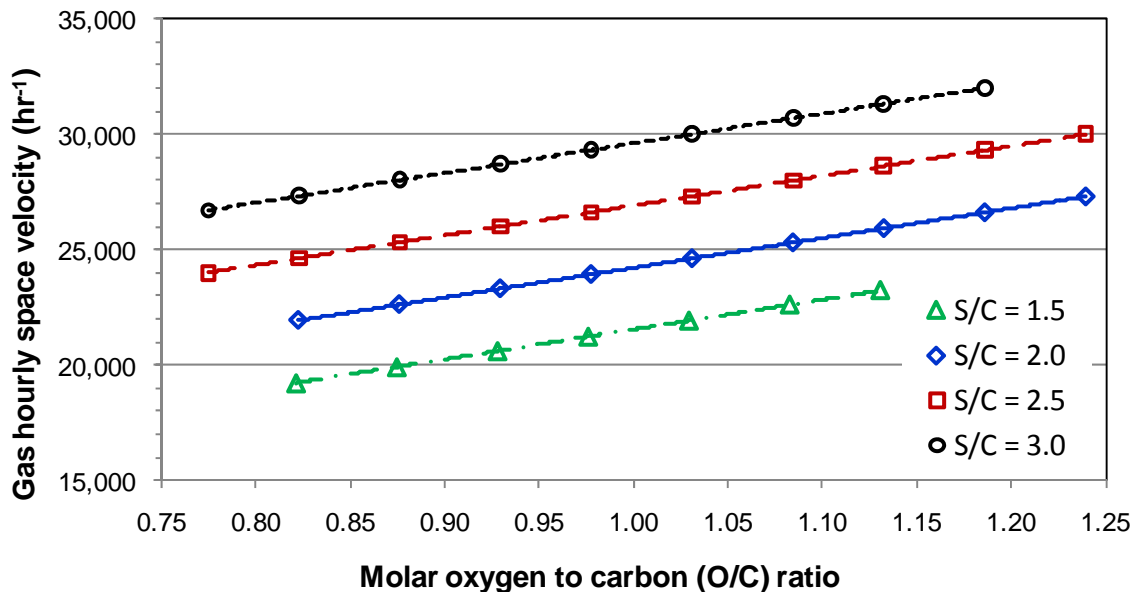


Figure 6.11 Gas hourly space velocity (GHSV) for JP-8 with flows of 5.9 ml/min. and S/C ratios of 1.5, 2.0, 2.5, and 3.0; reactor entrance temperature $425\text{ }^{\circ}\text{C} \pm 25\text{ }^{\circ}\text{C}$, and enrichment number (Ψ) of 1.0 (air).

6.3.2 Hydrogen and carbon monoxide yields under varying S/C ratios

The hydrogen and carbon monoxide yields are shown in Fig. 6.12. As would be expected, as the S/C ratio is increased, higher hydrogen yields and lower carbon monoxide yields are obtained. Also, at O/C ratio's above 1.15 (higher temperatures) the influence of S/C ratio diminishes. The reason for the convergence of hydrogen yield curves at high O/C ratio's is that although rising S/C ratio's increases hydrogen production, rising reactor operating temperatures biases the WGS equation (Eqn. 6-1) towards consumption of hydrogen and generation of carbon monoxide (as can be seen in Fig. 6.12b at $\text{O/C} > 1.15$). Similar results have been reported by Dreyer *et al* [190] when studying n-decane, n-hexadecane and JP-8, and also by Borup *et al.* [294] when conducting ATR experiments with gasoline and diesel.

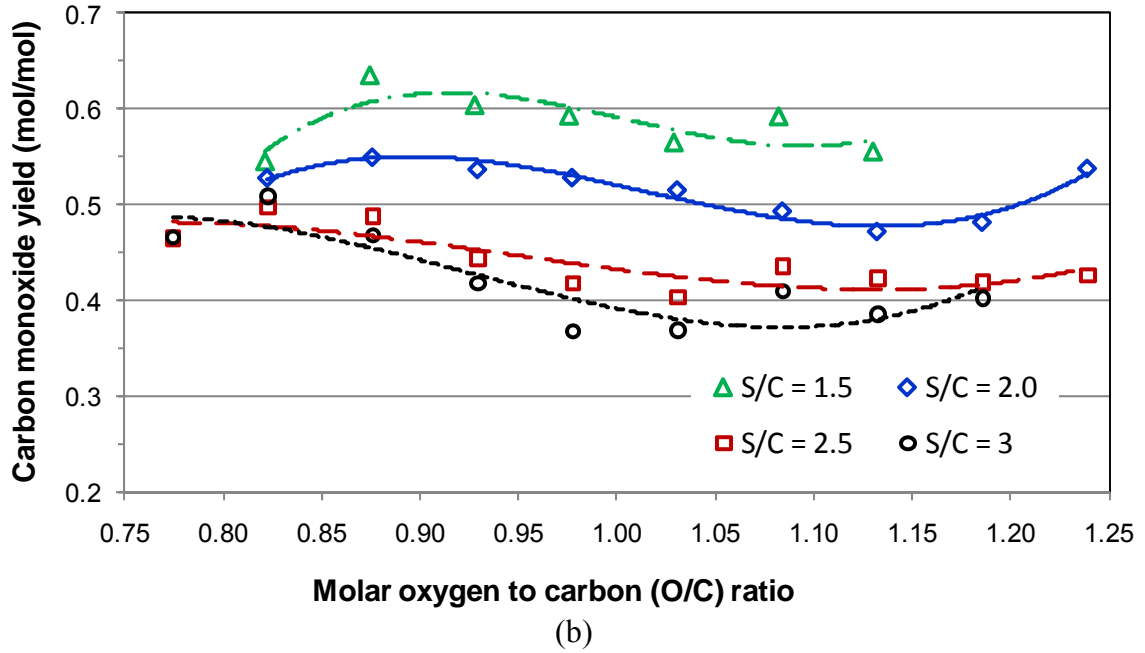
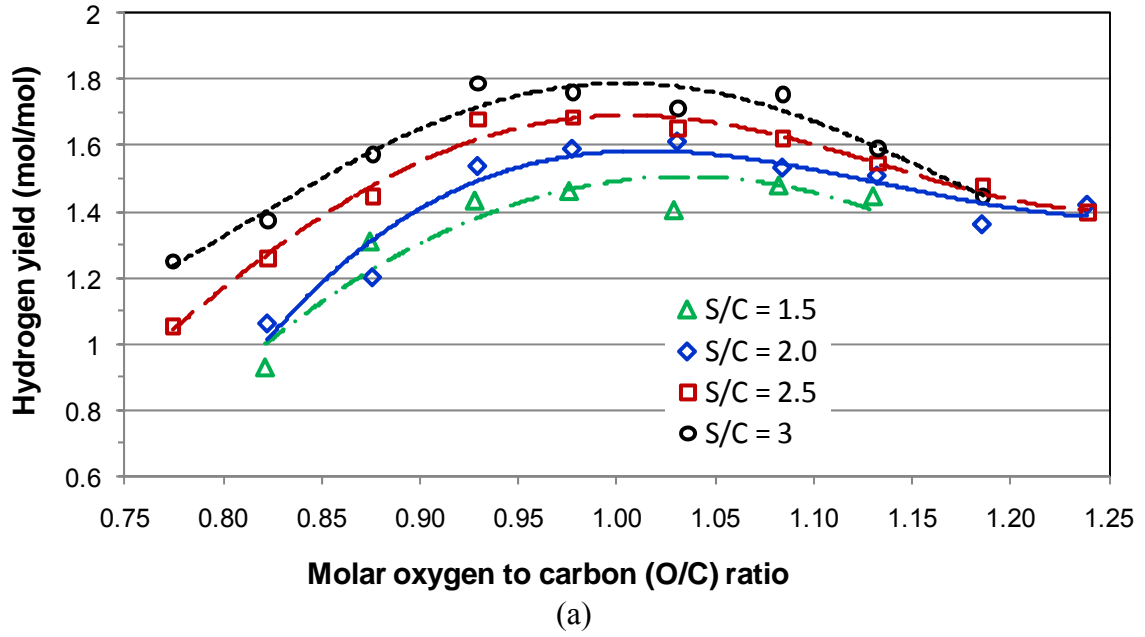
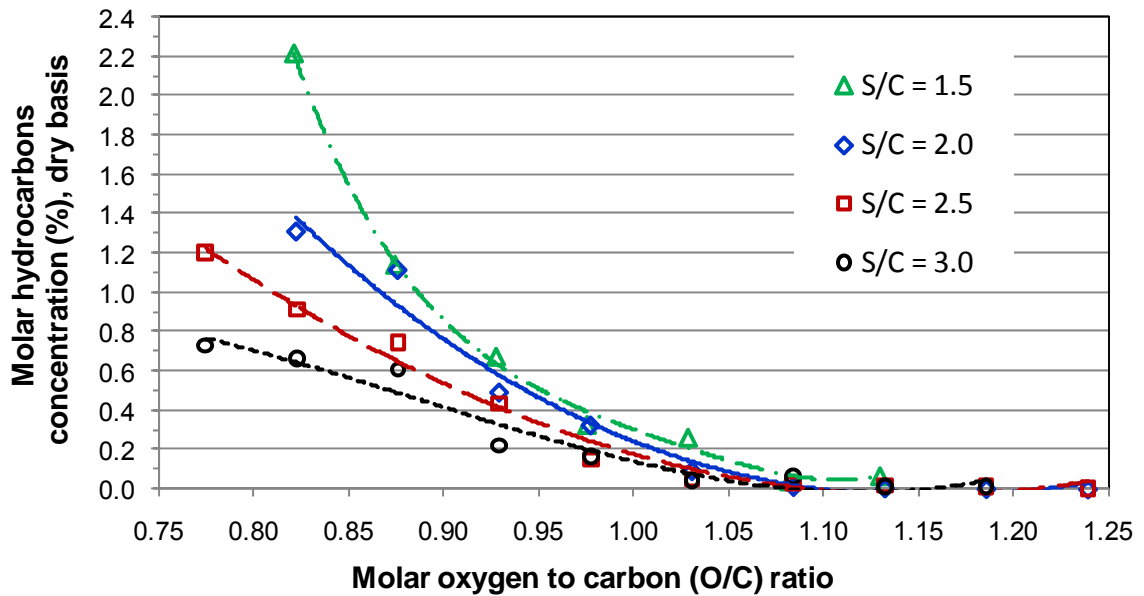


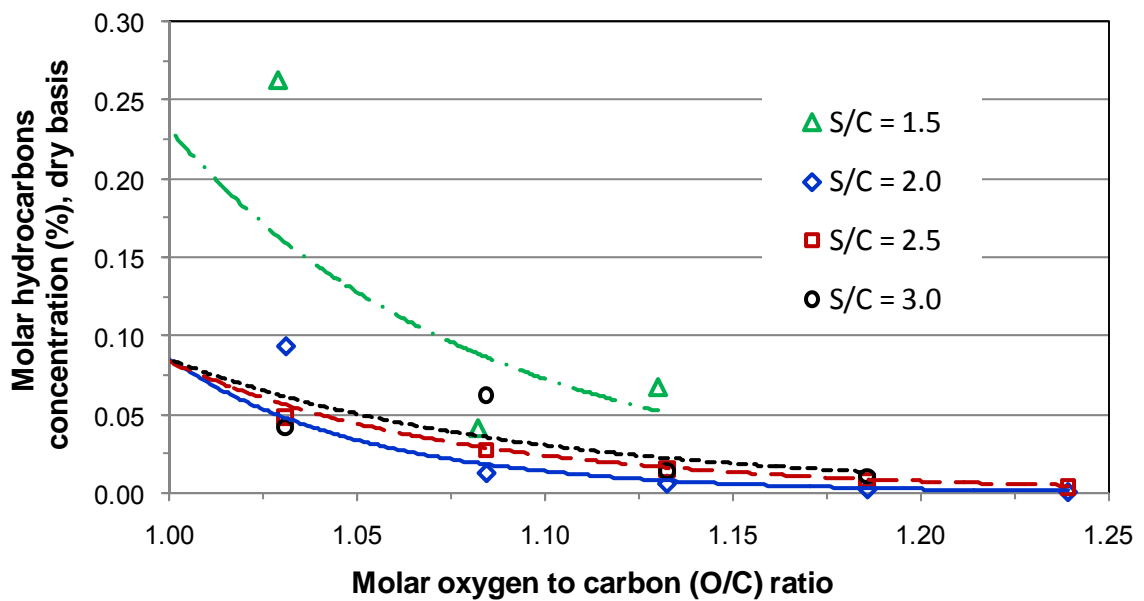
Figure 6.12 Hydrogen yield (a) and carbon monoxide yield (b) with JP-8 fuel flows of 5.9 ml/min. and S/C ratios of 1.5, 2.0, 2.5, and 3.0; reactor entrance temperature $425^{\circ}\text{C} \pm 25^{\circ}\text{C}$, and enrichment number (Ψ) of 1.0 (air). The GHSV for S/C = 1.5 was from $19,200\text{ hr}^{-1}$ to $23,200\text{ hr}^{-1}$, for S/C = 2.0 was from $21,900\text{ hr}^{-1}$ to $27,300\text{ hr}^{-1}$, for S/C = 2.5 was from $24,000\text{ hr}^{-1}$ to $30,000\text{ hr}^{-1}$, and for S/C = 3.0 was from $26,700\text{ hr}^{-1}$ to $32,000\text{ hr}^{-1}$.

6.3.3 Hydrocarbon and olefin conversion under varying S/C ratios

A significant challenge with heavy hydrocarbon fuel reforming is in managing carbon formation within the reactor. As was discussed in Chapter 2, hydrocarbon and olefin products in the reactor are precursors for carbon formation and the use of steam can be shown in both equilibrium modeling and in experimental results to help in reducing these products. Figures 6.13 and 6.14 shows the effects of steam addition on hydrocarbon and olefin products. For O/C ratios less than 1.0, increasing the S/C ratio results in reduced hydrocarbons and olefins in the product stream. For O/C ratios greater than 1.0, a significant drop in both hydrocarbons and olefins is achieved in going from S/C of 1.5 to 2.0. However, raising S/C to 2.5 and 3 results in an increase in hydrocarbons (shown in 6.13b) but with little change in olefins (Fig 6.14b). Comparing Fig. 6.13b with Fig. 6.14b reveals that the majority of hydrocarbons that are unconverted are olefins. Olefins are believed to be formed through homogeneous pyrolysis reactions towards the rear to the reactor after all oxygen is consumed [156]. Increased reactor temperature and lack of steam, as with S/C of 1.5, would encourage olefin production. Raising the S/C ratio beyond 2, while possibly helping to convert olefins via steam reforming also increases the space velocity (reduces reactor space time) and reduces the reactor's operating temperature; these changes reduce reaction kinetics and reactant residence time both having a negative impact on olefin conversion.

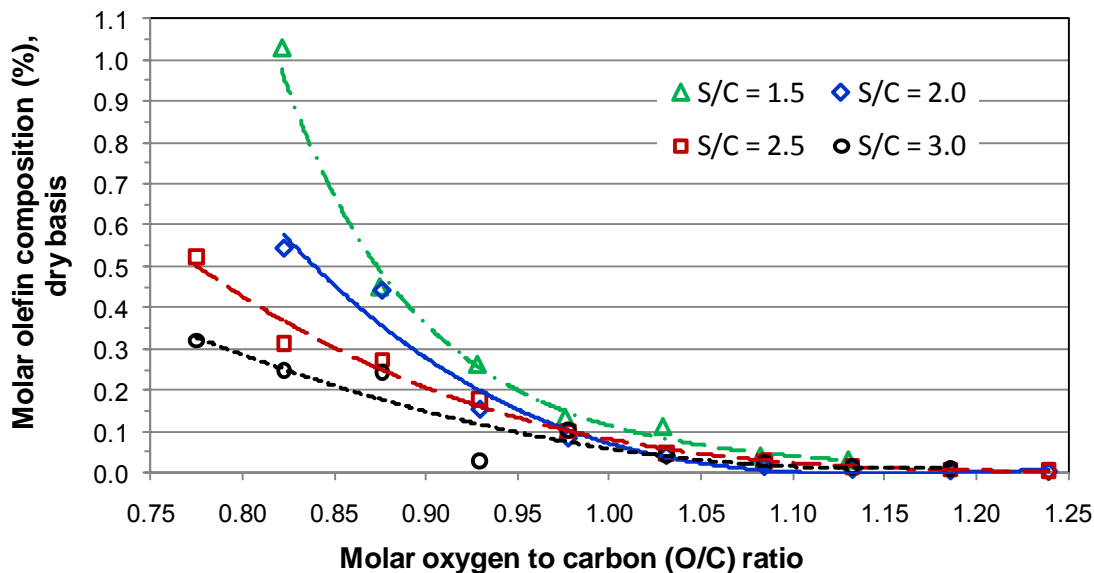


(a)

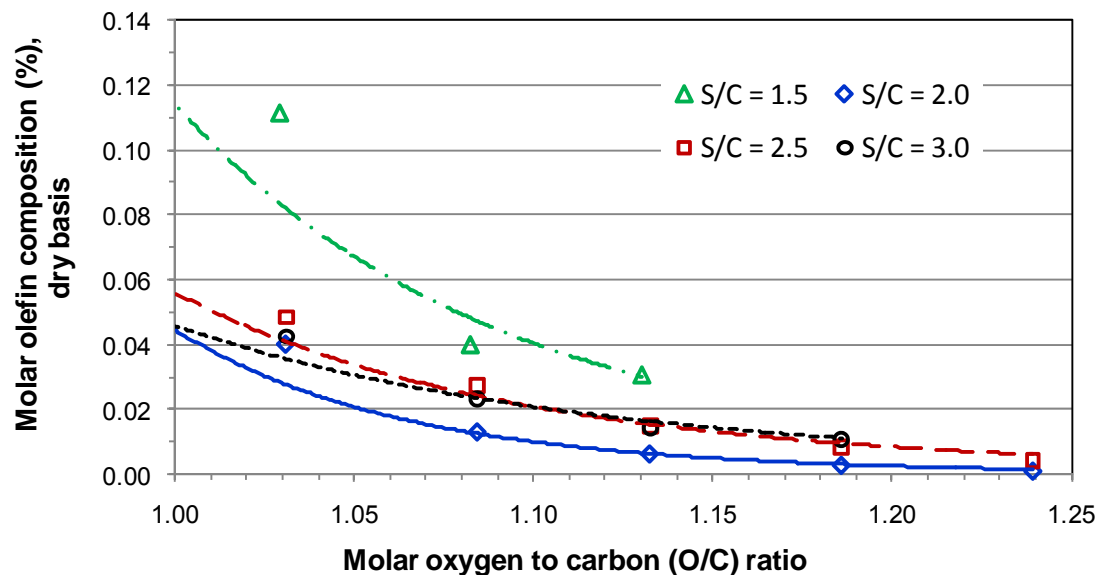


(b)

Figure 6.13 Hydrocarbon concentration as a function of S/C ratio with JP-8 fuel flows of 5.9 ml/min. and S/C ratios of 1.5, 2.0, 2.5, and 3.0; reactor entrance temperature $425^{\circ}\text{C} \pm 25^{\circ}\text{C}$, and enrichment number (Ψ) of 1.0 (air). The GHSV for S/C = 1.5 was from 19,200 hr^{-1} to 23,200 hr^{-1} , for S/C = 2.0 was from 21,900 hr^{-1} to 27,300 hr^{-1} , for S/C = 2.5 was from 24,000 hr^{-1} to 30,000 hr^{-1} , and for S/C = 3.0 was from 26,700 hr^{-1} to 32,000 hr^{-1} .



(a)



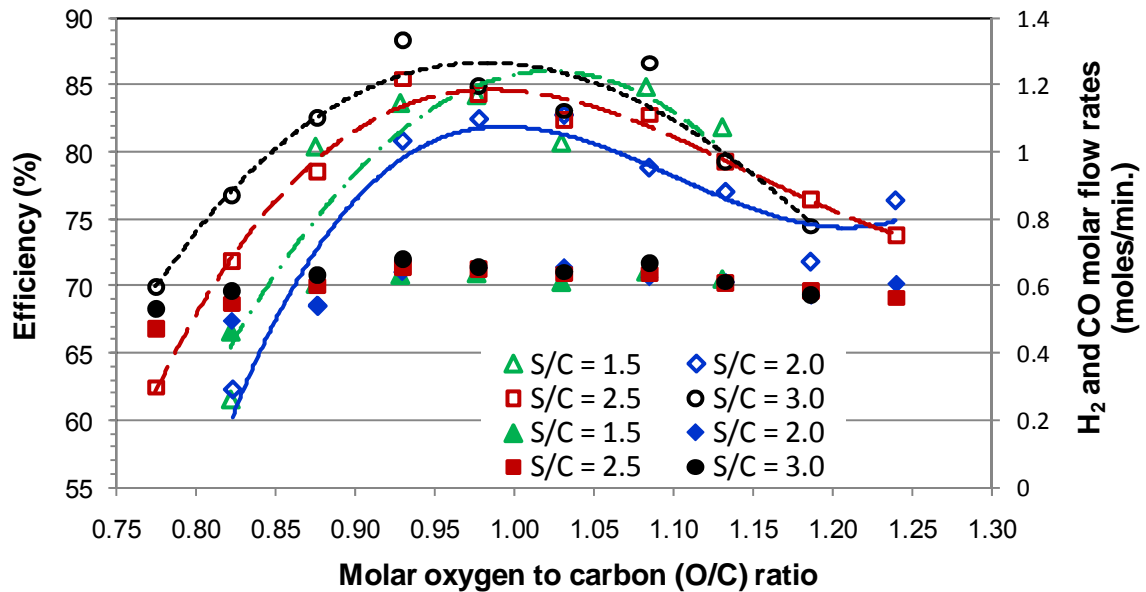
(b)

Figure 6.14 Olefin concentration as a function of S/C ratio with JP-8 fuel flows of 5.9 ml/min. and S/C ratios of 1.5, 2.0, 2.5, and 3.0; reactor entrance temperature $425^{\circ}\text{C} \pm 25^{\circ}\text{C}$, and enrichment number (Ψ) of 1.0 (air). The GHSV for S/C = 1.5 was from $19,200\text{ hr}^{-1}$ to $23,200\text{ hr}^{-1}$, for S/C = 2.0 was from $21,900\text{ hr}^{-1}$ to $27,300\text{ hr}^{-1}$, for S/C = 2.5 was from $24,000\text{ hr}^{-1}$ to $30,000\text{ hr}^{-1}$, and for S/C = 3.0 was from $26,700\text{ hr}^{-1}$ to $32,000\text{ hr}^{-1}$.

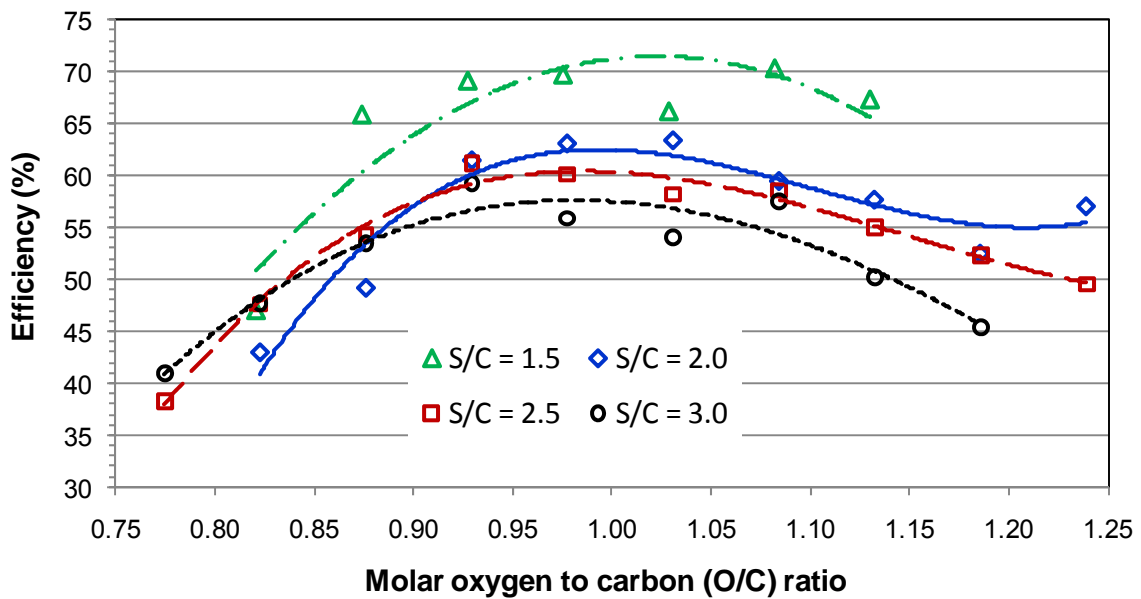
6.3.4 Reformer efficiency under varying S/C ratios

Figure 6.15a displays the reformer efficiency which is based on the lower heating value of products (hydrogen and carbon monoxide) over the lower heating value of the input fuel. The highest efficiency of 88% is obtained with S/C of 3.0 at an O/C ratio of 0.93, followed by 86% for S/C of 1.5 at O/C of 1.03, 84.5% for S/C of 2.5 at an O/C ratio of 0.97, and 82% for S/C of 2.0 at an O/C of 0.97. The results do not show a clear relationship between reforming efficiency and S/C ratio. This results from how reformer efficiency is defined; carbon monoxide is considered a useful product and as S/C ratios decrease, hydrogen production is diminished and carbon monoxide is increased on an equivalent basis. Fig. 6.15a shows that the combined hydrogen and carbon monoxide molar flow rates show little affect from S/C variations. This also implies that the WGS reaction (Eqn. 6-1) is largely responsible for changes in the hydrogen and carbon monoxide reformat composition as a result of water addition. In addition, the lower heating value for carbon monoxide on a molar basis (283.2 MJ/kmol) is higher than hydrogen (243.9 MJ/kmol) giving a preference for reformat streams higher in carbon monoxide as is the case with a S/C ratio of 1.5.

Another consideration in selecting an operating S/C ratio is the potential negative impact of having to vaporizer water. As we defined reformer efficiency, no penalty is assumed for the energy required to vaporize fuel and water, or to preheat air. In general, ATR systems on a whole are exothermic and contain “waste” streams with sufficient energy content to provide required liquid vaporization and air preheating needs (e.g. fuel cell



(a)



(b)

Figure 6.15 Reformer efficiency and combined hydrogen and carbon monoxide flow rates (a), and reformer efficiency when energy for water vaporization is considered (b) with JP-8 fuel flows of 5.9 ml/min. and S/C ratios of 1.5, 2.0, 2.5, and 3.0; reactor entrance temperature $425\text{ }^{\circ}\text{C} \pm 25\text{ }^{\circ}\text{C}$, and enrichment number (Ψ) of 1.0 (air). The GHSV for S/C = 1.5 was from $19,200\text{ hr}^{-1}$ to $23,200\text{ hr}^{-1}$, for S/C = 2.0 was from $21,900\text{ hr}^{-1}$ to $27,300\text{ hr}^{-1}$, for S/C = 2.5 was from $24,000\text{ hr}^{-1}$ to $30,000\text{ hr}^{-1}$, and for S/C = 3.0 was from $6,700\text{ hr}^{-1}$ to $32,000\text{ hr}^{-1}$.

stack typically have anode fuel utilization on the order of 70% leaving considerable available energy for other uses). However, when considering high S/C levels the water vaporization energy can be considerable and must be considered. Figure 6.15b shows reformer efficiencies based on the equation below, where the water vaporization energy is included.

$$\eta_{\text{reformer, w/ H}_2\text{O vaporization}} = \frac{LHV_{H_2} + LHV_{CO} - \dot{m}_{H_2O} \left(h_{g_{H_2O, 425^\circ\text{C}}} - h_{l_{H_2O, 25^\circ\text{C}}} \right)}{LHV_{\text{fuel}}} \cdot 100\% \quad 6-3$$

When the energy associated with water vaporization is considered the reformer efficiencies are inversely related to S/C ratio. To fully consider the impact from water addition, system level modeling would need to be performed which is beyond the scope of the research work contained here.

6.4 JP-8 surrogate reforming at varying fuel flows

JP-8 surrogate fuel at flow rates of 4.42 ml/min., 5.9 ml/min., 8.84 ml/min. and 11.8 ml/min. were reformed with air and steam at an S/C ratio of 2.0 in a noble metal monolithic reactor. The O/C ratio was varied from approximately 0.75 to 1.2. Under all fuel flows, complete fuel conversion was achieved (within measurement error) as shown in Fig. 6.16. The fuel flow of 8.84 ml/min. (shown as 5.0 kW_{th}) achieved full fuel conversion at the lowest O/C ratio of 0.942. Achieving full fuel conversion at the lowest possible O/C ratio is indicative of good performance in ATRs and CPOx reformers as

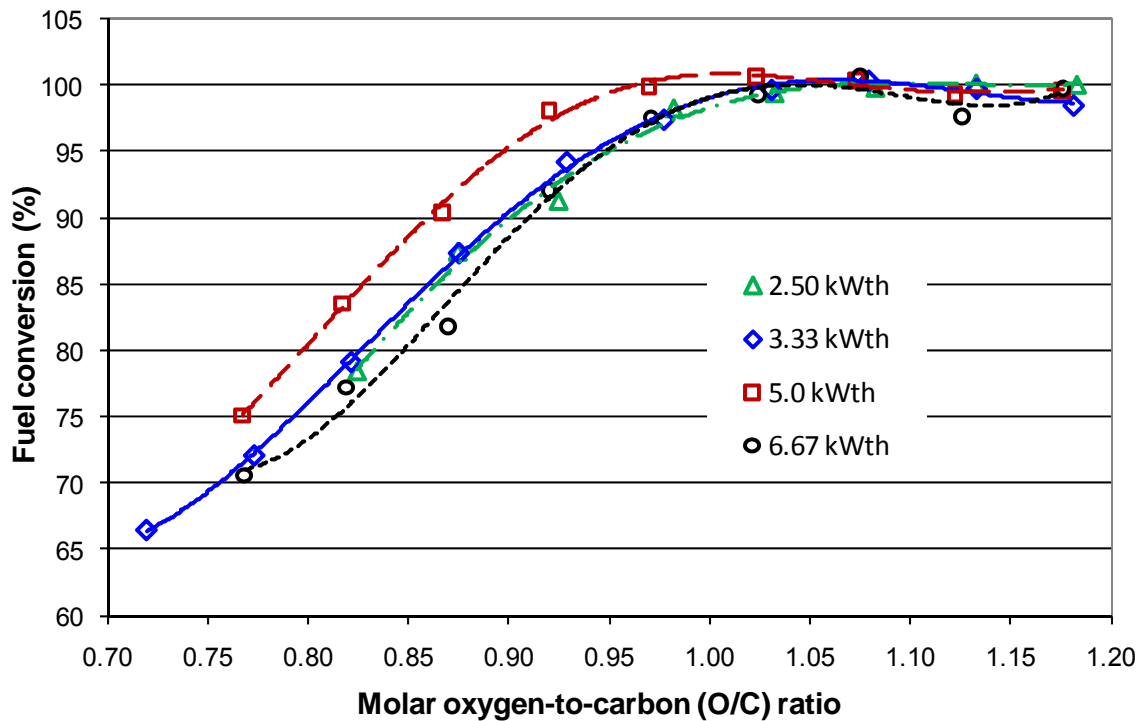


Figure 6.16 Normalized fuel conversion for JP-8 fuel flows of 4.42 ml/min. (2.5 kWth), 5.9 ml/min. (3.33 kWth), 8.84 ml/min. (5.0 kWth) and 11.8 ml/min. (6.67 kWth) with $S/C = 2.0$, reactor entrance temperature $425^{\circ}\text{C} \pm 25^{\circ}\text{C}$, and enrichment number (Ψ) of 1.0 (air). The GHSV for 2.50 ml/min. was from $16,000\text{ hr}^{-1}$ to $20,000\text{ hr}^{-1}$, for 3.33 kWth was from $20,500\text{ hr}^{-1}$ to $26,000\text{ hr}^{-1}$, for 5.0 kWth was from $32,500\text{ hr}^{-1}$ to $40,000\text{ hr}^{-1}$, and for 6.67 kWth was from $42,500\text{ hr}^{-1}$ to $53,500\text{ hr}^{-1}$.

increasing O/C ratios results in increasing full oxidation of fuel, reformat dilution by nitrogen and shorter reactor space times (larger space velocities). Operation at high O/C ratio's also negatively impacts system size and result in increased system pumping power; pumping power being directly related to reformat volume flow and system pressure drop which increases with fuel flow and O/C ratio as shown in Fig. 6.17. Good fuel conversion is a function of reactor operating temperature and sufficient time for all reactions to proceed to completion.

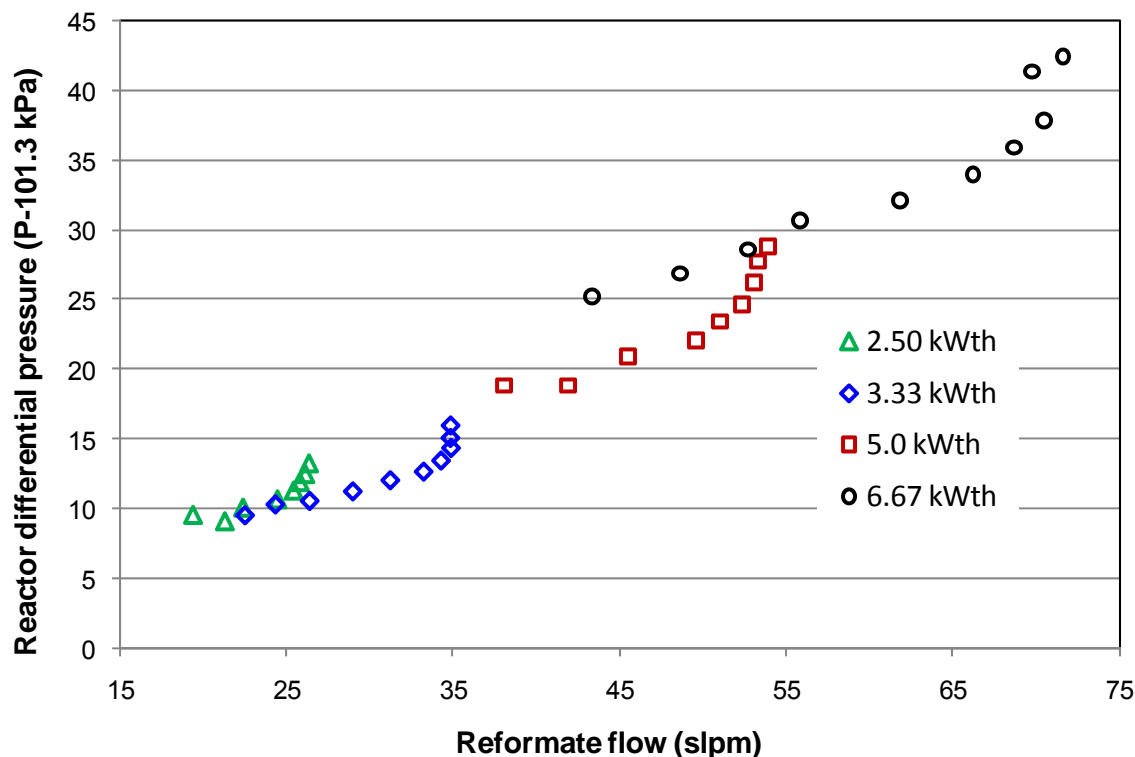


Figure 6.17 Reactor differential pressure as a function of fuel flow with JP-8 fuel flows of 4.42 ml/min. (2.5 kWth), 5.9 ml/min. (3.33 kWth), 8.84 ml/min. (5.0 kWth), and 11.8 ml/min. (6.67 kWth) with S/C = 2.0, reactor entrance temperature $425^{\circ}\text{C} \pm 25^{\circ}\text{C}$, and enrichment number (Ψ) of 1.0 (air). The GHSV for 2.50 ml/min. was from 16,000 hr^{-1} to 20,000 hr^{-1} , for 3.33 kWth was from 20,500 hr^{-1} to 26,000 hr^{-1} , for 5.0 kWth was from 32,500 hr^{-1} to 40,000 hr^{-1} , and for 6.67 kWth was from 42,500 hr^{-1} to 53,500 hr^{-1} .

Figure 6.18 shows the maximum and exit reactor temperatures for all four fuel flows with order of reactor temperatures following the order of fuel flows (i.e. higher temperature corresponding with higher fuel flows). The reactor operating temperature increased with increasing fuel flow because the reactor thermal losses are a function of the reactor operating temperature which does not increase linearly with increasing flows. Therefore, thermal losses relative to the energy released from fuel being oxidized in the reactor is

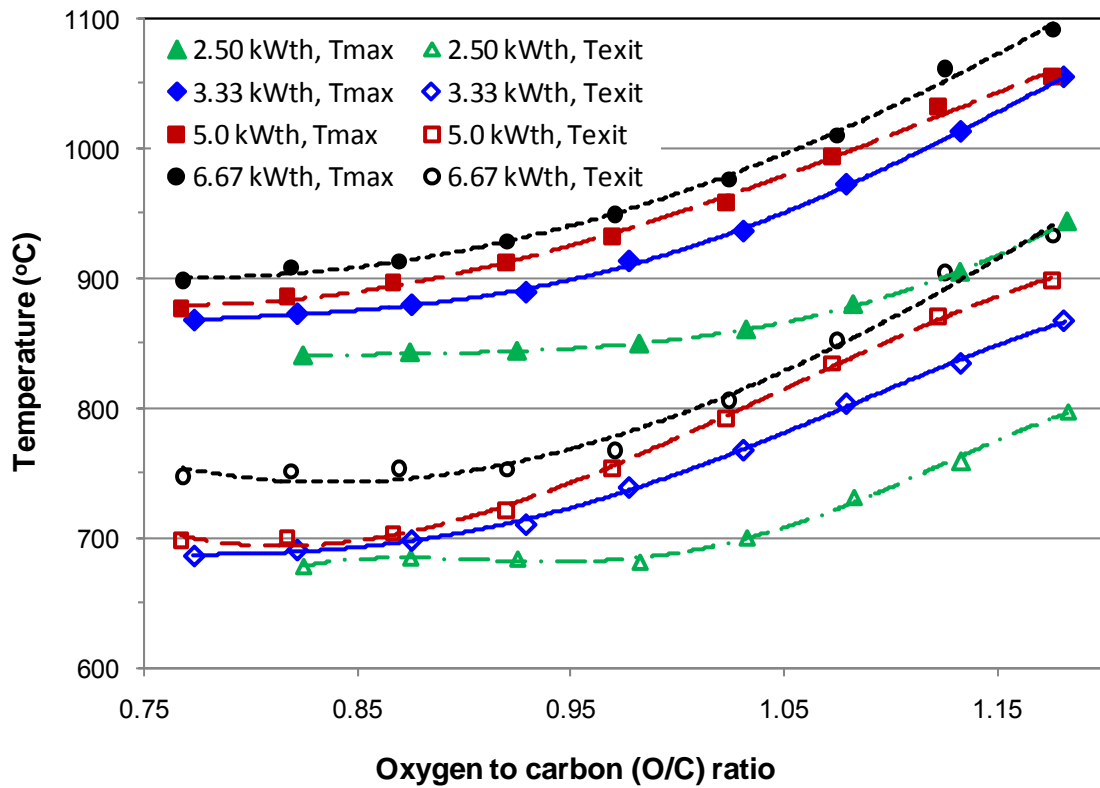


Figure 6.18 Reactor maximum and exit temperatures with JP-8 fuel flows of 4.42 ml/min. (2.5 kWth), 5.9 ml/min. (3.33 kWth), 8.84 ml/min. (5.0 kWth) and 11.8 ml/min. (6.67 kWth) with $S/C = 2.0$, reactor entrance temperature $425\text{ }^{\circ}\text{C} \pm 25\text{ }^{\circ}\text{C}$, and enrichment number (Ψ) of 1.0 (air). The GHSV for 2.50 ml/min. was from $16,000\text{ hr}^{-1}$ to $20,000\text{ hr}^{-1}$, for 3.33 kWth was from $20,500\text{ hr}^{-1}$ to $26,000\text{ hr}^{-1}$, for 5.0 kWth was from $32,500\text{ hr}^{-1}$ to $40,000\text{ hr}^{-1}$, and for 6.67 kWth was from $42,500\text{ hr}^{-1}$ to $53,500\text{ hr}^{-1}$.

reduced as the fuel flow rate is increased. Figure 6.19 gives the reactor space time which is inversely proportional to fuel flow. Figures 6.17, 6.18 and 6.19 provide some insight into reaction kinetics within the ATR from the perspective of fuel conversion. Table 6.1 provides a more convenient comparison of values at the point of full fuel conversion.

Looking at again at fuel conversions (Fig. 6.16) and Table 6.1, it appears that going from 3.33 kW_{th} to 5.0 kW_{th} the increase in reactor exit temperature results in better fuel

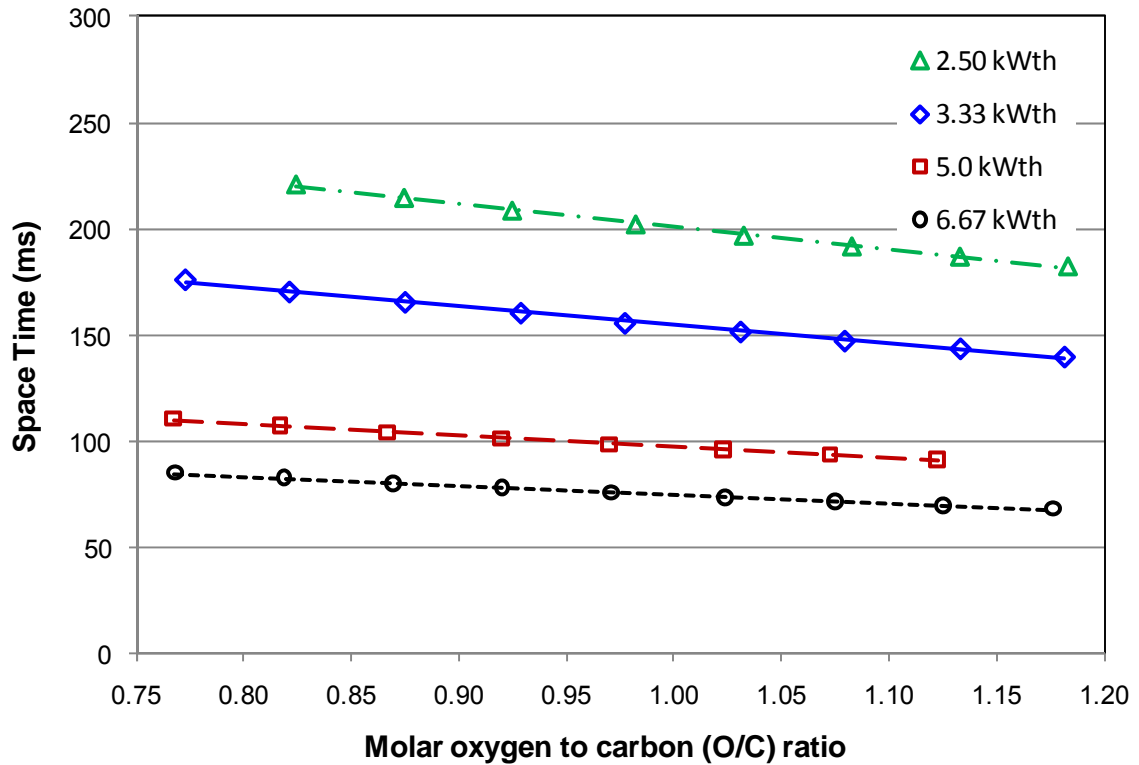


Figure 6.19 Space time for JP-8 fuel flows of 4.42 ml/min.(2.5 kWth), 5.9 ml/min. (3.33 kWth), 8.84 ml/min. (5.0 kWth) and 11.8 ml/min. (6.67 kWth) with S/C = 2.0, reactor entrance temperature $425^{\circ}\text{C} \pm 25^{\circ}\text{C}$, and enrichment number (Ψ) of 1.0 (air). Ideal gas behavior is assumed under standard conditions.

Table 6.1 Full fuel conversion

Thermal rating	O/C ratio	Reactor maximum temperature $^{\circ}\text{C}$	Reactor exit temperature $^{\circ}\text{C}$	Space time ms
2.50 kWth	1.038	863.2	683.3	307.6
3.33 kWth	0.992	895.0	700.6	242.8
5.0 kWth	0.942	945.9	793.8	151.5
6.67 kWth	1.042	987.6	852.0	116.2

conversion despite a shorter space times. This indicates that based on fuel conversion alone, the reactor as designed²² and currently configured²³ could be rated for fuel flows in excess of 3.33 kW_{th}. Below 3.33 kW_{th} the reactor exit temperature drops, slowing reaction kinetics, resulting in a non-optimum design. However, in moving from a rating of 5.0 kW_{th} to 6.67 kW_{th}, despite an increase in reactor exit temperature, full fuel conversion does not occur below an O/C ratio of 1.042, also indicating that the reactor is not optimized for this thermal rating. Interpolating the fuel conversion data as shown in Fig. 6.20 results in an optimized thermal rating for the reactor of approximately 4.61 kW_{th}. Further insight into the effects of fuel flow rate on reactor performance can be seen in reactor product yields.

Figure 6.21 displays the reformat product yields for hydrogen and carbon monoxide and Fig. 6.22 shows the reformer efficiency. As discussed previously, the hydrogen yield and reformer efficiency track very closely. Table 6.2 provides a comparison of peak value for full fuel conversion, hydrogen yield, and reformer efficiency and the O/C where the peaks where achieved. The maximum peak hydrogen yield obtained was 1.574 mols H₂/(mols H₂)_{fuel} attributed to a thermal rating of 5 kW_{th} at an O/C ratio of 1.005. The overall peak reformer efficiency was 90.0% obtained at an O/C ratio of 0.98 for thermal rating of 5.0 kW_{th}. The carbon monoxide yield within the syngas production region (typically, $0.95 \leq \text{O/C} \leq 1.20$) follows the order of reactor temperature with higher temperatures favoring the reverse WGS reaction, shown in Eqn. 6-1. In terms of O/C

²² This term refers to the fuel used, reactor size, reactor design and operating conditions.

²³ The reactor configuration refers to the catalysts, catalysts support structure and reactor geometry.

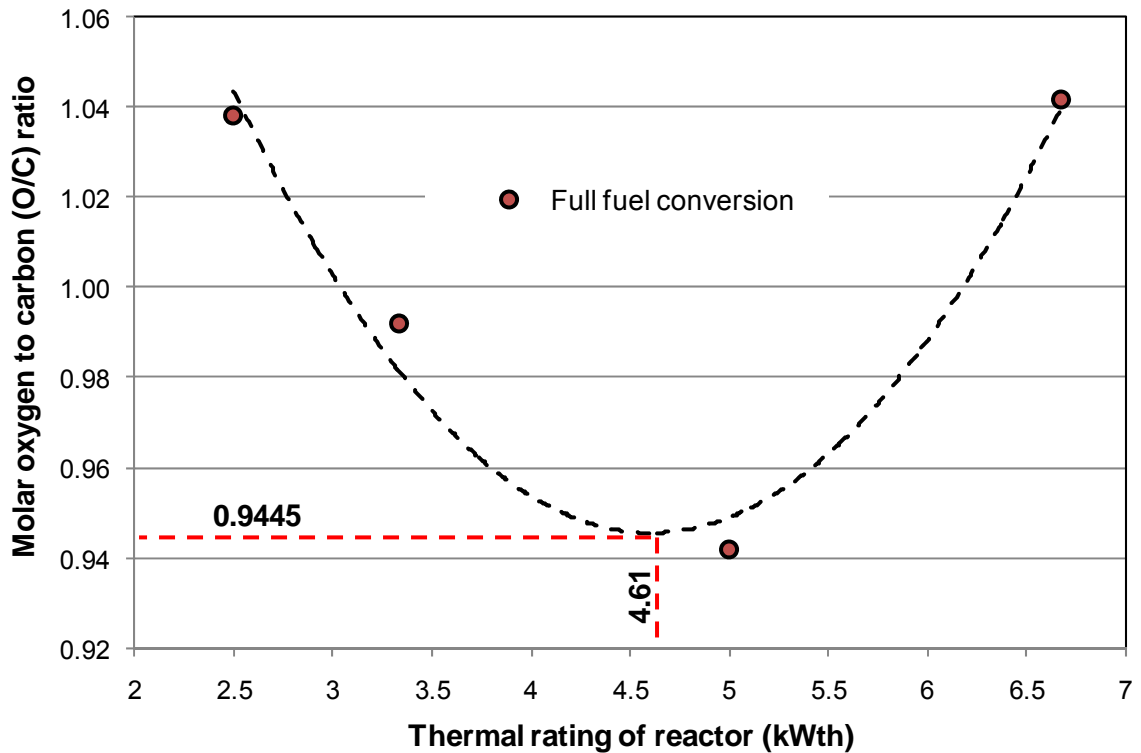
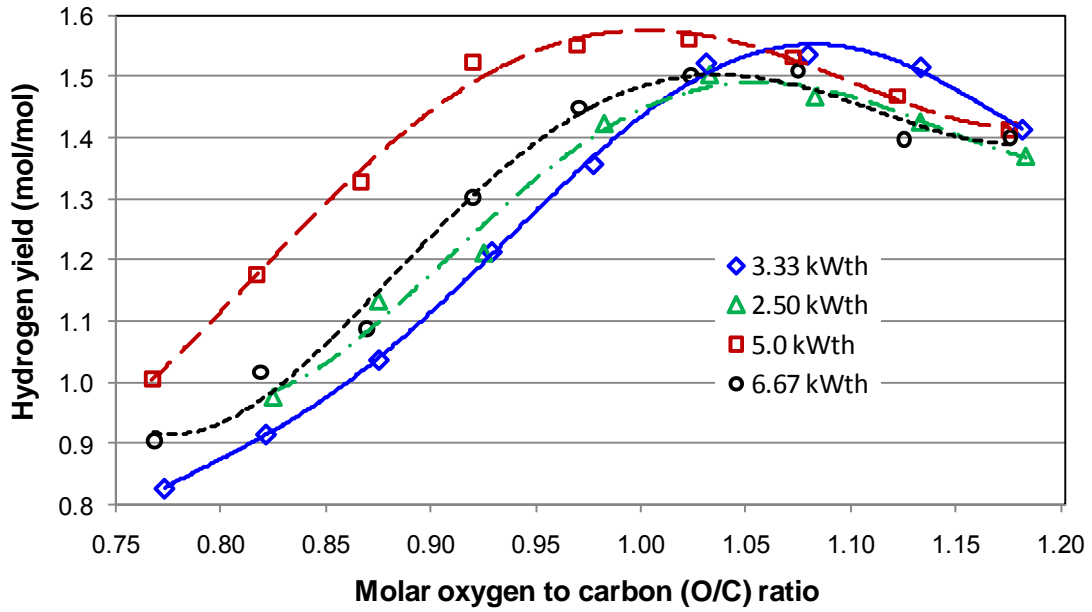
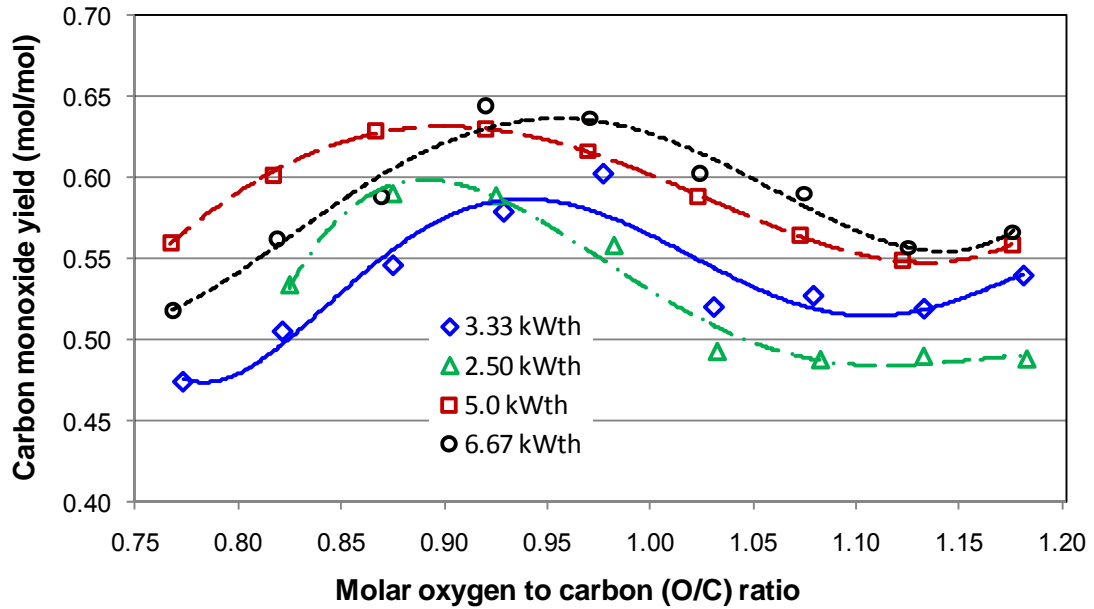


Figure 6.20 Graphical determination of optimum reactor thermal rating to achieve minimum O/C ratio for full fuel conversion with JP-8 fuel flows of 4.42 ml/min. (2.5 kWth), 5.9 ml/min. (3.33 kWth), 8.84 ml/min. (5.0 kWth) and 11.8 ml/min. (6.67 kWth) with S/C = 2.0, reactor entrance temperature $425^{\circ}\text{C} \pm 25^{\circ}\text{C}$, and enrichment number (Ψ) of 1.0 (air). The GHSV for 2.50 ml/min. was from $16,000\text{ hr}^{-1}$ to $20,000\text{ hr}^{-1}$, for 3.33 kWth was from $20,500\text{ hr}^{-1}$ to $26,000\text{ hr}^{-1}$, for 5.0 kWth was from $32,500\text{ hr}^{-1}$ to $40,000\text{ hr}^{-1}$, and for 6.67 kWth was from $42,500\text{ hr}^{-1}$ to $53,500\text{ hr}^{-1}$.

ratio, the peak hydrogen yields for all thermal rating tested occurred coincident with or just after the O/C ratio's corresponding to full fuel conversion. This is a very logical as unconverted fuel can contain a large portion of available hydrogen as is seen in the rapid fall in the hydrogen yield curves to the left of the point of full fuel conversion; and at O/C ratio's above full fuel conversion, hydrogen is being oxidized to water with increasing O/C ratio.



(a)



(b)

Figure 6.21 Hydrogen yield (a) and carbon monoxide yield (b) with JP-8 fuel flows of 4.42 ml/min. (2.5 kWth), 5.9 ml/min. (3.33 kWth), 8.84 ml/min. (5.0 kWth) and 11.8 ml/min. (6.67 kWth) with S/C = 2.0, reactor entrance temperature $425^{\circ}\text{C} \pm 25^{\circ}\text{C}$, and enrichment number (Ψ) of 1.0 (air). The GHSV for 2.50 ml/min. was from $16,000\text{ hr}^{-1}$ to $20,000\text{ hr}^{-1}$, for 3.33 kWth was from $20,500\text{ hr}^{-1}$ to $26,000\text{ hr}^{-1}$, for 5.0 kWth was from $32,500\text{ hr}^{-1}$ to $40,000\text{ hr}^{-1}$, and for 6.67 kWth was from $42,500\text{ hr}^{-1}$ to $53,500\text{ hr}^{-1}$.

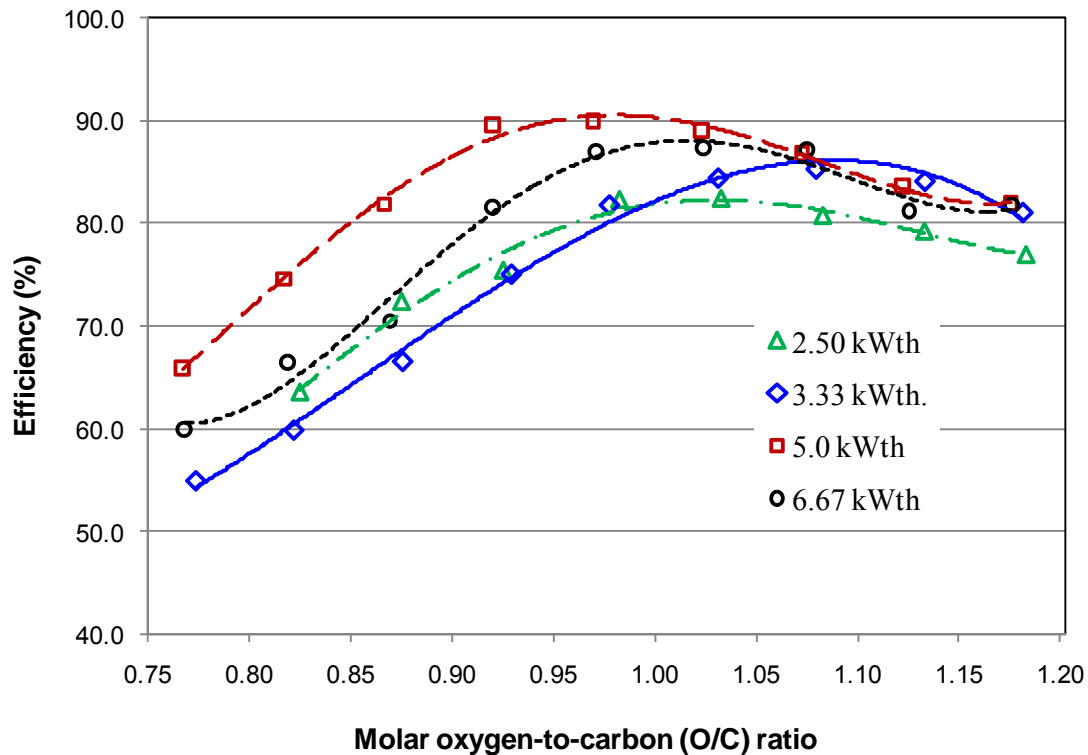


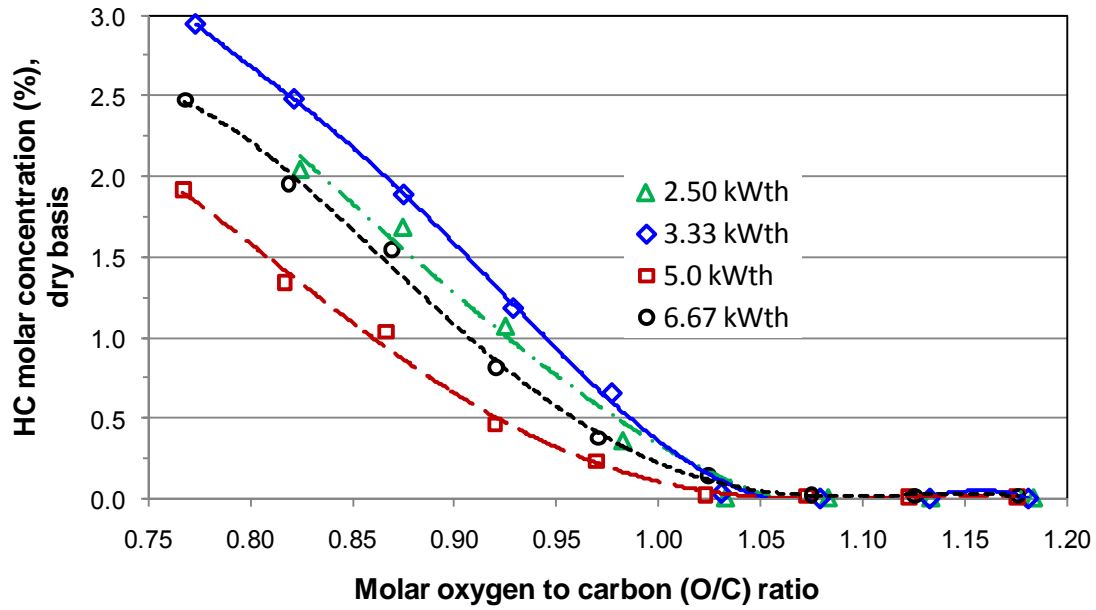
Figure 6.22 Reformer efficiency with JP-8 fuel flows of 4.42 ml/min. (2.5 kWth), 5.9 ml/min. (3.33 kWth), 8.84 ml/min. (5.0 kWth) and 11.8 ml/min. (6.67 kWth) with S/C = 2.0, reactor entrance temperature $425^{\circ}\text{C} \pm 25^{\circ}\text{C}$, and enrichment number (Ψ) of 1.0 (air). The GHSV for 2.50 ml/min. was from $16,000\text{ hr}^{-1}$ to $20,000\text{ hr}^{-1}$, for 3.33 kWth was from $20,500\text{ hr}^{-1}$ to $26,000\text{ hr}^{-1}$, for 5.0 kWth was from $32,500\text{ hr}^{-1}$ to $40,000\text{ hr}^{-1}$, and for 6.67 kWth was from $42,500\text{ hr}^{-1}$ to $53,500\text{ hr}^{-1}$.

Table 6.2 Comparison of peak full fuel conversion, hydrogen yield and reformer efficiency

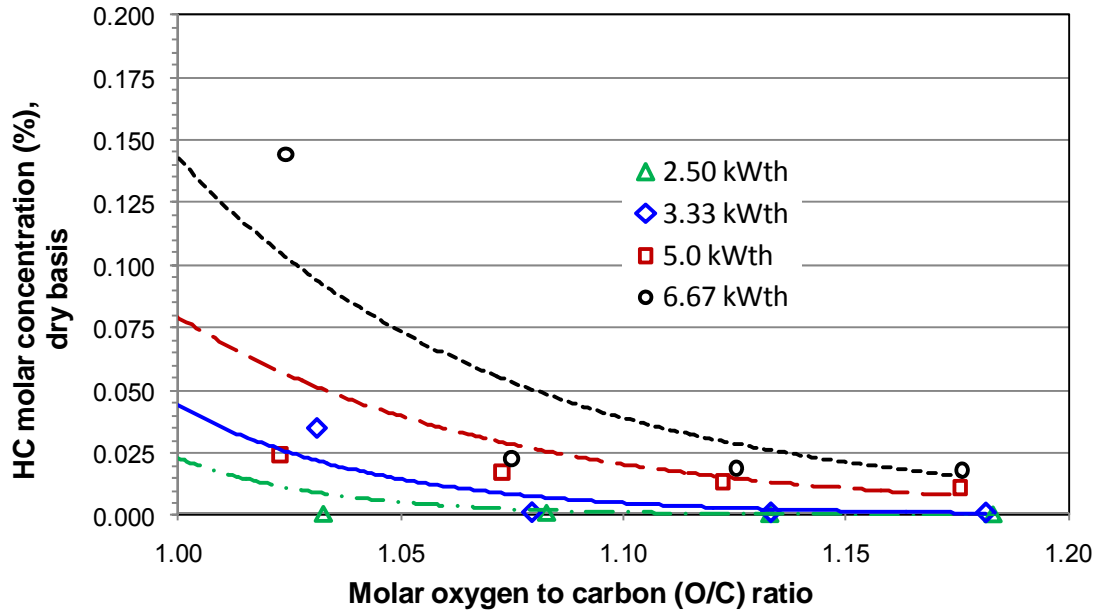
Thermal rating	Full fuel conversion		Maximum hydrogen yield		Maximum reformer efficiency	
	O/C ratio		O/C ratio	mol/mol	O/C ratio	%
2.50 kWth	1.038		1.055	1.506	1.030	82.2
3.33 kWth	0.992		1.090	1.542	1.088	86.1
5.0 kWth	0.942		1.005	1.574	0.980	90.0
6.67 kWth	1.042		1.040	1.050	1.016	88.3

In assessing the performance of an ATR, trace amounts of unconverted hydrocarbons and olefins must be evaluated. Olefins and hydrocarbons can lead to carbon formation in the reactor over time or can have deleterious effects on downstream processes (e.g. fuel cell stack, sulfur removal, etc.). Figure 6.23 displays the molar concentration of hydrocarbons as a function of O/C ratio. As a rule of thumb maintaining total hydrocarbons below 0.1% will reduce the likelihood of carbon formation and result in good catalysts durability. Looking at Fig. 6.23b all hydrocarbons are converted by an O/C ratio of 1.03 for a thermal rating of 2.50 kW_{th} and by 1.08 for 3.33 kW_{th}. However, for higher fuel flows (thermal rating of 5.0 kW_{th} and 6.67 kW_{th}) over the operating range tested, hydrocarbons were never completely converted but could be reduced to an acceptable level ($\leq 0.1\%$). Figure 6.24 displays the olefin concentration which is considered a strong precursor for catalysts deactivation from elemental carbon formation. For olefins a level of 0.03% or less is generally recommended to avoid carbon formation. Similar to hydrocarbon conversion, reformer thermal rating of 2.5 kW_{th} and 3.33 kW_{th} were able to fully convert all olefins by an O/C ratio of 1.08, but at the higher fuel flows the olefins could not be fully converted. For a thermal rating of 5.0 kW_{th} an O/C ratio of 1.022 or higher must be maintained to keep olefins within acceptable levels and for a thermal rating of 6.67 kW_{th} an O/C level of 1.080 or higher must be maintained.

The concentration of hydrogen has a direct effect on the performance of the fuel cells stack with higher concentration resulting in higher stack performance. In addition, higher

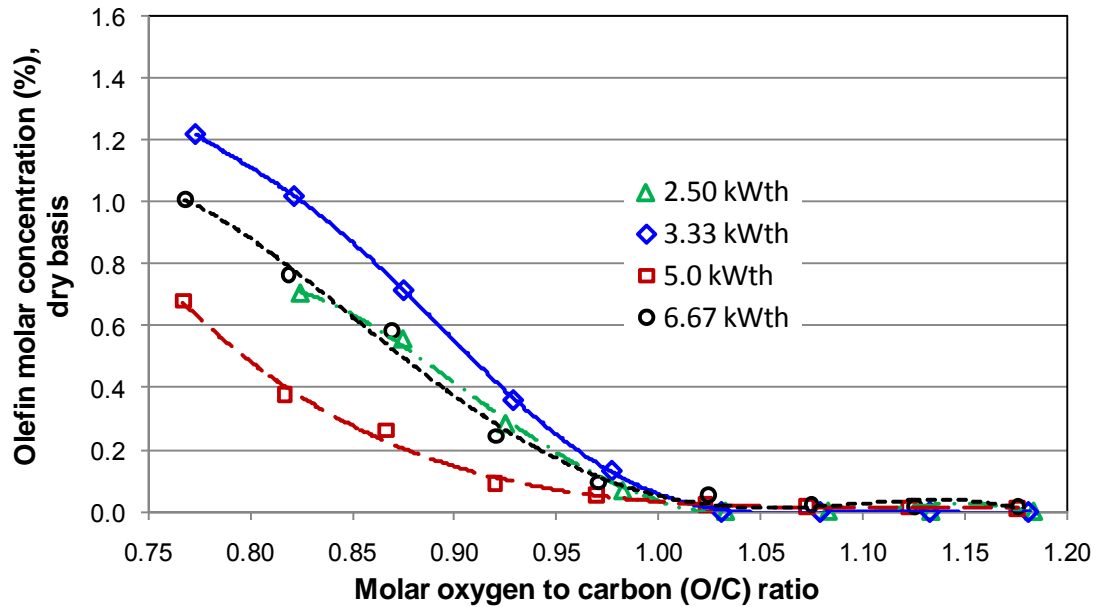


(a)

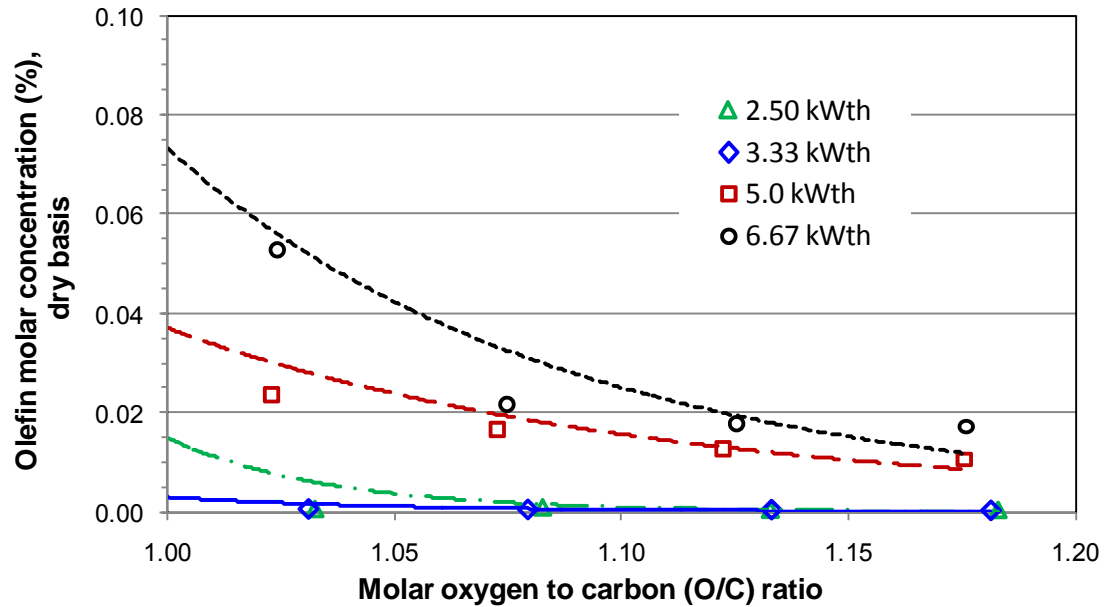


(b)

Figure 6.23 Molar concentration of hydrocarbons with JP-8 fuel flows of 4.42 ml/min. (2.5 kWth), 5.9 ml/min. (3.33 kWth), 8.84 ml/min. (5.0 kWth), and 11.8 ml/min. (6.67 kWth) with S/C = 2.0, reactor entrance temperature $425^{\circ}\text{C} \pm 25^{\circ}\text{C}$, and enrichment number (Ψ) of 1.0 (air). The GHSV for 2.50 ml/min. was from 16,000 hr^{-1} to 20,000 hr^{-1} , for 3.33 kWth was from 20,500 hr^{-1} to 26,000 hr^{-1} , for 5.0 kWth was from 32,500 hr^{-1} to 40,000 hr^{-1} , and for 6.67 kWth was from 42,500 hr^{-1} to 53,500 hr^{-1} .



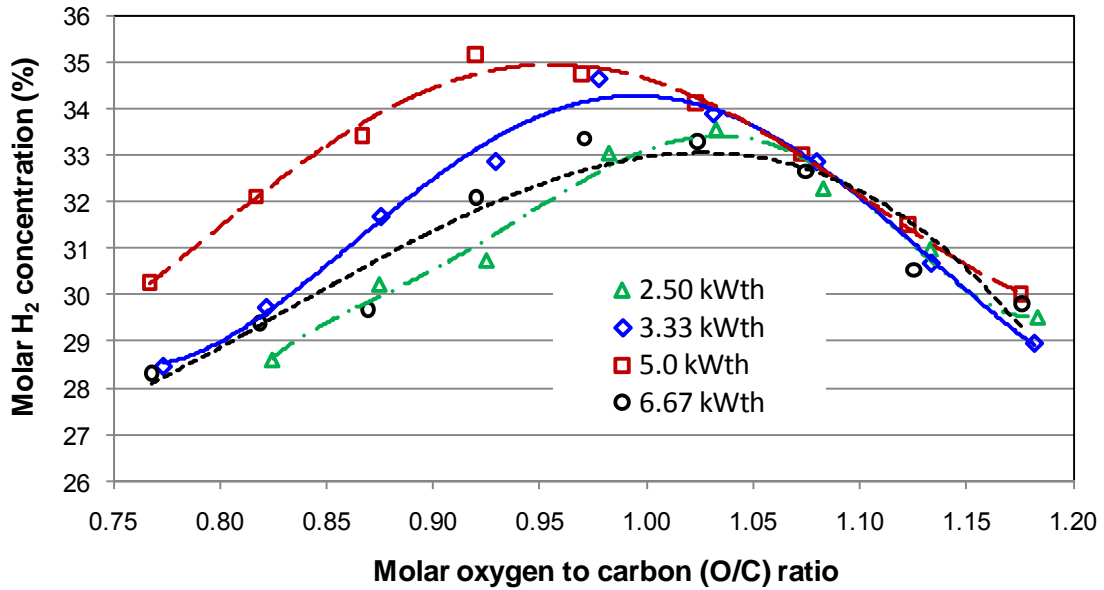
(a)



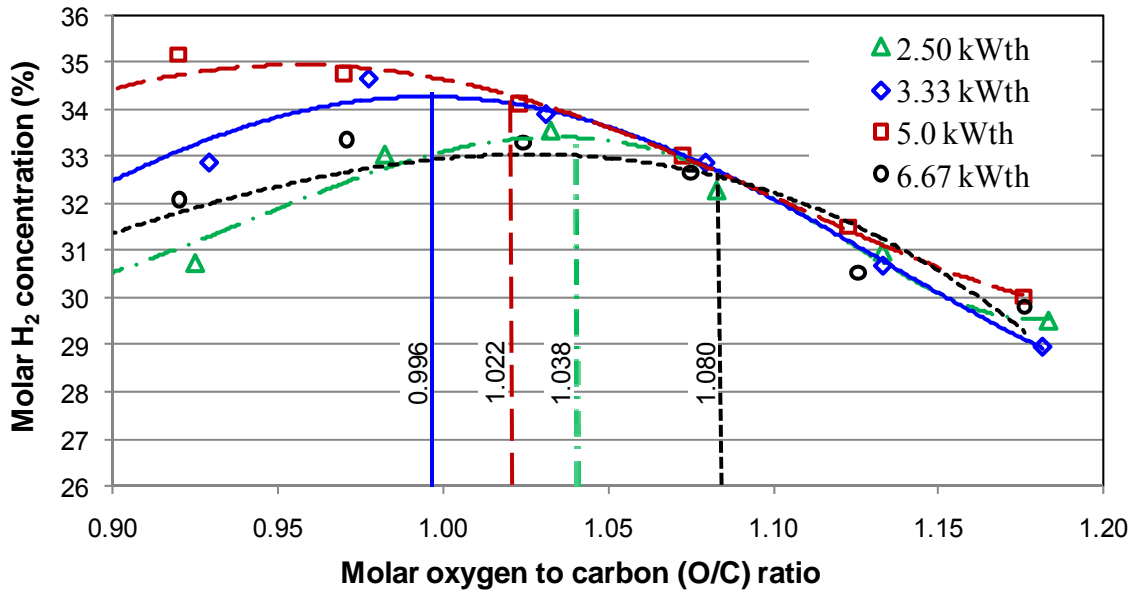
(b)

Figure 6.24 Molar concentration of olefins with JP-8 fuel flows of 4.42 ml/min. (2.5 kWth), 5.9 ml/min. (3.33 kWth), 8.84 ml/min. (5.0 kWth), and 11.8 ml/min. (6.67 kWth) with $S/C = 2.0$, reactor entrance temperature $425^{\circ}\text{C} \pm 25^{\circ}\text{C}$, and enrichment number (Ψ) of 1.0 (air). The GHSV for 2.50 ml/min. was from $16,000\text{ hr}^{-1}$ to $20,000\text{ hr}^{-1}$, for 3.33 kWth was from $20,500\text{ hr}^{-1}$ to $26,000\text{ hr}^{-1}$, for 5.0 kWth was from $32,500\text{ hr}^{-1}$ to $40,000\text{ hr}^{-1}$, and for 6.67 kWth was from $42,500\text{ hr}^{-1}$ to $53,500\text{ hr}^{-1}$.

concentrations of hydrogen also impact stack size as a result of mass transport effects at the fuel cell anode. Figure 6.25 displays the hydrogen concentration for the four thermal ratings evaluated. Figure 6.25a gives the peak hydrogen concentrations in descending order as: 35.0% at an O/C of 0.956 for 5.0 kW_{th}, 34.6% at an O/C of 0.996 for 3.33 kW_{th}, 33.0% at an O/C of 1.026 for 6.67 kW_{th}, and 32.2% at an O/C of 1.028 for 2.50 kW_{th}. In order to ensure good reformer operation, constraints on hydrocarbon and olefin reformat production, full fuel conversion and maximum operating temperature are needed. Table 6.3 provides a summary of operating constraints in terms of reformer O/C ratios and an allowable operating range is provided. Under these constraints shown in Fig. 6.25b, the maximum allowable hydrogen concentration obtained is 34.6% achieved by the thermal rating of 3.33 kW_{th} at an O/C of 0.996; this O/C operating point is well within the allowable O/C operating range and also represents the maximum hydrogen concentration for this thermal rating. At 5.0 kW_{th} the maximum allowable hydrogen concentration of 34.3% is obtained at an O/C ratio of 1.022; this operating point is constrained by allowable olefin levels. For 6.67 kW_{th} the maximum allowable hydrogen concentration of 32.6% is obtained at an O/C ratio of 1.080; this operating point is also constrained by allowable olefin levels. At 2.5 kW_{th} the maximum allowable hydrogen level of 32.2% is obtained at an O/C of 1.038; this operating point is constrained by full fuel conversion. Since a design goal for reactors is to be able to reform the highest quantity of fuel for a given reactor configuration, it is of interest to note that olefin levels limit the amount of fuel that can be handled. Further, looking back at Table 6.1 and Fig. 6.18, you can see that long space times associated with rating of 2.5 kW_{th} and 3.33 kW_{th} allow for full



(a)



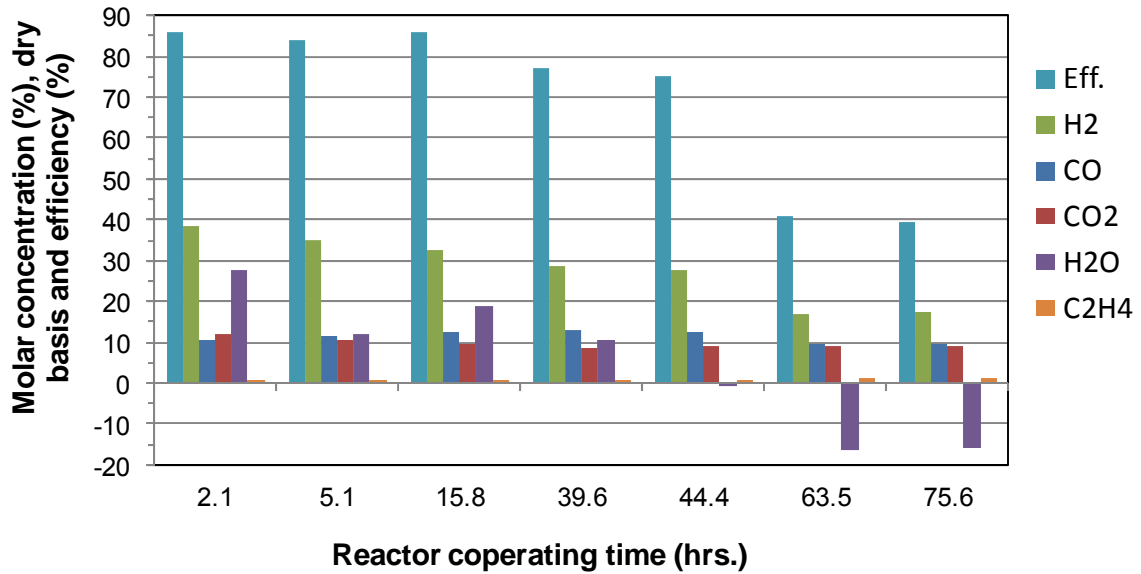
(b)

Figure 6.25 Hydrogen concentration (a) and maximum allowable hydrogen concentration points identified (b) with JP-8 fuel flows of 4.42 ml/min. (2.5 kWth), 5.9 ml/min. (3.33 kWth), 8.84 ml/min. (5.0 kWth), and 11.8 ml/min. (6.67 kWth) with S/C = 2.0, reactor entrance temperature $425\text{ }^{\circ}\text{C} \pm 25\text{ }^{\circ}\text{C}$, and enrichment number (Ψ) of 1.0 (air). The GHSV for 2.50 ml/min. was from $16,000\text{ hr}^{-1}$ to $20,000\text{ hr}^{-1}$, for 3.33 kWth was from $20,500\text{ hr}^{-1}$ to $26,000\text{ hr}^{-1}$, for 5.0 kWth was from $32,500\text{ hr}^{-1}$ to $40,000\text{ hr}^{-1}$, and for 6.67 kWth was from $42,500\text{ hr}^{-1}$ to $53,500\text{ hr}^{-1}$.

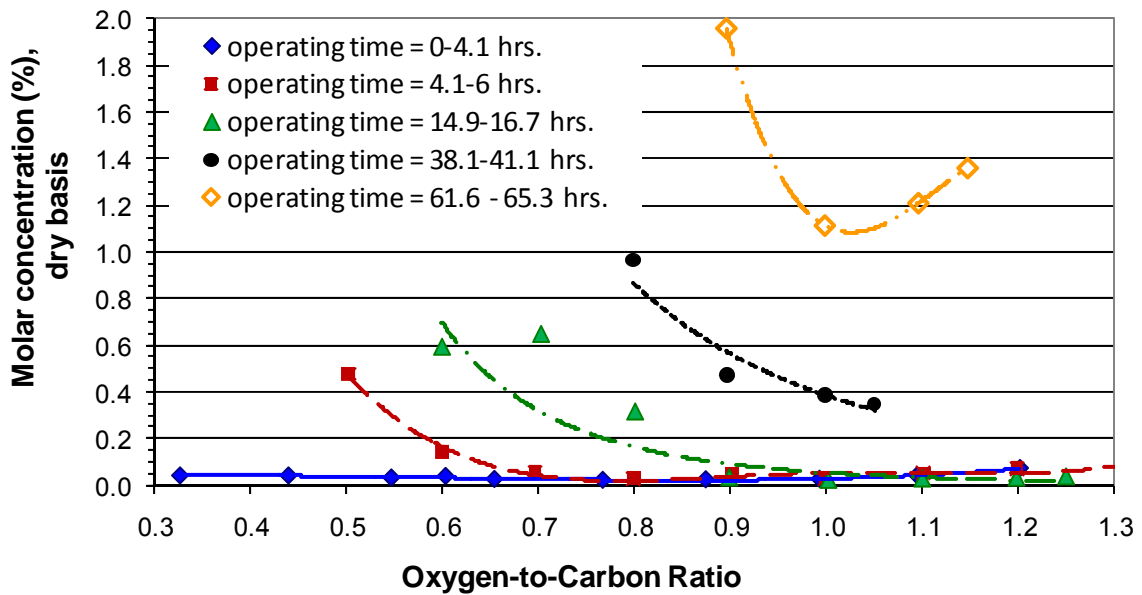
Table 6.3 Reformer operating constraints

Thermal rating	Full fuel conversion ($\pm 3.7\%$)	Maximum hydrogen yield ($\pm 2.4\%$)	Maximum reformer efficiency ($\pm 2.5\%$)	Olefins $\leq 0.03\%$ ($\pm 1.02\%$)	Hydrocarbons $\leq 0.10\%$ ($\pm 1.02\%$)	Maximum allowable reactor temperature ($1100\text{ }^{\circ}\text{C}$) ($\pm 44^{\circ}\text{C}$)	Allowable operating range
	O/C ratio	O/C ratio	O/C ratio	Min. O/C ratio	Min. O/C ratio	Max. O/C ratio	O/C ratio
2.5 kWth	1.038	1.055	1.030	0.976	0.952	1.307	1.038 - 1.307
3.33 kWth	0.992	1.090	1.088	0.890	0.965	1.237	0.965 - 1.237
5.0 kWth	0.942	1.005	0.980	1.022	0.984	1.221	1.022 - 1.221
6.67 kWth	1.042	1.040	1.016	1.080	1.026	1.180	1.080 - 1.180

conversion of olefin even though the reactor is operating at temperatures lower than at 5.0 kW_{th} and 6.67 kW_{th}. From these observations it appears that reactions leading to full conversion of olefins are slow and are less strongly influenced by temperature. Dreyer *et al.* [190] hypothesized that in heavy hydrocarbon ATR reforming olefins are generated through homogeneous reactions in the final third of the reactor once oxygen is consumed and water is less plentiful. Dreyer showed that operation at higher S/C ratio's had a positive effect on olefin reduction by enhancing heterogeneous steam reforming reactions. Similar results were observed in earlier reactor runs under this thesis; catalysts deactivation and olefin production were observed to occur and increase proportionally. Figure 6.26a shows the gradual deactivation of a reactor as a result of repeated exposure to elevated olefins levels; here reformer efficiency drops as olefin and hydrocarbon levels increase. Dreyer's conclusion that olefins are produced as a result of depleted oxygen and water in a reactor also support the observations made here that temperature appears to have little effect on olefin conversion; in fact, elevated temperature may result in increased homogeneous reactions resulting in increased olefin production. Figure 6.26 shows olefin level increasing with operating time for each experimental run. For each experimental run prior to the last run, olefin levels decrease with increasing O/C ratio (reactor temperature rises with increasing O/C ratio). This holds true until the last displayed run (operating time 61.6 to 65.3 hours), where increasing the reactor O/C ratio (increasing reactor temperature) results in increased olefin production.



(a)



(b)

Figure 6.26 Reactor performance degradation as a result of exposure to periodic high levels (≥ 1 mole%) of olefins. All at fuel flows 5.9 ml/min. (3.33 kWth) JP-8 with S/C = 2.0, O/C of 1.0 (for Fig. 6.18a and as shown for Fig. 6.18b), reactor entrance temperature $425\text{ }^{\circ}\text{C} \pm 25\text{ }^{\circ}\text{C}$, and enrichment number (Ψ) of 1.0 (air). The GHSV was from 20,500 hr^{-1} to 26,000 hr^{-1} . [* all percentages are liquid volume percent].

6.5 JP-8 reforming with air ($\Psi = 1$) summary

Based on the results from prior sections overall observations on ATR with air are highlighted below:

- The experimental apparatus designed for his thesis and discussed in Chapter 3 has demonstrated excellent performance, is controllable over a wide range of operating conditions and has avoided serious operating problems such as pre-reactor oxidation of reactants and associated sooting. Additionally, results are good (high hydrogen yields) and are corroborated by published results from similar experiments.
- It is possible to reform with air JP-8 and heavy hydrocarbons fuels to completion over a wide range of fuel flow rates and S/C ratios. Additionally, reformat products which are compatible with fuel cells can be produced. However, the reformat product stream is diluted by nitrogen.
- ATRs have a distinctive temperature profile consisting of zones where endothermic and exothermic reactions dominate. In the first third of the reactor, exothermic reactions dominate and maximum reactor temperatures are obtained. In the middle third of the reactor, endothermic reactions consisting of steam reforming and pyrolysis of long chain alkanes dominant and the temperature profiles shows a steep decrease. In the final third of the reactor both endothermic steam reforming of hydrocarbons and slightly exothermic WGS reactions dominant and the reactor temperature continues to gradually decrease. The O/C ratio has a direct and strong effect on reformer temperature profile.

- Variation in S/C ratio has a direct and positive effect on reformer efficiency assuming that excess energy is available to vaporize and preheat the water. Therefore, to the degree that waste heat and/or energy is available within the system, higher S/C ratios are beneficial. However, if additional fuel must be consumed to vaporize water, then higher S/C ratios can have a strong negative effect of reformer efficiency.
- S/C ratio does show a strong influence in the conversion of hydrocarbons and olefin within the reactor. This is very important as hydrocarbons and olefins in the product stream are closely associated with carbon formation within the reformer. Significant improvement in hydrocarbon conversion was observed when raising the S/C ratio to 2.0 from 1.5; however, no additional benefit was seen in going to S/C ratios of 2.5 and 3.0.
- Variation of fuel flow served to identify the optimum rating of the reactor which for this reactor is between 3.33 kW_{th} and 5.0 kW_{th}. The analysis based on fuel conversion indicated that the optimum rating of the reactor is closer to 5.0 kW_{th}, however, to minimize olefin production and ensure long-term durability a rating closer to 3.33 kW_{th} seem more appropriate. The optimum rating is a function of reactor physical configuration and selected fuel where there is a balance between endothermic and exothermic reactions, heat loss, reaction kinetics, mass transfer and residence time of reactant in order to achieve a desired reformat product. Raising the fuel flow with fixed reactor inlet temperature conditions places more energy into the reactor raising the reactors operating temperature and reducing the

thermal losses as a function of fuel flow all of which improve reformer performance. However, with increased fuel flow the space-time is significantly reduced and eventually insufficient time is available for fuel to fully convert into desired products and the reformer performance falls off.

- Every reactor configuration results in an optimum operating conditions that balances endothermic and exothermic reactions, heat loss, reaction kinetics, mass transfer and residence time of reactant in order to achieve a desired reformat product.

6.6 JP-8 surrogate fuel reforming with enriched air

Thus far all results have focused on reforming with air. An unavoidable consequence of this is that the reformat product stream typically consists of between 40% to 50% nitrogen. Nitrogen does not participate in reforming reactions and provides little useful benefit. The presence of nitrogen does dictate the size of systems, require parasitic energy for pumping and heating, significantly reduces reactant residence times and may interfere with reaction kinetics. The following sections address the performance of an ATR reactor with variable oxygen enrichment and the affects on an oxygen enriched ATR with varying fuel feeds. Based on the results from prior sections the S/C ratio was held a 2.0, which proved best for overall reformer performance, and hydrocarbon and olefin fuels conversion. For all tests with enriched oxygen; the enriched oxygen was obtained from compressed gas cylinders where the ratio of nitrogen and oxygen was set by the manufacturer (AirGas, Inc.) to prescribed ratios as a primary gas standard.

Primary gas standards, which are the most accurate grade available, meets or exceeds a blend tolerance of $\pm 1\%$ with an analytical tolerance of $\pm 0.02\%$.

6.6.1 JP-8 surrogate fuel reforming with enriched oxygen at 5.0 kW_{th}

At a fuel flow of 8.84 ml/min. (5.0 kW_{th}) an experimental ATR as described in Chapter 3 was operate under varying O/C ratios with oxygen concentrations (with balance nitrogen) of 17% ($\Psi = 0.477$), 20.95 % ($\Psi = 1.00$), 30% ($\Psi=1.43$), and 40% ($\Psi = 1.91$). Fuel conversion and reactor maximum and exit temperatures are shown in Fig. 6.27. Fuel conversion shown in Fig. 6.27a, shows that as the oxygen enrichment is increased, full fuel conversion occurs at lower O/C ratios. Reactor temperatures for O/C ratios greater than 0.95 also show a strong correlation to enrichment with higher maximum and exit temperatures going with higher enrichment numbers. At O/C ratios below 0.95, temperatures converge; however, there is still a distinct variation in fuel conversion. This difference in fuel conversion appears to be a function of reactor space time; with longer reactor space times resulting in more complete fuel conversion. Figure 6.28 displays reactor space time for each enrichment experiment. As would be expected space time is strongly influenced by oxygen enrichment and has an inverse relationship to the enrichment number. Based on the result of Fig. 6.27b and 6.28, it appears that at O/C ratios greater than 0.95 reactor temperature and reactant concentration strongly influence fuel conversion, but below an O/C of 0.95, where reactors temperatures are lower and reaction kinetics slow, the reactor space time and lower reactant concentrations strongly influence fuel conversion.

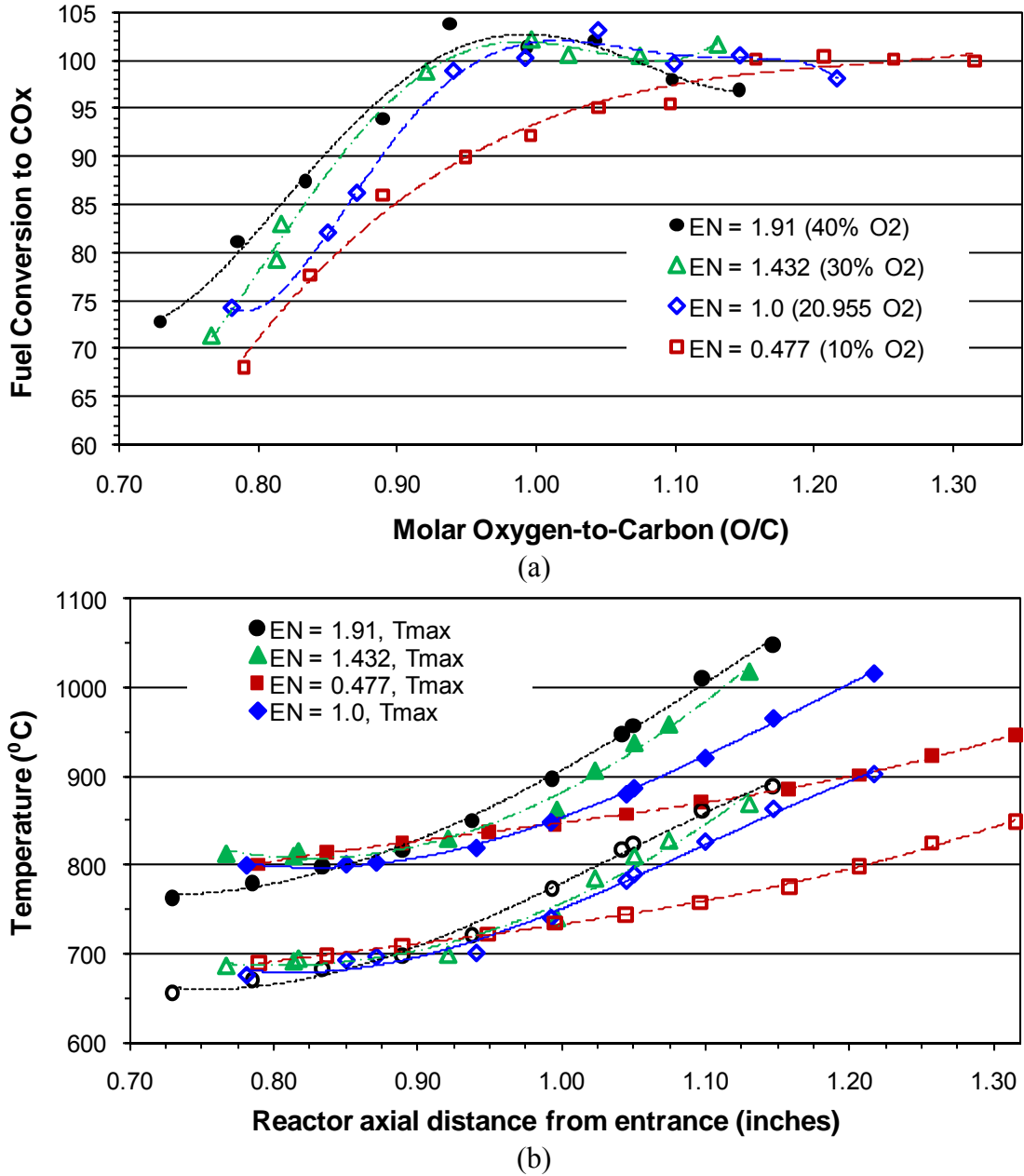


Figure 6.27 Normalized fuel conversion (a) and reactor maximum and exit temperatures (b) with JP-8 fuel flows of 8.84 ml/min. (5.0 kW_{th}) with oxygen enrichment (Ψ) of 0.477, 1.0, 1.432 and 1.91. The GHSV for $\Psi = 0.477$ was from 48,600 hr⁻¹ to 69,500 hr⁻¹, for $\Psi = 1.0$ was from 32,400 hr⁻¹ to 40,400 hr⁻¹, for $\Psi = 1.432$ was from 26,600 hr⁻¹ to 31,400 hr⁻¹, and for $\Psi = 1.91$ was from 23,600 hr⁻¹ to 27,800 hr⁻¹.

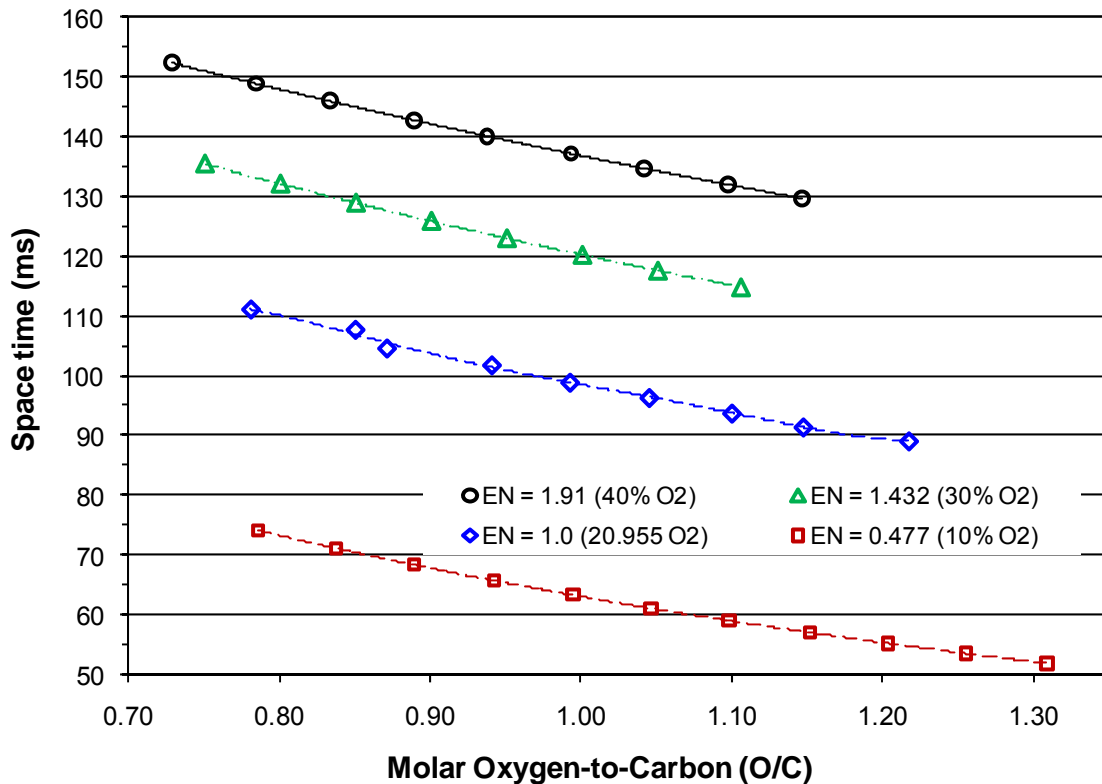


Figure 6.28 Space time for JP-8 fuel flows of 8.84 ml/min.(5.0 kW_{th}) with oxygen enrichment (Ψ) of 0.477, 1.0, 1.432 and 1.91 and reactor entrance temperature 425 °C \pm 25 °C. Ideal gas behavior is assumed under standard conditions.

Figures 6.29 and 6.30 display the hydrogen and carbon monoxide yields as a function of O/C ratio for four enrichment numbers. Peak hydrogen yield tends to follow enrichment number with higher hydrogen yields associated with higher enrichment numbers. Peak hydrogen yield correlates closely with the O/C ratio where full fuel conversion is achieved (Fig. 6.27a); therefore, the O/C ratio where peak hydrogen yield occurs is reduced as the enrichment number increases. Since operating at higher O/C ratios results in more fuel being oxidized and also greater nitrogen dilution downstream, the ability to operate at lower O/C ratios should result in better reformer and system

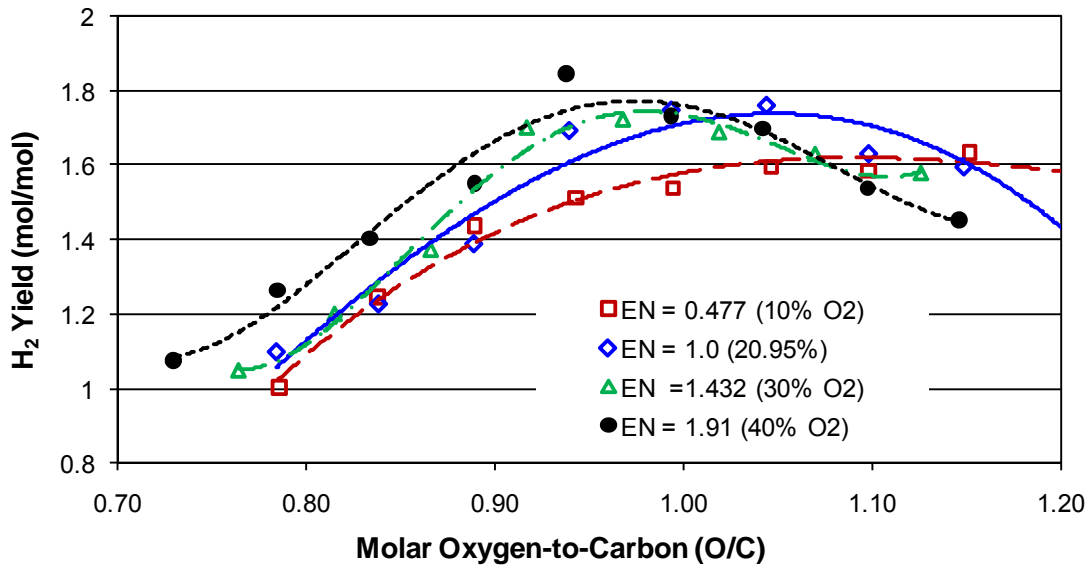


Figure 6.29 Hydrogen yield with surrogate JP-8 fuel flows of 8.84 ml/min.(5.0 kW_{th}) with oxygen enrichment (Ψ) of 0.477, 1.0, 1.432 and 1.91. The GHSV for Ψ = 0.477 was from 48,600 hr⁻¹ to 69,500 hr⁻¹, for Ψ = 1.0 was from 32,400 hr⁻¹ to 40,400 hr⁻¹, for Ψ = 1.432 was from 26,600 hr⁻¹ to 31,400 hr⁻¹, and for Ψ = 1.91 was from 23,600 hr⁻¹ to 27,800 hr⁻¹.

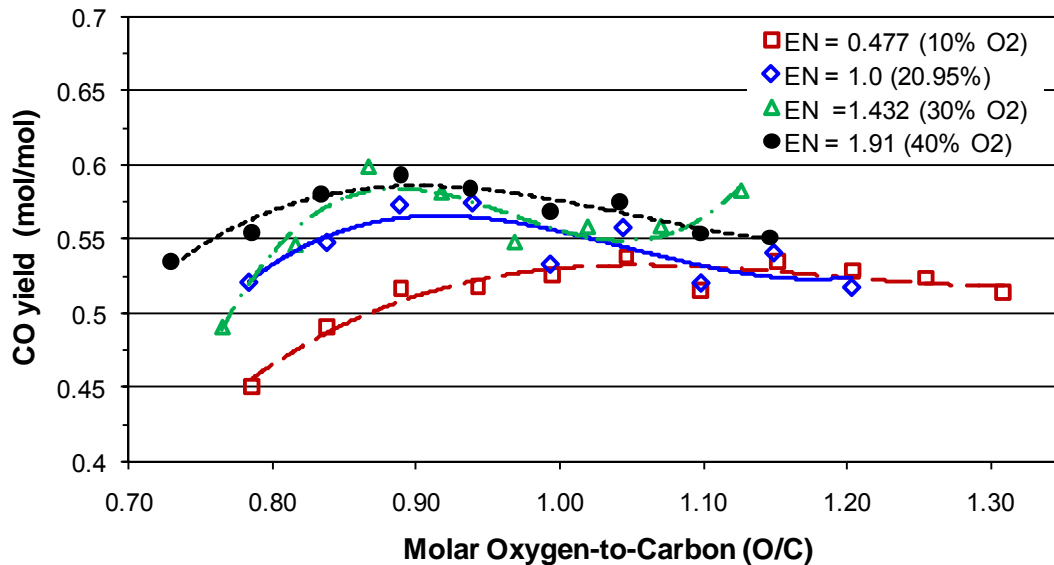
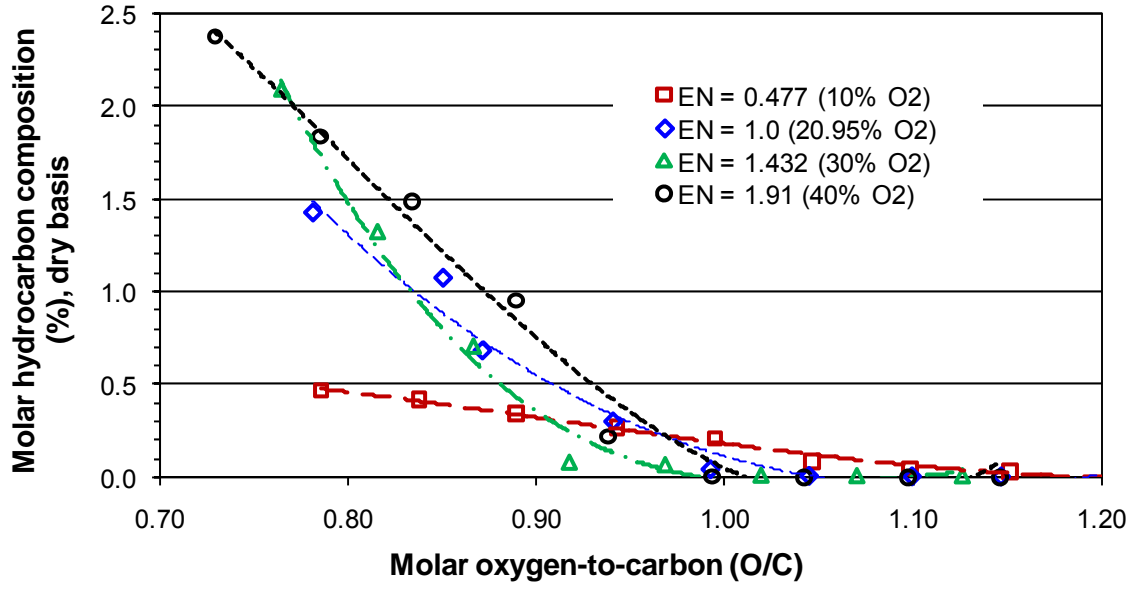


Figure 6.30 Carbon monoxide yield with surrogate JP-8 fuel flows of 8.84 ml/min.(5.0 kW_{th}) with oxygen enrichment (Ψ) of 0.477, 1.0, 1.432 and 1.91. The GHSV for Ψ = 0.477 was from 48,600 hr⁻¹ to 69,500 hr⁻¹, for Ψ = 1.0 was from 32,400 hr⁻¹ to 40,400 hr⁻¹, for Ψ = 1.432 was from 26,600 hr⁻¹ to 31,400 hr⁻¹, and for Ψ = 1.91 was from 23,600 hr⁻¹ to 27,800 hr⁻¹.

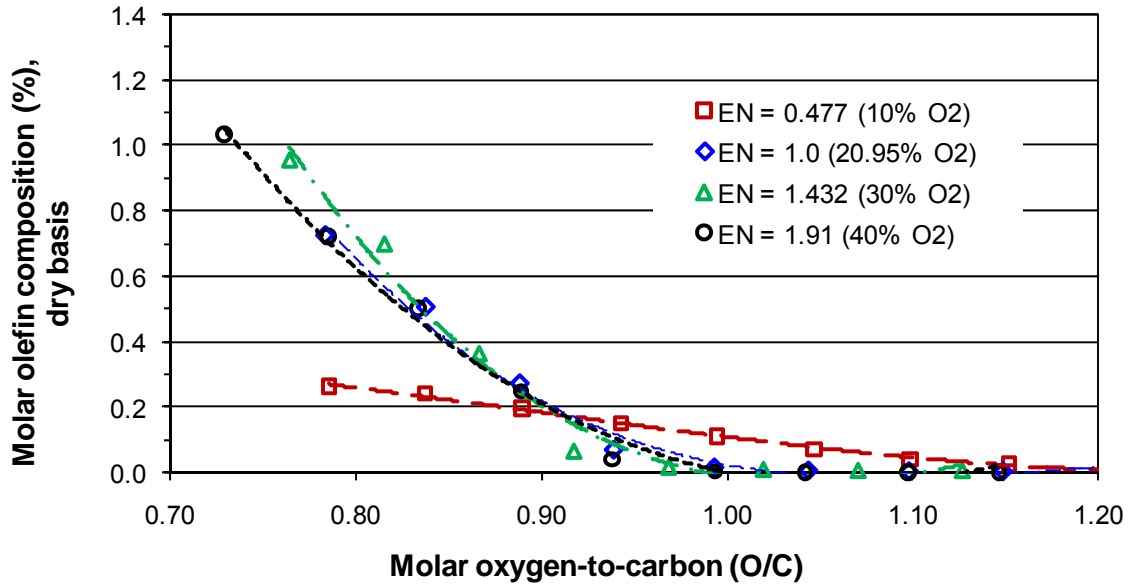
efficiencies. Carbon monoxide yield correlates well with enrichment number with higher enrichment numbers resulting in higher yields across all O/C ratios.

Figure 6.31 displays the composition of hydrocarbons species and olefins as a function of enrichment number and O/C ratio. There does not appear to be a clear and consistent relationship between enrichment number and olefin or hydrocarbon conversion. At O/C ratios above 1.0, increasing the enrichment number from 0.477 to 1.43 results in improved hydrocarbon and olefin conversion. However, at an enrichment number of 1.91, conversion for both hydrocarbons and olefins appears to occur at higher O/C ratios than for 1.43. Based on these results it appears that for hydrocarbon and olefin conversion there could be an optimum enrichment number. Further testing would be required to fully understand assess this observation.

Figure 6.32 displays the reformer efficiency as a function of enrichment number and O/C ratio. There is a very noticeable relationship between oxygen enrichment and efficiency with higher peak efficiencies, occurring at lower O/C ratios, correlating with higher oxygen enrichment levels. The peak reformer efficiencies for each enrichment number were 90% at an O/C ratio of 0.98 for enrichment number of 1.91, 88% at an O/C ratio of 1.02 for an enrichment number of 1.432, 86% at an O/C ratio of 1.08 for an enrichment number of 1.0, and 81% at an O/C ratio of 1.16 for an enrichment number of 0.477. The use of oxygen enrichment provides a direct and significant improvement on reformer efficiency over air ($\Psi = 1.0$). Additionally, Fig. 6.33 shows the molar hydrogen



(a)



(b)

Figure 6.31 Molar hydrocarbon and olefin composition in reformate with surrogate JP-8 fuel flows of 8.84 ml/min. (5.0 kW_{th}) with oxygen enrichment (Ψ) of 0.477, 1.0, 1.432 and 1.91. The GHSV for $\Psi = 0.477$ was from 48,600 hr⁻¹ to 69,500 hr⁻¹, for $\Psi = 1.0$ was from 32,400 hr⁻¹ and 40,400 hr⁻¹, for $\Psi = 1.432$ was from 26,600 hr⁻¹ to 31,400 hr⁻¹, and for $\Psi = 1.91$ was from 23,600 hr⁻¹ to 27,800 hr⁻¹.

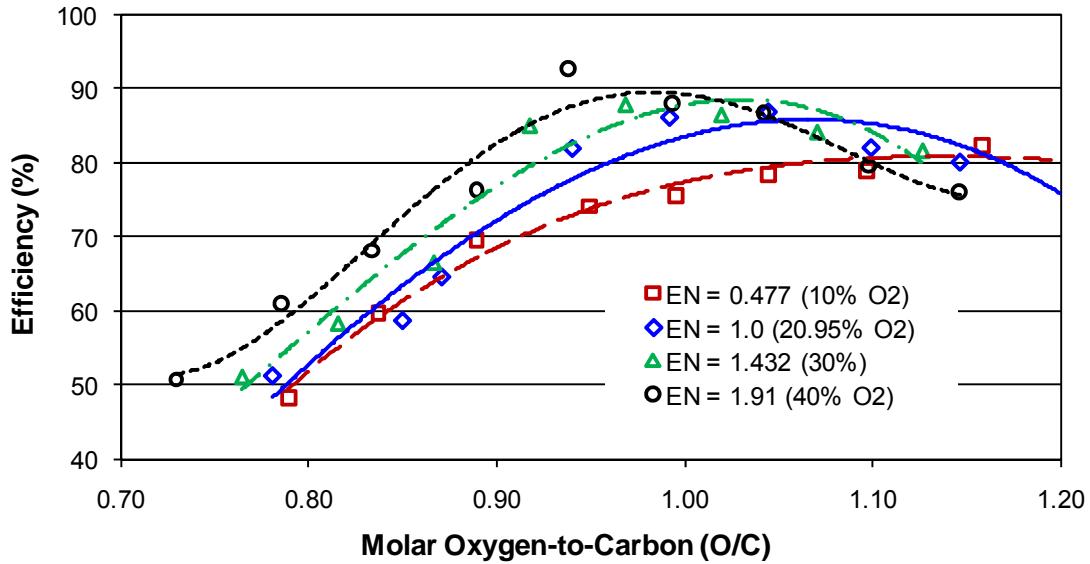


Figure 6.32 Reformer efficiency with surrogate JP-8 fuel flows of 8.84 ml/min. (5.0 kW_{th}) with oxygen enrichment (Ψ) of 0.477, 1.0, 1.432 and 1.91. The GHSV for Ψ = 0.477 was from 48,600 hr⁻¹ to 69,500 hr⁻¹, for Ψ = 1.0 was from 32,400 hr⁻¹ to 40,400 hr⁻¹, for Ψ = 1.432 was from 26,600 hr⁻¹ to 31,400 hr⁻¹, and for Ψ = 1.91 was from 23,600 hr⁻¹ to 27,800 hr⁻¹.

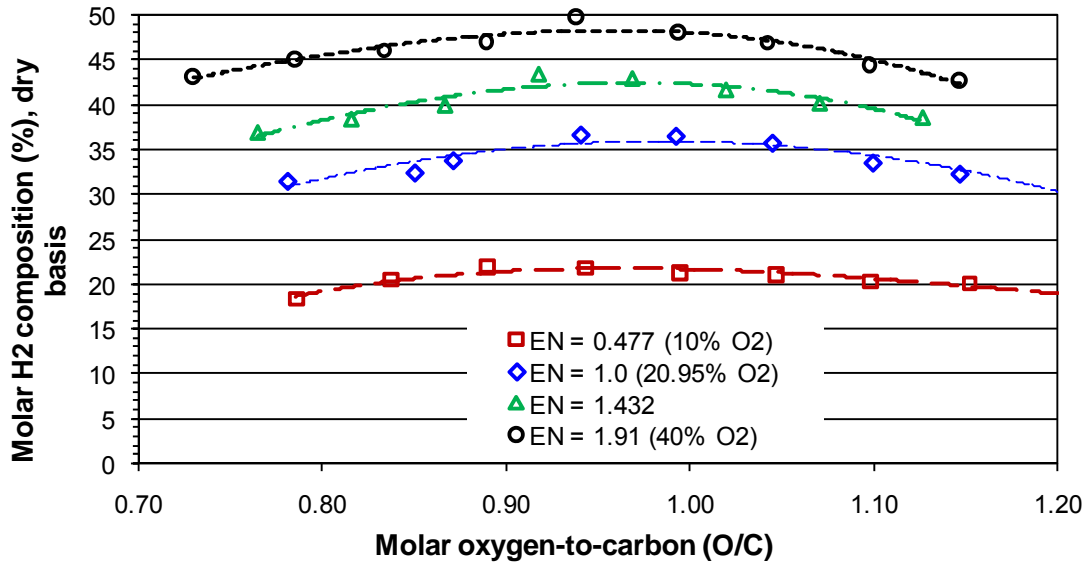


Figure 6.33 Molar hydrogen composition in reformate with surrogate JP-8 fuel flows of 8.84 ml/min. (5.0 kW_{th}) with oxygen enrichment (Ψ) of 0.477, 1.0, 1.432 and 1.91. The GHSV for Ψ = 0.477 was from 48,600 hr⁻¹ to 69,500 hr⁻¹, for Ψ = 1.0 was from 32,400 hr⁻¹ to 40,400 hr⁻¹, for Ψ = 1.432 was from 26,600 hr⁻¹ to 31,400 hr⁻¹, and for Ψ = 1.91 was from 23,600 hr⁻¹ to 27,800 hr⁻¹.

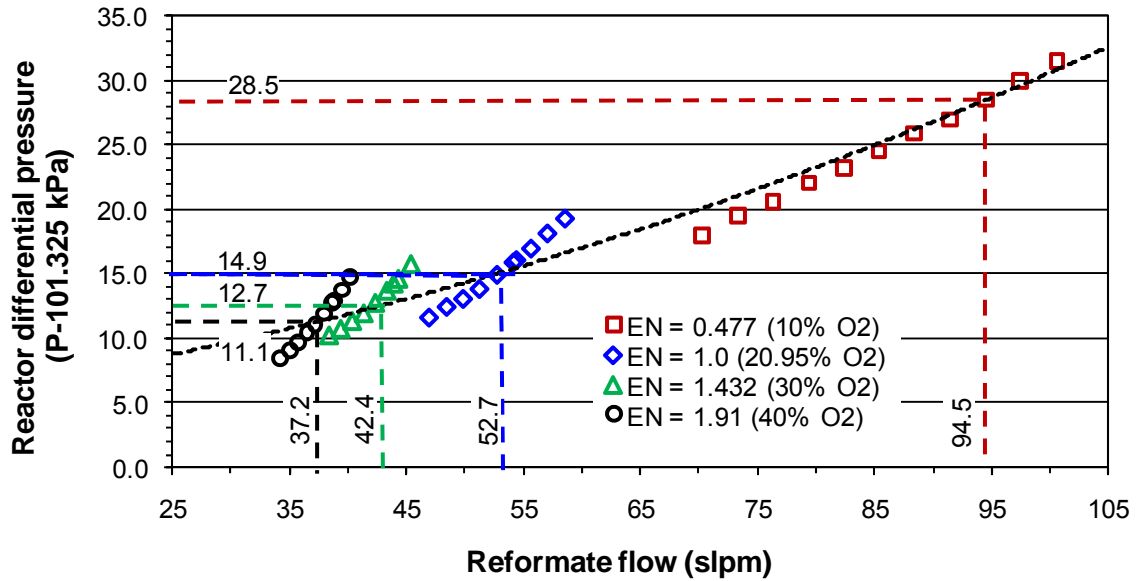
concentration in the reformat stream as a function of enrichment number and O/C ratio. Comparing oxygen enrichment of 1.91 (40% O₂) to 1.0 (20.95% O₂, air) a 39% increase in hydrogen concentration is achieved. The use of oxygen enrichment in autothermal reforming significantly increases the hydrogen concentration in reformat stream which has a direct influence on system parasitic pumping power and also can have a positive influence on the size and efficiency of the fuel cell stack. Figure 6.34a displays the reactor pressure drop as a function of enrichment number and reformat flow rate. Identified on Fig. 6.34a are the designs operating points for enrichment numbers of 0.477, 1.0, 1.432 and 1.91. The pumping power is calculated by Eqn. 6-4 below:

$$P_{flow} = \frac{\dot{V} \cdot \Delta p}{\eta_{pump}} \cdot 100\% \quad 6-4$$

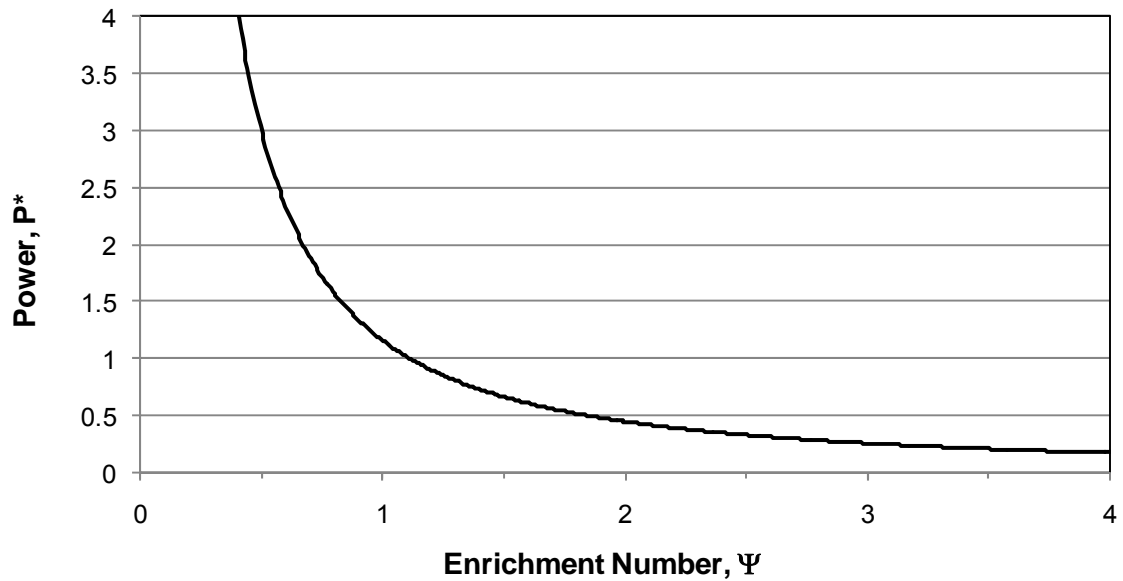
where \dot{V} is the reformat volume flow, Δp is the reformer pressure drop and η_{pump} is the efficiency of the gas pump²⁴. Based on the optimum operating points shown in Fig. 6.34a estimates for reformer operating pressure drop and reformat flow rate at other enrichment numbers can be derived. In Eqn. 6-5 below, a dimensionless number for power as a function of enrichment number is given:

$$P^* = \frac{P_{flow}(\Psi)}{P_{flow}(\Psi = 1)} \quad 6-5$$

²⁴ The effect of changes in reformer pressure drop will have an effect on the fuel and water pump, but since these are ideally pumping incompressible liquids little effect on power will result and have been ignored for simplification.



(a)



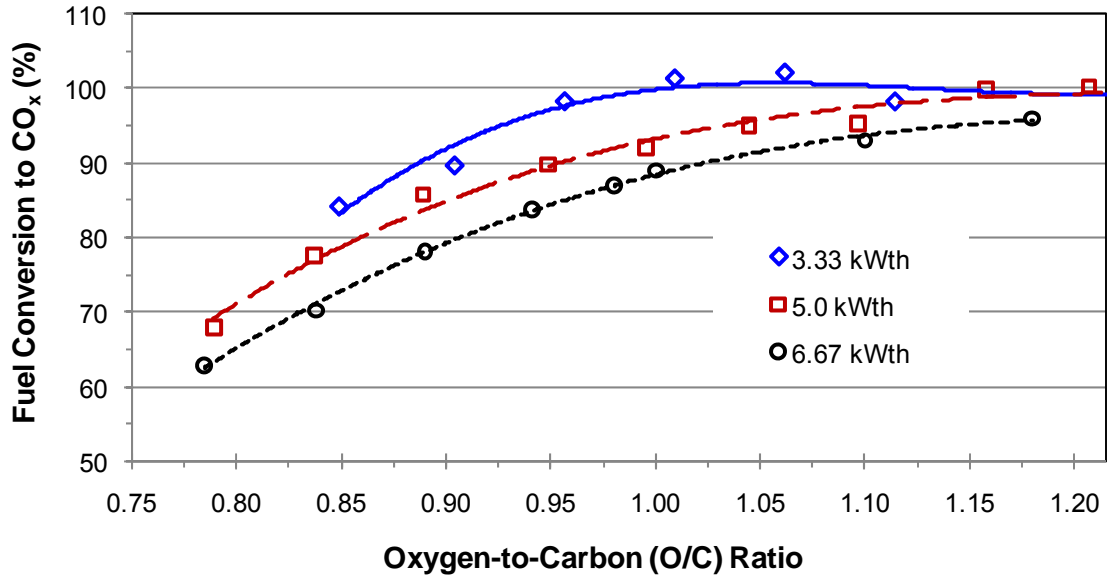
(b)

Figure 6.34 Reactor differential pressure with surrogate JP-8 fuel flows of 8.84 ml/min. (5.0 kW_{th}) with oxygen enrichment (Ψ) of 0.477, 1.0, 1.432 and 1.91. The GHSV for $\Psi = 0.477$ was from 48,600 hr⁻¹ to 69,500 hr⁻¹, for $\Psi = 1.0$ was from 32,400 hr⁻¹ and 40,400 hr⁻¹, for $\Psi = 1.432$ was from 26,600 hr⁻¹ to 31,400 hr⁻¹, and for $\Psi = 1.91$ was from 23,600 hr⁻¹ to 27,800 hr⁻¹.

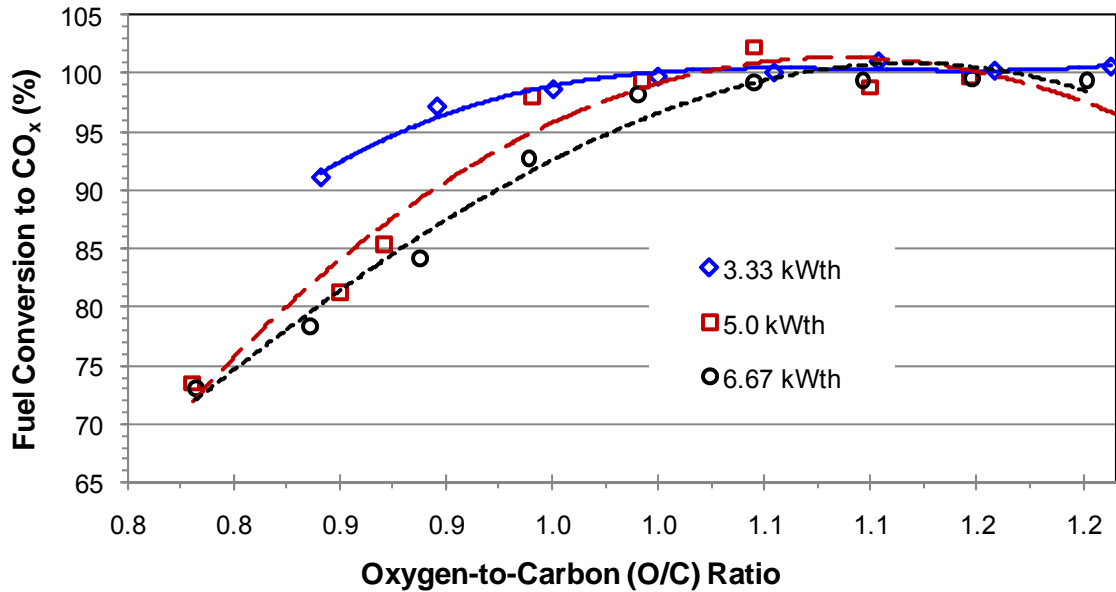
Figure 6.34b shows the relationship between enrichment number and the dimensionless power for optimum reforming at a 5 kW_{th} rating. A power reduction of 31.4% is achieved in going from an enrichment number of 1.0 to 1.432 and a power reduction of 47.4% is achieved from an enrichment number of 1.91.

6.6.2 JP-8 surrogate fuel reforming with enriched oxygen and varying fuel flows

Surrogate JP-8 fuel flows of 5.9 ml/min. (3.33 kW_{th}), 8.84 ml/min. (5.0 kW_{th}), 11.8 ml/min. (6.67 kW_{th}) and 14.75 ml/min. (8.33 kW_{th}) were reformed in an ATR as described in Chapter 3 with oxygen enrichment numbers of 0.477, 1.0, 1.432 and 1.91 and S/C ratio of 2.0. Figure 6.35 displays the fuel conversion for each of the four fuel flow conditions and enrichment numbers. For Fig.'s 6.35a and 6.35b the 8.33 kW_{th} fuel flow is not displayed, as this condition exceeds the pressure threshold of the reactor which is 34.5 kPa differential pressure. Figure 35a shows that with a very dilute oxygen stream ($\Psi = 0.477$) the point of full fuel conversion moves to higher O/C ratios as the fuel feed is increased. At a fuel feed equating to 6.67 kW_{th}, the reactor is unable to fully convert the fuel due to a combination of insufficient temperature and space time. As the enrichment is increased from 0.477 (Fig. 6.35a) to 1.0 (Fig. 35b) the points of full fuel conversion move to lower O/C ratios for each fuel flow. Also as the enrichment number increases the onset of full fuel conversion for different fuel flows begins to converge, and as shown in Fig. 35d, the fuel conversion curves become coincident.



(a)



(b)

Figure 6.35 Normalized fuel conversion for enrichment number (Ψ) of 0.477 (a) and 1.0 (b) with surrogate JP-8 fuel flows of 5.9 ml/min. (3.33 kW_{th}), 8.84 ml/min. (5.0 kW_{th}), 11.8 ml/min. (6.67 kW_{th}), and 14.7 ml/min. (8.33 kW_{th}). The GHSV for $\Psi = 0.477$ (a) was from 33,900 hr⁻¹ to 40,900 hr⁻¹ (3.33 kW_{th}), 48,600 hr⁻¹ to 69,500 hr⁻¹ (5.0 kW_{th}), and 54,700 hr⁻¹ to 67,200 hr⁻¹ (6.67 kW_{th}). The GHSV for $\Psi = 1.0$ (b) was from 22,200 hr⁻¹ to 26,900 hr⁻¹ (3.33 kW_{th}), 32,400 hr⁻¹ to 40,400 hr⁻¹ (5.0 kW_{th}), and 43,200 hr⁻¹ to 53,800 hr⁻¹ (6.67 kW_{th}).

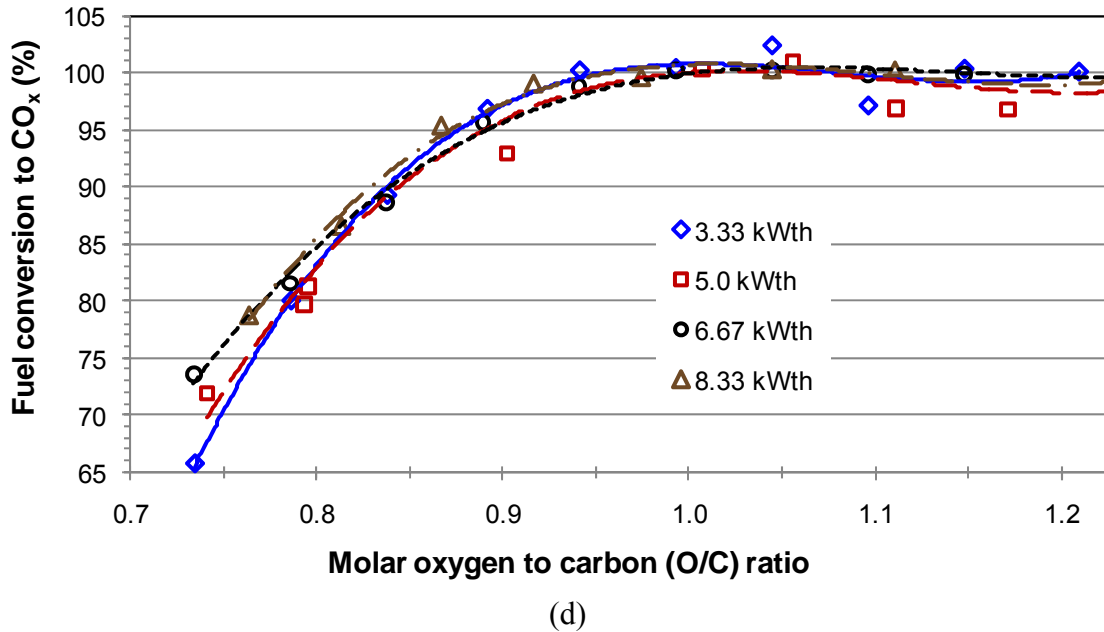
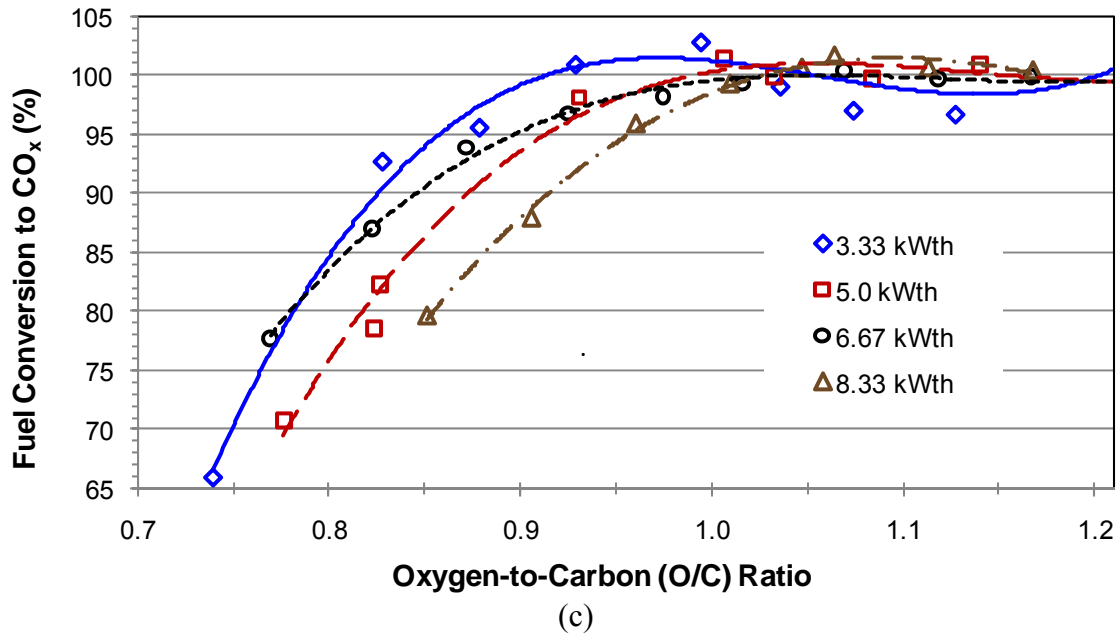


Figure 6.35 (con't) Normalized fuel conversion for enrichment number (Ψ) of 1.432 (c) and 1.91 (d) with surrogate JP-8 fuel flows of 5.9 ml/min. (3.33 kW_{th}), 8.84 ml/min. (5.0 kW_{th}), 11.8 ml/min. (6.67 kW_{th}), and 14.7 ml/min (8.33 kW_{th}). The GHSV for $\Psi = 1.432$ (c) was from 18,800 hr⁻¹ to 21,500 hr⁻¹ (3.33 kW_{th}), 26,600 hr⁻¹ to 31,300 hr⁻¹ (5.0 kW_{th}), 35,600 hr⁻¹ to 42,900 hr⁻¹ (6.67 kW_{th}), and 45,500 hr⁻¹ to 53,400 hr⁻¹ (8.33 kW_{th}). The GHSV for $\Psi = 1.91$ (d) was from 16,500 hr⁻¹ to 19,200 hr⁻¹ (3.33 kW_{th}), 23,600 hr⁻¹ to 27,800 hr⁻¹ (5.0 kW_{th}), and 31,900 hr⁻¹ to 37,400 hr⁻¹ (6.67 kW_{th}), and 41,100 hr⁻¹ to 46,800 hr⁻¹ (8.33 kW_{th}).

Reactor maximum and exit temperatures for each combination of enrichment number and fuel flow rating are displayed in Fig. 6.36. In general, with increasing fuel flow for a fixed enrichment number, the operating temperature of the reactor increases and the space time decreases. With increasing enrichment number the temperature of the reactor rises and the space time increases resulting in improved conditions for fuel conversion. The importance of the result in Fig. 6.35d is that under the test conditions the reactor has reached its equilibrium limits and is therefore, no longer limited by reaction kinetics or mass transfer. Further increases in enrichment number would not provide any additional benefit in terms of fuel conversion. Good reactor design, where the capability of the reactor is put to full use, is usually mass transfer limited. Therefore, the fuel flow capacity of the reformer has not been reached at the 8.33 kW_{th} rating. Further experimentation to determine the limit of the reactor could not be pursued due to limitation of reactor maximum design operating pressure. From the results of Fig. 6.35, the effective capacity of the reactor has been increased by a minimum of 150% through the use of oxygen enrichment.

The carbon monoxide yield is presented in Fig. 6.37. In general, carbon monoxide yield is directly related to fuel feed and the peak carbon monoxide yield increases slightly with increasing enrichment number. The shape of the carbon monoxide yield curve is usually sinusoidal and the water gas shift (WGS) equation (Eqn. 6-1) provides some insight into the relationship between carbon monoxide and hydrogen production. At O/C ratios less than 0.85 low carbon monoxide levels result from low fuel conversion and the presence

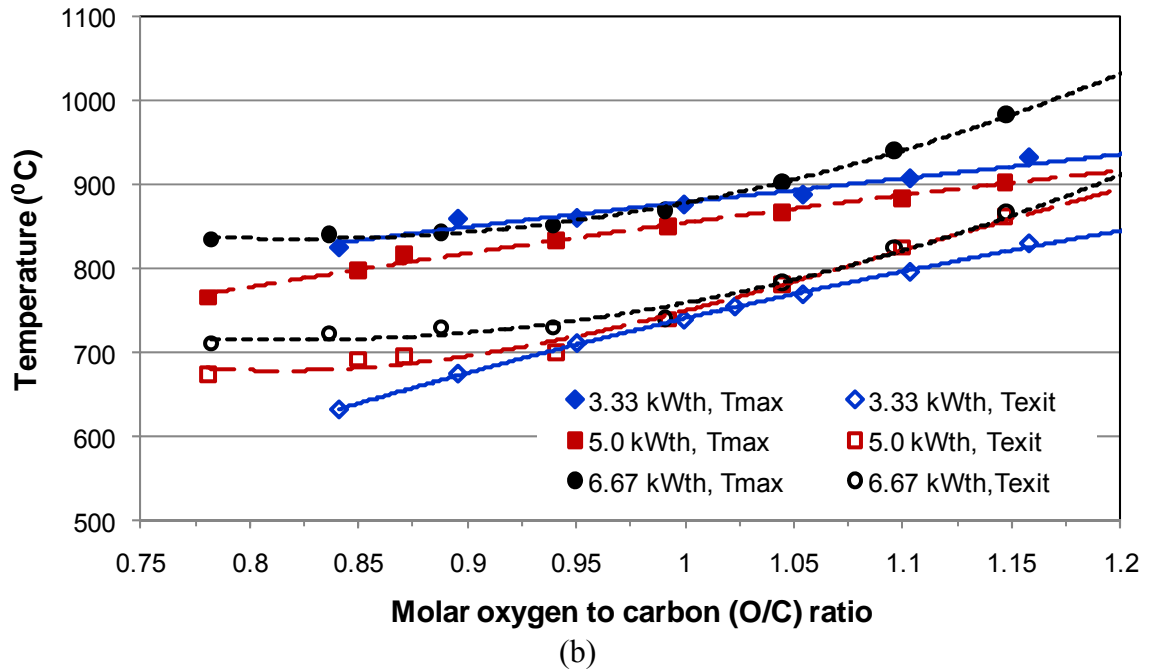
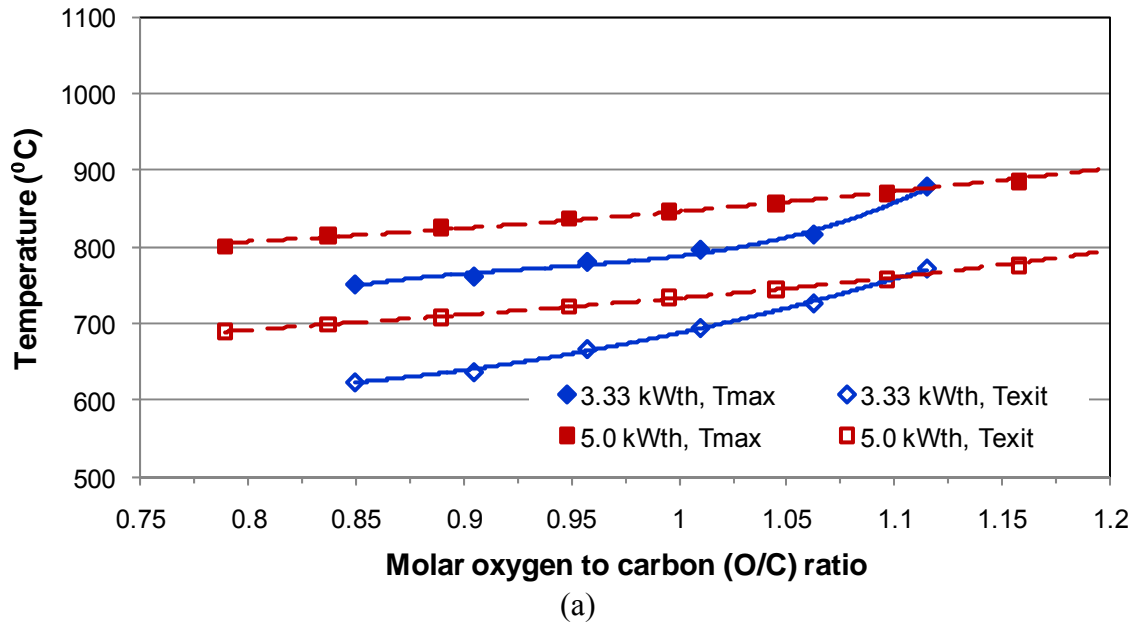


Figure 6.36 Reactor maximum and exit temperatures for enrichment number (Ψ) of 0.477 (a) and 1.0 (b) with surrogate JP-8 fuel flows of 5.9 ml/min. (3.33 kW_{th}), 8.84 ml/min. (5.0 kW_{th}), 11.8 ml/min. (6.67 kW_{th}), and 14.7 ml/min. (8.33 kW_{th}). The GHSV for $\Psi = 0.477$ (a) was from 33,900 hr⁻¹ to 40,900 hr⁻¹ (3.33 kW_{th}), 48,600 hr⁻¹ to 69,500 hr⁻¹ (5.0 kW_{th}), and 54,700 hr⁻¹ to 67,200 hr⁻¹ (6.67 kW_{th}). The GHSV for $\Psi = 1.0$ (b) was from 22,200 hr⁻¹ to 26,900 hr⁻¹ (3.33 kW_{th}), 32,400 hr⁻¹ to 40,400 hr⁻¹ (5.0 kW_{th}), and 43,200 hr⁻¹ to 53,800 hr⁻¹ (6.67 kW_{th}).

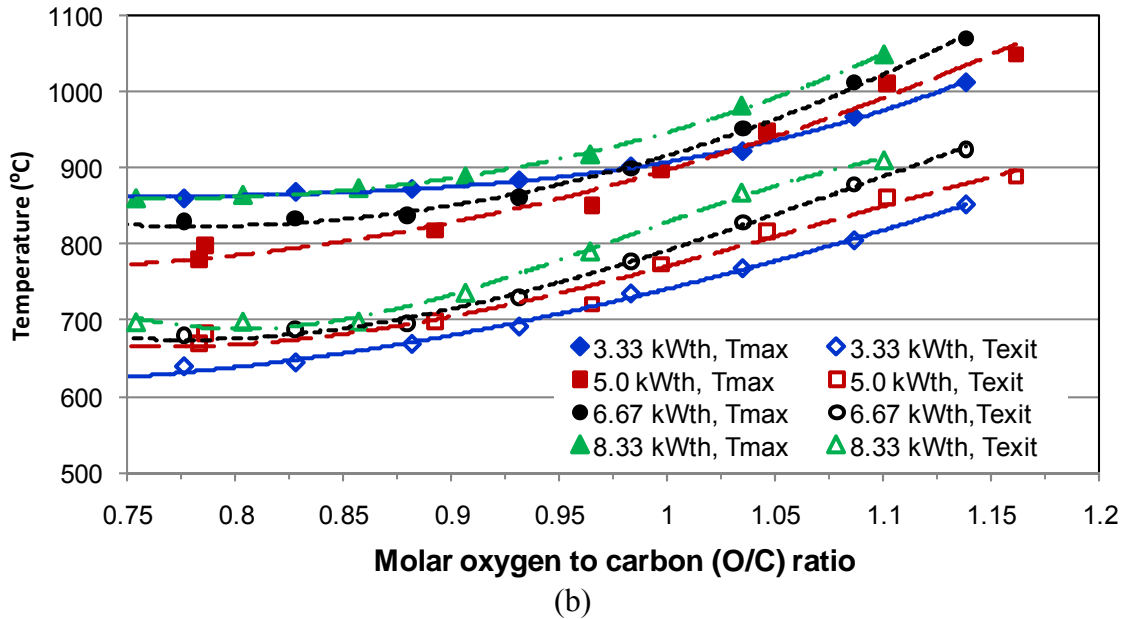
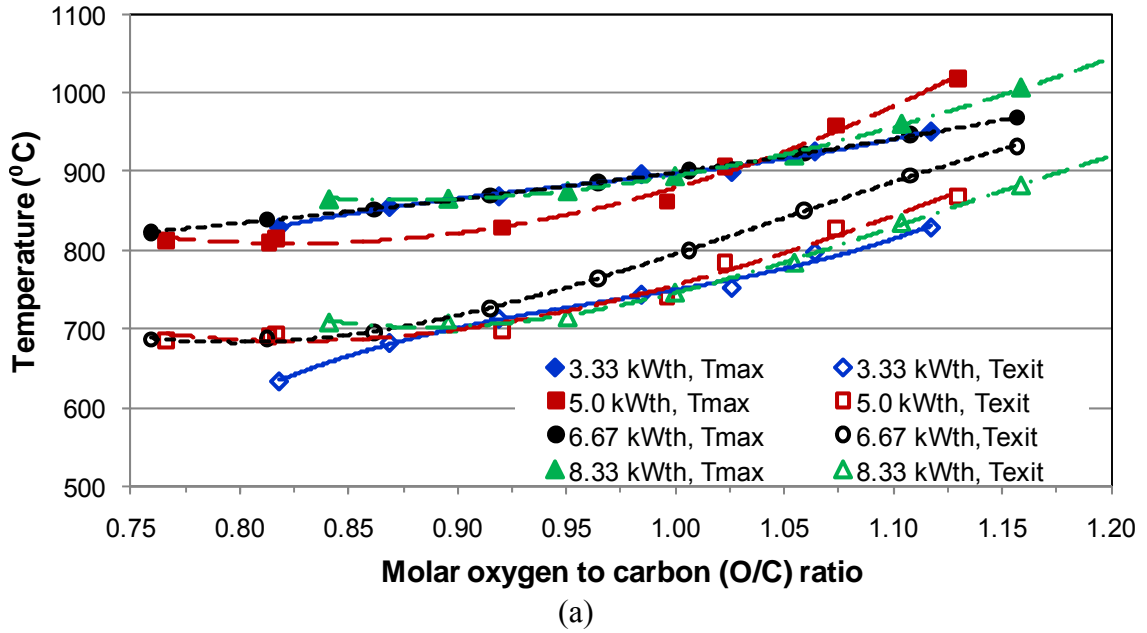
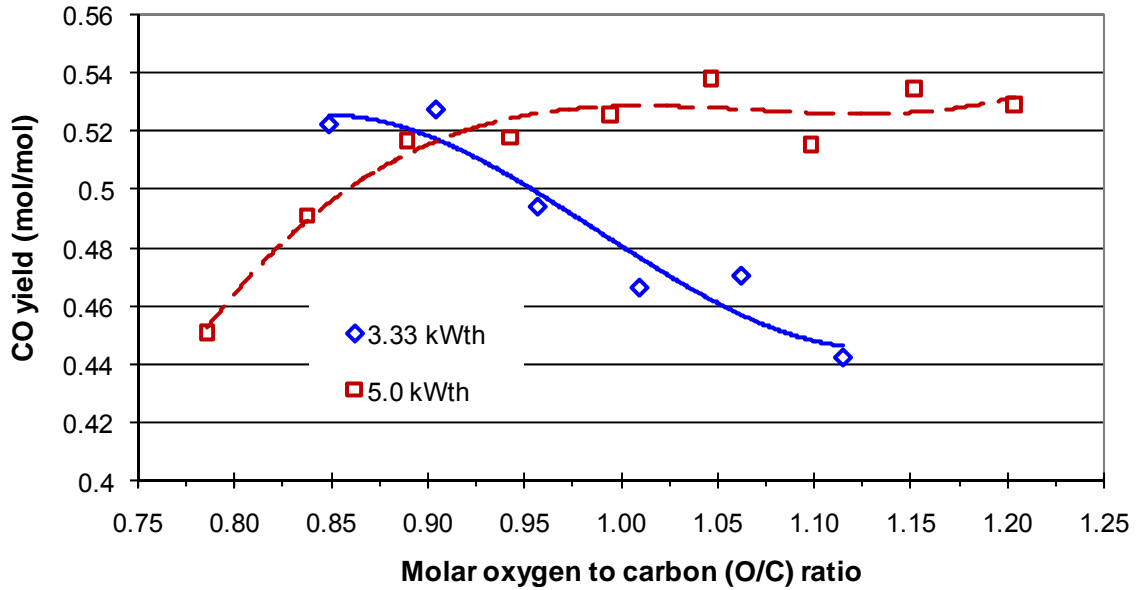
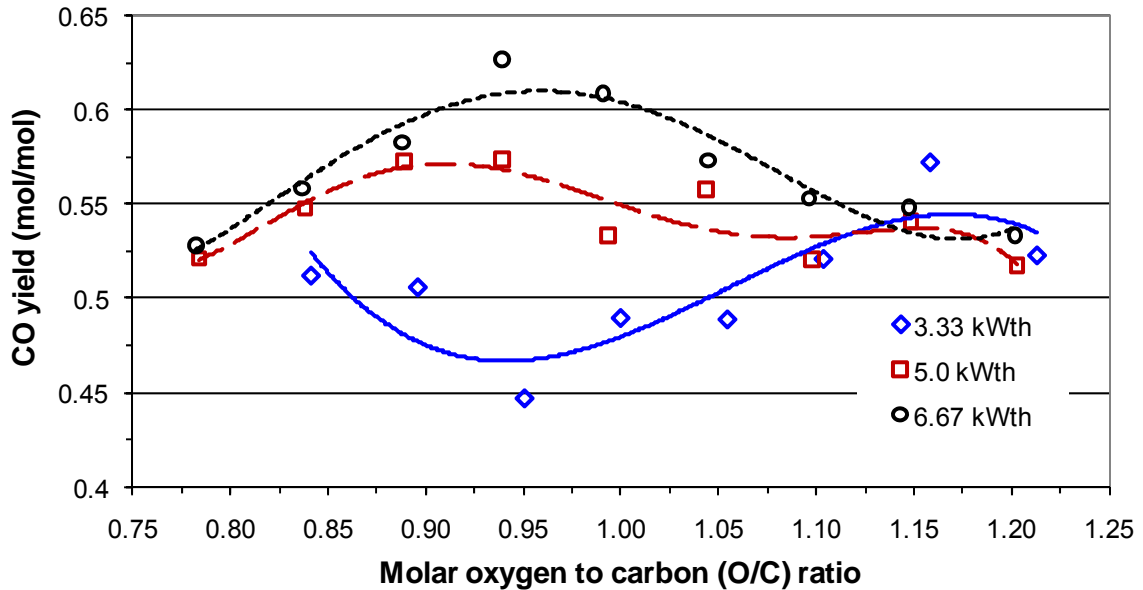


Figure 6.36 (con't) Reactor maximum and exit temperatures for enrichment number (Ψ) of 1.432 (c) and 1.91 (d) with surrogate JP-8 fuel flows of 5.9 ml/min. (3.33 kW_{th}), 8.84 ml/min. (5.0 kW_{th}), 11.8 ml/min. (6.67 kW_{th}), and 14.7 ml/min (8.33 kW_{th}). The GHSV for $\Psi = 1.432$ (c) was from 18,800 hr⁻¹ to 21,500 hr⁻¹ (3.33 kW_{th}), 26,600 hr⁻¹ to 31,300 hr⁻¹ (5.0 kW_{th}), 35,600 hr⁻¹ to 42,900 hr⁻¹ (6.67 kW_{th}), and 45,500 hr⁻¹ to 53,400 hr⁻¹ (8.33 kW_{th}). The GHSV for $\Psi = 1.91$ (d) was from 16,500 hr⁻¹ to 19,200 hr⁻¹ (3.33 kW_{th}), 23,600 hr⁻¹ to 27,800 hr⁻¹ (5.0 kW_{th}), and 31,900 hr⁻¹ to 37,400 hr⁻¹ (6.67 kW_{th}), and 41,100 hr⁻¹ to 46,800 hr⁻¹ (8.33 kW_{th}).



(a)



(b)

Figure 6.37 Carbon monoxide yields for enrichment number (Ψ) of 0.477 (a) and 1.0 (b) with surrogate JP-8 fuel flows of 5.9 ml/min. (3.33 kW_{th}), 8.84 ml/min. (5.0 kW_{th}), 11.8 ml/min. (6.67 kW_{th}), and 14.7 ml/min. (8.33 kW_{th}). The GHSV for $\Psi = 0.477$ (a) was from 33,900 hr⁻¹ to 40,900 hr⁻¹ (3.33 kW_{th}), 48,600 hr⁻¹ to 69,500 hr⁻¹ (5.0 kW_{th}), and 54,700 hr⁻¹ to 67,200 hr⁻¹ (6.67 kW_{th}). The GHSV for $\Psi = 1.0$ (b) was from 22,200 hr⁻¹ to 26,900 hr⁻¹ (3.33 kW_{th}), 32,400 hr⁻¹ to 40,400 hr⁻¹ (5.0 kW_{th}), and 43,200 hr⁻¹ to 53,800 hr⁻¹ (6.67 kW_{th}).

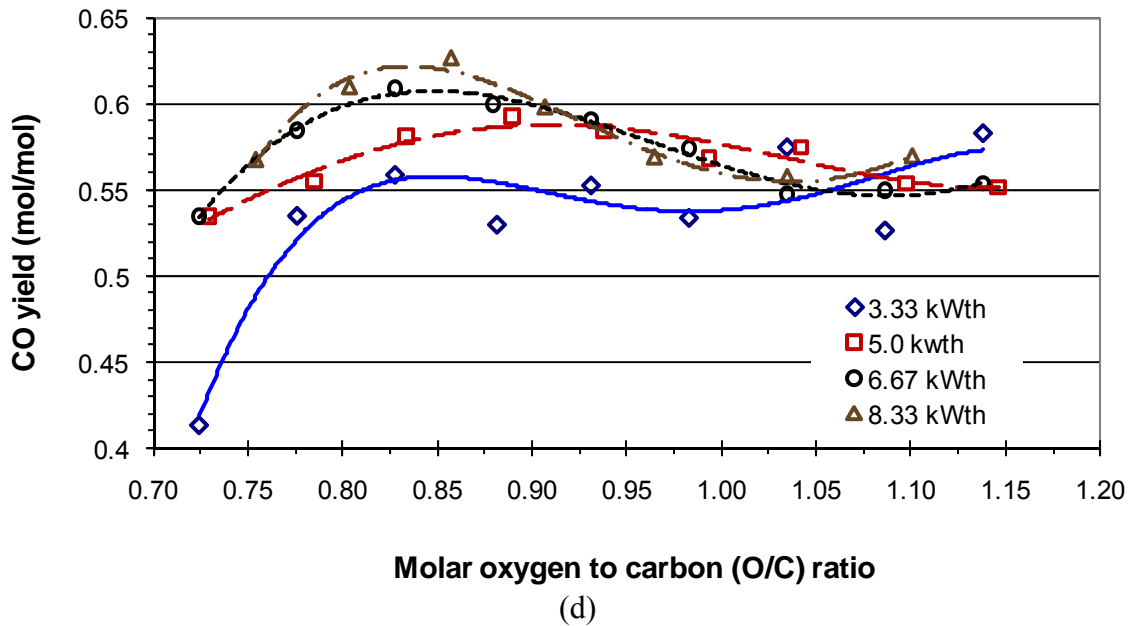
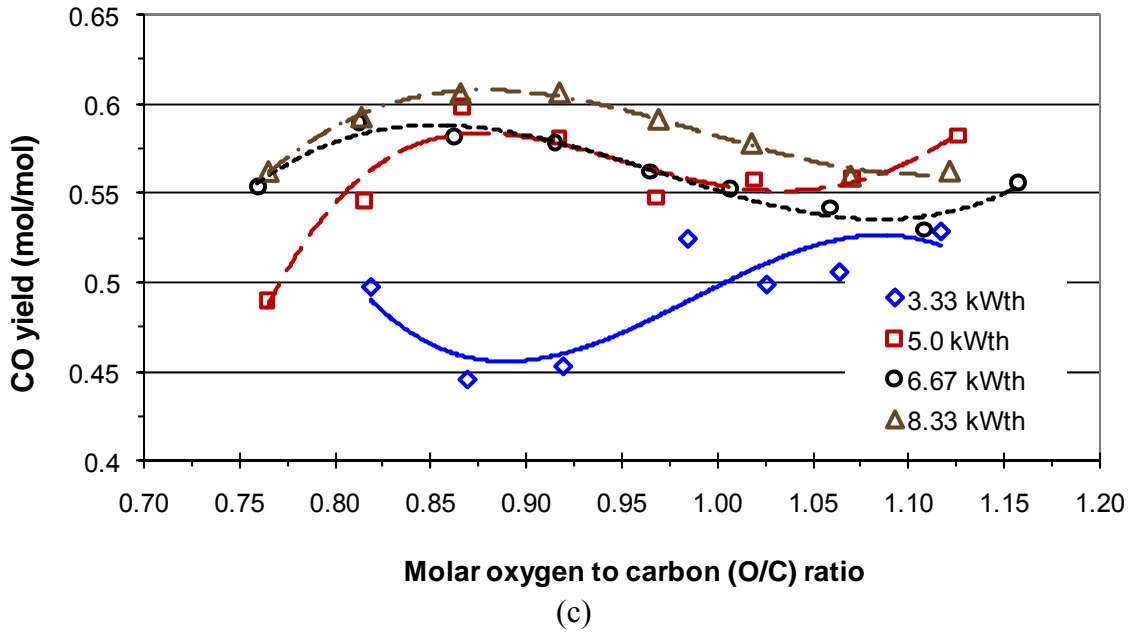
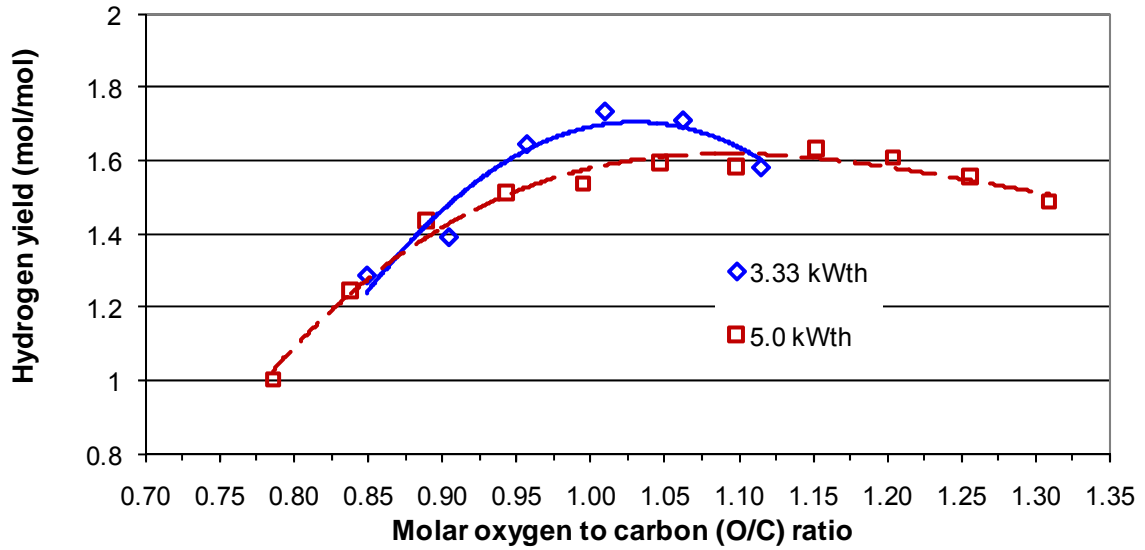


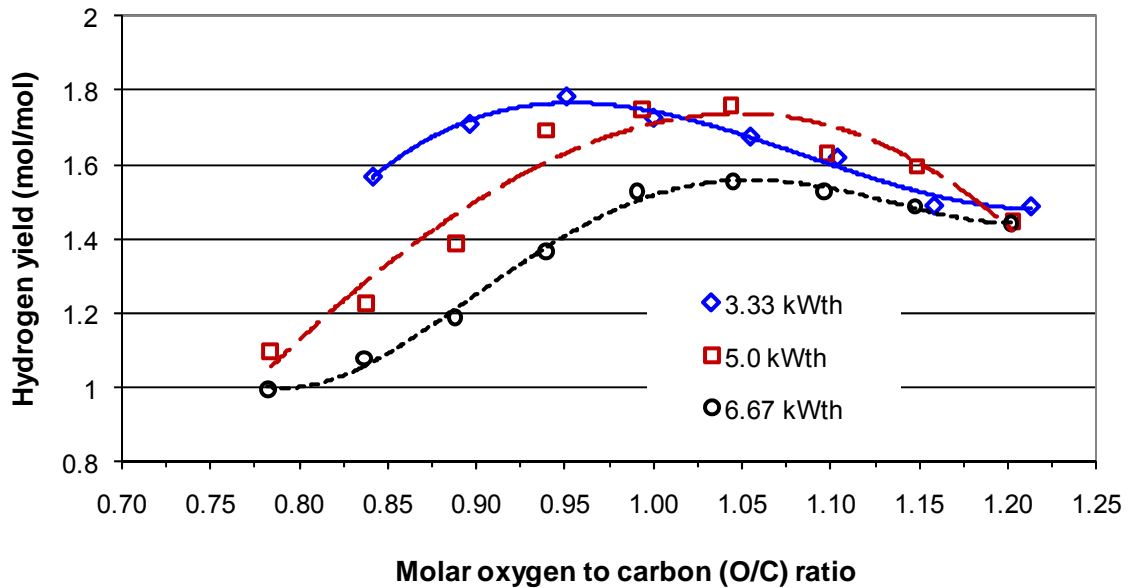
Figure 6.37 (con't) Carbon monoxide yield for enrichment number (Ψ) of 1.432 (c) and 1.91 (d) with surrogate JP-8 fuel flows of 5.9 ml/min. (3.33 kW_{th}), 8.84 ml/min. (5.0 kW_{th}), 11.8 ml/min. (6.67 kW_{th}), and 14.7 ml/min. (8.33 kW_{th}). The GHSV for $\Psi = 1.432$ (c) was from 18,800 hr⁻¹ to 21,500 hr⁻¹ (3.33 kW_{th}), 26,600 hr⁻¹ to 31,300 hr⁻¹ (5.0 kW_{th}), 35,600 hr⁻¹ to 42,900 hr⁻¹ (6.67 kW_{th}), and 45,500 hr⁻¹ to 53,400 hr⁻¹ (8.33 kW_{th}). The GHSV for $\Psi = 1.91$ (d) was from 16,500 hr⁻¹ to 19,200 hr⁻¹ (3.33 kW_{th}), 23,600 hr⁻¹ to 27,800 hr⁻¹ (5.0 kW_{th}), and 31,900 hr⁻¹ to 37,400 hr⁻¹ (6.67 kW_{th}), and 41,100 hr⁻¹ to 46,800 hr⁻¹ (8.33 kW_{th}).

of excess water. As fuel conversion increases, water is consumed in reforming reactions and the reactor temperature increases, all influencing the production of carbon monoxide. At O/C ratios associated with a high rates of hydrogen production, typically just prior to peak hydrogen yield (Fig. 6.38), the carbon monoxide yield is low (usually in the O/C range of 0.85 to 1.0). Peak hydrogen yield usually corresponds with a minimum in the carbon monoxide yield curve (at O/C's between 1.0 and 1.10). At O/C ratios from 1.10 to 1.25 the WGS equation is fairly balanced with hydrogen yield falling and carbon dioxide rising as a result of increased fuel oxidation resulting in a flat carbon yield curve.

Figure 6.38 displays the hydrogen yield as a function of enrichment number and fuel feed. As has been seen previously, peak hydrogen yield occurs at approximately the same O/C ratio as the point of full fuel conversion. For a given enrichment number, peak hydrogen yield is inversely related to fuel flow (lower fuel flows result in higher yields). However, reactor temperature increases with fuel flow. In general, most reactions are strongly influenced by temperature. An often quoted chemical reaction adage is, “..for every 10 °C increase, reaction rates double”. Looking at Fig. 6.38a for enrichment number 0.477, the average reaction temperature difference between 3.33 kW_{th} and 5.0kW_{th} is approximately 50 °C and the average space times are 96 ms for 3.33 kW_{th} and 60 ms for 5.0 kW_{th} (see Fig. 6.39 for reactor space time). The temperature difference would imply that reactions rates had increased on the order of 32 times; more than sufficient to overcome the increased amount of reactants and reduced space time. But here, this is not the case. Space time appears to strongly influence the ATR results. Most

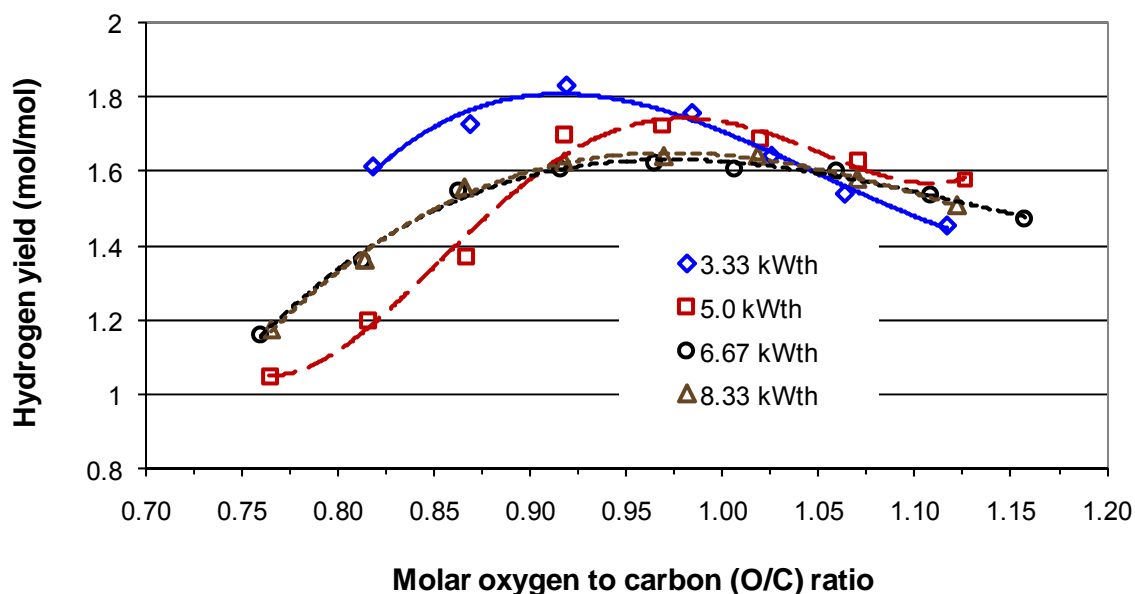


(a)

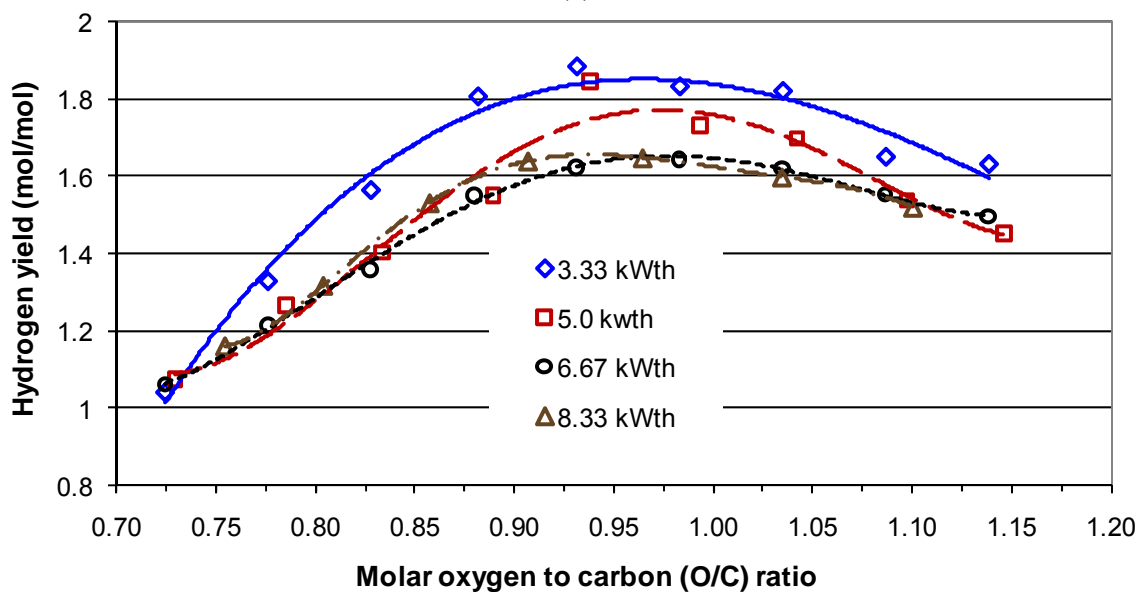


(b)

Figure 6.38 Hydrogen yield for enrichment number (Ψ) of 0.477 (a) and 1.0 (b) with surrogate JP-8 fuel flows of 5.9 ml/min. (3.33 kW_{th}), 8.84 ml/min. (5.0 kW_{th}), 11.8 ml/min. (6.67 kW_{th}), and 14.7 ml/min. (8.33 kW_{th}). The GHSV for $\Psi = 0.477$ (a) was from 33,900 hr⁻¹ to 40,900 hr⁻¹ (3.33 kW_{th}), 48,600 hr⁻¹ to 69,500 hr⁻¹ (5.0 kW_{th}), and 54,700 hr⁻¹ to 67,200 hr⁻¹ (6.67 kW_{th}). The GHSV for $\Psi = 1.0$ (b) was from 22,200 hr⁻¹ to 26,900 hr⁻¹ (3.33 kW_{th}), 32,400 hr⁻¹ to 40,400 hr⁻¹ (5.0 kW_{th}), and 43,200 hr⁻¹ to 53,800 hr⁻¹ (6.67 kW_{th}).

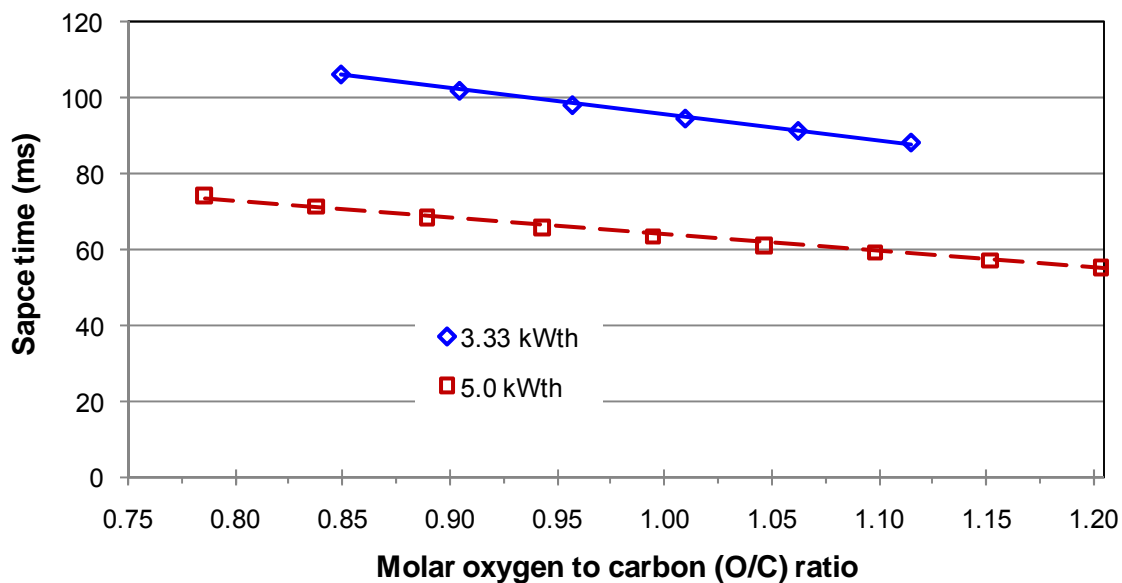


(c)

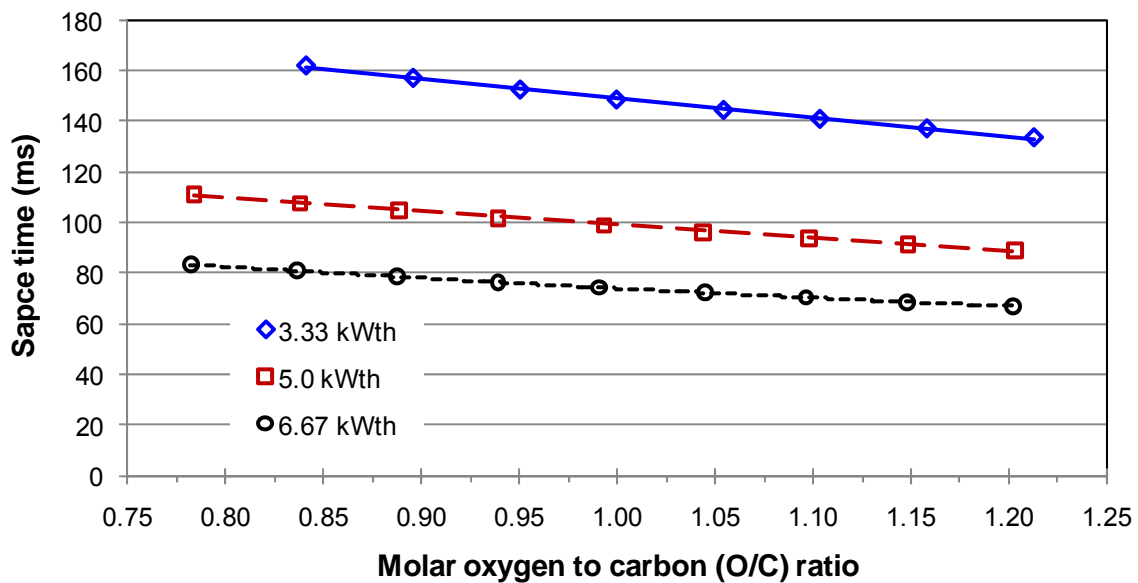


(d)

Figure 6.38 (con't) Hydrogen yields for enrichment number (Ψ) of 1.432 (c) and 1.91 (d) with surrogate JP-8 fuel flows of 5.9 ml/min. (3.33 kW_{th}), 8.84 ml/min. (5.0 kW_{th}), 11.8 ml/min. (6.67 kW_{th}), and 14.7 ml/min. (8.33 kW_{th}). The GHSV for $\Psi = 1.432$ (c) was from 18,800 hr⁻¹ to 21,500 hr⁻¹ (3.33 kW_{th}), 26,600 hr⁻¹ to 31,300 hr⁻¹ (5.0 kW_{th}), 35,600 hr⁻¹ to 42,900 hr⁻¹ (6.67 kW_{th}), and 45,500 hr⁻¹ to 53,400 hr⁻¹ (8.33 kW_{th}). The GHSV for $\Psi = 1.91$ (d) was from 16,500 hr⁻¹ to 19,200 hr⁻¹ (3.33 kW_{th}), 23,600 hr⁻¹ to 27,800 hr⁻¹ (5.0 kW_{th}), and 31,900 hr⁻¹ to 37,400 hr⁻¹ (6.67 kW_{th}), and 41,100 hr⁻¹ to 46,800 hr⁻¹ (8.33 kW_{th}).

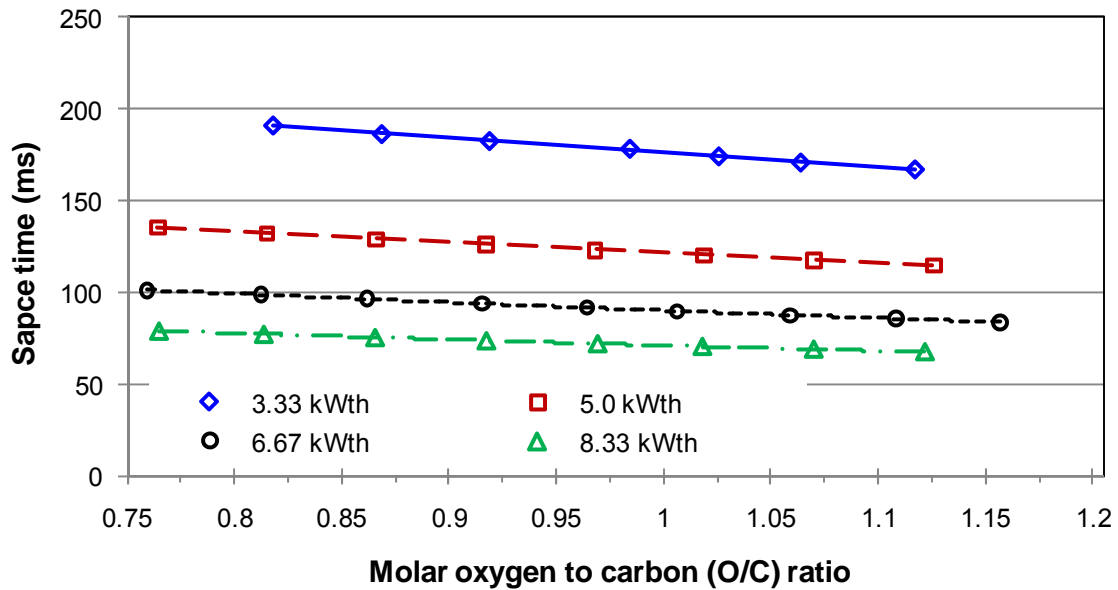


(a)

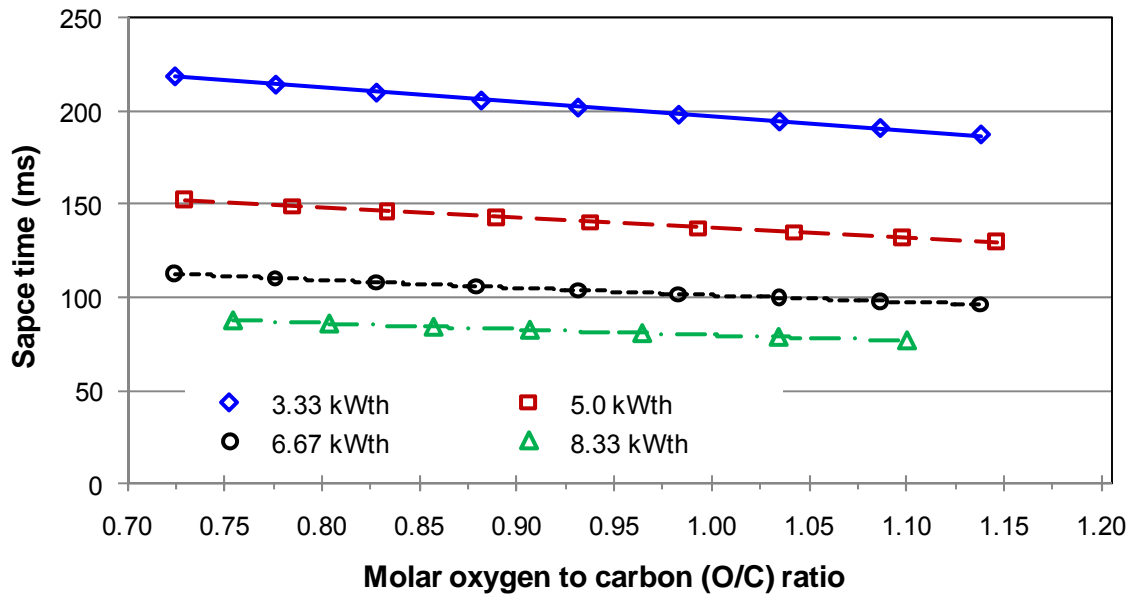


(b)

Figure 6.39 Space time for enrichment number (Ψ) of 0.477 (a) and 1.0 (b) with surrogate JP-8 fuel flows of 5.9 ml/min. (3.33 kW_{th}), 8.84 ml/min. (5.0 kW_{th}), 11.8 ml/min. (6.67 kW_{th}), and 14.7 ml/min (8.33 kW_{th}).



(c)

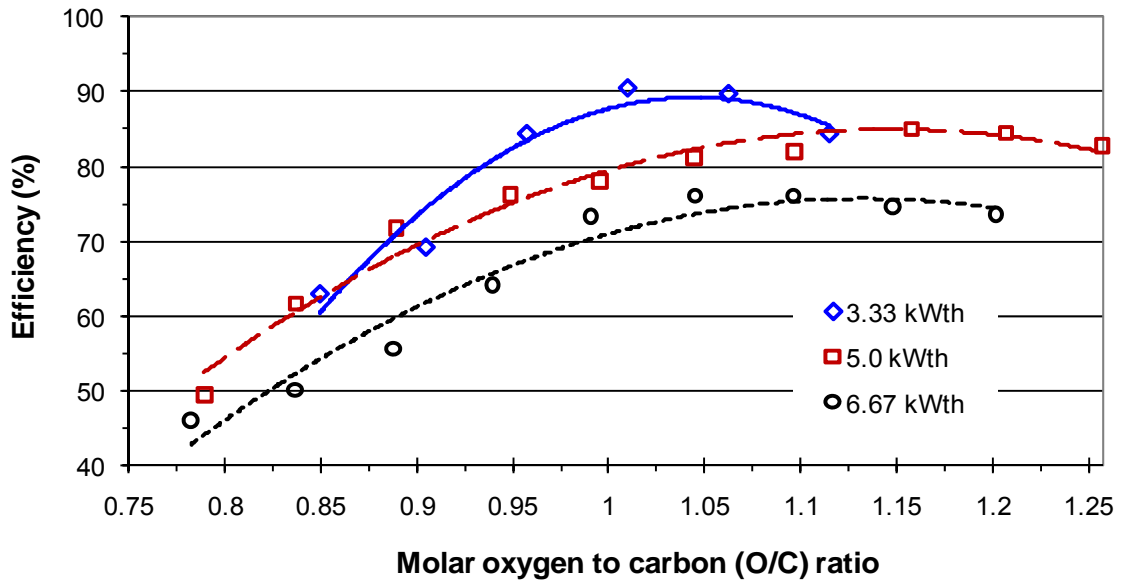


(d)

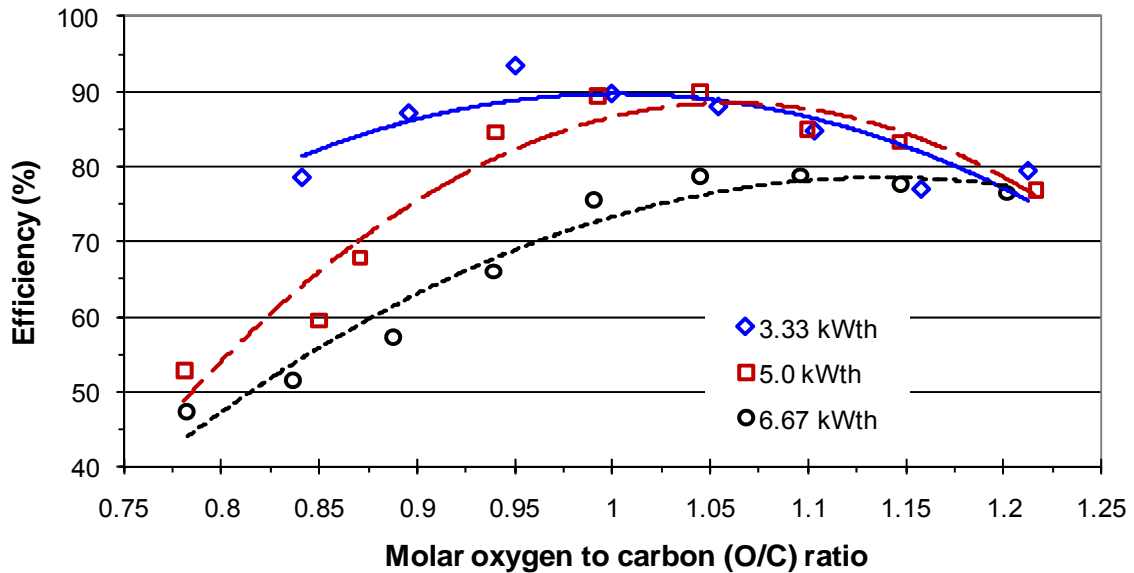
Figure 6.39 (con't) Carbon monoxide yield for enrichment number (Ψ) of 1.432 (c) and 1.91 (d) with surrogate JP-8 fuel flows of 5.9 ml/min. (3.33 kW_{th}), 8.84 ml/min. (5.0 kW_{th}), 11.8 ml/min. (6.67 kW_{th}), and 14.7 ml/min (8.33 kW_{th}).

Hydrogen production is associated steam reforming reactions which are considered kinetically slow. This may explain the observed results pertaining to the importance of reactor space time.

The reformer efficiency under varying fuel flow and enrichment number is shown in Fig. 6.40. For each enrichment number, the peak efficiencies are inversely related with fuel flow (i.e. higher efficiencies with lower fuel flows). Increased efficiency is also correlated with increased enrichment number. For a given fuel flow rate, as the enrichment number increases the reforming efficiency increases and the peak efficiency occurs at lower O/C ratios. The highest peak efficiency of 94.8% was obtained with a fuel flow corresponding to 3.33 kW_{th}, enrichment number of 1.91 and at an O/C ratio of 0.95 (Fig. 6.40d). Comparing efficiencies between enrichment numbers of 1.0 and 1.91; for fuel flow of 3.33 kW_{th} the efficiency increased from 89.7% to 94.8%, for 5.0 kW_{th} the efficiency increased from 89.9% to 92.8%, and for 6.67 kW_{th} the efficiency increased from 78.8% to 83.5%. No comparison can be made for 8.33 kW_{th} as this flow exceeded the reactors design capacity with enrichment number of 1.0. These results confirm the objective of this thesis that oxygen enriched reforming can result in improved performance of an autothermal reactor. Results indicate that with oxygen enrichment reformer efficiency can be improved by up to 6% (89.7% at $\Psi = 1.0$ and 94.8% at $\Psi = 1.91$) and pumping power reduced by 60% (42.0 W at $\Psi=1.0$ and 16.4 W at $\Psi = 1.91$).

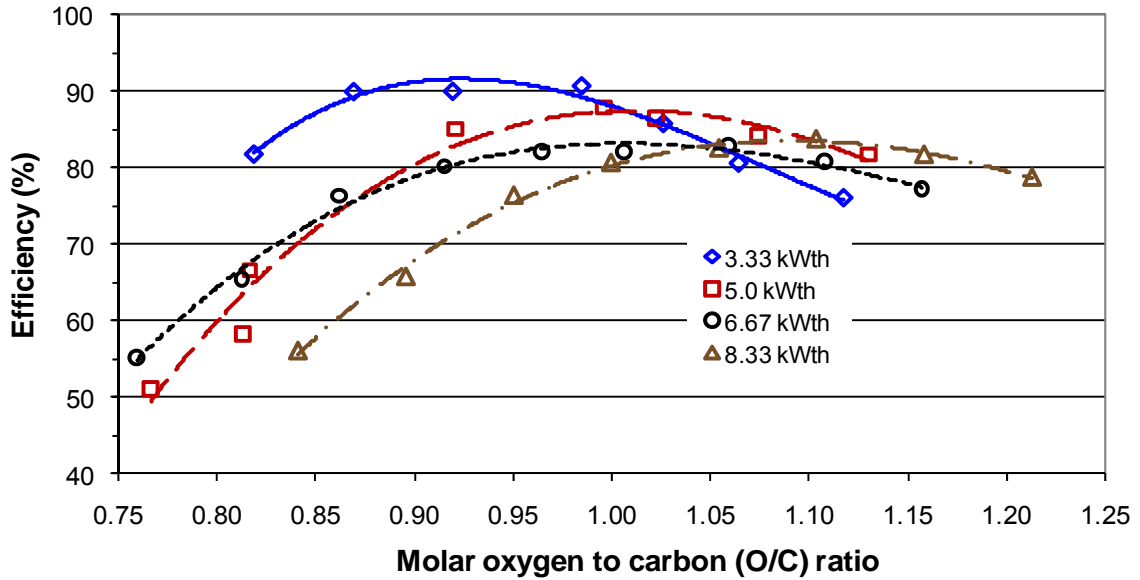


(a)

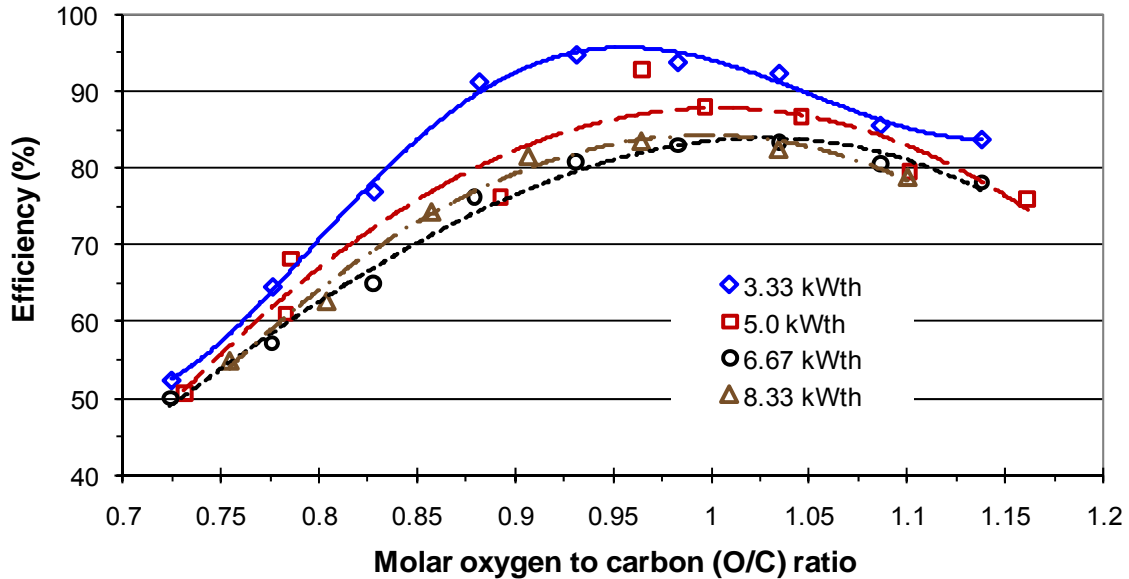


(b)

Figure 6.40 Reformer efficiency for enrichment number (Ψ) of 0.477 (a) and 1.0 (b) with surrogate JP-8 fuel flows of 5.9 ml/min. (3.33 kW_{th}), 8.84 ml/min. (5.0 kW_{th}), 11.8 ml/min. (6.67 kW_{th}), and 14.7 ml/min. (8.33 kW_{th}). The GHSV for $\Psi = 0.477$ (a) was from 33,900 hr⁻¹ to 40,900 hr⁻¹ (3.33 kW_{th}), 48,600 hr⁻¹ to 69,500 hr⁻¹ (5.0 kW_{th}), and 54,700 hr⁻¹ to 67,200 hr⁻¹ (6.67 kW_{th}). The GHSV for $\Psi = 1.0$ (b) was from 22,200 hr⁻¹ to 26,900 hr⁻¹ (3.33 kW_{th}), 32,400 hr⁻¹ to 40,400 hr⁻¹ (5.0 kW_{th}), and 43,200 hr⁻¹ to 53,800 hr⁻¹ (6.67 kW_{th}).



(c)



(d)

Figure 6.40 (con't) Reformer efficiency for enrichment number (Ψ) of 1.432 (c) and 1.91 (d) with surrogate JP-8 fuel flows of 5.9 ml/min. (3.33 kW_{th}), 8.84 ml/min. (5.0 kW_{th}), 11.8 ml/min. (6.67 kW_{th}), and 14.7 ml/min (8.33 kW_{th}). The GHSV for $\Psi = 1.432$ (c) was from 18,800 hr⁻¹ to 21,500 hr⁻¹ (3.33 kW_{th}), 26,600 hr⁻¹ to 31,300 hr⁻¹ (5.0 kW_{th}), 35,600 hr⁻¹ to 42,900 hr⁻¹ (6.67 kW_{th}), and 45,500 hr⁻¹ to 53,400 hr⁻¹ (8.33 kW_{th}). The GHSV for $\Psi = 1.91$ (d) was from 16,500 hr⁻¹ to 19,200 hr⁻¹ (3.33 kW_{th}), 23,600 hr⁻¹ to 27,800 hr⁻¹ (5.0 kW_{th}), and 31,900 hr⁻¹ to 37,400 hr⁻¹ (6.67 kW_{th}), and 41,100 hr⁻¹ to 46,800 hr⁻¹ (8.33 kW_{th}).

As an alternative to reformer and system efficiency improvements, you can significantly increase the throughput of the system with oxygen enrichment. Figure 6.41 displays the reactor capacity as a function of enrichment and reformer efficiency. Assuming a reformer efficiency of 90%, the thermal capacity of the reactor can be raised by 63% while maintaining 90% reformer efficiency ($3.36 \text{ kW}_{\text{th}}$ with $\Psi = 1.0$ to $5.44 \text{ kW}_{\text{th}}$ with $\Psi = 1.91$). A trade-off can be made between reformer throughput and efficiency. The maximum throughput successfully tested was $8.33 \text{ kW}_{\text{th}}$ (150% above the reformer design point of $3.33 \text{ kW}_{\text{th}}$) achieved under conditions of $\Psi = 1.91$ and resulted in a reformer efficiency of 83.5%.

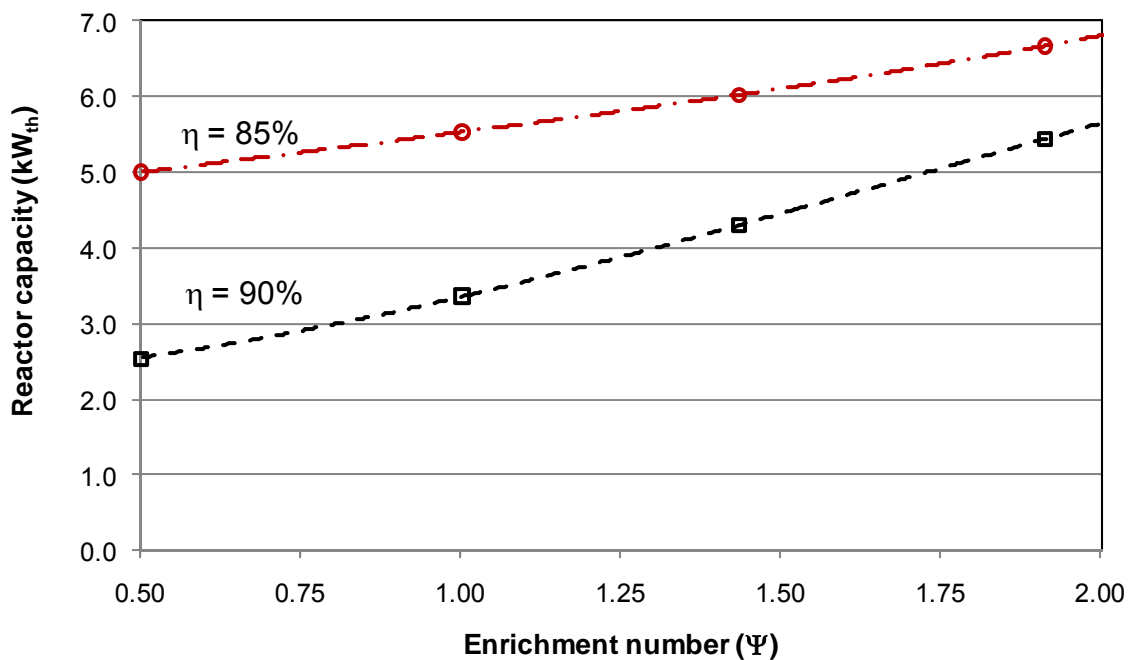


Figure 6.41 Reformer thermal capacity as a function of enrichment number. The reformer was operating at a S/C ratio of 2 and the O/C ratio was adjusted to achieve a constant reformer efficiency.

6.7 Fuel cell power system implications from oxygen enriched reforming

The motivation for the research addressed herein, is to improve fuel cell power system performance through oxygen enriched reforming of heavy hydrocarbon fuels. Although, the experimental work focused on reformer performance effects from oxygen enrichment, some concluding comments on fuel cell power system effects from oxygen enrichment are needed. The performance implications of oxygen enrichment on fuel reforming also provide benefits to other subsystems within a fuel cell power source. Modeling of fuel cell systems under oxygen enriched and unenriched conditions were performed.

Performance of the fuel reformer was based on experimental data; supporting analytical analysis of the fuel cell system and the membrane oxygen enrichment device were performed as described in Chapter 4. Overall modeling assumptions are shown in Table 6.4 and are based on published experimental results: blower and gas compressors [295,296,297], fuel cell auxiliary power systems[298,299], solid oxide fuel cells [300,301,302], power conditioning and control [303], emissions [304,305]. The analytical modeling was based on a 1 kW_e nominal design.

Figure 6.42 displays the overall fuel cell power system efficiency²⁵ and the contributions made by major subsystems. As previously discussed, reformer efficiency increases with enrichment number. The fuel cell stack also experiences large efficiency increases resulting from increased hydrogen partial pressure at the anode (i.e. increasing hydrogen concentration from the fuel reforming) and increased fuel utilization also resulting from

²⁵ Power source efficiency is based on net electric power out to the lower heating value (LHV) of fuel in.

6.4 System level modeling assumptions

Parameter	Value	Notes
Nominal net electrical power	1 kWe	
Reformer operating conditions		
S/C ratio	2	
O/C ratio	~1.0	adjusted to achieve maximum efficiency
Oxygen enrichment membrane		
material	polymeric	
thickness	0.035 μm	
selectivity	3.0	
permeability	3.0 Barriers	
Blower efficiency	50%	
Surface area	variable	adjusted to meet desired permeate flow
Fuel Cell Stack		
voltage	0.7 V/cell	
minimum H ₂ concentration at anode exit	15%	
anode fuel utilization	variable	adjusted to maintain H ₂ anode exit conditions.
cathode fuel utilization	50%	
System parameters		
air/enriched oxygen blower efficiency	60%	
electrical parasitics	15% of gross stack power	parasitics include: control, power conditioning, and control
system specific power (baseline)	30 W/kg	
system power density (baseline)	10 W/L	

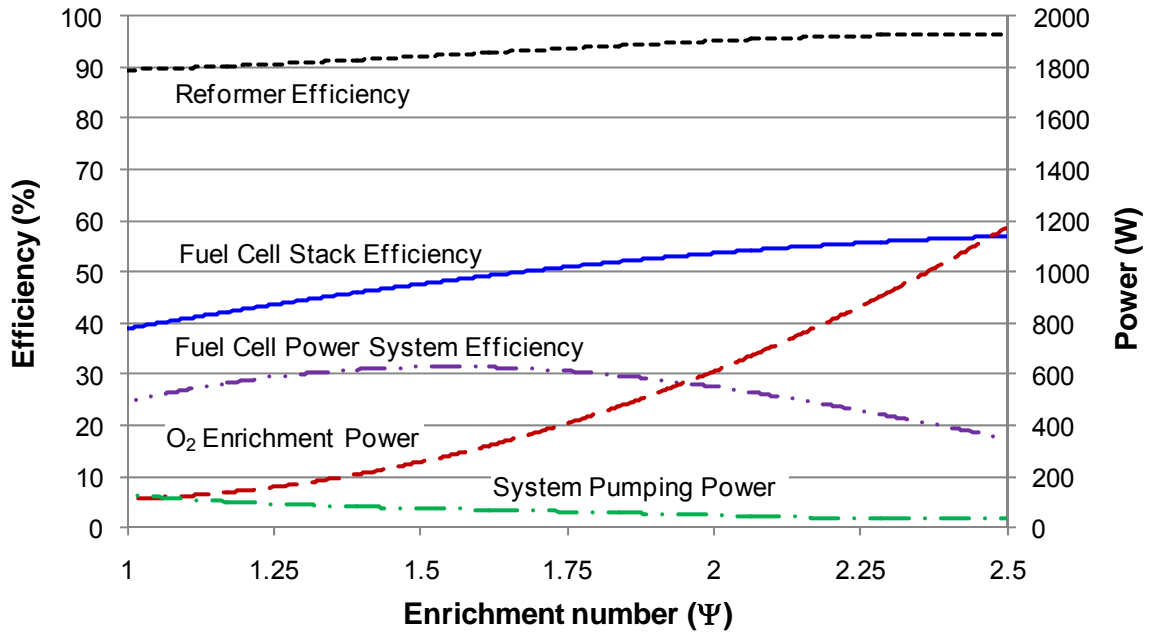


Figure 6.42 Overall power system performance based assumptions shown in Table 6.4.

higher hydrogen concentrations at the anode. Overall, fuel cell stack performance improvement between air operation ($\Psi = 1$) and $\Psi = 1.91$ is 31.9% ($\eta = 39.4\%$ at $\Psi = 1.0$ and $\eta = 52.0\%$ at $\Psi = 1.91$)²⁵. System pumping power is reduced resulting from removal of nitrogen and from increased reformer efficiency. Over the oxygen enrichment range of $1.0 \geq \Psi \geq 1.91$, the system pumping power is reduced from 133.8 W to 52.0 W; however, the power required for oxygen enrichment at $\Psi = 1.91$ is 563 W.

Displayed in Fig. 6.43 is the overall fuel cell power system results based on the assumptions of Table 6.4. Also, displayed in Fig. 6.43 for comparison, is the fuel cell power source efficiency on air at 27.4%²⁵. The peak fuel cell power system efficiency

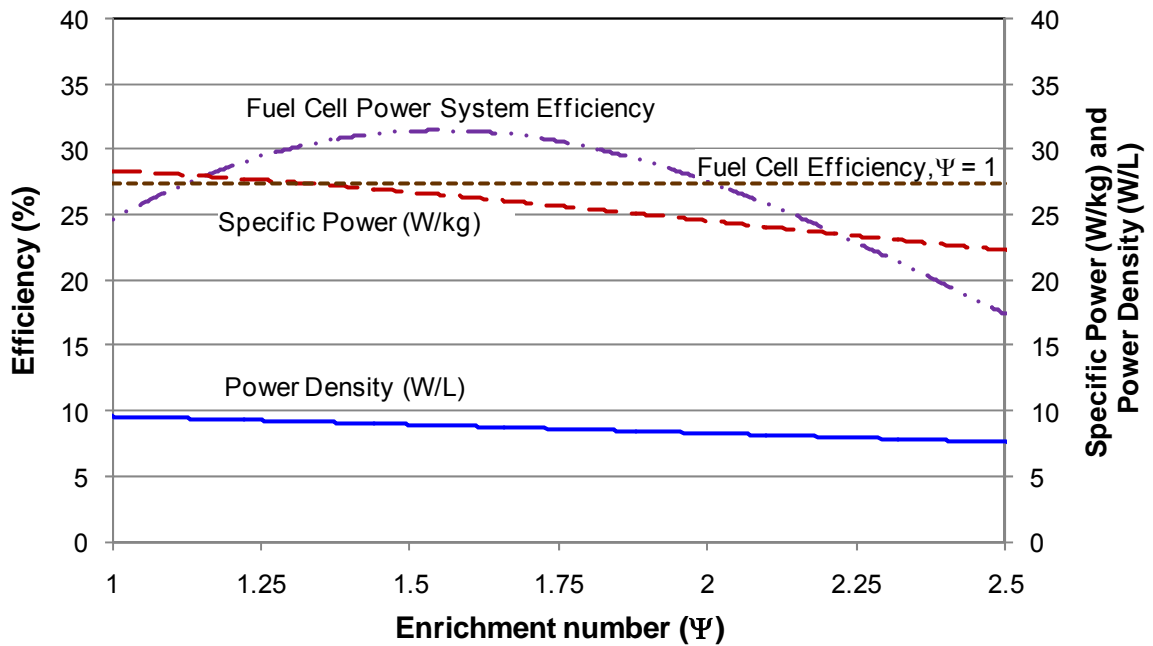


Figure 6.43 Impact to fuel cell power source performance on system efficiency, power density, and specific power as a function of oxygen enrichment of air. For comparison, the performance of a fuel cell power source without oxygen enrichment is shown. Overall power system performance based on assumptions of Table 6.4.

with enriched air is 31.4%²⁵ which occurs at an oxygen enrichment of 1.55 (32.5% O₂).

Thus, the use of oxygen enrichment results in an 18.5% increase in overall system efficiency. Also, shown in Fig. 6.43 is that for enrichment numbers below 1.2 or above 2.0 there is no advantage to the use of oxygen enrichment (subject to the modeling assumptions of Table 6.4).

As shown in Fig. 6.43 there is a negative impact to power system size and volume resulting from the addition of oxygen enrichment balance of plant (blower, membrane, and plumbing). Table 6.5 provides a comparison of emissions resulting from a fuel cell

power system with and without oxygen enrichment, in comparison to a diesel engine driven power source. Performance data for the diesel engine power source was based on a military grade power generator [306]. Across all three emission parameters of NO_x, particulate matter, and carbon dioxide the fuel cell with oxygen enrichment provides advantages over both the unenriched fuel cell and the diesel engine driven generator.

Table 6.5 Emissions comparisons

Parameter	Fuel cell Power system w/ O ₂ Enrichment	Fuel cell power system without O ₂ enrichment	Diesel driven generator
Efficiency	31.4%	27.4%	23.0%
NO _x (ppm/kW)	73	84	731
particulate matter (g/kW-hr)	0	0	0.61
CO ₂ (kg/kW-hr)	0.835	0.958	1.129
Fuel Consumption (kg/hr.)	0.265	0.304	0.362

Chapter 7

Conclusions and Recommendations

7.0 Introduction

The experimental and analytical work contain herein demonstrate that oxygen enriched fuel reforming of heavy hydrocarbon fuels provides performance and operational benefits to the fuel reformer and also to fuel cell system subcomponents. Over the course of this thesis, four primary areas of accomplishment were addressed: i) design and fabrication of an experimental reforming apparatus, ii) experimental evaluation of pure liquid hydrocarbons and hydrocarbon mixtures, leading to the definition of a surrogate JP-8 fuel, iii) successful reforming of JP-8 with air under widely varying, but well controlled conditions, and iv) oxygen enriched reforming of a JP-8 surrogate under varying enrichments and fuel flow conditions. In addition to these areas of accomplishment, a number of potential future research areas were identified and will be noted in this chapter.

7.1 Conclusions

- The experimental apparatus designed for his thesis and discussed in Chapter 3 has demonstrated excellent performance, is controllable over a wide range of operating conditions and has avoided serious operating problems such as pre-reactor oxidation of reactants and associated sooting. Additionally, results are

good (high hydrogen yields), reproducible, and are corroborated by published results by others on similar experiments.

- Eighteen different surrogate fuel candidates were investigated as possible JP-8 surrogates under autothermal reforming conditions. The best overall candidate was based on the hydrocarbon class components of paraffins, cyclo-paraffins and aromatics. These hydrocarbon class components represent 69% of the constituents of JP-8. Liquid hydrocarbons n-dodecane, decalin, and toluene were selected as representative components. Experimental results showed that the three-component mixture of n-dodecane, decalin and toluene in the liquid volume ratios of 7:1:2 results in a good approximation to the behavior of JP-8, particularly, in the oxygen to carbon ratio range of 0.95 to 1.10.

Overall observations on ATR with air are highlighted below:

- It is possible to reform JP-8 with air to completion over a wide range of fuel flow rates and S/C ratios. Additionally, reformat products which are compatible with fuel cells can be produced.
- Variation in S/C ratio has a direct and positive effect on reformer efficiency assuming that excess energy is available to vaporize and preheat the water. To the degree that waste heat and/or energy is available within the system, higher S/C ratios are beneficial. However, if additional fuel must be consumed to vaporize water, then higher S/C ratios can have a strong negative effect of reformer efficiency.

- S/C ratio does show a strong influence in the conversion of hydrocarbons and olefin within the reactor. This is very important as hydrocarbons and olefins in the product stream are closely associated with carbon formation within the reformer. Significant improvement in hydrocarbon conversion was observed when raising the S/C ratio to 2.0 from 1.5; however, no additional benefit was seen in going to S/C ratios of 2.5 and 3.0.
- Variation of fuel flow served to identify the optimum rating of the reactor which for this reactor is between 3.33 kW_{th} and 5.0 kW_{th}. The analysis based on fuel conversion indicated that the optimum rating of the reactor is closer to 5.0 kW_{th}, however, to minimize olefin production and ensure long-term durability a rating closer to 3.33 kW_{th} is more appropriate. The optimum rating is a function of reactor physical configuration and selected fuel, where there is a balance between endothermic and exothermic reactions, heat loss, reaction kinetics, mass transfer and residence time of reactant in order to achieve a desired reformat product. Raising the fuel flow with fixed reactor inlet temperature conditions places more energy into the reactor, raising the reactors operating temperature, and reducing the thermal losses as a function of fuel flow, all of which improve reformer performance. However, with increased fuel flow the space-time is significantly reduced and eventually insufficient time is available for fuel to fully convert into desired products and the reformer performance falls off.
- Every reactor configuration results in an optimum operating conditions that balances endothermic and exothermic reactions, heat loss, reaction kinetics, mass

transfer and residence time of reactant in order to achieve a desired reformat product.

Experimental oxygen enriched catalytic reforming of a JP-8 surrogate fuel under widely varying oxygen concentration, fuel flow rates, and variable oxygen-to-carbon ratios were performed. The experimental work was complimented by system level modeling that addressed other salient features of oxygen enrichment and its contribution to reforming and to system level components, most notably the fuel cell stack. Through experimental evaluation and analysis a number of conclusion and finding are noted below:

- The use of oxygen enrichment has a very positive pronounced effect on the concentration of hydrogen leaving the reformer. Nitrogen typically represents 40 to 50 percent of the reformat product stream with air reforming. Removal of nitrogen results in reduced pumping power, conservation of energy needed to heat nitrogen, reduced reactor volumetric reactant flow, and increased reactant concentrations.
 - The above greatly increases reactor space time and results in an increase in reformer temperature, all of which have a positive effect on reaction kinetic, fuel throughput, increased fuel yield and reformer efficiency.
- With oxygen enrichment, full fuel conversion, peak hydrogen and carbon monoxide yields occur at lower O/C ratios; this further reduces the amount of nitrogen introduced into the reformer resulting in further performance improvements.

- Oxygen enrichment results in a significant increase in hydrogen concentration. This increased concentration of hydrogen has a positive performance benefit to the fuel cell stack.
 - Increased fuel partial pressure at the anode results in a 4% performance increase when going from enrichment number of 1 to 2.
 - Increased fuel concentration allows for operation at higher stack fuel utilizations resulting in a 15.6% increase when going from enrichment number of 1 to 2.
- Oxygen enrichment improves reactor convective heat transfer as measured by constant pressure specific heat. Efficient transfers of heat from zones of exothermic reactions to zones of endothermic reactions are necessary for efficiency reformer operation.
- Oxygen enrichment reduces reformer volume flow resulting in a reduction in reactor pressure drop and an associated pumping power. Reduced reformer volume flow also increases reactor space time.
 - Or alternatively, the size of the reactor can be reduced while maintaining a constant reactor space time and pressure drop.
- Oxygen enrichment allows for independent variation of reactor space time and O/C ratio. This could have significant benefits for control applications as well as experimental research into kinetic and performance mapping of reactors.
 - The ability to independently vary space time and O/C ratio may also allow for fuel flexible reactor designs.

7.2 Recommendations for further study

Despite on-going research into fuel reformer little is known concerning reactions sequencing that take place within the reactor. Most research relies on reactor temperature profiles and reformat product analysis to deduce rating limiting reaction steps. As an initial step to understanding the progression of reactions within the reactor a segmented reactor study could be undertaken. A segmented reactor would consist of a reactor with physical gas sampling ports down the length of the reactor. This would provide some additional insight into the evolution of reaction and could provide further information into important reaction steps. This concept could be further explored via intra-channel gas analysis.

Intra-channel gas analysis consists of inserting a capillary probe axially into a channel of the reactor and collecting samples during reformer operation. The gas sample would be analyzed via a mass spectrometer for more rapid analysis (~ 0.5 s to 1s per scan). This technique has only recently been demonstrated and has never been attempted with liquid hydrocarbon fuel reforming. High reactor operating temperatures and the presence of condensable liquids will be channels, but this technique if successful, would allow for full axial sampling and would provide valuable information on reforming product evolution within a reformer. Along with the experimental studies computational fluid dynamics could be used to further explore reaction pathways.

Another area for further study would be experimental work leading to better understanding of hydrocarbon class effects on fuel reforming. Experimental work with hydrocarbon classes not represented in this study such as iso-paraffins, olefins and polyaromatics would be beneficial. There is significant development work taking place with the conversion of bio-mass and coal to straight chain heavy hydrocarbons fuel very similar to jet, diesel and kerosene fuels. These fuels can meet commercial and military fuel specifications, however, their composition is significantly different from petroleum based fuels and this has highlighted the lack of clear understanding of the contribution that different hydrocarbon classes make to combustion and reforming.

A potential third area of research would be to explore the potential of dual fuel combustion of a syngas stream and diesel and/or jet fuels. Significant research has shown that in spark ignition engines hydrogen can significantly improve combustion performance and reduce emission. Conceptually, the fast flame speed of hydrogen is believed to assist in combustion. With the maturing of fuel reforming catalysts it is possible to conceive of coupling a small fuel reformer with a compression ignition engine or other combustion process in order to gain better performance and/or reduce combustion emissions.

Appendix A

Propagation of Experimental Error Analysis

A.1 Error analysis

Test measurements of small liquid hydrocarbon fed power sources can inadvertently introduce errors that are a function of the test equipment capability and variability in data collection. The previous statement is always true, but can become more pronounced when working with small power sources that are fed by liquid heavy hydrocarbon fuels which have relatively high specific energy and high energy density. Fuel reformers are also very dynamic systems that operate with constant variation in temperatures, flows and pressures (even under constant load). All of these factors have an effect on measurement error in fuel reforming.

A.1.1 Error propagation

Definitions:

$f(\tilde{x}) \equiv$ function dependent on x

$\tilde{x} \equiv$ approximate value of x (i.e. measured value)

We want to understand how the discrepancy between x and \tilde{x} can affect $f(\tilde{x})$. In other words determine $\Delta f(x)$. Where,

$$\Delta f(x) = |f(x) - f(\tilde{x})| \quad \text{A1}$$

Equation A1 cannot be determined directly because $f(x)$ is unknown (i.e. x is unknown). If $f(\tilde{x})$ is continuous and differentiable (i.e. smooth function) then a Taylor Series can be used to determine $\Delta f(x)$. The Taylor Series states that as long as x and \tilde{x} are close in value then the following holds true:

$$f(x) = f(\tilde{x}) + f'(\tilde{x}) \cdot (x - \tilde{x}) + \frac{f''(\tilde{x})}{2!} \cdot (x - \tilde{x})^2 + \frac{f'''(\tilde{x})}{3!} \cdot (x - \tilde{x})^3 \dots + \frac{f^n(\tilde{x}) \cdot (x - \tilde{x})^n}{n!}$$

an estimate of the error in $f(x)$ can be determined by looking only at the higher order terms:

$$f(x) = f(\tilde{x}) + f'(\tilde{x}) \cdot (x - \tilde{x})$$

rearranging,

$$\Delta f(x) = f(x) - f(\tilde{x}) \cong f'(x) \cdot (x - \tilde{x})$$

We now have a way of approximating $\Delta f(x)$.

$$\Delta f(x) \cong |f'(\tilde{x})| \cdot (x - \tilde{x}) = |f'(\tilde{x})| \cdot \Delta \tilde{x}$$

where, $\Delta \tilde{x}$ is the measurement error.

The previous single variable system can be extended to multi-variable systems and the Taylor Series results in an error approximation as shown below:

$$\Delta f(x_1, x_2, \dots, x_n) \cong \left| \frac{\partial f(\tilde{x})}{\partial x_1} \right| \cdot \Delta \tilde{x}_1 + \left| \frac{\partial f(\tilde{x})}{\partial x_2} \right| \cdot \Delta \tilde{x}_2 + \dots + \left| \frac{\partial f(\tilde{x})}{\partial x_n} \right| \cdot \Delta \tilde{x}_n \quad A2$$

A.2 Instrument accuracy

Table A.1 Instrument measurement accuracy

Instrument	Error	Notes:
Agilent micro GC 3000A (4 channel)	1.02%	GC has a 1% error, but is calibrated to a primary standard with a 0.02% analytical error
Brooks 5851E mass flow controller	1%	Error is 1% of full scale (50 slpm for air and N2)
Ashcroft Analogue Guages	1%	Error is 1% of full scale reading
Reformate pressure, Dwyer Magnehelic Differential Pressure Gages	2%	full scale is 10 inches water gage
Reformate Flow Metrer (American Meter Company), AR250	1%	of reading
Thermocouples		
- Watlow, 1/16" stainless steel 316 sheathed	1.1 °C or 0.4%	response time is 0.22 s
- Watlow, 1/8" stainless steel 316 sheathed	1.1 °C or 0.4%	response time is 0.50 s
- Omega, K-type, 0.02" diameter	1.1 °C or 0.4%	which ever is greater; response time is 0.8s with 0.02" diameter
Gilson Piston Pump	1%	of reading
Scales (fuel, water, condensate)	0.001 gm	practicle limit of ± 0.05 gm due to air currents.

A.2.1 Example data

Actual data for n-dodecane below (Table A.2), is used in examples shown in this appendix unless otherwise stated.

Table A.2 Example experimental data from n-dodecane, fuel flow = 4.436 gm/min. (3.3 kWth); S/C = 2.0; O/C = 1.07	
Experimental value	Accuracy
$\tilde{T} = T_{std}$	$\Delta\tilde{T} = \pm 1.1\text{ }^{\circ}\text{C} = \pm 1.1\text{ }K$
$\tilde{P} = P_{std}$	$\Delta\tilde{P} = 24.89\text{ }Pa = 0.1''\text{ }wg$
$\dot{V}_{meter} = 33.728\text{ slpm}$	$\Delta\dot{V}_{meter} = 0.3\text{ slpm}$
$(\text{Air flow})_{in} = 19.4\text{ slpm}$	$(\text{Air flow})_{in} = 0.5\text{ slpm}$
$\tilde{X}_{N_2} = 0.4493$	$\Delta\tilde{X}_{N_2} = 0.004583$
$\% \tilde{N}_2\text{ in air} = 0.7809$	$\Delta\% \tilde{N}_2\text{ in air} = 0$
$\tilde{Fuel}_{in} = 88.72\text{ grams}$	$\Delta\tilde{Fuel}_{in} = 0.05\text{ gm}$
$(\tilde{\text{Reformat flow}})_{in} = 33.728\text{ slpm}$	$\Delta(\tilde{\text{Reformat flow}})_{in} = 1.2225\text{ slpm}$
$\tilde{X}_{H_2} = 0.3281$	$\Delta\tilde{X}_{H_2} = 0.003347$
$\tilde{LHV}_{H_2} = 33.603\text{ kW} - \text{hr/kg}$	$\Delta\tilde{LHV}_{H_2} = 0.33603\text{ kW} - \text{hr/kg}$
$\tilde{t} = 1200\text{ sec.}$	$\Delta\tilde{t} = 0.5\text{ sec.}$
$\tilde{LHV}_f = 12.26\text{ kW} - \text{hr/gm}$	$\Delta\tilde{LHV}_f = 0.01226\text{ kW} - \text{hr/gm}$

A.1.2 Data error analysis – mass flow of reactants

Common too many calculations to follow (yield, carbon balance, etc.) is determining the error associated with the mass flow rate of reactants.

$$\dot{m}_{fuel} = \frac{(Fuel)_{in}}{t} \quad A3$$

Using example data of Table A.2:

$$\dot{m}_{fuel} = \frac{88.72 \text{ gm}}{20 \text{ min.}} = 4.436 \text{ gm/min.}$$

and the associated error is determined by plugging equation A3 into equation A2.

$$\begin{aligned} \Delta Error_{\dot{m}_{fuel}} &= \left| \frac{\partial(\dot{m}_{fuel})}{\partial(\tilde{Fuel})_{in}} \right| \cdot \Delta(\tilde{Fuel})_{in} + \left| \frac{\partial(\dot{m}_{fuel})}{\partial(\tilde{t})} \right| \cdot \Delta(\tilde{t}) \\ \Delta Error_{\dot{m}_{fuel}} &= \frac{1}{\tilde{t}} \cdot \Delta(\tilde{Fuel})_{in} + \frac{(\tilde{Fuel})_{in}}{\tilde{t}^2} \cdot \Delta(\tilde{t}) \end{aligned} \quad A4$$

$$\Delta Error_{\dot{m}_{fuel}} = 0.0025 + 0.001848 = 0.00435 \text{ gm/min}$$

$$\dot{m}_{fuel} = 4.436 \text{ gm/min.} \pm 0.00435 \text{ gm/min}$$

From the above definition of error, it can be seen that the mass flow of fuel is a function of time (i.e. the longer the experiment runs the lower the associated error).

Figure 1 shows the relationship between the quantity of fuel used and error.

Operating at high fuel flows for long periods of time will result in reduced error.

Also, the design of the experiment can contribute to error (e.g. operating at higher flow rates will also improve accuracy).

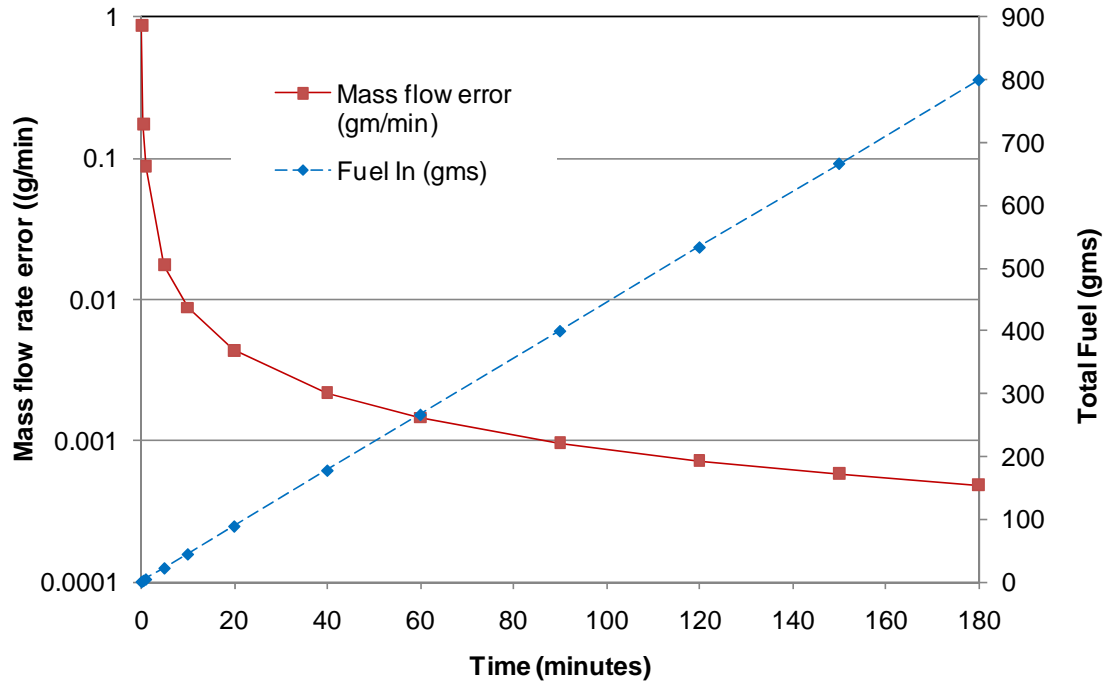


Figure 1. Fuel mass flow error as a function of time for flow condition of 4.436 g/min. and reformate flow of 33.73 slpm.

In general, the form of equation A4 is:

$$\Delta Error_{in_{fuel}} = \frac{0.05}{\tilde{t}} + \frac{(\tilde{Fuel})_{in}}{\tilde{t}^2} \cdot 0.5$$

A.1.3 Data error analysis – reformate flow

The reformate flow is needed to understand the quantity of reformate gaseous products being produced. Reformate flow can be determined by two means: 1) direct measurement via a positive displacement volume flow meter and 2) through the use of nitrogen as a reference. Under both scenarios, the reformate is considered an ideal gas.

The reformat molar flow rate of x is determined as follows:

$$\dot{V}_x = \dot{V}_{\text{Reformat}} \cdot X_x \quad \text{A5}$$

where,

$X_x \equiv$ molar concentration of x ; expressed as a fraction

For an ideal gas, molar flow and volume flow are directly proportional. A mole of any ideal gas occupies the same volume:

$$PV = nRT$$

rearranging,

$$\frac{V}{n} = \frac{RT}{P} = \frac{8314 \text{ J/kg} \cdot \text{mole K} \cdot 294.25 \text{ K}}{101325 \text{ Pa}} = 24.14404 \text{ l/gm-mole}$$

Case 1 – Direct Measurement:

I use a positive displacement volume flow meter (American Meter Company, AR250) with a 1% accuracy. The reading from the meter is corrected to standard conditions (1 atm, 20 °C) by a thermocouple and a pressure transducer placed just upstream of the meter.

$$\dot{V}_{\text{Ref corrected}} = \frac{T_{std}}{\tilde{T}} \cdot \frac{\tilde{P}}{P_{std}} \cdot \dot{V}_{meter} \quad \text{A6}$$

$$T_{std} = 20 \text{ } ^\circ\text{C} = 293.15 \text{ K}$$

$$P_{std} = 101325 \text{ Pa}$$

Applying equation A2 to equation A6 above,

$$\Delta Error_{\text{Reformat flow}} = \left| \frac{\partial(\dot{V}_{\text{Ref corrected}})}{\partial(\tilde{P})_{In}} \right| \cdot \Delta(\tilde{P})_{In} + \left| \frac{\partial(\dot{V}_{\text{Ref corrected}})}{\partial(\tilde{T})} \right| \cdot \Delta(\tilde{T}) + \left| \frac{\partial(\dot{V}_{\text{Ref corrected}})}{\partial(\tilde{V}_{\text{meter}})} \right| \cdot \Delta(\tilde{V}_{\text{meter}})$$

$$\begin{aligned} \Delta Error_{\text{Reformat flow}} &= \frac{T_{std}}{\tilde{T}} \cdot \frac{1}{P_{std}} \cdot \dot{V}_{\text{meter}} \cdot \Delta(\tilde{P})_{In} + \frac{T_{std}}{\tilde{T}^2} \cdot \frac{\tilde{P}}{P_{std}} \cdot \dot{V}_{\text{meter}} \cdot \Delta(\tilde{T}) + \\ &+ \frac{T_{std}}{\tilde{T}} \cdot \frac{\tilde{P}}{P_{std}} \cdot \Delta(\tilde{V}_{\text{meter}}) \end{aligned} \quad A7$$

Assuming the following:

$$\begin{aligned} \tilde{T} &= T_{std} & \Delta\tilde{T} &= \pm 1.1 \text{ } ^\circ\text{C} = \pm 1.1 \text{ K} \\ \tilde{P} &= P_{std} & \Delta\tilde{P} &= 24.891 \text{ Pa} = 0.1" \text{ wg} \\ \dot{V}_{\text{meter}} &= 33.728 \text{ slpm} & \Delta\dot{V}_{\text{meter}} &= 0.3 \text{ slpm} \end{aligned}$$

$$\Delta Error_{\text{Reformat flow}} = \frac{33.728 \text{ slpm}}{101325 \text{ Pa}} \cdot 24.891 \text{ Pa} + \frac{293.15 \text{ K}}{(293.15 \text{ K})^2} \cdot 33.728 \text{ slpm} \cdot 1.1 \text{ K} + 0.3 \text{ slpm}$$

$$\Delta Error_{\text{Reformat flow}} = 0.00828 \text{ slpm} + 0.11505 \text{ slpm} + 0.30 \text{ slpm} = 0.42085 \text{ slpm}$$

$$\dot{V}_{\text{meter}} = 33.728 \text{ slpm} \pm 0.42179 \text{ slpm}$$

Case 2 – using nitrogen as a reference

This scenario is based on knowing the nitrogen composition and flow into the reactor and also knowing the composition of nitrogen in the reformat you can determine the total reformat flow.

$$\dot{V}_{\text{Reformat}} = \frac{(\text{Air flow})_{\text{In}} \cdot (\% \text{ N}_2 \text{ in air})}{(X_{\text{N}_2})_{\text{Out}}} \quad \text{A8}$$

where,

$\text{Air flow} \equiv$ Air flow into reactor (at standard condition)

$\% \text{ N}_2 \text{ in air} \equiv 78.09 \%$ for air (0.7809)

Applying equation 3 to equation 6 above yields the following:

$$\Delta \text{Error}_{\text{Reformat flow}} = \left| \frac{\partial(\text{Reformat flow})}{\partial(\text{Air Flow})_{\text{In}}} \right| \cdot \Delta(\text{Air Flow})_{\text{In}} + \left| \frac{\partial(\text{Reformat flow})}{\partial(\% \text{ N}_2 \text{ in air})} \right| \cdot \Delta(\% \text{ N}_2 \text{ in air}) +$$

$$\left| \frac{\partial(\text{Reformat flow})}{\partial(X_{\text{N}_2})_{\text{Out}}} \right| \cdot \Delta(X_{\text{N}_2})_{\text{Out}}$$

where,

$\Delta \tilde{\text{Air Flow}} \equiv$ air flow into the reactor error

$\Delta \% \text{ N}_2 \text{ in air} \equiv$ volume percentage of nitrogen in air error

$\Delta \tilde{X}_{\text{N}_2} \equiv$ fractional concentration of nitrogen error

$$\Delta Error_{\text{Reformat flow}} = \frac{(\% \tilde{N}_2 \text{ in air})}{(\tilde{X}_{N_2})_{Out}} \cdot \Delta(\tilde{\text{Air Flow}})_{In} + \frac{(\tilde{\text{Air Flow}})_{In}}{(\tilde{X}_{N_2})_{Out}} \cdot \Delta(\% \tilde{N}_2 \text{ in air}) +$$

$$\frac{(\tilde{\text{Air Flow}})_{In} \cdot (\% \tilde{N}_2 \text{ in air})}{(\tilde{X}_{N_2})_{Out}^2} \cdot \Delta(\tilde{X}_{N_2})_{Out}$$

$$(\text{Air flow})_{In} = 19.4 \text{ slpm}$$

$$(\text{Air flow})_{In} = 0.5 \text{ slpm}$$

$$\% \tilde{N}_2 \text{ in air} = 0.7809$$

$$\Delta \% \tilde{N}_2 \text{ in air} = 0$$

$$\tilde{X}_{N_2} = 0.4493$$

$$\Delta \tilde{X}_{N_2} = 0.004583$$

$$\dot{V}_{\text{Reformat}} = \frac{(19.4 \text{ slpm})_{In} \cdot (0.7809)}{(0.4493)_{Out}} = 33.728 \text{ slpm}$$

$$\Delta Error_{\text{Reformat}} = 0.86902 + 0 + 0.34393 = 1.21295 \text{ slpm}$$

$$\dot{V}_{\text{Reformat}} = 33.728 \text{ slpm} \pm 1.21295 \text{ slpm}$$

A.1.4 Data error analysis – reformer efficiency

The efficiency (based on the lower heating value) is determined by the following equation:

$$\eta_{(H_2+CO)} = \left[\frac{(\dot{m}_{H_2} \cdot LHV_{H_2} + \dot{m}_{CO} \cdot LHV_{CO})_{out} \cdot t}{LHV_f \cdot (Fuel)_{in}} \right] \quad A9$$

where,

$\dot{m}_x \equiv$ molar (or mass) flow rate of x

$(Fuel)_{in} \equiv$ Fuel into the Reformer Test Bed (grams)

$LHV_f \equiv$ Lower Heating Value of f

$t \equiv$ elapsed time

Determining the efficiency of an autothermal reformer (ATR) is a function of the fuel cell system being employed. The efficiency equation above, equation 4, considers both the heating values from carbon monoxide and hydrogen implying that a solid oxide fuel cell will be used (versus a proton exchange membrane fuel cell where carbon monoxide is a poison). An additional implied assumption is that in a fuel cell power system the overall net reactions are exothermic leaving sufficient heat to vaporize the fuel and water input into the reactor. This assumption is generally correct for both partial oxidation and autothermal reforming reactors.

Putting equations 4, 5, and 6 together, gives:

$$\eta_{(H_2+CO)} = \left[\frac{(\tilde{\text{Reformate}})_{out} \cdot X_{H_2} \cdot LHV_{H_2} \cdot t \cdot MW_{H_2}}{LHV_f \cdot (Fuel)_{in} \cdot 24.144} \right]$$

Applying equation [3] yields,

$$\Delta Error_{\eta} = \left| \frac{\partial \eta}{\partial (\tilde{\text{Reformat}})_{out}} \right| \cdot \Delta (\tilde{\text{Reformat}})_{out} + \left| \frac{\partial \eta}{\partial X_{H_2}} \right| \cdot \Delta \tilde{X}_{H_2} + \left| \frac{\partial \eta}{\partial LHV_{H_2}} \right| \cdot \Delta \tilde{LHV}_{H_2} +$$

$$\left| \frac{\partial \eta}{\partial t} \right| \cdot \Delta \tilde{t} + \left| \frac{\partial \eta}{\partial LHV_f} \right| \cdot \Delta \tilde{LHV}_f + \left| \frac{\partial \eta}{\partial (Fuel)_{in}} \right| \cdot \Delta (\tilde{Fuel})_{in}$$

where,

$\Delta (\tilde{\text{Reformat}})_{out} \equiv$ reformat flow out of the reactor, error

$\Delta X_{H_2} \equiv$ fractional concentration of hydrogen, error

$\Delta \tilde{LHV}_{H_2} \equiv$ lower heating value of hydrogen, error

$\Delta \tilde{t} \equiv$ time measurement error

$\Delta \tilde{LHV}_f \equiv$ lower heating value of fuel error

$\Delta (\tilde{Fuel})_{in} \equiv$ fuel measurement error

$$\Delta Error_{\eta} \cong \left[\frac{\tilde{X}_{H_2} \cdot \tilde{LHV}_{H_2} \cdot \tilde{t} \cdot \tilde{MW}_{H_2}}{\tilde{LHV}_f \cdot (\tilde{Fuel})_{in} \cdot 24.144} \right] \cdot \Delta (\tilde{\text{Reformat}})_{out} +$$

$$\begin{aligned}
& \left[\frac{(\tilde{\text{Reformat}})_{\text{Out}} \cdot \tilde{LHV}_{H_2} \cdot \tilde{t} \cdot \tilde{MW}_f}{\tilde{LHV}_f \cdot (\tilde{F}_{\text{uel}})_{\text{in}} \cdot 24.144} \right] \cdot \Delta \tilde{X}_{H_2} + \left[\frac{(\tilde{\text{Reformat}})_{\text{Out}} \cdot \tilde{X}_{H_2} \cdot \tilde{t} \cdot \tilde{MW}_f}{\tilde{LHV}_f \cdot (\tilde{F}_{\text{uel}})_{\text{in}} \cdot 24.144} \right] \cdot \Delta \tilde{LHV}_{H_2} + \\
& \left[\frac{(\tilde{\text{Reformat}})_{\text{Out}} \cdot \tilde{X}_{H_2} \cdot \tilde{LHV}_{H_2} \cdot \tilde{MW}_f}{\tilde{LHV}_f \cdot (\tilde{F}_{\text{uel}})_{\text{in}} \cdot 24.144} \right] \cdot \Delta(\tilde{t}) + \left[\frac{(\tilde{\text{Reformat}})_{\text{Out}} \cdot \tilde{X}_{H_2} \cdot \tilde{LHV}_{H_2} \cdot \tilde{t}}{(\tilde{F}_{\text{uel}})_{\text{in}} \cdot (\tilde{LHV}_f)^2 \cdot 24.144} \right] \cdot \Delta \tilde{LHV}_f + \\
& \left[\frac{(\tilde{\text{Reformat}})_{\text{Out}} \cdot \tilde{X}_{H_2} \cdot \tilde{LHV}_{H_2}}{(\tilde{X}_{N_2})_{\text{Out}} \cdot \tilde{LHV}_f \cdot (\tilde{F}_{\text{uel}})_{\text{in}}^2 \cdot 24.144} \right] \cdot \Delta(\tilde{F}_{\text{uel}})_{\text{in}}
\end{aligned} \tag{A10}$$

Assume the following data:

$$\begin{aligned}
\tilde{F}_{\text{uel}}_{\text{in}} &= 88.72 \text{ grams} & \Delta \tilde{F}_{\text{uel}}_{\text{in}} &= 0.05 \text{ gm} \\
(\tilde{\text{Reformat}} \text{ flow})_{\text{Out}} &= 33.728 \text{ slpm} & (\Delta \tilde{\text{Reformat}} \text{ flow}_1)_{\text{Out}} &= 0.42915 \text{ slpm} \\
& & (\Delta \tilde{\text{Reformat}} \text{ flow}_2)_{\text{Out}} &= 1.2225 \text{ slpm} \\
\tilde{X}_{H_2} &= 0.3281 & \Delta \tilde{X}_{H_2} &= 0.0102 \\
\tilde{LHV}_{H_2} &= 33.603 \text{ kW} \cdot \text{hr/kg} & \Delta \tilde{LHV}_{H_2} &= 0.033603 \text{ kW} \cdot \text{hr/kg} \\
\tilde{X}_{N_2} &= 0.4493 & \Delta \tilde{X}_{N_2} &= 0.004583 \\
\tilde{t} &= 20 \text{ min.} & \Delta \tilde{t} &= 0.01667 \text{ min.} \\
\tilde{LHV}_f &= 12.26 \text{ kW} \cdot \text{hr/gm} & \Delta \tilde{LHV}_f &= 0.01226 \text{ kW} \cdot \text{hr/gm}
\end{aligned}$$

$$\eta = \frac{33.72 \cdot 0.3281 \cdot 20 \text{ min} \cdot 33.603 \text{ kW} \cdot \text{hr} / \text{kg} \cdot 2.01588 \text{ gm} / \text{mole}}{88.72 \text{ gms} \cdot 12.26 \frac{\text{kW} \cdot \text{hr}}{\text{kg}} \cdot 24.144 \text{ gm} \cdot \text{mole} / \text{l}} = 0.57066$$

$$\eta = 57.07 \%$$

$$\Delta Error_{\eta_1} \cong 0.00726383 \cdot 8 + 0.00582076 \cdot 9 + 0.00047555 \cdot 3 + 0.00057066 \cdot 4 + 0.00057066 \cdot 4 + 6.43219 \cdot 10^{-6} = 0.01470791 \cdot 9$$

$$\Delta Error_{\eta_2} \cong 0.02053051 \cdot 8 + 0.00582076 \cdot 9 + 0.0002378 \cdot 3 + 0.00057066 \cdot 4 + 0.00057066 \cdot 4 + 6.43219 \cdot 10^{-6} = 0.027737$$

$$\eta_1 = 57.07\% \pm 1.471\%$$

$$\eta_2 = 57.07\% \pm 2.774\%$$

A.1.5 Data error analysis – product flow

Measuring product flow of hydrogen (and carbon monoxide when solid oxide fuel cells are being considered) is an important parameter to determine. Hydrogen product flow is calculated by:

$$\dot{V}_{H_2} = \dot{V}_{\text{Reformate}} \cdot (X_{H_2})_{\text{Out}} \quad \text{A11}$$

with,

$$\dot{V}_{H_2} = 33.728 \text{ slpm} \cdot 0.3281 = 11.066 \text{ slpm}$$

Putting equation 7 above into equation 3 yields:

$$\Delta Error_{\dot{V}_{H_2}} = \left| \frac{\partial \dot{V}_{H_2}}{\partial (\dot{V}_{\text{Reformate}})} \right| \cdot (\Delta \dot{V}_{\text{Reformate}}) + \left| \frac{\partial \dot{V}_{H_2}}{\partial (X_{H_2})_{\text{Out}}} \right| \cdot \Delta (X_{H_2})_{\text{Out}}$$

$$\Delta Error_{\dot{V}_{H_2}} = (X_{H_2})_{\text{Out}} \cdot \Delta \dot{V}_{\text{Reformate}} + \dot{V}_{\text{Reformate}} \cdot \Delta (X_{H_2})_{\text{Out}}$$

$$\Delta Error_{\dot{V}_{H_2}} = 0.3281 \cdot 0.4292 \text{ slpm} + 33.728 \text{ slpm} \cdot 0.003346$$

$$\Delta Error_{\dot{V}_{H_2}} = 0.1408 \text{ slpm} + 0.1128 \text{ slpm} = 0.2536 \text{ slpm}$$

$$\dot{V}_{H_2} = 11.066 \text{ slpm} \pm 0.2536 \text{ slpm}$$

A.1.6 Data error analysis – product yield

Product yield is a molar ratio of desired products to the amount of desired product in the “fuel”.

$$\text{Yield}_x = \frac{\text{moles of } x \text{ in product}}{\text{moles of } x \text{ in fuel}}$$

Yield can be presented in many different forms (e.g. moles/moles, gm/gm, etc.).

When considering hydrogen yield in steam reforming and autothermal reforming it is possible to achieve yields of greater than 1.0 (or 100% if data is presented in percentages). This results from the presence of hydrogen in water which participates in reforming reactions and contributes to the amount of hydrogen in the product, but is not usually included in the dominator.

$$\text{Yield}_{H_2} = \frac{\dot{V}_{\text{Reformat}} \cdot X_{H_2}}{\frac{\dot{m}_{\text{fuel}}}{MW_{\text{fuel}}} (X_{H_2})_{\text{fuel}}} \cdot \frac{1}{24.144 \text{ gm-mole/l}} = \frac{\dot{V}_{H_2}}{\frac{\dot{m}_{\text{fuel}}}{MW_{\text{fuel}}} (X_{H_2})_{\text{fuel}} \cdot 24.144}$$

and,

$$\dot{m}_{\text{fuel}} = \frac{(Fuel)_{in}}{t}$$

$$\text{Yield}_{H_2} = \frac{\dot{V}_{H_2}}{\frac{(Fuel)_{in}}{MW_{\text{fuel}}} (X_{H_2})_{\text{fuel}} \cdot 24.144}$$

Plugging the above equation into equation 3, yields:

$$\Delta Error_{Yield_{H_2}} = \left| \frac{\partial(Yield_{H_2})}{\partial \dot{V}_{H_2}} \right| \cdot \Delta \dot{V}_{H_2} + \left| \frac{\partial(Yield_{H_2})}{\partial \dot{m}_{fuel}} \right| \cdot \Delta \dot{m}_{fuel} + \left| \frac{\partial(Yield_{H_2})}{\partial (\tilde{X}_{H_2})_{fuel}} \right| \cdot \Delta (\tilde{X}_{H_2})_{fuel}$$

$$\Delta Error_{Yield_{H_2}} = \frac{1}{\frac{\dot{m}_{fuel}}{MW_{fuel}} (\tilde{X}_{H_2})_{fuel} \cdot 24.144} \cdot \Delta \dot{V}_{H_2} + \frac{\dot{V}_{H_2}}{\left(\frac{\dot{m}_{fuel}}{MW_{fuel}} \right)^2 (\tilde{X}_{H_2})_{fuel} \cdot 24.144} \cdot \Delta \dot{m}_{fuel} +$$

$$\frac{\left(\frac{\dot{m}_{fuel}}{MW_{fuel}} \right) (\tilde{X}_{H_2})_{fuel}^2 \cdot 24.144}{\dot{V}_{H_2}} \cdot \Delta (\tilde{X}_{H_2})_{fuel} + \frac{\left(\frac{\dot{m}_{fuel}}{MW_{fuel}} \right) (\tilde{X}_{H_2})_{fuel}^2 \cdot 24.144}{\dot{V}_{H_2}} \cdot \Delta (\tilde{X}_{H_2})_{fuel}$$

$$\Delta Error_{Yield_{H_2}} = \pm 0.0310$$

$$Yield_{H_2} = 1.35 \pm 0.0310$$

A.1.7 Data error analysis – fuel conversion

Fuel conversion is a means for determining the degree to which the reactant fuel is being transformed into product. Because jet fuel is made up of many hydrocarbons compounds knowing exactly what you are starting with is difficult. Because the reactant composition is unknown, fuel conversion as defined below is essentially a carbon balance looking only at CO and CO₂.

$$\text{Fuel conversion to CO}_x (\%) = \frac{\dot{V}_{\text{Reformat}} \cdot (X_{CO} + X_{CO_2})}{m \cdot \frac{\dot{m}_{fuel}}{MW_{fuel}} \cdot 24.144 \text{ l/mol}} \cdot 100\% \quad A12$$

where, m is number of carbon atoms in fuel.

$$\begin{aligned}\tilde{X}_{CO} &= 0.12601 & \Delta\tilde{X}_{CO} &= 0.0012862 \\ \tilde{X}_{CO_2} &= 0.09324 & \Delta\tilde{X}_{CO_2} &= 0.0000951 \\ \tilde{m} &= 12\end{aligned}$$

$$(\text{Fuel conversion})_{CO_x} = \frac{33.715 \text{ slpm} \cdot (0.12601 + 0.09324)}{(12 \text{ C / mole fuel}) \cdot \frac{4.436 \text{ gm / min}}{170.32 \text{ gm / mole}} \cdot 24.144 \text{ l / mol}} \cdot 100\%$$

$$(\text{Fuel conversion})_{CO_x} = 97.96\%$$

$$\begin{aligned}\Delta Error_{(\text{Fuel conversion})_{CO_x}} &= \left| \frac{\partial(\text{Fuel conversion})_{CO_x}}{\partial \dot{V}_{\text{Reformat}}} \right| \cdot \Delta \dot{V}_{\text{Reformat}} + \left| \frac{\partial(\text{Fuel conversion})_{CO_x}}{\partial \tilde{X}_{CO}} \right| \cdot \Delta \tilde{X}_{CO} + \\ &\quad \left| \frac{\partial(\text{Fuel conversion})_{CO_x}}{\partial \tilde{X}_{CO_2}} \right| \cdot \Delta \tilde{X}_{CO_2} + \left| \frac{\partial(\text{Fuel conversion})_{CO_x}}{\partial \dot{m}_{fuel}} \right| \cdot \Delta \dot{m}_{fuel}\end{aligned}$$

$$\begin{aligned}\Delta Error_{(\text{Fuel conversion})_{CO_x}} &= \frac{(X_{CO} + X_{CO_2})}{m \cdot \frac{\dot{m}_{fuel}}{MW_{fuel}} \cdot 24.144 \text{ l / mol}} \cdot \Delta \dot{V}_{\text{Reformat}} + \frac{\dot{V}_{\text{Reformat}} \cdot (X_{CO_2})}{m \cdot \frac{\dot{m}_{fuel}}{MW_{fuel}} \cdot 24.144 \text{ l / mol}} \cdot \Delta \tilde{X}_{CO} + \\ &\quad \frac{\dot{V}_{\text{Reformat}} \cdot (X_{CO})}{m \cdot \frac{\dot{m}_{fuel}}{MW_{fuel}} \cdot 24.144 \text{ l / mol}} \cdot \Delta \tilde{X}_{CO_2} + \frac{\dot{V}_{\text{Reformat}} \cdot (X_{CO} + X_{CO_2})}{m \cdot \frac{(\dot{m}_{fuel})^2}{MW_{fuel}} \cdot 24.144 \text{ l / mol}} \cdot \Delta \dot{m}_{fuel}\end{aligned}$$

$$\Delta Error_{(\text{Fuel conversion})_{CO_x}} = \pm 1.0207\%$$

$$(\text{Fuel conversion})_{CO_x} = 97.96 \% \pm 1.0207 \%$$

Using nitrogen balance to determine the reformat flow:

$$(\text{Fuel conversion})_{CO_x} = 97.96 \% \pm 3.678 \%$$

Appendix B

Determining Experimental Operating Conditions

Prior to initiating experimental work in the lab, experimental operating parameters such as O/C ratio and S/C ratio must be translated into experimental operating conditions. In general, fuel reforming reactors are designed for a given fuel throughput in milliliters per minute (ml/min.) or in terms of fuel thermal value. In addition to fuel flow, air flow in standard liters per minute (slpm) and water flow in milliliters per minute (ml/min.).

Initial input operating point data are:

$\dot{m}_{fuel} \equiv$ mass flow rate of fuel

O/C ratio

S/C ratio

Enrichment number (Ψ)

Other known input data are:

$MW_{fuel} \equiv$ molecular weight of fuel.

$MW_{water} \equiv$ molecular weight of water.

$MW_{Air} \equiv$ molecular weight of air

$C_nH_m \equiv$ chemical composition of fuel. Or at least the average number of carbon atoms in the fuel need to be known.

$\rho_{fuel} \equiv$ density of the fuel

The oxygen flow is determined as follows:

$$\dot{n}_{O_2} \equiv \text{Oxygen molar flow} = \left(\frac{O}{C} \right) \cdot \dot{n}_{fuel} \cdot n_C \cdot \frac{O_2}{2 \cdot O}$$

where,

$$\dot{n}_{fuel} = \frac{\dot{m}_{fuel}}{MW_{fuel}}$$

and

$n_C \equiv$ average number of carbon atoms in fuel.

The air molar flow rate (\dot{n}_{Air}) is determined below:

$$\dot{n}_{Air} \equiv \text{Air molar flow} = \frac{\dot{n}_{O_2}}{X_{O_2}}$$

where,

$$X_{O_2} \equiv \text{molar fraction of oxygen in air/enriched air} = \Psi \cdot X_{O_2, 'Air/Enriched Air}$$

From the above the volumetric flow rate of air is determined as follows:

$$\dot{V}_{Air} = \frac{\dot{m}_{Air}}{\rho_{Air}}$$

where,

$$\dot{m}_{Air} = \dot{n}_{Air} \cdot MW_{Air}$$

The water flow rate is determined in a similar manner to air/enriched air.

$$\dot{n}_{H_2O} \equiv \text{Water molar flow} = \left(\frac{S}{C} \right) \cdot \dot{n}_{fuel} \cdot n_C$$

where,

$$\dot{m}_{H_2O} = \dot{n}_{H_2O} \cdot MW_{H_2O}$$

and the volumetric water flow rate is:

$$\dot{V}_{H_2O} = \frac{\dot{m}_{H_2O}}{\rho_{H_2O}}$$

Appendix C

Operational Calculations Based on Carbon and Hydrogen Content of Fuel

In dealing with “real” fuels that consist of many hundreds of individual hydrocarbons, the average molecular weight of the fuel is often not well established. This creates a problem in determining important operating conditions of oxygen-to-carbon ration (O/C) and steam-to-carbon rations (S/C); critical reactor operating conditions. However the mass percentage of hydrogen and carbon within the fuel can easily and accurately be determined through inexpensive fuel analysis. Knowing the hydrogen and carbon composition of the fuel, the carbon atom flow associated with the fuel can be determined and from this the operating O/C and S/C ratios can be determined. The procedure for determining the carbon atom flow is as follows:

Known parameters:

$$MW_C = 12.0107 \text{ g/mole}$$

$$MW_H = 1.00794 \text{ g/mole}$$

Obtained from fuel analysis:

$$\text{Mass percentage (\%) Carbon in fuel} = 85.72\%$$

$$\text{Mass percentage (\%) Hydrogen in fuel} = 13.91\%$$

Mass percentage (%) of X^1 in fuel = 0.37%

$$\rho_{fuel} = 0.785 \text{ g/ml}$$

$$LHV_{fuel} = 43.2 \text{ MJ/kg}$$

Determination of molecular percentages from mass percentages assuming a 100 g fuel sample:

Carbon	85.72 g	7.13697 moles
Hydrogen	13.91 g	13.8004 moles

From the above the molar hydrogen-to-carbon ratio can be determined.

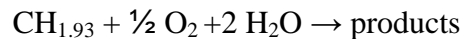
$$H/C = 1.93$$

A representative fuel ($CH_{1.93}$) can be and fuel composition can be developed from the above.

$$MW_{CH_{1.93}} = MW_C + \left(\frac{H}{C}\right)_{fuel} MW_H$$

$$MW_{CH_{1.93}} = 12.0107 + 1.93(1.00794) = 13.956 \text{ g/mole}$$

A representative reactant equation with $O/C = 1.0$ and $S/C = 2.0$ is shown below:



For a given reactor rating the mass flow rate of fuel can be determined. Assume a reactor rating of 3.33 kW_{th}.

¹ Jet fuels and diesel fuels primarily consist of hydrogen and carbon; however, other materials such as particulate matter and non-volatile materials exist in small quantities (for JP-8 required to be less than 1 vol% of fuel). Many of these materials are removed through fuel filtration prior to use of the fuel in engines or other combustion applications.

$$\dot{m}_{\text{fuel}} = \frac{3.33 \text{ kWth}}{43.2 \text{ MJ/kg}} = 4.629 \text{ g/min.}$$

$$\dot{n}_{\text{fuel}} = \frac{4.629 \text{ g/min.}}{13.956 \text{ g/mole}} = 0.3317 \text{ moles/min.}$$

Since, based on our representative fuel definition the fuel carbon atom flow is equivalent to the molar flow rate of fuel:

$$\dot{n}_{\text{Carbon in fuel}} = 0.3317 \text{ moles/min.}$$

We now have the fuel carbon atom flow rate and from this the flow rates of oxygen and steam can be determined from the given O/C ratio and S/C ratio.

Appendix D

Gas Chromatograph Calibration Properties

D.1 Gas chromatography development [1,2]

Gas chromatographs (GC) are a key analytical chemistry instrument for most modern chemistry labs. GC's operate by separating compounds and quantifying each separated compound. The underlying science that led to the development of the modern GC occurred in the 1950's and 1960's. The work of James and Martin [3] with the National Institute for Medical Research, UK is often cited as the first published work describing gas chromatography. Martin (Archer John Porter Martin) had earlier in 1941 developed liquid phased chromatography for which he won the 1952 Nobel Prize. Early gas chromatography work employed packed bed columns which were very slow in response often requiring hours to analyze a gas sample. In the 1980's, fused silica capillary column manufacturing techniques and experimentation with various liquid phase material coated on the walls of the column resulted in a significant improvements in GC analysis and reduced analysis time by an order of magnitude. Research and development in gas chromatography continues today with the goal of faster analysis times, use of new detector types including combination of detectors, and in broadening the types of chemical compounds that can be successfully analyzed.

D.2 Principles of operation

Gas chromatographs consist of five primary components: sample introduction apparatus, carrier gas, capillary column, oven or column heating apparatus, and the detector. In addition, computer interfaces are used today to store instrument setting and calibration tables, control GC components, conduct post processing of data, and produce reports.

The sample introduction apparatus can consist of a syringe/vaporizer for injecting liquid samples or as is employed in this thesis a gas sampling system that assure the sample gas is introduced at a constant pressure. The carrier gas is a high purity, usually inert gas, that is used to move the gas sample through the column and to move the eluted gas (absorbed sample leaving the absorbent) to the detector. Capillary columns are small diameter tubes into which the carrier gas and gas sample enter. The inside wall of the column is coated with a microscopic layer of material (usually a liquid or polymer material) that selectively absorbs and desorbs the sample gas. The selection of the column and absorbent material (also known as the stationary phase) is a function of the chemical compounds expected in the gas sample. The stationary phase selectively adsorbs and desorbs individual chemical compounds at different times known as the retention time. An oven or column heater is used to adjust the absorption/desorption process and provide separation between different compounds as they desorb (or elute). The detector provide a means to quantify the amount of a compound present that can through calibration tables determine the concentration of each calibrated compound.

D.3 Gas chromatograph calibration

With the proper selection of capillary columns, carrier gases and operating parameters chemical compounds can be separated and identified. Identification requires some prior knowledge of the general composition of the sample gas and order of elution of compounds. Figure D.1 (a) shows a typical result from a single column. Peak retention times are shown and each peak has good separation (necessary for quantification). Figure D.1 (b) shows the identification of each peak with its associated chemical compound. Once the GC peaks are identified, calibration gases can be used to quantify the amount of measured gas in the sample. For every compound measured at least a single calibration point is needed to interpolate a value. Calibration gases should span the anticipated range of concentrations for the compound being measured and extrapolation of values outside the calibration range should be avoided. For the experimental work in this thesis two point calibration gases were used as shown in Table D.1.

D.4 Gas chromatograph method

A gas chromatograph method is a pre-established set of all instrument set points for a particular analytical purpose. For the experimental work in this thesis a single method was established and the instrument parameters are shown in Table D.2.

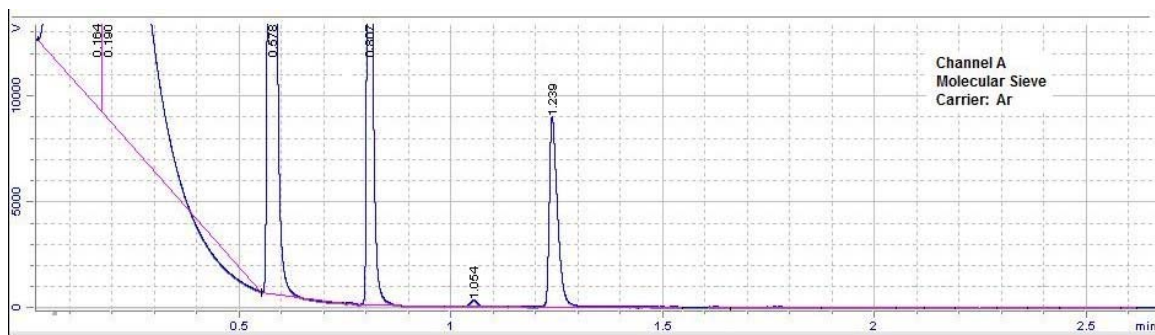
Table D.1 Calibration Gases for the Four Channel Micro Gas Chromatograph (Agilent 3000A)

		Compound	Calibration Gas 1		Calibration Gas 2	
Channel			Concentration	units	Concentration	units
1	A	Hydrogen	49.354	%	24.5271	%
2	A	Nitrogen	20.762	%	49.154	%
3	A	Methane	4.993	%	0.2965	%
4	A	CO	2.066	%	23.7396	%
5	B	CO2	18.219	%	0.9911	%
6	B	Ethylene	3.052	%	0.0991	%
7	B	Ethane	1.522	%	0.0792	%
8	B	Acetylene	10	ppm	570	ppm
9	C	Propane	30	ppm	987	ppm
10	C	Propylene	21	ppm	798	ppm
11	C	n-butane	20	ppm	775	ppm
12	C	t-2 butene	13	ppm	594	ppm
13	C	isobutylene	30	ppm	898	ppm
14	C	1-butene	21	ppm	695	ppm
15	C	c-2-butene	8	ppm	495	ppm
16	C	isopentane	31	ppm	999	ppm
17	C	n-pentane	20	ppm	801	ppm
18	C	pentenes		ppm		ppm
19	C	Cis-2-pentene	9	ppm	273	ppm
20	C	1-pentene	31	ppm	997	ppm
21	C	trans-2-pentene	22	ppm	720	ppm
22	C	2,3 dimethylpentane	10	ppm	97	ppm
19	D	isobutane	30	ppm	994	ppm
20	D	hexane plus		%		%
21	D	n-hexane	10	ppm	397	ppm
22	D	2-methyl-2-butene	0	ppm	8	ppm
23	D	2-methyl-1-butene	0	ppm	4	ppm
24	D	3-methylpentane	0	ppm	13	ppm
25	D	methylcyclopentane	0	ppm	17	ppm
26	D	2,2, dimethylpropane	0	ppm	3	ppm
		Total	100.000		100.000	

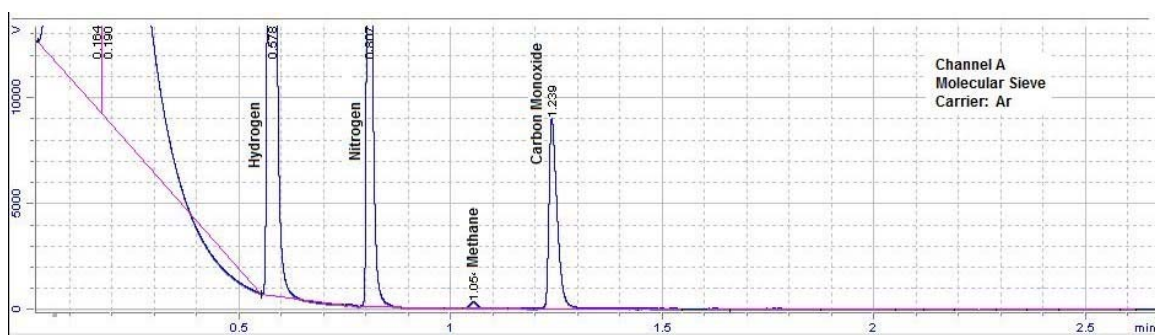
Table D.2 Method ATR1pt

Operating Parameters	A	B	C	D
Sample Inlet Temperature (°C)	80	80	80	80
Injector Temperature (°C)	80	80	80	80
Column Temperature (°C)	100	75	145	90
Sampling Times (s)	20	20	20	20
Injection Time (ms)	0	50	50	40
Run Time (s)	160	120	185	160
Post Run Time (s)	0	0	0	0
Pressure Equilibrium Time (s)	0	0	0	0
Column Pressure (psig)	32.00	32.00	32	30
Post Run Pressure (psig)	32.00	32.00	32	30
Detector Filament	Enabled	Enabled	Enabled	Enabled
Detector Sensitivity	Standard	High	High	High
Detector Data Rate (Hz)	50	50	50	50
Baseline Offset (mV)	0	0	0	0
Backflush Time (s)	10.0	8.0	5.0	n/a
3000 GC Configuration				
Injector Type	Backflush	Backflush	Backflush	Fixed Volume
Carrier Gas	Argon	Helium	Helium	Helium
Column Type	Molecular Sieve	Plot U	Alumina	OV-1
Detector	TCD*	TCD*	TCD*	TCD*
Inlet Type	Heated	Heated	Heated	Heated

* Thermal Conductivity Detector



(a)



(b)

Figure D.1 Channel A column from Micro GC 3000A showing retention times (a) and identified chemical compounds (b).

D.5 Reference

- 1 Fowles IA. Gas Chromatography, Second Edition. Analytical Chemistry by Open Learning, John Wiley & Sons, 1995.
- 2 Clemons JM, Thomas TJ. Fast Process Gas Chromatography. Analytical Products, Paper Sc7-42-400.
- 3 James AT, Martin AJP. Gas-liquid chromatography: the separation and micro-estimation of volatile fatty acids from formic acid to dodecanoic acid. *J. Biochem* 1952;50:679-90.

Bibliography

- 1 Conn, I., 2006, "Energy Trends and Technologies in the Coming Decades," Harvard University Center for the Environment, Cambridge, MA.
- 2 Vasquez, I., 2001, "Ending Mass Poverty," CATO Institute, <http://www.cato.org/research/articles/vas-0109.html>.
- 3 Global Carbon Project (GCP) – Global Carbon Budget Consortium, Carbon Budget 2008, May 11, 2010.
- 4 United Nations Human Development, Human Development Report 2009, Overcoming Barriers: Human mobility and development, Published for the United Nations Development Programme (UNDP)
- 5 Voeller, J.G., 2010, "The Era of Insufficient Plenty," *Mech Engr*, June.
- 6 Gates, W., 2010, "Energy: Innovating to Zero," Technology, Entertainment, Design (TED) 2010 Conference. http://www.ted.com/talks/lang/eng/bill_gates.html
- 7 Tully, S. R., 2005, "The Contribution of Human Rights to Universal Energy Access," Northwest University School of Law, Northwest Journal of International Human Rights, 4(3), pp. 518-548.
- 8 Bradbrook, A.J., Gardam, J.G., 2006, "Placing Access to Energy Services within a Human Rights Framework," *Human Right Quarterly*, 28(2), pp. 389-415.
- 9 International Energy Agency, 2009, *World Energy Outlook 2009*.
- 10 MacKay D.J.C., 2009, Sustainable Energy – without the hot air. UIT Cambridge Ltd.
- 11 Energy Information Administration. U.S. Carbon dioxide emissions from energy sources, 2008 flash estimates, May 2009.
- 12 Energy Information Agency, Annual Energy Review 2010, Report No. DOE/EIA-0383(2010), April 2010.
- 13 Smith, J., Bartley, G., 2000, "Stoichiometric operation of a Gas Engine Utilizing Synthesis Gas and EGR for NO_x Control," *ASME Journal of Engineering for Gas Turbines and Power* 122, pp.617-623.
- 14 Wilson, J.R., 2004, "Clean Diesels, Clean Diesel Fuel and Diesel Fuel Substitutes," Report to NextEnergy.
- 15 Energy Information Agency, Petroleum Products Consumption Information Sheet, www.eia.doe.gov, July 2005.
- 16 Stodolsky, F., Gaines, L., Vyas, A., 2000, "Analysis of Technology Options to Reduce the Fuel Consumption of Idling Trucks," Report ANL/EDS-43, Center for Transportation Research, Energy Systems Division, Argonne National Laboratory.

- 17 Filipi, Z., Louca, L., Stefanopoulou, A., Pukrushpan, J., Kittirungsi, B., Peng, H., 2004, "Fuel Cell APU for Silent Watch and Mild Electrification of a Medium Tactical Truck," *SAE paper 2004-01-1477*.
- 18 Zizelman, J., Shaffer, S., Mukerjee, S., 2002, "Solid Oxide Fuel Cell Auxiliary Power Unit – A Development Update," *SAE paper 2002-01-0411*, SAE 2002 World Congress, Detroit, Michigan.
- 19 Kokkolaras, M., Mourelatos, Z., Loucas, L., Filipi, Z., Delagrammatikas, G., Stephanopoulou, A., Papalambros, P., Assanis, D., 2005, "Design under Uncertainty and Assessment of Performance Reliability of a Dual-Use Medium Truck with Hydraulic-Hybrid Power Train and Fuel Cell Auxiliary Power Unit," *SAE paper 2005-01-1396*.
- 20 Lutsey, N., Brodrick, C., Sperling, D., Lipman, T., 2005, "Market Potential of Fuel Cell Auxiliary Power Units in Long-Haul Trucks," Transportation Research Board 2005 Annual Meeting.
- 21 Dobbs, H., Krause, T., Kumar, R., Krumpelt, M., *Proceedings of the 4th European Solid Oxide Fuel Cell Forum*, July 10-14, 2000, Lucerne, Switzerland, pp. 85-94.
- 22 Hirschenhofer, J., White, J., 2000, "Preliminary Assessment of Planar Solid Oxide Fuel Cells for Transportation Power Applications," Parsons Infrastructure and Technology.
- 23 Bromberg, L., Cohn, D.R., Rabinovich, A., Alexeev, J.B., Green, J.B., Domingo, N., Storey, J.M.E., Wagner, R.M., Armfield, J.S., 2007, "Experimental Evaluation of SI Engine Operation Supplemented by Hydrogen Rich Gas from a Compact Plasma Boosted Reformer," *SAE 2000-01-2206*.
- 24 Bromberg, L., Cohn, D.R., Rabinovich, A., 1999, "Aftertreatment of Diesel Vehicle Emissions Compact Plasmatron Fuel Converter-Catalyst Systems," Report PSFC/RR-00-1.
- 25 Crane, S., Khadiya, N. A., 2004, "Fast Start-up on-Board Fuel Reformer for NO_x Adsorber Regeneration and Desulfurization," 2004 Diesel Engine Emission Reduction (DEER) Conference.
- 26 Bromberg, L., Cohn, D.R., Heywood, J., Rabinovich, A., Hadidi, K., Alexeev, N., Samokhin, A., 2003, "Hydrogen Generation from Plasmatron Reformers and Use for Diesel Exhaust Aftertreatment," 2003 Diesel Engine Emission Reduction (DEER) Conference.
- 27 Kammen D.M., 2007, "Science and Policy for Dramatic Cuts in Carbon Emissions," National Academy of Sciences government-University-Industry Research Roundtable Meeting "global energy Policy Solutions II", Berkeley, CA.
- 28 Crowe, B.J., 1973, *Fuel Cells, A Survey*. National Aeronautics and Space Administration. NASA SP-5115.
- 29 Hoogers, G., 2003, *Fuel Cell Technology Handbook*. CRC Press.
- 30 Scott, J.H., 2006, "The Development of Fuel Cell Technology for Electric Power Generation: from NASA's Manned Space Program to the "Hydrogen Economy"," Proceeding of the *IEEE*, 94(1), pp. 1815-1825.
- 31 Taschek, W.G., 2008, "History of Fuel Cell R&D at Fort Belvoir, Virginia," *2008 Fuel Cell Seminar*, Phoenix, Arizona.

- 32 Acres, G.J.K., 2001, "Recent Advances in Fuel Cell Technology and Its Applications," *J. Power Sources* 100(1-2), pp. 60-66.
- 33 Appleby, A.J., McKetta, J.J., Cummingham, W.A., 1986, *Encyclopedia of Chemical Processing and Design*. Marcel Dekker: New York, NY, 24, pp 1-14.
- 34 McDonald, C.F., Rodgers, C., 2008, "Small Recuperated Ceramic Microturbines Demonstrator Concept," *Appl. Thermal Engr.*, 28, pp. 60-74.
- 35 Kalhammer, F.R., 2000, "Polymer Electrolytes and the Electric Vehicle," *Solid State Ionics*, 135, pp. 315 – 323.
- 36 Chalk, S.G., Miller, J.F., 2006, "Key Challenges and Recent Progress in Batteries, Fuel Cells, and Hydrogen Storage for Clean Energy Systems," *J. Power Sources*, 159(1), pp. 73-80.
- 37 Von Helmolt, R., Eberie, U., 2007, "Fuel Cell Vehicles: Status 2007," *J. Power Sources*, 165, pp. 833-843.
- 38 Shah, R.K., Desideri, U., Hsueh, K.L., Vikar, A.V., 2003, "Research Opportunities and Challenges in Fuel Cell Science and Engineering," 4th Baltic Heat Transfer Conference, Kaunas, Lithuania.
- 39 Wee, J.H., 2007, "Applications of Proton Exchange Membrane Fuel Cell Systems," *Renewable and Sustainable Energy Reviews* 11(8), pp. 1720-1738.
- 40 Cheekatamarla PK, Lane AM. Efficient bimetallic catalysts for hydrogen generation from diesel fuel. *Int. J. Hydrogen Energy*, 2005, 30,1277:1285.
- 41 Piwetz, M.M., Larsen, J.S., Christensen, T.S., 1996, "Hydrosulfurization and Pre-reforming of Logistic Fuels for Use in Fuel Cell Applications," *Fuel Cell Seminar Program and Abstracts*, Courtesy Associates, Inc.
- 42 Eastman, D., 1956, "Synthesis Gas by Partial Oxidation", *Ind. Eng Chem* 48(7), pp. 1118-1122.
- 43 Kurma, R., Ahmed, S., 1995, "Fuel Processing for Transportation Fuel Cell Systems," The First International Symposium on New Materials for Fuel Cell Systems, Montreal, Canada.
- 44 Rostrup-Nielsen J., 2001, "Conversion of Hydrocarbons and Alcohols for Fuel Cells," *Physical Chemistry Chemical Physics*, 3, pp. 283-288.
- 45 Hansen, J., 2004, "Fuels and Fuel Processing Options for Fuel Cells," 2004 Proceeding of The World Fuel Cell Conference, Lucerne, Switzerland.
- 46 Kumar, R., Ahmed, S., Krumpelt, M., 1996, "The Low-Temperature Partial Oxidation Reforming of Fuels for Transportation Fuel Cell Systems," *The 1996 Fuel Cell Seminar*, Kissimmee, Florida.
- 47 Froment, G.F., Bischoff, K.B., 1990, *Chemical Reactor Analysis and Design*. 2nd edition, Wiley Series in Chemical Engineering.

- 48 Holladay, J. , 2006, "Advanced Fuel Processing for Portable and Transportable Power," 6th Annual Logistics Fuel Processing Conference, Panama City, Florida.
- 49 Jensen, K., 2001, "Microreaction engineering – is small better," *Chemical Engineering Science* 56, pp. 293-303.
- 50 Shekawat, D., Berry, D., Gardner, T., 2004, "Diesel Fuel Reforming Kinetics," Office of Fossil Energy Fuel Cell Program, FY 2004 Annual Report.
- 51 Hsing, I., Srinivasan, R., Harold, M., Jensen, K., Schmidt, M., 2000, "Simulation of Micromachined Chemical Reactors for Heterogeneous Partial Oxidation Reactions," *Chem Eng Sci.*, 55, pp. 3-13.
- 52 Wegeng, R., Birmingham, J., Call, C., Drost, K., Friedrich, M., Kurath, D., Martin, P., TeGrotenhuis, W., Tonkovich, A., 1997, "Micro Chemical System Development Progress at the Pacific Northwest National Laboratory," First International Conference on Microreaction Technology, Frankfurt, Germany.
- 53 Hessel, V., de Croon, M., Guan, G., Kolb, G., Lowe, H., Rebrov, E., Schouten, J., Zapf, R., 2006, "Micro-channel Catalytic Layers for Fuel Processing – Prime Issues and Structuring Below the Micron Scale," Proceeding of the 2nd CONCORDE Conference on Nanostructured Catalysts, Seville, Spain.
- 54 Borup, R., Parkinson, W., Inbody, M., Guidry, D., Brosha, E., 2005, "Diesel Reforming for Solid Oxide Fuel Cell Auxiliary Power Units," Department of Energy, FY2005 Annual Report, pp. 156-161.
- 55 Rostrup-Nielsen, J., 1984, Catalytic Steam Refroming, reprinted from *Catalysis, Science and Technology*, 5, 1983, Springer-Verlag Berlin.
- 56 Whyatt, G., TeGrotenhuis, W., Geeting, J., Davis, J., Wegeng, R., Pederson, L. 2001, "Demonstration of Energy Efficient Steam Reforming in Microchannels for Automotive Fuel Processing," Proceeding of the fifth International Conference on Microreaction Technology, IMET.
- 57 Wegeng, R., Tegrotenhuis, W., Tonkovich, A., 1997, "In-Situ Propellant Production Based on Micro Chemical Systems," In Situ Resource Utilization (ISRU II), Technical Interchange Meeting, Lunar and Planetary Institute, Houston, Texas.
- 58 Wegeng, R., Birmingham, J., Call, C., Drost, K., Friedrich, M., Kurath, D., Martin, P., TeGrotenhuis, W., Tonkovich, A., 1997, "Micro Chemical System Development Progress at the Pacific Northwest National Laboratory", First International Conference on Microreaction Technology, Frankfurt, Germany.
- 59 Hsing, I., Srinivasan, R., Harold, M., Jensen, K., Schmidt, M., 2000, "Simulation of Micromachined Chemical Reactors for Heterogeneous Partial Oxidation Reactions," *Chem Eng Sci* , 55, pp. 3-13.
- 60 Palo, D., Holladay, J., Rozmiarek, R., Guzman-Leong, C., Wang, D., Hu, J., Chin, Y., Dagle, R., Baker, E., 2000, "Development of a Soldier-Portable Fuel Cell Power Systems, Part I: A Bread-board Methanol Fuel Processor," *J Power Sources*, 108, pp. 28-34.

- 61 Zalc, J.M., Loffler, D.G., 2002, "Fuel Processing for PEM Fuel Cells: Transport and Kinetic Issues of System Design," *J Power Sources* , 111, pp. 58-64.
- 62 Stodolsky, F., Gaines, L., Vyas, A., 2000, "Analysis of Technology Options to Reduce the Fuel Consumption of Idling Trucks," Report ANL/EDS-43, Center for Transportation Research, Energy Systems Division, Argonne National Laboratory.
- 63 Gellings, P.J., Bouwmeester, H.J.M., 1997, Dense Ceramic Membranes for Oxygen Separation, The CRC Handbook of Solid State Electrochemistry, CRC Press, Chapter 14, pp. 481-553.
- 64 Poola, R.B., 1998, Membrane-Based Air Composition Control for Light-Duty Diesel Vehicles: A Benefit and Cost Assessment, US Dept. of Energy Report under contract W-31-109-Eng-38.
- 65 Teraoka, Y., Nobunaga, T., Okamoto, K., Miura, N., Yamazoe, N., 1991, "Influence of Constituent Metal Cations in Substituted LaCoO₃ on Mixed Conductivity and Oxygen Permeability," *Solid State Ionics*, 48, pp. 207-212.
- 66 van den Berg, A.W.C., Arean, C.O., 2008, "Materials for Hydrogen Storage: Current Research Trends and Perspectives," *Chemical Communications, The Royal Society of Chemistry*, pp. 668-681.
- 67 Berry, G.D., Aceves, S.M., 1998, "Onboard Storage Alternatives for Hydrogen Vehicles," *Energy Fuels*, 12(1), pp. 49-55.
- 68 Ewald, R., 1996, "Requirements for Advanced Mobile Storage Systems," *Int J Hydrogen Energy*, 23(9), pp. 803-814.
- 69 Sarkar, A., Banerjee, R., 2005, "Net Energy Analysis of Hydrogen Storage Options," *Int J of Hydrogen Energy*, 30(8), pp. 867-877.
- 70 Takeichi, N., Senoh, H., Yokota, T., Tsuruta, H., Hamada, K., Takeshita, H.T., Tanaka, H., Kiyobayashi, T., Takano, T., Kuriyama, N., 2003, "Hybrid Hydrogen Storage Vessel, a Novel High-pressure Hydrogen Storage Vessel Combined with Hydrogen Storage Material," *Int J of Hydrogen Energy*, 28(10), 1121-29.
- 71 Rabinowitz, M., 2000, "Power Systems of the Future, Parts 1-3. *IEEE Power Engineering Review*, 20(1), pp. 5-16; 20(3), pp. 10-15; 20(5), pp. 21-24.
- 72 Bossel, U., Eliasson, B., Taylor, G., 2003, "The Future of the Hydrogen Economy: Bright or Bleak?," *2003 Fuel Cell Seminar*, Miami Beach, Florida.
- 73 Lawrence Livermore National Laboratory Project Report, FY2005 Annual Progress Report for DOE Hydrogen Program, November 2005, available at http://www.hydrogen.energy.gov/annual_progress05_storage.html.
- 74 Satyapal, S., Petrovic, J., Read, C., Thomas, G., Ordez, G., "The U.S. Department of Energy's National Hydrogen Storage Project: Progress Towards Meeting Hydrogen-Powered Vehicle Requirements," *Catalysis Today*, 120(3-4), pp. 246-256.
- 75 Schlappbach, L., Zuttel, A., 2001, "Hydrogen-Storage Materials for Mobile Applications," *Nature*, 414, pp. 353-358.

- 76 Ahluwalia, R.K., Peng, J.K., 2008, "Dynamics of Cryogenic Hydrogen Storage in Insulated Pressure Vessels for Automotive Applications," *Int J of Hydrogen Energy*, 33(17), pp. 4622-4633.
- 77 Dillion, A.C., Jones, K.M., Bekkedahl, T.A., Kiang, C.H., Bethune, D.S., Heben, M.J., 1997, "Storage of Hydrogen in Single-Walled Carbon Nanotubes," *Nature*, 386, pp. 377-79.
- 78 Mpourmpakis, G., Froudakis, G.E., Lithoxoos, G.P., Saminos, J., 2006, "SiC Nanotubes: A Novel Material for Hydrogen Storage," *Nano Lett.*, 6(8), pp. 1581-1583.
- 79 Dillion, A.C., Gilbert, K.E.H., Parilla, P.A., Alleman, J.L., 2002, "Hydrogen Storage in Carbon Single Wall Nanotubes," Proceedings of the 2002 U.S. DOE Hydrogen Program Review, NREL/CP-610-32405.
- 80 Vajo, J.J., Skeith, S.L., Mertens, F., 2005, "Reversible Storage of Hydrogen in Destabilized LiBH₄," *J. Phys. Chem B*, 109(9), pp. 3719-3722.
- 81 Bogdanovic, B., Schwickardi, M., 1997, "Ti-doped alkali metal aluminium as a potential novel reversible hydrogen storage material," *J. Alloy Compd.*, 253-254, 1-9.
- 82 Sakintuna, B., Lamari-Darkarkim, F., Hirscher, M., 2007, "Metal Hydride Materials for Solid Hydrogen Storage: A Review," *Int J Hydrogen Energy*, 32(9), pp. 1121-1140.
- 83 Schuth, G., Bogdanovic, B., Felderhoff, M., 2004, "Light Metal Hydrides and Complex Hydrides for Hydrogen Storage," *Chem. Commun.*, 20, pp. 2249-2258.
- 84 Luo, W., 2004, "(LiNH₂ - MgH₂): A Viable Hydrogen Storage System," *J Alloy Compd.*, 381(1-2), pp. 284-287.
- 85 Lu, J., Fang, Z.Z., Sohn, H.Y., 2006, "A New Li-Al-N-H System for Reversible Hydrogen Storage," *J Phys. Chem. B*, 110(29), pp. 14236-14239.
- 86 Pinkerton, F.E., Meisner, G.P., Meyer, M.S., Balogh, M.B., Kundrat, M.D., 2005, "Hydrogen Desorption Exceeding Ten Weight Percent from the New Quaternary Hydride Li₃BN₂H₈," *J Phys Chem B*, 109(1), pp. 6-8.
- 87 Ikeda, T., Mikami, Y., Haruki, T., 2007, "Mg-Promoted LiH-LiNH₂ Hydrogen Storage System Synthesized by Using the Mechanochemical Method," *J Phys. Chem. C.*, 111(23), pp. 8389-8396.
- 88 Schlesinger, H.I., Brown, H.C., Finholt, A.E., Gilbreath, J.R., Hoeksta, H.R., Hyde, E.K., 1953, "Sodium Borohydride, its Hydrolysis and its use as a Reducing Agent and in the Generation of Hydrogen," *J. Am. Chem. Soc.*, 72(1), pp. 215-219.
- 89 Brown, H.C., Brown, C.A., 1962, "New, Highly Active Metal Catalysts for the Hydrolysis of Borohydride," *J. Am. Chem. Soc.*, 84(1), pp. 1493-1494.
- 90 Kojima, Y., Suzuki, K., Fukumoto, K., Sasaki, M., Yamamoto, T., Kawai, Y., Hayashi, H., 2002, "Hydrogen Generation using Sodium Borohydride Solution and Metal Catalyst Coated on Metal Oxide," *Int J Hydrogen Energy*, 27(10), pp. 1029-1034.

- 91 Amendola, S.C., Sharp-Goldman, S.L., Janjua, M.S., Spencer, N.C., Kelly, M.T., Petillo, P.J., Binder, M., 2000, "A Safe, Portable, Hydrogen Gas Generator using Aqueous Borohydride Solution and Ru Catalyst," *Int J Hydrogen Energy*, 25(10), pp. 969-975.
- 92 Pinto, A.M.F.R., Falcao, D.S., Silva, R.A., Rangel, C.M., 2006, "Hydrogen Generation and Storage from Hydrolysis of Sodium Borohydride in Batch Reactors," *Int J Hydrogen Energy*, 31(10), pp. 1341-1347.
- 93 Wu, Y., Mohring, R.M., 2003, "Sodium Borohydride for Hydrogen Storage," Prepr. Pap.-Chem. Soc., Div. Fuel Chem., 48(2), p. 940.
- 94 Wu, Y., 2003, "Hydrogen Storage via Sodium Borohydride, Current Status, Barriers, and R&D Roadmap," Millenium Cell, Inc. presented at Global Climate and Energy Project (GCEP), Stanford University.
- 95 Pinkerton, F., Meyer, M., 2007, "Reversible Hydrogen Storage in the Lithium Borohydride-Calcium Hydride Coupled System," *Journal of Alloys and Compounds*, 464(1-2), pp. L1-L4.
- 96 Zuttel, A., Wenger, P., Rentsch, S., Sudan, P., Mauron, P., Emmengger, C., 2003, "LiBH₄ a New Hydrogen Storage Material," *J Power Sources*, 118(1-2), pp. 1-7.
- 97 Kong, V.C.Y., Foulkes, F.R., Kirk, D.W., Hinatsu, J.T., 1999, "Development of Hydrogen Storage for Fuel Cell Generators. I: Hydrogen Generation using Hydrolysis Hydrides," *Int J Hydrogen Energy*, 24(7), pp. 665-675.
- 98 Stephens, F.H., Pons, V., Baker, R.T., 2007, "Ammonia-Borane: The Hydrogen Source par Excellence?," *Dalton Transactions*, pp. 2613-2626.
- 99 Basu, S., Brockman, A., Gagare, P., Zheng, Y., Ramachandran, P.V., Delgass, W.N., Gore, J.P., 2009, "Chemical Kinetics of Ru-Catalyzed Ammonia Borane Hydrolysis," *J Power Sources*, 188(1), pp. 238-243.
- 100 Chandra, M., Xu, Q., 2007, "Room Temperature Hydrogen Generation from Aqueous Ammonia-Borane using Noble Metal Nano-Clusters as Highly Active Catalysts," *J Power Source*, 168(1), pp. 1235-142.
- 101 Yan, J.M., Zhang, X.B., Shioyama, H., Xu, Q., 2010, "Room Temperature Hydrolytic Dehydrogenation of Ammonia Borane Catalyzed by Co Nanoparticles," *J Power Sources*, 195(4), pp. 1091-1094.
- 102 Baitalow, F., Baumann, J., Wolf, G., Jaenicke-Roessler, K., Leitner, G., 2002, "Thermal Decomposition of B-N-H Compounds Investigated by using Combined Thermoanalytical Methods," *Thermochim. Acta*, 391(1-2), pp. 159-168.
- 103 Hausdorf, S., Baitalow, F., Wolf, G., Mertens, F.O.R.L., 2008, "A Procedure for the Regeneration of Ammonia Borane from BNH-Waste Products," *Int J Hydrogen Energy*, 33(2), pp. 608-614.
- 104 Neiner, D., Karkamka, A., Linehan, J.C., Arey, B., Autrey, T., Kauzlarich, S.M., 2008, "Promotion of Hydrogen Release from Ammonia Borane with Mechanically Activated Hexagonal Boron Nitride," *J. Phys. Chem. C*, 113(3), pp. 1098-1103.

- 105 Berzelius, J.J., 1836, "Quelques Idées sur une nouvelle force agissant dans les combinaisons des corps organiques," *Ann. Chim. Phys.*, 61, pp. 146-151.
- 106 Robertson, A.J.B., 1975, "The Early History of Catalysis," *Platinum Metals Rev.*, 19(2), pp. 64-69.
- 107 Davy, H., 1817, "Some New Experiments and Observations on the Combustion of Gaseous Mixtures, with an Account of a Method of Preserving a Continued Light in Mixtures of Inflammable Gases and Air without Flame," *Phil. Trans. Roy. Soc.*, 107, pp. 77-85.
- 108 Faraday, M., 1834, "Experimental Researches in Electricity. Sixth Series," *Phil. Trans. Roy. Soc.*, 124, pp. 55-76.
- 109 Hunt, L.B., 1958, "The Ammonia Oxidation Process for Nitric Acid Manufacture, Early Developments with Platinum Catalysts," *Platinum Metals Rev.*, 2(4), pp. 129-134.
- 110 Cook, E., 1926, "Peregrine Phillips, the inventor of the contact process for sulfuric acid," *Nature*, 117(2942), pp. 419-421.
- 111 *Nobel Lectures, Chemistry 1901-1921*, The Nobel Prize in Chemistry 1909, Wilhelm Ostwald, Elsevier Publishing Company, Amsterdam, 1966.
- 112 *Studies in Surface Science and Catalysts, Catalysis: An Integrated Approach*. Published by Elsevier Publishing Company, Amsterdam, 1999, 123, Edited by Averill, B.A., Moulijin, J.A., van Leeuwen, P.W.N.M., van Santen, R.A.
- 113 Johnson, S., 2008, *The Invention of Air*, Riverhead Books, New York, NY.
- 114 Dodge, J., 2008, "SMR Dominates Hydrogen Production, but there's many ways to make it," *Design News*, July.
- 115 Rostrup-Nielsen, J.R., 2002, "Syngas in Perspective," *Catalysis Today*, 71(3-4), pp. 243-247.
- 116 Nelson, W.L., 1958, *Petroleum Refinery Engineering*, 4th Edition. New York: McGraw-Hill Book Company.
- 117 Khor, C.S., 2007, "A Hybrid of Stochastic Programming Approaches for Decision-making in Petroleum Refinery Production-operations under Uncertainty," MSc Thesis, University of Waterloo, Canada.
- 118 Ritchey, S., McCollum, D., 2006, "Overview of the Interdependence of the Merchant Hydrogen and the Oil Refining Industries: A Potential Hydrogen Economy Springboard," Hydrogen Pathways Program Advisory Board Meeting, July.
- 119 Rampe, T., Heinzl, A., Vogel, B., 2000, "Hydrogen Generation from Biogenic and Fossil Fuels by Autothermal Reforming," *J Power Sources*, 86(1-2), pp. 636-541.
- 120 BCC Research, 2007, *Catalysts for Environmental and Energy Applications*. Report No. CHM020C, June.

- 121 Silvy, R.P., 2004, "Future Trends in the Refining Catalysts Market," *Appl. Catal. A: Gen.*, 261(2), pp. 247-252.
- 122 McCarthy, J.E., 2005, "Clean Air Act: A Summary of the Act and its Major Requirements," *CRS Report for Congress*, Order Code RL30853, May.
- 123 Feldman, B., 2004, "A Physicist's View of the Automobile Engine," *The Physics Teacher*, 42, pp. 543-547.
- 124 Bernstein, M., 2002, "Thomas Midgley and the Law of Unintended Consequences," *Invention & Technology*, 17(4), pp. 38-44.
- 125 Heck, R.M., Gulati, S., Farrauto, R.J., 2001, "The Application of Monoliths for Gas Phase Catalytic Reactions," *Chem Engr Journal*, 82(1-3), pp. 149-156.
- 126 Boger, T., Heibel, A., Sorensen, C.M., 2004, "Monolithic Catalysts for the Chemical Industry," *Ind. Eng. Chem Res.*, 43(16), pp. 4602-4611.
- 127 Cybulski, A., Moulijn, J.A., 1994, "Monoliths in Heterogeneous Catalysis," *Catal. Rev.-Sci. Eng.*, 36(2), pp. 179-270.
- 128 Voecks, G.E., 1998, Unconventional Utilization of Monolithic Catalysts for Gas-Phase Reactions. Structured Catalysts and Reactors; Cybulski, A., Moulijn, J.A., Eds.; Marcel Dekker: New York; Chapter 7, pp. 179-208.
- 129 Pereira, C., Wilkenhoener, S., Ahmed, S., Krumpelt, M., 2000, "Catalytic Reforming of Gasoline and Diesel Fuel," *American Institute of Chemical Engineering*, Spring.
- 130 Kreutz, T.G., Larson, E.D., Liu, G., Williams, R.H., 2008, "Fischer-Tropsch Fuels from Coal and Biomass," 25th Annual International Pittsburgh Coal Conference, Pittsburgh, Pennsylvania.
- 131 United Catalysts, Inc., Physical and thermodynamic properties of elements and compounds. Girdler Catalysts, Chemetron Division, Catalysts Division.
- 132 Pacheco, M., Sira, J., Kopasz, J., 2003, "Reaction Kinetics and Reactor Modeling for Fuel Processing of Liquid Hydrocarbons to Produce Hydrogen: Iso-octane Reforming," *Applied Catalysts A: Gen.*, 250(1), pp. 161-175.
- 133 Villegas, L., Guilhaume, N., Provendier, H., Daniel, C., Masset, F., Mirodatos, C., 2005, "A Combined Thermodynamic/Experimental Study for the Optimization of Hydrogen Production by Catalytic Reforming of Iso-octane," *Applied Catalyst*, 281(1-2), pp. 75-83.
- 134 Ersoz, A., Olgun, H., Ozdogan, S., Gungor, C., Akgun, F., Tiris, M., 2003, "Autothermal Reforming as a Hydrocarbon Fuel Processing Option for PEM Fuel Cell," *J Power Sources*, 118(1-2), pp. 384-392.
- 135 Oosthuizen, P., Hussain, S., Peppley, B., 2009, "A Numerical Study of the Performance of an Autothermal Reformer for use in a Fuel Cell Powered Auxiliary Power Unit for Trucks," *Chem Engr Trans*, 18, pp. 653-658.

- 136 Cheekatamarla, P.K., 2004, "Catalytic Autothermal Reforming of Diesel Fuel for Hydrogen Generation in Auxiliary Power Units," Ph.D. Dissertation, The University of Alabama, Chemical and Biological Engineering.
- 137 Dalle Nogare, D., Degenstein, N.J., Horn, R., Canu, L.D., Schmidt, L.D., 2008, "Modeling Spatially Resolved Profiles of Methane Partial Oxidation on a Rh Foam Catalysts with Detailed Chemistry," *J Catalysis*, 258(1), pp. 131-142.
- 138 Choi, J., Partridge, W., Maxey, C., Green, J., Fischer, G., Tan, E., Weissman, J., Kirwan, J., Hughes, D., 2006, "Spatially Resolved Species and Temperature Determination during Methane Partial Oxidation over Rh Catalysts," *AIChE National Meeting*, November.
- 139 Krumpelt, M., Krause, T.R., Carter, J.D., Kopasz, J.P., Ahmed, S., 2002, "Fuel Processing for Fuel Cell Systems in Transportation and Portable Power Applications," *Catalysts Today*, 77(1-2), pp. 3-16.
- 140 Ospinal-Jimenez, M., 2006, "Hydrogen production study using autothermal reforming of biodiesel and other hydrocarbons for fuel cell applications," M.S. thesis, University of Puerto Rico, Mayaguez Campus.
- 141 Zahedi, G., Yaghoobi, H., 2008, "Dynamic Modeling and Simulation of Heavy Paraffin Dehydrogenation Reactor for Selective Olefin Production in Linear Alkyl Benzene Production Plant," *Int. J. Chem. Bio. Engr.*, 1(3), pp. 114-119.
- 142 Bhasin, M.M., McCain, J.H., Vora, B.V., Imai, T., Pujado, P.R., 2001, "Dehydrogenation and Oxydehydrogenation of Paraffins to Olefins," *Appl Catalysis A: Gen*, 221(1-2), pp. 397-419.
- 143 Mundschau, M.V., Gribble, D.A., Henton, L.M., Jentzsch, N.R., Plassmeyer, P.N., 2010, "Reforming Diesel-Fuel Distillates with Membrane Reactors," *Asia-Pac. J. Chem. Eng.*, 5(1), pp. 160-168.
- 144 U.S. Department of Energy Hydrogen Program, Hydrogen Production, Fact Sheet, November 2008.
- 145 Haryanto, A., Fernando, S., Murali, N., Adhikari, S., 2005, "Current Status of Hydrogen Production Techniques by Steam Reforming of Ethanol: A Review," *Energy & Fuel*, 19(5), pp. 2098-2106.
- 146 Hoogers, G., 2003, *Fuel Cell Technology Handbook*. CRC Press.
- 147 Tonkovich, A.Y., Perry, S., Wang, Y., Qiu, D., LaPlante, T., Rogers, W.A., 2004, "Microchannel Process Technology for Compact Methane Steam Reforming," *Chem Engr Sci*, 59(22-23), pp. 4819-4824.
- 148 Thormann, J., Pfeifer, P., Schubert, K., Kunz, U., 2008, "Reforming of Diesel Fuel in a Micro Reactor for APU Systems," *Chem Engr J*, 135(1), pp. S74-S81.
- 149 Rostrup-Nielsen, J.R., 1984, *Catalytic Steam Reforming. Catalysis – Science and Technology*, Edited by John R. Anderson and Michel Boudart, Volume 5, Springer-Verlag, Berlin, Heidelberg.
- 150 Zheng, J., Strohm, J.J., Chunshan, S., 2008, "Steam Reforming of Liquid Hydrocarbon Fuels for Micro-Fuel Cells, Pre-reforming of Model Jet Fuels Over Supported Metal Catalysts," *Fuel Process Tech*, 89(4), pp. 440-448.

- 151 Farrauto, R., Hwang, S., Shore, L., Ruettinger, W., Lampert, J., Giroux, T., Liu, Y., Ilinich, O., 2003, "New Materials for Hydrocarbon Fuel Processing: Generating Hydrogen for the PEM Fuel Cell," *Annual Rev Mat'ls Res*, 33, pp. 1-27.
- 152 Armor, J.N., 1999, "The Multiple Roles of Catalysis in the Production of H₂" *Appl. Catal A: Gen.*, 176(2), pp. 159-176.
- 153 Ming, Q., Healey, T., Allen, L., Irving, P., 2002, "Steam Reforming of Hydrocarbon Fuels," *Catalysts Today*, 77(1-2), pp. 51-64.
- 154 Flytzani-Stephanopoulos, M., Voecks, G.E., 1983, "Autothermal Reforming of Aliphatic and Aromatic Hydrocarbon Liquids," *Int J Hydrogen Energy*, 8(7), pp. 539-548.
- 155 Hohn, K.L., Schmidt, L.D., 2001, "Partial Oxidation of Methane to Syngas at High Space Velocities over Rh-coated Spheres," *Appl Catalysis A: Gen.*, 211(1), pp. 53-68.
- 156 Krummenacher, J.J., West, K.N., Schmidt, L.D., 2003, "Catalytic Partial Oxidation of Higher Hydrocarbons at Millisecond Contact Times: Decane, Hexadecane, and Diesel Fuel," *J Catalysis*, 215(2), pp. 332-343.
- 157 Panuccio, G.J., Dreyer, B.J., Schmidt, L.D., 2007, "A Comparison of the Catalytic Partial Oxidation of C₁ to C₁₆ Normal Paraffins," *AIChE Journal*, 53(1), pp. 187-195.
- 158 Haynes, D.J., Campos, A., Berry, D.A., Shekhawat, D., Roy, A., Spivey, J.J., 2010, "Catalytic Partial Oxidation of a Diesel Surrogate Fuel using an Ru-substitute Pyrochlore." *Catalysis Today*, 155(1-2) pp. 84-91.
- 159 Shekhawat, D., Berry, D.A., Bardner, T.H., Spivey, J.J., 2006, "Catalytic Reforming of Liquid Hydrocarbon Fuels for Fuel Cell Applications," The Royal Society of Chemistry, *Catalysis*, 19, pp. 184-253.
- 160 Praharso, Adesina A.A., Trimm, D.L., Cant, N.W., 2004, "Kinetic Study of Iso-octane Steam Reforming over a Nickel-based Catalysts," *Chem. Eng. J.*, 99(2), pp. 131-136.
- 161 Pasel, J., Meibner, J., Pors, Z., Samsun, R.C., Peters, R., 2007, "Autothermal Reforming of Commercial Jet A-1 on a 5 kWe Scale." *Int J Hydrogen Energy*, 32(18), pp. 4847-4858.
- 162 Liu, D. J., Kaun, T. D., Liao, H. K., Ahmed, S., 2004, "Characterization of Kilowattscale Autothermal Reformer for Production of Hydrogen from Heavy Hydrocarbons," *Int J Hydrogen Energy*, 29(10), pp. 1035-1046.
- 163 Ahmed, S., Krumpelt, M., 2001, "Hydrogen from Hydrocarbon Fuels for Fuel Cells," *Int J Hydrogen Energy*, 26(4), pp. 291-301.
- 164 Ahmed, S., Pereira, C., Lee, S.H.D., Krumpelt, M., 2002, "Integrated Fuel Processor Development," SAE Paper 02FCC-161.
- 165 Lee, S.H.D., Pereira, C., Ahmed, S., Krumpelt, M., 2000, "Fuel Flexible Fuel Processor for Reforming Hydrocarbon-based Fuels," 2000 *AIChE Annual Meeting*, Los Angeles, California.

- 166 Kopasz, J.P., Wilkenhoener, R., Ahmed, S., Carter, J.D., Krumpelt, M., 1999, "Fuel-flexible Partial Oxidation Reforming of Hydrocarbons for Automotive Applications," *218th American Chemical Society National Meeting*, New Orleans, LA; also DOE Report ANL/CMT/CP-98970.
- 167 Lutz, A.E., Bradshaw, R.W., Bromberg, L., Rabinovich, A., 2004, "Thermodynamic Analysis of Hydrogen Production by Partial Oxidation Reforming," *Int J Hydrogen Energy*, 29(8), pp. 809-816.
- 168 Barrai, F., Castaldi, M.J., 2010, "Experimental Investigation of a JP8 Fuel Processor: Autothermal Reformer and CO-cleanup Train," *Ind Eng Chem Res*, 49(4), pp. 1577-1587.
- 169 Hartmann, L., Lucka, K., Koehne, H., 2003, "Mixture Preparation by Cool Flames for Diesel-Reforming Technologies," *J Power Source*, 118(1-2), pp. 286-297.
- 170 Turbine Fuel, Aviation, Kerosene Type, JP-8 (NATO F-34), NATO F-35, and JP-8+100 (NATO F-37); Detailed Specification, MIL-DTL-83133F, dated April 11, 2008.
- 171 Altin, O., Eser, S., 2001, "Analysis of Solid Deposits from Thermal Stressing of a JP-8 Fuel on Different Tube Surfaces in a Flow Reactor," *Ind Eng Chem Res*, 40(2), pp. 596-603.
- 172 Altin, O., Eser, S., 2000, "Characterization of Carbon Deposits from Jet Fuel on Inconel 600 and Inconel X Surfaces," *Ind Eng Chem Res*, 39(3), pp. 642-645.
- 173 Altin, O., Eser, S., 2001, "Analysis of Carbonaceous Deposits from Thermal Stressing of a JP-8 Fuel on Superalloy Foils in a Flow Reactor," *Ind Eng Chem Res*, 40(2), pp. 589-595.
- 174 Rubnick, L.R., Gul, O., Schobert, H.H., 2004, "The Effect of Chemical Composition of Coal-derived Jet Fuels on Carbon Deposits," *Prepr Pap.-Am. Soc Div Fuel Chem*, 49(2), pp. 220-772.
- 175 Chen, Y., Xu, H., Wang, Y., Jin, X., Xiong, G., 2006, "Hydrogen Production from Liquid Hydrocarbon Fuels for PEMFC Applications," *Fuel Process Technol*, 87(11), pp. 971-978.
- 176 Ming, Q., Lee, A., Harrison, J., Irving, P., 2005, "Engineering Aspects of Designing the Components in a Microchannel Fuel Processor. Chapter 14, Microreactor Technology and Process Intensification, Editors Wang T and Holladay J, American Chemical Society.
- 177 Szydlowski, D.F., Sederquist, R.A., 2000, Method and Apparatus for Injecting a Liquid Hydrocarbon Fuel into a Fuel Cell Power Plant Reformer. Patent Number 6,045,772.
- 178 Sarioglan, A., Olgun, H., Baranak, M., Ersoz, A., Atakul, H., Ozdogan, S., 2007, "The Effect of Heat Supply on Diesel Evaporation as the First Step of Hydrogen Production," *Int J Hydrogen Energy*, 32(14), pp. 2895-2901.
- 179 Lindstrom, B., Karlsson, J.A.J., Ekdunge, P., De Verdier, L., Haggendal, B., Dawody, J., Nilsson, M., Pettersson, L.J., 2009, "Diesel Fuel Reformer for Automotive Fuel Cell Applications," *Int J Hydrogen Energy*, 34(8), pp. 3367-3381.
- 180 Kang, I., Bae, J., Yoon, S., Yoo, Y., 2007, "Performance Improvement of Diesel Autothermal Reformer by Applying Ultrasonic Injector for Effective Fuel Delivery," *J Power Sources*, 172(2), pp. 845-852.

- 181 Personal conversation with Shabbir Ahmed, Electrochemical Technology Program, Chemical Technology Division, Argonne National Laboratory, September 15, 2005.
- 182 Boutin, O., Ferrer, M., Lede, J., 2002, "Flash Pyrolysis of Cellulose Pellets Submitted to a Concentrated Radiation: Experiments and Modeling," *Chem Eng Sci*, 57(1), pp. 15-25.
- 183 Salge, J.R., Dreyer, B.J., Dauenhauer, P.J., Schmidt, L.D., 2006, "Renewable Hydrogen from Nonvolatile Fuels by Reactive Flash Volatilization," *Science*, 314(5800), pp. 801-804.
- 184 Lenz, B., Aicher, T., 2005, "Catalytic Autothermal Reforming of Jet Fuel," *J Power Sources*, 149, pp. 44-52.
- 185 Campbell, T.J., Shaaban, A.H., Holcomb, F.H., Salavani, R., Binder, M.J., 2004, "JP-8 Catalytic Cracking for Compact Fuel Processors," *J Power Sources*, 129(1), pp. 81-89.
- 186 Barrai, F., Castaldi, M.J., 2010, "Experimental Investigation of a JP8 Fuel Processor: Autothermal Reformer and CO-cleanup Train," *Ind Eng Chem Res*, 49(4), pp. 1577-1587.
- 187 Liu, D.J., Krumpelt, M., Chien, H.T., Sheen, S.H., 2004, "Catalysts and Fuel Mixing for Diesel Reformer in Fuel Cell Auxiliary Power Unit," *Fuel Cell Seminar*, San Antonio, TX.
- 188 Kang, I., Bae, J., 2006, "Autothermal Reforming Study of Diesel for Fuel Cell Application," *J Power Sources*, 159(2), pp. 1283-1290.
- 189 Roychoudhury, S., Walsh, D., Chu, D., Kallio, E., 2006, "Performance of a Diesel, and JP-8 Logistic Fuel Processor," *J Power Sources*, 160(1), pp. 510-513.
- 190 Dreyer, B.J., Lee, I.C., Krummenacher, J.J., Schmidt, L.D., 2006, "Autothermal Steam Reforming of Higher Hydrocarbons: n-decane, n-hexadecane, and JP-8," *Appl Catal A: Gen.*, 307(2), pp. 184-194.
- 191 Navarro, R.M., Pena, M.A., Fierro, J.L.G., 2007, "Hydrogen Production reactions from Carbon Feedstocks: Fossil Fuels and Biomass," *Chem Rev*, 107(10), pp. 3952-3991.
- 192 Heck, R.M., Flanagan, P.; Englehard Corporation. U.S Patent 4,844,837, 1989, Catalytic Partial Oxidation Process.
- 193 Sud-Chime ATR Reforming Catalyst. http://www.sud-chemie.com/scmcms/web/page_en_6708.htm
- 194 Alfa Aesar, A Johnson Matthey Company brochure, Fuel Cells, Catalysts and Components.
- 195 Hansen, J.B., Rostrup-Nielsen, J., 2009, "Sulfur Poisoning on Ni Catalysts and Anodes. Chapter 65, Handbook of Fuel Cells – Fundamentals, Technology and Applications, edited by Yokokawa H and Gasteiger HA, John Wiley & Sons, Ltd.
- 196 Strohm, J.J., Zheng, J., Song, C., 2006, "Low-temperature Steam Reforming of Jet Fuel in the Absence and Presence of Sulfur over Rh and Rh-Ni Catalysts for Fuel Cells," *J Catal*, 238(2), pp. 309-320.
- 197 Luna, A.E.C., Iriarte, M.E., 2008, "Carbon Dioxide Reforming of Methane over a Metal Modified Ni-Al₂O₃ Catalyst," *Appl Catal*, 343(1-2), pp. 10-15.

- 198 Springman, S., Friedrich, G., Himmern, M., Sommer, M., Eigenberger, G., 2002, "Isothermal Kinetic Measurements for Hydrogen Production from Hydrocarbon Fuels using a Novel Kinetic Reactor Concept," *Appl Catal A: Gen*, 235(1-2), pp. 101-111.
- 199 Wang, Y., Wu, D., 2001, "The Experimental Research for Production of Hydrogen from n-octane through Partially Oxidizing and Steam Reforming Method," *Int J Hydrogen Energy*, 26(8), pp. 795-800.
- 200 Rostrup-Nielsen, J.R., Hansen, J.H.B., 1993, "CO₂-reforming of Methane over Transition Metals," *J Catal*, 144(1), pp. 38-49.
- 201 Krumpelt, M., Ahmed, S., Kumar, R., Doshi, R., 2000, "Partial Oxidation Catalysts," U.S. Patent 6,110,861.
- 202 Sheen, S.H., Chien, H.T., Liu, D.J., Krumpelt, M., 2005, "Engineering Issues in Catalytic Autothermal Diesel Fuel Reforming Process," *5th Annual Logistic Fuel Processing Conference*, Panama City Beach, Florida.
- 203 Krause, T., Mawdsley, J., Rossignol, C., Carter, J.D., Kopasz, J., Krumpelt, M., 2002, "Autothermal Reforming Catalysis," *Extended Abstracts – 2002 Fuel Cell Seminar*, Palm Springs, CA, pp. 571-574.
- 204 Liu, D.J., Krumpelt, M., 2005, "Activity and Structure of Perovskites as Diesel-reforming Catalysts for Solid Oxide Fuel Cell," *Int J Appl Ceramic Tech*, 2(4), pp. 301-307.
- 205 Mawdsley, J.R., Krause, T.R., 2008, "Rare Earth-first-row Transition Metal Perovskites as Catalysts for the Autothermal Reforming of Hydrocarbon Fuels to Generate Hydrogen," *Appl Catal A: Gen*, 334(1-2), pp. 311-320.
- 206 Erri, P., Dinka, P., Varma, A., 2006, "Novel Perovskite-based Catalysts for Autothermal JP-8 Fuel Reforming," *Chem Eng Sci*, 61(7), pp. 5328-5333.
- 207 Bartholomew, C.H., 2001, "Mechanisms of Catalyst Deactivation," *Appl Catal A: Gen*, 212(1-2), pp. 17-60.
- 208 Song, C.S., 2002, "Fuel Processing for Low-temperature and High-temperature Fuel Cells: Challenges, and Opportunities for Sustainable Development in the 21st Century," *Catal Today*, 77(1-2), pp. 17-49.
- 209 Mundschau, M.V., Gribble, D.A., Plassmeyer, P.N., Henton, L.M., Jentzsch, N.R., 2010, "Dry Catalytic Partial Oxidation of Diesel-fuel Distillates into Syngas," *Fuel*, 89(6), pp. 1202-1211.
- 210 Lobo, L.S., Trimm, D.L., 1973, "Carbon Formation from Light Hydrocarbons on Nickel," *J. Catal.*, 29(1), pp. 15-19.
- 211 Krause, T.R., Ahmed, S., Kumar, R., 2006, "Distributed Reforming of Diesel, JP-8, and other Heavy Hydrocarbon Fuels for Fuel Cell Applications: Challenges and Issues," FUECELL2006-97260, *The 4th International Conference on Fuel Cell Science, Engineering and Technology*, Irvine, CA.

- 212 Zheng, J., Song, C., 2003, "Reforming of Liquid Hydrocarbon Fuels for Micro Fuel Cells, Steam Reforming of Pre-reformate from Jet-fuel over Supported Metal Catalysts," *ACS Fuel Chemistry Division*, 48(1), pp. 378-380.
- 213 Adams, J.W., Cassarino, C., Lindstrom, J., Spangler, L., Binder, M.J., Holcomb, F.H., 2004, "Canola Oil Fuel Cell Demonstration. Volume 1 – Literature Review of Current Reformer Technologies," US Army Corps of Engineers, Engineer Research and Development Center, ERDC/CERL SR-04-24.
- 214 Coombe, H.S., 2007, "Oxygen-enriched Combustion of Hydrocarbon Fuels," PhD. Dissertation, The Catholic University of America.
- 215 Coombe, H.S., Nieh, S., 2007, "Polymer Membrane Air Separation Performance for Portable Oxygen Enriched Combustion Applications," *Energy Conversion and Management*, 48(5), pp. 1499-1505.
- 216 Li, N.N., Kulkarni, S.S., 200, Membrane Separations, *Access Science*, New York, NY, McGraw-Hill.
- 217 Thorogood, R.M., 191, "Developments in Air Separation," *Gas Separation & Purity*, 5(2), pp. 83-94.
- 218 Nemer, S.M., Roman, I.C., 1991, "Perfluorodioxide Membranes," U.S. Patent No. 5,051,114.
- 219 Nemser, S.M., Himmelreich, L., 2008, "Oxygen Enriched Air Supply Apparatus," U.S. Patent No. 6,126,721.
- 220 Rostrup-Nielsen, J.R., 2002, "Syngas in Perspective," *Catal. Today*, 71(3-4), pp. 243-247.
- 221 Appl, M., 1997, "The Haber-Bosch Heritage: The ammonia production technology," 50th Anniv. Of the IFA Technical Confr., Sevilla, Spain.
- 222 Rostrup-Nielsen, J.R., 1994, "Catalysis and Large-scale Conversion of Natural Gas," *Catal. Today*, 21(2-3), pp. 257-267.
- 223 Eltron Research & Development, Tech Brief, 2009, "Reformer for Conversion of Diesel Fuel into Synthesis Gas,"
http://www.eltronresearch.com/docs/Reformer_for_Converting_Diesel_Fuel_into_CO_and_Hydrogen.pdf
- 224 Czernichowski, A., Czernichowski, P., Czernichowski, M., Wesolowska, K., 2005, "Partial Oxidation of Fossil and Renewable Fuels into the Synthesis Gas," 17th Int. Symp. On Plasma Chemistry, Toronto, Canada.
- 225 Lambert, J., Sorin, M., Paris, J., 1997, "Analysis of Oxygen-Enriched Combustion for Steam Methane Reforming (SMR)," *Energy*, 22(8), pp. 817-825.
- 226 Personal conversation with Christian Junaedi, Research Engineer, Precision Combustion, Inc. September 2009.
- 227 Wegenr, R., Birmingham, J., Call, C., Drost, K., Friedrich, K., Kurath, M., Martin, K.D., TeGrotenhuis, W., Tonkovich, A., 1997, "Microchemical System Development Progress at the Pacific Northwest National Laboratory," *First International Conference on Microreaction Technology*, Frankfurt, Germany.

- 228 Salc, J.M., Loffler, D.G., 2002, "Fuel Processing of PEM Fuel Cells: Transport and Kinetic Issues of System Design," *J Power Sources*, 111(1), pp. 58-64.
- 229 Sheen, S., Chien, H., Liu, D., Krumpelt, M., 2005, "Engineering Issues in Catalytic Autothermal Diesel Fuel Reforming Process," *5th Annual Logistic Fuel Processing Conference*, Panama City Beach, Florida.
- 230 Kopaz, J., Applegate, D., Miller, L., Liao, H., Ahmed, S., 2005, "Unraveling the Maze: Understanding of Diesel Reforming through the use of Simplified Fuel Blends," *Int. J. Hydrogen Energy*, 30(11), pp. 1243-1250.
- 231 Krause, T., Kumar, R., 2006, "Distributed Reforming of Diesel, JP-8, and other Heavy Hydrocarbon Fuels for Fuel Cell Applications," *The 4th International Conference on Fuel Cell Science, Engineering and Technology*, Irvin, CA.
- 232 3M, InteramTM Catalytic converter Mat Products, Designer's Guide, Fourth Edition, 2003.
- 233 U.S. Army Research, Development and Engineering Command, U.S. Army Research, Development and Engineering Command Safety Program, RDECOM Regulation 385-10, dated 17 August 2010.
- 234 40 Code of Federal Regulation (CFR), Resource Conservation and Recovery Act (RCRA), Part 261 Identification and Listing of Hazardous Wastes.
- 235 40 Code of Federal Regulation (CFR), Resource Conservation and Recovery Act (RCRA), Part 262—Standards Applicable To Generators of Hazardous Waste.
- 236 Agilent 3000 Micro Gas Chromatograph, User Information, G2801-90117, 1ST Edition, April 2002, Agilent Technologies, Inc.
- 237 Faeber, E.A., Scoriah, R.L., 1948, "Heat Transfer to Water Boiling under Pressure," *Trans. ASME*, 70, pp. 369-384.
- 238 Forster, H.K., Zuber, N., 1959, "Growth of a Vapor Bubble in a Superheated Liquid," *J. Appl. Phys.*, 25(4), pp. 474-478.
- 239 Levy, S., 1959, "Generalized Correlation of Boiling Heat Transfer," *J. Heat Transfer, Trans. ASME*, 81, pp. 37-42.
- 240 Frass, A.P., Pzisk, M.N., 1965, Heat Exchanger Design, *Chapter 5 – Boiling Heat Transfer and Flow Stability*, John Wiley & Sons, Inc.
- 241 Babcock & Wilcox. Steam, Its Generation and Use. 39th Edition, 1978.
- 242 Wu, G., Qiu, S., Su, G., Jia, D., 2006, "Analysis of Flow Instabilities in Forced-convection Steam Generation," *Nuclear Science and Techniques*, 17(3), pp. 185-192.
- 243 Stookey, D., Majumdar, S., 2005, "Gas Permeance of High-flux, Commercial Membrane Elements," Compact Membrane Systems, Inc., North American Membrane Society, Annual Meeting, Providence, RI.

- 244 Prasad, R., Notaro, F., Thompson, D.R., 1994, "Evolution of Membranes in Commercial Air Separation," *J. Membrane Sci.*, 94(1), pp. 225-248.
- 245 Baker, R.W., 2002, "Future Directions of Membrane Gas Separation Technology," *Ind. Eng. Chem. Res.*, 41(6), pp. 1393-1411.
- 246 Coker, D.T., Freeman, B.D., Fleming, G.K., 1998, "Modeling Multi-component Gas Separation using Hollow Fiber Membrane Contactors," *AIChE J.*, 44(6), pp. 1289-1302.
- 247 Coombe, H.S., 2007, "Oxygen-enriched Combustion of Hydrocarbon Fuels," Ph.D thesis, The Catholic University of America.
- 248 Coombe, H.S., Nieh, S., 2007, "Polymer Membrane air Separation Performance for Portable Oxygen Enriched Combustion Applications," *J. Energy Conversion and Management*, 48(5), pp. 1499-1505.
- 249 Berry, D.A., Shekhawat, D., Gardner, T.H., 2003, "Development of Predictive Models for Diesel-based Fuel Processors," NETL Onsite Merit Review, Morgantown, West Virginia.
- 250 Penyazkov, O.G., Sevrouk, K.L., Tangirala, N.J., 2009, "Autoignition of Diesel Fuel/air Mixtures behind Reflected Shock Waves," Proceeding of the European Combustion Meeting 2009, Vienna.
- 251 Lindstrom, B., Karlsson, J.A.J., Ekdunge, P., De Verdier, L., Haggendal, B., Dawody, J., Nilsson, M., Pettersson, L.J., "Diesel Fuel Reformer for Automotive Fuel Cell Applications," *Int. J. Hydrogen Energy*, 34(8), pp. 3367-3381.
- 252 Dryer, F.L., 2006, "Chemical Kinetics in Support of Syngas Turbine Combustion," University Coal Research Contractors Review Meeting.
- 253 Laminie, J., Dicks, A., 2000, *Fuel Cell Systems Explained*. John Wiley & Sons, New York, NY.
- 254 Energy Information Agency, *Annual Energy Outlook 2009 (Early Release)*. Report #:DOE/EIA-0383(2009), December 2008.
- 255 Defense Energy Support Center, *Fact Book 2007*, thirteenth edition.
- 256 Department of Defense Directive, Number 4140.43, Fuel Standardization, March 11, 1988.
- 257 Department of Defense Directive, Number 4140.25, DoD Management Policy for Energy Commodities and Related Services, April 20, 1999.
- 258 Stucker, J.P., Schank, J.F., Dombey-Moore, B., 1995, "Assessment of DoD Fuel Standardization Policies," National Defense Research Institute, ISBN 0-8330-1546-X.
- 259 Military Specification MIL-T-83133D – Turbine Fuels, Aviation, Kerosene Types, NATO F-34 (JP-8), NATO F-35; January 29, 1992.
- 260 Exxon-Mobil Aviation, *World Jet fuel Specifications with Avgas Supplement*, 2008 Edition.

- 261 Defense Energy Support Center, Petroleum Quality Information System (PQIS), Annual Fuel Property Surveys, 2007.
- 262 Tsang, W., Hudgens, J., Allison, T.C., Burgess, D.R., Manion, J.A., Matheu, D., 2003, "Workshop on Combustion Simulation Databases for Real Transportation Fuels," Workshop Report, National Institute of Standards and Technology, Gaithersburg, MD.
- 263 Colket, M., Edwards, T.G., Williams, S., Cernansky, N.P., Miller, D.L., Egolfopoulos, F., *et al.*, 2007, "Development of an Experimental Database and Kinetic Models for Surrogate Jet Fuels," AIAA-2007-0770.
- 264 Wood, C.P., McDonell, V.G., Smith, R.A., Samuelson, G. S., 1989, "Development and Application of a Surrogate Distillate Fuel," *J Propul Power*, 5, pp. 399-405.
- 265 Edwards, T., Lourdes, M.Q., 2001, "Surrogate Mixtures to Represent Complex Aviation and Rocket Fuels," *J Propul Power*, 17, pp. 461-466.
- 266 Agosta, A., Cernansky, N.P., Miller, D.L., Faravelli, T., Ranzi, E., 2004, "Reference Components of Jet Fuel: Kinetic Modeling and Experimental Results," *Exp Therm Fluid Sci*, 23, pp. 701-708.
- 267 Violi, A., Yan, S., Eddings, E.G., Sarofim, A.F., 2002, "Experimental Formulation and Kinetic Model for JP-8 Surrogate Mixtures," *Combust Sci Tech*, 174, pp. 383-401.
- 268 Montgomery, C.J., Cannon, S.M., Mawid, M.A., Sekar, B., 2002, "Reduced Chemical Kinetic Mechanisms for JP-8 Combustion," AIAA 2002-0336.
- 269 Gokulakrishnan, P., Gaines, G., Currano, J., Klassen, M.S., Roby, R.J., 2007, "Experimental and Kinetic Modeling of Kerosene – type Fuels at Gas Turbine Operating Conditions," *J. Eng. Gas Turbines Power*, 129, pp. 655-664.
- 270 Irving, P., Allen, W.L., Ming, Q., Healey, T., 2001, "Novel Catalytic Fuel Reforming with Advanced Membrane Technology," Proceedings of the 2001 DOE Hydrogen Program Review.
- 271 Kataria, A., Abraham, M., 2005, "Understanding the Change in Reaction Pathways during Catalyst Deactivation in Diesel Fuel Steam Reforming," American Chemical Society, 2005 Annual Meeting.
- 272 Shekawat, D., Berry, D.A., Haynes, D.I., Spivey, J.J., 2009, "Fuel Constituent effects on Fuel Reforming Properties for Fuel Cell Applications," *Fuel*, 88, pp. 817-25.
- 273 Kaila, R.K., Krause, A.O.I., 2006, "Autothermal Reforming of Simulated Gasoline and Diesel Fuels," *Int J Hydrogen Energy* 31, pp. 1934-1941.
- 274 Gould, B.D., Tadd, A.R., Schwank, W., 2007, "Nickel-catalyzed Autothermal Reforming of Jet Fuel Surrogates: n-Dodecane, Tetralin, and their Mixture," *J Power Sourc*, 164, pp. 344-350.
- 275 Dinka, P., Mukasyan, A.S., 2007, "Perovskite Catalysts for the Auto-reforming of Sulfur Containing Fuels," *J Power Sourc*, 167, pp. 472-481.
- 276 Yonn, S., Kang, I., Bae, J., 2008, "Effects of Ethylene on Carbon Formation in Diesel Autothermal Reforming," *Int J Hydrogen Energy* 33, pp. 4780-4788.

- 277 Namazian, M., Sethuraman, S., Venkataraman, G., 2004, "Fuel Preprocessor (FPP) for a Solid Oxide Fuel Cell Auxiliary Power Units," Final Report, DOE Grant DE-FG36-02GO12058.
- 278 Huang, X., King, D.A., Zheng, F., Stenkamp, V.S., TeGrotenhuis, W.E., Roberts, B.Q., *et al.*, 2008, "Hydrodesulfurization of JP-8 and its Microchannel Distillate using Steam Reformate," *Catal Today*, 136, pp. 291-300.
- 279 Sandelli, G.J., Fokema, M., 2008, "Advancements in Military Logistic Fuel Processing," *2008 Fuel Cell Seminar & Exposition*, pp. 306-308.
- 280 Christensen, T.S., Primdahl, I.I., 1994, "Improve Syngas Production using Autothermal Reforming," *Hydrocarb Process*, 73, pp. 39-46.
- 281 DuBois, T.G., Nieh, S., 2008, "Design and Performance of an Experimental 3 kW_{th} Autothermal Reformer Test Bed for Heavy Hydrocarbon Fuels," *43rd Power Sources Conference*, pp. 133-136.
- 282 Horn, R., Williams, K.A., Degenstein, N.J., Schmidt, L.D., 2006, "Syngas by Catalytic Partial Oxidation of Methane on Rhodium: Mechanistic Conclusions from Spatially Resolved Measurements and Numerical Simulations," *J Catal* 242, pp. 92-102.
- 283 Defense Energy Support Center, Petroleum Quality Information System, Annual Fuel Property Surveys, available at: <http://www.desc.dla.mil/DCM/DCMPage.asp?pageid=99>.
- 284 Violi, A., Yan, S., Eddings, E.G., Sarofin, A.F., Granata, S., Faravelli, T., Ranzi, E., 2002, "Experimental Formulation and Kinetic Model for JP-8 Surrogates Mixtures," *2nd Mediterranean Combustion Symposium*, Sham El Sheik, Egypt.
- 285 Cernasky, N.P., Miller, D.L., 2006, "The Low Temperature Oxidation of JP-8 and its Surrogates at High Pressure," Army Research Office, Rpt. 44458.15-EG.
- 286 Humer, S., Frassoldati, A., Granata, S., Faravelli, T., Ranzi, E., Seiser, R., *et al.*, 2007, "Experimental and Kinetic Modeling Study of Combustion of JP-8, its Surrogates and Reference Components in Laminar Nonpremixed Flows," *Proceedings of the Comb Inst.* 31, pp. 393-400.
- 287 Rostrup-Nielsen, J.R., Christensen, T.S., Dybkjaer, I., 1998, "Steam Reforming of Liquid Hydrocarbons," *Stud Surf Sci Catal* 113, pp. 81-95.
- 288 Subramanian, R., Panuccio, G.J., Krummenacher, J.J., Lee, I.C., Schmidt, L.D., 2004, "Catalytic Partial Oxidation of Higher Hydrocarbons: Reactivities and Selectivities of Mixtures," *Chem Eng Sci*, 59, pp. 5501-5507.
- 289 Wang, X., Gorte, R.J., 2002, "A Study of Steam Reforming of Hydrocarbon Fuels on Pd/ceria," *Appl Catal Gen* 224, pp. 209-218.
- 290 Erri, P., Dinka, P., Varma, A., 2006, "Novel Perovskite-based Catalysts for Autothermal JP-8 Fuel Reforming," *Chem. Eng. Sci.* 61(16), pp. 5328-5333.
- 291 Barrai, F., Castaldi, M.J., 2010, "Experimental Investigation of a JP8 Fuel Processor: Autothermal Reformer and CO-cleanup Train," *Ind. Eng. Chem. Res.* 49(4), pp. 1577-1587.

- 292 Borup, R.L., Parkinson, W.J., Inbody, M.A., Brosha, E.L., Guidry, D., 2005, "Diesel Reforming for Fuel Cell Auxiliary Power Units," SECA Core Technology Program Review, Tampa, Florida.
- 293 Hohn, K.L., DuBois, T., 2008, "Simulation of a Fuel Reforming System Based on Catalytic Partial Oxidation," *J. Power Sources* 183(1), pp. 295-302.
- 294 Borup, R.L., Inbody, M.A., Semeisberger, T.A., Tafoya, J.I., Guidry, D.R., 2005, "Fuel Composition Effects on Transportation Fuel Cell Reforming," *Catalysis Today*, 99(3-4), pp. 263-270.
- 295 Kim, J.H., Seo, J.M., Sung, H.G., Rhyu, S.H., 2007, "Development of Blower for Air Management Systems of Fuel Cell Modules," *World Academy of Science, Eng. Tech.*, 28, pp. 212-216.
- 296 Clark, T., Arner, M., 2003, "Motor Blower Technologies for Fuel Cell Automotive Power Systems," DOE Merit Review, Hydrogen, Fuel Cells, and Infrastructure Technologies, Progress Report.
- 297 Agrawal, G., 2009, "Advances in Fuel Cell Blowers," *10th Annual SECA Workshop*, Pittsburg, PA.
- 298 Padulles, J., Ault, G.W., McDonald, J.R., 2000, "An Integrated SOFC Plant Dynamic Model for Power Systems Simulation," *J. Power Sources*, 86(1-2), pp. 495-500.
- 299 Dokiya, M., 2002, "SOFC System and Technology," *Solid State Ionics*, 152-153, pp. 383-392.
- 300 Brodrick, C.J., Lipman, T.E., Farshchi, M., Lutsey, N.P., Dwyer, H.A., Sperling, D., Gouse, S.W., Harris, D.B., King, F.G., 2002, "Evaluation of Fuel Cell Auxiliary Power Units for Heavy-Duty Diesel Trucks," *Transportation Res. Part D*, 7, pp. 303-315.
- 301 Gardner, F.J., Day, M.J., Brandon, N.P., Pashley, M.N., Cassidy, M., 2000, "SOFC Technology Development at Rolls-Royce," *J. Power Sources*, 86(1-2), pp. 122-129.
- 302 Stambouli, A.B., Traversa, E., 2002, "Solid Oxide Fuel Cells (SOFCs): A Review of an Environmentally Clean and Efficient Source of Energy," *Renewable and Sustainable Energy Reviews*, 6(5), pp. 433-455.
- 303 Khaleel, M., Sun X., Koepfel, B.J., Nguyen, B.N., Lu, N., 2005, "Modeling and Control of an SOFC APU," *DOE Hydrogen Program, FY 2005 Progress Report*.
- 304 DOE Report. The Impact of Future Diesel Fuel Specifications and Engine Emissions Standards on SOFC. June 29, 2004.
- 305 Hart, D., Hormandinger, G., 1998, "Environmental Benefits of Transport and Stationary Fuel Cells," *J. Power Sources*, 71(1-2), pp. 348-353.
- 306 Program Manager for Mobile Electric Power, 2 kW Military Tactical Generator (MTG) Technical Data, <https://www.pm-mep.army.mil/>.